Sergey P. Kuznetsov

# Hyperbolic Chaos

## A Physicist's View

高等教育出版社
HIGHER EDUCATION PRESS

Springer

Sergey P. Kuznetsov

# Hyperbolic Chaos

## A Physicist's View

*Author*

Sergey P. Kuznetsov
Kotel'nikov's Institute of Radio-Engineering and
Electronics of RAS, Saratov Branch
410019, Zelenaya 38, Saratov, Russian Federation
Email: spkuz@rambler.ru

ISBN 978-7-04-031964-4
Higher Education Press, Beijing

ISBN 978-3-642-23665-5 e-ISBN 978-3-642-23666-2
Springer Heidelberg Dordrecht London New York

Library of Congress Control Number: 2011935039



Printed on acid-free paper

Springer is part of Springer Science+Business Media (www.springer.com)

Sergey P. Kuznetsov

# Hyperbolic Chaos

## A Physicist's View

With 214 figures

高等教育出版社
HIGHER EDUCATION PRESS

Springer

# Preface

One of intensively developing research directions is exploration of complex dynamics and chaos in nonlinear systems. We regard an object as a *dynamical system*, if its state at any given time may be obtained from the initial state according to a certain rule defined for the given system. It is remarkable that such definition, although representing ideal of deterministic vision, does not exclude a possibility of *chaotic behavior* of the object, with dependence of the state on time looking like a random process. Chaos occurs in systems of different nature, e.g. relating to mechanics, hydrodynamics, electronics, laser physics and nonlinear optics, chemical kinetics, and biomedical disciplines. The main attribute of the dynamical chaos is *sensitivity to small perturbations of initial conditions*, which makes it impossible to predict the future states actually for times longer than some characteristic scale, which usually depends logarithmically on the inaccuracy of the initial conditions ("horizon of predictability").

For dissipative dynamical systems, chaos is associated with presence in the state space of a curious object called *the strange attractor*. At present, the collection of models with strange attractors is very rich, including artificial mathematical examples, models of physical, chemical, and biological systems.

A classic example of chaotic attractor is *Lorenz attractor*. It occurs in a set of three first-order differential equations modeling fluid convection or dynamics of a single-mode laser. The Lorenz model was a subject of extensive and careful studies in recent decades. Accurate mathematical foundation of chaotic nature of dynamics of the Lorenz model was found to be a subtle and delicate problem. It was announced as the 14-th Smale problem (from the list of difficult mathematical problems suggested by Steven Smale in 1998, as challenging mathematicians of the 21st century, similar to the list of Hilbert problems advanced for the 20th century). The solution was given by W. Tucker in 2002 by combination of technique of computer-assisted proof and careful analytic considerations.

Maybe, there was a lost opportunity for the nonlinear science to find out an alternative, a less painful way to discover physically meaningful and mathematically validated examples of chaotic behavior.

About 40 years ago, in mathematical studies a special type of chaotic attractors was introduced, namely, the *uniformly hyperbolic attractors*. They relate to systems belonging to the so-called *axiom A class* and are considered in the *hyperbolic theory* associated with the names of Anosov, Alekseev, Smale, Williams, Sinai, Plykin, Ruelle, Pesin, Newhouse and others. Chaotic nature of dynamics on the uniformly hyperbolic attractors is proved rigorously. They possess a property of *structural stability*, i.e., the phase space arrangement, character of dynamics, and its statistical characteristics are insensitive to variation of parameters and functions in the governing equations.

Originally, it was expected that the uniformly hyperbolic attractors will be relevant to many physical situations of occurrence of dynamical chaos. However, as time passed and many examples of chaotic systems of different nature had been suggested and studied, it became clear that these examples do not fit the narrow frames of the early hyperbolic theory. Therefore, people started to think of the uniformly hyperbolic attractors rather as of refined abstract image of chaos that has no relation to real systems. Efforts of mathematicians were redirected at developing generalizations applicable to broader classes of systems. For example, notions of singular-hyperbolic (or quasi-hyperbolic) attractors, non-uniformly hyperbolic attractors, partially hyperbolic attractors, and quasi-attractors were introduced, and certain progress in their exploration was achieved.

Abandoned for a long time and not clarified until recently is a question on a possibility of occurrence of the dynamical behavior associated with uniformly hyperbolic attractors in real world systems or, at least, in specially designed systems in physics and technology.

In textbooks on and reviews of nonlinear dynamics, the uniformly hyperbolic attractors are represented usually by artificial discrete time models based on geometric constructions, often explained qualitatively, in words, or by graphic images. Of course, for a physicist this is only a starting point for a research.

First of all, in addition to the geometric constructions it is desirable to have examples in a form of explicitly written equations, which allow application of computer methods for analyzing the dynamics and calculation of quantitative characteristics interesting to possible applications.

For some physical systems description in discrete time is very natural, and it would be worth examining possibilities of occurrence of the hyperbolic attractors in maps relating to such systems.

Next, it is important to turn to continuous time systems, which are of the first place importance, e.g., in physics and technology.

It is desirable to have a clear vision of how to implement the dynamics on uniformly hyperbolic attractors using combinations of structural elements known in the context of the theory of oscillations and in applications (oscillators, coupled systems, and feedback loops).

Finally, the proposed models should be implemented as real operating devices, for example, in electronics, mechanics, nonlinear optics, and technical applications of such devices should be indicated with explanation of advantages over alternative possible solutions.

In the theory of oscillations, since classic works of Andronov and his school, rough or structurally stable systems are regarded as those subjected to priority research, and as the most important for practice. It seems natural that the same should relate to systems with structurally stable uniformly hyperbolic attractors. The lack of physical examples in this regard looks as an evident dissonance. From a methodological point of view, the situation is similar to that in the early 20th century concerning the limit cycles, before their role as mathematical images for self-oscillations was established. In a similar way, the uniformly hyperbolic chaotic attractors should find their place as images for phenomena in real systems. It will help to link the abstract hyperbolic theory developed by mathematicians with description of real systems and attribute this theory to physical content.

This book is devoted to review the modern state of the outlined research program. The material is presented in four parts.

The introductory Part I consists of two chapters. Chapter 1 is devoted to the necessary basic concepts, including the notion of dynamical system, attractor, Poincaré map, and hyperbolicity. We introduce and discuss classic examples of uniformly hyperbolic attractors: Smale-Williams solenoid, DA-attractor of Smale, and attractors of Plykin type. An overview is given to the content of the hyperbolic theory (the cone criterion, structural stability, Markov partitions and symbolic dynamics, measures of Sinai-Ruelle-Bowen, etc.). Chapter 2 is a review of the literature indicating various possible situations of occurrence of uniformly hyperbolic attractors in dynamical systems.

Part II is the basic one. Here, we introduce a number of examples of systems, which allow physical implementation, and possess uniformly hyperbolic attractors with one-dimensional unstable manifolds (one positive Lyapunov exponent). In Chap. 3 we consider models, which admit a natural stroboscopic discrete time description. These are systems operating under periodic pulse kicks and systems whose dynamics is composed of a periodic sequence of stages, each of which is governed by a particular form of the differential equations. Chapter 4 discusses models designed on a base of two self-oscillators which are excited alternately because of forced external parameter modulation and transmit the excitation to each other in such way that its phase transforms in accordance with expanding circle map. Chapter 5 is devoted to autonomous systems operating according to the same principle. In Chap. 6 we consider schemes of parametric generators of chaos with hyperbolic attractors. Chapter 7 is devoted to methods of computer verification of the hyperbolic nature of attractors illustrated with the examples suggested in the previous chapters. Particularly, we consider technique of visualization of mutual location of stable and unstable manifolds, statistics of angles of intersections between them, visualization of the natural invariant measure distributions on the attractors, and verification of the cone criterion.

Part III is devoted to model systems, for which mathematical justification of the hyperbolic nature of the attractors is more problematic. Hypothetically, however, the hyperbolicity apparently takes place. This assertion is based on the fact that from a physical point of view, those models are built following the same principles as the systems considered in Chaps. 4 and 5, for which the hyperbolicity is justified at the level of computations. In Chap. 8 we consider non-autonomous systems of four alternately excited oscillators. Among them, there is a model, in which the transformation of phases during a period of parameter modulation follows the Anosov map on the torus, and a model associated with a map on the torus with hyperchaotic dynamics (more than one positive Lyapunov exponent). Also a system is considered constructed of two coupled elements, with each possessing a hyperbolic attractor. For this case, some details are studied for the transition corresponding to complete synchronization of chaos. In Chap. 9, an autonomous system is considered functioning due to dynamics nearby a heteroclinic cycle in the amplitude equations. On this basis, we implement an attractor of Smale-Williams type in the Poincaré map, an attractor with dynamics of cyclic (phase) variables governed by the Anosov map, and a hyperchaotic attractor. Chapter 10 is devoted to systems with delayed feedback, in which a chaotic map for the phases of successively generated oscillation trains is arranged due to the transfer of excitation from the previous stages of activity of a single oscillatory element (self-oscillator) to the next stages. In Chap. 11 we consider a high-dimensional system built on two ensembles of self-oscillators with global coupling within each of them. Due to the turning the coupling on and off alternately in two ensembles, they undergo periodic Kuramoto transitions from synchronization to desynchronization and back; the interaction between the ensembles is organized in such way that the phase of the oscillatory excitation for the mean field transferred to each other, follows the chaotic map.

Part IV is devoted to examples of hyperbolic (or hypothetically hyperbolic) attractors in electronic experiments available to date. In Chap. 12 we consider experiments with a non-autonomous system of two alternately excited self-oscillators manifesting dynamics on the attractor of Smale-Williams type. In Chap. 13 two variants of non-autonomous time-delay systems with periodic parameter modulation are discussed. One possesses presumably an attractor of Smale-Williams type, embedded in an infinite-dimensional state space of the respective stroboscopic Poincaré map, and the other corresponds to a partially hyperbolic attractor.

The Appendix address some matters, which are essential to the whole presentation and illustrations, but dropping out of the basic structure of the book. We consider algorithm for computing Lyapunov exponents based on the Gram-Schmidt orthogonalization, and derivation of the Hénon and Ikeda maps from physical considerations for systems with impulse kicks. Further, the construction of the Smale horseshoe is presented, which gives a nontrivial example of a non-attractive complicated invariant set. The Kaplan-Yorke formula is derived and explained connecting approximately the Lyapunov exponents and dimensions of chaotic attractors. Formal definition of the model of Hunt is reproduced, which implements suspension of attractor of Plykin type. A simple model of hyperbolic dynamics on a compact surface of negative curvature is considered. The final Appendix is devoted to the shadowing property of hyperbolic chaotic attractors, which is illustrated in computations for a model from Chap. 4 with added noise.

The book may be useful to physicists and engineers interested in the practical application of the theory of deterministic chaos, particularly in obtaining robust chaos insensitive to parameters and characteristics of components, fluctuations, interferences, etc. This may relate to various disciplines——mechanics, hydrodynamics, electronics, laser physics, and nonlinear optics.

Contents of the book can probably help to think about possibilities of occurrence of structurally stable chaos in systems of different physical nature. Intriguing area for contemplations may be the significance of such chaos in neurodynamics.

On the other hand, the book can be useful for mathematicians interested in concrete applications of the hyperbolic theory. For them, it may be of interest to see how the mathematical theories are refracted from the perspective of the applied disciplines.

The author tried to present the material in a style available to graduate and post graduate students of non-mathematical specialties and to make it, as far as possible, self-consistent to allow a study without recourse to other sources. I tried to avoid formal definitions and formulations with abusing mathematical symbolism, replacing them with rather intuitive qualitative arguments. Perhaps, a part of mathematically oriented readers will find it insufficient; they are referred to rich literature on mathematical theory of dynamical systems. Also, I must warn that the consideration of general content of nonlinear dynamics is restricted here by the minimum needed for understanding the substantive material of the book. So, it can not be regarded as a substitute for a systematic study of integral general courses of nonlinear dynamics, to which the interested reader is referred for this purpose.

I am grateful, for useful discussions, assistance, and constructive criticism, to V.S. Anishchenko, V.S. Afraimovich, B.P. Bezruchko, V.N. Belykh, A.Yu. Jalnine, A.Yu. Zhirov, O.B. Isaeva, A.P. Kuznetsov, P.V. Kuptsov, J. Kurths, A.Yu. Loskutov, R. MacKay, L.A. Mel’nikov, A. Pikovsky, V.I. Ponomarenko, A.G. Rozhnev, N.M. Ryskin, I.R. Sataev, E.P. Seleznev, W. Tucker, D.V. Treshchev, D.I. Trubetskov, L.V. Turukina.

Also, I thank all colleagues and administrative staff of Saratov Branch of Kotel’nikov’s Institute of Russian Academy of Sciences for many years of friendly collaboration, support, and creative atmosphere stimulating the scientific work.

The researches laying the foundation of this book were supported, in part, by RFBR grants 06-02-16619, 09-02-00426, 09-02-00707, and DFG-RFBR grants 04-02-04011, 08-02-91963. Additionally, the author acknowledges a support from program of Development of Scientific Potential of Higher Education of Ministry of Education of Ministry of Education and Science of Russian Federation (grant 2.1.1/1738).

*Sergey P. Kuznetsov*

Saratov, February 2011

# Contents

# Chapter 1
# Dynamical Systems and Hyperbolicity

**Abstract** In this chapter we review basic notions of the theory of dynamical systems essential for understanding subsequent chapters of the book. Particularly, a definition of the dynamical system is discussed and some important classes like continuous-time and discrete-time systems, conservative and dissipative systems, autonomous and non-autonomous systems are introduced. Interpretation of dynamics as evolution of a cloud of representative points in the state space is considered and implemented for explanation of chaos and, particularly, for the uniformly hyperbolic attractors, like Smale-Williams solenoid, DA attractor of Smale, and Plykin type attractors. Lyapunov exponents as a tool for quantitative approach to analyzing chaotic or regular dynamics are examined, and methodic of their computation is discussed. Main notions of the hyperbolic theory are considered, and its substational content is briefly reviewed.

## 1.1 Dynamical systems: basic notions

### *1.1.1 Systems with continuous and discrete time, and their mutual relation*

A finite-dimensional dynamical system is an object, for which one can specify a state by a collection of a finite number $N$ of real variables named a *state vector*, supposing that there exists a definite rule called the *evolution operator* that makes it possible to indicate precisely the state vector resulting from the initial one at any latter time instant (Birkhoff, 1927; Schuster and Just, 2005; Thompson and Stewart, 1986; Strogatz, 2001; Hasselblatt and Katok, 2003). A set of all possible states is a *phase space*, or *state space*; its dimension equals just the number of variables $N$ needed to specify the state vector. In other words, this is a space with coordinate axes, each of which is associated with one dynamical variable from the set of $N$ of them.

S. P. Kuznetsov, *Hyperbolic Chaos*

Both continuous-time and discrete-time systems are introduced and considered; in mathematical literature they are called *flows* and *cascades*, respectively.

Evolution of a state in time corresponds to motion of the representative point in the phase space along the *phase trajectory*, or *orbit.* A set in the phase space is called *invariant set* if all representative points from this set are transformed by the evolution operator again to the points belonging to the same set.

In order to describe continuous-time *autonomous* systems, one can use differential equations of the form

$$d\mathbf{x}/dt = \mathbf{F}(\mathbf{x}). \tag{1.1}$$

Here $\mathbf{x} = (x_1, x_2, \dots, x_N)$ is a state vector of dimension $N$, and $\mathbf{F} = (F_1(\mathbf{x}), F_2(\mathbf{x}), \dots, F_N(\mathbf{x}))$ is a vector function. In coordinate notation,

$$\begin{aligned} &dx_1/dt = F_1(x_1, x_2, \dots, x_N),\\ &dx_2/dt = F_2(x_1, x_2, \dots, x_N),\\ &\dots\dots\dots\dots\\ &dx_N/dt = F_N(x_1, x_2, \dots, x_N). \end{aligned} \tag{1.2}$$

By virtue of the theorem of existence and uniqueness of solutions for sets of differential equations (Arnold, 1978), with a given state at some instant $t_0$, one can determine states in the future $t > t_0$, as well as in the past $t < t_0$. In other words, the evolution of a state may be monitored both forward and backward in time.

If the right-hand side function $\mathbf{F}$ in the differential equation depends on time explicitly, the system is called *non-autonomous*. Physically, it corresponds to systems operating in the presence of external time-dependent forcing. To specify the state in this case, besides the vector $\mathbf{x}$ one needs to indicate the time instant it relates to. Therefore, we introduce the space of dimension $N$+1 with an additional coordinate axis $t$, which in this context is called the *extended phase space*. In this book, referring to non-autonomous systems, we will consider only the class of systems with the functions periodic in time: $\mathbf{F}(\mathbf{x}, t + T) = \mathbf{F}(\mathbf{x}, t)$.

Discrete time systems are described by evolution rules defined by *iterated maps*, which correspond to transformation of the states step by step,

$$\mathbf{x}_{n+1} = \mathbf{g}(\mathbf{x}_n). \tag{1.3}$$

Here $\mathbf{x}$ is a state vector, and $\mathbf{g}$ is a vector function specifying the evolution operator. In this case, a phase trajectory is a discrete sequence of points in the phase space. Evolution that takes place for $k$ steps corresponds to $k$-fold iteration of the map; it is designated as

$$\mathbf{x}_{n+k} = \mathbf{g}^k(\mathbf{x}_n) \equiv \underbrace{\mathbf{g}(\mathbf{g}(\cdots\mathbf{g}}_{k\text{ times}}(\mathbf{x}_n)\cdots)) \equiv \underbrace{\mathbf{g}\circ\mathbf{g}\circ\cdots\circ\mathbf{g}}_{k\text{ times}}(\mathbf{x}_n). \tag{1.4}$$

Continuous time systems and discrete time systems are closely related. Procedure of passage from one to another is known as the *Poincaré section* construction. In phase space of a continuous time system one selects some fixed surface in such a way that the phase trajectories cross it again and again in the course of the time evolution (Fig. 1.1(a)). Then we introduce a function **g**, which maps a point on the cross-section to another point at the next cross of the same surface by the trajectory emitting from the initial point. This function determines the *Poincaré map*, or *return map*. If the coefficients in differential equations have smooth dependence on the dynamical variables, then the Poincaré map is a *diffeomorphism*, a continuously differentiable function, having a uniquely defined inverse function, which is continuously differentiable too.

For non-autonomous systems with periodic functions of time in the right-hand part of the differential equations, a standard method of constructing the Poincaré map corresponds to *stroboscopic description*: the dynamics is monitored at discrete time instants with the period $T$. It means selection of the cross-section in the extended phase space with a family of planes $t{=}nT$, and the mapping is performed from one plane to the next one (Fig. 1.1(b)). All these planes may be regarded as identified because of the assumed time periodicity of the function **F**.

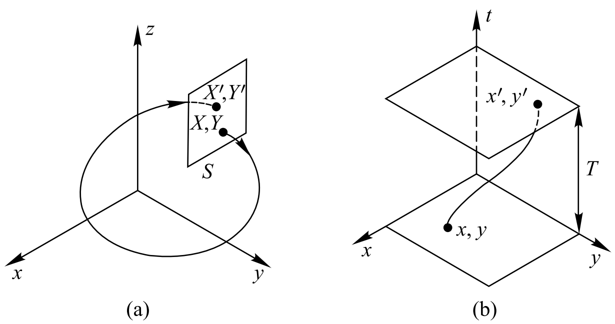


**Fig. 1.1** Poincaré map construction for 3-dimensional autonomous system **(a)** and for a non-autonomous system with 3-dimensional extended phase space **(b)**.

It is rather a rare case when the Poincaré map may be derived in explicit form; alternatively, one can construct it as a numerical algorithm.

For periodically non-autonomous systems the procedure is easy: we simply select a constant step of the finite-difference integration in such a way that the period of variation of coefficients in the differential equations contains an integer number of these steps. Starting with some initial state, after this number of steps we get the state corresponding to the result of the transformation of the original state under the stroboscopic Poincaré map.

For the case of autonomous dynamics, one has to define the preliminary Poincaré section by some equation, say $S(x_1,x_2,\ldots,x_N)=0$. Starting from initial state, which satisfies this condition, we should perform the integration till this condition will be valid again. Practically, of course, it will happen somewhere between the consecutive integration steps; here we have to stop and apply some interpolation procedure. An elegant recipe to do this in perfect consistency in accuracy with the finite-difference method was designed by Hénon. Shortly, we supplement the procedure with one non-standard final step of integration, which is produced with the same finite-difference method, but applied to the differential equations reformulated by taking $S(x_1, x_2, \ldots, x_N)$ as the independent variable (Hénon, 1982). The length of this additional step just corresponds to the value of $S$ obtained in the previous step.

A continuous time system restored from a given invertible map is referred to as a *suspension*.[1]

### 1.1.2 Dynamics in terms of phase fluid: Conservative and dissipative systems and attractors

Traditionally, two classes of dynamical systems are distinguished, the *conservative* and *dissipative* ones. In physics, the conservation means conserving the energy. For example, a mechanical oscillatory system without friction relates to the conservative class. In the presence of friction, it becomes a dissipative system. In the last case, the mechanical energy is not conserved, but gradually dissipates being transformed to heat, i.e. to the energy of microscopic motion of molecules of the physical system itself, and of its environment. Strictly speaking, now the temporal evolution should be determined not only by the macroscopic state of the system, but also by variables relating to the molecules. Nevertheless, in many cases, description of the framework of the theory of dynamical system in terms of macroscopic variables remains sufficient, reasonable and accurate; then, we get a dissipative dynamical system.

It would be good to have a definition appealing not to a particular class of objects of specific physical nature, but to the basic concepts of the theory of dynamical systems.

Let us consider an ensemble composed of a very large number of identical non-interacting dynamical systems, differing only in initial conditions. In the phase space the ensemble corresponds to a cloud of representative points. This cloud evolves in time, changing size and shape due to motion of all individual points in accordance with the dynamic equations of a single underlying system.

It may occur that each finite-size element of the cloud evolves in such a way that its phase volume remains constant (at least, with description of some properly chosen variables). This is the case of the *conservative systems*.

[1] The term *suspension* is preferable for flow systems in which the mapping of the required form takes place for a fixed time period, which corresponds to dynamics in a non-autonomous system governed by differential equations with coefficients periodic in time. In more general case, with respect to the system, for which the given map corresponds to the Poincaré map, the term *special flow* is used (Hasselblatt and Pesin, 2008).

In classic mechanics, Lagrangian and Hamiltonian formalisms are developed for the conservative systems of even dimension of the phase space $N$ (Landau and Lifshitz, 1976; Arnold, 1989). Traditionally, the twice less number $N/2$ is called the *number of degrees of freedom*.

Lagrangian description is based on a scalar-valued function $L(q_1,\dots,q_{N/2},\dot{q}_1,\dots,\dot{q}_{N/2})$ depending on generalized coordinates $q_i$ and generalized velocities $\dot{q}_i$. For mechanical systems it has a sense of difference of potential and kinetic energy. Differential equations are obtained from the Lagrange function in a standard way; they are called the *Euler-Lagrange equations*:

$$\frac{d}{dt}\frac{\partial L}{\partial \dot{x}_i} - \frac{\partial L}{\partial x_i} = 0 \quad (i = 1,\dots,N/2).$$

Considered in terms of variables $(q_i, \dot{q}_i)$, the dynamics of a conservative system, in general, does not obey the property of preserving phase volume. To have this property, another set of variables has to be used. Namely, instead of the generalized velocities the generalized momenta are introduced by means of the relations $p_i = \dot{q}_i \dfrac{\partial L}{\partial \dot{q}_i}$. To reformulate the description in terms of the canonical variables $(q_i, p_i)$, the Hamiltonian function is used

$$H(q_1,\dots,q_{N/2},p_1,\dots,p_{N/2}) = \sum_{i=1}^{N/2} \dot{q}_i \frac{\partial L}{\partial \dot{q}_i} - L.$$

Then, the dynamics is governed by the *Hamilton equations*

$$\begin{aligned} \dot{p}_i &= -\frac{\partial H(p_1,\dots,p_{N/2},q_1,\dots,q_{N/2})}{\partial q_i}, \\ \dot{q}_i &= \frac{\partial H(p_1,\dots,p_{N/2},q_1,\dots,q_{N/2})}{\partial p_i}, \quad i = 1,\dots,N/2. \end{aligned}$$

Conservation of phase volume of an element evolving in the state space $(q_i, p_i)$ is stated by the *Liouville theorem*.

For *non-autonomous* systems the formalism remains the same, although the Lagrangian and Hamiltonian functions depend additionally on the time variable $t$ in explicit way.

For the case of *discrete time*, correct description of Hamiltonian systems is defined by an implicit set of equations expressed via one scalar-valued function of $N$ variables $F(q_1,\dots,q_{N/2},q'_1,\dots,q'_{N/2})$ called the *generating function*:

$$\begin{aligned} p_i &= -\frac{\partial F(q_1,\dots,q_{N/2},q'_1,\dots,q'_{N/2})}{\partial q_i}, \\ p'_i &= \frac{\partial F(q_1,\dots,q_{N/2},q'_1,\dots,q'_{N/2})}{\partial q'_i}, \quad i = 1,\dots,N/2. \end{aligned}$$

(Here the values marked with prime relate to the next step of the discrete time.)

In dissipative systems the phase volume decreases in the course of time evolution, at least, in average. So, the cloud of representative points eventually settles on some subset in the phase space, called *attractor* (or, possibly, on several attractors). In conservative case the cloud of the representative points may be thought of as composed of incompressible fluid, while in the dissipative case it must be regarded as compressible substance, like vapor able to condensate with essential decrease of its volume.

Attractors represent sustained dynamical regimes in dissipative systems arising due to long-time evolution. The simplest example of attractor is a *stable fixed point*, or stable equilibrium. Another simple example is a *stable limit cycle*, a closed orbit, representing the periodic self-oscillations. An attractor associated with sustained quasiperiodic motion, which is a composition of two or more components of incommensurable frequencies is *torus* of respective dimension. Chaotic sustained regimes correspond to specific nontrivial sets in the phase space called the *strange attractors* (Ruelle and Takens, 1971).

In the case of coexistence of two or more attractors in the phase space, we talk about *bistability* or *multistability*. A set of states in the phase space, from which the orbits arrive at the given attractor, is called the *basin* of this attractor.

It appears to be a hard problem to give a satisfactory formal definition of attractor embracing all cases that may occur (Milnor, 1985). For aims of this book, sufficient is a definition of the so-called *maximal attractor*, which uses a notion of *absorbing domain*.

For a discrete time case, with evolution operator defined by a function $\mathbf{g}(\mathbf{x})$, consider a domain in the phase space mapped inside itself: $\mathbf{g}(D) \subset \mathrm{Int}(D)$. (Here $\mathbf{g}(D)$ means a set of images of representative points, which relate to $D$.) Then, the attractor $A$ certainly belongs to $D$, and may be defined as intersection of images of $D$ under successive $n$ iterations of the map, namely,

$$A = \bigcap_{n=1}^{\infty} \mathbf{g}^n(D). \tag{1.5}$$

For a continuous time case the notion of the maximal attractor implies that there exists a connected domain $D$ bounded by a surface $B$ of such kind that all orbits cross $B$ transversally (with non-zero angle) being directed inside the domain $D$.

### *1.1.3 Rough systems and structural stability*

In 1937 Andronov and Pontryagin introduced the concept of *rough systems* (Andronov and Pontrjagin, 1937; Andronov et al., 1966), later reformulated and developed under the name of *structural stability* (Smale, 1967; Shilnikov, 1997; Guckenheimer and Holmes, 1983; Katok and Hasselblatt, 1995; Shilnikov et al., 1998; 2002). The roughness is a property of a dynamical system to preserve the qualitative behavior of trajectories under small variation of parameters and functions in the definition of the evolution operator. A more accurate formulation is as follows: While those variations are small in the class of continuous functions with first derivatives (in the common notation, the functions of class $C^1$), the system remains topologically equivalent to the original one. It means that there exists a continuous invertible change of variables (a homeomorphism, class $C^0$), which transforms directed phase trajectories of the perturbed system to those of the original one.

Andronov and Pontryagin indicated a necessary and sufficient condition for roughness of two-dimensional flow systems in a bounded domain. (It is the presence of a finite number of fixed points and periodic orbits with eigenvalues of respective linearized problems distant from zero, and the absence of orbits connecting saddle fixed points.)

The notion of roughness is essential for physical and technical applications because one can be sure that the mathematical models for the case of rough systems describe correctly all relevant qualitative features of dynamical behavior in spite of inaccuracy of the models or of the presence of inevitable external interferences and noises.

The idea of roughness, or structural stability, became a foundation for a great research program in oscillation theory advanced and developed by Andronov and his school (Andronov et al., 1966; Shilnikov et al., 1998; Shilnikov et al, 2002). According to this program, rough systems are regarded as the most typical (that's true, at least, for the two-dimensional flow systems!) and, hence, subjected to priority research as the most important for practice. The next step is examination of systems of the first level of non-roughness, which may be thought of as separating rough classes in a space of systems, that corresponds to theory of bifurcations of codimension one. Next, one can turn to situations separating the systems of the first degree of non-roughness, and it will be theory of codimension-two bifurcations, and so on (Kuznetsov Yu., 1998).

The outlined research program was completely successful in application to the flow systems of dimension two, but attempts of generalization for dimension three and more met great difficulties.

For higher dimensions a straightforward generalization of the Andronov-Pontryagin approach was found appropriate only for a restricted class called the *Morse-Smale systems* (Smale, 1967; Palis, 1969; Guckenheimer and Holmes, 1983; Devaney, 2003), which are characterized by a finite number of fixed points and periodic orbits in a bounded domain of the phase space. Beside this class, the general picture for the multidimensional case is extremely complex, and the notion of roughness seems not helpful and elucidative. Particularly, it is known that whole regions may exist in parameter spaces, where structurally unstable systems occur on a dense set (the *Newhouse regions*) (Newhouse, 1979; Guckenheimer and Holmes, 1983). All these problems were actively studied in last several decades.

However, in the framework of the present book we must specially outline one more class of higher-dimensional rough systems (beside the Morse-Smale ones): these are just the systems with uniformly hyperbolic chaos. For them, the consistent theory was developed exclusively in mathematics (Smale, 1967; Williams, 1974; Katok and Hasselblatt, 1995; Afraimovich and Hsu, 2003; Bonatti et al., 2005; Hasselblatt et al., 2008). Lack of physical examples of this kind having existed until recently is a great dissatisfaction. It seems natural that general argumentation concerning theoretical and practical significance of rough systems must relate to the systems with hyperbolic chaos too; so, the problem deserves attention in concern of physical systems and technical devices.

### *1.1.4 Lyapunov exponents and their computation*

To distinguish regular and chaotic dynamics on a quantitative level, a useful and constructive method is concept of the Lyapunov exponents (Pesin, 1977; Rabinovich and Trubetskov, 1989; Guckenheimer and Holmes, 1983; Barreira and Pesin, 2001; Hilborn, 2000; Anishchenko, 2002; Ott, 2002; Schuster, and Just, 2005; Anishchenko et al., 2007).

Let $\mathbf{x}(t)$be some phase trajectory of the dynamical system (1.1). Consider an ensemble associated with a cloud of representative points forming initially a small ball of radius $\varepsilon$ centered at the starting point of the reference orbit $\mathbf{x}(t_0)$. How will this cloud evolve in time? While its size is small, it will take a form of an $N$-dimensional ellipsoid, like that shown in Fig. 1.2. Let us express the semi-principal axes of this ellipsoid at some time instant $t$ as $\{l_1, l_2, \ldots, l_N\} = \left\{\varepsilon e^{\lambda_1 t}, \varepsilon e^{\lambda_2 t}, \ldots, \varepsilon e^{\lambda_N t}\right\}$. Algebraically, they are related with the singular values of the matrix governing the evolution of the perturbation vectors along the reference orbit (Greene and Kim, 1987). In the limit of small $\varepsilon$ and large $t$, a set of the quantities $\{\lambda_1, \lambda_2, \ldots, \lambda_N\}$ determines

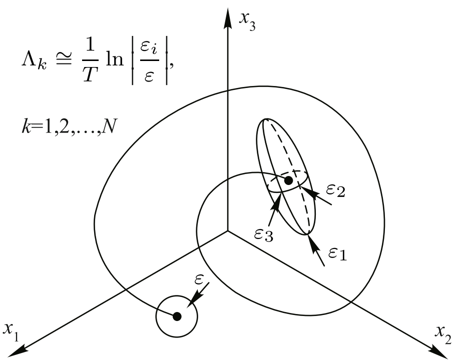


**Fig. 1.2** Geometric interpretation of spectrum of Lyapunov exponents: each exponent characterizes scale change along one of principle axes of ellipsoid arising from an infinitesimal ball centered at the starting point of the considered orbit.

the *spectrum of Lyapunov characteristic exponents*. A common convention is to order them in such a way that $\lambda_1 \geqslant \lambda_2 \geqslant \cdots \geqslant \lambda_N$. Each exponent may be thought of as indicating rate of expansion (if positive) or compression (if negative) for the cloud of representative points along the principal axes of the ellipsoid.

It should be understood that the above definition speaks about Lyapunov exponents of an *individual* reference orbit. Can this notion be applied to attractor, as a whole? Certainly, it is so for attractors consisting of a single orbit, like a limit cycle, or a stable fixed point. However, attractors being of more complex nature are composed of a *set* of trajectories, like a torus, or a strange attractor. Then, the question is not so trivial because distinct orbits may have different Lyapunov exponents.

In fact, appropriate generalization of the notion of Lyapunov spectra is possible: we refer to the Lyapunov spectrum of an attractor as defined for a *typical* trajectory on the attractor. This approach is justified mathematically by the so-called *multiplicative ergodic theorem* (Oseledets, 1968; Pesin, 1977; Raghunathan, 1979; Guckenheimer and Holmes, 1983).

Analytic evaluation of the Lyapunov exponents for dynamical systems is available rarely, so, usually we need to turn to the computational estimates.

To be concrete, consider a continuous-time autonomous system (1.1). Generalizations to a non-autonomous case and to diffeomorphisms are simple and straightforward. The computations are based on simultaneous solution of the dynamical equation (1.1) on the reference trajectory belonging to the attractor and the equation for small perturbation vector, linearized near that trajectory. To derive the last one, we substitute $\mathbf{x}(t) + \tilde{\mathbf{x}}(t)$ into (1.1) and expand the right-hand part in powers of the perturbation $\tilde{\mathbf{x}} = (\tilde{x}_1, \tilde{x}_2, \ldots, \tilde{x}_N)$ neglecting terms of order higher than one. It yields the so-called *variation equation*

$$\frac{d\tilde{\mathbf{x}}}{dt} = \mathbf{A}\left(\mathbf{x}(t)\right)\tilde{\mathbf{x}}, \tag{1.6}$$

where $\mathbf{A}(\mathbf{x}(t))$ is a matrix composed of all partial derivatives of the components of the vector function $\mathbf{F}(\mathbf{x})$ over the components of the vector $\mathbf{x}$:

$$\mathbf{A} = \begin{pmatrix} \dfrac{\partial F_1}{\partial x_1} & \dfrac{\partial F_1}{\partial x_2} & \cdots & \dfrac{\partial F_1}{\partial x_N} \\ \dfrac{\partial F_2}{\partial x_1} & \dfrac{\partial F_2}{\partial x_2} & \cdots & \dfrac{\partial F_2}{\partial x_N} \\ \vdots & \vdots & & \vdots \\ \dfrac{\partial F_1}{\partial x_N} & \dfrac{\partial F_2}{\partial x_N} & \cdots & \dfrac{\partial F_N}{\partial x_N} \end{pmatrix}. \tag{1.7}$$

In general, the matrix $\mathbf{A}$ depends on time via the variable $\mathbf{x}$ relating to the unperturbed reference trajectory. A linear vector space associated with each point on the reference orbit $\mathbf{x}$, where the perturbation vectors $\tilde{\mathbf{x}}$ live, is called the *tangent space*.

To compute more than one Lyapunov exponent, one needs to monitor a collection of the respective number of perturbation vectors evolving in time along the reference phase trajectory. However, without special measures, each vector in the collection typically contains a component characterized by the maximum Lyapunov exponent that will dominate at large time scale, and then evaluation of other Lyapunov exponents becomes impossible. Moreover, in the case of positive maximal exponent the norms of the vectors will manifest unbound growth with overfilling the memory registers in computer. To overcome these difficulties, it is recommended in the course of the algorithm operation to redefine from time to time the perturbation vectors applying the Gram-Schmidt orthogonalization process and renormalization (Benettin et al., 1980). The Lyapunov exponents are determined as mean rates for increase or decrease of accumulating sums for logarithms of ratios of norms of the vectors after orthogonalization but before the normalization (See explanation of the procedure in more detail in Appendix A).[2]

## 1.2 Model examples of chaotic attractors

### *1.2.1 Chaos in terms of phase fluid and baker's map*

Let us turn again to representation of dynamics in terms of ensemble of a large number of identical systems.

Chaos in dynamics occurs if the cloud of representative points in the course of evolution in the phase space undergoes repetitive deformations of stretching, folding, and transversal compression.

To illustrate, let us consider a dissipative version of the so-called *baker map* (Manneville, 1995; Schuster and Just, 1995; Tél and Gruiz, 2006), see Fig. 1.3. Take a unit square on the plane $(x, y)$ and deform it, like baker rolls a piece of dough. Next, cut the piece in half, and place the halves, one above the other, along the top and the bottom sides of the unit square, leaving a gap in the middle. Let us assume that

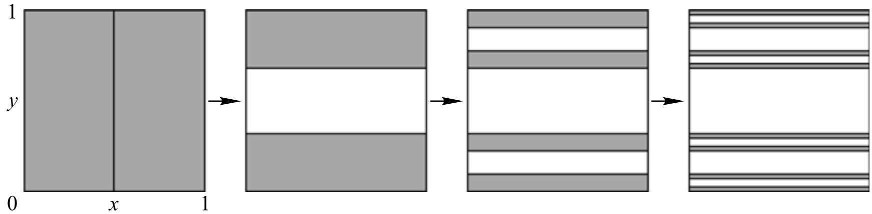


**Fig. 1.3** Geometric illustration of the dissipative baker's map.

[2] Now, some alternative approaches to computation of Lyapunov exponents have been suggested, e.g. (Geist et al., 1990; Christiansen and Rugh, 1997; Rangarajan et al., 1998).

in this process the horizontal size is doubled, and the vertical width becomes three times narrower. The total area then is decreasing; it reflects the dissipative nature of the mapping (the "dough" in this case should be imagined as a compressible substance). When the transformation is repeated many times, a layered structure appears containing horizontal bands, a number of which grows proportionally to $2^n$ ($n$ is the number of iterations), whereas the total width of the bands decreases proportionally to $3^{-n}$.

Attractor is the object arising in the limit of infinitely large number of iterations. In the cross-section it has structure of the Cantor set. Note that in this example distribution of the density of the "dough" along the layers tends to the uniform one.

It is worth stressing that the individual dynamics of particles of the "dough" is chaotic. Indeed, formally a one-step transformation of the instant state of a single particle in coordinates $(x, y)$ is governed by the equations

$$\begin{cases} x_{n+1} = 2x_n \\ y_{n+1} = \dfrac{1}{3}y_n \end{cases} \text{at } x_n \leqslant \frac{1}{2}, \quad \begin{cases} x_{n+1} = 2x_n - 1 \\ y_{n+1} = \dfrac{1}{3}y_n + \dfrac{2}{3} \end{cases} \text{at } x_n > \frac{1}{2}. \tag{1.8}$$

To explain chaotic nature of the dynamics, represent an initial value of $x$ by a real number in binary notation, for example, $0.0110010110111\ldots$. One step evolution of the system corresponds to a shift of the binary sequence by one position to the left discarding the leftmost digit. Note that a character at the first position after the binary point indicates residence of the particle at the present moment in the left or in the right half of the unit square for 0 or 1, respectively. When taking the initial condition as a random real number from the unit interval, we get a random set of zeros and ones in the binary notation; so the particle will appear in the left and right halves of the square in accordance with the prescribed random sequence of digits.

Despite its simplicity, the baker map shows many features common for chaotic attractors, for example, the transverse Cantor structure and specific combination of stability, in the sense of attraction of the orbits to the limit set in transverse direction, and instability, in the sense of mutual divergence of close orbits along the fibers of the attractor.

In this construction a natural dissatisfaction is the involved "cutting" the piece of the "dough". One can try to repair this unlikable feature, assuming the piece is not cut, but folded and placed again in the unit square (Fig. 1.4). Then, on the first steps one observes again formation of the layered structure. However, in the limit of a large number of iterations, no uniform distribution along the fibers (or at least close to that) arises! What is observed, the substance has a tendency to concentrate at folds, forming singularity of the density distribution. The reason is that at the place of folding the direction of the compression coincides with the vertical tangent at the edge of the "dough" piece, and the flattening gives rise to appearance of a local region of high density. In nonlinear dissipative systems, such situations may

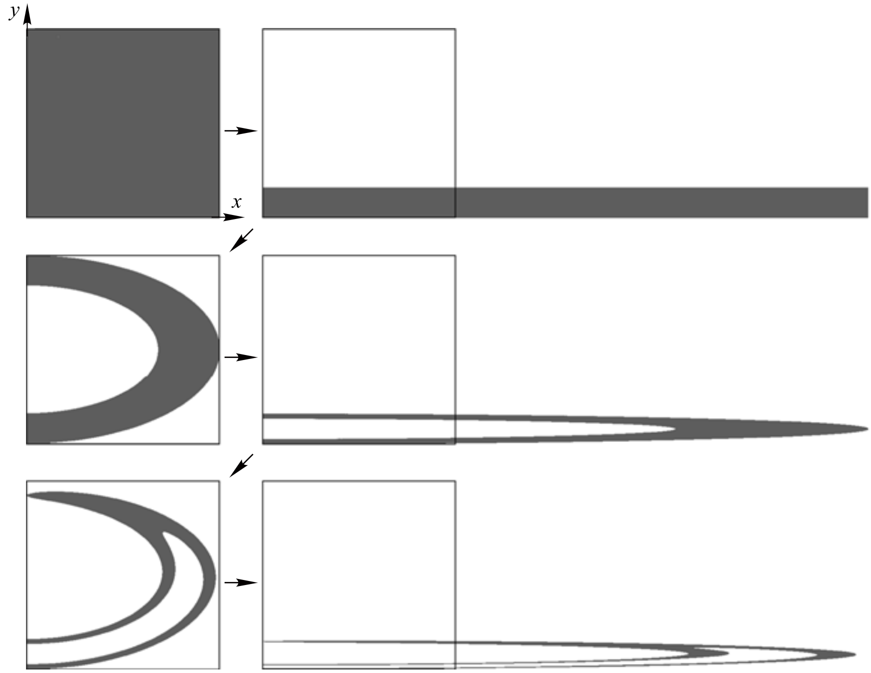


**Fig. 1.4** An attempt of modification of the dissipative baker map with folding instead of cut of the "dough"; two steps of successive iteration are shown. Formation of the layered structure is accompanied in this case with appearance of local singularities of density at places of folding.

be associated with non-hyperbolic chaos, like that in Hénon map (Appendix B), or with subsidence of the cloud on regular attractors (fixed points and cycles).[3]

> Hyperbolic chaos corresponds to situations when the transformation of a cloud of representative points, including the longitudinal stretch and transversal compression, is carried out perfectly, without cuts, discontinuities, and formation of local singular concentrations.

A principal possibility of occurrence of attractors with such properties may be proven by consideration of artificial examples. In each of them we, first, define the phase space, then indicate an absorbing domain $D$, and formulate a rule of evolution in discrete time $\mathbf{g}(\mathbf{x})$ in such a way that on one step this domain is mapped inside itself: $\mathbf{g}(D) \subset \mathrm{Int}(D)$. Then, the attractor is obviously located inside this domain being formally defined as $A = \bigcap_{n=1}^{\infty} \mathbf{g}^n(D)$.

[3] This type of dynamics is associated with the construction called *Smale's horseshoe* (see Appendix C).

### 1.2.2 Smale-Williams solenoid

The first example is *attractor of Smale-Williams* (Smale, 1967; Williams, 1974; Shilnikov, 1997; Guckenheimer and Holmes, 1983; Katok and Hasselblatt, 1995; Afraimovich and Hsu, 2003; Hasselblatt and Katok, 2003; Hasselblatt et al., 2008). The simplest case corresponds to a three-dimensional map. Consider a domain in the form of torus in three-dimensional space. Let us think of this torus as a plastic doughnut. One step of transformation is the following: we stretch the doughnut twice, squeeze it in the transversal direction, then fold it to get the double loop, and insert this loop within the original torus (Fig. 1.5). To fit it there, we must assume that the transverse size is reduced more than twice. At each next step of the transformation, the total volume decreases (that means the map is dissipative) and the number of coils is doubled. In the limit of infinite number of steps, it tends to infinity, and the object is formed, which is known as *solenoid*. In the transversal cross sections it has a Cantor-like structure.[4]

The essential point of the construction is that the angular coordinate undergoes doubling at each discrete time step: $\varphi_{n+1} = 2\varphi_n$ (Fig. 1.5). An obvious generalization is to carry out the procedure making a loop with a number of coils $M$. It corresponds to the mapping for the angular coordinate of the form $\varphi_{n+1} = M\varphi_n (\bmod 2\pi)$. With $M \geqslant 2$ it is termed an *expanding circle map*, or a *Bernoulli map*.

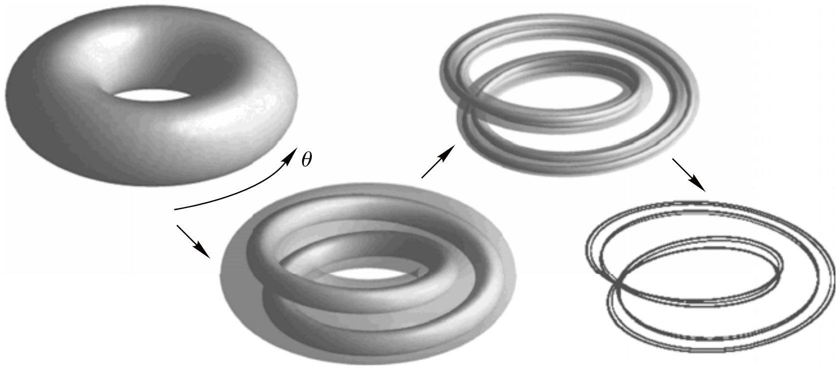


**Fig. 1.5** Absorbing toroidal domain in three-dimensional phase space, results of its transformation in the first two kinds of iteration, and the Smale-Williams solenoid, obtained after a large number of repetitive applications of the map (right).

[4] As a topological object, the solenoid was introduced by Vietoris and van Dantzig (Shilnikov, 1997), but as a chaotic attractor it appears due to Smale (Smale, 1967) and Williams (Williams, 1974). Interestingly, the solenoid occurs as well in a very different context in flow dynamical systems, as a non-chaotic attracting set at the Feigenbaum critical point of accumulation of period-doubling bifurcations (Vul et al., 1984). In the latter case, the formation of each new level of the intrinsic fractal structure is associated with doubling time scale, not with one step of discrete time as it is for the Smale-Williams attractor.

### 1.2.3 DA-attractor

The next example is the so-called *DA-attractor* proposed and named by Smale (DA stands for "Derived from Anosov"). It takes place for a two-dimensional map defined on a surface of a torus (Smale, 1967; Shilnikov, 1997; Katok and Hasselblatt, 1995).

Let us start with a map of Anosov, also known as the Arnold cat map (Arnold and Avez, 1968; Anosov et al., 1995; Devaney, 2003)

$$p_{n+1} = p_n + q_n, \quad q_{n+1} = p_n + 2q_n \;(\bmod 1), \tag{1.9}$$

where $\varphi = 2\pi p, \theta = 2\pi q$ are angular coordinates on the torus. Graphically, it is convenient to represent the phase space as a unit square, having in mind periodic continuation of all structures in the horizontal and vertical directions (Fig. 1.6).

The Anosov map is conservative and has a fixed point of saddle type in the origin, with stable and unstable directions given by the vectors $\mathbf{a}_1 = (1, W)$ and $\mathbf{a}_2 = (-W, 1)$, where $W = (\sqrt{5}+1)/2$.

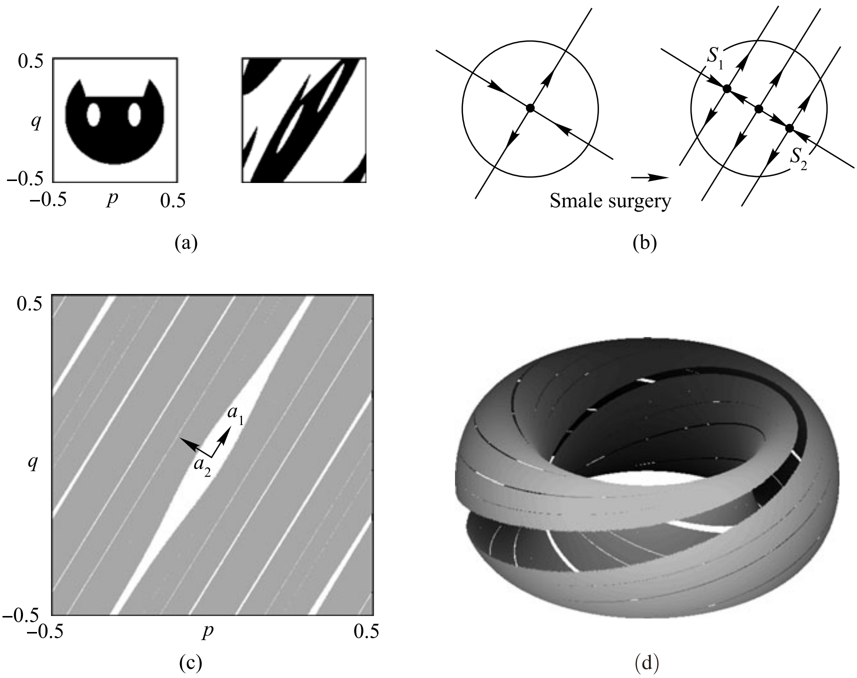


**Fig. 1.6** Illustration of the hyperbolic Anosov mapping, also known as the Arnold cat map, on the unit square representing the unfolding of the torus **(a)**. The Smale surgery performed in the vicinity of the fixed point at the origin **(b)**. Portrait of the DA-attractor depicted in the unit square **(c)** and on the surface of torus **(d)**.

To get a dissipative map with attractor, Smale suggested modifying the map by means of a “surgical operation” in a small neighborhood of the fixed point. The procedure is carried out in such a way that the motion along the unstable direction is not perturbed, but in the orthogonal direction it modifies; the fixed point becomes repulsive, and, hence, two saddle points $S_1$ and $S_2$ appear nearby (Fig. 1.6(b)). Outside the region subjected the “surgery”, the mapping does not change.

In this setup, the absorbing domain is the entire surface of the torus, except for a truncated circular neighborhood of the origin (the saddles $S_1$ and $S_2$ are inside this excluded neighborhood). Under iteration, the cut in the cloud of representative points elongates along the vector $\mathbf{a}_1$ with simultaneous contraction in the orthogonal direction $\mathbf{a}_2$, so that the cloud becomes a narrow strip stretching along the unstable direction. Since the slope coefficient is irrational, it covers the torus densely (Fig. 1.6 (c), (d)). This is the way the Cantor-like transverse structure of the hyperbolic attractor arises in this case. One particular variant of such attractor is described and visualized in the article (Coudene, 2006), devoted to computer illustrations of the hyperbolic theory.

### *1.2.4 Plykin type attractors*

The *Plykin attractor* takes place in a special two-dimensional map on a plane (Plykin, 1974; Sinai, 1979; Anosov et al., 1995; Katok and Hasselblatt, 1995; Shilnikov, 1997; Devaney, 2003). Figure 1.7 shows a region composed of three semi-discs with small semi-circular cutouts. The sub-domains on the figure are covered with hatching indicating two fields of directions defined in this area. The map is constructed in such a way that action on the states represented by points of the region produces a figure shown to the right. Note that the fields of directions after the transformation coincide with the initial fields. One corresponds to direction of stretch, and the other to direction of compression. This provides the hyperbolic nature of the attractor.

Understanding dynamics on the Plykin attractor becomes clearer due to the following observation. Consider representative points belonging to a common straight line segment of the radial hatching, or *foliation*, in the first figure. It is easy to see that all of them exhibit the same behavior in the sense that under iteration of the map they remain on a common segment of the foliation and visit simultaneously certain sub-areas on the diagram. We may agree not to distinguish points belonging to one and the same radial segment; then, instead of the dynamics in the two-dimensional phase space we can restrict consideration with the one-dimensional dynamics. The phase space for this dynamics is the so-called *one-dimensional branched manifold* (Williams, 1974). It can be thought of as a rubber thread; in the present case of the Plykin attractor it is a loop with two attached smaller loops. Initially, this thread is stretched to three nails, as shown in Fig. 1.7(b) (left). One iteration step implies stretching the thread and putting it again on the same nails, as shown in Fig. 1.7 (right).

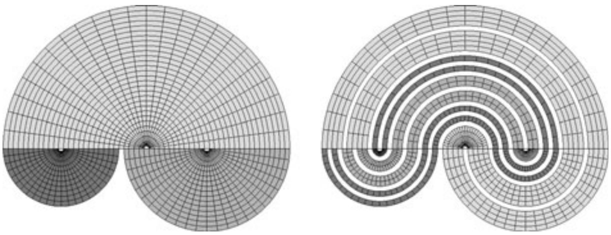

(a)

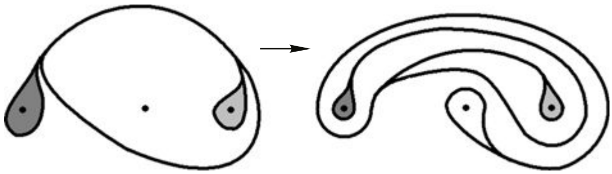

(b)

**Fig. 1.7** Absorbing domain and its transformation under application of the map **(a)** and description of the dynamics with the one-dimensional branched manifold **(b)** for the original Plykin attractor.

Description of the dynamics with a help of branched manifolds was used by Williams to develop a classification scheme for hyperbolic attractors in bounded two-dimensional domains with three or more holes. Now it is known that many distinct attractors of such kind exist (Williams, 1974; Zhirov, 1995; Grines and Zhuzhoma, 2006). They are called the *Plykin type attractors*. One of them, shown in Fig. 1.8, is of special interest for further consideration in the present book.

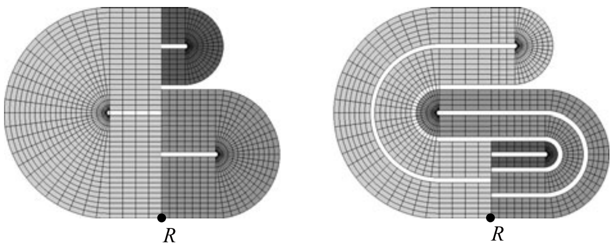


(a)

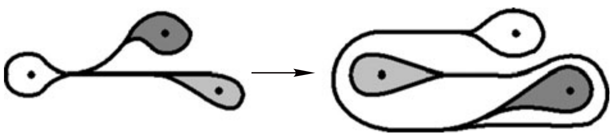

(b)

**Fig. 1.8** Absorbing domain and its transformation under application of the map **(a)** and description of the dynamics with the one-dimensional branched manifold **(b)** for an attractor of Plykin type essential for further consideration. Symbol $R$ indicates an unstable fixed point belonging to the attractor, which is of importance for the further consideration.

Attractors of Plykin type may be regarded as being placed on a sphere rather than on a plane. Indeed, mapping from the plane to the sphere and back may be performed with a change of variables called stereographic projection, well known from elementary geometry (Fig. 1.9).

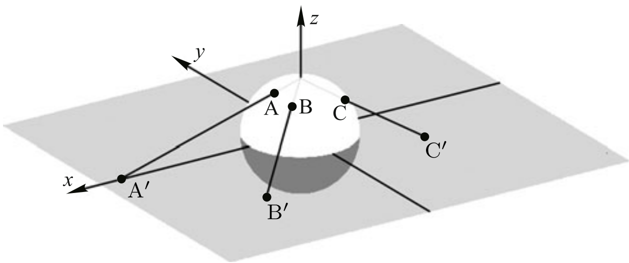


**Fig. 1.9** Correspondence of points A, B, C on the sphere and points A′, B′, C′ on the plane established by the stereographic projection.

On the sphere four holes are required minimally for a uniformly hyperbolic attractor of Plykin type could exist. This is consistent with the previous statements. Actually, if the center of the stereographic projection (mapped to infinity) is placed in one of the holes, then the transformed attractor is localized in a bounded domain with three holes on the plane.

## 1.3 Notion of hyperbolicity

A good way to begin introduction to the hyperbolic theory is discussion about a hyperbolic fixed point, the *saddle*. Figure 1.10 shows a pendulum and its phase

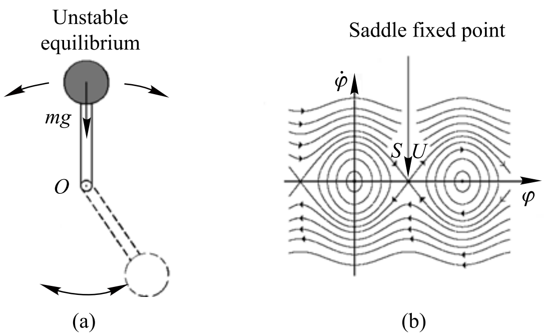


**Fig. 1.10** A picture of pendulum with unstable top equilibrium **(a)** and phase portrait of this system on the plane **(b)**. $S$ is a stable separatrix of the saddle point, and $U$ is the unstable separatrix. Locally near the saddle point trajectories look like hyperbolae, so it is called a hyperbolic fixed point.

portrait on the phase plane (Andronov et al., 1966; Sagdeev et al., 1988; Rabinovich and Trubetskov, 1989). The horizontal axis corresponds to the angular coordinate, and the vertical axis to instantaneous angular velocity. The pendulum can oscillate near the lower equilibrium $\varphi = 0$, but now an unstable state of equilibrium $\varphi = \pi$ is of interest for us. In the phase plane it corresponds to a saddle point $A$, located at the intersection of curves, called *separatrices*. From the state of equilibrium in the presence of a small perturbation the representative point departs along the unstable separatrix $U$. On the other hand, let the pendulum in the down position be kicked with a certain properly chosen momentum, so that it reaches the top point and stops there. In this case, the representative point moves along the stable separatrix $S$. The saddle point itself is a phase trajectory, and this trajectory is *hyperbolic*. The name stands for the fact that depicted on the phase plane phase trajectories near the saddle locally are of hyperbolic form.

A slightly more complex example is a closed hyperbolic trajectory, or a *saddle periodic orbit* (Fig. 1.11). It is an unstable limit cycle in the phase space, to which trajectories approach on the surface $S$, or depart being situated on the surface $U$. If we make a cross-section of the flow with a plane, as shown in the figure, we see two curves formed by the intersections of the plane with these surfaces. The point where these curves intersect each other belongs to the limit cycle, and it is a saddle point for the Poincaré map.

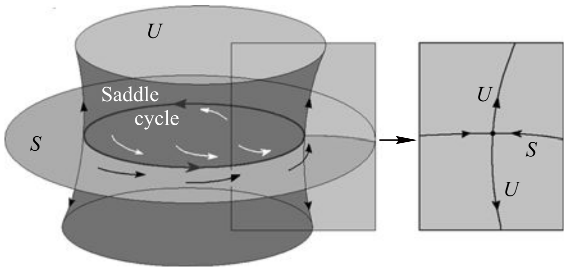


**Fig. 1.11** Phase space arrangement near a saddle cycle. $S$ is a surface representing the stable manifold, and $U$ is the unstable manifold. An inset shows a picture in the Poincaré section.

The next step is generalization of the notion of hyperbolicity for non-periodic phase trajectories (Fig. 1.12).

A phase trajectory is called *hyperbolic* if at each point of this orbit in the vector space of all possible infinitesimal perturbations $V$ one can define a subspace of vectors decreasing in norm in the course of evolution forward in time and a subspace of vectors decreasing in norm in reverse time. Moreover, the vectors belonging to these subspaces $V_S$, or $V_U$ must be bounded in norm by exponential functions of time, which decrease in forward, or inverted time, respectively. In the discrete-time case of a system governed by a diffeomorphism, all vectors in the space $V$ must allow representation as linear combinations of vectors belonging to $V_S$ and $V_U$. Mathematically, it means that the vector space $V$ is a direct sum of the subspaces $V_S$ and

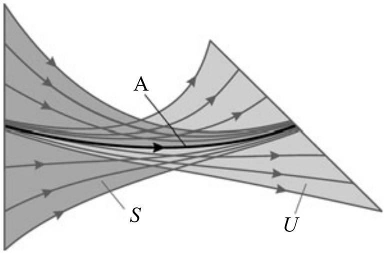


**Fig. 1.12** An illustration explaining the phase space structure near a general saddle phase trajectory; $S$ is the stable manifold and $U$ is the unstable manifold.

$V_U$: $V = V_U \oplus V_S$. In flow systems, a one-dimensional neutral subspace $V_N$ has to be added, corresponding to perturbations directed along the trajectory; such perturbations, on average, do not grow or decrease in the course of time evolution. In this case it is required that $V = V_U \oplus V_N \oplus V_S$.

The epithet *uniformly hyperbolic* means that the rates of exponential growth of decay of magnitudes of vectors relating to the stable and unstable manifolds are bounded and detached from zero by some (globally defined) constants.

In the phase space a set of trajectories, which approaches the reference orbit in the course of forward evolution in time, is called the *stable manifold*. Similarly, the *unstable manifold* is a set of trajectories, which approaches the reference orbit in reverse time. For hyperbolic orbits these sets are indeed manifolds, that means they are smooth objects like curves, surfaces or hyper-surfaces in the phase space; this is a conclusion of special theorem (known as *the Hadamard-Perron theorem*) (Anosov, 1967; Katok and Hasselblatt, 1995; Barreira and Pesin, 2001).

Uniformly hyperbolic saddle trajectories, and invariant sets composed of such trajectories may occur in phase spaces of both conservative and dissipative systems, but in this book we concentrate on the dissipative case. Hence, we will deal with such a kind of the hyperbolic invariant sets as the *uniformly hyperbolic attractors*.

The uniformly hyperbolic attractor is a bounded attracting invariant set in the phase space of a dissipative system, composed exclusively of uniformly hyperbolic saddle trajectories, and near all these trajectories the phase space is arranged locally in one and the same manner. Manifolds for all trajectories belonging to the attractor must have the same dimension. The intersections between stable and unstable manifolds are allowed only at nonzero angles (touches are excluded).

For the above example of Smale-Williams attractor, the stable manifolds are two-dimensional; they are represented by a family of meridianal plane sections of the torus domain (Fig. 1.5). By contrast, the unstable manifolds are one-dimensional. For each point on the attractor the unstable manifold is a fiber of the solenoid containing that point. As a whole, the unstable manifold actually coincides with the attractor.

For the DA-attractor (Fig. 1.6) the stable manifolds are one-dimensional, so are the unstable ones. The unstable manifolds follow approximately the direction of the expansion vector $\mathbf{a}_1$ (with some deflections nears the surgery area), and stable manifolds go along the orthogonal direction of the vector $\mathbf{a}_2$.

For attractors of Plykin type both stable and unstable manifolds are one-dimensional. The stable manifolds correspond to the family of lines, along which the compression of the phase volume takes place. The unstable manifolds run along the second family of lines associated with direction of stretching for the phase volume elements (Figs. 1.7 and 1.8).

Besides the uniform hyperbolicity we have to mention a notion of *partial hyperbolicity* developed as one of the generalizations in the mathematical theory (Pesin,2004; Bonatti et al., 2005; Pesin, 2007). It relates to a case when the vector space associated with perturbations at points of the reference orbit admits representation as a direct sum of subspaces $V = V_U \oplus V_S \oplus V_C$, where $V_U$ is an unstable subspace (corresponding to expansion), $V_S$ is a stable subspace (corresponding to contraction), and $V_C$is called the *central subspace*. The last one may correspond to expansion and/or contraction, but with rates in interval between the minimal expansion in $V_U$ and minimal contraction in $V_S$. In analysis, the dynamical properties appearing due to presence of the strong expansion and contraction may be distinguished and considered separately, and they provide features of dynamics analogous to those of uniformly hyperbolic systems. Meanwhile, dynamical properties associated with the central subspace may be of special nature for concrete systems. Although the current book is devoted to uniform hyperbolicity, we will need to refer to the partial hyperbolicity concerning some examples discussed in subsequent chapters.

## 1.4 Content and conclusions of the hyperbolic theory

Let us turn now to a brief overview of the substational part of the hyperbolic theory (Anosov, 1967; Smale, 1967; Williams, 1974; Sinai, 1979; Anosov et al., 1995; Eckmann and Ruelle, 1985; Shilnikov, 1997; Katok and Hasselblatt, 1995; Guckenheimer and Holmes, 1983; Afraimovich and Hsu, 2003; Hasselblatt and Katok, 2003; Devaney, 2003; Hasselblatt et al., 2008). For simplicity, we talk in this section about discrete time systems represented by maps (diffeomorphisms). For systems with continuous time the notions and results may be extended by means of appealing to the description in terms of the Poincaré map.

We begin with discussion of the *axiom A*, a statement formulated by Smale (Smale, 1967) which allows (together with the additional requirement of strict transversality) one to single out a class of structurally stable systems among the dynamical systems of arbitrary finite dimension.

A point in phase space of a dynamical system is called *wandering* if it has a neighborhood, into which a trajectory starting from the reference point never returns at time exceeding some fixed constant. From a physical point of view, such dynamics corresponds to transient motions. If this property does not hold, the point is called *non-wandering*; this may be regarded as some preliminary formalization for notion of sustained or stationary dynamical behavior (Birkhoff, 1927).

A system with discrete time, given by a diffeomorphism **g**, is said to obey the Axiom A if, first, a set of non-wandering points NW is hyperbolic, and, second, periodic points of **g** form a dense subset in NW. The latter means that an arbitrarily small neighborhood of any point of the set NW necessarily contains a point related to a periodic orbit, belonging to the same set.[5] Hyperbolicity is understood just as explained above: the linear space of vectors of perturbations (tangent space) is composed of spaces, $V_U$ and $V_S$ corresponding to exponential expansion or compression of vectors during their time evolution.[6] Strong transversality condition requires that the stable and unstable manifolds for an arbitrary pair of points belonging to NW are in a generic mutual disposition, i.e. crossings are allowed only with non-zero angles, and touches are excluded.

For the class of systems with Axiom A, Smale proved a *spectral decomposition theorem* (Smale, 1967; Katok and Hasselblatt, 1995; Afraimovich and Hsu, 2003). It asserts that the set of non-wandering points can be represented as a union of a finite number of disjoint invariant sets $B_i$, obeying the property of transitivity (i.e., each such set includes an orbit visiting an arbitrarily small neighborhood of any point of this set). They are called *basic* or *locally maximal* sets. For various concrete systems, it may be stable or unstable fixed points, periodic orbits, nontrivial attractive, repulsive, or saddle invariant sets. Definition of the local maximal set declares that it is an intersection of all images of some neighborhood $U$ containing this set under iteration of the map *forward and backward in time*: $B = \bigcap_{n=-\infty}^{\infty} \mathbf{g}^n(U)$. This is similar to the definition of a maximal attractor as intersection of images of the absorbing region in iteration in *forward time*; such attractors surely can occur as a particular case of the basic sets. Further, each basic set can be decomposed to a union of a finite number $k_i \geqslant 1$ of disjoint subsets $X_{i,j}$, visited in a certain fixed order under iteration of the map. Each set $X_{i,j}$ is an invariant set for the map iterated $k_i$ times. Uniformly hyperbolic attractors of Plykin type, Smale-Williams solenoid, DA-attractor are basic sets for certain model dynamical systems with Axiom A, for which the number $k$=1 (i.e., they do not allow further decomposition). Unless otherwise is not indicated specially (Part III of the present book), we will have in mind only attractors, whose unstable manifolds are one-dimensional.

---

[5] One particular class of systems with axiom A is represented by *Anosov systems*, like the Arnold cat map; their specificity is that for them the set of non-wandering points is the whole phase space.

[6] It does not exclude situations where one of the subspaces $V_U$ or $V_S$ is empty set; this makes it possible to incorporate simple structurally stable systems (with non-wandering sets of the type of fixed points or periodic orbits) in the framework of the axiom A reasoning.

### *1.4.1 Cone criterion*

Now, it should be noted that there exists *a rigorous criterion of hyperbolicity* formulated in such a way that it may be verified in computations (Sinai, 1979; Hasselblatt et al., 2008).

Let us assume that dynamics in discrete time is determined by a smooth invertible map $\mathbf{g}(\mathbf{x})$. The criterion requires that for some choice of a constant $\gamma > 1$, for each point $\mathbf{x}$ relating to the analyzed invariant set one can define expanding and contracting cones in the space of vectors of infinitesimal perturbations (the tangent space) (Fig. 1.13). An expanding cone is a set of vectors, norms of which increase by application of the mapping by factor $\gamma$ or more. A contracting cone is a set of vectors, norms of which grow by factor $\gamma$ or more by application of the inverse mapping. Bearing in mind the smooth dependence of all relevant objects on the position of the reference point in the phase space, we may talk on the fields of the expanding and contracting cones.

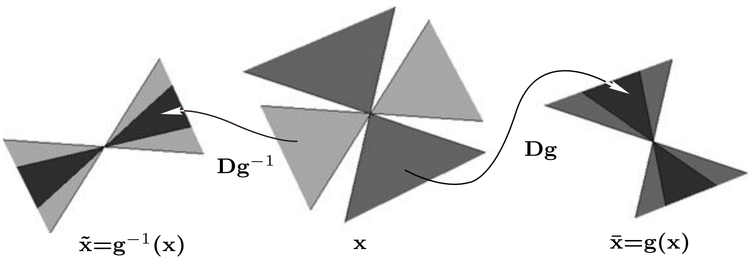


**Fig. 1.13** Explaining the criterion of hyperbolicity. The image of the expanding cone from a point $\mathbf{x}$ is located inside the expanding cone, defined for the image point $\bar{\mathbf{x}}$, and the pre-image of the compressing cone is situated inside the contracting cone defined at the pre-image point $\tilde{\mathbf{x}}$. The symbols $\mathbf{Dg}$ and $\mathbf{Dg}^{-1}$ denote the derivative matrices of the direct and inverse mappings, which define the transformation of the perturbation vectors on one step forward and backward in time.

The criterion holds if the expanding and contracting cones are invariant in the sense that for all points on the reference trajectory the image of the expanding cone belongs to interior of the expanding cone defined for the image point, and the pre-image of the contracting cone belongs to interior of the contracting cone defined for the pre-image point.

In subsequent chapters we consider in some detail technique of application of this criterion for verification of hyperbolic nature of attractors in concrete systems.

### 1.4.2 Instability

The fact that unstable manifold of any point on the attractor belongs to the attractor provides sensitivity of motion on the attractor in respect to small perturbations of initial conditions, which is the main attribute of dynamical chaos. Indeed, for two representative points, slightly shifted relative to each other along the unstable manifold, the images will evolve in time in such a way that they are moving apart from each other. While the distance between the images is small enough, it grows exponentially (in average), in accordance with the relation $\|\Delta\mathbf{x}\| \sim e^{\Lambda n}$. Here $n$ is the discrete time, and $\Lambda$ is the largest Lyapunov exponent.

If the unstable manifolds are one-dimensional, the spectrum of Lyapunov exponents contains one positive Lyapunov exponent, while all other exponents are negative. For maps all the Lyapunov exponents of a uniformly hyperbolic attractor are distanced from zero. Indeed, for individual trajectories on the attractor the positive exponents correspond to the perturbation vectors belonging to expanding cones defined at the points in these trajectories. Since the minimal degree of expansion is limited by a constant $\gamma > 1$ (used in the cone criterion), the positive Lyapunov exponent is not less than a positive number $\Lambda^+_{\min} = \ln\gamma$. This is true for all trajectories belonging to the attractor, and hence the same estimate holds for the exponent corresponding to the attractor as a whole. Similarly, the negative Lyapunov exponents, which are associated with the vectors belonging to the contracting cones, are bounded from above by a constant $\Lambda^-_{\max} = -\ln\gamma$.

### 1.4.3 Transversal Cantor structure and Kaplan-Yorke dimension

As seen from considered examples, essential attribute of the chaotic attractors is intrinsic Cantor-like transversal structure provided by the repetitive transformations of stretching, folding, and transversal compression for the phase space volume. For quantitative characterization of this structure, one has to use *the fractal dimension*. The main idea of the definition is that a number of elements of size $\varepsilon$ needed to cover the set grows with decrease of $\varepsilon$ according to the power law $N \sim \varepsilon^{-D}$, where $D$ is the dimension. It generalizes the familiar notion of dimension (1 for curves, 2 for surfaces, 3 for volumes); for such non-trivial sets as the strange attractors, it is usually a non-integer number. (See Appendix D for more details.) In due time, a formula was proposed to expresses the fractal dimension via the Lyapunov exponents (Kaplan and Yorke, 1979):

$$D_{KY} = m + S_m / |\lambda_{m+1}|\,, \quad S_m = \sum_{i=1}^{m} \lambda_i. \tag{1.10}$$

Here the Lyapunov exponents $\lambda_1, \ldots, \lambda_m, \ldots, \lambda_N$ are enumerated in decreasing order, and $m$ is such an integer that the sum $S_m$ is positive while $S_{m+1}$ is already negative. Empirically, this formula yields good results, remarkably close usually to correct dimensions of attractors. However, mathematically it is proved only for the case of attractors of two-dimensional maps. Then, as Solomon's solution, the scientific community used to regard the estimate (1.10) as a special kind of dimension called the *Kaplan-Yorke dimension*, or *Lyapunov dimension*. Great practical advantage of this dimension is simplicity of its evaluation, since it requires only the spectrum of Lyapunov exponents of the attractor.

Derivation of formula (1.10) explained in Appendix D is based on assumption of uniform contraction and expansion of phase space volume in the course of the dynamical evolution. This is precisely what occurs in a neighborhood of a uniformly hyperbolic attractor along the stable and unstable manifolds, respectively. Hence, we can assume that this formula has the most reliable foundation especially for the class of uniformly hyperbolic attractors, and it will be used widely in this book for operative estimates of their dimensions.

### 1.4.4 Markov partition and symbolic dynamics

Due to intrinsic structure formed by stable and unstable manifolds in a neighborhood of the uniformly hyperbolic attractor, it appears possible to construct a *partition* of a domain containing the attractor by *a finite number of non-overlapping connected sub-domains*, *whose boundaries follow the curves or surfaces corresponding to these manifolds*. Under some conditions (particularly, the images of boundaries coinciding with the stable manifolds under action of the mapping must fall back precisely on the boundaries of the same nature), it is called the *Markov partition* and can be used for complete description of the trajectories belonging to the attractor in terms of *symbolic dynamics* (Hasselblatt and Young, 2005; Sinai, 1979; Anosov et al., 1995; Katok and Hasselblatt, 1995; Hasselblatt and Katok, 2003; Devaney, 2003). Denoting each element of the partition with a certain symbol, a letter of the finite alphabet, a trajectory is encoded by these characters written in a string in order of visiting respective elements of the partition by this trajectory. For concrete attractors, these sequences may be subjected to certain restrictions, "the rules of grammar", which may be visualized by means of respective graph with a finite number of vertices and directed edges. The graph is represented formally by an *adjacency matrix* whose elements are zeros and ones. A unit at the position $(i, j)$ indicates the presence of a directed edge connecting the $i$-th and the $j$-th vertices of the graph, and zero means the absence of such an allowed transition.

Figure 1.14 illustrates the Markov partitions for the Smale-Williams attractor and for the attractor of Plykin type. Also, the respective graphs are drawn, which specify the grammar rules. In the first case the configuration is rather evident: one segment of the border between the partition elements is a plane cross-section mapped to itself; the other segment is a plane cross-section mapped to the first one. In the case of Plykin type attractor the border between the partition elements consists of a vertical line, which coincides with the stable manifold of the saddle-fixed point $R$

belonging to the attractor, and segments mapped to that vertical line by iteration of the map.

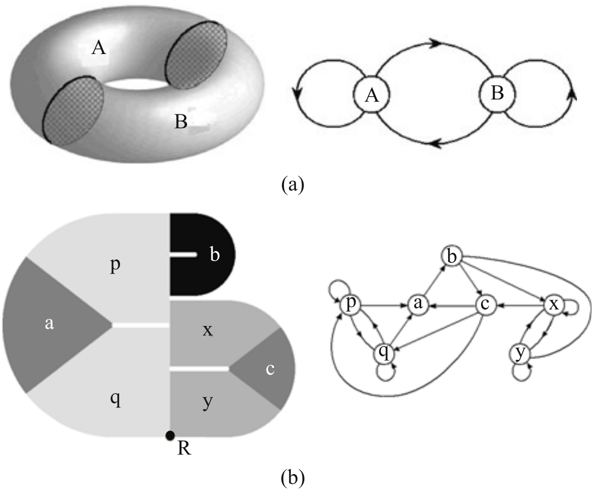


**Fig. 1.14** Markov partitions and graphs determining the allowed transitions for the attractor of Smale-Williams **(a)** and for the Plykin type attractor **(b)**. In the last case the border separating the partition elements is represented by the stable manifold of the saddle-fixed point R.

As seen, the structure of these graphs implies presence of transitions from each vertex to any other along the directed edges in a finite number of steps. Moreover there are vertices emitting more than one edge.[7] The last means that constructing a symbolic sequence we can select a transition from such vertex randomly from the allowed alternatives. Any code built in such a way will correspond to an orbit on the attractor with some definite initial conditions. It will manifest chaotic behavior visiting the elements of the partition in accordance with the prescribed code. It may be interpreted as the *Markov chain* (Feller, 1968), a random process with discrete time and finite number of states that correspond to the symbols of the alphabet. It justifies the term "Markov partition".

### *1.4.5 Enumerating of orbits and topological entropy*

The set of trajectories belonging to a hyperbolic attractor is in one-to-one correspondence with the set of all possible infinite sequences composed of symbols of the finite alphabet with certain grammar rules. It has the cardinality of continuum. The

[7] Adjacency matrix in this case has a property of *transitivity*. It means that for some power of this matrix all elements are nonzero. This is the case of the attractor having a single transitive component.

set of periodic orbits on the attractor corresponds to periodic symbolic sequences and has the cardinality of an infinite countable set. With the increase of period $T$ the number of periodic orbits of $N$ grows exponentially as $N \sim e^{hT}$. The characteristic index $h$ is called *the topological entropy* (Adler et al., 1965; Beck and Schlogl, 1993). It is interpreted as a quantity characterizing complexity of the set of orbits on the attractor.

It is clear that the possibility of complete symbolic description of trajectories on a uniformly hyperbolic attractor sustains a fundamental relationship of this issue with the information theory and coding theory. This may be of importance from the point of view of possible exploitation of systems with the uniformly hyperbolic attractors in information and communication applications.

### *1.4.6 Structural stability*

Structural stability of a uniformly hyperbolic attractor occurs due to the fact that the expansions and contractions of elements of phase volume always take place in directions, which have a non-zero angle between them (Smale, 1967; Williams, 1974; Sinai, 1979; Eckmann and Ruelle, 1985; Anosov et al., 1995; Katok and Hasselblatt, 1995; Shilnikov, 1997; Guckenheimer and Holmes, 1983; Afraimovich and Hsu, 2003; Devaney, 2003; Hasselblatt and Young, 2005). In terms of stable and unstable manifolds, it corresponds to their transversal (without touch) relative position at the intersections. If you slightly vary parameters, or functions used in the definition of the evolution operator, then, due to the transversal intersection of the manifolds, this perturbation does not destroy the associated topology of the phase space structure, at least while the perturbation is not too large. The same relates to a set of curves and surfaces used in the construction of Markov partitions. It means that the symbolic dynamics remains unchanged.

A more accurate formulation is as follows: While the considered perturbations are small in the class of continuous functions with first derivatives (of class $\mathrm{C}^1$), the system allows reduction to the original form by a homeomorphism that is a continuous invertible change of variables (of class $\mathrm{C}^0$), with the reversal variable change being continuous too. In other words, the perturbed system is topologically equivalent to the original one.

The Lyapunov exponents are obtained from the variation equations derived by linearization of the original equations near the reference trajectory, which implies the use of operation of differentiation. Therefore, under the change of variables, which may be not smooth, the Lyapunov exponents, generally speaking, are not invariant. Yet, due to the structural stability, with respect to their behavior under small variations of the system one can draw certain conclusions. Until the attractor remains uniformly hyperbolic, retaining the intrinsic topological structure of stable and unstable manifolds, the number of positive and negative exponents can not be changed. Moreover, those and others definitely remain distant from zero (we speak about maps here). Apparently, even stronger statement has to be valid that for a small variation of the system, at least the positive Lyapunov exponent also varies weakly. This assertion is confirmed by numerical data for models with uniformly hyperbolic attractors, discussed in subsequent chapters, but a mathematical result, to which in this context one could refer, is unknown to the author.

### *1.4.7 Invariant measure of Sinai-Ruelle-Bowen*

For the uniformly hyperbolic attractors there exists *an absolutely continuous invariant measure of Sinai-Ruelle-Bowen* (Sinai, 1972; Bowen, 1975; Ruelle, 1976). An abbreviation, *the SRB-measure*, is commonly used.

Let us turn again to interpretation of the dynamics as evolution of the cloud of representative points in the phase space. Assuming that initially the ensemble is characterized by a "good" distribution function (continuous and decreasing rapidly on the sides), let us ask, what will be the nature of the distribution at large times? It is easy to see that even in the simplest cases the arising distributions are singular; for example, for a stable attractive fixed point we have in the limit $t \to \infty$ a distribution represented by the Dirac delta function. A generalization embracing both smooth and singular distributions is delivered by a mathematical construct called a *measure*. This may be regarded as a generalization of familiar notions of length, area, and volume, which relate to simple one-, two-, and three-dimensional objects. In the context of dynamical systems, to define a measure means to prescribe non-negative numbers to subsets of phase space (not to any subset, but to those belonging to a sufficiently rich class of measurable subsets), which satisfy some natural requirements, say, a union of disjoint measurable sets must have a measure equal to the sum of the measures of its elements.

Let us consider a phase trajectory on the attractor and agree to prescribe to a domain of the phase space a measure equal to the relative duration of residence of the representative point in this domain as the observation time tends to infinity. It is called *the natural invariant measure*. For uniformly hyperbolic attractors a measure defined in such a way for any typical orbit relating to the attractor appears to be one and the same, and is called a measure *of Sinai-Ruelle-Bowen*. This measure may be thought of as a distribution of the phase fluid on the fibers of the attractor, i.e. along the unstable manifolds. Although across the structure of the fibers the distribution is of singular nature, it is described by a continuous function of coordinate measured along each fiber. In other words, the phase fluid substance is distributed on the fibers in a smooth manner, without pronounced local concentrations.

One more remark concerns relation of the Sinai-Ruelle-Bowen measure to systems subjected by noise.

In the presence of noise, instead of singular distributions we get the smooth ones, say, near a stable fixed point, instead of the Dirac delta function we will observe a finite-width Gauss-like distribution. Now, the assertion is that the distributions arising in systems with uniformly hyperbolic attractors under effect of small noise, in the limit of zero intensity of the noise tend precisely to those associated with the

Sinai-Ruelle-Bowen measures. So, these measures may be regarded as physically relevant.

### 1.4.8 Shadowing and effect of noise

The trajectories on uniformly hyperbolic attractors possess a remarkable property of *shadowing* (Guckenheimer and Holmes, 1983; Katok and Hasselblatt, 1995; Palmer, 2009). It refers to relationship between a true trajectory on the attractor and an approximate obtained, say, in the presence of small noise of bounded magnitude, or in computations with round-off at finite accuracy. The true orbit *shadows* a noisy trajectory in the sense that it remains close to it for arbitrarily long time. For the dynamics in the presence of noise this result was proven in due time by Kiefer (Kiefer, 1974). It shows that the stochastic behavior of dynamical origin is dominating in a sense over the stochastic motion caused by small random external force.

### 1.4.9 Ergodicity and mixing

Motion on a uniformly hyperbolic attractor (with one transitive component) is characterized by the properties of *ergodicity* and *mixing* (Sinai, 1979; Eckmann and Ruelle, 1985; Anosov et al., 1995; Katok and Hasselblatt, 1995; Shilnikov, 1997; Guckenheimer and Holmes, 1983; Afraimovich and Hsu, 2003; Devaney, 2003; Hasselblatt and Young, 2005). Ergodicity means that a typical trajectory on the attractor visits during the time evolution any neighborhood of any point on the attractor. It corresponds to equivalence of averaging over time and averaging over invariant measure and provides a statistical approach to the analysis of sustained regimes of dynamics. The mixing property is stronger. It means that for any element of phase volume for a sufficiently long time the corresponding cloud of representative points will be distributed throughout the attractor. The mixing allows describing statistically the process of approach of the ensemble to a state corresponding to the invariant distribution. The property of mixing is also associated with decay of correlations: the correlation function, calculated for the signal generated by dynamics of the discrete-time system on a uniformly hyperbolic attractor, is characterized by exponential decay. For continuous-time systems representing suspension of diffeomorphisms with uniformly hyperbolic attractors, the question of mixing and decay of correlations requires a special analysis in each case, as it depends on the nature of the distribution for times of returns to the Poincaré section.

### 1.4.10 Kolmogorov-Sinai entropy

Consider a set of all "words" occurring in symbolic representations of trajectories on the attractor and containing $n$ characters. For each $i$-th word one can determine a probability of its occurrence $p_i$. This value can be interpreted as a measure of Sinai-Ruelle-Bowen for a set of points in phase space, which correspond to the trajectory, having visited the elements of the Markov partition marked with the respective symbols in the previous $n$ steps. Now, let us define a sum $S_n = \sum p_i \log p_i$ over all words admissible by the grammar, divide it by $n$, and consider the limit $n \to \infty$. The quantity $h_{KS} = -\lim_{n\to\infty} S_n/n$ is called the *metric entropy* or *entropy of Kolmogorov-Sinai* (Kolmogorov, 1959; Sinai, 1959). As seen from the definition, it can be interpreted as amount of information generated by the dynamics on the attractor per unit of time. What is essential, the definition is appealing to an invariant measure associated with the attractor.

Positive metric entropy is a criterion of chaotic nature of the dynamics on the attractor. The metric entropy $h_{KS}$ and the topological entropy $h$ are related with an inequality $h \geqslant h_{KS}$. The result proved by Pesin relates spectrum of Lyapunov exponents and the Kolmogorov-Sinai entropy (Pesin, 1977). In general case, a sum of all positive Lyapunov exponents is the upper estimate for the metric entropy. For the uniformly hyperbolic attractors, the case of equality holds in the Pesin formula.

## References

Adler, R.L., Konheim, A.G., McAndrew, M.H.: Topological entropy. Trans. Amer. Math. Soc. **114**, 309–319 (1965).

Afraimovich, V., Hsu, S.-B.: Lectures on Chaotic Dynamical Systems. International Press, Somerville, MA (2003).

Andronov, A., Pontrjagin, L.: Systèmes Grossiers. Dokl. Akad. Nauk. SSSR **14**, 247–251 (1937).

Andronov, A.A., Vitt, A.A., Khaĭkin, S.Ė: Theory of oscillators. Pergamon Press (1966).

Anishchenko, V.S.: Nonlinear Dynamics of Chaotic and Stochastic Systems: Tutorial and Modern Developments. Springer, Heidelberg (2002).

Anishchenko, V.S., Astakhov, V., Vadivasova, T., Neiman, A., Schimansky-Geier, L.: Nonlinear Dynamics of Chaotic and Stochastic Systems. Tutorial and Modern Development. Springer, Berlin, Heidelberg (2007).

Anosov, D.V.: Geodesic flows on closed Riemannian manifolds of negative curvature. Trudy Mat. Inst. Steklov **90**, 3–210 (1967).

Anosov, D.V., Gould, G.G., Aranson, S.K., Grines, V.Z., Plykin, R.V., Safonov, A.V., Sataev, E.A., Shlyachkov, S.V., Solodov, V.V., Starkov, A.N., Stepin, A.M.: Dynamical Systems IX: Dynamical Systems with Hyperbolic Behaviour (Encyclopaedia of Mathematical Sciences) (v. 9). Springer, New York (1995).

Arnold, V.I.: Ordinary Differential Equations. The MIT Press, Somerville, MA (1978).

Arnold, V.I.: Mathematical Methods of Classical Mechanics. Springer-Verlag, Heidelberg (1989).

Arnold, V.I., Avez, A.: Ergodic Problems in Classical Mechanics. Benjamin, New York (1968).

Barreira, L, Pesin, Y.: Lectures on Lyapunov exponents and smooth ergodic theory. In: Smooth Ergodic Theory and Its Applications. Proceedings of Symposia in Pure Mathematics, pp. 3–90. AMS (2001).

Beck, C., Schlogl, F.: Thermodynamics of Chaotic Systems**:** An Introduction. Cambridge University Press, Cambridge (1993).
Benettin, G., Galgani, L., Giorgilli, A., Strelcyn, J.-M.: Lyapunov characteristic exponents for smooth dynamical systems and for Hamiltonian systems: A method for computing all of them. Meccanica **15**, 9–30 (1980).
Birkhoff, G.D.: Dynamical Systems. American Mathematical Society, Provindence RI (1927).
Bonatti, C., Diaz, L.J., Viana, M.: Dynamics Beyond Uniform Hyperbolicity. A Global Geometric and Probobalistic Perspective. Encyclopedia of Mathematical Sciences. Vol.102. Springer, Berlin, Heidelberg, New York (2005).
Bowen R.: Equilibrium States and Ergodic Theory of Anosov Diffeomorphisms. Lecture Notes in Math. 470**,** Springer, Heidelberg (1975).
Coudene, Y.: Pictures of hyperbolic dynamical systems. Notices of the American Mathematical Society **53**, 8–13 (2006).
Devaney, R.L.: An Introduction to Chaotic Dynamical Systems. Westview Press, New York (2003).
Eckmann, J.-P., Ruelle, D.: Ergodic theory of chaos and strange attractors. Rev. Mod. Phys. **57**, 617–656 (1985).
Feller, W.: An Introduction to Probability Theory and Its Applications **1**. Wiley, New York (1968).
Greene, J.M., Kim, J.-S.: The calculation of Lyapunov spectra. Physica D **24**, 213–225 (1987).
Grines, V.Z., Zhuzhoma, E.V.: Expanding attractors. Regular and Chaotic Dynamics **11** (2), 225–246 (2006).
Guckenheimer, J., Holmes, P.: Nonlinear Oscillations, Dynamical Systems, and Bifurcations of Vector Fields. Springer-Verlag, New York (1983).
Hasselblatt, B., Katok, A.A.: First Course in Dynamics: with a Panorama of Recent Developments. Cambridge University Press, Cambridge (2003).
Hasselblatt, B., Pesin, Y., Schmeling, J.: Pointwise Hyperbolicity Implies Uniform Hyperbolicity. Preprint ESI 2067, Vienna (2008).
Hasselblatt, B., Young, L.S.: Anosov and axiom a systems. In: Scott, A.(ed) Encyclopedia of Nonlinear Science, pp. 11–13. Routledge, New York (2005).
Hénon, M.: A two-dimensional mapping with a strange attractor. Commun. Math. Phys. **50**, 69–77 (1976).
Hilborn, R.C.: Chaos and Nonlinear Dynamics. Oxford University Press, Cambridge (2000).
Kaplan, J.L., Yorke, J.A.: A chaotic behavior of multi-dimensional differential equations. In: Peitgen, H.-O. and Walther, H.-O. (eds.) Functional Differential Equations and Approximations of Fixed Points. Lecture Notes in Mathematics, **730**, pp. 204–227. Springer, Berlin, New York (1979).
Katok, A., Hasselblatt, B.: Introduction to the Modern Theory of Dynamical Systems. Cambridge University Press, Cambridge (1995).
Kifer, Yu.I.: On small random perturbations of some smooth dynamical systems. Math. USSR Ivestija **8**, 1083–1107 (1974).
Kolmogorov, A.N.: Entropy per unit time as a metric invariant of automorphism. Doklady Acad. Sci. SSSR **124**, 754–755 (1959).
Kuznetsov, Yu.A.: Elements of Applied Bifurcation Theory. Springer, New York, Berlin, Heidelberg (1998).
Landau, L.D., Lifshitz, E.M.: Mechanics (Course of Theoretical Physics, vol.1). Butterworth-Heinemann , Oxford (1976).
Manneville, P.: Dissipative structures and weak turbulence. In: Chaos — The Interplay Between Stochastic and Deterministic Behaviour. Lecture Notes in Physics **457**, 257–272 (1995).
Milnor, J.: On the concept of attractor. Communications in Mathematical Physics, **99**, 177–195 (1985).
Newhouse, S.E.: The abundance of wild hyperbolic sets and non-smooth stable sets for diffeomorphisms. Publications Mathématiques de L'IHÉS **50**, 101–151 (1979).
Oseledets, V.I.: A multiplicative ergodic theorem: Lyapunov characteristic numbers for dynamical systems. Trans. Moscow Math. Soc. **19**, 197–231 (1968).
Ott, E.: Chaos in dynamical systems. Cambridge University Press, Cambridge (2002).

Palis, J.: On Morse-Smale dynamical systems. Topology **8,** 385–405 (1969).
Palmer, K. J.: Shadowing lemma for flows. Scholarpedia **4**(4), 7918 (2009).
Pesin, Y.B.: Characteristic Lyapunov exponents and smooth ergodic theory. Russian Math. Surveys **32**, 55–114 (1977).
Pesin, Ya.: Existence and genericity problems for dynamical systems with nonzero Lyapunov exponents. Regular and Chaotic Dynamics **12**, 476–489 (2007).
Pesin, Ya.B.: Lectures on Partial Hyperbolicity and Stable Ergodicity. Zurich lectures in advanced mathematics. European Mathematical Society (2004).
Plykin, R.V.: Sources and sinks of A-diffeomorphisms of surfaces. Math. USSR Sb. **23**, 233–253 (1974).
Rabinovich, M.I., Trubetskov, D.I.: Oscillations and Waves: In Linear and Nonlinear Systems, Kluwer Academic Publication, The Netherlands (1989).
Raghunathan, M.S. A proof of Oseledec's multiplicative ergodic theorem. Israel Journal of Mathematics **32** (4), 356–362 (1979)
Ruelle, D.: A measure associated with Axiom A attractors. Amer. J. Math. **98**, 619–654 (1976).
Ruelle, D., Takens, F.: On the nature of turbulence Commun. Math. Phys. **20**, 167–192 (1971).
Sagdeev, R.Z., Usikov, D.A., Zaslavsky, G.M.: Nonlinear physics: from the pendulum to turbulence and chaos. CRC Press, Boca Raton, FLA (1988).
Schuster, H.G., Just, W. Deterministic Chaos: An Introduction. Wiley-VCH Verlag GmbH & Co. KGaA, Weinheim, FRG (2005) .
Shilnikov, L.: Mathematical problems of nonlinear dynamics: a tutorial. Int. J. of Bifurcation and Chaos **7**, 1353–2001 (1997).
Shilnikov, L.P., Shilnikov, A.L., Turaev, D.V., Chua, L.O.: Methods of Qualitative Theory in Nonlinear Dynamics (Part 1). World Scientific, Singapore (1998).
Shilnikov, A.L., Turaev, D.V., Chua, L.O., Shilnikov, L.P.: Methods of Qualitative Theory in Nonlinear Dynamics (Part 2). World Scientific, Singapore (2002).
Sinai, Y.G.: On the Notion of Entropy of a Dynamical System. Doklady Acad. Sci. SSSR **124**, 768–771 (1959).
Sinai, Y.G.: Gibbs measures in ergodic theory. Russ. Math. Surv. **27**, 21–70 (1972).
Sinai, Y.G.: Stochasticity of dynamical systems. In: Gaponov-Grekhov, A.V. (ed.) Nolinear waves, pp.192–212. Moscow, Nauka (1979).
Schuster, H.G. and Just, W. Deterministic chaos: an introduction. Wiley-VCH (2005).
Smale, S.: Differentiable dynamical systems. Bull. Amer. Math. Soc. (NS) **73**, 747–817 (1967).
Strogatz, S.H.: Nonlinear Dynamics and Chaos: with Applications to Physics, Biology, Chemistry, and Engineering. Westview Press, MA (2001).
Tél, T. and Gruiz, M.: Chaotic dynamics: an Introduction Based on Classical Mechanics. Cambridge University Press, Cambridge (2006).
Thompson, J.M.T., Stewart, H.B.: Nonlinear Dynamics and Chaos. Wiley, New York (1986).
Vul, E.B., Sinai, Y.G., Khanin, K.M.: Feigenbaum universality and the thermodynamic formalism. Russ. Math. Surv. **39**, 1–40 (1984).
Williams, R.F.: Expanding attractors. Publications mathématiques de l'I.H.É.S. **43**, 169–203 (1974).
Zhirov, A.Yu.: Hyperbolic attractors of diffeomorphisms of orientable surfaces. Russ. Ac. Sci. Sb. Math. **83**, 23–66 (1995).

# Chapter 2
# Possible Occurrence of Hyperbolic Attractors

**Abstract** In this chapter we review some situations considered or mentioned in literature that may have relation to occurrence of uniformly hyperbolic attractors in dynamical systems represented by maps or differential equations. To date, the approaches under discussion are developed to different extents. Only few of them are elaborated up to such degree that may allow illustrating on a level of numerical computations. Nevertheless, the collected material is of undoubted significance for prospects of search for real-world systems with uniformly hyperbolic attractors or design of physical and technical devices operating due to the presence of such attractors.

## 2.1 The Newhouse-Ruelle-Takens theorem and its relation to the uniformly hyperbolic attractors

In the early 1970's, Ruelle and Takens advanced their scenario of origin of turbulence. They argued that under variation of a control parameter (the dimensionless Reynolds number in hydrodynamics) the transition to chaos happens after birth of a relatively small number of oscillatory components and is associated with emergence of a strange attractor (Ruelle and Takens, 1971). Detailed description and critical evaluation of this concept go far beyond the scope of the present review. However, it is worth emphasizing that Ruelle and Takens in their formulations meant specifically and definitely a uniformly hyperbolic attractor (not a strange attractor in a broad sense, as this term is commonly adopted now). So, it is interesting to ask to what extent their argumentation can be useful for design of concrete examples of dynamical systems with such attractors.

The basic theorem of Newhouse, Ruelle and Takens (Newhouse et al., 1978) establishes a possibility of occurrence of chaotic uniformly hyperbolic attractors for autonomous differential equations obtained by arbitrarily small perturbations from equations for quasiperiodic motions on tori of dimension $n \geqslant 3$ or $n \geqslant 4$.

Here we concentrate on their intermediate result. The formulated theorem relates to three cases: for diffeomorphisms (i) on a two-dimensional compact manifold, (ii) on a two-dimensional torus, and (iii) on a compact manifold of dimension $m \geqslant 3$. In case (i) the theorem says that a map having a uniformly hyperbolic attractor can be obtained by a perturbation of the identity map with a variation arbitrarily small in the class of functions with first derivatives $C^1$. In case (ii) a similar assertion holds, but the perturbation is small in the class of functions with two derivatives $C^2$, and in case (iii) it relates to the class of infinitely differentiable functions $C^\infty$.

As a starting point for reasoning, the authors refer to existence of a two-dimensional map $\mathbf{F}(\mathbf{X})$, which has a uniformly hyperbolic chaotic attractor in some bounded domain. This map is supposed to allow representation as a composition of a large number of maps close to the identity map:

$$\mathbf{F}(\mathbf{X}) = \mathbf{F}^{(N-1)}_{1/N} \circ \mathbf{F}^{(N-2)}_{1/N} \circ \cdots \circ \mathbf{F}^{(0)}_{1/N}(\mathbf{X}). \tag{2.1}$$

Here $N$ is a large integer, and

$$\mathbf{F}^{(k)}_{1/N}(\mathbf{X}) = \mathbf{X} + N^{-1}\tilde{\mathbf{F}}^{(k)}_{1/N}(\mathbf{X}). \tag{2.2}$$

In case (i) the authors suggest to consider a ring area of width $2\pi/N$ partitioned into $N$ sectors (Fig. 2.1(a)). By a shift and rescaling, one can place the domain of localization of the attractor of $\mathbf{F}(\mathbf{X})$ in the sector $k$=0. Next, a mapping of the ring into itself is constructed to map each sector of number $k$ into the sector $k$+1. This map is obtained from $\mathbf{F}^{(k)}_{1/N}$ by means of smooth variable changes for images and pre-images, with rescaling by factor $N$. Besides this, certain conditions are provided to arrange smooth matching at the boundaries of the sectors. The resulting map possesses a uniformly hyperbolic attractor. Indeed, after $N$ iterations, an orbit starting from the sector $k$=0 after visiting all other sectors returns to the original one, and the respective composite mapping is equivalent to the initial map $\mathbf{F}$ (up to the variable change).

The map from the $k$-th to the $k$+1-th sector contains, besides the trivial part, an additive perturbation term, which after the rescaling looks like $N^{-2}\tilde{\mathbf{F}}^{(k)}_{1/N}(N\xi)$, where $\xi$ designates the state vector transformed by the variable change. The perturbation is of order $N^{-2}$, and its derivative is of order $N^{-1}$. Hence, by increase of $N$ one can make the perturbation arbitrarily small together with its derivative. So, the map defined on the ring becomes arbitrarily close to the identity in the class of functions $C^1$ as $N$ is large enough, while the $N$-fold composition is equivalent to the map $\mathbf{F}$ that has the uniformly hyperbolic attractor.

For case (ii) consider a surface of two-dimensional torus partitioned into $N = M^2$ areas, small "squares" (Fig. 2.1(b)). Again, let us design a map, which ensures an orbit to visit successively all the elements of the partition, in such a way that after bypassing of all the elements (that requires $M^2$ steps) the resulting transformation is equivalent to the map (2.1). Thus, we represent the map equivalent to $\mathbf{F}$ as a composition of $M^2$ mappings, which contain the additive perturbation terms expressed

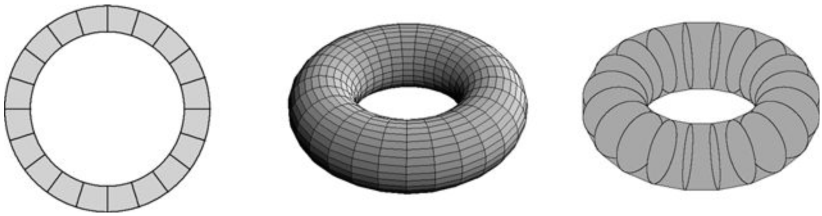

(a) (b) (c)

**Fig. 2.1** Geometric illustrations for constructions considered in cases (i), (ii), and (iii) of the theorem of Ruelle, Takens, and Newhouse; see the panels **(a)**, **(b)**, and **(c)**, respectively.

in the rescaled variables as $M^{-3}\tilde{\mathbf{F}}^{(k)}_{1/M^2}(M\xi)$, $k = 0, 1, \ldots, M^2 - 1$. The perturbation is of order $M^{-3}$, its first and second derivatives are of orders $M^{-2}$ and $M^{-1}$, respectively. Increasing $M$ we get the perturbation arbitrarily small in the class of functions $C^2$.

Finally, we turn to the situation (iii). Restricting discussion for simplicity with the three-dimensional case, $m$=3, let us consider a torus subdivided by cross-sections with meridianal planes into $N$ equal sectors (Fig. 2.1(c)). Assume that the dynamics along the azimuthal coordinate is governed by a one-dimensional map, which transforms each sector to the neighboring one. The map for the rest coordinates is supposed to be of form (2.1), where $\mathbf{X}$ specifies a position of the representative point in the transversal cross-section. Under $N$-fold application of the map an orbit arrives again in the original sector it started from, and the resulting mapping is equivalent to $\mathbf{F}$ in respect to variables associated with the coordinates in the transversal cross-section.

In the last case the rescaling of the dynamical variables is not needed, so, in the limit $N \to \infty$ the additive perturbation term $N^{-1}\tilde{\mathbf{F}}^{(k)}_{1/N}$ tends to zero together with all derivatives, i.e. becomes arbitrarily small in the class of functions $C^\infty$.

What can be said about potential application of the above considerations for practical design of physically realizable models with uniformly hyperbolic attractors? Certainly, such prospects seem very doubtful. As the reasoning starts from a given map with the uniformly hyperbolic attractor, it can not help, obviously, in finding out concrete examples of such maps. Moreover, the mathematical constructions, at least, in cases (i) and (ii), look absolutely non-physical, because of involvement of functions of extremely small characteristic scale in the phase space in the definitions of the dynamical systems.

## 2.2 Lorenz model and its modifications

One of the most famous systems in the context of nonlinear dynamics and chaos is the Lorenz model (Lorenz, 1963; Afraimovich et al., 1977; Sparrow, 1982; Guckenheimer and Holmes, 1983; Alligood et al., 1996; Ott, 2002; Schuster and Just, 2005)

$$\dot{x} = \sigma(y - x), \quad \dot{y} = rx - y - xz, \quad \dot{z} = -bz + xy. \tag{2.3}$$

Here $x$, $y$, $z$ are dynamical variables, and $\sigma, r, b$ are parameters. Such equations originate in the context of convection in the layer of fluid heated from bottom, in the theory of single-mode laser, in a model of water wheel, in the dissipative oscillator with inertial excitation and in some other problems.

In the work published in 1963 Lorenz reported observation of non-periodic sustained oscillations in the numerical solution of these equations, and interpreted these regimes as relating to the own complex dynamics of the system. Particularly, the author emphasized importance of sensitivity of the trajectories to small perturbations of initial conditions. Attractor of the Lorenz system is shown in Fig. 2.2. So far, due to deep and pervasive analysis made by many authors, the dynamical nature of chaos in the Lorenz model has been studied exhaustively. An important final advance in the long-term explorations is a computer-assisted proof published by Tucker (Tucker, 2002).

Historically, an important step in explaining many qualitative aspects of chaotic dynamics in the Lorenz model was a construction of a simplified model, the so-called *geometric Lorenz attractor* (Sparrow, 1982; Guckenheimer and Holmes, 1983) (Fig. 2.2(b)).

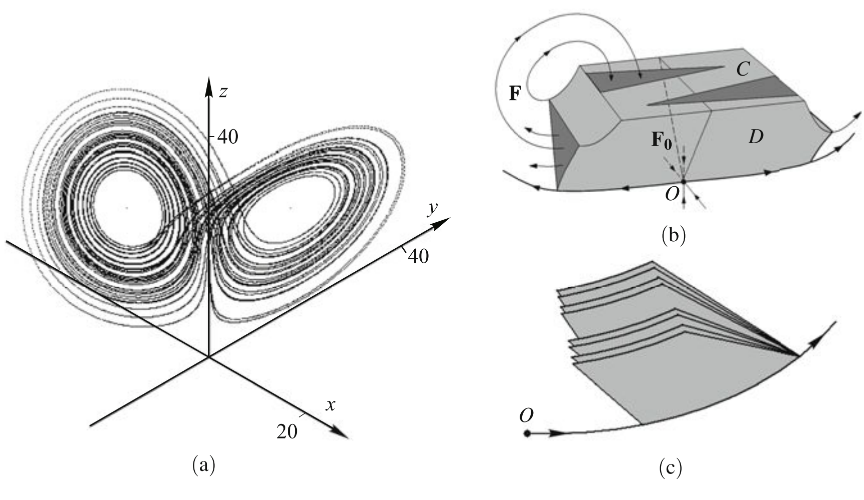


**Fig. 2.2** Portrait of the Lorenz attractor obtained from numerical solution of Eq. (2.3) at $r = 28$, $\sigma = 10$, $b = 8/3$ **(a)**, the geometric Lorenz model **(b)**, and illustration of the transverse structure of the attractor, the "Cantor book" **(c)**.

For organizing structure of the flow in the phase space of the Lorenz model a saddle fixed point $O$ at the origin is important. This point is characterized by one positive (unstable) and two negative (stable) eigenvalues of linearized equations that means it has one-dimensional unstable manifold and two-dimensional stable manifold. This point belongs to the attractor together with its one-dimensional unstable manifold. In domain $D$, shown in gray in Fig. 2.2(b), the flow is defined as that corresponding to linearization of the Lorenz system near the origin. By this flow $\mathbf{F}_0$ two halves of the "ceiling" $C$ of the domain $D$ are mapped to two curvilinear triangles on the sides of the domain. Further, by a flow defined in outside of $D$ by some field $\mathbf{F}$ these sides are transformed to two narrow elongated triangles inside the rectangle $C$. It corresponds to one step of the Poincaré map. In the Poincaré section the stretching is directed along these elongated triangles, and the compression takes place across them. The construction is built in such a way that the direction of the compression remains invariant under the action of the map. Attractor is not uniformly hyperbolic because of specific behavior of the trajectories near the singular orbit that is the unstable manifold of the point $O$. In the Poincaré cross-section the singular orbit corresponds to tips of the triangular regions. With decrease of distance from a certain trajectory to the singular one, the return time tends to infinity. The Cantor-like transversal structure of the attractor near the singular trajectory is arranged in a way illustrated in Fig. 2.2(c) that is the so-called "Cantor book". Attractor in the geometric model is classified as *quasi-hyperbolic* or *singular hyperbolic*. It does not possess structural stability in the usual sense. Markov partition can be constructed, but it requires an infinite alphabet. Following the Tucker result (Tucker, 2002), attractor in the original Lorenz equations (2.3) is of the same nature.

Now, we wonder whether it is possible to modify the system in such a way that it would have a uniformly hyperbolic attractor. A positive answer is given by Morales, though only on the level of the geometric constructions (Morales, 1996).

Let us turn to a model, in which the fixed point $O$ undergoes a kind of saddle-node bifurcation, and in other respects the system is similar to the geometric Lorenz model. In parameter range before the bifurcation, there is a pair of unstable fixed points. One of them is analogous to the fixed point in the Lorentz model and has one unstable and two stable directions, while the second fixed point has one stable and two unstable directions. As the parameter is varied, both fixed points move to meet each other at the bifurcation, and then annihilate. In the parameter range of coexistence of the pair of the fixed points the system has attractor of the Lorenz type. In the parameter range where the pair has disappeared, one of two options occurs, depending on the arrangement of the vector field in the remote parts of the phase space, through which the trajectory travels. The first variant is emergence of non-hyperbolic dynamics (somewhat like that in the Hénon map), and the second corresponds to appearance of attractor of Plykin type in the Poincaré map. In Fig. 2.3 the pictures in the Poincaré map are shown for the usual Lorenz attractor (a), and for the two cases indicated by Morales, (b) and (c). The last two are depicted for the dynamics arising after the bifurcation of merging and disappearance of the pair of the fixed points.

Possibility of occurrence of Plykin-type attractors in the modified Lorenz model seems interesting, and it may be significant for elaboration of physical examples, because the Lorenz model itself certainly has relation to a number of concrete systems

(a) (b) (c)

**Fig. 2.3** Qualitative illustrations of the action of the Poincaré map for the original geometric Lorenz attractor **(a)** and for the modified model in the work of Morales (**b** and **c**). The variant (b) corresponds to the emergent dynamics of Hénon type, and the variant (c) to the formation of the Plykin type attractor.

of different nature. However, so far no explicit examples of systems with uniformly hyperbolic chaos have been designed on this base.

## 2.3 Some maps with uniformly hyperbolic attractors

It is easy to write down a map possessing attractor of Smale-Williams type; it may be found in many textbooks (e.g. (Katok and Hasselblatt, 1995)). One can derive the map using variables $(\varphi, X, Y)$ of the following geometric sense. Let $X$ and $Y$ be Cartesian coordinates of a point in a meridianal plane section of a torus assuming $X^2 + Y^2 \leqslant 1$, and $\varphi$ is an angular coordinate specifying the given section. Coordinates in the three-dimensional phase space are expressed as

$$x = (R+X)\cos\varphi, \quad y = (R+X)\sin\varphi, \quad z = Y, \tag{2.4}$$

where $R$ is an additional parameter concretizing the geometry. Now, we define the map on one step of discrete time as

$$\varphi_{n+1} = 2\varphi_n, \quad X_{n+1} = \frac{3}{10}X_n + \frac{1}{2}\cos\varphi_n, \quad Y_{n+1} = \frac{3}{10}Y_n + \frac{1}{2}\sin\varphi_n.$$

It may be reformulated in terms of Cartesian coordinates $(x,y,z)$ as follows:

$$\begin{aligned}
x_{n+1} &= \left(\frac{7}{10}R + \frac{3}{10}\sqrt{x_n^2+y_n^2} + \frac{1}{2}\frac{x_n}{\sqrt{x_n^2+y_n^2}}\right)\frac{x_n^2-y_n^2}{x_n^2+y_n^2},\\
y_{n+1} &= \left(\frac{7}{10}R + \frac{3}{10}\sqrt{x_n^2+y_n^2} + \frac{1}{2}\frac{x_n}{\sqrt{x_n^2+y_n^2}}\right)\frac{2x_n y_n}{x_n^2+y_n^2},\\
z_{n+1} &= \frac{3}{10}z_n + \frac{1}{2}\frac{y_n}{\sqrt{x_n^2+y_n^2}}.
\end{aligned} \tag{2.5}$$

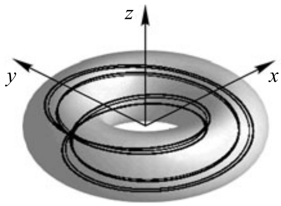


**Fig. 2.4** Portrait of attractor of Smale-Williams type obtained from iterations of the map (2.5) at $R = 2$ drawn on a background of the toroidal absorbing domain shown in gray.

Figure 2.4 shows a toroidal absorbing domain with a border expressed by the relation $X^2 + Y^2 = 1$ in the original variables, and portrait of the attractor obtained from iterations of the map (2.5) at $R = 2$. Observe visible transversal Cantor-like structure intrinsic to the Smale-Williams solenoid. The Lyapunov exponents for this attractor are $\Lambda_1 = \ln 2 = 0.6931\cdots$, $\Lambda_{2,3} = \ln(3/10) = -1.2039\cdots$, because one step of the iterations is accompanied by twofold stretch along the filaments of the attractor, i.e. along the angular coordinate $\varphi$, and by compression along two transversal directions by factor 3/10. The Kaplan-Yorke dimension of this attractor equals $D_{KY} = 1 + \Lambda_1/|\Lambda_2| \approx 1.576$.

Unfortunately, topologically this is *not* a kind of attractor that could occur in Poincaré maps of flow systems (Katok and Hasselblatt, 1995).

The geometric construction truly associated with the map (2.5) may be thought of as follows. Take a closed tube representing the surface of the torus, *cut it at some place by a meridianal plane*, then stretch the tube in length, compress it in width, fold in double loop, and *glue the edges* accurately at the place of the former cut (Ilyashenko, 2005).

If trying to perform the torus deformation continuously, without the cut (say, with a real rubber tube), one can observe that the tube inevitably undergoes additional azimuthal torsion. It means that we should glue the edges not directly, but with their relative rotation by the angle of $2\pi$. Hence, the map (2.5) is *not appropriate* as starting point for constructing physical flow systems suspending the Smale-Williams attractor, and alternative approaches must be developed.

Let us consider now an explicit example of a discrete-time system with DA-attractor on a torus (Kuznetsov, 2009). To start, we notice that the Arnold cat map (1.9) can be decomposed to two successively applied maps, which may be interpreted naturally as corresponding to two halves of a time step. Namely, if

$$p_{n+\frac{1}{2}} = p_n + q_n, \quad q_{n+\frac{1}{2}} = q_n, \tag{2.6}$$

and

$$p_{n+1} = p_{n+\frac{1}{2}}, \quad q_{n+1} = p_{n+\frac{1}{2}} + q_{n+\frac{1}{2}}, \tag{2.7}$$

then, on the whole step we get $p_{n+1} = p_n + q_n$, $q_{n+1} = p_n + 2q_n$. The symbols $\bmod 1$ are omitted for brevity.

As alternative to the Smale "surgery", let us perform the DA modification adding some analytical functions into the right-hand parts of (2.6) and (2.7). On the first half of the step the additional term is introduced in the first equation (2.6), as a function depending only on $x$. To preserve the fixed point in the origin, this function must be zero at $p$=0, and we assume the function to be odd. Then, as the dynamics takes place on the torus, it is natural to require this function to be of period 1 and represent it by the Fourier series. Accounting only the first and the second harmonics, we select their amplitudes in such a way that the function is as close to zero as possible at the middle of the unit interval; so, we select it as $\sin 2\pi p + \frac{1}{2}\sin 4\pi p$. On the second half-step analogous modification is performed in symmetric way by adding the function of $q$ in the second equation. Combining both half-steps, we arrive at the map

$$\begin{aligned}
p_{n+1} &= p_n + q_n + \varepsilon\left(\sin 2\pi p_n + \frac{1}{2}\sin 4\pi p_n\right)\Big/ 2\pi \ (\bmod 1), \\
q_{n+1} &= p_n + 2q_n + \varepsilon\left(\sin 2\pi p_n + \frac{1}{2}\sin 4\pi p_n + \sin 2\pi q_n\right. \\
&\quad \left. + \frac{1}{2}\sin 4\pi q_n\right)\Big/ 2\pi \ (\bmod 1).
\end{aligned} \tag{2.8}$$

Here $\varepsilon$ characterizes relative value of the added terms. The Jacobin matrix of the map (2.8)

$$\mathbf{M}(p,q) = \begin{pmatrix} 1+\varepsilon(\cos 2\pi p + \cos 4\pi p) & 1 \\ 1+\varepsilon(\cos 2\pi p + \cos 4\pi p) & 2+\varepsilon\cos 2\pi q + \varepsilon\cos 4\pi q \end{pmatrix} \tag{2.9}$$

has determinant strongly positive and detached from zero globally while $\varepsilon < \frac{8}{9}$. Hence, under this condition the mapping remains invertible (the diffeomorphism).

The map (2.8) has a fixed point in the origin, and for the matrix of linearization at this point $\mathbf{M}(0,0)$ the eigenvalues called the multipliers are

$$\mu_{1,2} = \frac{1}{2}(3+4\varepsilon) \pm \sqrt{\frac{5}{4} + 2\varepsilon}. \tag{2.10}$$

At $\varepsilon$=0 we have $\mu_1 = \frac{1}{2}(3+\sqrt{5}) > 1$ and $\mu_2 = \frac{1}{2}(3-\sqrt{5}) < 1$, that is a saddle. With increase of $\varepsilon$ both the multipliers grow, and the second one exceeds 1 at $\varepsilon > \varepsilon_1 = \frac{1}{2}$.

It corresponds to the situation that the fixed point accepts the properties required from the Smale surgery. So, we have to select $\frac{1}{2} < \varepsilon < \frac{8}{9}$.

Computations indicate that attractor of the map (2.8) is uniformly hyperbolic, e.g. at $\varepsilon = 0.7$. In Fig. 2.5 portraits of the attractor are shown in the unit square (a) and on the surface of torus (b). Observe transversal Cantor-like structure to the DA attractor. Lyapunov exponents computed by means of the Benettin algorithm are $\Lambda_1 = 0.9618, \Lambda_2 = -1.3445$. The largest exponent is close to $\ln \frac{3+\sqrt{5}}{2} \approx 0.9624$, the value associated with the Arnold cat map. Kaplan-Yorke dimension, respectively, is $D_{KY} = 1 + \Lambda_1/|\Lambda_2| \approx 1.715$.

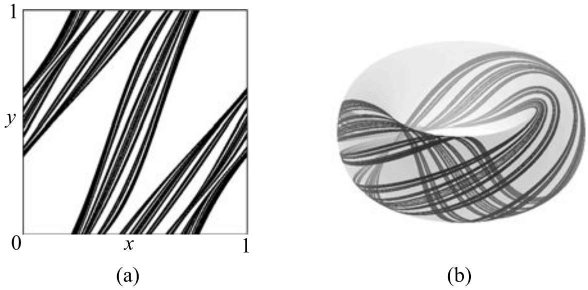


**Fig. 2.5** Attractor of the map (2.8) at $\varepsilon = 0.7$ depicted in the unit square (unfolding of torus) **(a)**, and in the torus surface **(b)**.

One more way to construct explicitly written maps with uniformly hyperbolic attractors was indicated by Lopez (Lopez, 1983). The author wonders what the degree of algebraic polynomials may be, representing a two-dimensional map with attractor of Plykin type. In fact, an example he has considered contains a function defined as a composition of polynomials of degree up to 9, and the result is represented by polynomials of very high order (over $10^5$). The author believes, however, that the lower limit of the order of polynomials defining the maps with the Plykin attractor is given by the number 7.

Regrettably, no one of the above examples indicates a straightforward way to construct continuous-time systems suspending the uniformly hyperbolic attractors.

## 2.4 From DA to the Plykin type attractor

It occurs that it is possible to come to a Plykin-type attractor on a plane or on a sphere departing from the DA-attractor of Smale (Katok and Hasselblatt, 1995; Hunt, 2000; Coudene, 2006). The initial step is introducing additional symmetry in such a way that the portrait of the attractor appears to be composed of four copies of the original version, as shown in Fig. 2.6 (left). To do so, in the map

$$p_{n+1} = p_n + q_n + f(p_n, q_n), \quad q_{n+1} = p_n + 2q_n + g(p_n, q_n), \tag{2.11}$$

obtained as result of the Smale surgery, we enlarge domain of definition in coordinates $(p, q)$ up to the square $2\times2$, and let this square represent the unfolding of the torus now. In other words, we regard $p$ and $q$ as variables defined modulo 2 while the functions $f$ and $g$ are evaluated in the same way as earlier, with the arguments defined modulo 1 (see Subsection 1.2.3). Next, let us perform consecutively the steps illustrated in Fig. 2.6. First, we take a top (or bottom) half of the square (a). Imaging the picture drawn on a transparent film, we fold it along the vertical middle line and glue along the left, top and bottom edges (b). Due to the symmetry, with such gluing the filaments of the attractor match accurately and correctly. Next, inflate the resulting square "envelope" like a balloon, and turn it into a sphere (c). Note that the corner singularities fall into the "holes", so, they are not relevant to the dynamics on the attractor. At this step we arrive at the Plykin type attractor on the sphere. Finally, by the variable change corresponding to the stereographic projection we obtain the attractor represented on the plane (e).

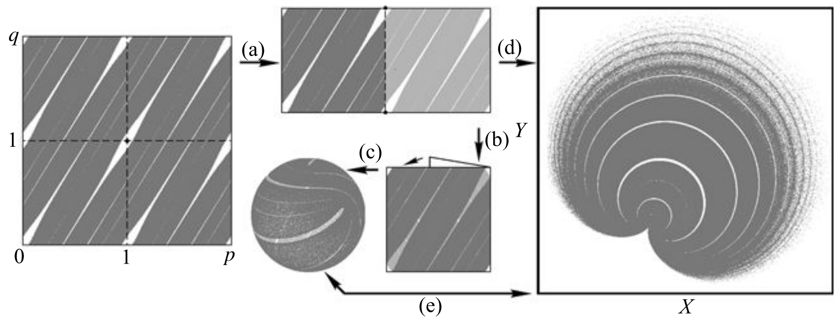


**Fig. 2.6** Transformations of the DA-attractor on a torus (left) to the Plykin attractor on a plane (left): **(a)** selecting of a rectangular that is the top half of the square $2 \times 2$; **(b)** double folding; **(c)** inflating the resulting "envelope" to the sphere; **(d)** transformation onto the plane with variable change involving the Weierstrass function; **(e)** mapping from the plane to the sphere or back by means of the stereographic projection.

Let us turn to more formal description. As the square $2\times2$ represents the unfolding of torus, the change of variables must be expressed by a function of complex variable $Z = p + iq$, with the fundamental periods of 2 and $2i$. As known, the doubly periodic analytic functions of complex variable relate to the class of elliptic functions (Abramowitz and Stegun, 1972; Akhiezer, 1990). Particularly, the Weierstrass function $\wp$ with the periods $2\omega_1$ and $2\omega_2$ is defined as

$$\wp(z) = z^{-2} + \sum_{\substack{m,n=-\infty \\ (m,n)\neq(0,0)}}^{\infty} \left[ (z - 2\omega_1 m - 2\omega_2 n)^{-2} - (2\omega_1 m + 2\omega_2 n)^{-2} \right]. \tag{2.12}$$

The evaluation of this function is inverse operation to the evaluation of the elliptic integral

$$z = \int_{\wp}^{\infty} \frac{dx}{\sqrt{4x^3 - g_2 x - g_3}}. \tag{2.13}$$

Here $g_2$ and $g_3$ are parameters called the invariants, and their values are selected to provide the required periods. Particularly, the half-periods $\omega_1 = 1$ and $\omega_2 = i$ are obtained at $g_2 = 11.817045$ and $g_3 = 0$.

The variable change

$$X + iY = \frac{2}{\sqrt{g_2}} \wp(p + iq) \tag{2.14}$$

transforms a bottom part of the square $2 \times 2$ to the plane $(X,Y)$. The fixed point in the origin is mapped to infinity, and three special points of the map (2.11) representing the period-three orbit $\cdots \to (0,1) \to (1,0) \to (1,1) \to \cdots$ are mapped, respectively, to $(-1,0)$, $(1,0)$ and $(0,0)$. In the new variables, the map formally may be written in analytical form as[1]

$$\begin{aligned}
X_{n+1} &= \frac{2}{\sqrt{g_2}} \mathrm{Re}\left[\wp((1+i)p + (1+2i)q + \varepsilon(1+i)f(p,q) + \varepsilon i f(p,q))\right], \\
Y_{n+1} &= \frac{2}{\sqrt{g_2}} \mathrm{Im}\left[\wp((1+i)p + (1+2i)q + \varepsilon(1+i)f(p,q) + \varepsilon i f(p,q))\right], \\
p = Re &\left[\wp^{-1}\left(\frac{\sqrt{g_2}}{2}(X_n + iY_n)\right)\right], \quad q = \mathrm{Im}\left[\wp^{-1}\left(\frac{\sqrt{g_2}}{2}(X_n + iY_n)\right)\right].
\end{aligned} \tag{2.15}$$

Here $\wp^{-1}$ designates the inverse for the Weierstrass function $\wp$. Surely, the analytical expression for the map is cumbersome. Practically, of course, it is much easier to perform the iteration in the variables $p$ and $q$, and convert them for graphical representation by the variable change (2.14). In Fig. 2.6 it corresponds to the step (d). Finally, by the variable change,

$$x + iy = 2\wp(Z)/(1 + |\wp(Z)|^2), \quad z = (1 - |\wp(Z)|^2)/(1 + |\wp(Z)|^2), \tag{2.16}$$

we may represent the picture in coordinates $x$, $y$, $z$ satisfying $x^2 + y^2 + z^2 = 1$ and consider the attractor as being placed on the sphere; this is the step (e) in Fig. 2.6.[2]

Perhaps, it is difficult to conclude the topological nature of the attractor from the portrait on the plane shown in Fig. 2.6 (right) because essential fine details are

---

[1] It should be noted that $\wp^{-1}$ is the double-valued function (as we regard the square $2 \times 2$ as the definition domain for $\wp$). For a given argument $Z = X + iY$ the function $\wp^{-1}$ defines two images, one in the top and other in the bottom part of the square $2 \times 2$, which are linked through the symmetry relations $(p,q) \leftrightarrow (2-p, 2-q)$. With an additional agreement not to distinguish such points, this peculiarity is not essential from the point of view of the dynamics of the system.

[2] Interestingly, the relation between the sphere and the torus exploited in the above reasoning has had an application in cartography. It lies in the basis of the so-called Guyou projection, through which the Earth surface is depicted in a rectangle with aspect ratio 2:1, or on a plane, as periodically reproduced pattern.

indistinguishable. Nevertheless, careful analysis indicates that this attractor is topologically equivalent to the Plykin type attractor drawn in Fig. 1.8.

Explicit design of a suspension for the obtained map with the Plykin type attractor is not trivial, as noticed in the PhD thesis of Hunt (Hunt, 2000). On the basis of this construction the problem was not resolved, but Hunt suggested an alternative approach for suspending the Plykin type attractor discussed in the next section.

The above considerations and the variable change (2.14) may be naturally applied to the map (2.8) as well; then we get an implicitly defined analytical map possessing the same kind of Plykin type attractor on the plane. Its portrait is shown in Fig. 2.7. Because of the use of the smooth variable change, the Lyapunov exponents and Kaplan-Yorke dimension of this attractor are the same as those for the DA-attractor of the map (2.8), namely, $\Lambda_1 = 0.9618, \Lambda_2 = -1.3445$, and $D_{KY} = 1.715$.

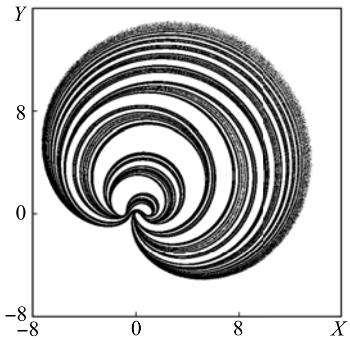


**Fig. 2.7** Attractor of Plykin type obtained by application of the approach discussed in the current section to the analytical map with DA attractor (2.8) by the variable change involving the Weierstrass function (2.14) at $\varepsilon = 0.7$.

## 2.5 Hunt's example: Suspending the Plykin type attractor

The Hunt model is a non-autonomous system governed by differential equations for two variables $x$ and $y$, with the right-hand parts depending on $x$, $y$, and the time variable $t$:

$$dx/dt = f_*(x,y,t), \quad dy/dt = g_*(x,y,t). \tag{2.17}$$

Here the functions $f_*$ and $g_*$ are continuously differentiable. They are assumed to be $2\pi$-periodic in respect to the argument $t$. Formal description and mathematical relations for computation of these functions are given in Appendix E.

Qualitatively the evolution rule constructed by Hunt is explained in Fig. 2.8. Panel (a) shows the initial configuration of the absorbing domain $U$, which consists of three sub-domains $U_i$. In each of them special curvilinear coordinates

$(r, \theta)^i (i = 1, 2, 3)$ are defined; the respective families of the coordinate lines are shown. Filled small black circles on the panel (a) indicate positions of the origins for the curvilinear coordinates.

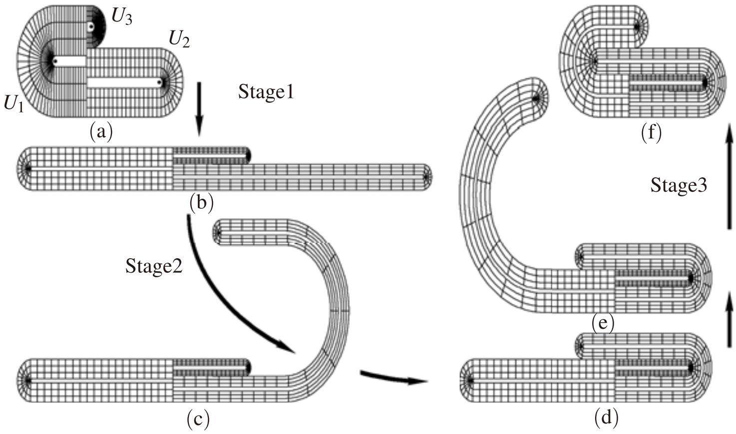


**Fig. 2.8** Evolution of the domain $U = U_1 \cup U_2 \cup U_3$ in time for one period $\Delta t = 2\pi$ for the Hunt model.

The cloud of representative points from the domain $U$ evolves in time as shown in the figure. On one time period $2\pi$ the dynamics consists of three consecutive stages, with each duration $2\pi/3$. At the first stage, the domain $U$ undergoes vertical compression and horizontal extension (see panel (b)). More accurately, compressing takes place along the coordinate lines of the curvilinear coordinate system $\theta = \text{const}$, and stretching along the lines $r = \text{const}$. In the second stage, the right-hand sub-domain $U_2$ smoothly bends up, left, and down (c), so that finally it is placed along the border of the domain $U_3$ (d). At the third stage, the left-hand sub-domain $U_1$ undergoes similar deformations, bending up, right, and down (e). The result is that its lower border is placed on the edge of the domain $U_2$ transformed in the previous stage (see panel (f)). The whole area takes the form of the original domain. Moreover, the coordinate lines in their new positions run along the lines of the original coordinates.

The described process of continuous deformation represents, say, the main content of the dynamics. Besides, the model includes some additional adjustments, by which the origins of the curvilinear coordinates become repelling, and the transverse compression of the figure is stronger, with the result that the transformed domain appears to be inside the original one. These adjustments are characterized by some parameter $\varepsilon$ (see details in the Appendix E). Additionally, relations are formulated for definition of the vector field $(f_*(x,y,t), g_*(x,y,t))$ outside the evolving domain $U(t)$.

Formal definition of the Hunt model is complicated and cumbersome, so it seems very doubtful that such a construction may be designed as a real physical device. In

Ref. (Aidarova and Kuznetsov, 2009) this model was used for tests of computational methods applicable to analysis of dynamics of hyperbolic attractors. Results of computer simulations were presented and discussed, and a technical error in the computer program in Hunt's work was noticed and corrected.

Figure 2.9 shows plots for observables $x$ and $y$ versus time, as obtained from numerical solution of the equations for the Hunt model. Irregular behavior of these curves indicates the chaotic nature of dynamics. The dependencies are characterized by the presence of matched parts of distinct behavior: the horizontal plateaus and sharp bursts. This is so due to specific nature of the Hunt model dynamics evolving on each period $2\pi$ in the consecutive three stages.

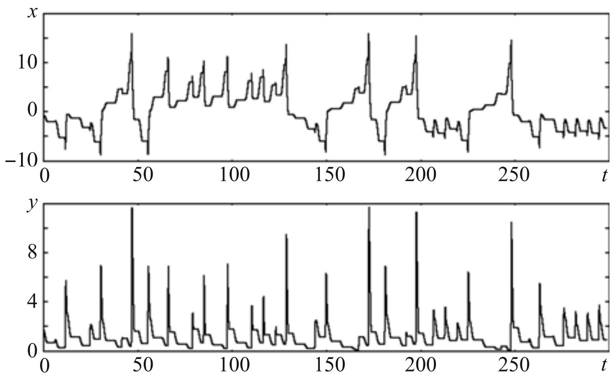


**Fig. 2.9** Dynamical variables $x$ and $y$ versus time in the Hunt model, $\varepsilon = 0.17$.

Portraits of the attractor in the Hunt model are shown in Fig. 2.10. Panel (a) depicts the attractor in the extended phase space. Panel (b) shows the same attractor in the projection on the plane $(x, y)$. Like the Lorenz attractor, it is composed of two "wings of a butterfly", which, however, are asymmetrical. For their formation, the second and third stages of the dynamics of the Hunt model are responsible, which include the deformations with rotations of the lateral sub-domains. Finally, the panel (c) shows the portrait of the attractor in the Poincaré section.

Clearly visible are the first few levels of the transverse fractal structure: the object is built of strips, each of which contains strips of the next level, and so on. The same object can be seen in the diagram (a) in the top plane cross-section of the figure. In accordance with Hunt's construction of the evolution rule, this attractor corresponds to the Plykin-type attractor shown in Fig. 2.10.

Because of complexity of the formal definition of the model, for computation of the Lyapunov exponents a version of the Benettin algorithm was applied basing on numerical integration of the differential equations along neighboring phase trajectories instead of the use of equations in variations. Namely, three sets of Equations (2.17) are integrated. One corresponds to the reference trajectory, and the other two correspond to close orbits, with fixed initial norm of the perturbation vector $\sqrt{(x_i - x_0)^2 + (y_i - y_0)^2} = \varepsilon_0 \ll 1$, $i$=1, 2. After each time interval of duration $2\pi$ the program performs orthogonalization of the vectors with the Gram-Schmidt process

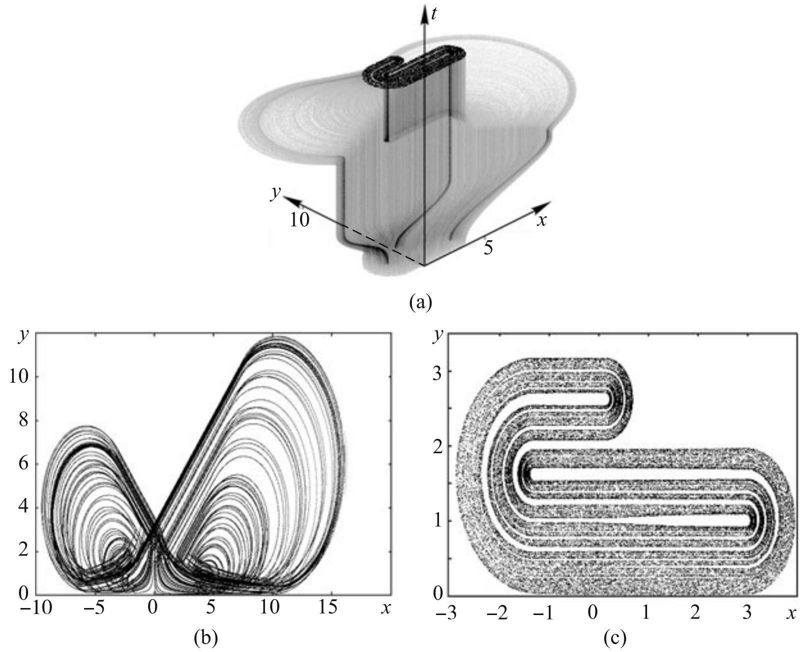


**Fig. 2.10** Attractor of the Hunt model in the extended phase space **(a)**, in projection on the plane of dynamical variables $x$ and $y$ **(b)**, and in the Poincaré cross-section **(c)**; the parameter value is $\varepsilon = 0.17$.

and normalization for the perturbation vectors to get again the norms $\varepsilon_0$. The Lyapunov exponents are evaluated as average rates for growth or decrease of accumulated sums of logarithms for norm ratios at the end and at the beginning of the intervals. It yields $\lambda_1 = 0.1532, \lambda_2 = -0.1930$. The Lyapunov exponents for the stroboscopic Poincaré map are $\Lambda_{1,2} = 2\pi\lambda_{1,2}$, and we get $\Lambda_1 = 0.9625, \Lambda_2 = -1.213$. Note that the largest exponent agrees with the estimate $\Lambda \cong \ln((3+\sqrt{5})/2) = 0.9624$, which may be derived directly from the procedure of constructing the Hunt model. Sum of the Lyapunov exponents is negative that corresponds to an exponential decrease of the volume of a cloud of representative points in the course of the approach to the attractor. Estimate of the attractor dimension with the Kaplan-Yorke formula yields $d_L = 1 + \lambda_1/|\lambda_2| \approx 1.79$. For the attractor as an object in the extended three-dimensional phase space, the dimension is larger by one: $D_L \approx 2.79$.

## 2.6 The triple linkage: A mechanical system with hyperbolic dynamics

Hunt and MacKay (Hunt and MacKay, 2003; Hunt, 2000; MacKay, 2005) established the hyperbolic nature of the dynamics for a mechanical system called the *triple linkage* that is a crank mechanism, earlier discussed in the popular mathematical article (Thurston and Weeks, 1984).

The triple linkage consists of three rods placed on a plane, free to rotate about pivots fixed at vertices of an equilateral triangle (Fig. 2.11(a)). The opposite ends are linked by floating pivots with three other rods, which have the opposite ends connected together with one more floating pivot. An instant configuration may be specified by the angular coordinates $\theta_1, \theta_2, \theta_3$, but only two of them are independent due to the mechanical constraints. Thus, the configuration space is a two-dimensional manifold. Topologically, as noted by Thurston and Weeks, this is a surface of genus 3 (a "pretzel" with three holes).

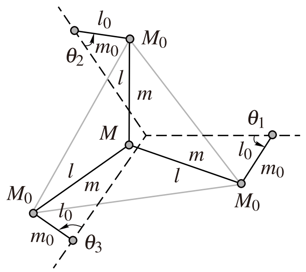


(a)

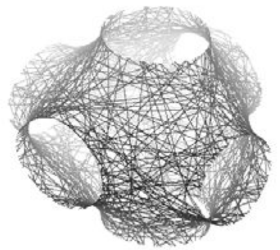

(b)

**Fig. 2.11** A mechanical system of Thurston and Weeks, the triple linkage **(a)**, and a trajectory in the three-dimensional space $(\theta_1, \theta_2, \theta_3)$ **(b)** obtained in computations for values of lengths and masses $l = \frac{41}{40}, l_0 = \frac{7}{40}, m = \frac{9}{100}, M = \frac{13}{100}, M_0 = \frac{1}{5}, m_0 = 0$. In accordance with the data of MacKay and Hunt, at these parameters the motion is hyperbolic because of globally negative curvature of the metric on the two-dimensional manifold in the configuration space.

In the absence of friction and external forces the motion by inertia takes place, with conservation of the kinetic energy. The kinetic energy is expressed as a quadratic form in terms of the generalized velocities, which are the time derivatives of the local coordinates on the two-dimensional manifold. This quadratic form with coefficients depending on the ratios of lengths and masses of the structural elements defines a metric on the two-dimensional manifold, and the motion takes place following the geodesics of this metric. By enumerating variants, the authors have found a set of parameter values, for which the metric is characterized by negative curvature everywhere in the configuration space (the two-dimensional manifold). As known due to Hadamard and others (Anosov, 1967; Balazs and Voros, 1986), in this situation a hyperbolic chaos occurs in its conservative version (see a simpler example in Appendix F). A sample trajectory is shown in Fig. 2.11(b) in the three-dimensional space $(\theta_1, \theta_2, \theta_3)$ as obtained from numerical solution of the mechanical equations of motion. The computations were performed for lengths and masses, at which the hyperbolicity must occur in accordance with the conclusions of MacKay and Hunt because of globally negative curvature of the metric on the manifold.

As MacKay and Hunt argued, providing additionally friction, potential field, and appropriate feedback control, it is possible to get a system with a hyperbolic attractor. So far, no concerned studies have been made, in which such attractors were demonstrated explicitly in computer simulations or in experiments.

## 2.7 A possible occurrence of a Plykin type attractor in Hindmarsh-Rose neuron model

In a rapidly developing field of neuroscience, a very popular and well studied is the *Hindmarsh-Rose model* (Hindmarsh and Rose,1984; Gonzalez-Miranda, 2007; Shilnikov and Kolomiets, 2008), which describes many features of dynamics of a single neuron. It is represented by an autonomous set of three differential equations

$$\begin{aligned} \dot{x} &= y - x^3 + 3x^2 - z, \\ \dot{y} &= 1 - 5x^2 - y, \\ \dot{z} &= \mu(4(x-c) - z - \delta). \end{aligned} \tag{2.18}$$

Here $x$, $y$, $z$ are dynamical variables, and $\delta$, $\mu$, $c$ are parameters. At fixed values of $\mu$ and $x_0$ (e.g., $\mu = 0.005$, $c = -1.56$) the model can demonstrate various dynamical regimes in dependence on the parameter $\delta$. In some range $\delta < \delta_1$, the relatively long-period self-oscillations occur, which are referred to as the *bursting activity*. In another range $\delta > \delta_2$, the relatively fast, short-period oscillations take place, and this is generation of *spikes*. In the intermediate interval $\delta_1 < \delta < \delta_2$ the spikes occur on a background of the bursts (Fig. 2.12), and this is just the parameter range where nontrivial dynamical phenomena may arise.

In the work of V. Belykh, I. Belykh, and E. Mosekilde (Belykh et al., 2005) the authors argue in favor of occurrence of the Plykin-type attractor in Poincaré map of a system of such kind. In fact, they examine equations in more formal generalized form

$$\dot{\mathbf{x}} = \mathbf{X}(\mathbf{x}, z), \ \dot{z} = \mu(Z(\mathbf{x}) - z - \delta).$$

Here $\mathbf{x}$ is a two-dimensional vector, and functions $\mathbf{X}(\mathbf{x}, z)$ and $Z(\mathbf{x})$ are concretized only on a qualitative level to justify the considerations.

The authors indicate a way to introduce the Poincaré map ensuring adequate description of the dynamics in the parameter range of interest, where the bursting and spiking activities coexist. In accordance with the undertaken qualitative analysis, in this parameter interval the two-dimensional Poincaré map acts in a domain in a form of a disc with several cut-offs (the holes). Particularly, a situation may occur in mapping on a disk with three holes that is a main non-trivial condition for appearance of attractor of Plykin type. The conclusion is that in the respective parameter domain an attractor of the three-dimensional flow system is hyperbolic, and appears as result of a secondary two-loop homoclinic bifurcation of a saddle.

These results are interesting because they relate to a system of natural origin (neuron model). It gives a motive to speculate about possible significance of the

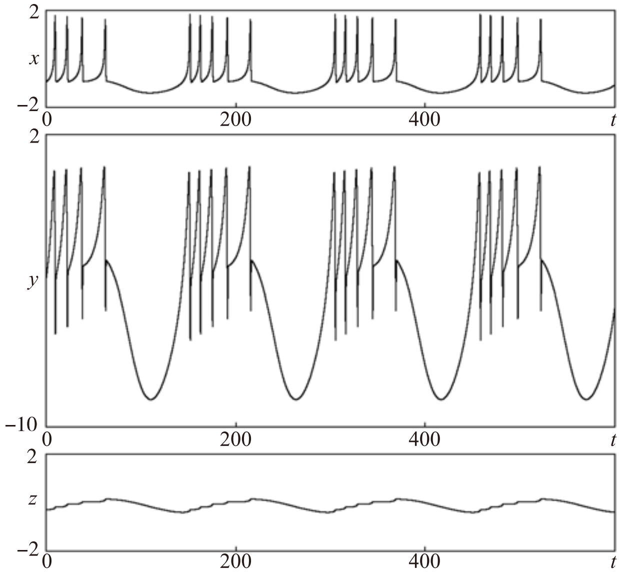


**Fig. 2.12** Bursts and spikes on a plot of the dynamical variable versus time in the model of Hindmarsh-Rose at $\mu = 0.005, c = -1.56, \delta = 2.8$.

uniform hyperbolicity for information processes in neurodynamics. Unfortunately, so far no concrete equations, expressions for the functions, and concrete recommendations for parameter selection have been presented associated with occurrence of the uniformly hyperbolic attractor. Obviously, setup of more detailed researches is needed, which would include detecting and demonstrating the uniformly hyperbolic attractors in computations, estimating their quantitative characteristics (like Lyapunov exponents, dimensions, etc.), and verifying the cone criterion. So far, no such studies have been made.

## 2.8 Blue sky catastrophe and birth of the Smale-Williams attractor

Shilnikov and Turaev (Turaev and Shilnikov, 1995; Shilnikov and Turaev, 1997) indicated a possibility of appearance of attractors of Smale-Williams type in Poincaré section of continuous-time systems undergoing a kind of the so-called *blue sky catastrophe*.

In the simplest version, a blue sky catastrophe occurs in three-dimensional phase space. At the bifurcation, a saddle-node limit cycle exists, from which the trajectories depart along the unstable manifold and return to the same cycle, but from the opposite side (Fig. 2.13(a)). With a shift of the control parameter value in one direction, the saddle-node cycle transforms to a pair of close limit cycles, one stable and the other unstable. With a parameter shift in the opposite direction, the saddle-node cycle disappears; instead, an attracting large-scale limit cycle emerges containing helical coils near the former saddle-node cycle.

Having initially an angular coordinate $\varphi$ near the saddle-node cycle, after a travel along the unstable manifold and subsequent return, the angular coordinate is expressed by a relation containing an additive term $m\varphi$, where an integer $m$ may be either 0, or 1 for the three-dimensional case. However, at higher dimensions, any integer can occur. Particularly, $m = 2$ corresponds to a birth of a hyperbolic strange attractor represented by a Smale-Williams solenoid in the Poincaré section (Fig. 2.13(b)). The authors stress that due to such bifurcation, a system of Morse-Smale class with simple dynamical behavior immediately converts to a system with complex dynamics associated with the structurally stable chaotic attractor.

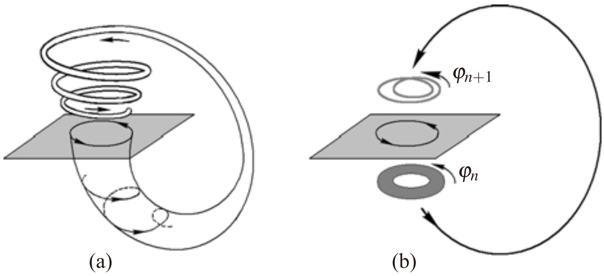


**Fig. 2.13** The phase space arrangement at the blue sky catastrophe in its simplest form in three-dimensional phase space **(a)**, and schematic representation of the situation of birth of the attractor of Smale-Williams, which is possible in the phase space of dimension 4 and more **(b)**.

To my knowledge, no concrete systems with the last variant of the blue sky bifurcation were described previously in the literature. Known examples have been presented so far only for the case of three-dimensional phase space (Gavrilov and Shilnikov, 1999; Shilnikov and Cymbalyuk, 2005; Glyzin et al., 2008), in which the transition to the attractor of Smale-Williams is not possible. A system of differential equations of the fourth order, in which such attractor indeed arises, has been suggested recently by the author (Kuznetsov, 2010) and is discussed in Chap. 5.

## 2.9 Taffy-pulling machine

A funny demonstration of feasibility of permanent stretching deformations for a continuous medium needed for a uniformly hyperbolic attractor, with no cuts and without appearance of local density singularities, is delivered by the so-called *taffy-pulling machine* used for preparation of cotton candy (Fig. 2.14) (MacKay, 2001; Halbert and Yorke, 2003; Hasselblatt and Katok, 2003). Due to the rotational motion of a set of transverse rods, the substance undergoes continuous stretching and folding with formation of a layered mixed pattern. In the paper by Halbert and Yorke a mathematical model was constructed in the form of a map describing the dynamics of local elements under deformation of the substance (Halbert and Yorke, 2003). It was said that such a machine can be regarded as a variant of the physical realization of a hyperbolic attractor. However, this is not appropriate physical situation we mean in the context of the present book. In fact, the whole device is *not* a low-dimensional dynamical system, as it contains distributed medium that is the continuum undergoing deformations, while its local elements are governed by the map possessing the hyperbolic dynamics. In other words, here we deal with dynamics of a real substance in the real space, rather than dynamics of a phase fluid in the phase space of a low-dimensional dynamical system.

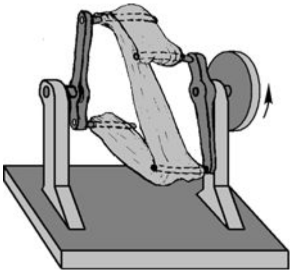

**Fig. 2.14** The taffy-pulling machine for preparing cotton candy. The reader can find photos and videos illustrating operation of such machines in the Internet using the key word “taffy-pulling machine” for the search.

## References

Abramowitz, M., Stegun, I.A.(eds.): Handbook of Mathematical Functions With Formulas, Graphs, and Mathematical Tables. National Bureau of Standards USA (1972).

Afraimovich, V.S., Bykov, V.V., Shilnikov, L. P.: Origin and structure of the Lorenz attractor. Akad. Nauk SSSR Doklady **234**, 336–339 (1977).

Aidarova, Yu.S., Kuznetsov, S.P.: Chaotic dynamics of the Hunt model, an artificially constructed flow system with a hyperbolic attractor. Preprint. arXiv: 0901.2727 (2009).

Akhiezer, N.I.: Elements of the Theory of Elliptic Functions. American Mathematical Society, Providence, RI (1990).

Alligood, K., Sauer, T., Yorke, J.A.: Chaos. An Introduction to Dynamical Systems. Springer-Verlag, New York (1996).

Anosov, D.V.: Geodesic flows on closed Riemannian manifolds of negative curvature. Trudy Mat. Inst. Steklov **90**, 3–210 (1967).

Balazs, N.L., Voros, A.: Chaos on the pseudosphere. Physics Reports **143**, 109–240 (1986).

Belykh, V., Belykh, I., Mosekilde, E.: The hyperbolic Plykin attractor can exist in neuron models. Int. J. of Bifurcation and Chaos **15**, 3567–3578 (2005).

Coudene, Y.: Pictures of hyperbolic dynamical systems. Notices of the American Mathematical Society **53**, 8–13 (2006).

Gavrilov, N.K., Shilnikov, A.L.: An example of blue sky catastrophe. In: Methods of qualitative theory of differential equations and related topics. Amer. Math. Soc. Transl., II Ser. **200**, pp. 165–188. AMS, Providence, RI (1999).

Glyzin, S.D., Kolesov, A.Yu., Rozov, N.Kh.: Blue Sky Catastrophe in Relaxation Systems with One Fast and Two Slow Variables. Differential Equations **44**, 161–175 (2008).

Gonzalez-Miranda, J.M.: Complex bifurcation structures in the Hindmarsh-Rose neuron model. Int. J. Bifurcation and Chaos **17**, 3071–3083 (2007).

Guckenheimer, J., Holmes, P.: Nonlinear Oscillations, Dynamical Systems, and Bifurcations of Vector Fields. Springer-Verlag, New York (1983).

Halbert, J.T., Yorke, J.A.: Modeling a chaotic machine's dynamics as a linear map on a "square sphere". http://www.math.umd.edu/∼halbert/taffy-paper-1.pdf (2003).

Hasselblatt, B., Katok, A.A.: First Course in Dynamics: with a Panorama of Recent Developments. Cambridge University Press, Cambridge (2003).

Hindmarsh, J.L., Rose, R.M.: A model of neuronal bursting using three coupled first order differential equations. Proc. Roy. Soc. London. Ser. B, Biological Sciences. **221** (1222), 87–102 (1984).

Hunt, T.J.: Low Dimensional Dynamics: Bifurcations of Cantori and Realisations of Uniform Hyperbolicity. PhD Thesis. Univercity of Cambridge (2000).

Hunt, T.J., MacKay, R.S.: Anosov parameter values for the triple linkage and a physical system with a uniformly chaotic attractor. Nonlinearity **16**, 1499–1510 (2003).

Ilyashenko, Y.S.: Attractors and their fractal dimension. MCCME, Moscow (2005).

Katok, A., Hasselblatt, B.: Introduction to the Modern Theory of Dynamical Systems. Cambridge University Press, Cambridge (1995).

Kuznetsov, S.P.: Plykin-type attractor in nonautonomous coupled oscillators. Chaos **19**, 013114 (2009).

Kuznetsov, S.P.: Example of blue sky catastrophe accompanied by a birth of Smale-Williams attractor. Regular and Chaotic Dynamics **15**, 348–353 (2010).

Lopez, A.O.: An Example of Polynomial Interpolation of an Hyperbolic Attractor. In: Lecture Notes in Mathematics **1007**, pp. 498–511. Springer-Verlag, Berlin (1983).

Lorenz, E.N.: Deterministic nonperiodic flow. J. Atmos. Sci. **20**, 130–141 (1963).

MacKay, R.S.: Chaos in three physical systems. In: Dumortier, F., Broer, H., Mawhin, J., Vanderbauvohede, A., Verduyn Lunel S. (eds) Equadiff 2003, pp. 59–72, World Science Press, Singapore (2005).

MacKay, R.S.: Complicated dynamics from simple topological hypotheses. Phil. Trans. R. Soc. Lond. A **359**, 1479–1496 (2001).

Vanderbauwhede, A., Verduyn Lunel S. (eds.) Equadiff 2003, pp. 59–72, World Science Press, Singapore (2005)

Morales, C.A.: Lorenz attractor through saddle-node bifurcations. Ann. de l'Inst. Henri Poincaré **13**, 589–617 (1996).

Newhouse, S., Ruelle, D., Takens, F.: Occurrence of strange Axiom-A attractors near quasi periodic flows on $T^m$, m≧ 3. Comm. Math. Phys. **64**, 35–40 (1978).

Ott, E.: Chaos in Dynamical Systems. Cambridge University Press, Cambridge (2002).

Ruelle, D., Takens, F.: On the nature of turbulence Commun. Math. Phys. **20**, 167–192 (1971).

Schuster, H.G., Just, W.: Deterministic Chaos: An Introduction. Wiley-VCH Verlag GmbH & Co. KGaA, Weinheim, FRG (2005).

Shilnikov, A., Cymbalyuk, G.: Transition between tonic spiking and bursting in a neuron model via the blue-sky catastrophe. Phys. Rev. Lett. **94**, 048101 (2005).

Shilnikov, A., Kolomiets, M.: Methods of the qualitative theory for the Hindmarsh-Rose model: a case study. Int. J. Bifurcation and Chaos **18**, 2141–2168 (2008).

Shilnikov, L.P., Turaev, D.V.: Simple bifurcations leading to hyperbolic attractors. Computers Math. Appl. **34**, 173–193 (1997).

Sparrow, C.: The Lorenz Equations: Bifurcations, Chaos, and Strange Attractors. Springer-Verlag, New York, Heidelberg, Berlin (1982).

Thurston, W.P., Weeks, J.R.: The mathematics of three-dimensional manifolds. Sci. Am. **251**, 94–106 (1984).
Tucker, W.: A rigorous ODE solver and Smale's 14th problem. Comp. Math. **2**, 53–117 (2002).
Turaev, D.V., Shilnikov, L.P.: On blue sky catastrophes. Doklady Akademii Nauk **342,** 596–599 (1995).

# Chapter 3
# Kicked Mechanical Models and Differential Equations with Periodic Switch

**Abstract** Some physical systems admit very natural description in discrete time. For example, it relates to mechanical or electronic systems under action of periodic pulses (kicks). Instead considering the motion in continuous time, one can derive a map, which expresses the state variables just before (or after) the next kick via the state just before (or after) the previous kick. In papers and textbooks on nonlinear dynamics, maps of Hénon, Ikeda, and Chirikov-Taylor-Zaslavsky are derived and studied in this context (Heagy, 1992; Kuznetsov et al., 2008; Sagdeev et al., 1988). Is it possible for the uniformly hyperbolic attractors to occur for diffeomorphisms arising in description of periodically kicked systems? In this chapter we introduce some simple physically motivated toy models with dynamics described by maps possessing attractors of Smale-Williams type.

One more approach to design of non-autonomous systems with uniformly hyperbolic attractors is to organize evolution in time as certain periodically repeated distinct stages, in such a way that the right-hand parts in the differential equations are defined in a special form for each of the successive stages. In other words, the right-hand parts may be thought of as being represented by functions piece-wise continuous and periodic in time. It may be referred to as *differential equations with periodic switch*. One example of such kind will be suggested with attractor of Smale-Williams type.

Earlier, the approach based on the periodically switching equations was developed by Hunt (Hunt, 2000) in the context of the problem of suspending attractor of Plykin type, as mentioned in Chap. 2. We introduce a simpler model with analogous attractor governed by equations with right-hand parts represented by periodic piece-wise continuous functions of time. Then, exploiting the structural stability, we modify the model to obtain differential equations with smooth coefficients possessing attractor of the same type.

S. P. Kuznetsov, *Hyperbolic Chaos*

## 3.1 Smale-Williams solenoid in mechanical model: Motion of a particle on a plane under periodic kicks

Let us turn to mechanical setup giving rise to maps with uniformly hyperbolic attractors of Smale-Williams type (Kuznetsov and Turukina, 2010).

Consider motion of a particle of unit mass on a plane $(x, y)$ with friction force proportional to the instant velocity. Let the motion take place in the presence of a stationary potential field; the potential function is $U(x,y) = -\frac{1}{2}\mu(x^2+y^2)+\frac{1}{4}\mu(x^2+y^2)^2$. This function possesses circular symmetry being minimal on the unit circle. Let us assume that short pulses kick the particle with period $T$, and the direction and magnitude of the kicks depend on the instant position of the particle. In other words, some force field is switched on for a short time, and then switched off, again and again. Let us assume that momentum accepted by the particle from a single kick is expressed as $\mathbf{P} = P_x(x,y)\,\mathbf{i}+P_y(x,y)\,\mathbf{j}$. Here $x$ and $y$ are the instant coordinates of the particle, the functions $P_{x,y}(x,y)$ describe the spatial distribution of the force field, $\mathbf{i}$ and $\mathbf{j}$ are unit vectors in the $x$ and $y$ directions, respectively. For simplicity we set the unite friction coefficient and write down the equations of the motion in the form

$$\begin{aligned} \ddot{x}+\dot{x} &= \mu x(1-x^2-y^2)+P_x(x,y)\sum_{n=-\infty}^{\infty}\delta(t-nT), \\ \ddot{y}+\dot{y} &= \mu y(1-x^2-y^2)+P_y(x,y)\sum_{n=-\infty}^{\infty}\delta(t-nT). \end{aligned} \tag{3.1}$$

To select appropriate spatial distribution for the field $\mathbf{P}(x, y)$ we proceed as follows. Let us assume that initially we set a ring of particles resting on a unit circle, with coordinates $x = \cos\varphi$ and $y = \sin\varphi (0 \leqslant \varphi < 2\pi)$. After a kick caused by the force field, each particle characterized by initial angular coordinate $\varphi$ accepts the momentum components $P_x(x,y)$ and $P_y(x,y)$ that entails certain displacement of the particle after some time. If the potential field is not taken into account $(\mu = 0)$, the particle would stop because of the friction at the coordinates

$$x' = x+P_x(x,y), \quad y' = y+P_y(x,y). \tag{3.2}$$

Let us specify the functions $P_x(x,y)$ and $P_y(x,y)$ requiring the particles to arrive again on the unit circle, but in such a manner that a single bypass of the original ring would correspond to an $M$-fold bypass for the new disposition, with an integer $M \geqslant 2$. In other words, the angular coordinate has to undergo the multiplication by $M$

$$\varphi' = M\varphi \pmod{2\pi}. \tag{3.3}$$

For this, the final coordinates of the particle must satisfy

$$x' = \cos\varphi' = \cos M\varphi, \quad y' = \sin\varphi' = \sin M\varphi. \tag{3.4}$$

It will be the case if the functions characterizing the distribution of the pulse force field are selected in such a way that

$$\begin{aligned} P_x(x,y) &= x' - x = \cos M\varphi - \cos\varphi = \mathrm{Re}(e^{iM\varphi} - e^{i\varphi}), \\ P_y(x,y) &= y' - y = \sin M\varphi - \sin\varphi = \mathrm{Im}(e^{iM\varphi} - e^{i\varphi}). \end{aligned} \tag{3.5}$$

Taking into account the relation of the Cartesian coordinates and the angular variable on the unit circle ($x = \cos\varphi$ and $y = \sin\varphi$), one easily obtains

$$P_x(x,y) + iP_y(x,y) = (x+iy)^M - (x+iy). \tag{3.6}$$

In the relations for $P_{x,y}(x,y)$ it is allowable to express even powers of one variable through the other, as on the unit circle the relation $y^2 = 1 - x^2$ is valid. Then, we obtain for $M$=2:

$$P_x(x,y) = 2x^2 - x - 1, \quad P_y(x,y) = 2xy - y, \tag{3.7}$$

and for $M = 3$ :

$$P_x(x,y) = 4x^3 - 4x, \quad P_y(x,y) = -4y^3 + 2y. \tag{3.8}$$

Note that in the last case the field of the pulse force is potential; moreover, the components $x$ and $y$ depend only on one single respective coordinate, that may be regarded as an advantage of this model from the point of view of simplicity of its implementation.

Parameter $\mu$ may be selected as relatively small value; then, during the characteristic time of the motion caused by the kick, a displacement of the particle caused by the potential field $U(x,y)$ is rather negligible. On the other hand, the period of kicks $T$ is assumed large enough to have time for the particle to approach the potential minimum. These conditions are not strong and have to be valid at least in a rough approximation. It is so because of structural stability of the hyperbolic attractor we intend to construct. With initial state just before the $n$-th kick $\mathbf{x}_n = \{x, \dot{x}, y, \dot{y}\}_{t=nT-0}$, one can determine the state before the next, $n+1$-th kick from solution of Eqs. (3.1) in the period $T$:

$$\ddot{x} + \dot{x} = \mu x(1 - x^2 - y^2), \quad \ddot{y} + \dot{y} = \mu y(1 - x^2 - y^2) \tag{3.9}$$

with the initial conditions specified by the state just after the kick:

$$\begin{aligned} x|_{t=nT+0} &= x_n, \quad \dot{x}|_{t=nT+0} = \dot{x}_n + P_x(x_n, y_n), \\ y|_{t=nT+0} &= y_n, \quad \dot{y}|_{t=nT+0} = \dot{y}_n + P_y(x_n, y_n). \end{aligned} \tag{3.10}$$

It is easy to write down additionally the variation equations linearized near the reference trajectory needed for computation of Lyapunov exponents. Substituting $(x+\tilde{x}, y+\tilde{y})$ into Eqs. (3.9), for small perturbations $\tilde{x}$, $\tilde{y}$ we obtain equations

$$\ddot{\tilde{x}} + \dot{\tilde{x}} = \mu\tilde{x} - \mu(y^2\tilde{x} + 3x^2\tilde{x} + 2xy\tilde{y}), \quad \ddot{\tilde{y}} + \dot{\tilde{y}} = \mu\tilde{y} - \mu(x^2\tilde{y} + 3y^2\tilde{y} + 2xy\tilde{x}) \tag{3.11}$$

supplemented by the initial conditions just after the kick following from (3.10):

$$\begin{aligned} \tilde{x}|_{t=nT+0} &= \tilde{x}_n, \quad \dot{\tilde{x}}|_{t=nT+0} = \dot{\tilde{x}}_n + \tilde{x}_n \partial_x P_x(x_n, y_n) + \tilde{y}_n \partial_y P_x(x_n, y_n), \\ \tilde{y}|_{t=nT+0} &= \tilde{y}_n, \quad \dot{\tilde{y}}|_{t=nT+0} = \dot{\tilde{y}}_n + \tilde{x}_n \partial_x P_y(x_n, y_n) + \tilde{y}_n \partial_y P_y(x_n, y_n). \end{aligned} \tag{3.12}$$

Relations (3.9) and (3.10) give rise to a *four-dimensional Poincaré map* $\mathbf{x}_{n+1} = \mathbf{f}(\mathbf{x}_n)$. This map is invertible because all the state transformations produced by the kicks and by the continuous time evolution governed by the differential equations are invertible. Although the exact form for the map is not derived analytically, the action of this map can be easily reproduced by means of numerical solution of the differential equations (3.9) by a computer program.

What is of relevance to occurrence of the Smale-Williams attractor, that's the topological property of the ensemble after the transformation, namely, emergence of a configuration encircling the origin two or three times. Compression in the transversal direction in the phase space is provided by the friction and by the effect of the potential field, due to which the particle drifts towards the potential minimum at the unit circle. In contrast to the classic construction discussed in Chap. 1, in these models the attractors of Smale-Williams type are embedded in the four-dimensional phase space of the Poincaré map rather than in the three-dimensional one.

In Figs. 3.1 — 3.4 illustrations are shown obtained from numerical solution of the equations of motion of the particle under pulsing driving force for the case $M$=2, with the force field specified by (3.7). Figure 3.1 shows a trajectory of the particle in the course of its motion on the plane $(x, y)$ that corresponds to the dynamics of the system on the attractor. Portrait of the attractor in the stroboscopic cross-section is presented in Fig. 3.2 in projection on the plane $(x, y)$. Its visual similarity to the Smale-Williams solenoid is obvious. The inset shows a magnified fragment of the picture, and the intrinsic Cantor-like transversal structure may be seen. In Fig. 3.3 an iteration diagram is drawn for the angular coordinate $\varphi_n = \arg(x(nT-0) + iy(nT-0))$ determined just before each kick. Observe that in very good approximation the angular coordinate behaves in accordance with the expanding circle map, or Bernoulli map. One bypass of the circle for pre-image corresponds to a two-fold bypass for the image.

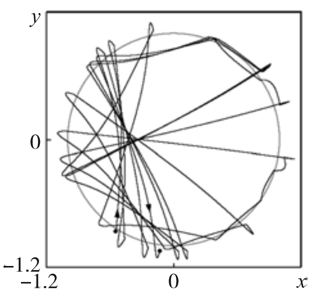


**Fig. 3.1** Trajectory of the particle on the plane $(x, y)$ in the models (3.1), (3.7) at $\mu = 0.44$, $T = 5$ for 30 periods of the driving. Arrows indicate directions of the motion.

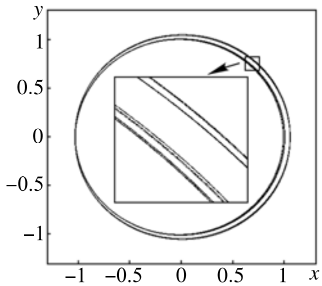


**Fig. 3.2** Portrait of attractor for the systems (3.1), (3.7) in projection on the plane $(x, y)$ in the stroboscopic cross-section at $\mu = 0.44$, $T = 5$. A fragment is shown with magnification to resolve the transversal Cantor-like structure of the object.

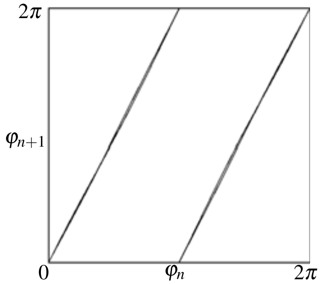


**Fig. 3.3** Iteration diagram for the angular coordinate obtained from numerical solution of Eqs. (3.1) with the distribution of the force field (3.7) at $\mu = 0.44$, $T = 5$.

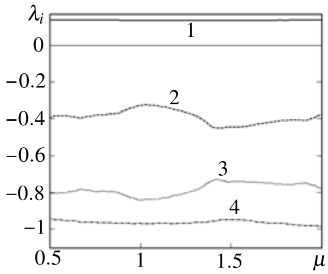


**Fig. 3.4** Plot for Lyapunov exponents of the models (3.1), (3.7) versus parameter $\mu$ at $T = 5$.

In Fig. 3.4 plots for the Lyapunov exponents are shown versus the parameter $\mu$ at fixed $T$. The Lyapunov exponents were computed by means of joint numerical solution of Eq. (3.9) for reference orbit with relations (3.10) at the kicks and a collection of four variation equations (3.11) with relations (3.12) at the kicks; Gram-Schmidt orthogonalization and normalization of the perturbation vectors were performed after each kick. Observe that the largest Lyapunov exponent remains nearly constant, and for the stroboscopic map it is very close to the estimate $\Lambda_1 \approx \ln 2$. It corresponds to the Lyapunov exponent for the Bernoulli map describing approximately the dynamics of the angular coordinate. Other Lyapunov exponents are negative. Estimate of the fractal dimension of the attractor in the Poincaré section at $\mu$=0.44 yields $D$=1.328.

In Figs. 3.5 — 3.8 analogous illustrations are presented for the model with $M$=3, and the force field is specified by (3.8). Figure 3.5 shows a trajectory of the particle on the plane $(x, y)$. Portrait of the attractor in the stroboscopic cross section is shown in Fig. 3.6 that corresponds to a variant of the Smale-Williams solenoid (with tripling of number of coils at each next step of the construction) and manifests Cantor-like transversal structure distinguished in the inset. In Fig. 3.7 an iteration diagram is shown for the angular coordinate determined just before the kicks. It behaves in very good approximation in accordance with the three-fold expanding circle map. In Fig. 3.8 the Lyapunov exponents are plotted versus the parameter $\mu$ at fixed $T$. The largest Lyapunov exponent is nearly constant, and for the stroboscopic map it is close to the estimate $\Lambda_1 \approx \ln 3$. Other Lyapunov exponents are negative. Estimate of the fractal dimension of the attractor in the Poincaré section at $\mu$=0.22 yields $D$=1.47.

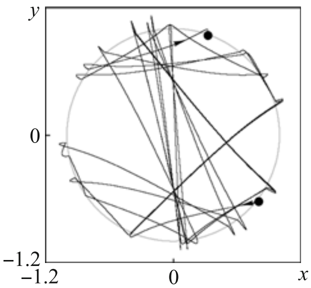


**Fig. 3.5** Trajectory of the particle on the planes $(x, y)$ in the models (3.1), (3.8) at $\mu = 0.22$, $T = 8$ for 30 periods of the driving. Arrows indicate directions of the motion.

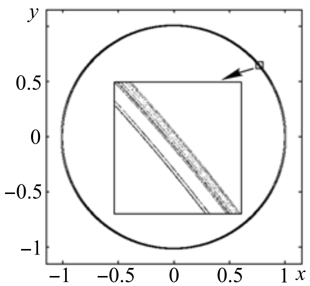


**Fig. 3.6** Portrait of attractor for the system (3.1) with distribution of the force field (3.8) in projection on the plane $(x, y)$ in the stroboscopic cross-section at $\mu = 0.22, T = 8$. A fragment is shown with magnification to resolve the transversal Cantor-like structure of the object.

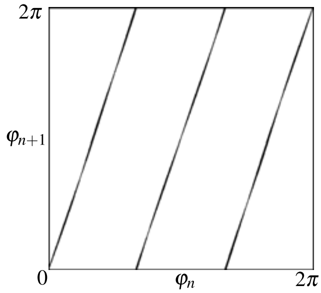


**Fig. 3.7** Iteration diagram for the angular coordinate obtained from numerical solution of Eqs. (3.1) with the distribution of the force field (3.8) at $\mu = 0.22, T = 8$.

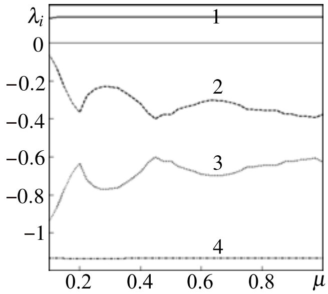


**Fig. 3.8** Plot for Lyapunov exponents of the models (3.1), (3.8) versus parameter $\mu$ at $T = 8$.

## 3.2 A set of switching differential equations with attractor of Smale-Williams type

The advantage of the above mechanical models is their simplicity. However, the dimension of the phase space is larger by one than the minimal dimension required for maps with attractors of Smale-Williams type.

Let us construct now a non-autonomous system in which the state at fixed time is given by a three-dimensional vector $(x, y, z)$, and the extended phase space is four-dimensional. Consider four periodically repeated stages of continuous transformations, with each unit time duration governed by the differential equations, as follows:

**I. Differential rotation around *x*-axis:**

$$\dot{x} = 0, \quad \dot{y} = -\frac{\pi}{2}xz, \quad \dot{z} = \frac{\pi}{2}xy. \tag{3.13}$$

**II. Non-uniform shift with compression in *y*-direction:**

$$\dot{x} = 0, \quad \dot{y} = -d_1(y - 2x^2 + 1), \quad \dot{z} = 0. \tag{3.14}$$

**III. Rotation by angle $\pi/2$ around *y*-axis:**

$$\dot{x} = -\frac{\pi}{2}z, \quad \dot{y} = 0, \quad \dot{z} = \frac{\pi}{2}x, \tag{3.15}$$

**IV. Compression towards unit circle in the plane *z*=0** :

$$\dot{x} = \mu x(1 - x^2 - y^2), \quad \dot{y} = \mu y(1 - x^2 - y^2), \quad \dot{z} = -d_2 z. \tag{3.16}$$

The dynamical equations may be written in the unified form as

$$\begin{aligned} \dot{x} &= -\frac{\pi}{2}zf_3(t) + \mu x(1 - x^2 - y^2)f_4(t), \\ \dot{y} &= -\frac{\pi}{2}xzf_1(t) - d_1(y - 2x^2 + 1)f_2(t) + \mu y(1 - x^2 - y^2)f_4(t), \\ \dot{z} &= \frac{\pi}{2}xyf_1(t) + \frac{\pi}{2}xf_3(t) - d_2 zf_4(t), \end{aligned} \tag{3.17}$$

where $f_k(t) = 1$, if $k - 1 \leqslant t - 4[t/4] < k$, and 0 otherwise. Considering all four stages successively, one can derive the following map from analytic solution of Eqs. (3.13) —- (3.16):

$$\mathbf{x}_{n+1} = \mathbf{b}(\mathbf{x}_n), \tag{3.18}$$

where

$$\mathbf{b}(\mathbf{x}) = \begin{pmatrix} -\dfrac{e^{\mu}z}{\sqrt{1+(e^{2\mu}-1)\left(z^2+\left(e^{-d_1}(y\cos\frac{\pi}{2}x - z\sin\frac{\pi}{2}x)+(2x^2-1)(1-e^{-d_1})\right)^2\right)}} \\ \dfrac{e^{\mu-d_1}(y\cos\frac{\pi}{2}x - z\sin\frac{\pi}{2}x)+e^{\mu}(2x^2-1)(1-e^{-d_1})}{\sqrt{1+(e^{2\mu}-1)\left(z^2+\left(e^{-d_1}(y\cos\frac{\pi}{2}x - z\sin\frac{\pi}{2}x)+(2x^2-1)(1-e^{-d_1})\right)^2\right)}} \\ e^{-d_2}x \end{pmatrix}.$$

As well, the inverse map may be written down explicitly

$$\mathbf{b}^{-1}(\mathbf{x}) = \begin{pmatrix} ze^{d_2} \\ \dfrac{ye^{d-\mu}\cos(\frac{\pi}{2}e^{d_2}z) - xe^{-\mu}\sin(\frac{\pi}{2}e^{d_2}z)}{\sqrt{1+(x^2+y^2)(e^{-2\mu}-1)}} + (2z^2e^{2d_2}-1)(1-e^{d})\cos(\frac{\pi}{2}e^{d_2}z) \\ \dfrac{-ye^{d-\mu}\sin(\frac{\pi}{2}e^{d_2}z) - xe^{-\mu}\cos(\frac{\pi}{2}e^{d_2}z)}{\sqrt{1+(x^2+y^2)(e^{-2\mu}-1)}} - (2z^2e^{2d_2}-1)(1-e^{d})\sin(\frac{\pi}{2}e^{d_2}z) \end{pmatrix}. \tag{3.19}$$

Figure 3.9(a) shows an absorbing domain appropriately selected at the parameter values $d_1 = d_2$=2, $\mu$=2 defined by the inequality $(p\sqrt{x^2+y^2} - 1)^2 + qz^2 \leqslant 1$, $p = 12.5$, $q = 25$, and its image under application of the Poincaré map (3.18). The action of the map agrees qualitatively with the Smale-Williams construction. Diagram (b) shows portrait of the attractor of the map. In the inset one can observe intrinsic transversal Cantor-like structure of filaments. Although local directions of expansion do not coincide precisely with directions of the filaments, and local compressions are directed with different angles dependent on position in the phase space, the present degree of correspondence with the geometric construction of Smale-

Williams appears to be sufficient for existence of the uniformly hyperbolic attractor. The panel (c) illustrates the iteration diagram for the angular variable determined at the $n$-th iteration of the map by the relation $\varphi_n = \arg(x_n + iy_n)$. Its form corresponds to expanding circle map, slightly deformed Bernoulli map: variation of the argument by $2\pi$ implies variation of the function by $4\pi$.

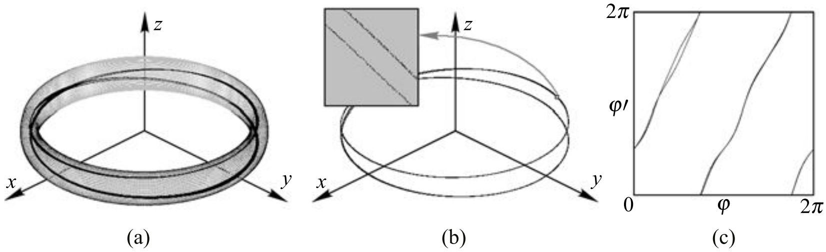


**Fig. 3.9** Absorbing domain in the phase space and its image after application of the map (3.18) **(a)**; portrait of the attractor **(b)** and iteration diagram for the angular coordinate **(c)**. Parameter values are $d_1 = d_2$=2, $\mu = 2$.

The Lyapunov exponents are found to be $\Lambda_1 = 0.661$, $\Lambda_2 = -2.601$, $\Lambda_3 = -2.650$, and the Kaplan-Yorke dimension of the attractor is $D_L \approx 1 + \Lambda_1/|\Lambda_2| \approx 1.25$. Numerical computations confirm the cone criterion in the entire absorbing domain.

Figures 3.10 and 3.11 illustrate some features of the dynamics in continuous time in accordance with the differential equation (3.17). In Fig. 3.10 the dependence of the dynamical variables versus time is plotted manifesting visually chaotic dynamics. Figure 3.11 shows three-dimensional projection of the attractor from the extended phase space of the continuous-time system. The picture is drawn in the gray-scale technique: the deepness of the gray tone indicates relative duration of

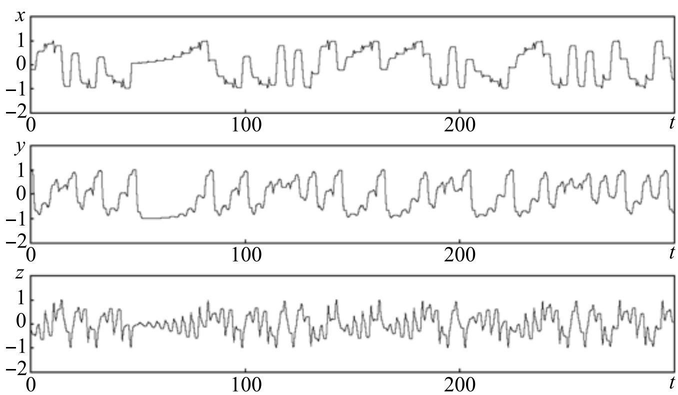


**Fig. 3.10** Dependence of variable $x$, $y$, $z$ on time obtained from numerical solution of Eqs. (3.17) at $d_1 = d_2$=2, $\mu = 2$.

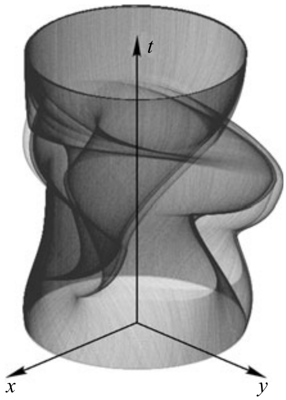


**Fig. 3.11** Portrait of the attractor of the continuous-time system (3.17) in three-dimensional projection from the four-dimensional extended phase space. Gray tones indicate relative duration of presence of the phase trajectories in the respective pixels.

presence of the phase trajectories in the respective pixels. In cross-section of the object by the hyper-plane $t$=const the solenoid shown in Fig. 3.9b takes place.

## 3.3 Explicit dynamical system with attractor of Plykin type

The present section is aimed at explicit construction of a non-autonomous flow system with Plykin type attractor (Kuznetsov, 2009a,b,c, 2011). The starting point is some map composed of successive periodically repeating stages of continuous geometrically evident transformations defined on a two-dimensional sphere.

### *3.3.1 Plykin type attractor on a sphere*

Let us consider a sphere of unit radius (Fig. 3.12). A point on the sphere can be specified in angular coordinates $(\theta,\varphi)$, or in Cartesian coordinates

$$x=\cos\varphi\sin\theta,\quad y=\sin\varphi\sin\theta,\quad z=\cos\theta, \tag{3.20}$$

which satisfy the relation $x^2+y^2+z^2=1$. As proven by Plykin, a map on a sphere can possess hyperbolic attractor in the presence of at least four holes, the areas not visited by trajectories belonging to the attractor. In our construction the holes will be represented by neighborhoods of points A, B, C, D with coordinates $(x,y,z)=(\pm1/\sqrt{2},0,\pm1/\sqrt{2})$. North and south poles of the sphere are denoted by N and S, respectively.

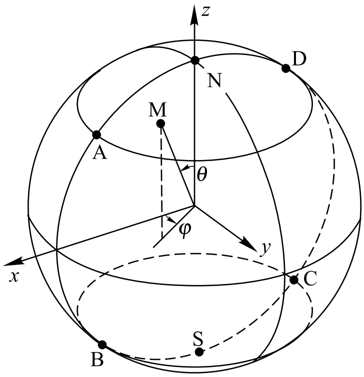


**Fig. 3.12** A sphere with marked points A, B, C, D, neighborhoods of which will correspond to the holes not visited by trajectories on the attractor. The north and south poles are indicated with N and S, respectively. The angular coordinates $(\theta, \varphi)$ are shown for some point M, and axes of the Cartesian coordinates $x$, $y$, $z$ are depicted.

Let us consider a periodic sequence of four successive continuous transformations, each unit time duration.

**I. Flow down along circles of latitude:** This is the motion of representative points on the sphere away from the meridians NABS and NDCB towards the meridians equally distant from the arcs AB and CD. In Cartesian coordinates it is governed by equations

$$\dot{x} = -\varepsilon x y^2, \quad \dot{y} = \varepsilon x^2 y, \quad \dot{z} = 0, \tag{3.21}$$

where $\varepsilon$ is a parameter.

**II. Differential rotation around $z$-axis** with angular velocity depending on $z$ linearly, in such a way that points B and C do not move, while A and D exchange their positions; it corresponds to equations

$$\dot{x} = \pi(z/\sqrt{2} + 1/2)y, \quad \dot{y} = -\pi(z/\sqrt{2} + 1/2)x, \quad \dot{z} = 0. \tag{3.22}$$

**III. Flow down to the equator:** That is motion of representative points along circles centered on the $x$-axis; the motion takes place on the sphere from the great circle ABCD, towards the equator:

$$\dot{x} = 0, \quad \dot{y} = \varepsilon y z^2, \quad \dot{z} = -\varepsilon y^2 z. \tag{3.23}$$

**IV. Differential rotation around $x$-axis** with angular velocity depending on $x$ linearly, in such a way that in the plane orthogonal to $x$-axis and containing the point C the representative points do not move, while those in the plane containing the point B undergo a turn by $180^\circ$:

$$\dot{x} = 0, \quad \dot{y} = -\pi(x/\sqrt{2} + 1/2)z, \quad \dot{z} = \pi(x/\sqrt{2} + 1/2)y. \tag{3.24}$$

Note symmetry of the procedure: The first and the second pairs of the transformations are identical to exchange of the variables $x$ and $z$.

Intuitively, it looks reasonable that this sequence of transformations will generate a flow on the sphere accompanying with formation of filaments of fine transversal structure that is a characteristic feature of the Plykin type attractors.

One can accept an interpretation that an instant speed of a representative point on the sphere is determined by combination of two vector fields switched on and off, turn by turn. One corresponds to dynamics during the stages of flow down, and the other to the stages of differential rotation. We can introduce angles $\bar{\alpha}$ and $\bar{\beta}$ determining directions of the fields, and coefficients $p$ and $q$ responsible for switching them on and off:

$$\bar{\alpha} = \bar{\beta} = \frac{\pi}{4}(-1)^{[t/2]} - \frac{\pi}{4}, \quad p = \frac{1}{2} + \frac{1}{2}(-1)^{[t]}, \quad q = \frac{1}{2}(-1)^{[t/2]} - \frac{1}{2}(-1)^{[t/2+1/2]}.$$

(Here $[\tau]$ designates the integer part of $\tau$.) Setting $K = \pi/\sqrt{2}$, we write down Eqs. (3.21) —- (3.24) in a compact unified form, which will be used for modification considering in the next section:

$$\begin{aligned}
\dot{x} &= -p\varepsilon y^2 (x\cos\bar{\alpha} + z\sin\bar{\alpha})\cos\bar{\alpha} + qKy\left(-x\sin\bar{\beta} + z\cos\bar{\beta} + \frac{1}{\sqrt{2}}\right)\cos\bar{\beta},\\
\dot{y} &= p\varepsilon y(x\cos\bar{\alpha} + z\sin\bar{\alpha})^2 - qK(x\cos\bar{\beta} + z\sin\bar{\beta})\left(-x\sin\bar{\beta} + z\cos\bar{\beta} + \frac{1}{\sqrt{2}}\right),\\
\dot{z} &= -p\varepsilon y^2 (x\cos\bar{\alpha} + z\sin\bar{\alpha})\sin\bar{\alpha} + qKy\left(-x\sin\bar{\beta} + z\cos\bar{\beta} + \frac{1}{\sqrt{2}}\right)\sin\bar{\beta}.
\end{aligned} \tag{3.25}$$

The Poincaré map, which determines transformation of a state vector $\mathbf{x}_n = (x_n, y_n, z_n)$ per period $T = 4$, may be derived explicitly. From successive solution of the differential eqs. (3.21) — (3.24) with account of the mentioned symmetry, one can express the resulting state vector $\mathbf{x}_{n+1}$ as

$$\mathbf{x}_{n+1} = \mathbf{f}_+(\mathbf{f}_-(\mathbf{x}_n)) \equiv \mathbf{f}(\mathbf{x}_n), \tag{3.26}$$

where

$$\mathbf{f}_\pm(\mathbf{x}) = \begin{pmatrix} \pm z \\ \dfrac{ye^{\frac{\varepsilon}{2}(x^2+y^2)}\cos\dfrac{\pi}{2}(z\sqrt{2}+1) \pm xe^{-\frac{\varepsilon}{2}(x^2+y^2)}\sin\dfrac{\pi}{2}(z\sqrt{2}+1)}{\sqrt{\cosh\varepsilon(x^2+y^2) + \varepsilon(y^2-x^2)\dfrac{\sinh\varepsilon(x^2+y^2)}{\varepsilon(x^2+y^2)}}} \\ \dfrac{ye^{\frac{\varepsilon}{2}(x^2+y^2)}\sin\dfrac{\pi}{2}(z\sqrt{2}+1) \mp xe^{-\frac{\varepsilon}{2}(x^2+y^2)}\cos\dfrac{\pi}{2}(z\sqrt{2}+1)}{\sqrt{\cosh\varepsilon(x^2+y^2) + \varepsilon(y^2-x^2)\dfrac{\sinh\varepsilon(x^2+y^2)}{\varepsilon(x^2+y^2)}}} \end{pmatrix}.$$

The relation (3.26) determines a map of the sphere to itself **f**, for which C is a fixed point, while A, B and D compose a period-3 unstable orbit: A → D → B → A. The map **f** is invertible. The inverse map appears as a result of the same transformations in backward order, with reversed directions of the rotations.

Figure 3.13 shows attractor of the map **f** at $\varepsilon = 0.77$. Observe specific fractal-like transversal structure of the attractor: the object looks like composed of strips, each of which contains narrower strips of the next level, etc.

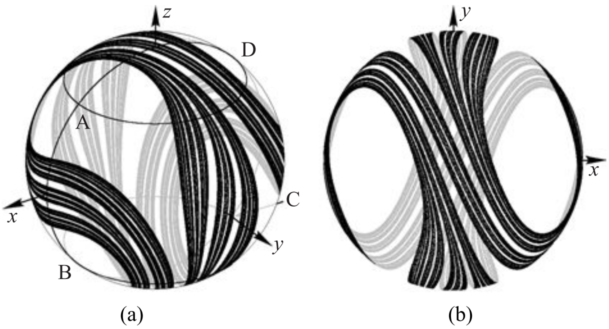


**Fig. 3.13** Attractor of the map (3.26) at $\varepsilon = 0.77$ on the unit square in an axonometric projection **(a)** and in polar azimuthal projection **(b)**.

Two Lyapunov exponents of the attractor are plotted in Fig. 3.14 versus the parameter $\varepsilon$. The procedure of computation of the Lyapunov exponents is based on the Benettin algorithm (see Appendix A), with the joint iteration of the mapping (3.26) together with two sets of the variational equations

$$\tilde{\mathbf{x}}_{n+1} = \mathbf{f}'_{+}(\mathbf{f}_{-}(\mathbf{x}_n))\mathbf{f}'_{-}(\mathbf{x}_n)\tilde{\mathbf{x}}_n \tag{3.27}$$

with orthogonalization of the perturbation vectors to the radius vector $\mathbf{x} = (x, y, z)$ and to each other, and their normalization to a fixed constant.

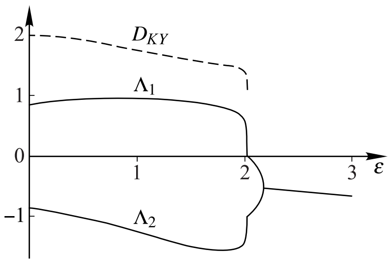


**Fig. 3.14** Dependence of Lyapunov exponents on the parameter $\varepsilon$ (solid line) and the Kaplan-Yorke dimension of the attractor (dotted line) for the map (3.26). The range of hyperbolic chaos according to the numerical verification of the cone criterion is approximately $0.35 < \varepsilon < 2$. At $\varepsilon > \varepsilon_c \approx 2.023$ there is no chaos; the dynamics become periodic.

In the range $\varepsilon < \varepsilon_c \approx 2.03$ one of two Lyapunov exponents is positive, which indicates the presence of chaos, and the other is negative. If $\varepsilon > \varepsilon_c$ (strong dissipation on the stages I and III), chaos disappears. Note smooth dependence of the positive Lyapunov exponent on the parameter, without drops to negative values intrinsic to many systems with non-hyperbolic attractors (see Appendix B). Additionally, a plot is shown for the Kaplan-Yorke dimension, which in this case is $D_{KY} = 1 + \Lambda_1/|\Lambda_2|$. With growth of $\varepsilon$, the dimension gradually decreases from 2 (that corresponds to extremely small dissipation) approximately to 1. Particularly, at $\varepsilon$=0.77 the Lyapunov exponents are $\Lambda_1 = 0.959$ and $\Lambda_2 = -1.141$, so the Kaplan-Yorke dimension is $D_{KY} \approx 1.84$.

Numerical verification of the cone criterion confirms hyperbolic nature of the attractor in the parameter interval $0.35 < \varepsilon < 2$ (Kuznetsov, 2009a,b). Figure 3.15 illustrates how the attractor structure evolves as the parameter is varied in this range: the strips forming the transversal Cantor-like structure look fat at smaller $\varepsilon$ and becomes narrower with increase of it.

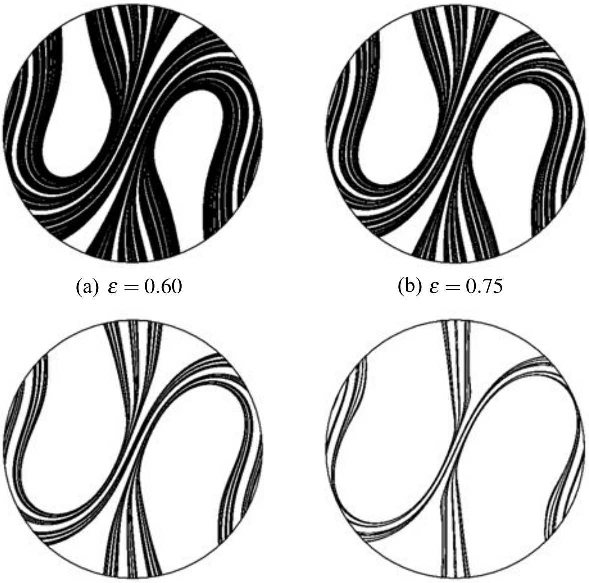

(a) $\varepsilon = 0.60$ (b) $\varepsilon = 0.75$

(c) $\varepsilon = 1.20$ (d) $\varepsilon = 1.75$

**Fig. 3.15** Portraits of attractors of the map (3.26) depicted in the polar azimuthal projection in the northern hemisphere for different values of $\varepsilon$ in the range of hyperbolicity. (The maps for the southern hemisphere look similarly northern, being obtained as mirror images about the vertical axis on the plots.)

### 3.3.2 Plykin type attractor on the plane

Description of the dynamics can be reformulated to represent states of the system on a plane. To do this, the following variable change is appropriate

$$W = X + iY = \frac{x - z + iy\sqrt{2}}{x + z + \sqrt{2}}. \tag{3.28}$$

It corresponds to stereographic projection from the sphere to the plane, with selection of the projection point at $\mathrm{C}(-1/\sqrt{2}, 0, -1/\sqrt{2})$. This point does not belong to the attractor (it is in the "hole"), so the attractor on the plane appears to be located in a bounded domain. The backward variable change is expressed as

$$x = \frac{1 - |W|^2 + 2\mathrm{Re}\,W}{\sqrt{2}(1 + |W|^2)}, \quad y = \frac{2\mathrm{Im}\,W}{1 + |W|^2}, \quad z = \frac{1 - |W|^2 - 2\mathrm{Re}\,W}{\sqrt{2}(1 + |W|^2)}. \tag{3.29}$$

Now, the dynamical eqs. (3.21) — (3.24) may be rewritten in new variables. The advantage is that the third redundant variable is excluded. Computing time derivative of (3.29), substituting derivatives of the old variables from (3.21) — (3.24), and expressing the result via $X$ and $Y$ we obtain the following equations in the four stages.

**Stage I:**

$$\begin{aligned} \dot{X} &= \varepsilon Y^2 \frac{(1 + 2X - X^2 - Y^2)(X - 1)}{(1 + X^2 + Y^2)^2}, \\ \dot{Y} &= \varepsilon Y \frac{(1 + 2X - X^2 - Y^2)(1 + 2X - X^2 + Y^2)}{2(1 + X^2 + Y^2)^2}. \end{aligned} \tag{3.30}$$

**Stage II:**

$$\dot{X} = \frac{\pi}{\sqrt{2}} \frac{Y(1 - X)^2}{1 + X^2 + Y^2}, \quad \dot{Y} = -\frac{\pi}{2\sqrt{2}} \frac{(1 - X)(1 + 2X - X^2 + Y^2)}{1 + X^2 + Y^2}. \tag{3.31}$$

**Stage III:**

$$\begin{aligned} \dot{X} &= \varepsilon Y^2 \frac{(1 - 2X - X^2 - Y^2)(X + 1)}{(1 + X^2 + Y^2)^2}, \\ \dot{Y} &= \varepsilon Y \frac{(1 - 2X - X^2 - Y^2)(1 - 2X - X^2 + Y^2)}{2(1 + X^2 + Y^2)^2}. \end{aligned} \tag{3.32}$$

**Stage IV:**

$$\dot{X} = -\frac{\pi}{\sqrt{2}} \frac{Y(1 + X)^2}{1 + X^2 + Y^2}, \quad \dot{Y} = -\frac{\pi}{2\sqrt{2}} \frac{(1 + X)(1 - 2X - X^2 + Y^2)}{1 + X^2 + Y^2}. \tag{3.33}$$

The Poincaré map may be derived either from direct analytic solution of the dynamical equations (step by step on the four stages), or from (3.26), by means of the variable changes (3.28) and (3.29). The resulting map is expressed as

$$\mathbf{W}_{n+1} = \mathbf{T}_+(\mathbf{T}_-(\mathbf{W}_n)) \equiv \mathbf{T}(\mathbf{W}_n), \tag{3.34}$$

$$\mathbf{T}_\pm(\mathbf{W}) = \begin{pmatrix} \dfrac{\pm(1-|W|^2-2X) - \frac{2\sqrt{2}Ye^{\rho/2}\sin\Phi \mp (1-|W|^2+2X)e^{-\rho/2}\cos\Phi}{\sqrt{\cosh\rho+\gamma\sinh\rho/\rho}}}{\pm(1-|W|^2-2X) + \frac{2\sqrt{2}Ye^{\rho/2}\sin\Phi \mp (1-|W|^2+2X)e^{-\rho/2}\cos\Phi}{\sqrt{\cosh\rho+\gamma\sinh\rho/\rho}} + 2 + 2|W|^2} \\ \dfrac{\sqrt{2}\frac{2\sqrt{2}Ye^{\rho/2}\cos\Phi \pm (1-|W|^2+2X)e^{-\rho/2}\sin\Phi}{\sqrt{\cosh\rho+\gamma\sinh\rho/\rho}}}{\pm(1-|W|^2-2X) + \frac{2\sqrt{2}Ye^{\rho/2}\sin\Phi \mp (1-|W|^2+2X)e^{-\rho/2}\cos\Phi}{\sqrt{\cosh\rho+\gamma\sinh\rho/\rho}} + 2 + 2|W|^2} \end{pmatrix},$$

where

$$|W|^2 = X^2 + Y^2, \quad \rho = \varepsilon\frac{8Y^2 + (1-|W|^2-2X)^2}{2(1+|W|^2)^2},$$

$$\gamma = \varepsilon\frac{8Y^2 - (1-|W|^2-2X)^2}{2(1+|W|^2)^2}, \quad \Phi = \pi\frac{1-X}{1+|W|^2}.$$

Portrait of the attractor on the plane obtained from iteration of the map (3.34) at $\varepsilon$=0.77 is shown in Fig. 3.16(a).

To reveal that this attractor is of Plykin type, and to confirm the uniform hyperbolicity, it is appropriate to turn to graphical representation of the stable and unstable foliations. To draw the stable and unstable manifolds with computer, we do the following. First, for a given point on the attractor $\mathbf{x}$ we obtain the image by iteration of the Poincaré map $\overline{\mathbf{x}} = \mathbf{f}^N(\mathbf{x})$, and the pre-image by iteration of the inverse map $\tilde{\mathbf{x}} = \mathbf{f}^{-N}(\mathbf{x})$, where $N$ is some empirically chosen integer. Then, with random initial conditions $\tilde{\mathbf{y}}$ in a small neighborhood of $\tilde{\mathbf{x}}$, we get by iteration of the Poincaré map a set of points $\mathbf{y} = \mathbf{f}^N(\tilde{\mathbf{y}})$, which mark the unstable manifold. In a similar way, starting with random initial conditions $\overline{\mathbf{y}}$ in a small neighborhood of $\overline{\mathbf{x}}$, we draw the stable manifold by a set of points $\mathbf{y} = \mathbf{f}^{-N}(\overline{\mathbf{y}})$. The accuracy the manifolds are depicted grows fast with increase of $N$. Actually, already selected $N = 6$ is enough to get so small errors that they are visually indistinguishable in the plot.

In Fig. 3.16(b) the stable and unstable foliations are drawn in the domain $D$ containing the attractor.The stable and unstable manifolds run along the black and gray curves, respectively. As seen, the unstable manifolds follow filaments of the attractor, while the stable ones are transversal to them. Mutual disposition of the stable and unstable manifolds in the domain $D$ certainly excludes their tangencies.

Markov partition of the domain $D$ can be obtained. A border separating the elements of the partition is just the stable manifold of the saddle-fixed point $R$, which belongs to the attractor (at $\varepsilon$=0.77 it is located at $X$=0, $Y = -3.45524253$). The partition is depicted in Fig. 3.16(c) as obtained from computations using the above technique of drawing the stable manifolds. Comparison of topology of the partition (mutual location of the sub-areas) with that shown in Fig. 1.14(b) for the Plykin type attractor clearly indicates that the attractor relates to the same class. Respectively,

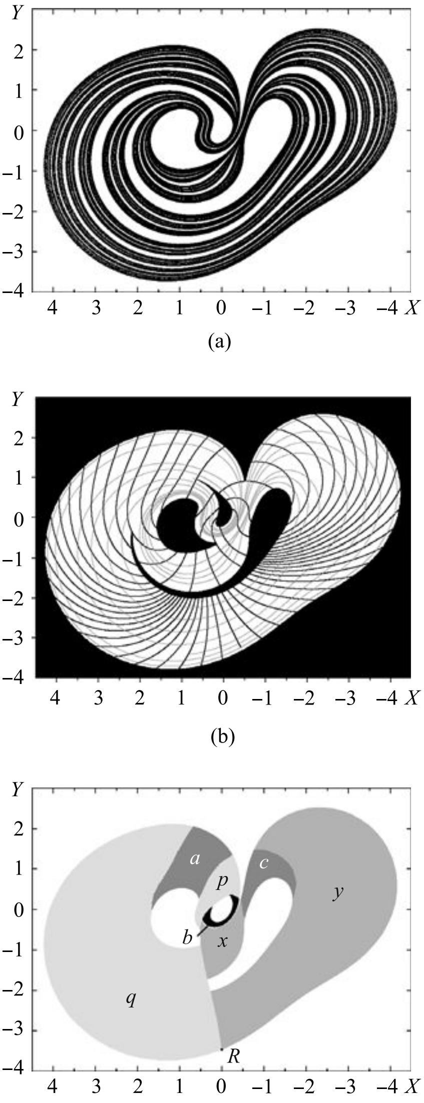


**Fig. 3.16** **(a)** Portrait of the attractor of the map (3.34) at $\varepsilon$=0.77. **(b)** Stable and unstable foliation obtained in computations in the absorbing domain $D$ shown in white. The stable and unstable manifolds run along the black and gray curves, respectively. **(c)** Markov partition: the border between the sub-areas is the stable manifold of the saddle fixed point $R$ belonging to the attractor. The partition may be compared to that shown in Fig. 1.14(b) that indicates relation of the attractor to the same Plykin type class. For clearness of the comparison, direction of the horizontal coordinate axis is inverted here, and the same colors and letters are used for the sub areas as those in Fig. 1.14(b).

the attractor discussed in the previous section has to be interpreted as the Plykin type attractor on the sphere.

Both representations, on the sphere and on the plane, differ only by a smooth variable change. Hence, the Lyapunov exponents for the attractor on the plane correspond exactly to those plotted in Fig. 3.14. The attractor is uniformly hyperbolic as follows from the numerical verification of the cone criterion at least in the parameter range $0.35 < \varepsilon < 2$. Figure 3.17 illustrates transformation of structure of the attractor portraits drawn on the plane as the parameter is varied in this interval.

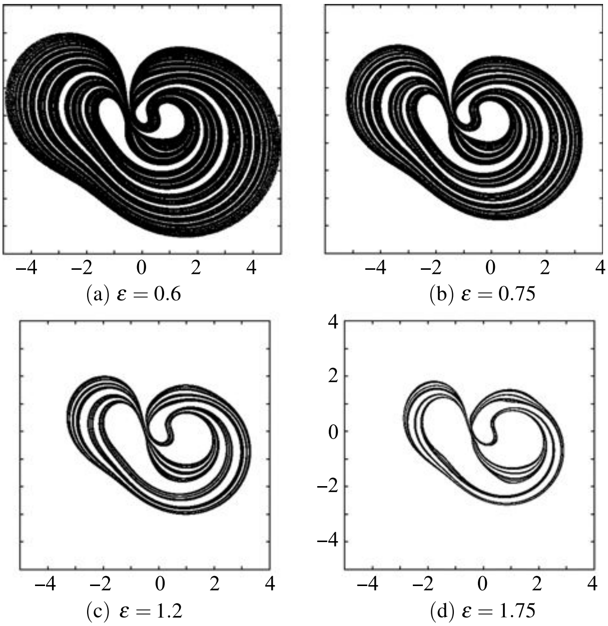


**Fig. 3.17** Portraits of attractors on the plane for different values of $\varepsilon$ in the range of hyperbolicity.

## 3.4 Plykin-like attractor in smooth non-autonomous system

One can object that the above examples are not completely satisfactory from the point of view of the classic hyperbolic theory as they are based on discontinuous evolution in time. Nevertheless, their evolution in a finite time (the period of the sequence of the stages) is governed by a diffeomorphism, which is a composition of the diffeomorphisms relating to the stages. So, they deliver examples of discrete-time evolution rules possessing the hyperbolic attractors. Moreover, we may try to modify slightly the evolution rules to exclude the discontinuities. If the modification is in some sense weak, one may expect that the variations in the stroboscopic map are also small, and, by virtue of the structural stability, the uniformly hyperbolic attractor will survive. Here we consider such approach in application to the system discussed in Sect. 3.3.

So, we intend to construct a version of the non-autonomous model containing only smooth functions. Let us return to Eqs. (3.25), which define a flow on the sphere, and set there

$$\bar{\alpha} = \frac{\pi}{4}\cos\frac{\pi}{2}t - \frac{\pi}{4}, \quad \bar{\beta} = \frac{\pi}{4}\sin\frac{\pi}{2}t - \frac{\pi}{4}, \quad p = 1, \quad q = \sin\frac{\pi}{2}t. \tag{3.35}$$

Now, two vector fields, responsible for the flow down and for the differential rotation, vary in time continuously and smoothly, undergoing rotations in space in such a way that the original configuration is repeated with the period $T = 4$. The second field oscillates, reversing the direction twice per period. To retain the alternating stages of flow down and of differential rotation, the variations of one and other fields are shifted in time relatively by a quarter of period. So, the extremal values of the fields are achieved by turns. The action of the fields on the motion of the representative points is mostly significant at the extremal values, hence, it is reasonable to specify them as the same like those in the original version of the model. Because of structural stability of the hyperbolic attractor, one can hope that it survives the modification, at least in a properly selected range of the parameters. As seen from the computations, it is so, e.g. at $\varepsilon = 0.72$ and $K = 1.9$.

In contrast to the previous version of the model, the Poincaré map can not be expressed analytically. However, it may be easily performed with a computer program integrating the equations with a finite-difference method in a time period $T = 4$.

We can exclude a redundant variable in the equations by means of the variable change (3.28), and rewrite them in terms of $W = X + iY$. After separation of the real and imaginary parts, we obtain

$$\begin{aligned}
\frac{dX}{dt} &= -2\varepsilon Y^2 \Omega_1(X,Y,t)\left(\cos\left(\frac{\pi}{4}\cos\frac{\pi}{2}t\right) - X\sin\left(\frac{\pi}{4}\cos\frac{\pi}{2}t\right)\right) \\
&\qquad + KY\Omega_2(X,Y,t)\left(\cos\left(\frac{\pi}{4}\sin\frac{\pi}{2}t\right) - X\sin\left(\frac{\pi}{4}\sin\frac{\pi}{2}t\right)\right)\sin\frac{\pi t}{2}, \\
\frac{dY}{dt} &= 2\varepsilon Y\Omega_1(X,Y,t)\left(X\cos\left(\frac{\pi}{4}\cos\frac{\pi}{2}t\right) + \frac{1}{2}(1 - X^2 + Y^2)\sin\left(\frac{\pi}{4}\cos\frac{\pi}{2}t\right)\right) \\
&\qquad - K\Omega_2(X,Y,t)\left(X\cos\left(\frac{\pi}{4}\sin\frac{\pi}{2}t\right) + \frac{1}{2}(1 - X^2 + Y^2)\sin\left(\frac{\pi}{4}\sin\frac{\pi}{2}t\right)\right)\sin\frac{\pi t}{2},
\end{aligned} \tag{3.36}$$

where

$$\begin{aligned}
\Omega_1(X,Y,t) &= \frac{2X\cos\left(\frac{\pi}{4}\cos\frac{\pi}{2}t\right) + (1 - X^2 - Y^2)\sin\left(\frac{\pi}{4}\cos\frac{\pi}{2}t\right)}{(1 + X^2 + Y^2)^2}, \\
\Omega_2(X,Y,t) &= \frac{-2X\sin\left(\frac{\pi}{4}\sin\frac{\pi}{2}t\right) + (1 - X^2 - Y^2)\cos\left(\frac{\pi}{4}\sin\frac{\pi}{2}t\right)}{1 + X^2 + Y^2} + \frac{1}{\sqrt{2}}.
\end{aligned} \tag{3.37}$$

The expressions (3.36), (3.37) look awkward, but this is *the first explicit example of a set of differential equations with smooth coefficients, which has attractor of Plykin type on a plane in the Poincaré cross-section.*

Figure 3.18 shows variables $X$ and $Y$ in dependence on time as obtained from numerical integration of the differential equations (3.36) at $\varepsilon = 0.72$ and $K = 1.9$, after exclusion of transients. Visually they look like samples of random processes, as they should be for the dynamics on the chaotic attractor.

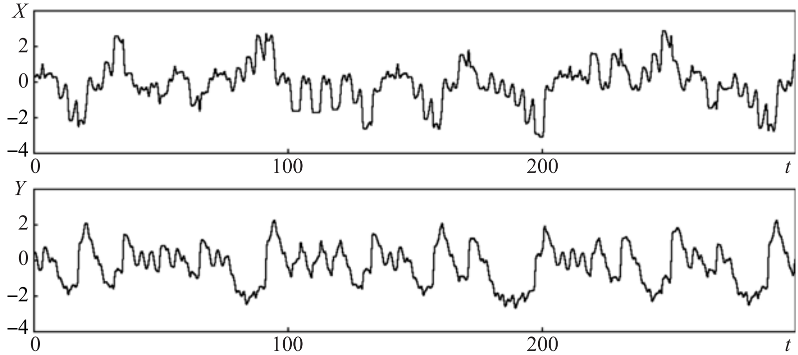


**Fig. 3.18** Variables $X$ and $Y$ versus time obtained numerically from integration of the differential equations (3.36) at $\varepsilon$=0.72 and $K$=1.9. The plot relates to sustained chaotic regime associated with motion on the attractor; the transients are excluded.

Figure 3.19 shows portrait of the attractor in the three-dimensional extended phase space $(X, Y, t)$. To make the inherent structure visible, the picture is presented with the gray-scale technique. Brighter tones correspond to relatively larger probability of visiting pixels by orbits on the attractor. Time interval on the vertical axis corresponds just to a period of variation of coefficients in the equations. In the cross-section of the attractor with the horizontal plane, one can observe an object with fractal structure, remarkably similar to that discussed in the previous section (Fig. 3.16(a)). At a qualitative level, it may be regarded as an argument in favor of persistence of the hyperbolic attractor under modification of the model we undertake.

Computation of the Lyapunov exponents for the model (3.36) by means of the Benettin algorithm (Appendix A) at $\varepsilon = 0.72$ and $K = 1.9$ yields $\lambda_1 \approx 0.221$ and $\Lambda_2 \approx -0.315$. It corresponds to the Lyapunov exponents of the Poincaré map $\Lambda_1 = \lambda_1 T \approx 0.884$ and $\Lambda_2 = \lambda_2 T \approx -1.260$. Estimate of the attractor dimension in the Poincaré section by the Kaplan-Yorke formula is $D_{KY} \approx 1.70$.

The hyperbolic nature of the attractor was verified by means of graphical representation of manifolds in the Poincaré section (like in Fig. 3.16(b)) and the computations based on the cone criterion (Kuznetsov, 2009a,b). Following those results, the attractor is hyperbolic in some parameter range around $\varepsilon = 0.72$ and $K = 1.9$.

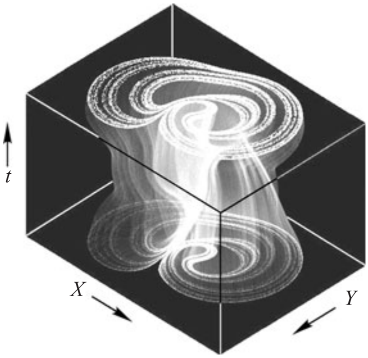


**Fig. 3.19** Portrait of the attractor of the model (3.36) at $\varepsilon = 0.72$ and $K = 1.9$ in the extended three-dimensional phase space. The gray-scale technique is used: brighter tones correspond to areas of relatively large probability of visiting by orbits on the attractor.

# References

Heagy J.F.: A physical interpretation of the Hénon map. Physica D **57**, 436–446 (1992).

Hunt, T.J.: Low dimensional dynamics: bifurcations of Cantori and realisations of uniform hyperbolicity. PhD Thesis. Univercity of Cambridge (2000).

Kuznetsov, A.P., Savin, A.V., Savin, D.V.: On some properties of nearly conservative dynamics of Ikeda map and its relation with the conservative case. Physica A **387**, 1464-1474 (2008).

Kuznetsov, S.P.: Hyperbolic strange attractors of physically realizable systems. Izvestija VUZov-Applied Nonlinear Dynamics (Saratov) **17** (4), 5-34 (2009a).

Kuznetsov, S.P.: A non-autonomous flow system with Plykin type attractor. CNSNS **14**, 3487–3491 (2009b).

Kuznetsov, S.P.: An example of a non-autonomous continuous-time system with attractor of Plykin type in the Poincaré map. Nonlinear Dynamics **5**, 403-424 (2009c).

Kuznetsov, S.P., Turukina, L.V.: Attractors of Smale-Williams type in periodically kicked model systems. Izvestija VUZov-Applied Nonlinear Dynamics (Saratov) **18**, 80-92 (2010).

Kuznetsov, S.P.: Dynamical chaos and uniformly hyperbolic attractors: from mathematics to physics. Physics-Uspekhi **54** (2), 119 (2011).

Sagdeev, R.Z., Usikov, D.A., Zaslavsky, G.M.: Nonlinear physics: from the pendulum to turbulence and chaos. CRC Press, Boca Raton, FLA (1988).

# Chapter 4
# Non-Autonomous Systems of Coupled Self-Oscillators

**Abstract** In this chapter we examine models composed of coupled limit-cycle self-oscillators. We start with discussion of a single van der Pol oscillator and pay attention, particularly, to its description in terms of slow complex amplitudes. This oscillator will be used as a building block for design of models with hyperbolic attractors. Some years ago the author suggested a system admitting physical realization, in which the Poincaré map possesses the uniformly hyperbolic attractor of Smale-Williams type (Kuznetsov, 2005). It is composed of two van der Pol oscillators, which become active by turns because of external modulation of parameters responsible for the birth of the limit cycle. The partial oscillators pass the excitation each other in such a way that on a whole cycle of this transfer the phase of the oscillations undergoes transformation corresponding to the expanding circle map. The last section of the chapter is devoted to another approach: it will be shown how the dynamics associated with the Plykin type attractor considered in the previous chapter may be realized in a system of two coupled self-oscillators described in terms of complex amplitudes.

## 4.1 Van der Pol oscillator

Let us start with discussion of the van der Pol oscillator, which will be used as a building block for the systems discussed in the main part of this chapter. This model is well known, popular and significant in nonlinear science because it represents the simplest example of self-oscillatory system able to manifest sustained periodic oscillations of magnitude, period, and wave-form determined by the system itself, not by some external force. Originally, this model was designed by Dutch physicist and radio-engineer B. van der Pol in application to an electronic generator of non-dumping radio-frequency oscillations. Later, it acquired status of a universal model of theory of oscillations used for description of systems of different physical nature (Andronov et al., 1966; Davis, 1962; Hayashi, 1964; Rabinovich and Trubetskov, 1989; Landa, 1996; Strogatz, 2001; Pikovsky et al., 2002).

S. P. Kuznetsov, *Hyperbolic Chaos*

The van der Pol oscillator is a system governed by differential equation of the second order

$$\ddot{x} - (A - x^2)\dot{x} + \omega_0^2 x = 0. \tag{4.1}$$

Here $\omega_0$ is characteristic frequency; $A$ is control parameter that determines character of dynamical regime of the system. An instant state of the system is specified by two dynamical variables, the generalized coordinate $x$ (its concrete physical sense depends on the problem in consideration, say, in electronics it is some time-dependent voltage) and the generalized velocity $\dot{x}$. So, the states are represented by points on the phase plane $(x, \dot{x})$.

At $A < 0$ the system has a unique attractor on the phase plane, the stable fixed point at the origin (Fig. 4.1(a)). At $A > 0$ the equilibrium state in the origin becomes unstable; an attractive closed orbit appears nearby, which is the stable limit cycle corresponding to the self-oscillations in the system. At small positive $A$ the oscillations are close to sinusoid with frequency $\omega_0$ and amplitude proportional to $\sqrt{A}$ (Fig. 4.1(b)). At large $A$ the oscillations accept some peculiar form (called the relaxation oscillations), and their main frequency undergoes graduate decrease with growth of $A$ (Fig. 4.1(c)). The phenomenon of birth of the limit cycle at $A$=0 is a particular case of the *normal (or supercritical) Andronov-Hopf bifurcation* (Andronov et al., 1966; Kuznetsov, 1998).

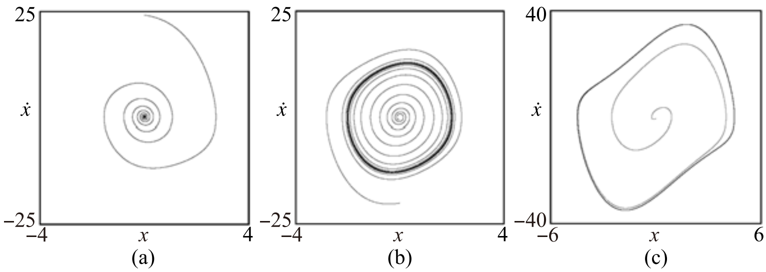


**Fig. 4.1** Phase portraits for the van der Pol oscillator (4.1) at $\omega_0 = 2\pi$, $A = -1$ **(a)**, $A = 1$ **(b)**, and $A = 5$ **(c)** on the phase plane $(x, \dot{x})$. Transient trajectories are shown in gray, and attractor (the stable fixed point in the first, and the limit circles on the second and the third pictures) in black.

A useful and luminous approach to analytical description of the model is based on the *method of slow complex amplitudes*. The early version of this approach was developed by van der Pol himself; later important contributions were made by Andronov, Bogolyubov and Mitropolsky, and others (Andronov et al., 1966; Nayfeh, 2000; Grebenikov, 2004). It is convenient to explain this method in the version we use hereafter.

Let us set

$$x = a(t)e^{i\omega_0 t} + a^*(t)e^{-i\omega_0 t}, \tag{4.2}$$

where $a(t)$ is a complex-valued function of time, and assume

$$\dot{x} = i\omega_0 a e^{i\omega_0 t} - \omega_0 a^* e^{-i\omega_0 t}, \tag{4.3}$$

which implies that

$$\dot{a}e^{i\omega_0 t} + \dot{a}^* e^{-i\omega_0 t} = 0. \tag{4.4}$$

(The relation (4.2) introduces two unknown functions, the real and the imaginary parts of the complex amplitude, instead of one real function $x(t)$; so, we are in our right to impose one additional functional condition that is just the relation (4.4).) Then, accounting (4.4), we get

$$\ddot{x} + \omega_0^2 x = i\omega_0 \dot{a} e^{i\omega_0 t} - i\omega_0 \dot{a}^* e^{-i\omega_0 t} = 2i\omega_0 \dot{a} e^{i\omega_0 t}. \tag{4.5}$$

So, Equation (4.1) may be rewritten through the complex amplitudes as

$$\dot{a} = \frac{1}{2}[A - (ae^{i\omega_0 t} + a^* e^{-i\omega_0 t})^2](ae^{i\omega_0 t} - a^* e^{-i\omega_0 t})e^{-i\omega_0 t}. \tag{4.6}$$

So far, all the algebra transformations have been rigorous, but now we will turn to approximation and assume that the complex amplitudes are *slow-varying functions of time*. To account this, we perform averaging in Eq. (4.6) over a period of the relatively fast oscillations of frequency $\omega_0$. Practically, this may be done simply by dropping all terms on the right-hand side, which contain fast time dependencies like $e^{\pm i\omega_0 t}, e^{\pm 2i\omega_0 t}$, etc. Then, we obtain what is called the *amplitude equation,* or the *shortened van der Pol equation*

$$\dot{a} = \tfrac{1}{2}(A - |a|^2)a. \tag{4.7}$$

Advantage over the original model is that the last equation is analytically solvable. Namely, if the initial complex amplitude at $t$=0 equals $a_0$, then the explicit solution is expressed as

$$a(t) = \frac{a_0 e^{At/2}}{\sqrt{1 + |a_0|^2 (e^{At} - 1)/A}}. \tag{4.8}$$

Observe that in the limit $t \to \infty$ in accordance with this relation the solution at $A < 0$ decays to zero, and at $A > 0$ it saturates at finite amplitude $|a| = \sqrt{A}$ that corresponds to the stable limit cycle.

One can regard Eq. (4.7) not only as a certain approximation for the original system (4.1), but as a self-contained object for studies and analysis. Sometimes, these or similar equations can appear in much more wide context than the original van der Pol model. A good example is the so-called Landau-Stewart equation for description of initial stages of development of turbulence (Landau and Lifshitz, 1959 Kuramoto, 1984; Strogatz, 2001).

## 4.2 Smale-Williams attractor in a non-autonomous system of alternately excited van der Pol oscillators

For an attractor of Smale-Williams type to occur, of principal significance is presence of some angular variable, which is multiplied by factor of two (or by a larger integer) under the action of the Poincaré map, while in other directions the phase volume undergoes compression.

Let us assume that the angular variable is a phase of some oscillatory process. Can we design a non-autonomous system with expanding transformation for the phase after each period of variation of coefficients in the differential equations? It is not a so trivial task because transformations of oscillatory signals produce usually only a shift of the output phase, equivalent to a shift of the input phase; so, realization of the expanding circle map seems problematic. Nevertheless, a solution does exist: we can use two or more oscillatory elements, which transfer excitation each other in such a way that the required transformation for phases takes place on the whole cycle of the transfer.[1] It is worth noticing that in this situation each oscillator cannot be characterized by globally defined phase during the whole process; otherwise expanding map for the phase would be impossible.

Consider two coupled van der Pol oscillators of frequencies $\omega_0$ and $2\omega_0$, respectively, governed by equations

$$\begin{aligned} &\ddot{x} - (A\cos(2\pi t/T) - x^2)\dot{x} + \omega_0^2 x = \varepsilon y \cos\omega_0 t, \\ &\ddot{y} - (-A\cos(2\pi t/T) - y^2)\dot{y} + 4\omega_0^2 y = \varepsilon x^2. \end{aligned} \tag{4.9}$$

The generalized coordinates $x$ and $y$ relate to two subsystems activated by turns due to the externally forced modulation of the parameter responsible for the bifurcation of birth of the limit cycle in a single oscillator. Its magnitude is determined by the parameter $A$. Interaction between the subsystems is characterized by coupling constant $\varepsilon$. The first oscillator affects the second one due to the quadratic term $\varepsilon x^2$ in the right-hand part of the second equation. The backward coupling is introduced by a product of the dynamical variable and the auxiliary signal of frequency $\omega_0$ (the right-hand term in the first equation). It is assumed that a period of the parameter modulation contains an integer number of periods of the auxiliary signal $T = 2\pi N/\omega_0$. Thus, the external driving is periodic, and description of the dynamics in terms of the stroboscopic Poincaré map is appropriate.

Equations (4.9) may be rewritten as a set of equations of the first order

[1] On a base of analogous approach, feasible systems were suggested also for implementation of some phenomena of complex dynamics discussed earlier only on a level of abstract constructions. It relates to a robust strange non-chaotic attractor of Hunt and Ott type (Hunt and Ott, 2001; Kim et al., 2003) considered in (Jalnine and Kuznetsov, 2007), and phenomena of complex analytic dynamics, like Mandelbrot and Julia sets (Devaney, 2003) considered in (Isaeva et al., 2007; 2008).

$$\begin{aligned}
\dot{x} &= \omega_0 u, \\
\dot{u} &= (A\cos(2\pi t/T) - x^2)u - \omega_0 x + \varepsilon\omega_0^{-1} y \cos\omega_0 t, \\
\dot{y} &= 2\omega_0 v, \\
\dot{v} &= (-A\cos(2\pi t/T) - y^2)v - 2\omega_0 y + \frac{1}{2}\varepsilon\omega_0^{-1} x^2,
\end{aligned} \tag{4.10}$$

where the variables $u$ and $v$ represent normalized generalized velocities of two oscillators. To introduce the Poincaré map, assume the state at $t = t_n = nT$ is specified by a vector $\mathbf{x}_n = \{x(nT), u(nT), y(nT), v(nT)\}$. Solution of Eqs. (4.10) in the time interval $T$ with the initial conditions $\mathbf{x}_n$ generates a new vector $\mathbf{x}_{n+1}$, and so we define the four-dimensional map $\mathbf{x}_{n+1} = \mathbf{T}(\mathbf{x}_n)$. Geometrically, in the five-dimensional extended phase space of the non-autonomous system $\{x, u, y, v, t\}$ it corresponds to cross-section of the flow of trajectories by the four-dimensional hyper-planes $t = t_n = nT$.

Qualitatively, the system operates as follows. Let the first oscillator have some phase $\varphi$ at a stage of activity: $x \sim \cos(\omega_0 t + \varphi)$. The squared variable $x^2$ contains the second harmonic component because of the trigonometric equality

$$x^2 \sim \cos^2(\omega_0 t + \varphi) = \frac{1}{2} + \frac{1}{2}\cos(2\omega_0 t + 2\varphi), \tag{4.11}$$

and the phase of this component is $2\varphi$. As the half-period comes to the end, the term $x^2$ stimulates excitation of the second oscillator, and oscillations of the variable $y$ get the phase $2\varphi$. Half a period later, the mixture of these oscillations with the auxiliary signal stimulates excitation of the first oscillator, which accepts now this phase $2\varphi$. Thus, in subsequent periods of the parameter modulation, the phase of the first oscillator follows approximately the relation

$$\varphi_{n+1} = 2\varphi_n + \text{const} \pmod{2\pi}. \tag{4.12}$$

Here the constant term accounts phase shifts in the course of the transfer of the excitation from one oscillator to another; this term may be removed by displacement of the origin for the phase variable. The relation (4.12) is the expanding circle map, or Bernoulli map, which is commonly known as the simplest model example in the chaos theory.

We emphasize that the phase $\varphi$ cannot be determined as continuous variable in the whole time interval $T$. Indeed, at the stage when the oscillator is suppressed, its amplitude is small, and the phase is not well defined.

The process we have described indeed occurs in numerical simulations in a wide parameter range. Figure 4.2 shows a typical sample of time dependence for variables $x$ and $y$ obtained from numerical solution of Eqs. (4.9) at particular parameter values $\omega_0 = 2\pi$, $T = 6$, $A = 5$, $\varepsilon = 0.5$. Being represented by periodic alternation of excitation and suppression for the first and the second oscillators, the process, in fact, is chaotic. Chaos reveals itself in variations of phases of the oscillators at successive stages of activity. More accurate analysis shows that these variations of the phases follow the Bernoulli map (in reasonable approximation). In Fig. 4.3 an empirical

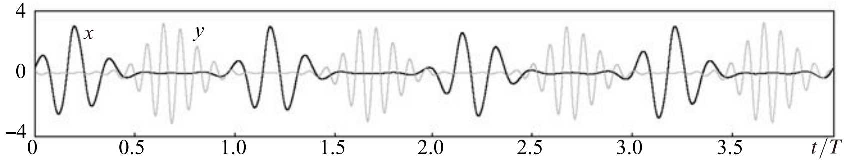


**Fig. 4.2** Typical sample of time dependence for the generalized coordinates $x$ and $y$ obtained from numerical solution of Eqs. (4.9) at $\omega_0 = 2\pi$, $T = 6$, $A = 5$, $\varepsilon = 0.5$.

diagram is shown for the phases determined in the process of numerical simulations at successive excitation stages for the first oscillator as $\varphi_n = \arg(x(nT) - iu(nT))$ and plotted for sufficiently large number of the basic periods. The mapping for the phase surely looks topologically equivalent to the Bernoulli map (4.12). Some distortions arise due to imperfection of the above qualitative considerations and of the definition of the phase; the correspondence becomes better at larger period ratios $N$. Of principal significance is topological nature of the phase transformation: one complete bypass for the pre-image $\varphi_n$ (that is variation by $2\pi$) corresponds to the two-fold bypass for the image $\varphi_{n+1}$.

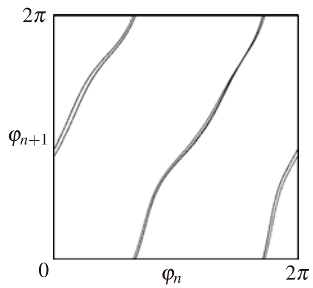


**Fig. 4.3** Diagram illustrating transformation of the phase for the first oscillator from one stage of activity to the next one obtained from numerical solution of Eqs. (4.9) at $\omega_0 = 2\pi$, $T = 6$, $A = 5$, $\varepsilon = 0.5$.

For computation of Lyapunov exponents one integrates Eqs. (4.10) together with collection of four replicas of variation equations

$$\begin{aligned}
\dot{\tilde{x}} &= \omega_0 \tilde{u}, \\
\dot{\tilde{u}} &= (A\cos(2\pi t/T) - x^2)\tilde{u} - 2x\tilde{x}u - \omega_0 \tilde{x} + \varepsilon\omega_0^{-1}\tilde{y}\cos\omega_0 t, \\
\dot{\tilde{y}} &= 2\omega_0 \tilde{v}, \\
\dot{\tilde{v}} &= (-A\cos(2\pi t/T) - y^2)\tilde{v} - 2y\tilde{y}v - 2\omega_0 \tilde{y} + \varepsilon\omega_0^{-1}x\tilde{x},
\end{aligned} \tag{4.13}$$

and the procedure is supplemented with normalization and orthogonalization of four perturbation vectors (as explained in Appendix A) at each period $T$. The Lyapunov exponents are evaluated as average rates of growth or decrease of accumulating sums of logarithms of norms of the perturbation vectors before the normalizations. According to the calculations, the Lyapunov exponents for the attractor of the Poincaré map at the specified parameters are the following

$$\Lambda_1 = 0.6832, \quad \Lambda_2 = -2.602, \quad \Lambda_3 = -4.605, \quad \Lambda_4 = -6.538. \tag{4.14}$$

The positive exponent $\Lambda_1$ indicates chaotic nature of the dynamics. It is close to $\ln 2 = 0.693\ldots$, which is in good correspondence with the approximate description of the evolution for the phase variable in terms of the one-dimensional Bernoulli map (4.12). Estimate of the Kaplan-Yorke dimension of the attractor through the Lyapunov exponents yields $D \approx 1.263$.

Action of the Poincaré map $\mathbf{T}$ in the four-dimensional space is accompanied by expansion in the directions locally associated with the angular variable, or phase, in Eq. (4.12), and by compression in the rest three phase space directions. Empirically, one can indicate a toroidal absorbing domain $D$, which is topologically a product of a one-dimensional circle and a three-dimensional ball. An iteration of the Poincaré map in application to the representative points from this domain generates an object $\mathbf{T}(D)$ in a form of a closed "tube" that is stretched in length, compressed in width and folded in double loop inside the original toroidal domain. It precisely corresponds to the Smale-Williams construction, but in the four-dimensional phase space.

To write down an analytic expression for the domain $D$ it is convenient to redefine the coordinate system and introduce new variables $\{x_0, x_1, x_2, x_3\}$ as follows:

$$\begin{gathered} x_0 = x/r_0, \quad x_1 = (u - c_{ux}x)/r_1, \\ x_2 = y - c_{yx}x - c_{yu}u, \quad x_3 = v - c_{vx}x - c_{vu}u - c_{vy}y, \end{gathered} \tag{4.15}$$

where $c_{ux}, c_{yx}, c_{yu}, c_{vx}, c_{vu}, c_{vy}$, $r_0$, $r_1$ are some constants, which can be determined for concrete mode of operation of the system as follows. First, by numerical solution of Eqs. (4.9) we accumulate a large number of points $\{x, u, y, v\}$ on the attractor in the Poincaré section. Then, by the least square method we determine the coefficients to minimize the mean-square values $<(u - c_{ux}x)^2>$, $<(y - c_{yx}x - c_{yu}u)^2>$, $<(v - c_{vx}x - c_{vu}u - c_{vy}y)^2>$. Geometrically, it means directing the coordinate axes along the principal axes of ellipsoid that roughly approximates the attractor. Additionally, we normalize the first two variables $x_0$ and $x_1$ by factors $r_0$ and $r_1$ to have $<x_0^2> = <x_1^2> \approx 1/2$. Finally, at the parameters of the system $\omega_0 = 2\pi$, $T = 6$, $A = 5$, $\varepsilon = 0.5$ we get

$$\begin{aligned} &c_{ux} = 0.438, \quad c_{yx} = -0.042, \quad c_{yu} = 0.226, \quad c_{vx} = -0.218, \\ &c_{vu} = 0.029, \quad c_{vy} = -0.118, \quad r_0 = 0.812, \quad r_1 = 0.721. \end{aligned}$$

In the new coordinates the absorbing domain $D$ is defined *by* the inequality:

$$\left(\left(\sqrt{x_0^2 + x_1^2} - r\right) \Big/ d_r\right)^2 + (x_2/d)^2 + (x_3/d)^2 \leqslant 1. \tag{4.16}$$

Here the empirically selected constants are $r = 0.94, d_r = 0.4, d = 0.15$.

Figure 4.4 shows a three-dimensional projection of the objects in the four-dimensional space to give impression of how the image $\mathbf{T}(D)$ is embedded inside the original toroid $D$. The mutual location of the domains $D$ and $\mathbf{T}(D)$ is analogous to that at the first step of the construction of the Smale-Williams attractor. The domain $\mathbf{T}(D)$ looks like a narrow band because of strong transversal compression in the course of evolution in one period of the parameter modulation.

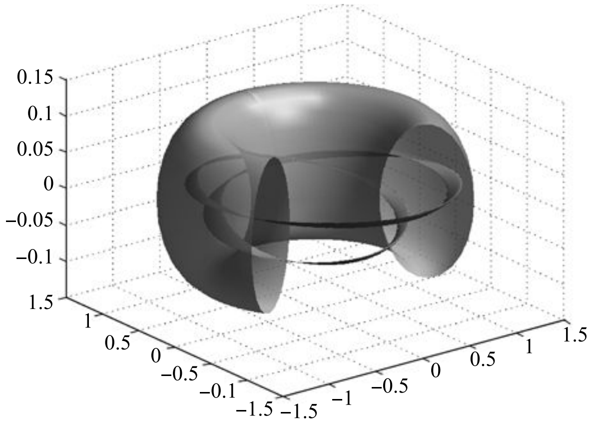


**Fig. 4.4** Absorbing domain $D$ and its image $\mathbf{T}(D)$ under the Poincaré map in three-dimensional projection.

It is interesting to examine process of deformation of the toroidal domain in continuous time that ensures the embedding of the image inside the original domain being folded in a double loop. It is illustrated by a series of pictures in Fig. 4.5. Each of them represents projection of the four-dimensional object into the three-dimensional space of variables $\{x_0, x_1, x_2\}$ along the axis of the fourth variable $x_3$. The first picture (a) corresponds to initial time instant $t = 0$ and depicts the original toroidal domain. Then, this toroid is compressed strongly in transversal directions (b). The compression differs in different directions, and the image takes a form of a closed narrow band. Then, the image undergoes expansion in the longitudinal direction and deformation of such kind that the double loop is formed ((c), (d)). At final stages of the process, this double loop widens in size and appears to be placed inside the original domain ((e), (f)). Actually, the process reproduces the continuous deformations of plastic doughnut used for popular explanation of the Smale-Williams construction as considered in Chap. 1.

Figure 4.6 shows portraits of attractor on a plane of variables of the first oscillator. The panel (a) represents a projection of the attractor from the five-dimensional extended phase space on the plane of original variables $(x, u)$. The portrait is depicted in gray scales (the darkness reflects a relative duration of presence of the orbit inside a given pixel). Black dots relate to the stroboscopic Poincaré cross-section, i.e., to the instants $t_n = nT$. The panel (b) shows the attractor in the Poincaré cross-section

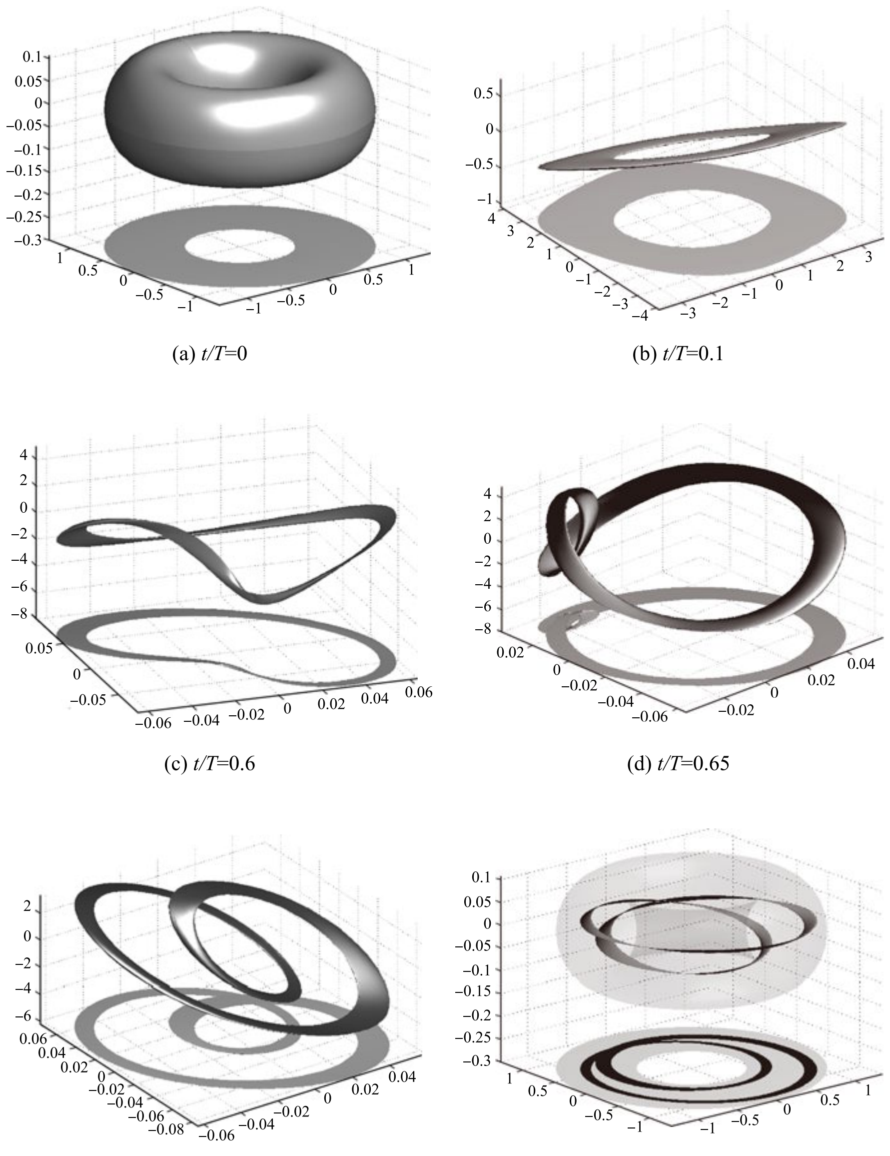


(a) $t/T$=0 (b) $t/T$=0.1

(c) $t/T$=0.6 (d) $t/T$=0.65

(e) $t/T$=0.69 (f) $t/T$=1

**Fig. 4.5** Illustration of transformation of the original toroidal domain **(a)** in the course of the continuous time evolution on one period $T$ (**(b)**-**(f)**). Each picture is a three-dimensional projection for the four-dimensional object into the space of variables $\{x_0, x_1, x_2\}$ along the axis of the fourth variable $x_3$. Notice essentially different scales along the coordinate axes on the diagrams.

on the plane of the redefined coordinates $(x_0, x_1)$ (see (4.15)). The transverse Cantor-like structure is illustrated separately by magnified fragments of the initial picture. Note evident visual similarity with the Smale-Williams attractor (Fig. 1.5).

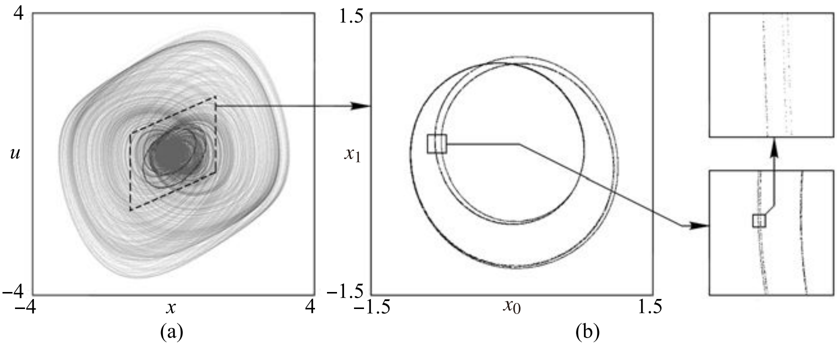


**Fig. 4.6** Attractor of the system of coupled non-autonomous van der Pol oscillator in projection onto phase plane of the first oscillator in the original variables and portrait in the stroboscopic cross-section on the plane $(x_0, x_1)$.

For quantitative characterization of the fractal structure of the attractor in the Poincaré cross-section, the correlation dimension was estimated in computations by means of the algorithm of Grassberger and Procaccia (Grassberger and Procaccia, 1983; Tong, 1994; Schuster, H.G. and Just, 2005; Hilborn,2000; Ott, 2002). A 4-component time series $\mathbf{x}_n = \{x_0(t_n), x_1(t_n), x_2(t_n), x_3(t_n)\}$ ($n$=1÷$M$, $M$=40000) was obtained from numerical iteration of the Poincaré map. The resulting dimension $D_2 \approx 1.252$ may be compared with the estimate from the Kaplan-Yorke formula $D \approx 1.263$.

In Fig. 4.7 all four Lyapunov exponents are plotted versus the amplitude of slow modulation $A$ at fixed other parameters. As seen, the largest exponent remains almost constant in a wide range of the parameter, and is close to the value $\ln 2 = 0.693\ldots$ characteristic to the Bernoulli map. Such behavior of the largest Lyapunov exponent responsible for the chaotic nature of the dynamics agrees with structural stability of the hyperbolic attractor, which evidently persists in this parameter interval (for comparison, see plots of the Lyapunov exponents for models, which do not possess the structural stability in Appendix B). The rest exponents are large negative. They correspond to strong compression of the phase volume along three of four dimensions of the phase space of the Poincaré map.

For the system (4.9) with the used parameter values the computations were carried out to confirm hyperbolicity (see Chap. 7). It was demonstrated in computations that the cone criterion is valid in the toroidal domain, containing the attractor of the Poincaré map (Kuznetsov and Sataev, 2007). Recently, the hyperbolic nature of the attractor in this system has been established rigorously, on the basis of the computer-assisted proof (Wilczak, 2010).

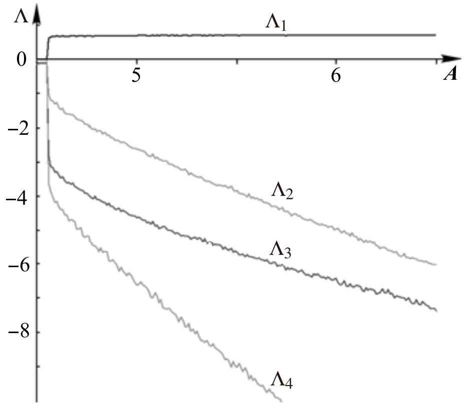


**Fig. 4.7** Lyapunov exponents of the Poincaré map for the system (4.9) plotted versus the amplitude of slow modulation $A$ at fixed other parameters $\omega_0 = 2\pi$, $T = 6$, $\varepsilon = 0.5$.

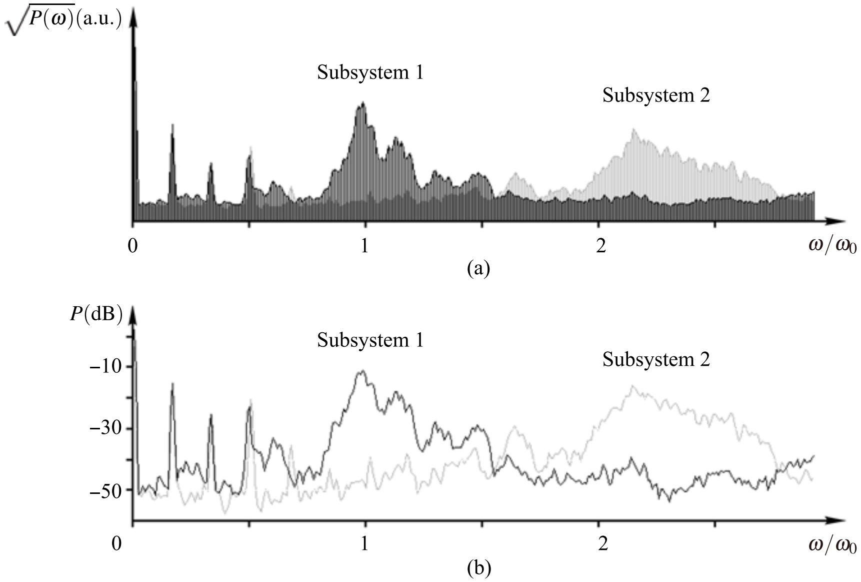


**Fig. 4.8** Power spectrum generated by the system (4.9) at $\omega_0 = 2\pi$, $T = 6$, $\varepsilon = 0.5$ obtained by processing data of the numerical simulation: the square root of the spectral power density **(a)** and the spectral power density in logarithmic scale **(b)**.

Figure 4.8 shows power spectra of two oscillators constituting the system (4.9) as obtained from processing time series for $x$ and $y$ sampled from data of numerical simulation of the dynamics on the attractor. The spectrum is computed according to the method of statistical evaluation of the spectral power density recommended in the theory of random processes (Jenkins and Watts, 1968). The procedure includes breaking the time series onto pieces of certain length, performing the Fourier transform for each segment, and then averaging the squares of the amplitudes of spectral components over all pieces. Panel (a) shows a plot for square root of the power density versus frequency, and panel (b) plots this quantity in logarithmic scale, in decibels traditionally used in electronics (10 dB correspond to 10-fold ratio of the compared power levels).[2]

As can be seen from the figure, the spectrum of one oscillator is concentrated in a certain range near the natural frequency $\omega_0$, and the second near the doubled frequency $2\omega_0$. The continuous component in the power spectrum is an attribute of chaotic dynamics. Discrete peaks in the left part of the picture appear due to the presence of periodic component in the dynamics of the system because of the slow modulation of the parameter.

In Appendix G features of dynamics on hyperbolic attractor under effect of external noise are considered using this model as an example.

It was found out that in the considering system the hard excitation and hysteresis can be observed in a quite wide range of parameters. To demonstrate this phenomenon, let us supplement Eqs. (4.9) with an additional parameter $h$, which regulates relative duration of excitation and damping stages of the oscillators:

$$\begin{aligned}\ddot{x}-(h+A\cos(2\pi t/T)-x^2)\dot{x}+\omega_0^2 x=\varepsilon y\cos\omega_0 t,\\ \ddot{y}-(h-A\cos(2\pi t/T)-y^2)\dot{y}+4\omega_0^2 y=\varepsilon x^2.\end{aligned} \tag{4.17}$$

The above-described mode of operation corresponds to excitation of the first oscillator entering the activity stage by stimulation from the partner. The respective driving force is proportional to the squared amplitude of oscillations of the partner at the previous stage of activity. If one sets the initial conditions with characteristic amplitude small enough, the excitation of the whole system does not occur because of negligible level of the squared amplitude, and the oscillations do not develop. Generation regime can be restored by increasing parameter $h$, i.e. by increase of the part of the modulation period, during which the oscillators are linearly unstable. With gradual growth of $h$, at some point one observes an abrupt transition to the large amplitude chaotic regime. Now, if one starts to decrease $h$, it does not lead immediately to breakdown of the chaotic oscillations since the excitation in the system is transferred from the previous stages of activity to the next ones. Only at large enough negative values of $h$ the oscillations decay. The hysteresis phenomenon is illustrated in Fig. 4.9. In the course of computation, small random perturbation was added at each step of the numeric integration on a level of order $\Delta x \sim 0.0001$ to ensure departure of the system from the trivial stationary state at zero as it becomes unstable. The insets in Fig. 4.9 show portraits of attractors in the Poincaré map at representative points of the hysteresis loop, from which one can see that its type corresponds to the Smale-Williams solenoid.

[2] The first form of presentation is selected to make possible a qualitative comparison with experimental data in Chap. 12 available in this scale; the second is used to make possible visual comparison with data relating to time-delay systems in experiment in Chap. 13 and in numerics in Chap. 10.

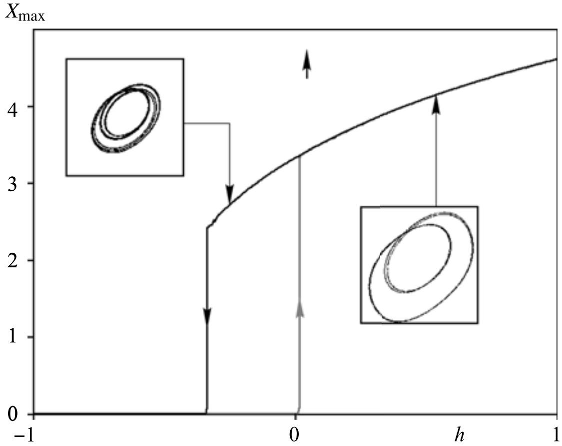


**Fig. 4.9** A diagram illustrating the hard excitation and hysteresis in the system: Dependence of the maximum amplitude of the first oscillator on the parameter $h$ in (4.17) at $\omega_0 = 2\pi$, $T = 6$, $A = 5$, $\varepsilon$=0.5. The parameter $h$ is varied, first, from left to right that corresponds to motion along the lower branch, and then from right to left that corresponds to motion along the upper branch of the hysteresis loop.

## 4.3 System of alternately excited van der Pol oscillators in terms of slow complex amplitudes

In assumption that $N = \omega_0 T/2\pi \gg 1$, and for parameters $A$ and $\varepsilon$ being not too large, the problem may be reformulated in terms of slow complex amplitudes, with decrease of a number of relevant control parameters. For this, we set

$$\begin{aligned} x &= ae^{i\omega_0 t} + a^* e^{-i\omega_0 t}, \quad \dot{x} = i\omega_0 a e^{i\omega_0 t} - i\omega_0 a^* e^{-i\omega_0 t}, \\ y &= be^{2i\omega_0 t} + b^* e^{-2i\omega_0 t}, \quad \dot{y} = 2i\omega_0 b e^{2i\omega_0 t} - 2i\omega_0 b^* e^{-2i\omega_0 t}, \end{aligned} \tag{4.18}$$

and up on substitution in Eqs. (4.9) and averaging we obtain

$$\begin{aligned} \dot{a} &= \frac{1}{2}(aA\cos(2\pi t/T) - |a|^2 a) - i\bar{\varepsilon} b, \\ \dot{b} &= \frac{1}{2}(-bA\cos(2\pi t/T) - |b|^2 b) - i\bar{\varepsilon} a^2, \end{aligned} \tag{4.19}$$

where $\bar{\varepsilon} = \varepsilon/4\omega_0$. A study of this system was made in (Kuptsov et al., 2008). It was shown that in a wide parameter range attractor of Smale-Williams type takes place in the stroboscopic Poincaré map, particularly, it is the case at $A$=3, $T$=10, $\bar{\varepsilon} = 0.05$.

It may be speculated that such equations will arise in a broader context than the approximating dynamics of the concrete model. Arguing in the spirit of theory of onset of turbulence of Landau and Hopf (Landau and Lifshitz, 1959; Hopf, 1948), one can imagine the following situation. Suppose we have some spatially extended system, in which two oscillatory modes occur with frequency ratio close to 1:2 on the background of an additional slow periodic motion; they alternately come beyond the threshold of excitation and back, because the nonlinear interactions transfer excitation to each other. Then, we have the conditions for the realization of a hyperbolic attractor of Smale-Williams type.

## 4.4 Non-resonance excitation transfer

As mentioned above, the system (4.9) is designed in such a way that the coupling terms contain frequency components *in resonance* with the oscillator to which the excitation is passed. It occurs that attractor of Smale-Williams type can arise in the system of two alternately active self-oscillators as well with *non-resonance* transfer of the excitation (Kuznetsov et al., 2007). Indeed, accounting finite characteristic time of excitation of the partner oscillator, the spectrum of signal ensuring the excitation transfer occupies a band of some width around the central frequency having decaying tails on both sides. If, say, the central frequency is $2\omega_0$, and natural frequency of the excited oscillator is $\omega_0$, then, under certain conditions presence of the components on the tail of the spectral distribution near $\omega_0$ may arrange the excitation transfer, accounting that on the activity stage at finite super-criticality the growth of the perturbation is exponential. Of course, in this case conditions of parameters of the system are essentially more restricted.[3]

As an example, consider a system

$$\begin{aligned} &\ddot{x} - (A\cos(2\pi t/T) - x^2)\dot{x} + \omega_0^2 x = \varepsilon y, \\ &\ddot{y} - (-A\cos(2\pi t/T) - y^2)\dot{y} + 4\omega_0^2 y = \varepsilon x^2, \end{aligned} \tag{4.20}$$

which operates without the auxiliary signal in contrast to (4.9). According to results of numerical simulation of the dynamics at $T = 10, \omega_0 = 2\pi, \varepsilon = 0.5, A = 6$, attractor of Smale-Williams type occurs in the stroboscopic Poincaré map, although the transfer of the excitation from the second oscillator to the first one is of non-resonance character. Figure 4.10 shows the iteration diagram for phases at successive stages of activity of the first oscillator, the attractor in projection from extended phase space onto the plane $(x, \dot{x})$, and the portrait of the attractor in the stroboscopic Poincaré map. Lyapunov exponents estimated numerically for the Poincaré map in this regime are $\Lambda_1 = 0.6808, \Lambda_2 = -3.625, \Lambda_3 = -8.326, \Lambda_4 = -17.633$, and estimate of the Kaplan-Yorke dimension yields $D_{KY} = 1.188$.

[3] Apparently, in many applications, say, in microwave electronics, laser physics, nonlinear optics, the resonance mechanism should be regarded as preferable. Indeed, it seems problematic that non-resonance transfer may be arranged on a level significantly exceeding noises under frequency larger in order or more than the modulation frequency.

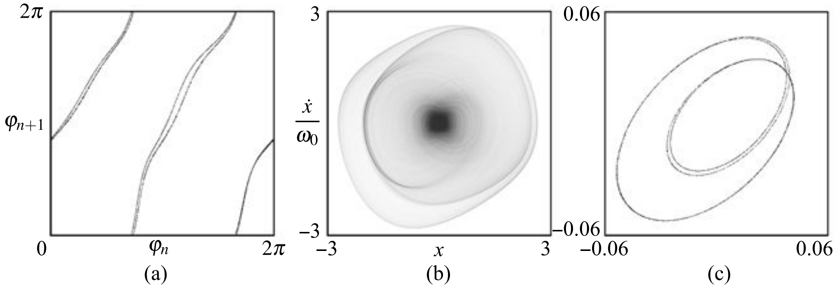


**Fig. 4.10** Diagram for phases determined from formula $\varphi = \arg(x - i\dot{x}/\omega_0)$ at successive instants $t = nT$ **(a)**, attractor in projection onto the phase plane of the first oscillator **(b)**, and portrait in the Poincaré section **(c)** for the system with non-resonance excitation transfer governed by Eqs. (4.20) at $T = 10, \omega_0 = 2\pi, \varepsilon = 0.5, A = 6$.

## 4.5 Plykin-like attractor in non-autonomous coupled oscillators

In the present section it will be shown how to implement the dynamics associated with attractor of Plykin type in a system of coupled non-autonomous oscillators. As believed, it opens prospects for design of physical and technical systems, e.g. electronic devices with Plykin type attractors (Kuznetsov, 2009).

### *4.5.1 Representation of states on a sphere and equations of the model*

Let us start with a system of two self-oscillators with compensation of losses from the common energy source; the equations for slow complex amplitudes $a$ and $b$ read

$$\begin{aligned} \dot{a} &= \frac{1}{2}\mu(1-|a|^2-|b|^2)a, \\ \dot{b} &= \frac{1}{2}\mu(1-|a|^2-|b|^2)b, \end{aligned} \tag{4.21}$$

where $\mu$ is a positive parameter. Let us set

$$b = \sqrt{\rho}e^{i\varphi/2+i\psi}\sin(\theta/2), \quad a = \sqrt{\rho}e^{-i\varphi/2+i\psi}\cos(\theta/2). \tag{4.22}$$

Clearly, in the sustained regime of the self-oscillations, the equality $\rho = |a|^2 + |b|^2 = 1$ has to be valid. Identifying the states of the system, differing only in the overall phase, under condition $\rho = 1$ one can associate them with points on a unit sphere (Fig. 3.12). Also, the Cartesian coordinates may be introduced

$$x = \rho\cos\varphi\sin\theta, \quad y = \rho\sin\varphi\sin\theta, \quad z = \rho\cos\theta. \tag{4.23}$$

Via the complex amplitudes they are expressed as

$$x+iy=2a^*b, \quad z=|a|^2-|b|^2. \tag{4.24}$$

We are going to modify the model (4.21) in order to obtain a set of equations with coefficients periodically varying in time, in such a way that in the stroboscopic description the Plykin type attractor will occur.

Let us consider a sequence of continuous transformations on the sphere, which is equivalent in a whole period to those discussed in Sect. 3.3. However, in order to simplify the equations written for the complex amplitudes, it is more convenient here to perform the transformations in six rather than in four stages. Duration of each of the stages is accepted equal to a unit time interval.

**I. Flow down along circles of latitude**. At this stage we require the angular velocity of representative points on the sphere to be proportional to $\sin 2\varphi$. An appropriate form of the differential equations is

$$\dot{a}=-i\varepsilon a\mathrm{Im}(a^*b)^2, \quad \dot{b}=i\varepsilon b\mathrm{Im}(a^*b)^2. \tag{4.25}$$

Indeed, substituting $b=e^{i\varphi/2+i\psi}\sin(\theta/2)$, $a=e^{-i\varphi/2+i\psi}\cos(\theta/2)$, after some simple manipulations we get $\dot{\varphi}=\frac{1}{2}\varepsilon\sin^2\theta\sin 2\varphi, \dot{\theta}=0$. Physically, the right-hand terms in (4.25) ensure a frequency shift of opposite sign for two oscillators. Magnitude of the shift is proportional to the amplitude of a low-frequency signal produced from mixing of the second harmonic components of both oscillators on a quadratic nonlinear element.

**II. Differential rotation** around $z$-axis with angular velocity depending on $z$. At this stage we set

$$\dot{a}=-\frac{1}{4}i\pi(\sqrt{2}-1-2\sqrt{2}|a|^2)a, \quad \dot{b}=-\frac{1}{4}i\pi(\sqrt{2}+1-2\sqrt{2}|b|^2)b. \tag{4.26}$$

In angular variables $(\varphi,\theta)$, these equations reduce to $\dot{\varphi}=-\frac{1}{2}\pi(\sqrt{2}\cos\theta+1)$, $\dot{\theta}=0$. Note that the angular velocity $\dot{\varphi}$ depends linearly on $z=\cos\theta$ and vanishes at $z=-1/\sqrt{2}$. At this stage two subsystems behave like uncoupled classic non-isochronous oscillators. At small amplitudes their frequencies are detuned from the reference point by $\Delta\omega_{a,b}=-\frac{1}{4}i\pi(\sqrt{2}\mp 1)$. With growth of the amplitudes, the frequencies undergo a shift proportional to the squared amplitude for both subsystems.

**III. Rotation** of the sphere by 90° around the $y$-axis in accordance with the equations

$$\dot{a}=\frac{1}{4}\pi b, \quad \dot{b}=-\frac{1}{4}\pi a. \tag{4.27}$$

It corresponds to a conservative system of coupled oscillators with equal frequencies, with the coupling coefficient of such value that the energy exchange between the partial oscillators corresponds precisely to the duration of the stage.

**IV. Flow down along circles of latitude**, like at the first stage:

$$\dot{a} = -i\varepsilon a \mathrm{Im}(a^* b)^2, \quad \dot{b} = i\varepsilon b \mathrm{Im}(a^* b)^2. \tag{4.28}$$

**V. Inverse differential rotation** around $z$-axis:

$$\dot{a} = \frac{1}{4} i\pi(\sqrt{2} - 1 - 2\sqrt{2}|a|^2)a, \quad \dot{b} = \frac{1}{4} i\pi(\sqrt{2} + 1 - 2\sqrt{2}|b|^2)b. \tag{4.29}$$

**VI. Inverse rotation** by 90° around the $y$-axis:

$$\dot{a} = -\frac{1}{4}\pi b, \quad \dot{b} = \frac{1}{4}\pi a. \tag{4.30}$$

The procedure is symmetric in the sense that the operations for the stages (I) and (IV) are identical, while the stages (II) and (III) differ from (V) and (VI) only by directions of the rotations.

Now, we can write down equations for the complex amplitudes embracing the complete time period $T = 6$. For this, we compose the right-hand sides as combinations of terms (4.25), (4.26), (4.27), which are supposed to be switched on, or off, during the respective stages of the time evolution. As to the terms from (4.21), we account them only at the stages of rotation. Their exclusion for other stages is not so significant, but we do so, because it simplifies the derivation of the Poincaré map. Thus, we arrive at the equations

$$\begin{aligned}
\dot{a} &= -i\varepsilon(1 - \sigma^2 - s^2)\mathrm{Im}(a^2 b^{*2})a \\
&\quad + \frac{1}{4} i\sigma\pi(\sqrt{2} - 1 - 2\sqrt{2}|a|^2)a - \frac{\pi}{4} sb + \frac{1}{2} s^2 \mu(1 - |a|^2 - |b|^2)a, \\
\dot{b} &= i\varepsilon(1 - \sigma^2 - s^2)\mathrm{Im}(a^2 b^{*2})b \\
&\quad + \frac{1}{4} i\sigma\pi(\sqrt{2} + 1 - 2\sqrt{2}|b|^2)b + \frac{\pi}{4} sa + \frac{1}{2} s^2 \mu(1 - |a|^2 - |b|^2)b.
\end{aligned} \tag{4.31}$$

Here the factors $\sigma$ and $s$ depend on time with period $T = 6$, and on a single period are defined by the relations

$$\sigma = \begin{cases} -1, & 1 \leqslant t < 2 \\ 1, & 4 \leqslant t < 5, \\ 0, & \text{otherwise,} \end{cases} \qquad s = \begin{cases} -1, & 2 \leqslant t < 3 \\ 1, & 5 \leqslant t < 6, \\ 0, & \text{otherwise.} \end{cases} \tag{4.32}$$

Let us derive the Poincaré map, which determines transformation of the state over one period $T$=6 and delivers stroboscopic description of the time evolution. Let the initial conditions for Eqs. (4.31) at $t_n = nT$ be defined as the state vector $\mathbf{X}_n = (a_n, b_n)$. Solving the equations in each successive unit interval analytically, we can represent the map explicitly:

$$\mathbf{X}_{n+1} = \mathbf{G}_+(\mathbf{G}_-(\mathbf{X})) \equiv \mathbf{G}(\mathbf{X}), \tag{4.33}$$

where

$$\mathbf{G}_{\pm}(\mathbf{X}) = \left\{ \begin{array}{c} \dfrac{aD(a,b)e^{\pm\frac{1}{4}i\pi(\sqrt{2}-1-2\sqrt{2}|a|^2)} \mp bD^*(a,b)e^{\pm\frac{1}{4}i\pi(\sqrt{2}+1-2\sqrt{2}|b|^2)}}{\sqrt{1+(|a|^2+|b|^2)(e^{\mu}-1)}} e^{\frac{1}{2}\mu} \\ \dfrac{\pm aD(a,b)e^{\pm\frac{1}{4}i\pi(\sqrt{2}-1-2\sqrt{2}|a|^2)} + bD^*(a,b)e^{\pm\frac{1}{4}i\pi(\sqrt{2}+1-2\sqrt{2}|b|^2)}}{\sqrt{1+(|a|^2+|b|^2)(e^{\mu}-1)}} e^{\frac{1}{2}\mu} \end{array} \right\}, \tag{4.34}$$

and

$$D(a,b) = \frac{1}{\sqrt{2}} \left( \frac{|a|^2|b|^2 - (a^*b)^2 \tanh(2\varepsilon|a|^2|b|^2)}{|a|^2|b|^2 - (ab^*)^2 \tanh(2\varepsilon|a|^2|b|^2)} \right)^{\frac{1}{4}}. \tag{4.35}$$

### *4.5.2 Numerical results for the coupled oscillators*

Figure 4.11 shows plots for the amplitudes of the coupled oscillators $|a|$ and $|b|$ versus time obtained from numerical solution of the differential equations (4.31). As initial conditions, some small in absolute value and random in phase complex amplitudes $a$ and $b$ are taken, so the plot depicts the transient evolution prior to the regime of chaotic self-oscillations. In the right-hand part of the diagram the dependences look like samples of a random process, that associates with motion on the chaotic attractor. Locally, some features can be seen because of the piecewise continuous nature of the process composed of successive stages. Particularly, the horizontal plateaus relate to the stages of evolution (I), (II), (IV), (V), on which the amplitudes $|a|$ and $|b|$ remain constant. Note that the dependence on $|a|$ and $|b|$ is interconnected: in the sustained regime they obey the relation $|a|^2 + |b|^2 = 1$.

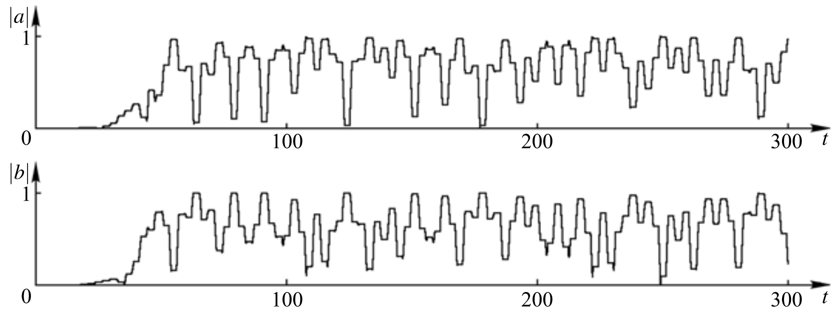


**Fig. 4.11** Plots of the real amplitudes $|a|$ and $|b|$ versus time in the transient process obtained from numerical solution of the differential equations (4.31) at $\varepsilon = 0.77$ and $\mu = 1$.

Fig. 4.12(a) shows portrait of the attractor of the stroboscopic Poincaré map corresponding to the instants $t_n = nT, T = 6$. To make visible the intrinsic transversal Cantor-like structure, special coordinates $\mathrm{Re}(a^*b), \mathrm{Im}(a^*b)$ are used. The points are shown in black, if the amplitude of the first oscillator is larger than that of the second oscillator, and in gray otherwise. As seen from relations (4.22), such visualization corresponds to a definite plane projection of the attractor from the sphere. It may be observed that this attractor exactly corresponds to the attractor of the formal model from the previous chapter (compare Fig. 4.12(a) with 3.13(b)).

Figure 4.12(b) presents a portrait of the attractor for the continuous-time system (4.31). As the dimension of the state space is sufficiently high (vector $\mathbf{X} = (a,b)$ is four-dimensional, and the extended state space of the non-autonomous system is five-dimensional), depicting the image to resolve subtle fractal transverse structure intrinsic to the attractor is not a trivial task. The portrait is shown on the plane of two values of real amplitude $|a(t)|$ and $|a(t-3)|$, which relate to instants separated by a half of time period of variation of the coefficients in Eqs. (4.31). Presentation of the object in gray scales is used: brighter tones correspond to pixels visited by the representative point with higher probability. Here, again one can distinguish the fractal-like transverse structure linked with the dynamics of the Plykin type. This method of visualization may be appropriate in experiments with systems of the class under consideration.

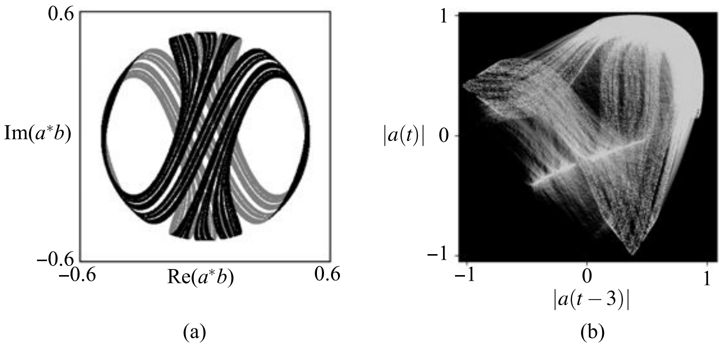


**Fig. 4.12** Portrait of attractor for the Poincaré map (4.33) in the coordinates $\mathrm{Re}(a^*b), \mathrm{Im}(a^*b)$ **(a)** and attractor of the continuous-time system (4.31) on the plane of real amplitudes of one oscillator separated by time interval $T/2 = 3$ in gray scales: brighter tones correspond to higher probability of visiting the pixels by the orbit **(b)**. The parameter values are $\varepsilon = 0.77$, $\mu = 1$.

Two Lyapunov exponents for the Poincaré map are equal to those for the map (3.24). Besides, there is a zero exponent associated with a simultaneous equal phase shift for both oscillators, and a negative exponent corresponding to approach of the trajectories to the invariant set $|a|^2 + |b|^2 = 1$. Figure 4.13 presents the results graphically. The first plot (a) shows four Lyapunov exponents $\Lambda_i$ in dependence on parameter $\varepsilon$ at fixed $\mu = 1$. In the range $\varepsilon < \varepsilon_c \approx 2.03$ one of the exponents is positive that means chaos. Among other exponents one is zero (up to numerical errors), and two are negative. Note a smooth dependence of the largest exponent on the parameter in that range. For larger $\varepsilon$ (strong dissipation is brought in at the stages I and IV) chaos disappears. The second plot (b) shows the Lyapunov exponents versus $\mu$ at fixed $\varepsilon = 1$. Observe that variation of $\mu$ notably effects only one exponent, which corresponds, obviously, to approach of orbits to the invariant sphere. Presence of

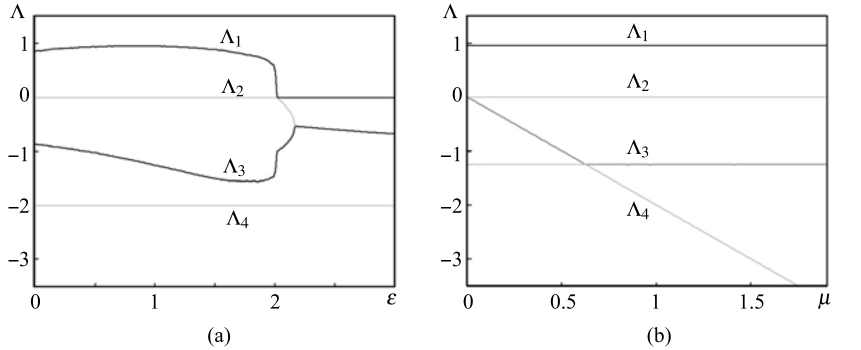


**Fig. 4.13** Four Lyapunov exponents versus parameter $\varepsilon$ at $\mu = 1$ **(a)** and versus parameter $\mu$ at $\varepsilon = 1$ **(b)** for the Poincaré map represented in terms of complex amplitudes. A zero exponent occurs due to invariance of the equations in respect to the overall phase shift.

a zero exponent reflects invariance of the equations in respect to the overall phase shift. Of course, results of computations agree with the data from the previous chapter: at identical $\varepsilon$ two of the nonzero exponents coincide (up to numerical errors) with those obtained for the two-dimensional map.

Formally, in our complex amplitude equations the attractor should not be interpreted as uniformly hyperbolic, because of presence of a neutral direction in the state space associated with the overall phase (presence of the zero-value Lyapunov exponent in the Poincaré map). Instead, it has to be related to the class of *partially hyperbolic attractors* (Pesin,2004; Bonatti et al., 2005; Pesin, 2007). Nevertheless, in the form used here, the invariance of the equations in respect to the overall phase is exact; it means that one can accept a legal agreement not to distinguish states distinct only in the phase.[4] In a frame of this convention, we can treat the dynamics as being true hyperbolic. However, in systems, for which description in terms of slow complex amplitudes will be an approximation, one can expect appearance of peculiarities associated with features of the partially hyperbolic attractor. If the deflections from the slow-amplitude approximation are small, the overall phase will manifest slow random walk, while the dynamics of the rest variables will retain its character because of intrinsic robustness.

In conclusion of this section, it is worth mentioning that there are some other situations in physics where the states are naturally associated with points on a sphere. For example, it relates to representation of two-level systems and, particularly, of particles of spin $1/2$, on the Bloch sphere (Mark Fox, 2006), or to the description of light polarization in terms of Stokes parameters (Goldstein and Collet, 2003). We can assume that under certain manipulations in such systems the dynamics corresponding to attractors of Plykin type could be implemented.

[4] Anologous reasoning was used to decrease the phase-space dimension handled in many models considered in literature, including the derivation of the celebrating Lorenz model.

## References


Andronov, A.A., Vitt, A.A., Khaĭkin, S.Ė.: Theory of Oscillators, Pergamon Press, Oxford (1966).

Bonatti, C., Diaz, L.J., Viana, M.: Dynamics Beyond Uniform Hyperbolicity. A Global Geometric and Probobalistic Perspective. Encyclopedia of Mathematical Sciences. Vol.102. Springer, Berlin, Heidelberg, New York (2005).

Davis, H.T.: Introduction to Nonlinear Differential and Integral Equations. Dover Publications, New York (1962).

Devaney, R.L.: An Introduction to Chaotic Dynamical Systems. Westview Press, New York (2003).

Goldstein, D.H., Collet, E.: Polarized Light, Revised and Expanded. CRC Press, Boca Raton (2003).

Grassberger, P., Procaccia, I.: Measuring the strangeness of strange attractors. Physica D **9,** 189–208 (1983).

Grebenikov, E., Mitropolsky, Yu.A., Ryabov, Y.A.: Asymptotic Methods in Resonance Analytical Dynamics. CRC Press, Boca Raton (2004).

Hayashi, C.: Nonlinear Oscillations in Physical Systems. McGraw-Hill, New York (1964).

Hilborn, R.C.: Chaos and Nonlinear Dynamics. Oxford University Press, Cambridge (2000).

Hopf, E.: A mathematical example displaying features of turbulence. Communications on Pure and Applied Mathematics **1**, 303–322 (1948)

Hunt, B.R., Ott, E.: Fractal properties of robust strange nonchaotic attractors. Phys. Rev. Lett. **87**, 254101 (2001).

Isaeva, O.B., Kuznetsov, S.P., Osbaldestin, A.H.: Complex Analytic Dynamics Phenomena in a System of Coupled Nonautonomous Oscillators with Alternative Excitation. Tech. Phys. Lett. **33,** 748–751 (2007)

Isaeva, O.B., Kuznetsov, S.P., Osbaldestin, A.H.: A system of alternately excited coupled non-autonomous oscillators manifesting phenomena intrinsic to complex analytical maps. Physica D **237**, 873–884 (2008).

Jalnine, A.Yu., Kuznetsov, S.P.: On the realization of the hunt-ott strange nonchaotic attractor in a physical system. Technical Physics **52,** 401–408 (2007).

Jenkins, G.M., Watts, D.G.: Spectral Analysis and its Application. Holden-Day, Inc., San Francisco (1968).

Kim, J-W., Kim, S.-Y. Hunt, B., Ott, E.: Fractal properties of robust strange nonchaotic attractors in maps of two or more dimensions. Phys. Rev. E **67**, 036211 (2003).

Kuptsov, P.V., Kuznetsov, S.P., Sataev, I.R.: Hyperbolic attractor of Smale-Williams type in a system of two coupled non-autonomous amplitude equations. Preprint nlin. arXiv: 0804.3677 (2008).

Kuramoto, Y.: Chemical Oscillations, Waves, and Turbulence. Springer, Berlin (1984).

Kuznetsov, A.P., Kuznetsov, S.P., Pikovsky, A.S., Turukina, L.V.: Chaotic dynamics in the system of coupling nonautonomous oscillators with resonance and nonresonance transfer of excitation. Izvestija VUZov-Applied Nonlinear Dynamics (Saratov) **15** (6), 75–85 (2007) (In Russian).

Kuznetsov, S.P.: Example of a physical system with a hyperbolic attractor of the Smale-Williams type. Phys. Rev. Lett. **95**, 144101 (2005).

Kuznetsov, S.P., Sataev, I.R.: Hyperbolic attractor in a system of coupled non-autonomous van der Pol oscillators: Numerical test for expanding and contracting cones. Physics Letters A **365**, 97–104 (2007).

Kuznetsov, Yu.A.: Elements of Applied Bifurcation Theory. Springer, New York, Berlin, Heidelberg (1998).

Kuznetsov, S.P. and Sataev, I.R.: Hyperbolic attractor in a system of coupled non-autonomous van der Pol oscillators: Numerical test for expanding and contracting cones. Physics Letters A **365**, 97–104 (2007).

Landa, P.S.: Nonlinear Oscillations and Waves in Dynamical Systems. Kluwer Academic Publisher, The Netherlands (1996).

Landau, L.D., Lifshitz, E.M.: Fluid Mechanics (Course of Theoretical Physics, vol.6). Pergamon Press, London (1959).

Mark Fox, A.: Quantum Optics: An Introduction. Oxford University Press, Cambridge (2006).

Nayfeh, A.H.: Perturbation Methods. Wiley, NewYork (2000).

Ott, E.: Chaos in dynamical systems. Cambridge University Press, Cambridge (2002).

Pesin, Ya.B.: Lectures on Partial Hyperbolicity and Stable Ergodicity. Zurich Lectures in Advanced Mathematics. European Mathematical Society (2004).

Pesin, Ya.: Existence and genericity problems for dynamical systems with nonzero Lyapunov exponents. Regular and Chaotic Dynamics **12**, 476–489 (2007).

Pikovsky, A., Rosenblum, M., Kurtz, J.: Synchronization: A Universal Concept in Nonlinear Sciences. Cambridge University Press, Cambridge (2002).

Rabinovich, M.I., Trubetskov, D.I.: Oscillations and Waves: In Linear and Nonlinear Systems, Kluwer Academic Publication, The Netherlands (1989).

Schuster, H.G., Just, W.: Deterministic Chaos: An Introduction. Wiley-VCH Verlag GmbH & Co. KGaA, Weinheim, FRG (2005) .

Strogatz, S.H.: Nonlinear Dynamics and Chaos: with Applications to Physics, Biology, Chemistry, and Engineering. Westview Press, MA (2001).

Tong, H.(Ed.): Dimension Estimation and Models (Nonlinear Time Series and Chaos). World Scientific Publication, Singapore (1994).

Wilczak, D.: Uniformly Hyperbolic attractor of the Smale-Williams type for a Poincaré map in the Kuznetsov system. SIAM J. Applied Dynamical Systems **9**, 1263–1283 (2010).

# Chapter 5
# Autonomous Low-dimensional Systems with Uniformly Hyperbolic Attractors in the Poincaré Maps

**Abstract** The idea of manipulating by phases in the course of the excitation transfer between the alternately active oscillators may be applied to design of autonomous systems with hyperbolic chaos. To develop such models one needs to ensure self-modulation accompanying with alternating activating and damping of self-oscillations in two interacting subsystems. Several examples will be considered in the present chapter. One of them may serve as illustration of intriguing problem of origin of hyperbolic attractors under variation of parameters of the system; it relates to the scenario of birth of the Smale-Williams attractor via the so-called blue-sky catastrophe in accordance with mechanism suggested by Shilnikov and Turaev. All systems we examine here are based on non-resonance transfer of excitation; in some respect, it may be regarded as a disadvantage because it may be problematic to implement these models, say, in electronics and nonlinear optics, at large ratios of characteristic frequencies of the self-oscillation and self-modulation.

## 5.1 Autonomous system of two coupled oscillators with self-regulating alternating excitation

Let us try to construct an autonomous continuous-time system with Smale-Williams attractor in the Poincaré map departing from the coupled alternately excited oscillators discussed in the previous chapter.

There are two kinds of time dependence of coefficients, which make Eqs. (4.9) non-autonomous. The first is slow periodic variation of parameters responsible for the Andronov-Hopf bifurcation, and the second is the auxiliary signal of frequency $\omega_0$. In the averaged equations for complex amplitudes (4.17) the last kind of the time dependence is excluded, so, to get a set of autonomous differential equations we need only one step: to replace the external slow periodic driving by appropriate evolution of an additional real internal variable $z$, which enters equations for two oscillators with opposite signs:

S. P. Kuznetsov, *Hyperbolic Chaos*

$$\dot{a} = \frac{1}{2}(z - |a|^2)a - i\varepsilon b,$$
$$\dot{b} = \frac{1}{2}(-z - |b|^2)b - i\varepsilon a^2. \tag{5.1}$$

This additional variable has to decrease while the first oscillator is active, and to grow as the second one is active, in symmetric way. To obtain the alternating excitation of the oscillators as a self-supporting process, we supplement Eqs. (5.1) with a differential equation of the first order for the variable $z$; the right-hand part contains the difference of the squared amplitudes of two oscillators and a term linear in $z$, with some positive coefficient. So, we assume

$$\dot{z} = \alpha z + |b|^2 - |a|^2. \tag{5.2}$$

Now, setting $a = X + iY, b = U + iV$ in (5.1) and (5.2) we arrive at an autonomous five-dimensional system in real variables

$$\begin{aligned}
\dot{X} &= \frac{1}{2}(z - X^2 - Y^2)X + \varepsilon V,\\
\dot{Y} &= \frac{1}{2}(z - X^2 - Y^2)Y - \varepsilon U,\\
\dot{U} &= \frac{1}{2}(-z - U^2 - V^2)U + 2\varepsilon XY,\\
\dot{V} &= \frac{1}{2}(-z - U^2 - V^2)V - \varepsilon(X^2 - Y^2),\\
\dot{z} &= \alpha z + U^2 + V^2 - X^2 - Y^2.
\end{aligned} \tag{5.3}$$

It delivers an explicit example of an autonomous set of differential equations possessing attractor of Smale-Williams type in the Poincaré map.[1]

Figure 5.1 shows time dependence on amplitudes and phases obtained from numerical simulation of the dynamics at appropriately selected parameter values. Observe alternating self-oscillating excitations of the first and the second partial oscillators. As will be shown below, they are accompanied with the transformation of phases, like in the prototypical system corresponding to the Bernoulli type map on each cycle of oscillations of the variable $z$.

To proceed, we have to define Poincaré section in the five-dimensional phase space; it appears appropriate to use a hyper-plane $z$=0 accounting cross-sections of it by orbits, say, in direction of increase of the variable $z$, i.e., with the additional condition $\dot{z} > 0$.

[1] Although we have derived equations departing from a model associated with physically non-autonomous system, what is worth outlining here is formal relation of the differential equations (5.1) by their mathematical entity to the autonomous class. At the moment, we do not concern the question of concrete physical realization of the dynamics.

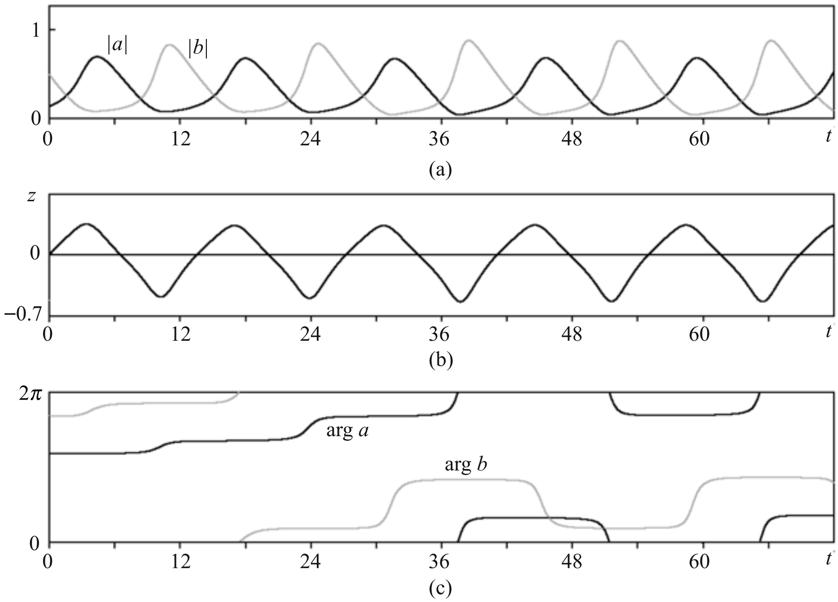


**Fig. 5.1** Plots of the real amplitudes $|a|$ and $|b|$ versus time in the sustained regime obtained from numerical solution of the differential equations (5.3), at $\varepsilon = 0.1$ and $\alpha = 0.6$.

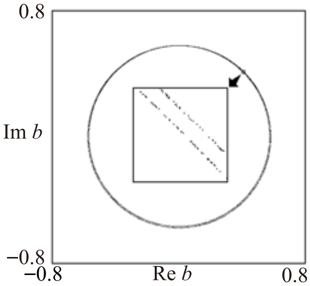


**Fig. 5.2** Portrait of attractor for the system (5.3) in projection on the plane $(U, V)$ in the Poincaré section with the hyper-plane $z = 0$ passed by the orbits with $\dot{z} > 0$. Parameter values are $\varepsilon = 0.1$ and $\alpha = 0.6$. A fragment is shown with magnification to resolve the transversal Cantor-like structure of the object. A mean time interval between successive cross-sections of the hyper-plane in right direction is $< T > \approx 13.77$.

Figure 5.2 shows portrait of attractor of the Poincaré map in projection on a plane of variables relating to one of the alternately exciting subsystems. In fact, the attractor is a kind of the Smale-Williams solenoid embedded in the four-dimensional phase space of the Poincaré map. In the inset a fragment of the picture is magnified that allows resolving the intrinsic transversal Cantor-like structure of the filaments of the attractor. Figure 5.3 shows the diagram illustrating transformation of the angular coordinate, or phase for the second subsystem defined at successive returns at the cross-sections as $\varphi_n = \arg(U + iV)|_{z=0,\dot{z}>0}$. It may be seen that for the cyclic coordinate $\varphi$ the expanding circle map takes place with high accuracy producing the doubling of the phase. In other directions in the phase space the phase volume undergoes compression.

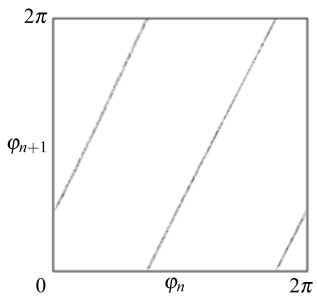


**Fig. 5.3** Iteration diagram for the phase of the second partial oscillator $\varphi_n = \arg(U + iV)|_{z=0,\dot{z}>0}$ obtained from numerical solution of Eqs. (5.3) at $\varepsilon = 0.1$ and $\alpha = 0.6$.

Computation of the Lyapunov exponents for the attractor of the flow system (5.3) at $\varepsilon = 0.1$ and $\alpha = 0.6$ yields

$$\begin{gathered}\lambda_1 = 0.05036, \quad \lambda_2 = 0.00000, \quad \lambda_3 = -0.3351, \\ \lambda_4 = -0.3933, \quad \lambda_5 = -0.4787.\end{gathered} \tag{5.4}$$

Accounting that the average period of transfer of the excitation according to the computations is found to be $T_{\rm av} \approx 13.77$, the largest Lyapunov exponent for the Poincaré map is $\Lambda_1 = \lambda_1 T_{\rm av} \approx 0.6934$, which is in excellent agreement with the estimate based on the Bernoulli map, $\Lambda_1 = \ln 2$. The second exponent $\lambda_2$ is zero up to numerical errors and corresponds to perturbation vector directed along the reference trajectory as it always takes place in autonomous systems. All other Lyapunov exponents are negative being responsible for compression of the phase volume and approach of phase trajectories to the attractor. The estimate of the Kaplane-Yorke dimension for the attractor embedded in the five-dimensional phase space of Eqs. (5.3) yields $D_{KY} = 2 + (\lambda_1 + \lambda_2)/|\lambda_3| \approx 2.15$.

The numerical simulations agree with the structural stability expected for the attractor. Qualitatively the same behavior with Bernoulli type dynamics of the phase for successive epochs of activity persists in a rather wide area on the parameter plane (Fig. 5.4).

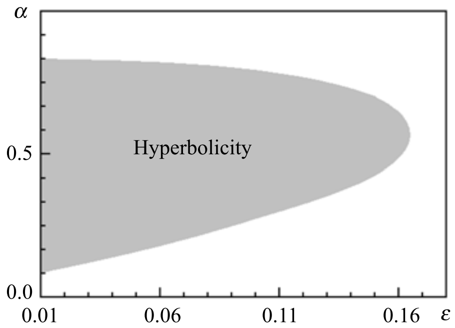


**Fig. 5.4** Domain of persistence of dynamics associated with Bernoulli type transformation of phases for successive epoch of activity of subsystems of the model (5.3) shown as gray area on the parameter plane.

## 5.2 System constructed on a base of the predator-prey model

A number of examples of autonomous systems with hyperbolic attractors were suggested in our joint work with Pikovsky (Kuznetsov and Pikovsky, 2007). Let us turn to one, which is characterized by the minimal phase space dimension allowing existence of attractor of Smale-Williams (other examples will be discussed in Chap. 8).

We begin with a two-dimensional predator-prey system with instant state specified by two non-negative variables $r_1, r_2$:

$$\dot{r}_1 = 2\left(1 - r_2 + \frac{1}{2}r_1 - \frac{1}{50}r_1^2\right)r_1, \quad \dot{r}_2 = 2(r_1 - 1)r_2. \tag{5.5}$$

The system has a limit cycle which passes very close to the saddle fixed point in the origin, goes around the unstable focus A (at $r_1 = 1$, $r_2 = 37/25$), passes near the saddle point B (at $r_1 = 26.86$, $r_2 = 0$) and then the loop is closed (see the phase portrait of trajectories on the plane of variables $\sqrt{r_1}$ and $\sqrt{r_2}$ in Fig. 5.5(a)). During this process, the growth rates represented by the factors $m_1 = 1 - r_2 + \frac{1}{2}r_1 - \frac{1}{50}r_1^2$ and $m_2 = r_1 - 1$ in Eqs. (5.5) alternately change sign.

Let us regard $r_1$ and $r_2$ as squared amplitudes of two oscillators of some frequency $\omega_0$, and represent them as $r_1 = x^2 + u^2$ and $r_2 = y^2 + v^2$. The new variables $x$, $u$ and $y$, $v$ correspond to real and imaginary parts of two complex amplitudes: $a_1 = x + iu$ and $a_2 = y + iv$. Then, we write down

$$\dot{a}_1 = -i\omega_0 a_1 + m_1(|a_1|, |a_2|)a_1, \quad \dot{a}_2 = -i\omega_0 a_2 + m_2(|a_1|, |a_2|)a_2, \tag{5.6}$$

or

$$
\begin{aligned}
\dot{x} &= \omega_0 u + m_1(x^2+u^2, y^2+v^2)x, \\
\dot{u} &= -\omega_0 x + m_1(x^2+u^2, y^2+v^2)u, \\
\dot{y} &= \omega_0 v + m_2(x^2+u^2, y^2+v^2)y, \\
\dot{v} &= -\omega_0 y + m_2(x^2+u^2, y^2+v^2)v.
\end{aligned} \tag{5.7}
$$

At this point, what we have is a system of two oscillators alternately undergoing growth and decay, and their phases are uncoupled. Finally, we complement (5.7) with additional coupling terms in the first and the third equations, which are proportional to $vy$ and $x$, respectively, and arrive at the following model

$$
\begin{aligned}
\dot{x} &= \omega_0 u + [1-(y^2+v^2)+\frac{1}{2}(x^2+u^2)-\frac{1}{50}(x^2+u^2)^2]x+\varepsilon yv, \\
\dot{u} &= -\omega_0 x + [1-(y^2+v^2)+\frac{1}{2}(x^2+u^2)-\frac{1}{50}(x^2+u^2)^2]u, \\
\dot{y} &= \omega_0 v + (x^2+u^2-1)y+\varepsilon x, \\
\dot{v} &= -\omega_0 y + (x^2+u^2-1)v.
\end{aligned} \tag{5.8}
$$

Here $\varepsilon$ is the coupling constant. In the numerical computations discussed below, we fix the parameters $\omega_0 = 2\pi$, $\varepsilon = 0.3$.

At $\varepsilon = 0$ the equations for variables $r_1 = |a_1|^2 = x^2+u^2$ and $r_2 = |a_2|^2 = y^2+v^2$ coincide precisely with relations (5.5). At $\varepsilon$ small enough, motion of a representative point on the plane $r_1, r_2$ follows approximately a closed limit cycle, like that in Fig. 5.5(a), visiting again and again a neighborhood of the origin. Qualitatively, for each such passage, the following stages may be specified: excitation of the first oscillator (i), excitation of the second oscillator (ii), damping of the first oscillator (iii), and slower damping of the second oscillator (iv). Activation of the sec-

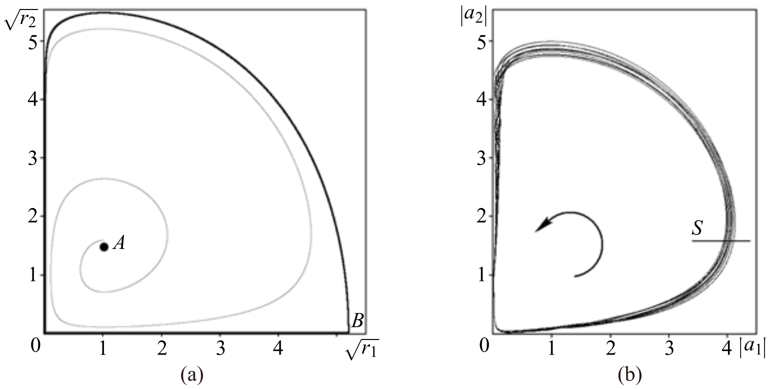


**Fig. 5.5** Portrait of trajectories on the phase plane of Eqs. (5.5) in variables $\sqrt{r_1}$ and $\sqrt{r_2}$ **(a)** and portrait of a trajectory on attractor of the model (5.8) at $\omega_0 = 2\pi$ and $\varepsilon = 0.3$ depicted on a plane of the same variables expressed as absolute values of the complex amplitudes **(b)**. The arrow indicates direction of the motion. Segment $S$ corresponds to the hyper-plane used in the definition of the Poincaré map.

ond oscillator occurs in the presence of driving from the partner, due to the coupling term proportional to $\varepsilon$ in the second equation, so, it inherits the phase from the first oscillator. During the damping stage of the second oscillator, its residual oscillations stimulate the first one. The corresponding term in the equations $\varepsilon yv$ is selected in such a way that the stimulation is determined by the second harmonic of the oscillations. Indeed, if $y \sim \sin(\omega_0 t + \varphi)$ and $v \sim \cos(\omega_0 t + \varphi)$, then $y_k v_k \sim \sin(\omega_0 t + \varphi)\cos(\omega_0 t + \varphi) = \frac{1}{2}\sin(2\omega_0 t + 2\varphi)$. As a result, the first oscillator inherits the doubled phase $2\varphi$ on its active stage. Observe that the frequency of driving is essentially different from the natural frequency of the stimulated oscillator: $2\omega_0$ versus $\omega_0$; so we talk of the *non-resonant* transfer of the excitation. As time passes, it is the turn for the first oscillator to decay, but it transfers the excitation back to the second oscillator and so on. This successive exchange by the excitation repeats again and again, and each complete cycle of the process corresponds to the expanding circle map of Bernoulli for the phase variable $\varphi_{n+1} = 2\varphi_n + \text{const}$, at least in a rough approximation. In spite of the non-resonant nature of the excitation transfer on a certain stage, everything works; the dynamics in accordance with the explained mechanism is clearly observed in computations, at least while one sets the frequency parameter $\omega_0$ not too large.[2]

Figure 5.5(b) shows portrait of the attractor as it looks in projection onto the plane of the same variables as those used for depicting the limit cycle of the initial version of Eqs. (5.5).

In Fig. 5.6 the panel (a) presents time dependence for oscillating variables $x$ and $y$ relating to the first and the second oscillators. Observe alternating stages of activity of the partial oscillators. The mean time interval of repetitions of the stages estimated in this operation mode is found to be $< T >= 7.248$. The panel (b) shows a three-dimensional portrait of the attractor in the space $(y, v, \rho)$, where $\rho = \sqrt{x^2 + u^2}$. Rotation of the orbit approximately on the horizontal plane corresponds to epochs of excitation and slow decay for the second oscillator and of silence for the first one.

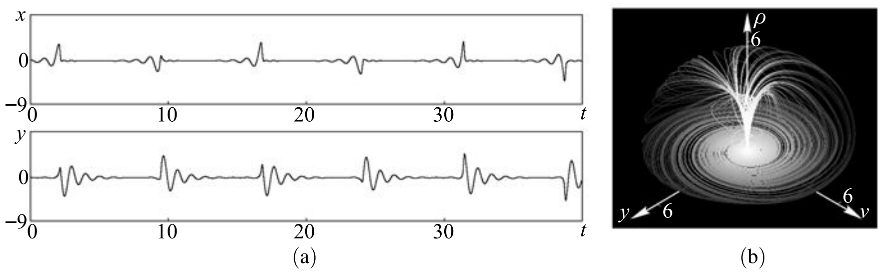


**Fig. 5.6** Plots for time dependence for oscillating variables $x$ and $y$ relating to the first and the second oscillators **(a)** and portrait of attractor in 3D projection **(b)** for the model (5.8) at $\omega_0 = 2\pi$ and $\varepsilon = 0.3$.

[2] In computations at different initial conditions one and the same chaotic attractor is always observed; no phenomena of multistability have been noticed. The same kind of dynamics is observed in a rather wide parameter range.

The excitation of the first oscillator gives rise to the departure of the orbit from the origin with the subsequent excitation of the second oscillator, its decay, and the next return into a neighborhood of the origin.

To proceed, we introduce the Poincaré map in the four-dimensional phase space of the system $(x, u, y, v)$. From Fig. 5.5(b) it is clear that it is appropriate to define the Poincaré section with a hyper-surface specified by the equation $r_1 = c$ that is $y^2 + v^2 = c$ taking into account crossings in direction of increase of $r_1$. At the parameters assigned here, an appropriate constant is $c = 2.5$. In Fig. 5.5(b) it corresponds to a horizontal segment $S$. In the three-dimensional cross-section we use the coordinates $\{x, u, z\}$, here $x$ and $u$ are just variables appearing in the original equations, and the third variable is determined as

$$z = \arg(y + iv) - \arg(x + iu) \tag{5.9}$$

in such a way that $z \in (-\pi, \pi]$.

The procedure for computation of the Poincaré map for a given initial vector $\mathbf{x} = \{x, u, z\}$ is arranged as a computer program based on numerical solution of differential equations (5.8) complemented with Hénon's interpolation procedure, consistent in accuracy with the applied finite-difference scheme (Hénon, 1982). As the trajectory segment starting and finishing at the Poincaré section is computed, the updated variables $\overline{\mathbf{x}} = (\bar{x}, \bar{u}, \bar{z}) = \mathbf{T}(\mathbf{x})$ are determined at the final point.

Performing the computations for some representative trajectory on the attractor we can determine sequence of phases at successive intersections of the surface $S$ at $t_n$ as $\varphi_n = \arg(x(t_n) + iu(t_n))$ to check whether it satisfies the Bernoulli map as it should be according to the above qualitative intuitive argumentation. Figure 5.7 shows a plot for the phases obtained from iteration of the Poincaré map $\mathbf{T}$ in the computations for the model (5.8) at $\omega_0 = 2\pi$, $\varepsilon = 0.3$. Observe that the plot is indeed close to that of the Bernoulli map. The most important is the intrinsic visible topological nature of the map: a single bypass of the complete circle by the pre-image implies the two-fold bypass for the image. It gives a foundation for suggestion that the Smale-Williams attractor occurs because the Poincaré map ensures the two-fold

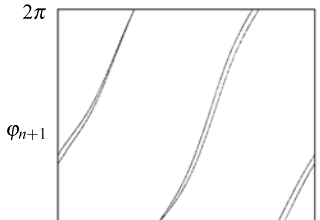


**Fig. 5.7** Iteration diagram for the phases of the first partial oscillator at successive crossing the Poincaré section $\varphi_n = \arg(x + iu)|_{z=0,\dot{z}>0}$ obtained from numerical solution of Eqs. (5.8) at $\omega_0 = 2\pi$ and $\varepsilon = 0.3$.

stretching along the angular phase coordinate, and compressions in other directions for the evolving elements of phase volume.

Let us consider a toroidal domain D in the three-dimensional phase space of the Poincaré map **T(x)** specified by the following parametric equations:

$$\begin{aligned} x &= (r + \rho b \sin\vartheta)\cos\psi, \\ u &= (r + \rho b \sin\vartheta)\sin\psi, \\ z &= \rho d \cos\vartheta, \end{aligned} \tag{5.10}$$

where $0 \leqslant \rho \leqslant 1$, $0 \leqslant \psi < 2\pi$, $0 \leqslant \theta \leqslant \pi$, and the constants are $r = 4.05$, $b = 0.3$, $d = 0.1$. As it was validated in computations, this is an absorbing domain for the attractor of the Poincaré map **T(x)**. Figure 5.8 shows this domain and its image under a single application of the Poincaré map. Observe that the image looks exactly as it is assumed in the construction of the Smale-Williams attractor: this is a narrow double folded loop embedded inside the toroidal absorbing domain. In Fig. 5.9 a portrait of the attractor of the Poincaré map is plotted in projection onto the phase

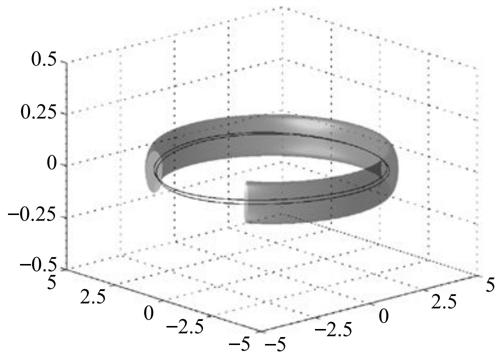


**Fig. 5.8** Absorbing domain parameterized by Eqs. (5.10) is image in the 3D phase space of the Poincaré map of the system (5.8) at $\omega_0 = 2\pi$, $\varepsilon = 0.3$.

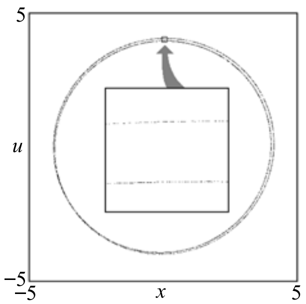


**Fig. 5.9** Attractor of the Poincaré map of the system (5.8) at $\omega_0 = 2\pi$, $\varepsilon = 0.3$ in projection onto the phase plane of the first oscillator $(x, u)$.

plane of the first oscillator $(x, u)$. Observe visible Cantor-like transversal structure of the attractor, which is a characteristic feature of the Smale-Williams solenoid.

Calculation of Lyapunov exponents using the algorithm of Benettin in application to the model (5.7) yields the following data:

$$\lambda_1 = 0.0918, \quad \lambda_2 = 0.0000, \quad \lambda_3 = -0.982, \quad \lambda_4 = -1.330. \tag{5.11}$$

Accounting the autonomous nature of the system, it is natural to regard the exponent $\lambda_2$ as precisely zero. Next, as mentioned, the average period between successive passages of the Poincaré section is $T_{\text{av}} = 7.248$. Then, in accordance with the approach based on the Bernoulli map, the largest Lyapunov exponent must be equal to $T_{\text{av}}^{-1} \ln 2 \approx 0.096$. This is in reasonable agreement with the value of $\lambda_1$ obtained in numerical calculations. Estimate of the dimension of the attractor according to the Kaplan-Yorke formula yields $D_L = 2 + (\lambda_1 + \lambda_2)/\lambda_3 \approx 2.094$.

For the system governed by Eqs. (5.8) with the above-mentioned parameters values the computations were carried out, confirming that the cone criterion is valid in the toroidal domain, containing the attractor of the Poincaré map (see (Kuznetsov et al., 2007) and Sect. 7.3 of this book); so, this is really the hyperbolic attractor.

## 5.3 Example of blue sky catastrophe accompanied by a birth of Smale-Williams attractor

As mentioned in Chap. 2, attractors of Smale-Williams type in Poincaré sections of continuous-time systems may arise under variation of a parameter via the so-called blue sky catastrophe (Turaev and Shilnikov, 1995; Shilnikov and Turaev, 1997).

To construct an example with birth of the Smale-Williams attractor, one must have the phase space dimension at least equal to four. The phase-space flow has to be organized in such a way that a toroidal domain close initially to the saddle-node cycle, in the course of travel and returning to that cycle would form a double-folded loop, with thinner coils. To do this, the model considered in the previous section may be applied with certain modifications.

Let us revise the prototype model (5.5) as follows (Kuznetsov, 2010):

$$\dot{r}_1 = 2\left(1 - r_2 + \frac{1}{2}r_1 - \frac{1}{50}r_1^2\right) r_1, \quad \dot{r}_2 = 2\left(r_1 - \mu + \frac{1}{2}r_2 - \frac{1}{50}r_2^2\right) r_2. \tag{5.12}$$

These equations differ from (5.5) with additional nonlinear terms in the second ("predator") equation, and contain now a control parameter $\mu$. If the value of $\mu$ is slightly less than $\mu_0 = 3\frac{1}{8}$, a picture of orbits on the phase plane $r_1, r_2$ looks like that shown in Fig. 5.10(a). There are four fixed points: an unstable focus A, saddles B and $\mathrm{C}_1$, and a node $\mathrm{C}_2$. With increase of $\mu$, the fixed points $\mathrm{C}_1$ and $\mathrm{C}_2$ move to meet each other at $\mu = \mu_0$, and then disappear (see the panels (b) and (c), respectively). Instead of the former pair of fixed points, a domain of relatively slow motion appears, and the attractor is now a limit cycle, which passes close to the origin and to the saddle B.

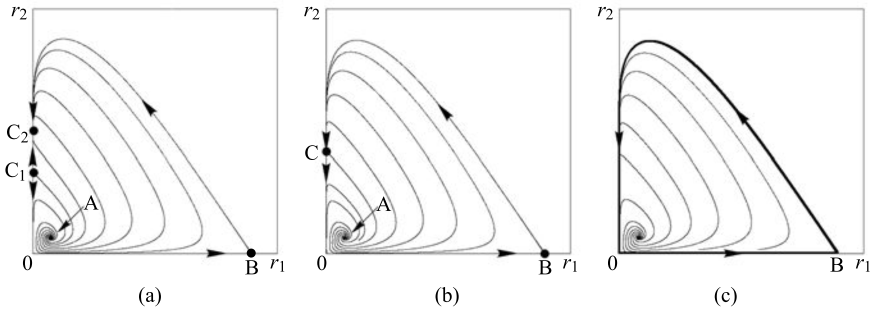


**Fig. 5.10** Phase portraits of the system (5.12) with increase of $\mu$ from (a) to (c) show that two fixed points, a stable node $C_2$ and a saddle $C_1$ **(a)** meet together at the bifurcation **(b)**, and a limit cycle appears shown with a bold curve **(c)**.

Like in the previous section, let us regard the quantities $r_1, r_2$ as squared absolute values of complex amplitudes for two oscillators and introduce additional coupling between them. The equations read

$$\begin{aligned}
\dot{x} &= \omega_0 u + \left(1 - (y^2+v^2) + \frac{1}{2}(x^2+u^2) - \frac{1}{50}(x^2+u^2)^2\right) x + \varepsilon y v, \\
\dot{u} &= -\omega_0 x + \left(1 - (y^2+v^2) + \frac{1}{2}(x^2+u^2) - \frac{1}{50}(x^2+u^2)^2\right) u, \\
\dot{y} &= \omega_0 v + \left(x^2+u^2 - \mu + \frac{1}{2}(y^2+v^2) - \frac{1}{50}(y^2+v^2)^2\right) y + \varepsilon x, \\
\dot{v} &= -\omega_0 y + \left(x^2+u^2 - \mu + \frac{1}{2}(y^2+v^2) - \frac{1}{50}(y^2+v^2)^2\right) v.
\end{aligned} \tag{5.13}$$

At $\varepsilon = 0$, equations for $r_1 = |a_1|^2 = x^2+u^2$ and $r_2 = |a_2|^2 = y^2+v^2$ can be easily derived from (5.13), which coincide with Eqs. (5.12). At $\varepsilon$ small enough, and at values of $\mu$ notably less than $\mu_0$, the sustained dynamics of the model (5.12), being represented graphically on the plane $r_1, r_2$, takes place nearby the node $C_2$. For nonzero $\varepsilon$, this is a limit cycle of such kind that the second oscillator has some notable amplitude, while the amplitude for the first one is very small. Besides, there is a close unstable limit cycle close to $C_1$. With gradual increase of the parameter, both cycles come closer, meet together and coincide at some $\mu = \mu_c(\varepsilon) \approx \mu_0$, forming a semi-stable limit cycle. At $\mu > \mu_c(\varepsilon)$ it disappears. Now, motion of a representative point on the plane $r_1, r_2$ follows approximately a closed large-scale path, like in Fig. 5.10(c), visiting again and again a neighborhood of the origin. As explained in the previous section, transformation of the phase at each next cycle of the excitation exchange in this regime will correspond approximately to the Bernoulli map, $\varphi_{n+1} = 2\varphi_n + \text{const.}$

These considerations suggest that at $\mu = \mu_c$ a kind of blue sky bifurcation occurs, which corresponds to the case $m = 2$ (see Sect. 2.7). So, in accordance with argumentation of (Shilnikov and Turaev, 1997) it has to be accompanied by a birth of hyperbolic attractor, the Smale-Williams solenoid in the Poincaré section.

Figure 5.11 shows portraits of phase trajectories in projection on the plane of real amplitudes of two oscillators as obtained from numerical solution of Eqs. (5.13). Parameter values in the computations are specified as $\omega_0 = 2\pi$ and $\varepsilon = 0.5$.

Taking into account configuration of the attractor, in the supercritical domain $\mu > \mu_c$ it is appropriate to define the Poincaré section with a hypersurface $S$ in the 4D phase space by equation $|a_2| = c$ with $c = 2.5$, taking into to account only crossings in direction of increase of $|a_2|$ (see a horizontal segment and an arrow in panel (b) of Fig. 5.11).

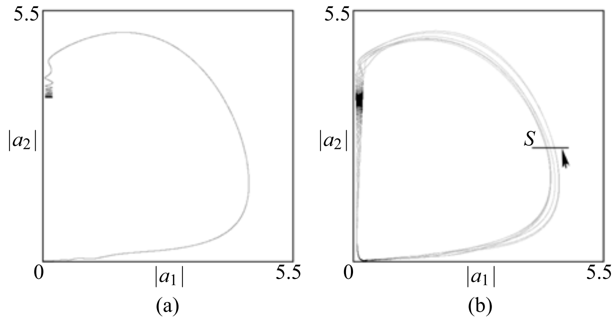


**Fig. 5.11** A transient trajectory (gray) and limit cycle (black) before the bifurcation at $\mu = 3.14$ **(a)** and portrait of attractor after the bifurcation, at $\mu = 3.1442$ **(b)**, projected onto a plane of real amplitudes $|a_1|$ and $|a_2|$. Other parameters are $\omega_0 = 2\pi$ and $\varepsilon = 0.5$.

As mentioned in (Shilnikov and Turaev, 1997), near the bifurcation, the characteristic time of return of orbits at the Poincaré section depends on the control parameter like $T(\mu) \sim 1/\sqrt{\mu - \mu_c}$. In computations, the numerical data are found to agree well with this relation. Evidence is delivered by a plot of squared inverse averaged time of returns against parameter $\mu$ shown in Fig. 5.12. The bifurcation threshold corresponds to intersection of the curve with the horizontal coordinate axis, and locally the dependence is linear (see the dotted line). From extrapolation, the bifurcation is located with high accuracy at $\mu_c \approx 3.144196$.

Diagrams in Fig. 5.13 illustrate evolution of phases at successive crossings of the Poincaré section $S$ in the course of the motion on the attractor. The phase $\Phi_n$ relates to the first oscillator at $t = t_n$, which is the $n$-th crossing of the orbit with the hypersurface $S$ in the correct direction. It is determined as $\Phi_n = \arg(x(t_n) + iu(t_n))$. Observe that topologically the discrete-step evolution of phases corresponds to Bernoulli map. Such topological nature persists in a wide range of parameter $\mu$ above the bifurcation threshold. It supports the qualitative argument that the case

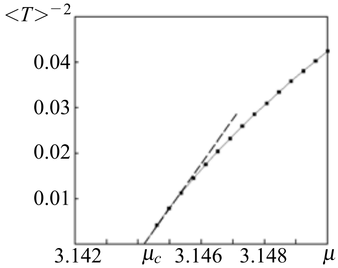


**Fig. 5.12** Squared inverse averaged time of returns at the Poincaré section for orbits on the attractor versus control parameter $\mu$; the label $\mu_c$ marks the blue sky bifurcation point. Other parameters are $\omega_0 = 2\pi$ and $\varepsilon = 0.5$.

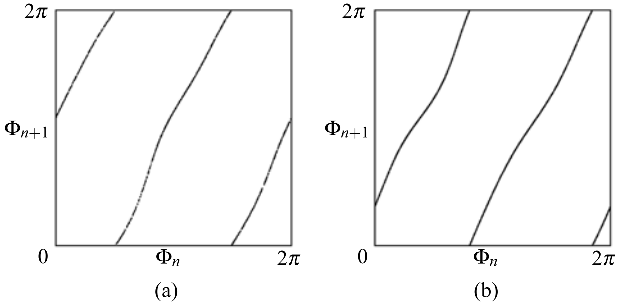


**Fig. 5.13** Diagrams for discrete-step evolution of phases for the first oscillator at passages of the Poincaré section $S$. Parameters are $\omega_0 = 2\pi$, $\varepsilon = 0.5$, $\mu = 3.1442$ **(a)** and $\mu = 3.15$ **(b)**.

$m$=2 does occur associated with presence of structurally stable hyperbolic attractor represented by the Smale-Williams solenoid in the Poincaré map. Figure 5.14 shows the attractor in the Poincaré section in projection on the phase plane of the first oscillator. Although it looks like a simple closed curve, a high enough zoom resolves intrinsic transversal Cantor-like structure.

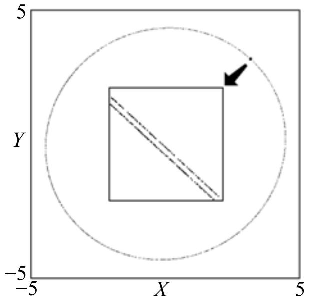


**Fig. 5.14** Attractor of the system (5.13) at $\mu = 3.15$ in the Poincaré section projected onto the phase plane of the first oscillator. Transversal Cantor-like structure becomes visible at great resolution, as shown in the inset.

In Fig. 5.15 a plot for the Lyapunov exponents is shown, as they behave under parameter variation through the blue sky catastrophe, which occurs at $\mu = \mu_c$ (see panel (a)). In the left part of the plot, the largest Lyapunov exponent is zero, and three others are negative. Here attractor is a stable limit cycle, like that in Fig. 5.11(a). At the bifurcation, both larger exponents meet at zero, and two others remain negative. After the bifurcation, there is one positive exponent, which grows with increase of $\mu$. The second exponent remains zero, and two others are negative, with gradually decreasing absolute value. In this range the Smale-Williams attractor persist.

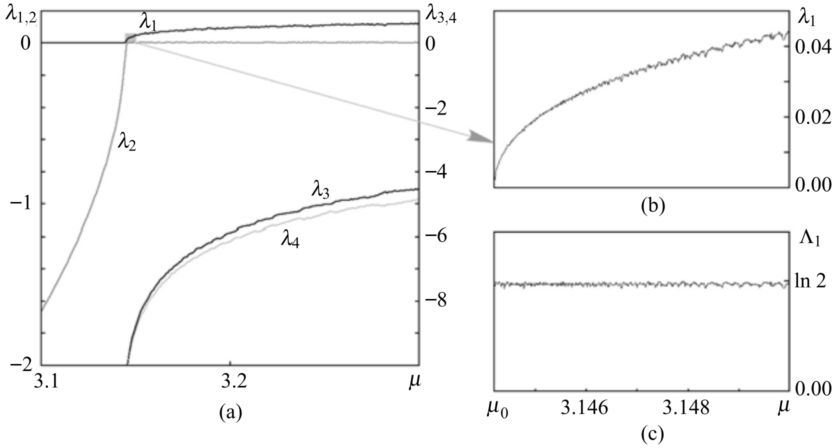


**Fig. 5.15** Lyapunov exponents of the system (5.13) plotted versus parameter $\mu$ **(a)**, a magnified part for the largest Lyapunov exponent near the bifurcation threshold in supercritical domain **(b)**, and the plot for the Lyapunov exponent of the Poincaré map **(c)**. Observe that the Lyapunov exponent for the Poincaré map is approximately constant close to ln 2 that corresponds to the Bernoulli map.

Particularly, at $\mu = 3.15$ the Lyapunov exponents are

$$\lambda_1 = 0.0434, \quad \lambda_2 = 0.0000, \quad \lambda_3 = -8.75, \quad \lambda_4 = -8.85. \tag{5.14}$$

The second exponent is zero (up to numerical error) and must be regarded as being associated with neutral infinitesimal perturbation along the trajectory on the attractor. Estimate of the attractor dimension from the Kaplan-Yorke formula (Appendix D) yields $D_L = 2 + \lambda_1/|\lambda_3| \approx 2.005$.

The growth of the positive Lyapunov exponent in the supercritical domain, $\mu > \mu_c$ (see a separate plot (b)), occurs because of a decrease of the characteristic time scale observed with departure from the bifurcation point. In the supercritical domain, one can determine Lyapunov exponents $\Lambda_1, \Lambda_2, \Lambda_3$ for the Poincaré map as well. The zero-value exponent is excluded, and others are in obvious relation with those for the differential equations, namely, $\Lambda_1 = \lambda_1 < T >$, $\Lambda_2 = \lambda_3 < T >$,

$\Lambda_3 = \lambda_4 < T >$. Here $< T >$ is characteristic time of return at the Poincaré section, averaged over orbits on the attractor. Observe that the positive exponent for the Poincaré map remains almost constant in a wide parameter range (up to fluctuations because of the numerical inaccuracy). It is close to $\ln 2$, the value corresponding to the Bernoulli map (see panel (c) in Fig. 5.15).

The present model essentially supplements a collection of known explicit examples of blue sky catastrophes (Gavrilov and Shilnikov, 1999; Shilnikov and Cymbalyuk, 2005; Glyzin et al., 2008), which were restricted, until now, with transitions involving only regular attractors, the limit cycles. This and similar examples may be of interest for understanding variety of dynamical behavior, e.g. in neurodynamics. Indeed, some models with the blue sky catastrophes relate to this discipline (Shilnikov and Cymbalyuk, 2005; Shilnikov, A. and Kolomiets, 2008), as well as a hypothetical example of a uniformly hyperbolic strange attractor suggested in (Belykh et al., 2005).

## References


Belykh, V., Belykh, I., Mosekilde, E.: The hyperbolic Plykin attractor can exist in neuron models. Int. J. of Bifurcation and Chaos **15**, 3567–3578 (2005).

Gavrilov, N.K., Shilnikov, A.L.: An example of blue sky catastrophe. In: Methods of qualitative theory of differential equations and related topics. Amer. Math. Soc. Transl., II Ser. **200**, pp.165–188. AMS, Providence, RI (1999).

Glyzin, S.D., Kolesov, A.Yu., Rozov, N.Kh.: Blue sky catastrophe in relaxation systems with one fast and two slow variables. Differential Equations **44**, 161–175 (2008).

Hénon, M.: On the numerical computation of Poincaré maps. Physica D **5**, 412–414 (1982).

Kuznetsov, S.P.: Example of blue sky catastrophe accompanied by a birth of Smale-Williams attractor. Regular and Chaotic Dynamics **15**, 348–353 (2010).

Kuznetsov, S.P., Pikovsky, A.: Autonomous coupled oscillators with hyperbolic strange attractors. Physica D **232**, 87–102 (2007).

Kuznetsov, S.P., Pikovsky, A.S., Sataev, I.R.: Hyperbolic Smale–Williams attractor in Poincaré map of a four-dimensional autonomous system. In: Proc. of the III Int. Conf. "Frontiers of Nonlinear Physics". Nizhny Novgorod – Saratov – Nizhny Novgorod, pp. 66-67 (2007).

Shilnikov, A., Cymbalyuk, G.: Transition between tonic spiking and bursting in a neuron model via the blue-sky catastrophe. Phys. Rev. Lett. **94**, 048101 (2005).

Shilnikov, L.P., Turaev, D.V.: Simple bifurcations leading to hyperbolic attractors. Computers Math. Appl. **34**, 173–193 (1997).

Shilnikov, A., Kolomiets, M.: Methods of the qualitative theory for the Hindmarsh-Rose model: a case study. Int. J. Bifurcation and Chaos **18**, 2141–2168 (2008).

Turaev, D.V., Shilnikov, L.P.: On blue sky catastrophes. Doklady Akademii Nauk **342,** 596–599 (1995).

# Chapter 6
# Parametric Generators of Hyperbolic Chaos

**Abstract** Excitation transfer between alternately active oscillators with phases transformed in accordance with chaotic maps, like that in the previous two chapters, may be regarded as some general principle of design of systems with attractors of the Smale-Williams type. Appropriate and convenient for implementation of this principle, are *parametric oscillatory systems* (Mandelshtam, 1972; Louisell, 1960; Akhmanov and Khokhlov, 1966; Rabinovich and Trubetskov, 1989; Damgov, 2004). The term relates to a class of systems with excitation of oscillations caused by periodic variation of some parameter. Parametric oscillations occur in systems of mechanics, electronics, acoustics, nonlinear optics, etc. In mechanics, a commonly known example relates to a person on a swing, who gradually increases the amplitude of the oscillations due to variation of the body position that corresponds to periodic change of the effective length of the equivalent pendulum (Fig. 6.1 (a) and (b)). In electric LC-circuit one can increase amplitude of the oscillations step by step if vary periodically the capacity: increasing the distance between the plates of the capacitor at the instants of its maximal charge, and decreasing it back at the instants of maximal current in the inductance, when the charge of the capacitor is close to zero (Fig. 6.1(c)). Clearly, the mechanical work against the force of attraction of the charged plates in the course of the process converts into the energy of electromagnetic oscillations in the circuit; so, the amplitude will grow gradually. The main part of this chapter starts with consideration of the *three-frequency parametric oscillator* (Louisell, 1960), in which the excitation takes place in two coupled oscillators of frequencies $\omega_1$ and $\omega_2$ due to periodic variation of the coupling strength with the pump frequency $\omega_3 = \omega_1 + \omega_2$. Saturation of the excitation may be ensured by nonlinear damping in the scheme, which manifests then regular sustained regime of parametric generation. After that, we turn to designs, in which phases of the parametrically excited oscillators undergo transformations corresponding to the expanding circle map in some period of time. Accounting compression of the phase volume in the state space along other directions, these will be systems with attractors of Smale-Williams type in the stroboscopic Poincaré maps. In the systems examined here, the phase manipulation is performed as energy is transferred between oscillators, whereas the key role in systems discussed in the previous two chapters is played by

a non-oscillatory external source of energy that compensates for oscillator losses, rather than by the energy transfer.

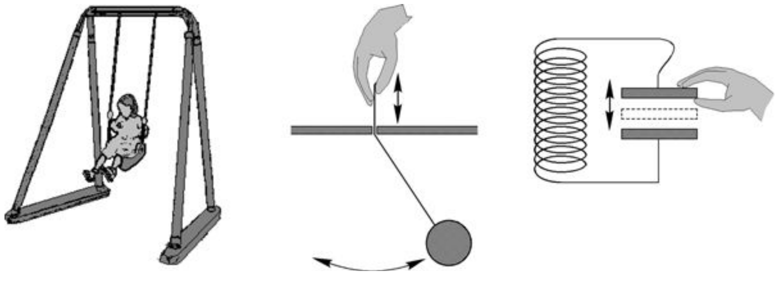


**Fig. 6.1** Simple examples of parametric excitation: **(a)** a child increases amplitude of the swing by variation of the body position that is equivalent to periodic variation of the effective length of a pendulum **(b)**; in LC-circuit the electromagnetic oscillations grow in amplitude due to periodic variation of the capacity **(c)**.

## 6.1 Parametric excitation of coupled oscillators. Three-frequency parametric generator and its operation

Let us start with a system composed of two oscillators of frequencies $\omega_1$ and $\omega_2$ (Fig. 6.2) coupled via a linear element characterized by strength of coupling periodically varied with frequency $\omega_3$, and the frequencies are related as

$$\omega_3 = \omega_1 + \omega_2. \tag{6.1}$$

The values $\omega_1$ and $\omega_2$ are called the signal and the idler frequency, and $\omega_3$ is the pump frequency. The relation (6.1) is the *parametric resonance condition*.

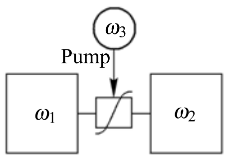


**Fig. 6.2** Block diagram of a three-frequency parametric generator. Blocks marked with $\omega_1$ and $\omega_2$ represent the signal and idler oscillators, and the block with the wavy crossing is the non-dissipative coupling element characterized by parameter oscillating with a frequency of pump $\omega_3$.

To derive differential equations for systems of some physical nature one should use relations specific for each respective sub-discipline; say, Newton equations in mechanics, Kirchhoff equations in electric circuits, etc. Alternatively, we may turn to formalism elaborated for general description of conservative dynamics, like the Lagrangian or Hamiltonian method. Then, the equations are derived in elegant and straightforward way in correct and general form. To apply them to concrete parametric systems, one needs only to specify physical sense of the used dynamical variables and parameters.

A Lagrange function in our case is composed of terms $\frac{1}{2}\dot{x}^2 - \frac{1}{2}\omega_1^2 x^2$ and $\frac{1}{2}\dot{y}^2 - \frac{1}{2}\omega_2^2 y^2$ representing differences of the kinetic and potential energy for two partial oscillators, expressed via generalized coordinates and velocities, and of the coupling term containing product of the generalized coordinates and the pump signal of frequency $\omega_3$:

$$L(x,\dot{x},y,\dot{y},t) = \frac{1}{2}(\dot{x}^2 + \dot{y}^2 - \omega_1^2 x^2 - \omega_2^2 y^2) + \kappa xy \sin\omega_3 t. \tag{6.2}$$

Here parameter $\kappa$ characterizes strength of the coupling and intensity of the pump. Explicit dependence of the Lagrangian on time indicates that we deal with a non-autonomous system.

The differential equations governing dynamics of the system are obtained from the Lagrange function in standard way, as a set of Lagrange-Euler equations

$$\begin{aligned} \frac{d}{dt}\frac{\partial L}{\partial \dot{x}} - \frac{\partial L}{\partial x} = 0, \\ \frac{d}{dt}\frac{\partial L}{\partial \dot{y}} - \frac{\partial L}{\partial y} = 0. \end{aligned} \tag{6.3}$$

With the Lagrangian (6.2) we get the linear equations

$$\begin{aligned} \ddot{x} + \omega_1^2 x &= \kappa y \sin\omega_3 t, \\ \ddot{y} + \omega_2^2 y &= \kappa x \sin\omega_3 t. \end{aligned} \tag{6.4}$$

As the parametric excitation occurs, in these linear equations the amplitude will grow unboundedly. To avoid this, we have to introduce into the model some factor responsible for saturation. The simplest and physically justified way is to add nonlinear damping; moreover, it is reasonable because we wish to have a model possessing an attractor in the state space.

To account dissipation, the Lagrangian formalism is complemented with introduction of the *Rayleigh dissipation function* (Marsden and Raţiu, 1999), which we specify in the form

$$R(\dot{x},\dot{y}) = \frac{1}{2}(\alpha_1\dot{x}^2 + \alpha_2\dot{y}^2) + \frac{1}{4}(\beta_1\dot{x}^4 + \beta_2\dot{y}^4). \tag{6.5}$$

Here the parameters $\alpha_{1,2}$ and $\beta_{1,2}$ will be responsible for the linear and nonlinear dissipation, respectively. Now, instead of Eqs. (6.3) we have to use

$$\frac{d}{dt}\frac{\partial L}{\partial \dot{x}} - \frac{\partial L}{\partial x} = -\frac{\partial R}{\partial \dot{x}},$$
$$\frac{d}{dt}\frac{\partial L}{\partial \dot{y}} - \frac{\partial L}{\partial y} = -\frac{\partial R}{\partial \dot{y}}, \tag{6.6}$$

that yields

$$\begin{aligned}\ddot{x} + \omega_1^2 x &= \kappa y \sin \omega_3 t - \alpha_1 \dot{x} - \beta_1 \dot{x}^3, \\ \ddot{y} + \omega_2^2 y &= \kappa x \sin \omega_3 t - \alpha_2 \dot{y} - \beta_2 \dot{y}^3.\end{aligned} \tag{6.7}$$

To illustrate the dynamics, we present results of numerical solution of Eqs. (6.7) in Fig. 6.3. In the computations we set $\omega_1 = 2\pi$, $\omega_2 = 4\pi$, $\omega_3 = 6\pi$ (the natural period of the first oscillator is the time unit), and the resonance condition is obviously valid. Other parameters are $\kappa = 35$, $\alpha_1 = \alpha_2 = 0.6$, $\beta_1 = \beta_2 = 0.1$. The variables $x_1$, $x_2$, and the pump signal $\kappa \sin \omega_3 t$ are shown in dependence on time. Observe saturation of the transient process resulting in stationary regime of parametric generation with fixed amplitudes of the signal and idler oscillations. In stroboscopic Poincaré map attractor is represented by a stable fixed point. Also, there is an unstable fixed point in the origin: departing orbits from that point correspond to transients.

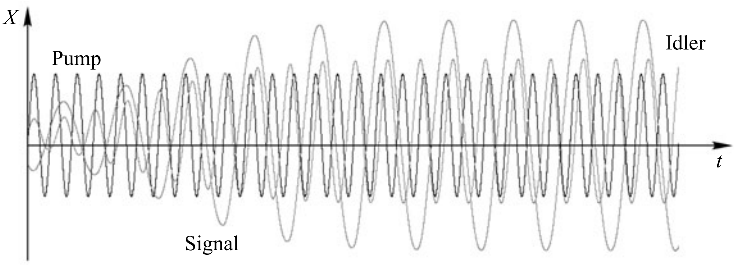


**Fig. 6.3** Plots for signal and idler oscillations versus time, and the pump signal $\omega_3$ for the model (6.7) at $\kappa = 35$, $\alpha_1 = \alpha_2 = 0.6$, $\beta_1 = \beta_2 = 0.1$, $\omega_1 = 2\pi$, $\omega_2 = 4\pi$, $\omega_3 = 6\pi$.

A useful approach to description of the dynamics of the system under consideration is the *method of slow complex amplitudes*, analogous to that mentioned in Chap. 4. For parametric systems this method is commonly exploited giving rise to very special, easily recognizable form of equations common for parametric systems of different physical nature. Here we explain this method in application to the system (6.7).

Let us set

$$x = ae^{i\omega_1 t} + a^* e^{-i\omega_1 t}, \quad y = be^{i\omega_2 t} + b^* e^{-i\omega_2 t}, \tag{6.8}$$

where $a(t) = a' + ia''$ and $b(t) = b' + ib''$ are complex functions of time variable obeying the additional condition

$$\dot{a}e^{i\omega_1 t} + \dot{a}^* e^{-i\omega_1 t} = 0, \quad \dot{b}e^{i\omega_2 t} + \dot{b}^* e^{-i\omega_2 t} = 0. \tag{6.9}$$

With substitution of these expression in (6.7), multiplication of the first equation by factor $e^{-i\omega_1 t}$ and the second by factor $e^{-i\omega_2 t}$, accounting the frequency resonance relation, and performing averaging over a period of fast oscillations, we obtain

$$\begin{aligned}\dot{a} &= -\frac{\kappa}{4\omega_1}b^* - \frac{1}{2}\alpha_1 a - \frac{3}{2}\omega_1^2\beta_1 a|a|^2,\\ \dot{b} &= -\frac{\kappa}{4\omega_2}a^* - \frac{1}{2}\alpha_2 b - \frac{3}{2}\omega_2^2\beta_2 b|b|^2.\end{aligned} \tag{6.10}$$

To give evidence for the parametric instability, consider these equations for a case of equal coefficients of linear dissipation $(\alpha_1 = \alpha_2 = \alpha)$ and without nonlinear dissipation $(\beta_{1,2} = 0)$. Then, they can be solved analytically; the solution is

$$\begin{aligned}a &= (C_+ e^{\kappa t/4\sqrt{\omega_1\omega_2}} + C_- e^{-\kappa t/4\sqrt{\omega_1\omega_2}})e^{-\alpha t},\\ b &= -\sqrt{\omega_2/\omega_1}(C_+^* e^{\kappa t/4\sqrt{\omega_1\omega_2}} + C_-^* e^{-\kappa t/4\sqrt{\omega_1\omega_2}})e^{-\alpha t},\end{aligned}$$

where $C_+$ and $C_-$ are complex constants determined by initial conditions. There is a finite threshold: at $\kappa > \alpha$ unbounded growth of both amplitudes $|a|$ and $|b|$ occurs. Saturation takes place only with account of the nonlinear dissipative terms in the equation.

## 6.2 Hyperbolic chaos in parametric oscillator with Q-switch and pump modulation

Let us consider a system similar to that discussed in the previous section but with periodic modulation of parameters, including the pump amplitudes and the dissipation parameters in both oscillators (Kuznetsov et al., 2010). The system composed of two oscillators with natural frequencies $\omega_1$ and $\omega_2 = 2\omega_1$ undergoes parametric excitation due to a sequence of pulses of pump signal of frequency $\omega_3 = \omega_1 + \omega_2 = 3\omega_1$ following one after another with a period $T \gg 1/\omega_3$. With the same period, the damping strengths (Q-factors) for both oscillators are modulated, as well as a coefficient of the additional quadratic coupling of the oscillators. For clearness of the presentation, we consider modulation of all mentioned parameters with a rectangular waveform, assuming instantaneous switching from one parameter value to another at certain points in time (at zeros of the pump signal). In other words, evolution in time in one period $T$ is supposed to consist of four stages of equal duration.

### 6.2.1 Dynamical equations

Let $x$ and $y$ be generalized coordinates of two oscillators with natural frequencies $\omega_1$ and $\omega_2 = 2\omega_1$. The pump frequency will be $\omega_3 = \omega_1 + \omega_2 = 3\omega_1$.

In terms of the Lagrange and Rayleigh functions we describe the dynamical evolution as follows. At the first stage, parametric excitation takes place because of oscillations of the coupling parameter with the pump frequency. Nonlinear dissipation is present ensuring saturation of the parametric instability. The Lagrangian is $L = \frac{1}{2}(\dot{x}^2 + \dot{y}^2 - \omega_1^2 x^2 - \omega_2^2 y^2) + \kappa xy \sin\omega_3 t$, and the Rayleigh function is $R = \frac{1}{4}(\beta_1 \dot{x}^4 + \beta_2 \dot{y}^4)$. At the second stage, interaction of the oscillators is switched off, and linear damping of the second oscillator takes place. It corresponds to $L = \frac{1}{2}(\dot{x}^2 + \dot{y}^2 - \omega_1^2 x^2 - \omega_2^2 y^2)$, and $R = \frac{1}{2}\alpha_2 \dot{y}^2$. At the third stage, there is no dissipation, and the oscillators are coupled via quadratic nonlinear element. Here we account a term proportional to $x^2 y$ in the Lagrangian, and assume $L = \frac{1}{2}(\dot{x}^2 + \dot{y}^2 - \omega_1^2 x^2 - \omega_2^2 y^2) + \varepsilon x^2 y$, while $R = 0$. At the fourth stage, linear damping of the first oscillator takes place that corresponds to $L = \frac{1}{2}(\dot{x}^2 + \dot{y}^2 - \omega_1^2 x^2 - \omega_2^2 y^2)$, and $R = \frac{1}{2}\alpha_1 \dot{x}^2$. The durations of all stages are assumed equal and containing an integer number of the high-frequency oscillations of the pump signal, i.e. $T/4 = 2\pi N/\omega_3$.

The dynamical equations for each of the four stages obtained from the relations (6.6) are the following.

**I. Stage of parametric excitation:**

$$\ddot{x} + \omega_1^2 x = \kappa y \sin\omega_3 t - \beta_1 \dot{x}^3, \quad \ddot{y} + \omega_2^2 y = \kappa x \sin\omega_3 t - \beta_2 \dot{y}^3. \tag{6.11}$$

**II. Stage of damping of the second oscillator:**

$$\ddot{x} + \omega_1^2 x = 0, \quad \ddot{y} + \omega_2^2 y = -\alpha_2 \dot{y}. \tag{6.12}$$

**III. Stage of interaction through the quadratic nonlinearity:**

$$\ddot{x} + \omega_1^2 x = 2\varepsilon xy, \quad \ddot{y} + \omega_2^2 y = \varepsilon x^2. \tag{6.13}$$

**IV. Stage of damping of the first oscillator:**

$$\ddot{x} + \omega_1^2 x = -\alpha_1 \dot{x}, \quad \ddot{y} + \omega_2^2 y = 0. \tag{6.14}$$

Alternatively, the dynamics may be represented by a single set of differential equations with piecewise-continuous coefficients:

$$\begin{aligned} \ddot{x} + \omega_1^2 x &= f_1(t)(\kappa y \sin\omega_3 t - \beta_1 \dot{x}^3) - \alpha_1 f_4(t)\dot{x} + 2\varepsilon f_3(t) xy, \\ \ddot{y} + \omega_2^2 y &= f_1(t)(\kappa x \sin\omega_3 t - \beta_2 \dot{y}^3) - \alpha_2 f_2(t)\dot{y} + \varepsilon f_3(t) x^2, \end{aligned} \tag{6.15}$$

where $f_k(t) = 1$, if $k - 1 \leqslant 4\{t/T\} < k$, and 0 otherwise. Here the braces designate the fractional part of a number. Parameter $\kappa$ determines strength of parametric coupling because of presence of the pump; $\varepsilon$ is parameter of quadratic coupling;

parameters $\alpha_{1,2}$ are responsible for linear, and $\beta_{1,2}$ for nonlinear dissipation in the first and the second oscillators, respectively.

A state of the system at fixed time instant $t$ is defined by a four-dimensional vector $\mathbf{x} = (x, u, y, v)$, where $u = \dot{x}/\omega_1$ and $v = \dot{y}/\omega_2$ are normalized generalized velocities of the oscillators. Transformation of the vector in a full period of variation of the coefficients in the equations from $t = nT$ up to $t = (n+1)T$ corresponds to the stroboscopic Poincaré map,

$$\mathbf{x}_{n+1} = \mathbf{f}(\mathbf{x}_n). \tag{6.16}$$

The mapping may be performed by means of the computer program solving the set of differential eqs. (6.11) — (6.14) in the period $T$ at four successive stages by a finite-difference integration method. It is natural to specify the integration step to have an integer number of steps at each stage.

If the period of parameter modulation is much larger than the period of high-frequency oscillations, $N \gg 1$, and parameters of coupling and dissipation are small enough, we may reformulate the problem in terms of slow complex amplitudes of the same kind as considered in Sect. 4.1. For this, we set

$$x = ae^{i\omega_1 t} + a^* e^{-i\omega_1 t}, \quad \dot{x} = i\omega_1 a e^{i\omega_1 t} - i\omega_1 a^* e^{-i\omega_1 t}, \tag{6.17}$$

and

$$y = be^{i\omega_2 t} + b^* e^{-i\omega_2 t}, \quad \dot{y} = i\omega_2 b e^{i\omega_2 t} - i\omega_2 b^* e^{-i\omega_2 t}. \tag{6.18}$$

Substitution into (6.11) — (6.14) with multiplication by $e^{-i\omega_1 t}$ (in the equations for $a$), and by $e^{-i\omega_2 t}$ (in the equations for $b$), and averaging over period of the fast oscillations accounting the frequency relation (6.1) yield the shortened equations for slow amplitudes at four stages of the dynamics as follows:

**Stage I.** $\dot{a} = -(\kappa/4\omega_1)b^* - \frac{3}{2}\beta_1\omega_1^2|a|^2 a, \dot{b} = -(\kappa/4\omega_2)a^* - \frac{3}{2}\beta_2\omega_2^2|b|^2 b.$

**Stage II.** $\dot{a} = 0, \dot{b} = -\frac{1}{2}\alpha_2 b.$

**Stage III.** $\dot{a} = -i\varepsilon\omega_1^{-1}a^* b, \dot{b} = -\frac{1}{2}i\varepsilon\omega_2^{-1}a^2.$

**Stage IV.** $\dot{a} = -\frac{1}{2}\alpha_1 a, \dot{b} = 0.$

Equivalently, it may be represented by a set of differential equations

$$\begin{aligned}
\dot{a} &= -(\kappa/4\omega_1)b^* f_1(t) - \frac{3}{2}f_1(t)\beta_1\omega_1^2|a|^2 a - if_3(t)\varepsilon\omega_1^{-1}a^* b - \frac{1}{2}f_4(t)\alpha_1 a, \\
\dot{b} &= -(\kappa/4\omega_2)a^* f_1(t) - \frac{3}{2}f_1(t)\beta_2\omega_2^2|b|^2 b - \frac{1}{2}if_3(t)\varepsilon\omega_2^{-1}a^2 - \frac{1}{2}f_2(t)\alpha_2 b,
\end{aligned} \tag{6.19}$$

where, again, $f_k(t) = 1$, if $k - 1 \leqslant 4\{t/T\} < k$, and 0 otherwise.

### 6.2.2 Qualitative explanation of the operation

At the first stage of parametric excitation amplitudes of both oscillators grow, and their final phases appear to be fixed in certain relation. To explain this point, let us assume for simplicity that the dissipation is absent. Then, the complex amplitudes evolve in accordance with equations $\dot{a} = -\kappa b^*/4\omega_1, \dot{b} = -\kappa a^*/4\omega_2$, and we get $a = -\sqrt{\omega_1/\omega_2}(C_+^* e^{\kappa t/4\sqrt{\omega_1\omega_2}} + C_-^* e^{-\kappa t/4\sqrt{\omega_1\omega_2}})$, $b = C_+ e^{\kappa t/4\sqrt{\omega_1\omega_2}} + C_- e^{-\kappa t/4\sqrt{\omega_1\omega_2}}$. The constants $C_+ = Re^{i\varphi}$ and $C_- = Re^{-i\varphi}$ are determined by initial conditions at the onset of the stage. The second terms in both expressions decay, and at the end of the stage the first terms dominate; so, we have $b \sim R \cdot e^{i\varphi} e^{\kappa t/4\sqrt{\omega_1\omega_2}}$ and $a \sim -\sqrt{\omega_1/\omega_2} R \cdot e^{-i\varphi} e^{\kappa t/4\sqrt{\omega_1\omega_2}}$. It corresponds to $y \sim R \cdot e^{\kappa t/4\sqrt{\omega_1\omega_2}} \cos(\omega_2 t + \varphi)$ and $x \sim R \cdot \sqrt{\omega_1/\omega_2} e^{\kappa t/4\sqrt{\omega_1\omega_2}} \cos(\omega_1 t - \varphi - \pi)$. Thus, the oscillations arising due to the parametric instability on the first harmonic $(\omega_1)$ and the second harmonic $(\omega_2 = 2\omega_1)$ have related phases determined by a single constant $\varphi$, which depends on the initial conditions. With account of the nonlinear dissipation, the amplitudes undergo saturation, but the phase relation is retained, at least approximately.

At the second stage the oscillators are decoupled. The first one demonstrates free oscillations of constant amplitude, and in the second one the oscillations decay up to some very low level. The phase shift of the first oscillator remains nearly constant, and we have $a \sim -e^{-i\varphi}$ and $x \sim \cos(\omega_1 t - \varphi - \pi)$.

At the third stage, interaction of the oscillators through the quadratic nonlinearity takes place. The second oscillator is driven by the resonance action from the second harmonic component of the first oscillator because of the assumed relation $\omega_2 = 2\omega_1$. From the equation $\dot{b} = -\frac{1}{2} i\varepsilon\omega_2^{-1} a^2$, with amplitude of the first oscillator $a \sim -e^{-i\varphi}$, we obtain $b \sim -ia^2 = -ie^{-2i\varphi}$, and $y \sim \cos(\omega_2 t - 2\varphi - \pi/2)$. Hence, the value of the phase for the second oscillator appears to be doubled (up to a sign and a constant shift).

At the fourth stage, the first oscillator decays up to negligible level while the second one retains its amplitude and phase shift, namely, $b \sim -ie^{-2i\varphi}$ and $y \sim \cos(\omega_2 t - 2\varphi - \pi/2)$. At the end of the stage, it determines the initial conditions for the next stage of parametric excitation.

Updated coefficients in the expression for the solution determining growth of oscillations at the next stage of parametric excitation $C'_+$ and $C'_-$ are expressed as $b = C'_+ + C'_- \sim -ie^{-2i\varphi}, a \sim C'_+ - C'_- \approx 0$. Then, $C'_+ = R' e^{i\varphi'} \sim -ie^{-2i\varphi}$ and it means that in the approximation we use the new and the old phase shifts $\varphi$ related as

$$\varphi' = -2\varphi - \pi/2. \tag{6.20}$$

So, transformation of the system state in a full period of four stages corresponds to expanding map for the phase. It is a kind of chaotic expanding circle map, which differs from the usual Bernoulli map only in inversion of the direction of the bypass for the image around the circle. A perturbation of the variable $\varphi$ is multiplied by factor 2, so, the positive Lyapunov exponent is $\Lambda = \ln 2$.

Each iteration of the Poincaré map is accompanied with expansion of elementary phase volume by factor 2 along a cyclic coordinate associated with the phase variable $\varphi$, and with compression in all the rest directions in the phase space. It corresponds to situation, where presence of the Smale-Williams attractor has to be expected.

### 6.2.3 Numerical results

Let us turn to results of numerical simulation of the dynamics of the system. It is convenient to set $\omega_1 = 2\pi$, $\omega_2 = 4\pi$, and $\omega_3 = 6\pi$ that correspond to the choice of the unit time period of natural oscillations for the first oscillator. Figure 6.4 shows typical examples of time dependence in the sustained regime of parametric generation obtained by solving Eqs. (6.15) with computer finite-difference method at the parameters

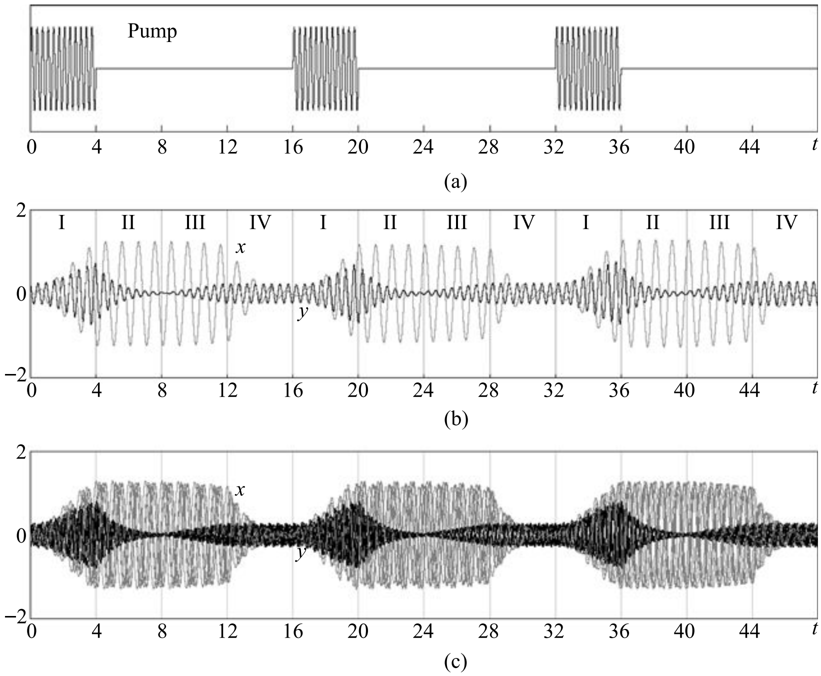


**Fig. 6.4** Plots of the time dependence for the pump **(a)** and for variables associated with signal and idler oscillations in the sustained regime of parametric generation **(b)**. Roman numbers denote the four stages of the system operation. Presence of chaos reveals itself in irregular evolution of the phase of the carrier signal relatively to the envelope; it becomes visually evident with plotting several samples of the signals on one diagram **(c)**.

$$T = 16, \quad \alpha_1 = \alpha_2 = 1.6, \quad \beta_1 = \beta_2 = 0.02, \quad \varepsilon = 2.2, \quad \kappa = 25. \tag{6.21}$$

The time interval depicted contains three periods of the pump modulation; the plot of the pump signal is shown in the upper diagram (a). As seen from the diagram (b), each of the two oscillators that constitute the system generates oscillatory trains, which follow with time interval corresponding to the period of pump modulation. However, both signal and idler oscillations are in fact non-periodic: the phases of the high-frequency filling vary from pulse to pulse chaotically. The non-periodicity is visually evident from the diagram (c), where several successive sections of the signals are superimposed on one and the same plot.

Figure 6.5(a) shows the iteration diagram obtained from the numerical solution of Eqs. (6.15); the phases are determined at the end of the stages of the parametric excitation from the formula $\varphi = \arg(x - iu)$ and are reduced to fit the interval $[0, 2\pi)$. Observe that the phase diagram is consistent with the qualitative description in the previous subsection. Indeed, it is obvious that one complete bypass of a full cycle for pre-image gives rise to two-fold bypass for the image (in the reverse direction). Figure 6.5(b) shows a portrait of the attractor in the Poincaré section projected on the phase plane of the first oscillator $(x, u)$, which corresponds to the expected solenoid of Smale-Williams type. The transversal Cantor-like structure characteristic for such attractor is noticeable. The hyperbolic nature of this attractor was verified numerically with the technique considered in the next chapter (Kuznetsov et al., 2010).

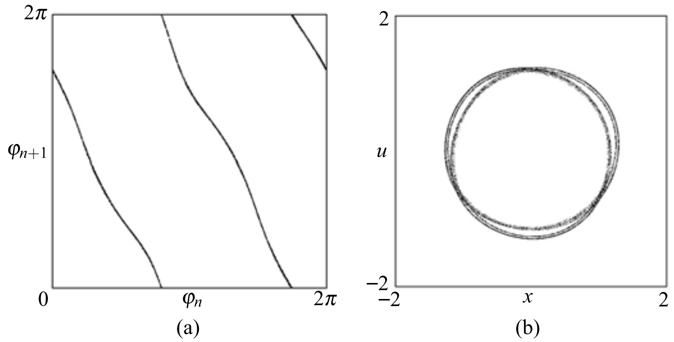


**Fig. 6.5** Iteration diagram for the phases of the first oscillator in the final parts of the stages of the parametric excitation **(a)** and a portrait of the attractor in the Poincaré section (stroboscopic section), corresponding to the same points in time **(b)**.

To have evidence for chaos on the quantitative level, we turn to the calculation of Lyapunov exponents with a standard method discussed in Appendix A and carry out a joint solution of Eqs. (6.15) and four replicas of variation equations

$$\begin{aligned}\ddot{\tilde{x}} + \omega_1^2 \tilde{x} &= f_1(t)(\kappa \tilde{y} \sin \omega_3 t - 3\beta_1 \dot{x}^2 \dot{\tilde{x}}) - \alpha_1 f_4(t) \dot{\tilde{x}} + 2\varepsilon f_3(t)(\tilde{x} y + x \tilde{y}),\\ \ddot{\tilde{y}} + \omega_2^2 \tilde{y} &= f_1(t)(\kappa \tilde{x} \sin \omega_3 t - 3\beta_2 \dot{y}^2 \dot{\tilde{y}}) - \alpha_2 f_2(t) \dot{\tilde{y}} + 2\varepsilon f_3(t) x \tilde{x},\end{aligned} \tag{6.22}$$

accompanied by the Gram-Schmidt orthogonalization and normalization for the perturbation vectors $\tilde{\mathbf{x}}_i = \{\tilde{x}_i, \dot{\tilde{x}}_i, \tilde{y}_i, \dot{\tilde{y}}_i\}$, $i = 1,2,3,4$. The Lyapunov exponents are determined as mean rates for increase or decrease of accumulating sums for logarithms of ratios of norms of the vectors (after orthogonalization but before the normalization). Full spectrum of Lyapunov exponents for the attractor at the parameter values (6.21), according to the calculations, is the following:

$$\lambda_1 \approx 0.0402, \quad \lambda_2 \approx -0.0631, \quad \lambda_3 \approx -0.559, \quad \lambda_4 \approx -0.675. \tag{6.23}$$

For the stroboscopic Poincaré map, the Lyapunov exponents are expressed as $\Lambda_k = \lambda_k T$. Then, $\Lambda_1 \approx 0.643$ that agrees well with the estimate $\Lambda = \ln 2$ in the approximation corresponding to the one-dimensional expanding circle map for the phase variable.

The presence of a positive exponent $\Lambda_1$ is a quantitative confirmation of chaos. The remaining exponents $\Lambda_2$, $\Lambda_3$, $\Lambda_4$ are all negative. It means that an element of phase volume undergoes stretching in one direction associated with the cyclic phase variable, and contraction in three other directions in the four-dimensional phase space of the Poincaré map. The Kaplan-Yorke dimension of the attractor of the Poincaré map (see Appendix D) is $D = 1 + \Lambda_1/|\Lambda_2| \approx 1.64$.

### *6.2.4 Numerical results in the frame of method of slow complex amplitudes*

Equations obtained in Subsection 6.2.1 for the complex amplitudes can be regarded not only as an approximation for the original system (6.15), but also as a separate object of study. It is essential that this formulation reveals the universal nature of the model: the combinations of complex amplitudes and conjugate values are characteristic for equations describing parametric systems of different physical nature. Note that the number of essential parameters in this formulation is less than in the original equations, because the absolute value of the fundamental frequency $\omega_1$ does not enter the equations, except in combination with other parameters. The evolution equation can be rewritten as follows:

$$\begin{aligned} \dot{a} &= -\bar{\kappa} b^* f_1(t) - \frac{3}{2} f_1(t)\bar{\beta}_1 |a|^2 a - i f_3(t)\bar{\varepsilon} a^* b - \frac{1}{2} f_4(t)\alpha_1 a, \\ \dot{b} &= -\frac{1}{2}\bar{\kappa} a^* f_1(t) - \frac{3}{2} f_1(t)\bar{\beta}_2 |b|^2 b - \frac{1}{4} i f_3(t)\bar{\varepsilon} a^2 - \frac{1}{2} f_2(t)\alpha_2 b, \end{aligned} \tag{6.24}$$

where $\bar{\kappa} = \kappa/4\omega_1$, $\bar{\beta}_{1,2} = \beta_{1,2}\omega_{1,2}^2$, $\bar{\varepsilon} = \varepsilon/\omega_1$. Hereafter we select the parameters to have correspondence to the previous subsection, namely,

$$\begin{aligned} &T = 16, \quad \alpha_1 = \alpha_2 = 1.6, \quad \beta_1 = 0.7896, \\ &\beta_2 = 3.1583, \quad \varepsilon = 0.3501, \quad \kappa = 0.9947. \end{aligned} \tag{6.25}$$

Figure 6.6 provides time dependence of the amplitudes and phases of the complex variables $a$ and $b$, obtained by computer numerical solution of Eqs. (6.24). As seen, the amplitude dependence corresponds well to the envelopes for the plots of oscillations of two subsystems in Fig. 6.4. The dependence of the phases on time is irregular (see panel (b)). One can check that the phase transformation in each period of repetition of stages appears to be in good correspondence with the expanding circle map discussed above. It is seen from the diagram shown in Fig. 6.7(a), which should be compared with Fig. 6.5(a). Portrait of the attractor in the Poincaré section in Fig. 6.7(b) demonstrates an obvious correspondence with attractor of the original model in Fig. 6.5(b).

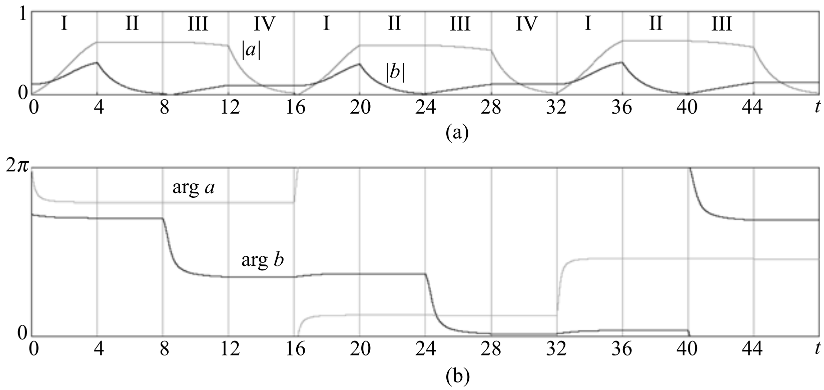


**Fig. 6.6** Plots for amplitudes **(a)** and phases **(b)** of complex variables for the two partial oscillators obtained from computer numerical solution of Eqs. (6.24). Roman numerals designate the four stages of evolution of the system.

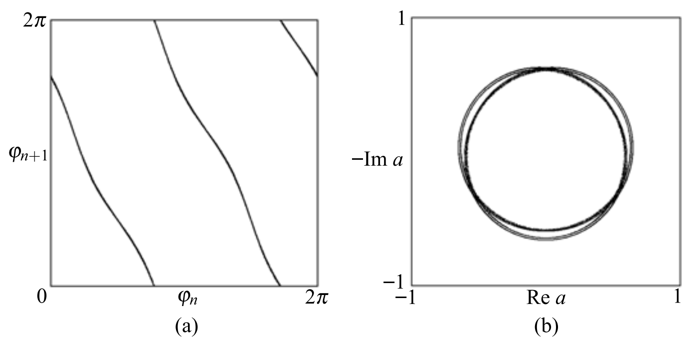


**Fig. 6.7** Iteration diagram for the phases of the first oscillator in the final parts of the stages of the parametric excitation **(a)** and a portrait of the attractor in the stroboscopic Poincaré section **(b)** obtained from numerical solution of the amplitude equations (6.24).

Computation of Lyapunov exponents for the attractor by the method of Benettin (see Appendix A) is based on solving the equations for slow amplitudes, supplemented by four replicas of linearized equations for perturbations of the reference phase trajectory, and yields the spectrum of Lyapunov exponents

$$\lambda_1 \approx 0.0413, \quad \lambda_2 \approx -0.0656, \quad \lambda_3 \approx -0.558, \quad \lambda_4 \approx -0.685, \tag{6.26}$$

which is in good agreement with the results (6.23). Observe that the largest exponent for the Poincaré map $\Lambda_1 = \lambda_1 T \approx 0.661$ is close to the value $\ln 2$ corresponding to approximate description of the evolution of the phase in terms of the expanding circle map.

Figure 6.8 shows a plot for Lyapunov exponents of the Poincaré map versus the parameter of the pump intensity $\bar{\kappa}$. As seen, the largest Lyapunov exponent in a wide parameter range remains almost constant and close to the value $\ln 2$. This character of the dependence is consistent with the suggested presence of a structurally stable hyperbolic attractor.

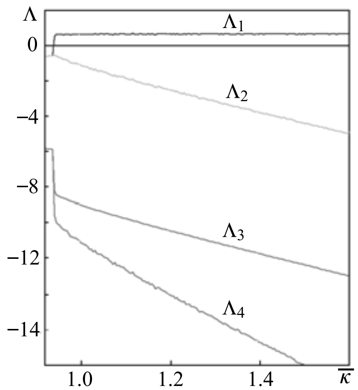


**Fig. 6.8** Lyapunov exponents for the Poincaré map plotted against the parameter of intensity of pump for the model (6.24) at $T = 16, \alpha_1 = \alpha_2 = 1.6$, $\beta_1 = 0.7896$, $\beta_2 = 3.1583$, $\varepsilon = 0.3501$.

## 6.3 Parametric generator of hyperbolic chaos based on four coupled oscillators with pump modulation

Consider a system composed of two subsystems A and B, each of which represents a parametric generator consisting of two parametrically coupled oscillators with frequencies $\omega_1$ and $\omega_2 = 2\omega_1$, like what discussed in Sect. 6.1 (Kuznetsov, 2008). The block diagram is shown in Fig. 6.9. Pumping frequency is assumed to be equal to $\omega_3 = \omega_1 + \omega_2 = 3\omega_1$; so, the condition of parametric resonance is satisfied. The oscillator of frequency $\omega_1$ is coupled to the oscillator of frequency $\omega_2$ in the other subsystem via an element with quadratic nonlinearity. The pump is switched on and off alternately in both subsystems, so the parametrically excited oscillations grow and decay in them by turns. Each excitation of a subsystem is stimulated by a second harmonic component generated by the other subsystem. Due to this, the oscillation phase is doubled in the course of each signal transfer; hence, it is multiplied by a factor of 4 over a whole period of pump modulation. As a result, the system generates a sequence of oscillatory trains following with the modulation period, whose carrier phase chaotically varies from pulse to pulse.

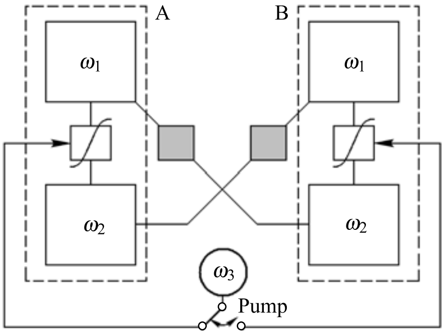


**Fig. 6.9** Block diagram of the parametric chaos generator. Blocks labeled as $\omega_1$ and $\omega_2$ represent the oscillators with these natural frequencies; those labeled with a wave-like crossing are reactive elements with coupling parameter oscillating at the pump carrier frequency; the gray squares are coupling elements characterized by the quadratic nonlinearity.

## *6.3.1 Model, operation principle and basic equations*

Consider the Lagrangian function

$$\begin{aligned} L = &\frac{1}{2}(\dot{x}_1^2+\dot{x}_2^2+\dot{y}_1^2+\dot{y}_2^2-\omega_1^2x_1^2-\omega_2^2x_2^2-\omega_1^2y_1^2-\omega_2^2y_2^2) \\ &+\kappa[x_1x_2f(t)+y_1y_2g(t)]\sin\omega_3 t+\varepsilon(x_1^2y_2+y_1^2x_2), \end{aligned} \tag{6.27}$$

where $x_{1,2}$ and $y_{1,2}$ are generalized coordinates of two coupled pairs of oscillators, $\dot{x}_{1,2}$ and $\dot{y}_{1,2}$ are the corresponding generalized velocities, $\omega_1$ and $\omega_2 = 2\omega_1$ are the respective natural frequencies of the oscillators in both pairs. The parameter $\kappa$ quantifies the pump strength and the functions $f(t)$ and $g(t)$ determine the respective slowly varying amplitudes of the pump signals that drive the two pairs of oscillators. The pump carrier frequency is $\omega_3 = \omega_1+\omega_2 = 3\omega_1$. The parameter $\varepsilon$ characterizes the coupling between oscillators belonging to different pairs.

The nonlinear damping needed for saturation of parametric instability and for existence of an attractor is introduced by means of the Rayleigh dissipation function defined as follows:

$$R = \frac{1}{2}(\alpha_1 \dot{x}_1^2 + \alpha_2 \dot{x}_2^2 + \alpha_1 \dot{y}_1^2 + \alpha_2 \dot{y}_2^2) + \frac{1}{4}(\beta_1 \dot{x}_1^4 + \beta_2 \dot{x}_2^4 + \beta_1 \dot{y}_1^4 + \beta_2 \dot{y}_2^4), \tag{6.28}$$

where $\alpha_{1,2}, \beta_{1,2}$ are positive constants. The equations of motion for the system

$$\frac{d}{dt}\left(\frac{\partial L}{\partial \dot{x}_i}\right) = \frac{\partial L}{\partial x_i} - \frac{\partial R}{\partial \dot{x}_i}, \quad \frac{d}{dt}\left(\frac{\partial L}{\partial \dot{y}_i}\right) = \frac{\partial L}{\partial y_i} - \frac{\partial R}{\partial \dot{y}_i}, \quad i = 1, 2 \tag{6.29}$$

are then written as

$$\begin{aligned}
\ddot{x}_1 + \omega_1^2 x_1 &= \kappa x_2 f(t) \sin \omega_3 t + 2\varepsilon x_1 y_2 - \alpha_1 \dot{x}_1 - \beta_1 \dot{x}_1^3, \\
\ddot{x}_2 + \omega_2^2 x_2 &= \kappa x_1 f(t) \sin \omega_3 t + \varepsilon y_1^2 - \alpha_2 \dot{x}_2 - \beta_2 \dot{x}_2^3, \\
\ddot{y}_1 + \omega_1^2 y_1 &= \kappa y_2 g(t) \sin \omega_3 t + 2\varepsilon y_1 x_2 - \alpha_1 \dot{y}_1 - \beta_1 \dot{y}_1^3, \\
\ddot{y}_2 + \omega_2^2 y_2 &= \kappa y_1 g(t) \sin \omega_3 t + \varepsilon x_1^2 - \alpha_2 \dot{y}_2 - \beta_2 \dot{y}_2^3.
\end{aligned} \tag{6.30}$$

Let us specify the functions $f(t)$ and $g(t)$ so that the pump signals for two subsystems should be modulated in counter-phase:

$$f(t) = \sin^2(\pi t/T), \quad g(t) = \cos^2(\pi t/T). \tag{6.31}$$

The modulation period is assumed to be an integer multiple of the pump carrier period, i.e. $T = 2\pi N/\omega_3$, where $N$ is an integer. This condition implies that (6.30) is just a system of equations with $T$-periodic coefficients, and its dynamics can be rigorously represented by the stroboscopic Poincaré map using sections of the extended phase space with time step $T$.[1]

In the case $N \gg 1$, following a standard technique of the method of slow amplitudes, we set

$$\begin{aligned}
x_1 &= A_1 e^{i\omega_1 t} + A_1^* e^{-i\omega_1 t}, \quad x_2 = A_2 e^{i\omega_2 t} + A_2^* e^{-i\omega_2 t}, \\
y_1 &= B_1 e^{i\omega_1 t} + B_1^* e^{-i\omega_1 t}, \quad y_2 = B_2 e^{i\omega_2 t} + B_2^* e^{-i\omega_2 t},
\end{aligned} \tag{6.32}$$

where $A_{1,2}(t) = A'_{1,2} + iA''_{1,2}$ and $B_{1,2}(t) = B'_{1,2} + iB''_{1,2}$ are slowly varying complex functions of time subject to the additional conditions

$$\begin{aligned}
\dot{A}_1 e^{i\omega_1 t} + \dot{A}_1^* e^{-i\omega_1 t} &= 0, \quad \dot{A}_2 e^{i\omega_2 t} + \dot{A}_2^* e^{-i\omega_2 t} = 0, \\
\dot{B}_1 e^{i\omega_1 t} + \dot{B}_1^* e^{-i\omega_1 t} &= 0, \quad \dot{B}_2 e^{i\omega_2 t} + \dot{B}_2^* e^{-i\omega_2 t} = 0.
\end{aligned} \tag{6.33}$$

Substituting these relations into (6.30), multiplying the equations for $A_1$ and $B_1$ by $e^{-i\omega_1 t}$, and for $A_2$ and $B_2$ by $e^{-i\omega_2 t}$, averaging the resulting equations over a period of fast oscillations, and using the assumed relation between $\omega_{1,2,3}$ we obtain

[1] This condition can be ignored in the approach based on slowly varying amplitudes considered below.

$$\begin{aligned}
\dot{A}_1 &= -\frac{\kappa}{4\omega_1} f(t) A_2^* - i\frac{\varepsilon}{\omega_1} A_1^* B_2 - \frac{1}{2}\alpha_1 A_1 - \frac{3}{2}\omega_1^2 \beta_1 A_1 |A_1|^2, \\
\dot{A}_2 &= -\frac{\kappa}{4\omega_2} f(t) A_1^* - i\frac{\varepsilon}{2\omega_2} B_1^2 - \frac{1}{2}\alpha_2 A_2 - \frac{3}{2}\omega_2^2 \beta_2 A_2 |A_2|^2, \\
\dot{B}_1 &= -\frac{\kappa}{4\omega_1} g(t) B_2^* - i\frac{\varepsilon}{\omega_1} B_1^* A_2 - \frac{1}{2}\alpha_1 B_1 - \frac{3}{2}\omega_1^2 \beta_1 B_1 |B_1|^2, \\
\dot{B}_2 &= -\frac{\kappa}{4\omega_2} g(t) B_1^* - i\frac{\varepsilon}{2\omega_2} A_1^2 - \frac{1}{2}\alpha_2 B_2 - \frac{3}{2}\omega_2^2 \beta_2 B_2 |B_2|^2.
\end{aligned} \tag{6.34}$$

If $\varepsilon = 0$, the system splits into two symmetric isolated subsystems A and B, each comprising two parametrically coupled oscillators. Consider one of the subsystems. For the constant pump amplitude, as explained in the previous section, the parametrically excited oscillations at the frequencies $\omega_1$ and $\omega_2 = 2\omega_1$ are characterized by a common phase shift constant $\varphi$, depending on the initial conditions.

Now, consider the regime when the coupled subsystems A and B with nonzero $\varepsilon$ are driven by turns due to the modulated pump.

In each subsystem, the oscillator with natural frequency $\omega_2 = 2\omega_1$ is excited, stimulated by the second harmonic of the oscillator of frequency $\omega_1$ from the opposite subsystem, produced by the quadratic nonlinear coupling element. The double phase shift in the second harmonic is inherited then by the excited oscillator. During the next modulation half-period, the subsystems A and B exchange roles, and the phase shift of the passed signal doubles once again. Thus, the phase shift after a modulation period can be approximately represented by the map $\varphi_{new} = 4\varphi_{old} + \mathrm{const}(\bmod 2\pi)$. It is a Bernoulli type map with chaotic dynamics characterized by the Lyapunov exponent $\Lambda = \ln 4 \approx 1.386$.

Description of the dynamics may be done in discrete time by sampling the eight-dimensional state vectors $\mathbf{X}_n$ at time instants $t_n = nT$. From solution of Eqs. (6.30) or (6.34) at a time interval $T$ starting from a particular $t_n$, we obtain a new state vector $\mathbf{X}_{n+1}$. The function

$$\mathbf{X}_{n+1} = \mathbf{T}(\mathbf{X}_n), \tag{6.35}$$

which maps the eight-dimensional phase space into itself, is the stroboscopic Poincaré map associated with the system of differential evolution equations whose right-hand sides are smooth and bounded in a finite domain in the phase space. By virtue of the existence, uniqueness, continuity, and differentiability of the solution to the system, the map $\mathbf{T}$ is a diffeomorphism (Arnold, 1978).

### *6.3.2 Chaotic dynamics: results of computer simulation*

Hereafter we assign $\omega_1 = 2\pi$, $\omega_2 = 4\pi$, $\omega_3 = 6\pi$ that correspond to measuring of time in units of the natural period of one of the involved oscillators.

Figure 6.10 shows typical samples of waveforms obtained from numerical solution of Eqs. (6.30) for the generalized coordinates $x$ and $y$, with modulated amplitudes (6.31) of the pump signals plotted separately on the panel (a). Parameter values are assigned as follows:

$$T = 40, \quad \varepsilon = 0.5, \quad \kappa = 35, \quad a = 0.6, \quad b = 0.01. \tag{6.36}$$

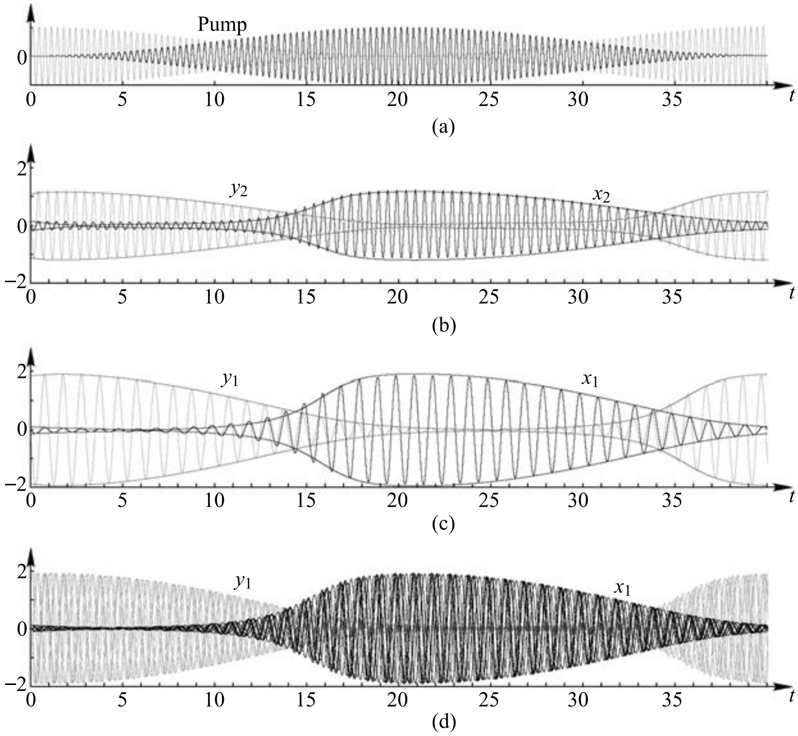


**Fig. 6.10** Time-domain waveforms obtained from numerical solution of Eqs. (6.30) with parameter values (6.36): **(a)** pump signals; **(b)**, **(c)** single samples; **(d)** superimposed samples of the same signal realization. The envelopes in panels (b) and (c) are obtained by numerical solution of equations for complex amplitudes (6.34).

As observed, in the course of the evolution in time both subsystems are active alternately, in correspondence with the action of the pump (panels (a), (b), and (c)). Each subsystem produces a train of oscillations following with the pump modulation period; however, the waveform is not periodic: the carrier phase varies irregularly from pulse to pulse. An illuminating visual illustration is provided by panel (d), which shows several superimposed signal samples corresponding to successive modulation periods. Panels (b) and (c) illustrate additionally the time dependence obtained from numerical solution of the amplitude equations (6.34).[2] The figure demonstrates good agreement between the results obtained by the slowly varying amplitude method and the exact solution.

Figure 6.11 shows iteration diagram for phases of the carrier in successive oscillatory trains generated by one of the subsystems. The abscissa and ordinate are the phases of oscillations in the subsystem B relating to the time instants $t_n = nT$ and $t_{n+1}$, respectively. The plot in panel (a) is obtained for the original equations (6.30), and that in panel (b) for the amplitude equations (6.34). In the first case the phase is determined from the formula $\varphi_n = \arg(y_1(t_n) + \dot{y}_1(t_n)/i\omega_1)$, and in the second case from $\varphi_n = \arg B_1(t_n)$. Note that the phase is defined only within a time interval of activity of the subsystem, when the output amplitude does not approach zero.[3] According to Fig. 6.11, as $\varphi_n$ varies from 0 to $2\pi$, the point associated with the phase $\varphi_{n+1}$ goes around the unit circle four times; i.e., the mapping is topologically equivalent to the Bernoulli type map.

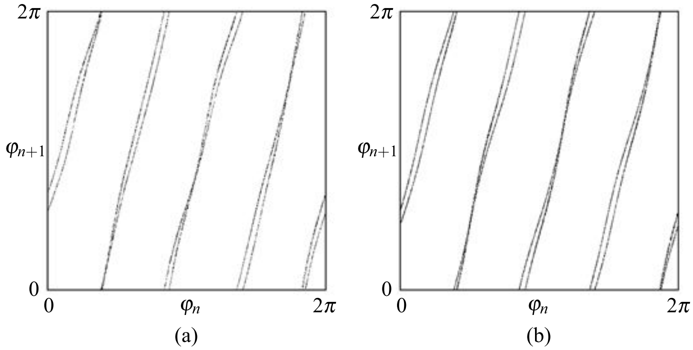


**Fig. 6.11** Iteration diagram for phases at the stage of activity of one of the subsystems, composed on the basis of the numerical solution of the original equations (6.30) **(a)** and the equations for complex amplitudes (6.34) **(b)**; the parameters assigned in accordance with (6.36).

Because of good agreement between the results obtained with the original and the amplitude equations, the analysis below is restricted to the amplitude equations.

Quantitative evidence of chaotic behavior is obtained by calculating the Lyapunov exponents. To find the Lyapunov spectrum by Benettin algorithm (Appendix A), Equations (6.34) are computed simultaneously with eight replicas of variation equations

[2] To correlate the waveforms, the initial conditions set at the starting point in time were calculated for the corresponding state of the system (6.30) by using relations (6.32) and (6.33).

[3] The phase cannot be defined globally on the entire time axis, because the amplitude is nearly zero when the subsystem is not active. If such a definition were possible, then the map for the phase could not belong to the appropriate topological class.

$$\begin{aligned}
\dot{\tilde{A}}_1 &= -\frac{\kappa}{4\omega_1} f(t)\tilde{A}_2^* - i\frac{\varepsilon}{\omega_1}(\tilde{A}_1^* B_2 + A_1^*\tilde{B}_2) - \frac{1}{2}\alpha_1\tilde{A}_1 - \frac{3}{2}\omega_1^2\beta_1 A_1^2\tilde{A}_1^* - 3\omega_1^2\beta_1 A_1^* A_1\tilde{A}_1,\\
\dot{\tilde{A}}_2 &= -\frac{\kappa}{4\omega_2} f(t)\tilde{A}_1^* - i\frac{\varepsilon}{\omega_2} B_1\tilde{B}_1 - \frac{1}{2}\alpha_2\tilde{A}_2 - \frac{3}{2}\omega_2^2\beta_2 A_2^2\tilde{A}_2^* - 3\omega_2^2\beta_2 A_2^* A_2\tilde{A}_2,\\
\dot{\tilde{B}}_1 &= -\frac{\kappa}{4\omega_1} f(t)\tilde{B}_2^* - i\frac{\varepsilon}{\omega_1}(A_2\tilde{B}_1^* + B_1^*\tilde{A}_2) - \frac{1}{2}\alpha_1\tilde{B}_1 - \frac{3}{2}\omega_1^2\beta_1 B_1^2\tilde{B}_1^* - 3\omega_1^2\beta_1 B_1^* B_1\tilde{B}_1,\\
\dot{\tilde{B}}_2 &= -\frac{\kappa}{4\omega_2} f(t)\tilde{B}_1^* - i\frac{\varepsilon}{\omega_2} A_1\tilde{A}_1 - \frac{1}{2}\alpha_2\tilde{B}_2 - \frac{3}{2}\omega_2^2\beta_2 B_2^2\tilde{B}_2^* - 3\omega_2^2\beta_2 B_2^* B_2\tilde{B}_2.
\end{aligned} \tag{6.37}$$

Each time after a certain number of integration steps have been performed, the Gram-Schmidt orthonormalization process is applied to the perturbation vectors $\{\tilde{A}'_1, \tilde{A}''_1, \tilde{A}'_2, \tilde{A}''_2, \tilde{B}'_1, \tilde{B}''_1, \tilde{B}'_2, \tilde{B}''_2\}$. (Prime and double prime designate real and imaginary parts, respectively.) The Lyapunov exponents are calculated by averaging the growth rates of the sum of logarithms of norms of the perturbation vectors after orthogonalization, but before normalization. The Lyapunov spectrum obtained for the attractor corresponding to parameter set (6.36) is as follows:

$$\begin{aligned}
&\lambda_1 = 0.03456, \quad \lambda_2 = -0.1320, \quad \lambda_3 = -0.2247, \quad \lambda_4 = -0.5220,\\
&\lambda_5 = -0.6826, \quad \lambda_6 = -0.9012, \quad \lambda_7 = -1.4189, \quad \lambda_8 = -2.3248.
\end{aligned} \tag{6.38}$$

The corresponding Lyapunov exponents of the stroboscopic Poincaré map are determined from (6.38) as $\Lambda_k = \lambda_k T$. Particularly, $\Lambda_1 = 1.3823$, which is in good agreement with the value $\ln 4 = 1.3862\cdots$ obtained from the Bernoulli type map $\varphi_{n+1} = 4\varphi_n + \text{const}(\bmod 2\pi)$. A positive $\Lambda_1$ is an indicator of chaos. Since the remaining exponents $\Lambda_2 \cdots \Lambda_8$ are negative, an element of phase space volume undergoes expanding in one direction in the phase space of the Poincaré map, associated with the angular coordinate $\varphi$, and the others are contracting. Figure 6.12 plots two larger Lyapunov exponents of the Poincaré map calculated as functions of the cou-

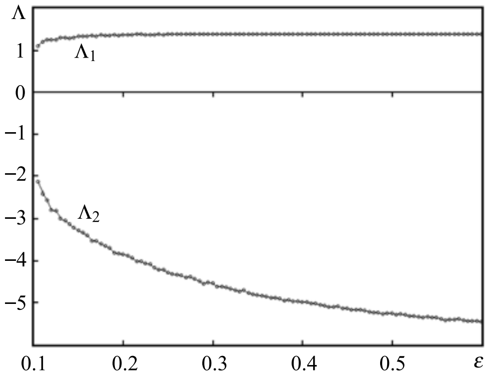


**Fig. 6.12** The largest two Lyapunov exponents of stroboscopic Poincaré map vs. parameter $\varepsilon$ computed for $\omega_1 = 2\pi$, $\omega_2 = 4\pi$, $\omega_3 = 6\pi$, $T = 40$, $\kappa = 35, a = 0.6, b = 0.01$. The largest exponent is consistent with the estimate $\Lambda_1 = \ln 4$.

pling strength $\varepsilon$ while the remaining parameters are held constant. It is clear from Fig. 6.12 that the value of $\Lambda_1$ is close to ln 4 over a wide interval of $\varepsilon$. The positive exponent smoothly depends on the parameter and has no sharp dips characteristic for non-hyperbolic attractors (See for comparison of Figs. B. 4 and B. 7 in Appendix B.)

The Kaplan-Yorke dimension of the attractor of the stroboscopic Poincaré map with the Lyapunov spectrum (6.38) is

$$D = 1 + \Lambda_1/|\Lambda_2| \approx 1.26 \tag{6.39}$$

(since $\Lambda_1 > 0$ and $\Lambda_1 + \Lambda_2 < 0$). Accordingly, the total dimension of the attractor embedded in the nine-dimensional extended phase space is $D' = D + 1 \approx 2.26$.

Figure 6.13(a) shows portrait of the attractor in the Poincaré section obtained by projection onto the phase plane of oscillator $\omega_1$ in subsystem B. An enlarged fragment is shown to resolve details of the intrinsic transverse Cantor-like fractal structure. Figure 6.13(b) presents an analogous phase portrait corresponding to a coupling strength value near the threshold for existence of the chaotic attractor, where the transverse fractal structure is visible much better.

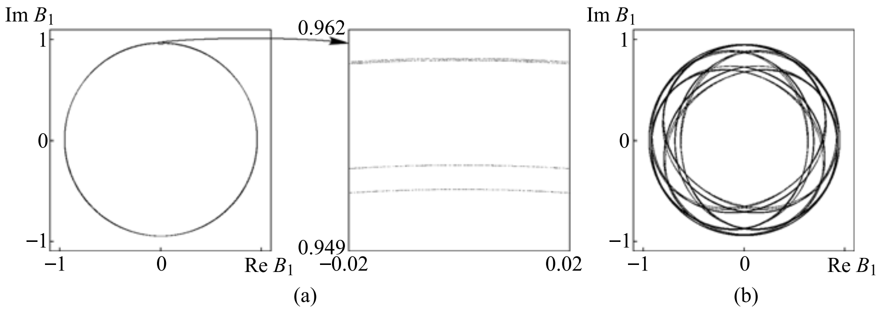


**Fig. 6.13** Poincaré section of the attractor portrait projected onto the complex amplitude plane of the first oscillator in subsystem B for $\varepsilon = 0.5$ **(a)** and $\varepsilon = 0.125$ **(b)**. Remaining parameters are assigned in accordance with (6.36).

The underlying mechanism of operating of the parametric generator of chaos, as well as numerical results confirming implementation of this mechanism allow suggesting that the observed chaotic attractor is uniformly hyperbolic. Interpreting the action of the Poincaré map geometrically, we can imagine a toroid embedded in an eight-dimensional space (that is a direct product of one-dimensional circle and the seven-dimensional ball) and associate a single iteration of the map with the longitudinal expanding and transversal compression of the object, then folded to a quadruple loop deposited inside the original domain. At each step of repetition of this procedure, the number of turns is increased by four times. In the limit, we obtain a solenoid containing an infinite number of coils and transverse structure of the Cantor set, that is one of the variants of attractors of the Smale-Williams type. Confirmation of relation of this attractor to the uniformly hyperbolic class could be based on the use of computational procedures described in the next chapter, although in this case the phase space dimension is relatively high, and the problem requires excessive computational resources.

Despite the hypothetical nature of the conclusion of the hyperbolic nature of the chaotic attractor in the last model, the schemes of the parametric generators of chaos considered in this chapter certainly open up possibility for generation of robust chaos insensitive to the variation of parameters and characteristics of elements, e.g. in the systems of radio-engineering and electronics, mechanics, acoustics, nonlinear optics.

## References

Akhmanov, S.A., Khokhlov, R.V.: Parametric amplifiers and generators of light. Soviet Physics Uspekhi **9** (2), 210 (1966).

Arnold, V.I.: Ordinary Differential Equations. The MIT Press, Somerville, MA (1978).

Damgov, V.: Nonlinear and parametric phenomena: theory and applications in radiophysical and mechanical systems . World Scientific Publ. (2004).

Kuznetsov, S.P.: On feasibility of a parametric generator of hyperbolic chaos. JETP **106**, 380–387 (2008).

Kuznetsov, A.S., Kuznetsov, S.P., Sataev, I.R.: Parametric generator of hyperbolic chaos based on two coupled oscillators with nonlinear dissipation. Technical Physics **55**, 1707–1715 (2010).

Louisell, W.H.: Coupled Mode and Paramagnetic Electronics. Wiley, New York (1960).

Mandelshtam, L.I.: Lectures on oscillation theory. Nauka, Moscow (1972) (In Russian).

Marsden, J.E., Raţiu, T.S.: Introduction To Mechanics And Symmetry: A Basic Exposition Of Classical Mechanical Systems. Springer, New York (1999).

Rabinovich, M.I., Trubetskov, D.I.: Oscillations and Waves: In Linear and Nonlinear Systems, Kluwer Academic Publication, The Netherlands (1989).

# Chapter 7
# Recognizing the Hyperbolicity: Cone Criterion and Other Approaches

**Abstract** Physical and technical devices usually are not specially suited to admitting simple mathematical proofs. So, it is vital to employ numerical tools for verification of the hyperbolicity in systems, which potentially may possess uniformly hyperbolic chaotic attractors. Substantiation of hyperbolicity is essential to accounting relevant conclusions of the mathematical theory, like availability of description in terms of Markov partitions with a finite alphabet, or structural stability of the chaotic attractors, which may be of natural practical significance. Section 7.1 is devoted to approaches based on verification of a fundamental property of the hyperbolic invariant sets that is transversality of mutual location of stable and unstable manifolds for all orbits belonging to the invariant set. In Sect. 7.2 we turn to a technique of visualization of natural invariant measures along filaments of attractors, which shows presence or absence of singularities in the distributions. For comparison, besides models with uniformly hyperbolic attractors, some systems not relating to this class are considered in terms of the same approaches. Final part of the chapter is devoted to the cone criterion based on a rigorous mathematical result and appropriate for validation of hyperbolicity in computations. Here it is reexamined in some detail, with explanation of technical hints, and with concrete examples of its application.

## 7.1 Verification of transversality for manifolds

One of the main properties, which must be valid for a hyperbolic invariant set, is transversal mutual location of stable and unstable manifolds for all orbits relating to the invariant set (Smale, 1967; Williams, 1974; Sinai, 1979; Shilnikov, 1997; Guckenheimer and Holmes, 1983; Katok and Hasselblatt, 1995; Afraimovich and Hsu, 2003; Hasselblatt and Katok, 2003; Hasselblatt and Pesin, 2008). It means that intersections between the manifolds can occur exclusively without tangencies (or there are no intersections at all, but that is not the case for the attractors we deal with).

In this section we consider two approaches to verification of the transversality.

S. P. Kuznetsov, *Hyperbolic Chaos*

The first one is based on visualization of the manifolds by their graphical representation. For this purpose it is sufficient to have an accuracy about one pixel of the picture; it is achieved easily with a simple method explained in Subsection 7.2.1. It is worth noting, however, that more accurate methods are also available (Krauskopf, 2005). For application of this technique the most appropriate is the case of two-dimensional Poincaré maps, when a nontrivial attractor has one positive and one negative Lyapunov exponents.

The second method is based on computation of angles between vectors tangent to the stable and unstable manifolds at their intersections for a representative collection of points on the examined invariant set, with subsequent inspection of the statistical distribution of these angles. If the uniform hyperbolicity holds, all the observed angles have to be distant from zero. The procedure may be easily expanded to analyze attractors with dimension of the stable manifolds larger than one. This method was suggested in (Lai et al., 1993) and then used with modifications in (Hirata et al., 1999; Anishchenko et al., 2000; Kuznetsov, 2005; Kuznetsov and Seleznev, 2006; Ginelli et al., 2007; Kuptsov and Kuznetsov, 2009).

### *7.1.1 Visualization of the manifolds*

Let us consider a dissipative discrete-time system governed by a map $\mathbf{x}_{n+1} = \mathbf{f}(\mathbf{x}_n)$; alternatively, it may be a Poincaré map for a continuous time system. The map is assumed to be a diffeomorphism, with nontrivial attractor $A$. In our considerations it is supposed that the map is available for evaluation by means of a computer program together with the respective inverse map.

To have a possibility of simple graphical representation, we restrict ourselves here with two-dimensional maps assuming that for the attractor $A$ both stable and unstable manifolds are one-dimensional: $N_S = 1$ and $N_U = 1$. Hence, one Lyapunov exponent is negative, and the other one is positive.

To draw the stable and unstable manifolds with computer, we proceed as follows. First, for an arbitrarily given point on the attractor $\mathbf{x} \in A$ we obtain its image under $N$-fold application of the map, i.e. $\overline{\mathbf{x}} = \mathbf{f}^N(\mathbf{x})$, and pre-image by means of the inverse map $\tilde{\mathbf{x}} = \mathbf{f}^{-N}(\mathbf{x})$, where $N$ is some empirically chosen integer. Then, with random initial conditions $\tilde{\mathbf{y}}$ in a small neighborhood of $\tilde{\mathbf{x}}$, by forward iteration of the map we get a set of points $\mathbf{y} = \mathbf{f}^N(\tilde{\mathbf{y}})$ close to the unstable manifold containing the initial point $\mathbf{x}$, which marks this manifold on the plot. In a similar way, starting with random initial conditions $\overline{\mathbf{y}}$ in a small neighborhood of $\overline{\mathbf{x}}$, we can draw the stable manifold with a set of points $\mathbf{y} = \mathbf{f}^{-N}(\overline{\mathbf{y}})$. Formally speaking, the accuracy the manifolds depict grows fast with increase of $N$; an actual selection of this number implicates a compromise between the graphical accuracy and the numerical errors arising as $N$ becomes too large.

In the cases we consider here, the unstable manifolds are one-dimensional and coincide with filaments of the attractor; so, to judge of the transversality it is sufficient to plot only *stable manifolds* for some representative set of points on the attractor. The pictures obtained in this way are illuminating and convincing to conclude qualitatively presence or absence of touches of the manifolds, and respectively, absence or presence of the uniform hyperbolicity. Nevertheless, this should not be regarded as a substitute for legitimate mathematical proofs!

The pictures shown in Fig. 7.1 relate to two uniformly hyperbolic attractors mentioned in the previous chapters. Diagrams (a) and (b) correspond, respectively, to attractor of Plykin type in the map on the plane (3.34) and to DA-attractor of the map on the torus (2.6). Portraits of the attractors are shown in gray, and families of stable manifolds are depicted in black on its background. One can see clearly that they are transversal (form nonzero angles) with the filaments of the attractors. Note that the families of the stable manifolds visually look representative: one can easily imagine intermediately missed curves.

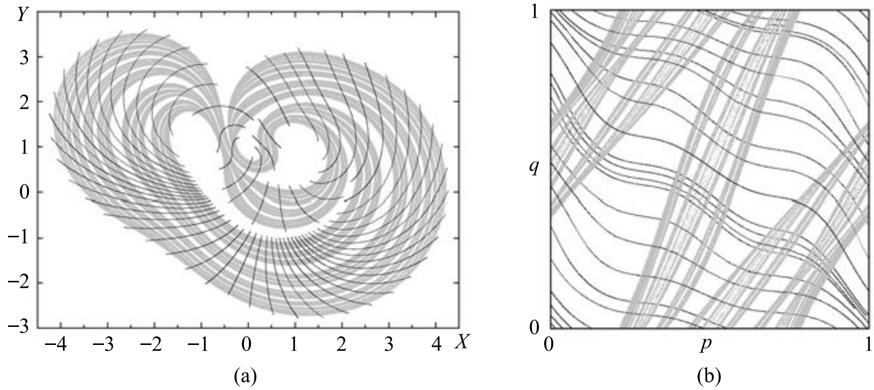


**Fig. 7.1** Portraits of chaotic uniformly hyperbolic attractors shown in gray with families of stable manifolds computed as explained in the text and plotted in black. Observe clearly visible transversality of the stable manifolds globally over the whole attractor to the filaments forming its structure. The diagram **(a)** relates to the Plykin type attractor of the map (3.34) at $\varepsilon$=0.77, and **(b)** corresponds to the DA-attractor of the map (2.6) at $\varepsilon$=0.7.

For comparison, in Fig. 7.2 the pictures are shown for another kind of attractors, which do not relate to the uniformly hyperbolic class. One is attractor of the Hénon map (a), and the other for the Ikeda map (b), at parameters corresponding to chaotic dynamics. There is one positive and one negative Lyapunov exponents. The numerical technique applied to plotting the diagrams is exactly the same as explained. Again, the families of the stable manifolds are representative; one can easily supplement them mentally with intermediate curves. However, the pictures look essentially distinct in comparison to those relating to the uniformly hyperbolic case. Namely, the stable manifolds are disposed in such a way that the touches with filaments of the attractors occur inevitably.

It is interesting to consider the Lorenz attractor, which is in some sense special, being classified as quasi-hyperbolic, or singular hyperbolic. In Fig. 7.3 the respective diagram is shown for the attractor in the Lorenz model (2.1) at the traditional

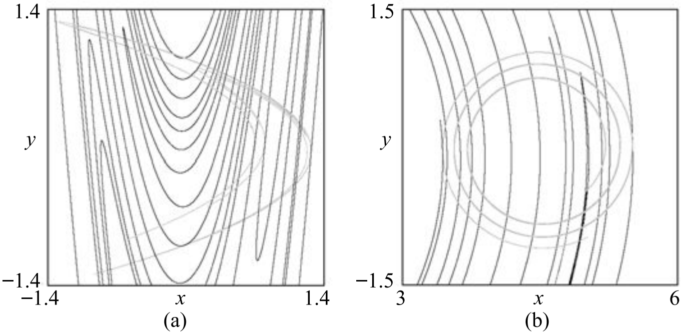


**Fig. 7.2** Portraits of chaotic attractors for Hénon map (F.4) at $a$=1.4, $b$=0.3, and Ikeda map (F.35) at $A$=4.5, $B$=0.2, $\varphi$=0 shown in gray with families of stable manifolds computed as explained in the text and plotted in black. Observe tangencies, which clearly occur either for shown or for intermediate (mentally supplemented) curves of the stable manifold families.

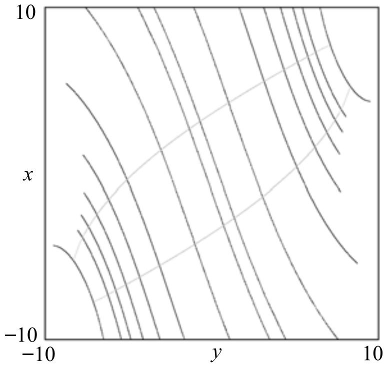


**Fig. 7.3** Lorenz attractor of Eqs. (2.1) at $r$=28, $b$=8/3, $\sigma$=10 (gray) and the family of stable manifolds (black) in the Poincaré section by the plane $z = r - 1$ (only crossings in direction of decrease of $z$ are accounted to be plotted).

values of parameters $r$=28, $b$=8/3, $\sigma$=10. The Poincaré section is used with the plane $z = r - 1$. In this case, no visible tangencies occur, but there is a special situation of mutual location of the attractor and the stable manifolds near the sharp ends of the curved segments representing two branches of the attractor in the Poincaré section. These are just the features, which do not allow relating the Lorenz attractor to the uniformly hyperbolic class.

### *7.1.2 Distributions of angles of the manifold intersections*

To my knowledge, the idea of verification of hyperbolicity by analysis of statistical distribution of angles between local stable and unstable manifolds for dynamical systems having one stable direction and one unstable direction at each point of the invariant set was advanced in (Lai et al., 1993). Such approach was applied to some saddle hyperbolic sets (Hirata et al., 1999) and to attractors not relating to the uniformly hyperbolic class (Anishchenko et al., 2000; Ginelli et al., 2007). Later, it was developed in application to the case of attractor of Smale-Williams type for stroboscopic maps of coupled non-autonomous oscillators to embrace the case of higher-dimensional stable manifold (Kuznetsov, 2005; Kuznetsov and Seleznev, 2006). [1]

In this procedure, the angles between the directions of small perturbations are evaluated at points of one and the same trajectory calculated forward and backward in time. If the set of the angles does not contain values close to zero, it indicates that the invariant set is hyperbolic. If the distribution demonstrates nonzero probability of zero angles, then the tangencies between stable and unstable manifolds occur that implies non-hyperbolicity. These tangencies may be interpreted as indicator of presence of a quasi-attractor in a dissipative system under consideration that is a complex invariant set containing beside chaotic orbits longperiod stable periodic trajectories with extremely narrow domains of attraction (Shilnikov, 1997).

For the case of a two-dimensional map $\mathbf{x}_{n+1} = \mathbf{f}(\mathbf{x}_n)$ the procedure is very simple. First, by iteration we generate a long orbit $\mathbf{x}_n$ belonging to the attractor we analyze. Then, with random initial conditions from the variation equations we produce two sequences of perturbation vectors, one by iteration forward in time, $\tilde{\mathbf{u}}_{n+1} = \mathbf{f}'(\mathbf{x}_n)\tilde{\mathbf{u}}_n$, and the other by backward iteration, $\tilde{\mathbf{v}}_n = (\mathbf{f}'(\mathbf{x}_n))^{-1}\tilde{\mathbf{v}}_{n+1}$, where $\mathbf{f}'(\mathbf{x}_n)$ designates the matrix derivative of the map, and $(\mathbf{f}'(\mathbf{x}_n))^{-1}$ is the inverse matrix. To avoid divergences, the vectors at each step are normalized: $\tilde{\mathbf{u}}'_{n+1} = \tilde{\mathbf{u}}_{n+1}/\|\tilde{\mathbf{u}}_{n+1}\|$ and $\tilde{\mathbf{v}}'_n = \tilde{\mathbf{v}}_n/\|\tilde{\mathbf{v}}_n\|$. The angle between each pair of the vectors $\tilde{\mathbf{u}}_n$ and $\tilde{\mathbf{v}}_n$ is determined from their inner product (dot product): $\theta_n = \arccos(\tilde{\mathbf{u}}_n \cdot \tilde{\mathbf{v}}_n)$. For the collection of the angles $\{\theta_n\}$ we can plot a histogram and judge whether there is or not statistically significant occurrences of angles close to zero.

In Fig. 7.4 the histograms are shown obtained in computations for uniformly hyperbolic attractors, one for the Plykin type attractor in the map (3.34) and the other for the DA-attractor of the map on torus (2.6). Observe clearly visible gap separating the distribution from zero angle on both plots.

It is illuminating to compare these diagrams with those relating to attractors, which are not uniformly hyperbolic (Fig. 7.5). One is plotted for the Hénon attractor in the map (F.4) and the other for the attractor of the Ikeda map (F.35) at their parameters corresponding to chaotic dynamics (with one positive and one negative Lyapunov exponents).

One more object for comparison is the Lorenz attractor classified as the quasi-hyperbolic, or singular hyperbolic one. The computations were performed for the Poincaré map obtained by means of numerical solution of the Lorenz equations (2.1) at classic parameter set $r$=28, $\sigma$=10, $b$=8/3 supplemented with the Hénon interpolation procedure at the intersections (Hénon, 1982). First, a sufficiently long reference orbit belonging to the Lorenz attractor was generated, and then respec-

[1] An advanced version of the approach is based on computation of covariant Lyapunov vectors and evaluation of principal angles between the stable and unstable manifolds (Kuptsov and Kuznetsov, 2009).

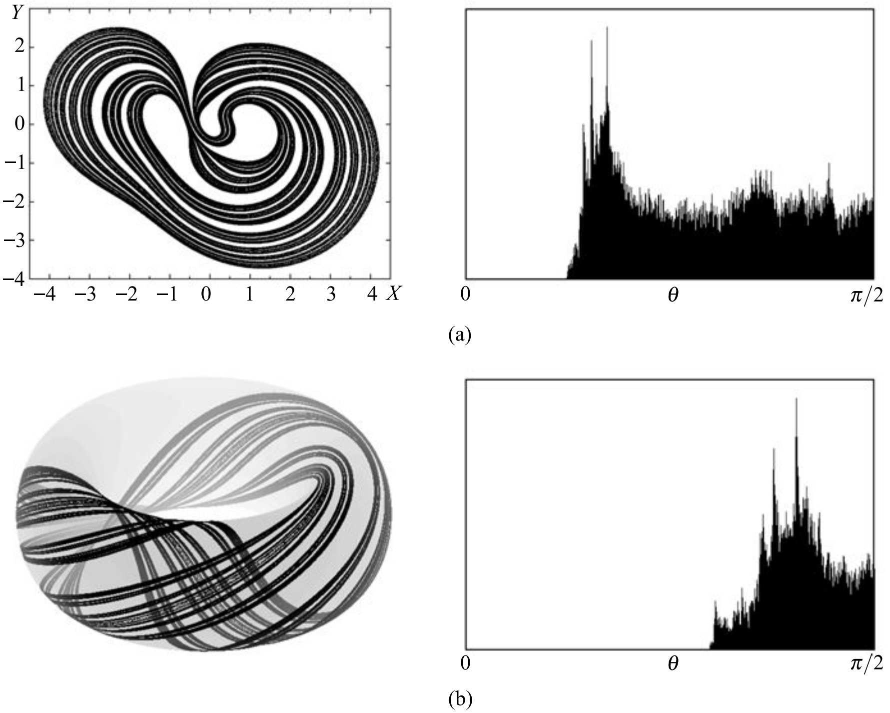


**Fig. 7.4** Chaotic uniformly hyperbolic attractors and histograms for distributions of angles for intersections of local stable and unstable manifolds: **(a)** Plykin type attractor of the map (3.34) at $\varepsilon = 0.77$ and **(b)** DA-attractor on the torus for the map (2.6) at $\varepsilon = 0.7$.

tive linearized equations were solved along this orbit in forward and inverse time to obtain normalized perturbation vectors at crossings with the Poincaré section (the plane $z = r - 1$ in the phase space; crossings by the orbits are accounted only in the direction of decrease of $z$). The histogram for the distribution of the angles of the respective vectors is shown in Fig. 7.6. In this case the distribution looks distant from zero, like in the above-discussed cases of uniform hyperbolicity, in contrast to the non-hyperbolic situations of Fig. 7.5. So, this method fails to distinguish the Lorenz attractor from uniformly hyperbolic ones.

Now, let us turn to generalization of the method, which would be appropriate for the case of larger dimensions of the stable manifolds. Then, the technique of computations for the local stable manifolds and determination of angles with the unstable manifolds has to be reconsidered. Examples are systems with attractors of Smale-Williams type described in the previous chapters. For instance, in the Poincaré map of the models (4.9) and (5.5) the stable manifolds are three-dimensional, i.e. $N_s = 3$; for the models (3.18) and (4.17) they are two-dimensional, $N_s = 2$.

Again, we start with computation of a representative orbit $\mathbf{x}(t)$ on the attractor for sufficiently long time interval. Then, we consider linearized equations for per-

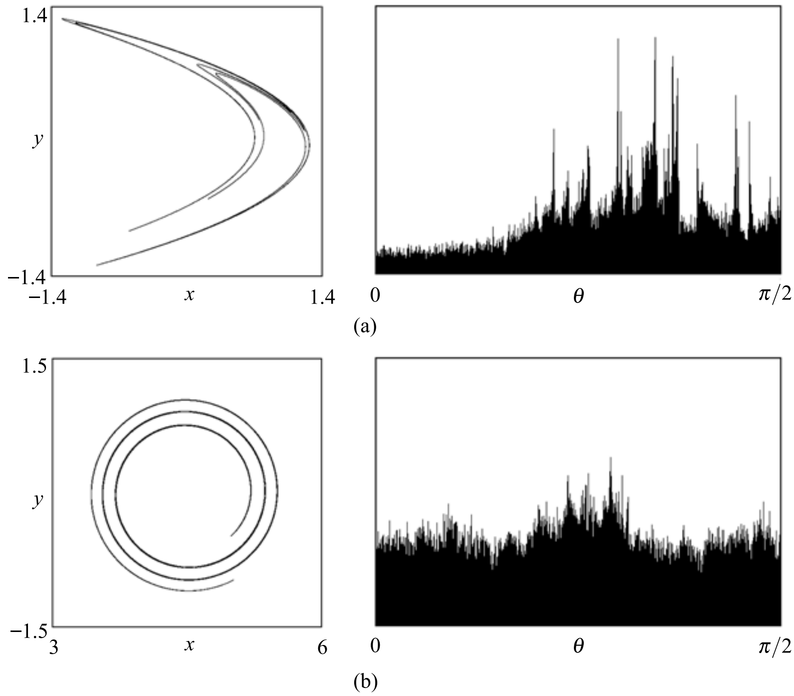


**Fig. 7.5** Chaotic non-hyperbolic attractors and histograms for distributions of angles for intersections of local stable and unstable manifolds for: **(a)** Hénon map (F.4) at $a$=1.4, $b$=0.3, and **(b)** Ikeda map (F.35) at $A$=4.5, $B$=0.2, $\varphi$=0. Observe non-vanishing probability of occurrence of angles close to zero.

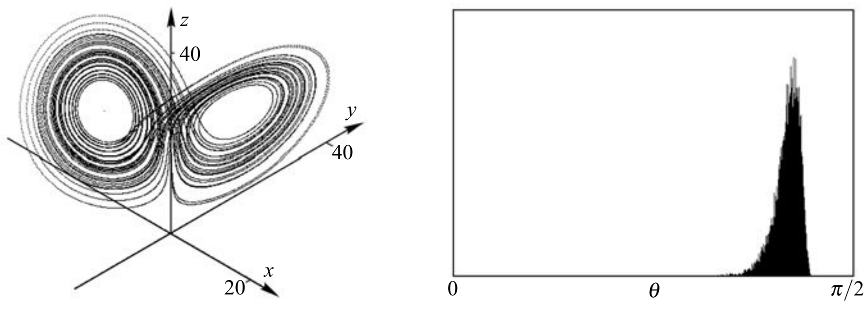


**Fig. 7.6** A histograms for distributions of angles for intersections of local stable and unstable manifolds for the singular hyperbolic attractor in the Poincaré map of the Lorenz model governed by Eqs. (2.1) at $r$=28, $b$=8/3, $\sigma$=10. The Poincaré section is defined with the plane $z = r - 1$ accounting crossings by the orbits in the direction of decrease of the variable $z$.

turbations and integrate them in computations along the reference orbit, initially in forward time, with renormalization of the vector at each next step of the Poincaré map to have a fixed norm to preclude divergence. The result is a set of vectors $\{\mathbf{u}_n\}$.

Next, we perform solution of the linearized equations backward in time, along the same reference orbit, for a collection of $N_s$ perturbation vectors. For them, at each step of iteration for the Poincaré map we perform the Gram-Schmidt orthogonalization and normalization procedure (like that used in the computations of the Lyapunov exponents) to avoid divergence and predominance of one of these vectors. The result is a set of vectors $\{\mathbf{v}_n^{(1)}, \mathbf{v}_n^{(2)}, \ldots, \mathbf{v}_n^{(N_s)}\}$. Now, at each $n$ the vector $\mathbf{u}_n$ defines the local unstable direction, and the span of the vectors $\{\mathbf{v}_n^{(1)}, \mathbf{v}_n^{(2)}, \ldots, \mathbf{v}_n^{(N_s)}\}$ defines the local $N_s$-dimensional stable manifold. To evaluate the angle $\theta_n$ between the manifolds, we, first, determine a vector $\mathbf{z}_n$ orthogonal to the stable manifold by solving the linear system of $N_s$ equations

$$\begin{aligned}
&\mathbf{z}_n \cdot \mathbf{v}_n^{(1)} = 0, \\
&\mathbf{z}_n \cdot \mathbf{v}_n^{(2)} = 0, \\
&\ldots\ldots\ldots\ldots \\
&\mathbf{z}_n \cdot \mathbf{v}_n^{(N_s)} = 0.
\end{aligned}$$

Then, we calculate the angle $\beta_n \in [0, \pi/2]$ between $\mathbf{u}_n$ and $\mathbf{z}_n$ from $\cos\beta_n = |\mathbf{u}_n \cdot \mathbf{z}_n| / |\mathbf{u}_n||\mathbf{z}_n|$ and, finally, set $\theta_n = \pi/2 - \beta_n$. Plotting the histograms for the computed angles $\theta_n$ one can judge whether the distribution is distant from zero that testifies in favor of hyperbolicity, or there is non-vanishing probability of occurrence of near-zero angles that means non-hyperbolicity.

Examples are presented in Fig. 7.7, where the panels (a) and (b) correspond to models with three-dimensional Poincaré maps, and the panels (c), (d) to the models with four-dimensional Poincaré maps.

Panel (a) relates to the model with attractor of Smale-Williams type constructed in Sect. 3.2 as a flow system governed by a set of switched differential equations of the third order. The stroboscopic Poincaré map is expressed explicitly by (3.18). Parameter values are $d_1 = d_2 = 2$, $\mu = 2$.

Panel (b) presents data for attractor of Smale-Williams type in the three-dimensional Poincaré map of the autonomous model developed in (Kuznetsov and Pikovsky,

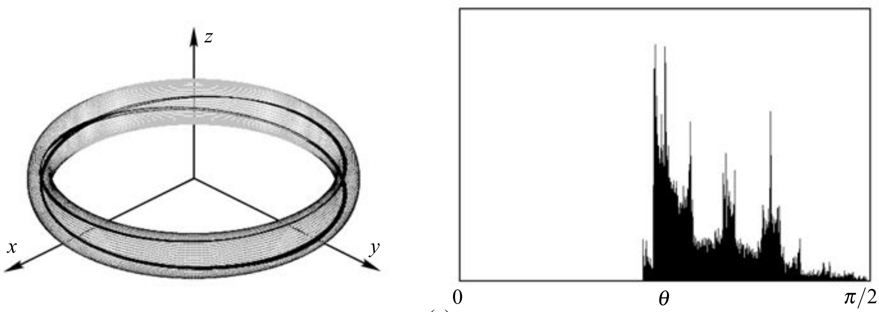


(a)

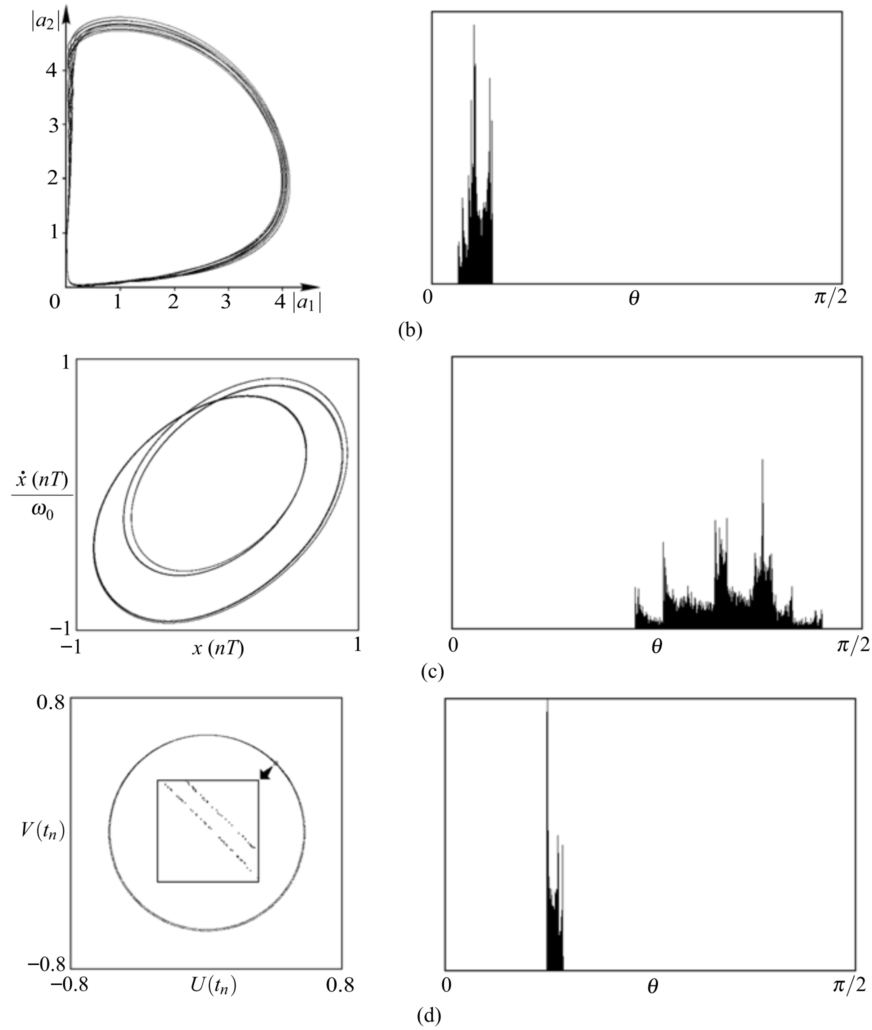


**Fig. 7.7** Attractors of Smale-Williams type and histograms for distributions of angles between local stable and unstable manifolds: **(a)** model map (3.16) at $d_1 = d_2 = 2$, $\mu = 2$; **(b)** three-dimensional Poincaré map of the autonomous model (5.13); **(c)** the stroboscopic map of alternately excited non-autonomous oscillators (4.9) at $\omega_0 = 2\pi$, $T = 6$, $A = 5$, $\varepsilon = 0.5$; **(d)** Poincaré map of the model (5.5) at $\varepsilon = 0.1$, $a = 0.6$; developed on the base of predator-prey system, $\omega_0 = 2\pi$, $\varepsilon = 0.3$.

2007) on the base of predator-prey system and discussed in Sect. 5.3 (see Eqs. (5.13)). Parameter values are $\omega_0$=$2\pi$, $\varepsilon$=0.3.

Panel (c) corresponds to the basic model governed by Eqs. (4.9) of two non-autonomous alternately excited van der Pol oscillators transferring the excitation each other with transformation of the phase approximating by the expanding circle map. The stroboscopic Poincaré map is four-dimensional. Parameter values are $\omega_0=2\pi$, $T=6$, $A=5$, $\varepsilon=0.5$.

Panel (d) relates to the autonomous model with attractor of Smale-Williams type introduced in Sect. 5.1 (see Eqs. (5.3)). The Poincaré map is four-dimensional. Parameter values are $\omega_0=2\pi$, $\varepsilon=0.3$.

Observe that all histograms of Fig. 7.7 manifest a well expressed gap separating the distributions from the domain of angles close to zero. It indicates absence of touches of the stable manifolds with unstable ones associated with hyperbolic nature of the attractors in agreement with other methods of their analysis.

## 7.2 Visualization of invariant measures

If we consider dynamics in terms of evolution of a cloud of representative points in phase space of a dissipative dynamical system, there is some stationary distribution arising in a limit of large observation time; according to the accepted terminology, this is the invariant measure associated with the attractor. In accordance with theorem of Krylov and Bogolyubov (Anosov, 1994), natural invariant measure, as relative probability of residence of a representative orbit on the measured set in phase space, may be introduced under very general circumstances; but for non-hyperbolic attractors it is characterized by presence of local singularities. Hyperbolic chaos takes place in a situation of evolution of the clouds including stretching, folding, and compression in a perfect way, without breaks and without appearance of local seals. In these cases we deal with the invariant measure of Sinai-Ruelle-Bowen (Sinai, 1972; Bowen, 1975; Ruelle, 1976). It is absolutely continuous that means the smooth distribution along the filaments of the attractor occurs. Hence, visualization of the distributions of the invariant measures is a useful and illuminating tool to distinguish hyperbolic and non-hyperbolic attractors.

In computations the simplest way to visualize the invariant measure is to define a grid of cells in the phase space domain containing the attractor, and in the course of the simulation to accumulate array of the quantities indicating relative time of residence in all the cells. Afterwards, probabilities of the residence are estimated and plotted in appropriate coordinates (Tél and Gruiz, 2006). A disadvantage of this method is presence of relatively large statistical fluctuations of the probability estimates, that makes the distinction between smooth and singular distributions visually not so impressive. For this reason, it is worth turning to modification of the method, which we consider here in application to attractors with one-dimensional unstable manifolds.

The modified approach consists in plotting just the one-dimensional probability distribution along the one-dimensional unstable manifold, that is the same, along a filament of the attractor. In application to some map $\mathbf{g}(\mathbf{x})$ corresponding to a discrete-time system, or to a Poincaré map of a continuous-time system, the algorithm operates as follows (Kuznetsov and Sataev, 2011).

1. Select a point on the attractor $\mathbf{x}_0^{(0)}$, and another one $\mathbf{x}_0^{(1)}$ at a small distance $\|\Delta\mathbf{x}\| = \varepsilon_0$ (practically, it may be $\varepsilon_0 \sim 0.001$).

2. Consider iterates of the map $\mathbf{g}(\mathbf{x})$ starting from both initial points, while the distance between them becomes greater than $10\varepsilon_0$; the resulting points will be $\mathbf{x}_n^{(0)}$ and $\mathbf{x}_n^{(1)}$.

3. Then, update the initial pair of points and set $\mathbf{x}_0^{(0)} = \mathbf{x}_n^{(0)}$ and $\mathbf{x}_0^{(1)} = \mathbf{x}_n^{(0)} + \varepsilon(\mathbf{x}_n^{(1)} - \mathbf{x}_n^{(0)})/\|\mathbf{x}_n^{(1)} - \mathbf{x}_n^{(0)}\|$.

4. Repeat the steps 2 and 3 quite a lot of times (practically, about $10^3$); then both initial points will sit on the unstable manifold.

5. The segment between the initial points obtained is divided onto a large number of equal small segments by inserting intermediate points (the number of them may be about $10^5$)

6. Starting from all these points iterate the map, while the maximum distance for points of some adjacent pair remains less than a prescribed constant, say, $50\varepsilon$.

7. Each of the resulting segments is attributed to the value of the inverse of its length, which is proportional to the density measure in this interval.

8. For visualization, the resulting values are normalized to the maximal one to get the numbers in the unit interval from 0 to 1, and plotted in appropriate coordinates in proportional, or logarithmic scale.

The pictures obtained are representative, if the finally obtained segment of the unstable manifold covered by the examined points is long enough to cover the attractor for many times, revealing its thin fractal transverse structure up to a sufficiently deep level.

Diagrams obtained by means of the above computational scheme in application to model systems with uniformly hyperbolic attractors discussed in the previous chapters are shown in Figs. 7.8—7.10.

Figure 7.8 shows the distribution of the invariant measure for DA-attractor in the map (2.6) at $\varepsilon$=0.7. The unit square in the horizontal plane corresponds to unfolding of the torus surface, on which the map is defined. Figure 7.9 relates to the Plykin type attractor on the plane for the model governed by the map (3.34) at $\varepsilon$=0.77. Figure 7.10 corresponds to the attractor of Smale-Williams type in the stroboscopic Poincaré map of the system of two alternately excited non-autonomous van der Pol equations (4.9) at $\omega_0 = 2\pi$, $T$=6, $A$=5, $\varepsilon$=0.5. In this case the Poincaré map is four-dimensional; so, the distribution of the invariant measure is shown over a projection of the attractor onto the plane of two dynamical variables $(x, \dot{x}/\omega_0)$. Observe that in all these cases, which relate to the uniformly hyperbolic attractors, smooth dependence of the probability distribution takes place along the filaments of the attractors. In the used technique of visualization it is seen very clear.

For comparison, let us discuss examples of non-hyperbolic attractors, e.g. those relating to the Hénon and Ikeda maps. The diagrams obtained for them by means of the above computational scheme are shown in Figs.7.11 and 7.12. The distributions of probability along the filaments of these attractors look essentially non-uniform, and contain singularities represented by narrow and high peaks. To show them in comparable scale with the rest part of the distribution functions we use the logarith-

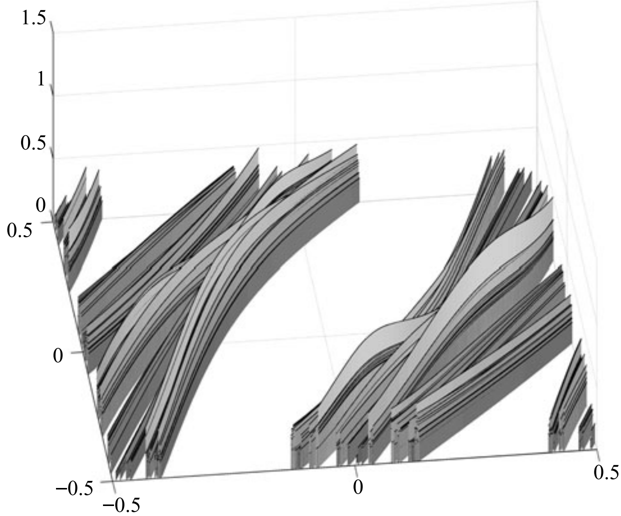


**Fig. 7.8** Diagram illustrating the distribution of the invariant measure of Sinai-Ruelle-Bowen along unstable manifolds of a uniformly hyperbolic attractor of DA type for the map (2.6) at $\varepsilon$=0.7.

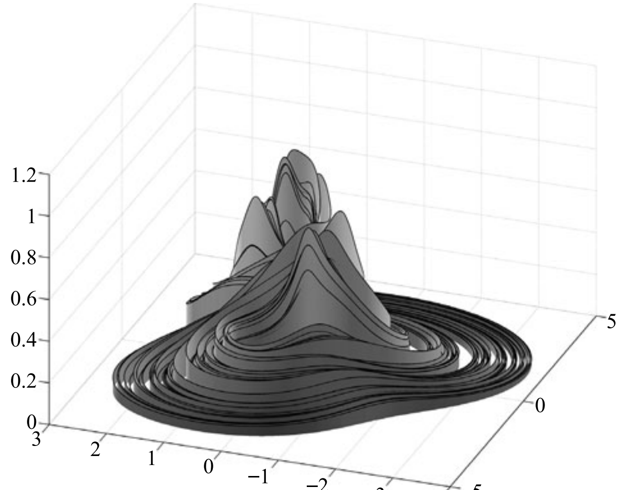


**Fig. 7.9** Diagram illustrating the distribution of the invariant measure of Sinai-Ruelle-Bowen along unstable manifolds of Plykin type attractor on the plane obtained for the map (3.34) at $\varepsilon$=0.77.

mic scale along the vertical axis. The plots are in impressive contrast with the case of the uniformly hyperbolic attractors.

Finally, it is interesting to consider a special case of quasi-hyperbolic (or singular-hyperbolic) Lorenz attractor. The respective diagram is shown in Fig. 7.13 obtained for the two-dimensional Poincaré map of the Lorenz model (2.3) at parameter values

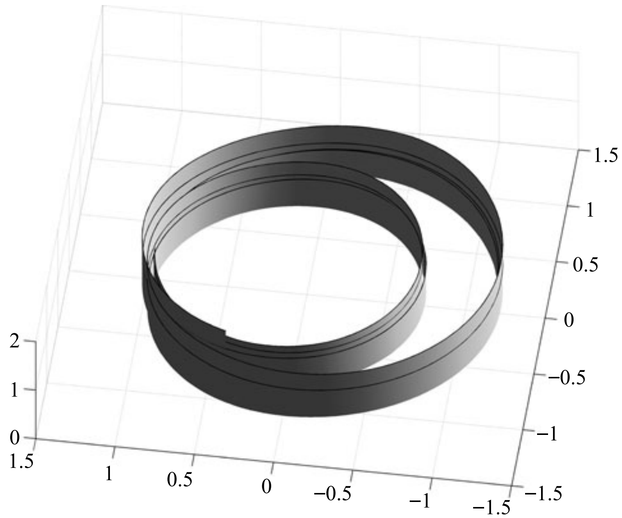


**Fig. 7.10** Diagram illustrating the distribution of the invariant measure of Sinai-Ruelle-Bowen along unstable manifolds of attractor of Smale-Williams type in the stroboscopic Poincaré map of the system of two alternately excited non-autonomous van der Pol equations (4.9) at $\omega_0 = 2\pi$, $T$=6, $A$=5, $\varepsilon$=0.5.

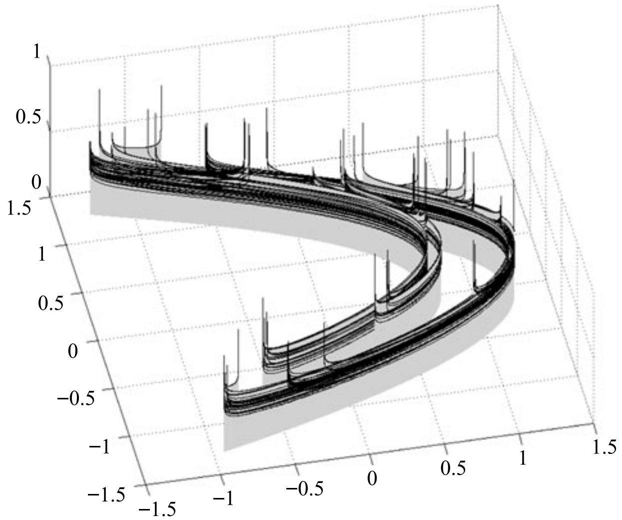


**Fig. 7.11** Diagram illustrating the distribution of the invariant measure for the attractor of the Hénon map (F.4) at $a$=1.4, $b$=0.3. Logarithmic scale is used along the vertical axis to visualize both singular and non-singular components of the distribution.

$r$=28, $b$=8/3, $\sigma$=6. The Poincaré section is defined with the plane $z = r - 1$ accounting orbits crossings this surface in the direction of decrease of the variable $z$. In

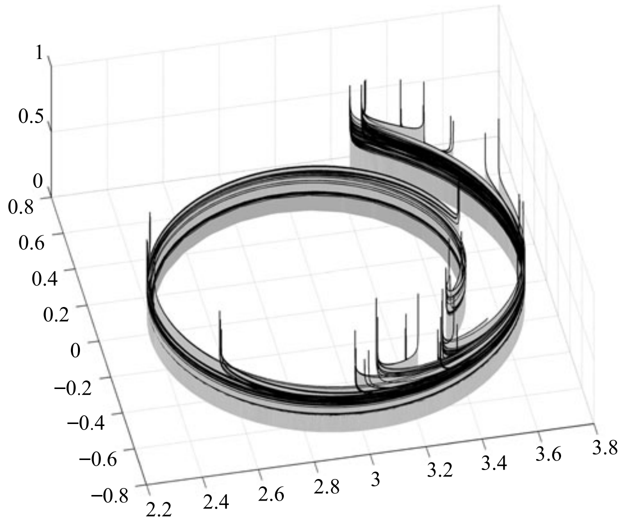


**Fig. 7.12** Diagram illustrating the distribution of the invariant measure for the attractor of the Ikeda map (F.35) at $A$=3, $B$=0.2, $\varphi$=0. Logarithmic scale is used along the vertical axis to visualize both singular and non-singular components of the distribution.

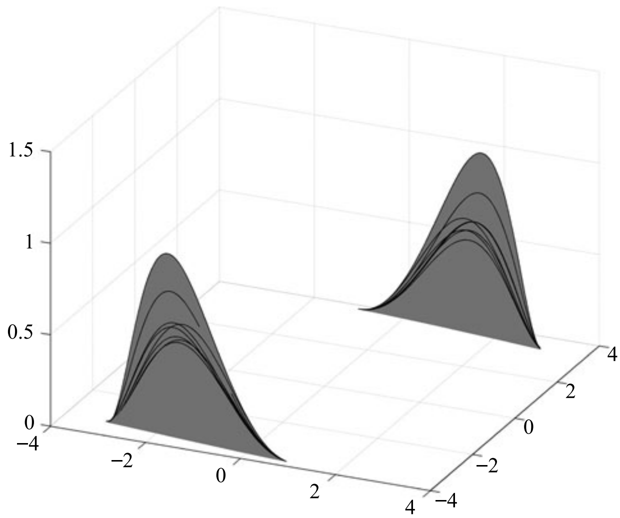


**Fig. 7.13** Diagram illustrating the distribution of the invariant measure for the Lorenz attractor of the model (2.3) at $r$=28, $b$=8/3, $\sigma$=6 in the Poincaré section by the plane $z = r - 1$.

this case the picture does not show singularities of the distribution of the invariant measure, like in two previous examples. However, there is a visible difference in comparison with the case of uniformly hyperbolic attractors. It is vanishing of the distribution function at some end points of the fragments representing the unstable manifolds in the Poincaré section; for uniformly hyperbolic attractors the distributions are locally smooth and not vanishing along the entire unstable manifolds.

To conclude, the developed technique provides an effective tool for detection of hyperbolic or non-hyperbolic nature of attractors in numerical calculations, at least on a qualitative level.

## 7.3 Cone criterion and examples of its application

In Chap. 1, reviewing content and conclusions of the hyperbolic theory, we told about the cone criterion (Sinai, 1979; Hasselblatt and Pesin, 2008), which provides a necessary and sufficient condition for hyperbolicity of an invariant set, appropriate for computer verification. The first known attempt of application of this criterion to verification of chaotic nature of attractor in computations was presented in (Sinai and Vul, 1981). Recently, this criterion was applied to computer validation of hyperbolicity of attractors in models suggested in Chap. 3—6 (e.g. (Kuznetsov and Sataev, 2007; Kuznetsov et al., 2007; Kuznetsov, 2009; Kuznetsov et al., 2010)). Let us return to this issue and consider it in more constructive manner to explain concretely the content of the computations.

### *7.3.1 Procedure of verification of the cone criterion*

We will discuss here the cone criterion only for attractors with one positive Lyapunov exponent in application to maps represented by diffeomorphisms. They may be thought of as relating either to discrete-time dynamics, or to description of continues-time systems in terms of Poincaré sections.

Let us have a dissipative map $\mathbf{x}_{n+1} = \mathbf{g}(\mathbf{x}_n)$, where $\mathbf{x}$ is an $N$-dimensional vector, and this map possesses attractor $A$, which has to be analyzed. Additionally, we define the linear map $\mathbf{u}_{n+1} = \mathbf{g}'(\mathbf{x}_n)\mathbf{u}_n$ governing infinitesimal perturbations. Here $\mathbf{g}'(\mathbf{x})$ is the matrix derivative of the map $\mathbf{g}$ at the point $\mathbf{x}$; it is a square matrix of size $N \times N$ called the Jacobian matrix. In our considerations it is assumed that the map $\mathbf{g}$ and the matrices $\mathbf{g}'(\mathbf{x})$ are available for evaluation for the dynamical system under study by means of a computer program.

Let us consider details of the procedure of verification for the cone criterion at some reference point in the phase space $\mathbf{x}$. To proceed, we need to specify the image point $\overline{\mathbf{x}} = \mathbf{g}(\mathbf{x})$, and the pre-image point $\tilde{\mathbf{x}}$, so that $\mathbf{x} = \mathbf{g}(\tilde{\mathbf{x}})$. Let $\gamma$ be some fixed constant larger than 1.

The matrix derivative of the map $\mathbf{g}$ at the reference point $\mathbf{v} = \mathbf{g}'(\mathbf{x})$ acts in the linear space of vectors $\mathbf{u} = \{u_0, u_2, \ldots, u_{N-1}\}$ called the tangent space at $\mathbf{x}$. Via the auxiliary symmetric matrix $\hat{\mathbf{b}} = \mathbf{v}^{\mathrm{T}}\mathbf{v}$ (the superscript T means the transpose), the Euclidean norm of the vector $\overline{\mathbf{u}} = \mathbf{v}\mathbf{u}$ may be expressed as

$$||\bar{\mathbf{u}}||^2 = \mathbf{u}^{\mathrm{T}}\hat{\mathbf{b}}\mathbf{u}. \tag{7.1}$$

A set of vectors

$$S_{\mathbf{x}} = \{\mathbf{u}|\mathbf{u}^{\mathrm{T}}\hat{\mathbf{b}}\mathbf{u} \geqslant \gamma^2\mathbf{u}^{\mathrm{T}}\mathbf{u}\} \tag{7.2}$$

represents the expanding cone at the point $\mathbf{x}$. With the same matrix $\hat{\mathbf{b}}$ one can define a set

$$C'_{\bar{\mathbf{x}}} = \{\mathbf{u}|\gamma^2\mathbf{u}^{\mathrm{T}}\hat{\mathbf{b}}\mathbf{u} \leqslant \mathbf{u}^{\mathrm{T}}\mathbf{u}\}. \tag{7.3}$$

This set corresponds to the pre-image for the contracting cone defined at the point $\bar{\mathbf{x}} = \mathbf{g}(\mathbf{x})$.

Now, consider the matrix derivative for the inverse map $\mathbf{w} = (\mathbf{g}^{-1}(\mathbf{x}))'$. Note that this matrix may be evaluated without handling the inverse map itself, via the inverse matrix of the derivative of the map $\mathbf{g}$ at the pre-image point $\tilde{\mathbf{x}}$: $\mathbf{w} = (\mathbf{g}'(\tilde{\mathbf{x}}))^{-1}$. Introducing symmetric matrix $\hat{\mathbf{a}} = \mathbf{w}^{\mathrm{T}}\mathbf{w}$ we represent the norm of the vector $\tilde{\mathbf{u}} = \mathbf{w}\mathbf{u}$ as

$$||\tilde{\mathbf{u}}||^2 = \mathbf{u}^{\mathrm{T}}\hat{\mathbf{a}}\mathbf{u}. \tag{7.4}$$

With the matrix $\hat{\mathbf{a}}$ one can define a set

$$C_{\mathbf{x}} = \{\mathbf{u}|\mathbf{u}^{\mathrm{T}}\hat{\mathbf{a}}\mathbf{u} \geqslant \gamma^2\mathbf{u}^{\mathrm{T}}\mathbf{u}\}, \tag{7.5}$$

which represents the contracting cone at $\mathbf{x}$, and a set

$$S'_{\tilde{\mathbf{x}}} = \{\mathbf{u}|\gamma^2\mathbf{u}^{\mathrm{T}}\hat{\mathbf{a}}\mathbf{u} \leqslant \mathbf{u}^{\mathrm{T}}\mathbf{u}\}, \tag{7.6}$$

which corresponds to an image for the expanding cone relating to the point $\tilde{\mathbf{x}} = \mathbf{g}^{-1}(\mathbf{x})$.

In computations it is necessary to check, first, existence of nonempty cones satisfying the definitions, and, second, invariance of the cones that means validity of the inclusions $S'_{\tilde{\mathbf{x}}} \subset S_{\mathbf{x}}$ and $C'_{\bar{x}} \subset C_{\mathbf{x}}$.

The required inclusions may be formulated in terms of quadratic forms associated with the matrices $\mathbf{b} = \hat{\mathbf{b}} - \Gamma^2\hat{\mathbf{e}}$ and $\mathbf{a} = \hat{\mathbf{a}} - \Gamma^{-2}\hat{\mathbf{e}}$, where $\hat{\mathbf{e}}$ is a unit matrix. A constant factor $\Gamma$ is assumed to be equal to either $\gamma$, or $1/\gamma$, considering the expanding, or contracting cones, respectively. Obviously, the equations

$$\sum_{m,n=0}^{N-1} b_{mn}u_m u_n = 0 \tag{7.7}$$

and

$$\sum_{m,n=0}^{N-1} a_{mn}u_m u_n = 0 \tag{7.8}$$

determine the borders of the cones.

The $N \times N$ matrix $\hat{\mathbf{b}}$ is symmetric and positively definite (as it is a product of two mutually transposed matrices). Eigenvalues of this matrix are all positive, and one can determine respective orthogonal basis, the set of unit vectors $\mathbf{d}_0, \mathbf{d}_1, \ldots, \mathbf{d}_{N-1}$. We suppose that the eigenvalues are enumerated in the decreasing order. Then, using the matrix $\mathbf{D} = (\mathbf{d}_0, \mathbf{d}_1, \ldots, \mathbf{d}_{N-1})$ we transform the matrix $\hat{\mathbf{b}}$ to the diagonal form

$$\mathbf{D}^{\mathrm{T}}\hat{\mathbf{b}}\mathbf{D} = \begin{pmatrix} \Lambda_0^2 & 0 & \cdots & 0 \\ 0 & \Lambda_1^2 & \cdots & 0 \\ \vdots & \vdots & & \vdots \\ 0 & 0 & \cdots & \Lambda_{N-1}^2 \end{pmatrix}. \tag{7.9}$$

For the case we deal with, there should be one expanding direction, and others contracting, so, we must check in computations that $\Lambda_0^2 > \Gamma^2, \Lambda_1^2, \ldots, \Lambda_{N-1}^2 < \Gamma^2$. If this is the case, the matrix

$$\mathbf{D}^{\mathrm{T}}(\hat{\mathbf{b}} - \Gamma^2\hat{\mathbf{e}})\mathbf{D} = \begin{pmatrix} \Lambda_0^2 - \Gamma^2 & 0 & \cdots & 0 \\ 0 & \Lambda_1^2 - \Gamma^2 & \cdots & 0 \\ \vdots & \vdots & & \vdots \\ 0 & 0 & \cdots & \Lambda_{N-1}^2 - \Gamma^2 \end{pmatrix} \tag{7.10}$$

has one positive and all other negative elements on the diagonal. By an additional scale change along the coordinate axes, the matrix is transformed to the canonical form:

$$\mathbf{S}^{\mathrm{T}}\mathbf{D}^{\mathrm{T}}(\hat{\mathbf{b}} - \Gamma^2\hat{\mathbf{e}})\mathbf{D}\mathbf{S} = \begin{pmatrix} 1 & 0 & \cdots & 0 \\ 0 & -1 & \cdots & 0 \\ \vdots & \vdots & & \vdots \\ 0 & 0 & \cdots & -1 \end{pmatrix}, \tag{7.11}$$

where

$$\mathbf{S} = \begin{pmatrix} 1/\sqrt{\Lambda_0^2 - \Gamma^2} & 0 & \cdots & 0 \\ 0 & 1/\sqrt{\Gamma^2 - \Lambda_1^2} & \cdots & 0 \\ \vdots & \vdots & & \vdots \\ 0 & 0 & \cdots & 1/\sqrt{\Gamma^2 - \Lambda_{N-1}^2} \end{pmatrix}. \tag{7.12}$$

In the new variables $\mathbf{u}' = \mathbf{S}^{\mathrm{T}}\mathbf{D}^{\mathrm{T}}\mathbf{u}$ the quadratic form (7.7) reduces to

$$u_0'^2 - u_1'^2 - \cdots - u_{N-1}'^2 = 0. \tag{7.13}$$

Under the same transformations, Equation (7.8) converts to

$$\sum_{m,n=0}^{N-1} a'_{mn} u'_m u'_n = 0, \tag{7.14}$$

where $a'_{mn}$ are elements of the matrix $\mathbf{a}' = \mathbf{S}\mathbf{D}^{\mathrm{T}}(\hat{\mathbf{a}} - \Gamma^{-2}\hat{\mathbf{e}})\mathbf{D}\mathbf{S}$.

Let us examine vectors $\mathbf{u}' = \{1, c_1, c_2, \ldots, c_{N-1}\}$. The relation (7.13) corresponds to a unit sphere in the space of $N-1$ coefficients: $c_1^2 + c_2^2 + \cdots + c_{N-1}^2 = 1$. On the other hand, the expression (7.14) for such vectors can be rewritten as

$$a'_{00} + \sum_{m=1}^{N-1} (a'_{0m} c_m + a'_{m0} c_m) + \sum_{m,n=1}^{N-1} a'_{mn} c_m c_n = 0. \tag{7.15}$$

The required inclusion of the cones means that the last equation has to determine a surface in a form of ellipsoid placed inside the unit sphere. We prefer to use a sufficient condition for such situation, which is easy for derivation and application.

First, we determine a center point $\bar{\mathbf{c}}$ for the second-order hyper-surface from the set of equations

$$\begin{aligned} a'_{11}\bar{c}_1 + a'_{12}\bar{c}_2 + \cdots + a'_{1,N-1}\bar{c}_{N-1} &= -a'_{10}, \\ a'_{21}\bar{c}_1 + a'_{22}\bar{c}_2 + \cdots + a'_{2,N-1}\bar{c}_{N-1} &= -a'_{20}, \\ \cdots\cdots\cdots\cdots \\ a'_{N-1,1}\bar{c}_1 + a'_{N-1,2}\bar{c}_2 + \cdots + a'_{N-1,N-1,}\bar{c}_{N-1} &= -a'_{N-1,0}. \end{aligned} \tag{7.16}$$

and evaluate its distance from the center of the unit sphere:

$$\rho = \sqrt{\bar{c}_1^2 + \bar{c}_2^2 + \cdots + \bar{c}_{N-1}^2}. \tag{7.17}$$

By transfer of the origin to the point $\bar{\mathbf{c}}$ we rewrite Eq. (7.15) in variables $\tilde{c}_m = c_m - \bar{c}_m$ as

$$\sum_{m,n=1}^{N-1} a'_{mn} \tilde{c}_m \tilde{c}_n = R^2. \tag{7.18}$$

For the symmetric matrix

$$\mathbf{h} = \begin{pmatrix} a'_{11} & a'_{12} & \cdots & a'_{1,N-1} \\ a'_{21} & a'_{21} & \cdots & a'_{2,N-1} \\ \vdots & \vdots & & \vdots \\ a'_{N-1,1} & a'_{N-1,1} & \cdots & a'_{N-1,N-1} \end{pmatrix} \tag{7.19}$$

of size $(N-1)\times(N-1)$, all eigenvalues $l_1, l_2, \ldots, l_{N-1}$ are real. Let $\mathbf{q}_1, \ldots, \mathbf{q}_{N-1}$ be respective eigenvectors. Diagonal representation of this matrix is obtained by orthogonal coordinate transformation. To do this, we set $\mathbf{h}' = \mathbf{Q}^{\mathrm{T}}\mathbf{h}\mathbf{Q}$ and $\mathbf{c}' = \mathbf{Q}^{\mathrm{T}}\mathbf{c}$, where $\mathbf{Q} = (\mathbf{q}_1, \ldots, \mathbf{q}_{N-1})$. Then, Equation (7.15) reduces to

$$\sum_{m=1}^{N-1} l_m c_m'^2 = H, \tag{7.20}$$

where

$$H = -a'_{00} - \sum_{m=1}^{N-1} (a'_{0m}\bar{c}_m + a_{m0}\bar{c}_m) - \sum_{m,n=1}^{N-1} a'_{mn}\bar{c}_m\bar{c}_n. \tag{7.21}$$

If all the eigenvalues $l_m$ are of the same sign as the sign of the quantity $H$, Equation (7.20) determines an ellipsoid with the largest semi-axis expressed via the eigenvalue of minimal magnitude $l_{\min}$; the length equals $\sqrt{H/l_{\min}}$. A sufficient condition for the ellipsoid to belong to the interior of the unit sphere is the inequality

$$\rho + \sqrt{H/l_{\min}} < 1. \tag{7.22}$$

If all the above conditions are true simultaneously both for $\Gamma = \gamma$ and $\Gamma = 1/\gamma$ with some $\gamma > 1$, one can conclude about correct inclusions for the expanding and contracting cones at the reference point $\mathbf{x}$.

Indeed, in the variables $\mathbf{c}'$ the cross-section of the expanding cone $S_\mathbf{x}$ is the closed unit ball in the space of dimension $N-1$, and cross-section of the cone $S'_{\tilde{\mathbf{x}}}$ is represented by closure of the interior of the small ellipsoid obtained at $\Gamma = \gamma$. So, the required inclusion $S'_{\tilde{\mathbf{x}}} \subset S_\mathbf{x}$ is valid, as shown schematically in Fig. 7.14(a). On the other hand, cross-section of the contracting cone $C_\mathbf{x}$ is a closure of exterior of the small ellipsoid obtained at $\Gamma = 1/\gamma$. Cross-section of the cone $C'_{\tilde{\mathbf{x}}}$ corresponds to a closure of exterior of the unit sphere. Hence, the inclusion $C'_{\tilde{\mathbf{x}}} \subset C_\mathbf{x}$ is valid as illustrated in Fig. 7.14(b).

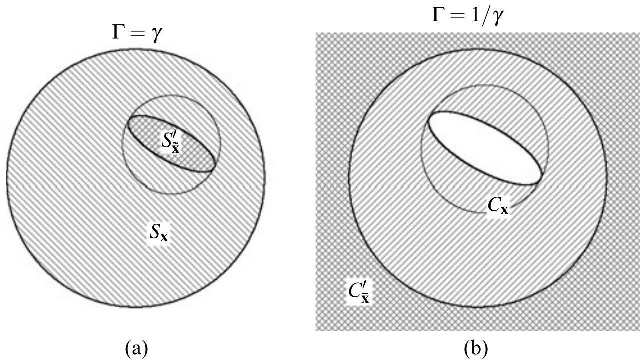


**Fig. 7.14** Schematic illustration of disposition of cross-sections of the expanding cones $S'_{\tilde{\mathbf{x}}} \subset S_\mathbf{x}$ **(a)** and contracting cones $C'_{\tilde{\mathbf{x}}} \subset C_\mathbf{x}$ **(b)**. A circle circumscribed around the ellipse corresponds to circumscribed ball around ellipsoid that should be located inside the unit ball if the condition (7.22) is valid.

For the particular case of two-dimensional maps ($N$=2), the last part of the procedure is simplified essentially. In this case the cross-sections of the cones correspond to one-dimensional intervals, for which the appropriate inclusions have to be checked. The matrix $\mathbf{h}$ degenerates to a single real number $a'_{11}$, and $l_{\min} = l_1 = a'_{11}$. Then, the relation (7.22) represents correct necessary and sufficient condition for the required inclusions to hold.

The procedure we have described relates to a single reference point $\mathbf{x}$, but we need to be sure that all the required conditions are true on the whole attractor $A$.

One way to organize the calculations may be used if an absorbing domain $D$ is specified from some preliminary analysis, or in computations, namely, $\mathbf{g}(D) \subset \operatorname{Int} D$, and $A = \bigcap_{m=1}^{\infty} \mathbf{g}^m(D)$. We may arrange scanning of this domain $D$ on a grid in the $N$-dimensional phase space and perform the above computational procedure at each node of the grid, with one and the same constant $\gamma > 1$. What is essential is selection of sufficiently small size of the grid cells. All relevant involved characteristics (elements of the matrices, eigenvalues, and eigenvectors) have to be nearly constant at the scale of a single cell. If all the imposed conditions are valid at the nodes of the grid covering the domain $D$, we may be sure that they are true on the attractor $A$ as it belongs to this domain. One disadvantage of this method is a necessity of preliminary knowledge of the absorbing domain. Another is a rapid increase of the volume of computations with the growth of the phase space dimension $N$.

Alternative approach consists in verification of the conditions of the cone criterion for a representative set of points on the attractor itself. These points are obtained step by step from iteration of the map $\mathbf{g}$. In this case we do not need to determinate the absorbing domain, and the method can be easily applied to systems of high dimensions $N$.

At first glance, the second method might seem much less convincing than the first one. However, the practice of calculations shows that being essentially easier in use, it allows reliable recognizing of situations of hyperbolic chaos, not more worthful than the first approach. It may be explained as follows. For smooth systems, the objects involved in the procedure of verification of the cone criterion in the region of interest depend on the state variables in smooth manner as they are determined by the dynamics in finite time intervals. It means that validity of the conditions at some point $\mathbf{x}$ with constant $\gamma$ distant from 1 implies that the conditions of the cone criterion hold as well in a neighborhood of $\mathbf{x}$ (the wider, the larger the value $|\gamma - 1|$). Hence, a positive result of the test for a representative set of points implies validity of the criterion on the entire attractor, if it is covered completely by the union of the mentioned neighborhoods. Practically, such situation is achieved by increase of the number of representative points on the attractor subjected to the test, i.e. the number of iterations of the map under consideration.

It is worth noting that the computational procedure may be recommended in some cases for application to $k$-fold iteration of the map, where $k$ is some integer, as the hyperbolicity recognition often becomes better with increase of $k$. On the other hand, at large $k$ the involved operations of linear algebra become ill-conditioned, because of coexistence of divergence and convergence for nearby orbits at the hyperbolic trajectories. So, the most appropriate selection of $k$ may require some compromise.

### 7.3.2 Examples of application of the cone criterion

Let us turn to concrete examples of application of the computational verification of the cone criterion to model systems discussed in previous chapters. For all of them we present materials in a unified form, basing on the computations at representative sets of points on the attractors. For some of the models the computations were performed as well with the technique of scanning the absorbing domains over appropriate grids; for these results we refer the reader to publications (Kuznetsov and Sataev, 2007; Kuznetsov et al., 2007; Kuznetsov, 2009; Kuznetsov et al., 2010).

First, let us consider *the system governed by switched differential equations* introduced in Sect. 3.2. It is rather a simple example for application of the computational procedure because the stroboscopic Poincaré map may be written down explicitly so does the inverse map (see formulas (3.18) and (3.19)). The map is three-dimensional, and it corresponds to the minimal dimension, for which the Smale-Williams type attractor can occur. The matrix derivatives may be obtained analytically:

$$\mathbf{g}'(\mathbf{x}_n) = \begin{pmatrix} \dfrac{\partial x_{n+1}}{\partial x_n} & \dfrac{\partial x_{n+1}}{\partial y_n} & \dfrac{\partial x_{n+1}}{\partial z_n} \\ \dfrac{\partial y_{n+1}}{\partial x_n} & \dfrac{\partial y_{n+1}}{\partial y_n} & \dfrac{\partial y_{n+1}}{\partial z_n} \\ \dfrac{\partial z_{n+1}}{\partial x_n} & \dfrac{\partial z_{n+1}}{\partial y_n} & \dfrac{\partial z_{n+1}}{\partial z_n} \end{pmatrix} \text{ and } (\mathbf{g}^{-1}(\mathbf{x}))' = \begin{pmatrix} \dfrac{\partial x_{n-1}}{\partial x_n} & \dfrac{\partial x_{n-1}}{\partial y_n} & \dfrac{\partial x_{n-1}}{\partial z_n} \\ \dfrac{\partial y_{n-1}}{\partial x_n} & \dfrac{\partial y_{n-1}}{\partial y_n} & \dfrac{\partial y_{n-1}}{\partial z_n} \\ \dfrac{\partial z_{n-1}}{\partial x_n} & \dfrac{\partial z_{n-1}}{\partial y_n} & \dfrac{\partial z_{n-1}}{\partial z_n} \end{pmatrix}.$$

Explicit expressions are too cumbersome, and we omit them for brevity.

Figure 7.15 presents data illustrating all essential components of the procedure of verification of the cone criterion. The quantities are plotted obtained in the course of the computations at successively visited points on the attractor in the sustained chaotic regime. The horizontal axis corresponds to the angular coordinate counted around the toroid containing the attractor (Fig. 3.9). In panel (a) one can see a plot for three eigenvalues of the matrix $\hat{\mathbf{b}} = \mathbf{v}^{\mathrm{T}}\mathbf{v} = \mathbf{g}'^{\mathrm{T}}\mathbf{g}'$. Observe that the first eigenvalue is straightly larger than 1 on the entire attractor, while the others are straightly less than 1. It indicates presence of the one-dimensional expansion and the two-dimensional contraction in the phase space, and the families of expanding and contracting cones may be defined all over the attractor. Panel (b) presents the data for eigenvalues of the auxiliary matrix $\mathbf{h}$ (see (7.19)), which is of size $2\times 2$ in this case. Observe that the ratios of the eigenvalues to the quantity $H$ (see (7.20)) for both of them are positive all over the attractor, that means that in the cross-section the cones produce the ellipses. Although the diagram is drawn for $\Gamma$=1, all filaments observed on the plot are clearly separated from zero, so, the situation will be qualitatively the same for values of $\Gamma$ slightly larger or less than 1. Finally, panel (c) gives the evidence for the correct inclusions for the cones. The value $\rho + \sqrt{H/l_{\min}}$ is plotted (see (7.22)), which is the maximal distance between the centre of the unit circle and a point on the small ellipse that must be inside the unit circle for the criterion to hold. Observe that this positive quantity is straightly less than 1. This situation occurs

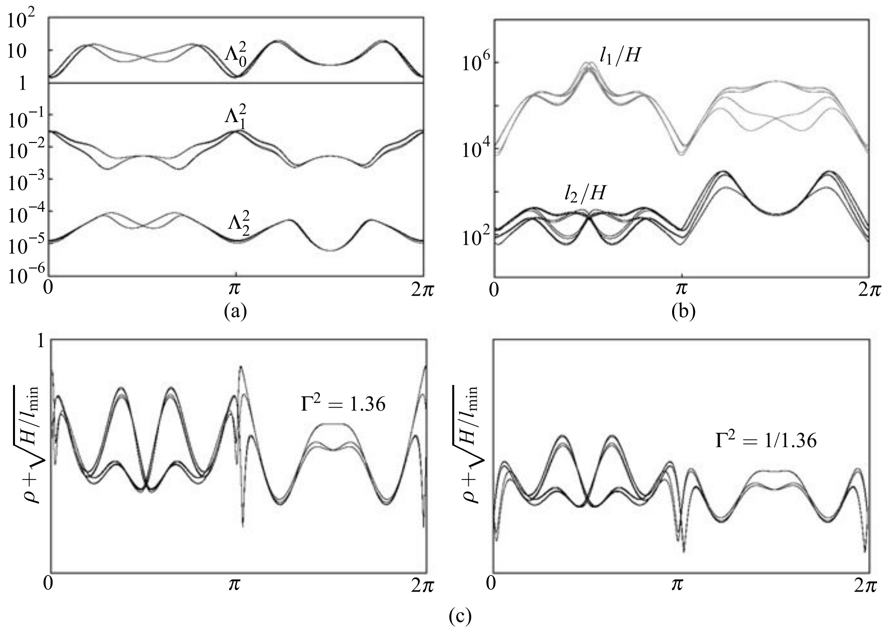


**Fig. 7.15** Relevant quantities computed in the course of verification of the cone criterion in dependence on the angular coordinate counted around the coils of the solenoid for the system governed by the three-dimensional map (3.18): **(a)** eigenvalues of symmetric matrix used for definition of the cones; **(b)** eigenvalues of the auxiliary matrix used for analysis of mutual location of cross-sections of the cones; **(c)** the distance, which is less than 1 in the case of correct inclusions for the expanding cones (the left diagram) and for the contracting cones (the right diagram). Parameters values assigned are $d = d_2$=2, $\mu$=2.

for $\Gamma = \gamma$ and $1/\gamma$ with some $\gamma$ larger than 1. For example, it is true at $\Gamma^2 = 1.36$; so, the required inclusions for the expanding and the contracting cones are valid at $\gamma = \sqrt{1.36} > 1$.

In Fig. 7.16 portrait of the attractor in the stroboscopic Poincaré section is shown supplemented on the periphery with diagrams indicating the mutual location for the expanding cones and the images of the expanding cones at several points of the attractor. The expanding cone is represented by a unit disc, and the image of the expanding cone from the previous point is a small ellipse inside the disc. The circumscribed circle around the ellipse in all cases belongs to the unit disc as well; this is the content of the sufficient condition (7.22).

The next example we consider is the model map with DA attractor (2.6). This is a two-dimensional map for the state vector $\mathbf{x}_n = \{p_n, q_n\}$. The matrix derivative may be obtained analytically,

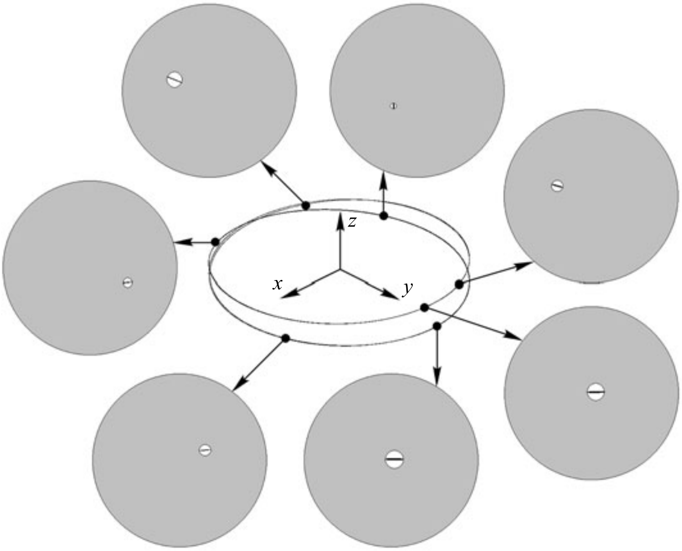


**Fig. 7.16** Illustrations of validity of the criterion for the expanding cones for $\gamma^2$=1.36 checked at seven representative points for the attractor of map (3.18) depicted in the centre. Parameters values assigned are $d = d_2 = 2$, $\mu = 2$. The expanding cone at each point is represented by a unit disc, and the image of the expanding cone from the previous point is a small ellipse inside the disc. The circumscribed circle around the ellipse is used in formulation of the sufficient condition of the correct inclusion for the cones (7.22).

$$\mathbf{g}'(\mathbf{x}_n) = \begin{pmatrix} \dfrac{\partial p_{n+1}}{\partial x_n} & \dfrac{\partial x_{n+1}}{\partial x_n} \\ \dfrac{\partial x_{n+1}}{\partial x_n} & \dfrac{\partial x_{n+1}}{\partial x_n} \end{pmatrix}.$$

While $\varepsilon < \frac{8}{9}$, its Jacobian determinant is positive, so, the map is invertible, but the analytical expression for the inverse map is not available.

Figure 7.17 presents data relating to the computational procedure of verification of the cone criterion for the map (2.6) at $\varepsilon = 0.7$. The abscissa axis corresponds to the coordinate $p$ counted around the torus, on which the map is defined. In panel (a) one can see a plot for two eigenvalues of the matrix $\hat{\mathbf{b}} = \mathbf{v}^{\mathrm{T}}\mathbf{v} = \mathbf{g}'^{\mathrm{T}}\mathbf{g}'$. The first eigenvalue is everywhere larger than 1, and the second is straightly less than 1. In the two-dimensional case, instead of the matrix $\mathbf{h}$ we have simply a single number $l_1$; its ratio to the quantity $H$ (see (7.20)) is plotted in panel (b). Observe that it is positive all over the attractor. The panel (c) gives the evidence for the correct inclusions for the cones. The value $\rho + \sqrt{H/l_{\min}}$ in this case is the maximal distance between the centre of the unit interval and a border of smaller interval that must be inside the unit interval for the criterion to hold. This situation occurs for $\Gamma = \gamma$ and $1/\gamma$, for example, at $\gamma^2 = 5$, as seen from the right diagram (c).

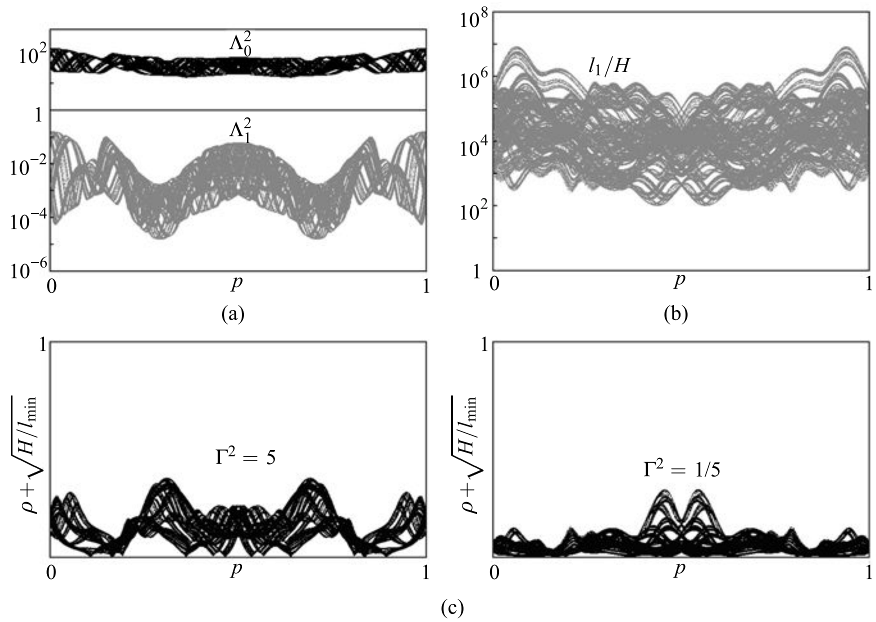


**Fig. 7.17** Relevant quantities for the cone criterion in dependence on the coordinate around the torus for the system governed by the map (2.6) at $\varepsilon = 0.7$: **(a)** two eigenvalues of the symmetric matrix used for definition of the cones; **(b)** the auxiliary value used for analysis of mutual location of intervals representing cross-sections of the two-dimensional cones; **(c)** the distance, which is less than 1 in the case of correct inclusions for the expanding cones (the left diagram) and for the contracting cones (the right diagram).

Let us examine the Plykin type attractor on the plane in the two-dimensional map introduced in Sect. 3.2. In this case, again the map has an analytical expression (3.34). Also, an inverse map can be derived analytically, so do the matrix derivatives $\mathbf{T}'$ and $(\mathbf{T}')^{-1}$. In the course of computations performed at $\varepsilon$=0.77 it appears that degree of non-uniformity of transformations over the attractor in the representation on the plane is quite high; so, the cone criterion in the version we formulate here is successful only for at least four-fold iteration of the original map. Panel (a) of Fig. 7.18 shows a plot for two eigenvalues of the matrix $\hat{\mathbf{b}} = \mathbf{v}^{\mathrm{T}}\mathbf{v} = \mathbf{g}'^{\mathrm{T}}\mathbf{g}'$, where $\mathbf{g} = \mathbf{T}^4$, and the abscissa axis corresponds to the coordinate $X$ used in the definition of the map. Note that the first eigenvalue is straightly higher than 1, and the second is straightly less then 1. The ratio of the auxiliary values l and $H$ is plotted in panel (b) and is positive all over the attractor. Finally, panel (c) gives evidence for the correct inclusions for the cones. The value $\rho + \sqrt{H/l_{\min}}$ is straightly less than 1 for both $\Gamma = \gamma$ and $1/\gamma$ with $\gamma^2 = 1.2$.

Now we turn to more complex examples, for which the Poincaré maps and derivative matrices have to be obtained in computations from numerical integration of the respective differential equations.

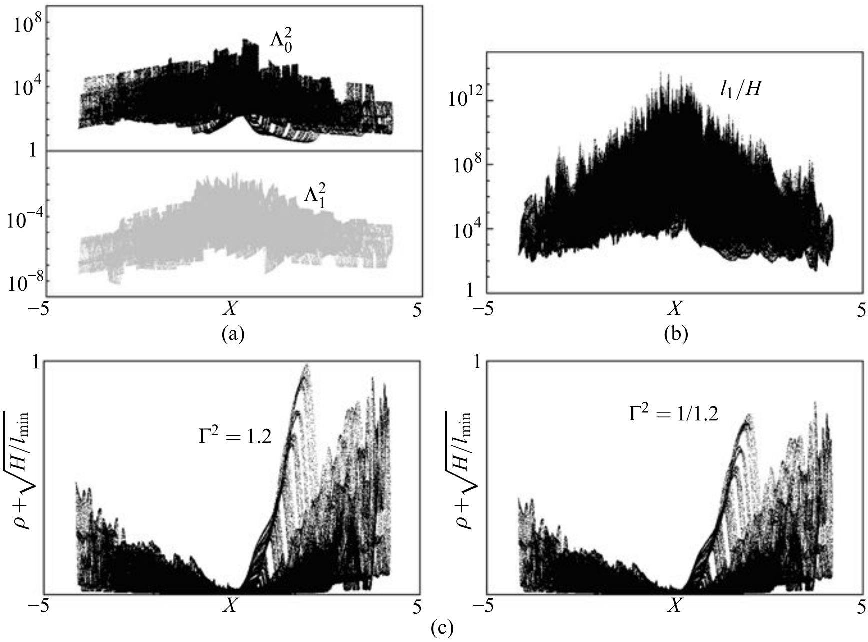


**Fig. 7.18** Relevant quantities for the cone criterion in dependence on the coordinate for the Plykin type attractor of the map (3.34) at $\varepsilon = 0.77$: **(a)** two eigenvalues of the symmetric matrix used for definition of the cones; **(b)** the auxiliary value used for analysis of mutual location of intervals representing cross-sections of the two-dimensional cones; **(c)** the distance, which is less than 1 in the case of correct inclusions for the expanding cones (the left diagram) and for the contracting cones (the right diagram).

The **model constructed on a base of the predator-prey equations** was introduced in the joint work (Kuznetsov and Pikovsky, 2007) and discussed in Chap. 5. It is governed by Eqs. (5.8), which may be rewritten as a set of four differential equations for real variables $x = \text{Re } a_1, u = \text{Im } a_1, y = \text{Re } a_2, v = \text{Im } a_2$. The parameter values assigned are $\omega_0 = 2\pi, \varepsilon = 0.3$. As mentioned in Chap. 5, it is appropriate to define the Poincaré section with a hyper-surface in the 4D phase space specified by the equation $y^2 + v^2 = c$, with account of crossings in direction of increase of $y^2 + v^2$. In the parameter range of interest, an appropriate value of the constant is $c = 2.5$. In the three-dimensional hyper-surface of the cross-section we use coordinates $\{x, u, z\}$, where $z = (2\pi)^{-1} \arg[(y + iv)/(x + iu)]$. The procedure for computation of the Poincaré map is arranged as a computer program basing on numerical solution of differential equations (5.8) complemented with interpolation consistent in accuracy with the applied finite-difference scheme (Hénon, 1982). The initial conditions are formulated in terms of the variables $\{x, u, z\}$ at the Poincaré section. As the part of the trajectory starting and finishing at the Poincaré section has been computed, this results in the updated variables $\bar{x}, \bar{u}, \bar{z}$. Then, the variational equations are integrated along the same trajectory with initial conditions $\tilde{x}, \tilde{u}, \tilde{z}$; in the course of integration the original variables and their variations are used. After returning to the Poincaré section, the updated perturbation vector is obtained. From the last one the component associated with a shift along the trajectory is subtracted. The rest vector is expressed in terms of the updated variations $\tilde{x}, \tilde{u}, \tilde{z}$.

For evaluation of the matrix derivative one performs the procedure of computation three times along the same reference trajectory with initial conditions for the variations (1,0,0), (0,1,0), and (0,0,1). Three resulting final vectors form three columns of the derivative matrix.

Figure 7.19 illustrates verification of the cone criterion for the attractor of Smale-Williams type in the Poincaré map of the system (5.3). Panel (a) shows a plot for three eigenvalues of the matrix $\hat{\mathbf{b}} = \mathbf{v}^{\mathrm{T}}\mathbf{v}$. One of them is straightly higher than 1, and others are straightly less than 1. Panel (b) presents the data for eigenvalues of the auxiliary matrix $\mathbf{h}$ of size $2 \times 2$ in this case. The ratios of the eigenvalues to the quantity $H$ are positive all over the attractor. The diagram is drawn for $\Gamma = 1$, but all observed filaments of the formation on the picture are clearly separated from zero, so, the situation will be the same for $\Gamma$ at least slightly higher or less than 1. Panel (c)

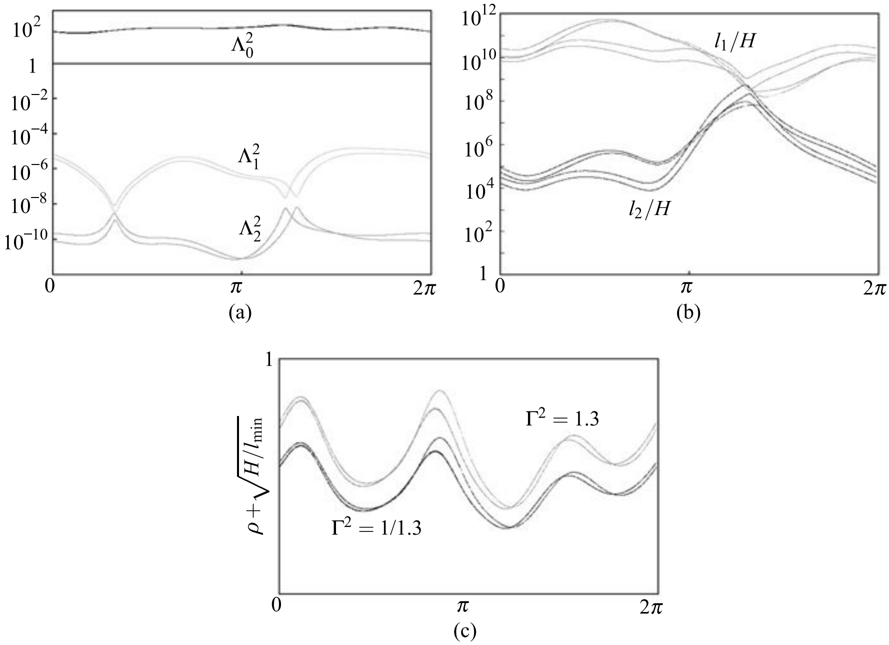


**Fig. 7.19** Relevant quantities computed in the course of verification of the cone criterion in dependence on the angular coordinate counted around the coils of the solenoid for the system governed by differential equations (5.3): **(a)** eigenvalues of symmetric matrix used for definition of the cones; **(b)** eigenvalues of the auxiliary matrix used for analysis of mutual location of cross-sections of the cones; **(c)** the distance, which is less than 1 in the case of correct inclusions for the expanding cones (the gray plot) and for the contracting cones (the black plot). Parameters values assigned are $\omega_0 = 2\pi$, $\varepsilon = 0.3$.

indicates that the value $\rho + \sqrt{H/l_{\min}}$ is straightly less than 1. This situation occurs at $\Gamma^2 = 1.3$, as well as at $\Gamma^2 = 1/1.3$. It means that the required inclusions for both the expanding and the contracting cones are valid at $\gamma = \sqrt{1.3} > 1$. In (Kuznetsov et al., 2007) the cone criterion for this model was verified by scanning the absorbing domain on a grid of small cell size and was found valid at $\gamma$=1.3.

The next example is the *system of two coupled alternately excited non-autonomous self-oscillators* introduced by the author in (Kuznetsov, 2005). It is governed by Eqs. (4.9). The parameter values selected for detailed analysis are $\omega_0 = 2\pi, A = 5, T = 6, \varepsilon = 0.5$. All the time-dependent coefficients in the equations have the least common period $T$, so, the dynamics may be described in terms of stroboscopic Poincaré map, which transforms the initial four-dimensional state vector $\mathbf{x}_n = (x, \dot{x}/\omega_0, y, \dot{y}/\omega_0)|_{t=nT} = (x,u,y,v)|_{t=nT}$ to the state vector $\mathbf{x}_{n+1} = (x,u,y,v)|_{t=(n+1)T}$. It is easily performed with numerical solution of the differential equations by a standard finite-difference method of Runge-Kutta assuming the time interval $T$ contains an integer number of time steps of the finite-difference scheme. Together with the integration, along the reference orbit, a collection of four linearized equations for variations $(\tilde{x}, \tilde{u}, \tilde{y}, \tilde{v})$ is integrated with initial conditions (1,0,0,0), (0,1,0,0), (0,0,1,0),

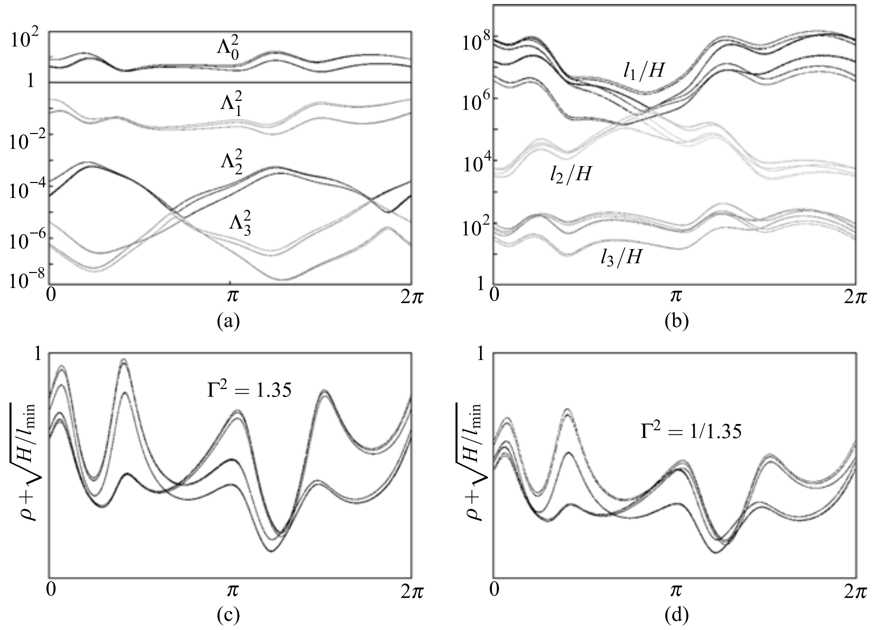


**Fig. 7.20** Relevant quantities for the cone criterion in dependence on the angular coordinate counted around the solenoid for the system governed by differential equations (4.9): **(a)** eigenvalues of the symmetric matrix used for definition of the cones; **(b)** eigenvalues of the auxiliary matrix used for analysis of mutual location of cross-sections of the cones; the distance, which is less than 1 in the case of correct inclusions for the expanding cones **(c)** and for the contracting cones **(d)**. Parameters values assigned are $A = 5, T = 6, \varepsilon = 0.5$.

and (0,0,0,1) to obtain columns of the derivative matrix for the stroboscopic four-dimensional map.

As stated in Sect. 4.2, attractor of the Poincaré map at the selected parameters is a kind of Smale-Williams solenoid embedded in the four-dimensional state space. Fig. 7.20 illustrates verification of the cone criterion for a set of representative points on the attractor obtained by successive iteration of the Poincaré map for the system (4.9). Panel (a) shows a plot for four eigenvalues of the matrix $\hat{\mathbf{b}} = \mathbf{v}^{\mathrm{T}}\mathbf{v}$, one is straightly higher than 1, and three others are straightly less than 1. Panel (b) presents eigenvalues for the matrix $\mathbf{h}$ of size $3\times3$; the ratios of the eigenvalues to $H$ are positive all over the attractor. Panels (c) and (d) show that the value $\rho + \sqrt{H/l_{\min}}$ is straightly less than 1 at $\Gamma^2 = 1.35$ and at $\Gamma^2 = 1/1.35$. So, the cone criterion is valid at $\gamma = \sqrt{1.35} > 1$.

An absorbing domain for this attractor was specified (see formula (4.16) and Fig. 4.3). For expanding cones the criterion was verified on a grid covering this absorbing domain $D$, and for contracting cones that was verified for the domain $\mathbf{T}^2(D)$ (Kuznetsov and Sataev, 2007). It was found valid, e.g. at $\gamma^2 = 1.1$.

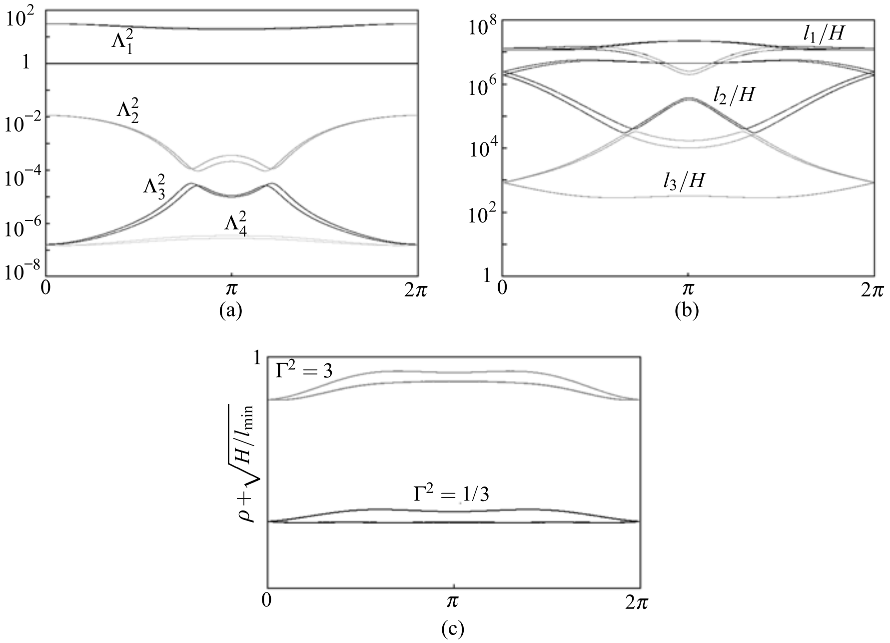


**Fig. 7.21** Relevant quantities for the cone criterion in dependence on the angular coordinate counted around the solenoid for the system governed by differential equations (5.5): **(a)** eigenvalues of the symmetric matrix used for definition of the cones; **(b)** eigenvalues of the auxiliary matrix used for analysis of mutual location of cross-sections of the cones; **(c)** the distance, which is less than 1 in the case of correct inclusions for the expanding cones (the gray plot) and for the contracting cones (the black plot). Parameters values assigned are $\alpha = 0.6, \varepsilon = 0.1$.

A final example of attractor of Smale-Williams type relates to the *five-dimensional autonomous system* introduced in Sect. 5.2 and governed by differential equations (5.5). The Poincaré map is four-dimensional, like in the previous system, but because of its autonomous nature the construction of the Poincaré map requires a little bit more care. The computation of the Poincaré map is performed by a computer program basing on numerical solution of differential equations (5.5) complemented with procedure of (Hénon, 1982). The initial conditions are specified by the variables $\{X, Y, U, V\}$ at $z = 0$. As the part of the trajectory starting and finishing at the Poincaré section has been computed, the updated values are obtained. Then, the variation equations are integrated along the same trajectory; there is a collection of four vectors to construct columns of the derivative matrix for the Poincaré map. After returning to the Poincaré section, from each perturbation vector the component associated with a shift along the trajectory is subtracted, to ensure zero value of variation of the variable $z$; the resulting vectors determine columns of the derivative matrix.

Figure. 7.21 illustrates verification of the cone criterion for a set of representative points on the attractor obtained by successive iteration of the Poincaré map. The panels have the same sense as for the previous system. Panel (c) shows that the required cone inclusions take place at $\gamma = \sqrt{3} > 1$.

## References


Afraimovich, V., Hsu, S.-B.: Lectures on Chaotic Dynamical Systems. International Press, Somerville, MA (2003).

Anishchenko, V.S., Kopeikin, A.S., Kurths, J., Vadivasova, T.E., Strelkova G.I.: Studying hyperbolicity in chaotic systems. Physics Letters A **270**, 301–307 (2000).

Anosov, D.V.: On the contribution of N.N. Bogolyubov to the theory of dynamical systems. Russ. Math. Surv. **49**, 1–18 (1994).

Bowen R.: Equilibrium states and ergodic theory of Anosov diffeomorphisms. Lecture Notes in Math. 470**,** Springer, Heidelberg (1975).

Ginelli, F., Poggi, P., Turchi, A., Chaté, H., Livi, R., Politi, A.: Characterizing dynamics with covariant Lyapunov vectors. Phys. Rev. Lett. **99**, 130601 (2007).

Guckenheimer, J., Holmes, P.: Nonlinear Oscillations, Dynamical Systems, and Bifurcations of Vector Fields. Springer-Verlag, New York (1983).

Hasselblatt, B., Katok, A.A.: First Course in Dynamics: with a Panorama of Recent Developments. Cambridge University Press, Cambridge (2003).

Hasselblatt, B., Pesin, Y.: Hyperbolic dynamics. Scholarpedia **3**, 2208 (2008).

Hénon, M.: On the numerical computation of Poincaré maps. Physica D **5**, 412–414 (1982).

Hirata, Y., Nozaki, K., Konishi, T.: The intersection angles between $N$-dimensional stable and unstable manifolds in $2N$-dimensional symplectic mappings. Prog. Theor. Phys. **102**, 701–706 (1999).

Katok, A., Hasselblatt, B.: Introduction to the Modern Theory of Dynamical Systems. Cambridge University Press, Cambridge (1995).

Krauskopf, B., Osinga, H.M., Doedel E.J., Henderson, M.E., Guckenheimer, J., Vladimirsky, A., Dellnitz, M., Junge, O.: A survey of methods for computing (un) stable manifolds of vector fields. Int. J. Bifurcation and Chaos **15**, 763–791(2005).

Kuptsov, P.V., Kuznetsov, S.P.: Violation of hyperbolicity in a diffusive medium with local hyperbolic attractor. Phys. Rev. E **80**, 016205 (2009).

Kuznetsov, A.S., Kuznetsov, S.P., Sataev, I.R.: Parametric generator of hyperbolic chaos based on two coupled oscillators with nonlinear dissipation. Technical Physics **55**, 1707–1715 (2010).

Kuznetsov, S.P.: Example of a physical system with a hyperbolic attractor of the Smale-Williams type. Phys. Rev. Lett. **95**, 144101 (2005).

Kuznetsov, S.P.: A non-autonomous flow system with Plykin type attractor. CNSNS **14**, 3487–3491 (2009).

Kuznetsov, S.P. and Pikovsky, A.: Autonomous coupled oscillators with hyperbolic strange attractors. Physica D **232**, 87–102 (2007).

Kuznetsov, S.P., Sataev, I.R.: Hyperbolic attractor in a system of coupled non-autonomous van der Pol oscillators: Numerical test for expanding and contracting cones. Physics Letters A **365**, 97–104 (2007).

Kuznetsov, S.P., Sataev, I.R.: Visualization of invariant measures and comparison of hyperbolic and non-hyperbolic chaotic attractors. Preprint. SB IRE RAS, Saratov (2011).

Kuznetsov, S.P., Seleznev, E.P.: A strange attractor of the Smale-Williams type in the chaotic dynamics of a physical system. JETP **102**, 355–364 (2006).

Kuznetsov, S.P., Pikovsky, A.S., Sataev, I.R.: Hyperbolic Smale-Williams attractor in Poincaré map of a four-dimensional autonomous system. In: Proc. of the III Int. Conf. “Frontiers of Nonlinear Physics”. Nizhny Novgorod-Saratov-Nizhny Novgorod, pp. 66–67 (2007)

Lai, Y.-C., Grebogi, C., Yorke, J. A., Kan, I.: How often are chaotic saddles nonhyperbolic? Nonlinearity **6**, 779–798 (1993).

Ruelle, D.: A measure associated with Axiom A attractors. Amer. J. Math. **98**, 619–654 (1976).

Shilnikov, L.: Mathematical problems of nonlinear dynamics: a tutorial. Int. J. Bifurcation and Chaos **7**, 1353–2001 (1997).

Sinai, Y.G.: Gibbs measures in ergodic theory. Russ. Math. Surv. **27**, 21–70 (1972).

Sinai, Y.G.: Stochasticity of dynamical systems. In: Gaponov-Grekhov, A.V. (ed.) Nolinear waves, pp. 192–212. Moscow, Nauka (1979).

Sinai, J.G., Vul, E.B.: Hyperbolicity conditions for the Lorenz model. Physica D **2**, 3–7 (1981).

Smale, S.: Differentiable dynamical systems. Bull. Amer. Math. Soc. (NS) **73**, 747–817 (1967).

Tél, T., Gruiz, M.: Chaotic dynamics: an Introduction Based on Classical Mechanics. Cambridge University Press, Cambridge (2006).

Williams, R.F.: Expanding attractors. Publications mathématiques de l’I.H.É.S. **43**, 169–203 (1974).

# Chapter 8
# Systems of Four Alternately Excited Non-autonomous Oscillators

**Abstract** This chapter is devoted to non-autonomous models generating successive trains of oscillations with phase chaotically varying from one train to the other. In contrast to Chap. 4, here we examine dynamics in the phase space of larger dimensions; so, the models are composed of four oscillators activating by turns (usually in pairs). Particularly, we consider a model, in which evolution of the phases in successive epochs of activity is described by the Arnold cat map and by a hyperchaotic torus map that has two positive Lyapunov exponents. Then, a system will be discussed that can be thought of as being composed of two coupled pairs of oscillators, each of which corresponds to a system with hyperbolic attractor of Smale-Williams type in the Poincaré map. This may be regarded as initial step of a research program for ensembles of coupled elements with hyperbolic chaotic dynamics, like coupled map lattices considered, e.g. in (Bunimovich and Sinai, 1988; 1993; Bricmont and Kupiainen, 1997; Järvenpää, 2005), but on a base of concrete physically realizable systems.

## 8.1 Arnold's cat map dynamics in a system of coupled non-autonomous van der Pol oscillators

As mentioned in Chap. 1, one special class of objects with chaotic dynamics corresponds to Anosov hyperbolic automorphisms of torus (Arnold and Avez, 1968; Anosov et al., 1995; Devaney, 2003). The most popular example is known also as Arnold's cat map:

$$\begin{aligned} p_{n+1} &= p_n + q_n \; (\bmod 1), \\ q_{n+1} &= p_n + 2q_n \; (\bmod 1). \end{aligned} \tag{8.1}$$

For graphical representation one can use a unit square with the opposite pairs of sides identified (Fig. 1.6(a)). The map (8.1) is a conservative system: any domain in the $(p,q)$ plane (say, that cat face) conserves its area under the iteration.

It is known that the map (8.1) demonstrates chaotic dynamics in a sense of hyperbolic theory, with such attributes as existence of continuous invariant measure, description in terms of Markov partition and symbolic dynamics, positive topological and metric entropies (Devaney, 2003). Two Lyapunov exponents are expressed via eigenvalues of the matrix associated with the map, namely,

$$\Lambda_1 = \ln(3+\sqrt{5})/2 \approx 0.9624, \quad \Lambda_2 = -\ln(3+\sqrt{5})/2 \approx -0.9624. \tag{8.2}$$

The largest exponent is positive that reflects occurrence of chaos characterized by exponential sensitivity to initial conditions.

The Arnold cat map may be represented as a two-fold composition of a simpler map:

$$\begin{aligned} p_{n+1} &= q_n \ (\mathrm{mod}\, 1), \\ q_{n+1} &= p_n + q_n \ (\mathrm{mod}\, 1). \end{aligned} \tag{8.3}$$

Expressed in terms of one variable, as $p_{n+1} = p_n + p_{n-1}$, it is called *the Fibonacci map*.

To implement the corresponding dynamics, we consider the following set of coupled non-autonomous van der Pol oscillators (Isaeva et al., 2006):

$$\begin{aligned} \ddot{x} - (A\cos(2\pi t/T) - x^2)\dot{x} + \omega_0^2 x &= \varepsilon z \cos\omega_0 t, \\ \ddot{y} - (A\cos(2\pi t/T) - y^2)\dot{y} + \omega_0^2 y &= \varepsilon w, \\ \ddot{z} - (-A\cos(2\pi t/T) - z^2)\dot{z} + 4\omega_0^2 z &= \varepsilon xy, \\ \ddot{w} - (-A\cos(2\pi t/T) - w^2)\dot{w} + \omega_0^2 w &= \varepsilon x. \end{aligned} \tag{8.4}$$

Three of them associated with variables $x, y$, and $w$ have equal natural frequencies $\omega_0$, and the rest one ($z$) has a frequency $2\omega_0$. The control parameter responsible for the Andronov-Hopf bifurcation in the partial systems is forced to vary slowly with some period $T$. In each half-period, at the beginning of activity stage for one pair of the oscillators $(x, y)$, or $(z, w)$, the other pair stimulates its excitation because of presence of respective coupling terms in the equations proportional to $\varepsilon$, one of which contains also an auxiliary signal of frequency $\omega_0$. A period of the slow parameter modulation is assumed to contain an integer number of periods of the auxiliary signal $N_0 = \omega_0 T/2\pi$, so the external driving is periodic.

Let us derive approximate relations for transformation of phases of the oscillators in the course of the process. Suppose that the first and the second oscillators at a stage of activity are characterized by some initial phases:

$$x \sim \cos(\omega_0 t + \varphi_x), \quad y \sim \cos(\omega_0 t + \varphi_y). \tag{8.5}$$

The coupling term in the third equation contains a product $xy$ and, hence, may be represented as

$$\cos(\omega_0 t + \varphi_x)\cos(\omega_0 t + \varphi_y) = \frac{1}{2}\cos(\varphi_x - \varphi_y) + \frac{1}{2}\cos(2\omega_0 t + \varphi_x + \varphi_y). \tag{8.6}$$

The last additive term in this expression is a resonance drive for the oscillator $z$ and stimulates its excitation at the beginning of the activity stage. So, the third oscillator inherits the phase $\varphi_z \approx \varphi_x + \varphi_y + \text{const}$, while the fourth one simply accepts the phase from the first oscillator: $\varphi_w \approx \varphi_x + \text{const}$. At the next stage of activity for the first pair of the oscillators, the coupling term in the first equation

$$z\cos 2\pi t \sim \frac{1}{2}(\cos(6\pi t + \varphi_x + \varphi_y) + \cos(2\pi t + \varphi_x + \varphi_y)) \tag{8.7}$$

stimulates the oscillator $x$, and it acquires the phase $\varphi_x' \approx \varphi_z + \text{const} \approx \varphi_x + \varphi_y + \text{const}$. The oscillator $y$ inherits the phase from $w$: $\varphi_y' \approx \varphi_w \approx \varphi_x + \text{const}$. So, the mapping for the phases is expressed as follows:

$$\begin{aligned} \varphi_x' &= \varphi_x + \varphi_y + \text{const}, \\ \varphi_y' &= \varphi_x + \text{const}. \end{aligned} \tag{8.8}$$

Accounting that the phases are defined in the interval from 0 to $2\pi$ and using the normalization $q = \varphi_x/2\pi$ and $p = \varphi_y/2\pi$, we obtain exactly the map (8.3), up to additive constants; they obviously may be removed by appropriate shift of the origin. Hence, for the phases of oscillators $(x, y)$ the stroboscopic dynamics with sampling with time interval $2T$ follows the Arnold cat map, at least in rough approximation.

To support the drawn conclusion, let us turn to direct numerical computations for the set of non-autonomous differential equations (8.4). Figure 8.1 shows the dynamical variables versus time in the system (8.4), at parameter values

$$\omega_0 = 2\pi,\ N_0 = T = 20,\ A = 2,\ \varepsilon = 0.4. \tag{8.9}$$

Observe that the system operates in correspondence with the discussed mechanism. Chaos reveals itself in random phases of the carrier oscillations in respect to the envelope in subsequent periods of the slow modulation.

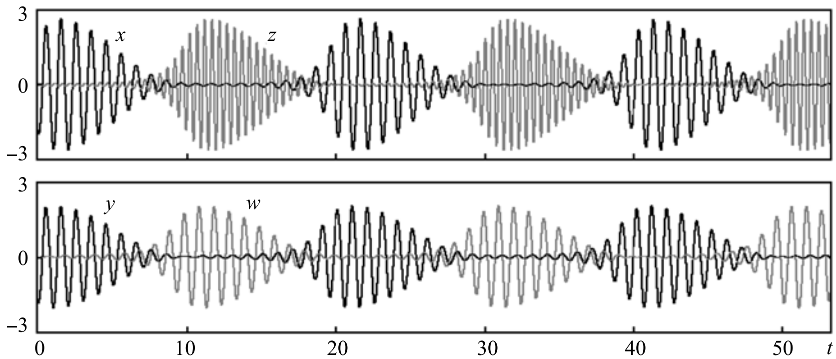


**Fig. 8.1** Time dependence for the dynamical variables of the system (8.4) at $\omega_0 = 2\pi, T = 20, A = 2, \varepsilon = 0.4$.

To demonstrate correspondence of the transformation of phases in the system of oscillators with the Arnold cat map, we implement the following procedure. In the course of numerical integration of Eqs. (8.4) we determine the phases for the first and the second oscillators in the middle of their activity stage[1]

$$\varphi_x = \arg(x + i\omega_0^{-1}\dot{x}), \quad \varphi_y = \arg(y + i\omega_0^{-1}\dot{y}). \tag{8.10}$$

If the point $(q, p) = (\varphi_x/2\pi, \varphi_y/2\pi)$ belongs to the area of the cat face drawn in the unit square, we mark the dot on the diagram, and also mark the dot for the images after time intervals $2T$ and $4T$ on two succeeding plots. If it is not the case, the dot is not marked. By accumulation of a great number of dots, we can see the cat face on the first picture, and images corresponding to once and twice iterating of the Arnold map on the second and the third diagrams, respectively (Fig. 8.2(a)).

The pictures may be compared with those obtained directly from iteration of the Arnold cat map. For better correspondence, we must account the additive constant terms in the equations for phases, which appear in the course of the transfer of excitations from oscillators to their partners. With these constants empirically selected (for the particular case under consideration, see (8.9)) the map reads

$$\begin{aligned} p' &= p + q + 0.07 \pmod 1, \\ q' &= p + 2q - 0.38 \pmod 1. \end{aligned} \tag{8.11}$$

The plots illustrating evolution of the cat face in accordance with this map are shown in Fig. 8.2(b). Observe a nice correspondence of the phase dynamics in the system of non-autonomous van der Pol oscillators and in the modified Arnold cat map (8.11).

For more accurate discrete-time description, we turn to the stroboscopic Poincaré map. Let us have a certain state of the system at $t_n = 2nT$ associated with a vector $\mathbf{x}_n = \{x, \dot{x}/\omega_0, y, \dot{y}/\omega_0, z, \dot{z}/2\omega_0, w, \dot{w}/\omega_0\}$. From solution of the differential equations (8.4) with the initial state $\mathbf{x}_n$, after time interval $2T$, we get a new vector $\mathbf{x}_{n+1}$ and introduce a function that maps the eight-dimensional space into itself:

$$\mathbf{x}_{n+1} = \mathbf{T}(\mathbf{x}_n). \tag{8.12}$$

Geometrically, in the nine-dimensional extended phase space of our non-autonomous system $\{\mathbf{x}, t\}$ we have a cross-section of the flow by the eight-dimensional hyper-planes $t = t_n = 2nT$. The Poincaré map $\mathbf{T}$ is a diffeomorphism in $\mathbf{R}^8$, a one-to-one differentiable map of class $C^\infty$ (Arnold, 1978).

Figure 8.3 shows portrait of the attractor in projection from the extended phase space onto the plane of variables of the first oscillator $(x, \dot{x})$. The attractor is shown in gray scales reflecting relative duration of residence of the orbit inside pixels. Black dots relate to the Poincaré cross-section, i.e., to the instants $t_n = 2nT$.

---

[1] The phases $\varphi_x$ and $\varphi_y$ cannot be defined globally, in the whole time interval $T$: they are attributed to a stage of excitation of the pair of oscillators and may be used in the context of the discrete time description. Indeed, when this pair of oscillators is not active, the respective amplitudes are small, and the phases are not well defined.

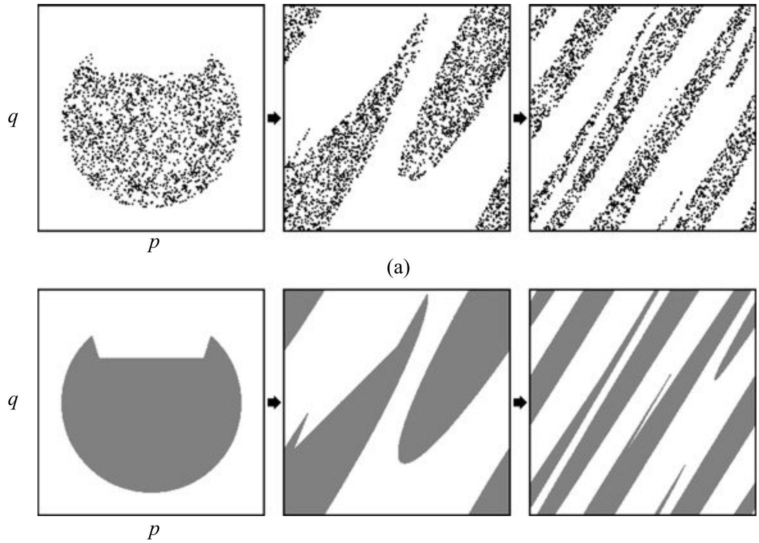


**Fig. 8.2** Transformation of an area in the form of a cat face in a plane of phase variables in the system of van der Pol oscillators (8.4) after time intervals $2T$ and $4T$ **(a)** and analogous pictures obtained from the map (8.10) **(b)**.

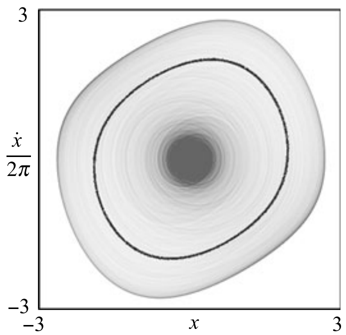


**Fig. 8.3** Portrait of attractor at $\omega_0 = 2\pi, T = 6, A = 6.5, \varepsilon = 0.4$: projection from the extended phase space on the plane of variables $(x, \dot{x})$ and the Poincaré cross-section corresponding to the instants $t_n = 2nT$ (black dots), which looks like projection of a narrow two-dimensional torus.

The spectrum of Lyapunov exponents is evaluated with a help of algorithm based on simultaneous numerical integration of Eqs. (8.1) together with eight replicas of the linearized equations for perturbations:

$$\begin{aligned}
\ddot{\tilde{x}} + 2x\dot{x}\tilde{x} - (A\cos(2\pi t/T) - x^2)\dot{\tilde{x}} + \omega_0^2\tilde{x} &= \varepsilon\tilde{z}\cos\omega_0 t,\\
\ddot{\tilde{y}} + 2y\dot{y}\tilde{y} - (A\cos(2\pi t/T) - y^2)\dot{\tilde{y}} + \omega_0^2\tilde{y} &= \varepsilon\tilde{w},\\
\ddot{\tilde{z}} + 2z\dot{z}\tilde{z} - (-A\cos(2\pi t/T) - z^2)\dot{\tilde{z}} + 4\omega_0^2\tilde{z} &= \varepsilon(\tilde{x}y + x\tilde{y}),\\
\ddot{\tilde{w}} + 2w\dot{w}\tilde{w} - (-A\cos(2\pi t/T) - w^2)\dot{\tilde{w}} + \omega_0^2\tilde{w} &= \varepsilon\tilde{x}.
\end{aligned} \tag{8.13}$$

In the course of the solution, at each next period $2T$, the Gram-Schmidt orthogonalization and normalization were performed for eight vectors $\tilde{\mathbf{x}} = \{\tilde{x}, \dot{\tilde{x}}/\omega_0, \tilde{y}, \dot{\tilde{y}}/\omega_0, \tilde{z}, \dot{\tilde{z}}/2\omega_0, \tilde{w}, \dot{\tilde{w}}/\omega_0\}$, and the mean rates of growth or decrease of the accumulated sums of logarithms of the norm ratios are estimated (Appendix A). As found, at the parameters (8.9) the Lyapunov exponents for the attractor of the Poincaré map are [2]

$$\begin{array}{llll} \Lambda_1 = 0.962, & \Lambda_2 = -0.970, & \Lambda_3 = -15.525, & \Lambda_4 = -19.074, \\ \Lambda_5 = -20.053, & \Lambda_6 = -21.315, & \Lambda_7 = -32.444, & \Lambda_8 = -32.898. \end{array} \tag{8.14}$$

Figure 8.4 shows a plot for all eight Lyapunov exponents of the system versus the amplitude $A$ of slow modulation at fixed other parameters. As seen, the largest two exponents remain almost constant in a wide range and are close to the values characteristic of the Arnold cat map (8.2). The rest exponents are largely negative. They correspond to strong compression of the phase volume along six remaining dimensions in the phase space of the Poincaré map.

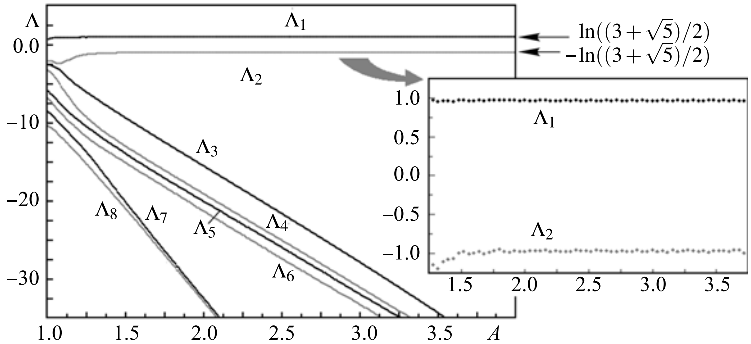


**Fig. 8.4** Lyapunov exponents for the system (8.4) versus the amplitude of parameter modulation at $\omega_0 = 2\pi, T = 20, \varepsilon = 0.4$.

Figure 8.5 illustrates distribution of invariant measure on the attractor as it looks on the plane of two phase variables used to show the Arnold cat face. Here one can see subtle fractal-like structure intrinsic to the distribution, which appears due to some deflections from the linear toral map. Such distributions were discussed in the context of the problem of the so-called "non-strange chaotic attractor" (Farmer et al., 1983; Anishchenko et al., 2002). In fact, attractor in the Poincaré map of our system is not "non-strange": it certainly has a transverse fractal structure in the eight-dimensional phase space, but distribution of the invariant measure over the torus approximately representing the attractor is of the nature that has been suggested for the "non-strange chaos".

To have quantitative characteristics for the fractal invariant measure on the attractor, we have estimated the correlation dimensions from the Grassberger-Procaccia

[2] We use here $2T$ as the normalization time interval in definition of the Lyapunov exponents to have a correspondence with the cat map model.

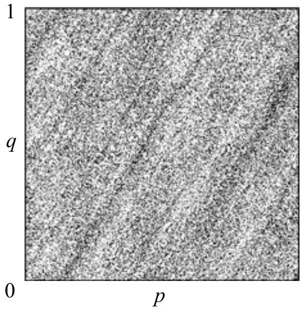


**Fig. 8.5** Distributions of points on the attractor in projection on a plane of phases of the first pair of oscillators in Poincaré cross-section obtained from computations or the system (8.1).

algorithm (Grassberger and Procaccia, 1983) by processing a two-component time series composed of data for phases (8.10) form $10^5$ iteration of the Poincaré map obtained in numerical solution of Eqs. (8.4) (Fig. 8.6). At the present parameter values (8.18) we get the dimension $D_2$=1.98 distinct from the value 2, which would correspond to a uniform distribution of the invariant density over a surface of 2D torus. The estimate from Kaplan-Yorke formula (Appendix D) using the Lyapunov exponents (8.19) yields $D_L = 1 + \Lambda_1/|\Lambda_2| \approx 1.99$.

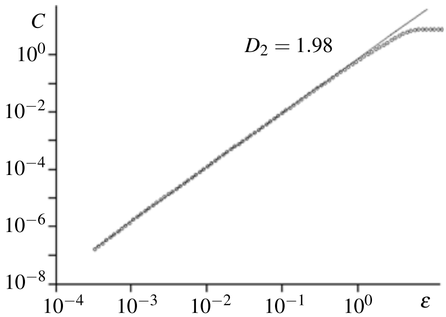


**Fig. 8.6** Plot of the correlation integral versus the partition size in double logarithmic scale obtained from processing of two-component time series of $10^5$ pairs of phases (8.10) in the Poincaré cross-section from numerical solution of (8.4). The respective estimate for the correlation dimension corresponds to a slope in the range of linear dependence.

The considered system of four coupled non-autonomous van der Pol oscillators delivers a realistic example of dynamics approximately described by hyperbolic maps on a torus. In fact, we deal with an attractor in the eight-dimensional phase space of Poincaré map. Due to strong phase volume compression, it reduces approximately to a two-dimensional map for the phases of a pair of the oscillators that corresponds to the Arnold cat map. It may be hypothesized that the attractor in the Poincaré map is uniformly hyperbolic and, hence, structurally stable, although an accurate check of this assumption seems not easy because of high dimension of the phase space.

## 8.2 Dynamics corresponding to hyperchaotic maps

The term *hyperchaos* was introduced by Rössler and relates to dynamical regimes characterized by two or more positive Lyapunov exponents (Rössler, 1979; Matsumoto et al., 1986; Stoop et al., 1989; Reiterer et al., 1998; Letellier and Rössler, 2007). To date, no compelling reasons have been seen for relating the known in the literature examples of hyperchaotic behavior to uniformly hyperbolic attractors. Here we turn to models, which can pretend to deliver appropriate examples.

### *8.2.1 System implementing toral hyperchaotic map*

First, let us consider a system of four coupled van der Pol oscillators

$$\begin{aligned} \ddot{x} - (A\cos(2\pi t/T) - x^2)\dot{x} + \omega_0^2 x &= \varepsilon z \cos\omega_0 t, \\ \ddot{y} - (A\cos(2\pi t/T) - y^2)\dot{y} + \omega_0^2 y &= \varepsilon w \cos 2\omega_0 t, \\ \ddot{z} - (-A\cos(2\pi t/T) - z^2)\dot{z} + 4\omega_0^2 z &= \varepsilon xy, \\ \ddot{w} - (-A\cos(2\pi t/T) - w^2)\dot{w} + 9\omega_0^2 w &= \varepsilon x^3, \end{aligned} \tag{8.15}$$

two of which have the natural frequencies $\omega_0$, and the third and the fourth have, respectively, the frequencies $2\omega_0$ and $3\omega_0$. Control parameters, responsible for the Andronov-Hopf bifurcation in the autonomous subsystems, are slowly modulated periodically in time. In the first half-period of modulation the first pair of oscillators is active, and the second is damped. In the second half-period the situation is reversed.

Suppose that the first oscillator in the epoch of activity is characterized by an initial phase $\varphi_x$, and the second by the phase $\varphi_y$; so, the respective dynamical variables oscillate as $x \sim \cos(\omega_0 t + \varphi_x)$ and $y \sim \cos(\omega_0 t + \varphi_y)$. Then, when the second pair is activating, the third oscillator is stimulated by the coupling term in the equation proportional to

$$xy \sim \cos(\omega_0 t + \varphi_x)\cos(\omega_0 t + \varphi_y) = \frac{1}{2}\cos(\varphi_x - \varphi_y) + \frac{1}{2}\cos(2\omega_0 t + \varphi_x + \varphi_y).$$

Then, it accepts the phase $\varphi_z = \varphi_x + \varphi_y + \text{const}$ because the last term in the sum is resonant for this oscillator. The fourth oscillator, in turn, accepts the tripled phase from the first one, as can be deduced from the relation

$$x^3 \sim \cos^3(\omega_0 t + \varphi_x) = \frac{3}{4}\cos(\omega_0 t + \varphi_x) + \frac{1}{4}\cos(3\omega_0 t + 3\varphi_x).$$

The resonance stimulation occurs due to the last term of the tripled frequency. So, we have $\varphi_w = 3\varphi_x + \text{const}$. Then, at the next transfer of the excitation, these phases are transmitted to the first and the second oscillators at their next activity stage. So, the mapping for the phases in the complete period of modulation is

$$\varphi_x' = \varphi_x + \varphi_y + \text{const}, \quad \varphi_y' = 3\varphi_x + \text{const}, \tag{8.16}$$

where the constants may be removed by a shift of the origin on the plane $(\varphi_x, \varphi_y)$. Accounting that the phases are defined modulo $2\pi$, for normalized variables $q = \varphi_x/2\pi i$ and $p = \varphi_y/2\pi$, we get

$$\begin{aligned} p_{n+1} &= p_n + q_n \ (\bmod 1). \\ q_{n+1} &= 3p_n \ (\bmod 1), \end{aligned} \tag{8.17}$$

or

$$\begin{pmatrix} p \\ q \end{pmatrix}_{n+1} = \begin{pmatrix} 1 & 1 \\ 3 & 0 \end{pmatrix} \begin{pmatrix} p \\ q \end{pmatrix}_n . \tag{8.18}$$

Eigenvalues of the matrix in the last expressions are $(1 \pm \sqrt{13})/2$. Respectively, the Lyapunov exponents for the map are

$$\Lambda_1 = \ln(\sqrt{13}+1)/2 = 0.834, \quad \Lambda_2 = \ln(\sqrt{13}-1)/2 = 0.264. \tag{8.19}$$

Both of them are positive, so, the map generates hyperchaos.

Figure 8.7 depicts chaotic attractor in the projection from the eight-dimensional phase space in the stroboscopic section on the plane of phase variables $(\varphi_x, \varphi_y)$. Note that the points fill the unit square almost uniformly. Figure 8.8 shows the Lyapunov exponents of the attractor versus magnitude of the parameter modulation. Observe that two larger Lyapunov exponents remain approximately constant and close to the approximated values (8.19) in a wide range. This indirectly confirms the robustness of the observed hyperchaotic attractor.

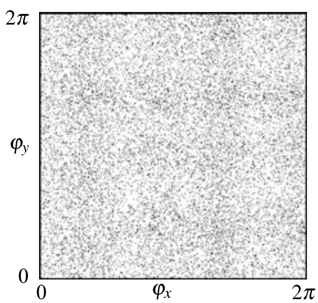


**Fig. 8.7** Portrait of the trajectory on the hyperchaotic attractor in stroboscopic map of the model (8.15) onto the plane of phase variables $(\varphi_x, \varphi_y)$ at $\omega_0 = 2\pi, T = 20, A = 2.5, \varepsilon = 0.5$.

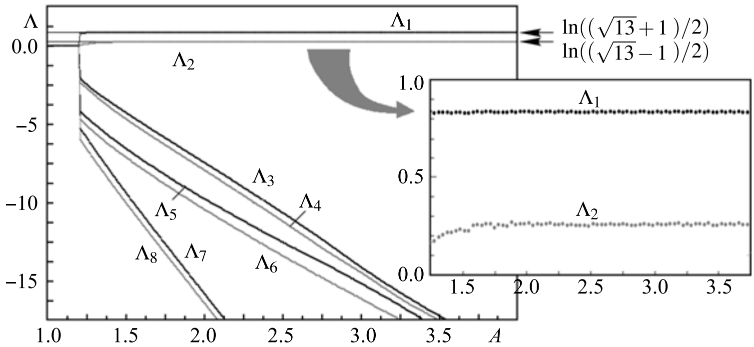


**Fig. 8.8** Lyapunov exponents of the stroboscopic Poincaré map of the model (8.15) at $\omega_0 = 2\pi, T = 20, A = 2.5, \varepsilon = 0.5$.

### *8.2.2 Model with cascade transfer of excitation upward the frequency spectrum*

The following example is inspired by the concept that underlies understanding of developed hydrodynamic turbulence. As known, it is based on the idea of a cascade energy transfer through the spectrum, from formations in the turbulent flow characterized by large spatial and temporal scales to smaller scales (Landau and Lifshitz, 1959; Monin and Yaglom, 2007).

Obviously this idea in nature is general and, apparently, it makes sense to use it as a guiding principle for design of various systems with chaotic dynamics even in situations where equations are not similar to the hydrodynamic ones.

Consider a system of four van der Pol oscillators with natural frequencies $\omega_0, 2\omega_0, 4\omega_0, 8\omega_0$ shown schematically in Fig. 8.9, operation of which is provided by a cascade transfer of excitation from one oscillator to another with successive frequency doubling (Kuznetsov and Sokha, 2010). Parameters controlling the Andronov-Hopf bifurcation in each oscillator are forced to vary slowly in time, with amplitude $A$ and period $T = 2\pi/\Omega$, where $\Omega \ll \omega_0$. The modulation takes place in the same phase for the first and the third oscillators, and in the counter-phase for the second and the fourth oscillators. An appropriate model is the system of differential

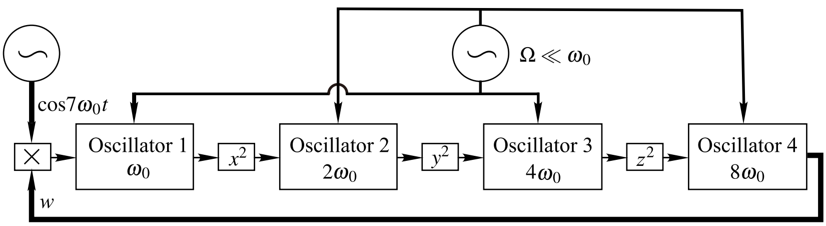


**Fig. 8.9** Block-diagram of the system with cascade transfer of excitation with frequency doubling.

equations

$$\begin{aligned}
\ddot{x} - (A\cos\Omega t - x^2)\dot{x} + \omega_0^2 x &= \varepsilon w \cos 7\omega_0 t,\\
\ddot{y} - (-A\cos\Omega t - y^2)\dot{y} + 4\omega_0^2 y &= \varepsilon x^2,\\
\ddot{z} - (A\cos\Omega t - z^2)\dot{z} + 16\omega_0^2 z &= \varepsilon y^2,\\
\ddot{w} - (-A\cos\Omega t - w^2)\dot{w} + 64\omega_0^2 w &= \varepsilon z^2,
\end{aligned} \tag{8.20}$$

where the variables $x, y, z, w$ are the generalized coordinates of the oscillators from the first to the fourth, respectively. We assume that the relation $\omega_0 T = 2\pi N$ holds, where $N$ is an integer, so that the non-autonomous set of equations has periodic time dependence of the coefficients.

Due to the assumed parameter modulation, two pairs of oscillators become active in turn. Stimulations for the oscillators 2, 3 and 4 at the beginning of each new stage of activity are provided by the excitation transfer from the previous oscillators of twice less frequencies through the quadratic nonlinear element. In the course of the excitation transfer, the phase shift constant intrinsic to the signal is doubled. Indeed, from the signal $\cos(\omega t + \varphi)$ we obtain $\cos^2(\omega t + \varphi) = \frac{1}{2}\cos(2\omega t + 2\varphi) + \frac{1}{2}$; here one can account only the component of doubled frequency resonant with the newly excited oscillator. The feedback is closed with final nonlinear transformation of mixing of the output signal from the chain with a reference signal of frequency $7\omega_0$ and with fixed phase shift to obtain the difference frequency response in the resonance band of the first oscillator. Indeed, $\cos(8\omega_0 t + \theta)\cos 7\omega_0 t = \frac{1}{2}\cos(\omega_0 t + \theta) + \cdots$ here the non-resonance term is omitted, which is negligible for stimulation of the oscillator of frequency $\omega_0$.

For a clearer understanding of the phase transformations in the course of operation of the system, refer to Table 8.1. The columns correspond to oscillators 1, 2, 3, 4, and the rows relate to successive half-periods of slow modulation. The first row corresponds to the stage of activity of the oscillators 1 and 3 characterized by phases $\varphi_0$ and $\theta_0$. The oscillators 2 and 4 at this stage are damped and do not possess a well defined phase, so that the corresponding cells are left empty. The oscillators 2 and 4 are excited on the next half-period of modulation. Following the above explanations, they accept the phases, respectively, $2\varphi_0$ and $2\theta_0$ (up to additive constants). Then, the process is repeated. In the table, for clarity, a few lines corresponding to successive steps of the conversion are given.

**Table 8.1** Transformation of phases for oscillators 1–4 at successive stages of activity.

| | 1 | 2 | 3 | 4 |
|---|---|---|---|---|
| 0 | $\varphi_0$ | | $\theta_0$ | |
| $\frac{1}{2}$ | | $2\varphi_0 + \text{const}$ | | $2\theta_0 + \text{const}$ |
| 1 | $2\theta_0 + \text{const}$ | | $4\varphi_0 + \text{const}$ | |
| $\frac{3}{2}$ | | $4\theta_0 + \text{const}$ | | $8\varphi_0 + \text{const}$ |
| 2 | $8\varphi_0 + \text{const}$ | | $8\theta_0 + \text{const}$ | |

As seen from the table, after each next period of slow modulation of parameters the phases of two initially active oscillators are transformed according to the relations

$$\begin{aligned} \varphi_{n+1} &= 2\theta_n + \text{const} \ (\bmod 2\pi), \\ \theta_{n+1} &= 4\varphi_n + \text{const} \ (\bmod 2\pi). \end{aligned} \tag{8.21}$$

In other words, a two-dimensional vector $\mathbf{v}_n = (\varphi_n, \theta_n)$ whose components are defined modulo $2\pi$, is mapped to another vector $\mathbf{v}_{n+1} = (\varphi_{n+1}, \theta_{n+1})$ of the same type, i.e. this may be interpreted as a map defined on a torus. It has specific degeneration, namely, the complete phase sequence of $\varphi_n$ (or $\theta_n$) is composed of two independent subsequences, so that in the course of the time evolution their members alternate. Subsequences manifest chaotic dynamics. In two steps, small perturbations to each of them increase by eight times. Therefore, the map (8.21) is characterized by presence of two equal positive Lyapunov exponents $\Lambda_{1,2} = \frac{1}{2}\ln 8 \approx 1.0397$.

The results of the numerical solution of differential equations (8.20) show that the expected type of dynamics indeed occurs in a wide range of parameters. For a detailed analysis we select the case $\omega_0 = 2\pi, T = 8, A = 4.5, \varepsilon = 0.6$. Figure 8.10 shows the dynamic variables for the four oscillators plotted as functions of time.

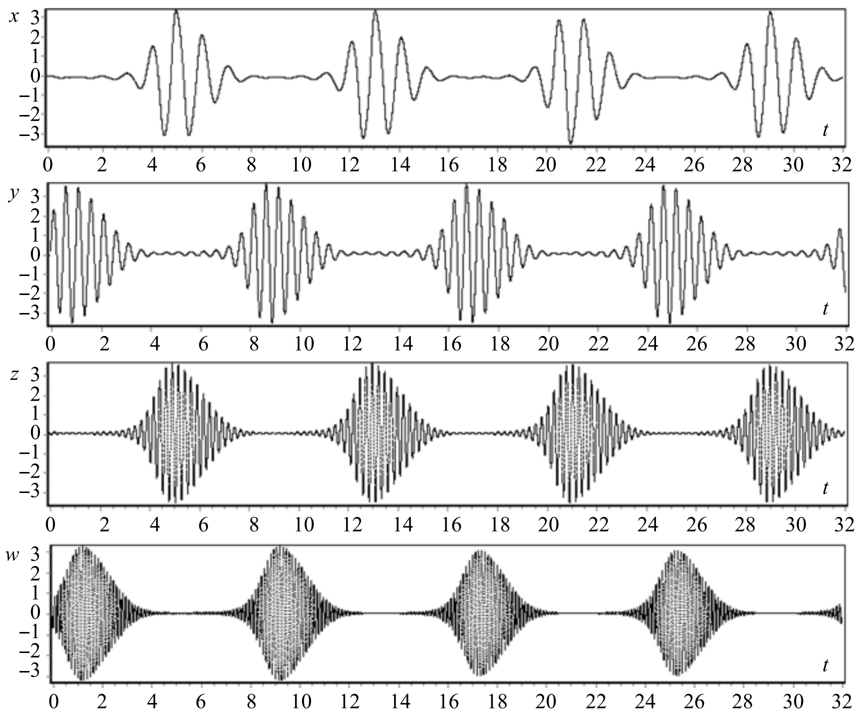


**Fig. 8.10** Dynamical variables for four oscillators constituting the system (8.20) plotted as functions of time at $\omega_0 = 2\pi, T = 8, A = 4.5, \varepsilon = 0.6$.

Each oscillator generates a sequence of pulses following one another with time intervals $T$. The carrier frequencies correspond to the natural frequencies of the partial oscillators. Chaos reveals itself in chaotic variation of the phases of the carrier in respect to envelops of the signals. The presence of chaos is caused by the described mechanism of phase transfer between the oscillators from the previous stages of the process to the next ones.

Figure 8.11 shows the iteration diagrams for the phases, which indicate that their dynamics actually correspond in certain approximation to the map (8.21). Phases, each corresponding to the next stage of the activity of the oscillators 1 and 3, are determined at a time instant fixed with respect to the modulation signal according to the formulas

$$\varphi_n = \arg(x - i\dot{x}/\omega_0), \quad \theta_n = \arg(z - i\dot{z}/\omega_0). \tag{8.22}$$

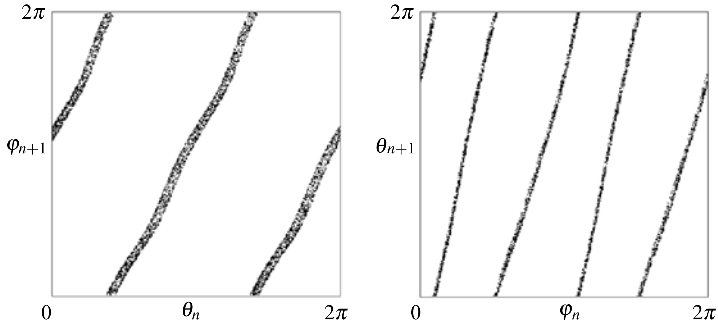


**Fig. 8.11** Iteration diagrams for phases of the oscillators 1 and 3, respectively, $\varphi_n$ and $\theta_n$ at successive stages of their activity at $\omega_0 = 2\pi, T = 8, A = 4.5, \varepsilon = 0.6$.

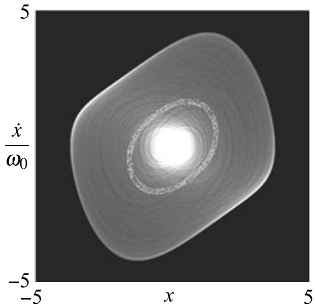


**Fig. 8.12** Attractor projection onto the phase plane of the oscillator 1 shown in gray scale. White dots correspond to the stroboscopic Poincaré section.

Figure 8.12 shows portrait of the attractor in the projection from the extended nine-dimensional phase space to the phase plane of the first oscillator. The picture is presented in gray scale, so that lighter pixels correspond to a relatively great probability for the residence of the representative orbit there. White dots correspond to instants of reaching the maximum values of the modulated bifurcation parameter in the first oscillator; they form a portrait of the attractor in the Poincaré section.

To evaluate the Lyapunov exponents, in a computer program we calculate the Poincaré map from numerical solution of Eqs. (8.20) and the Jacobian matrix by simultaneous solution of eight replicas of the linearized variation equations. With multiple iteration of this procedure, the evolution of the eight vectors of small perturbations is monitored by multiplying them by the Jacobian matrices. After each step of the iterations the Gram-Schmidt orthogonalization process is applied and normalization is performed for the eight vectors (Appendix A). Lyapunov exponents are defined as the average rates of growth or decrease the accumulated sums of logarithms of the norms of the vectors.

Figure 8.13 shows the dependence of the Lyapunov exponents for the stroboscopic Poincaré map on the parameter modulation magnitude $A$ at fixed other parameters. In a wide range of parameter variation the largest two exponents remain almost constant and close to (ln 8)/2. Particularly, at $A = 4.5$ the Lyapunov exponents are

$$\begin{array}{llll} \Lambda_1 = 1.038, & \Lambda_2 = 1.037, & \Lambda_3 = -4.622, & \Lambda_4 = -5.077, \\ \Lambda_5 = -7.914, & \Lambda_6 = -8.403, & \Lambda_7 = -10.335, & \Lambda_8 = -10.722, \end{array} \tag{8.23}$$

and the attractor dimension in the Poincaré section from the Kaplan-Yorke formula is 2.449.

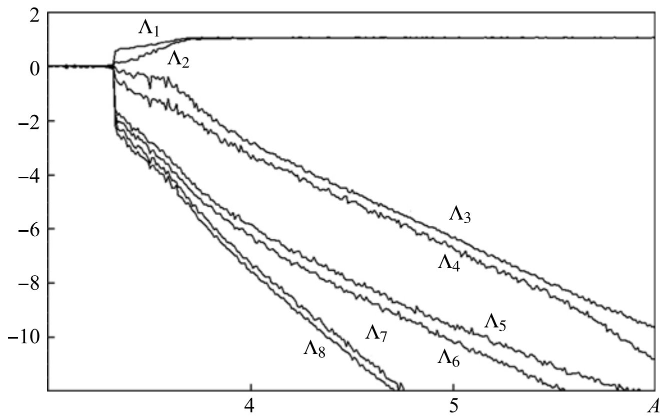


**Fig. 8.13** Lyapunov exponents versus the parameter of the modulation depth $A$ at $\omega_0 = 2\pi, T = 8, \varepsilon = 0.6$.

Figure 8.14 shows the Fourier power spectrum of the signal represented as the sum of the variables related to all four oscillators $X = x + y + z + w$. Spectrum is continuous that reflects the chaotic nature of the dynamics on the attractor. In the spectrum one can see four well-defined widened peaks, which correspond to the natural frequencies of four oscillators constituting the system. Discrete component, which is distinguishable on the left side of the spectrum corresponds to the frequency of slow periodic modulation of parameters.

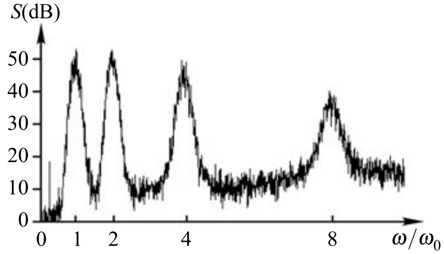


**Fig. 8.14** The power spectrum of the signal $X = x+y+z+w$ generated by the system at $\omega_0 = 2\pi, T = 8, A = 4.5, \varepsilon = 0.6$.

Summarizing, we outline a fascinating moment that the considered scheme exploits one of the key ideas of the theory of hydrodynamic turbulence——a cascade transfer of energy over the spectrum. The analogy, of course, is rather qualitative and heuristic in nature: in this case we talk about the transfer of excitation along a chain of oscillators that become active alternately with successive doublings of the frequency. A feature of the system is a quite broad total frequency band of the generated signal. This is due to the presence of a set of oscillators with essentially different natural frequencies. Number of oscillators in the chain can be increased that will further expand the frequency band of the generated chaotic signal. In a wide range of parameters the dynamics is characterized by the presence of two positive Lyapunov exponents, which are close in value and weakly depend on the parameters. The scheme obviously can be realized as an electronic device.

## 8.3 Hyperchaos and synchronous chaos in a system of coupled non-autonomous oscillators

Important research direction in nonlinear science concerns lattice models composed of blocks, or cells, manifesting certain types of dynamical behavior. Particularly, these studies are relevant to some fundamental challenging problems like foundation of statistical mechanics or origin of turbulence. In this context, one can mention seminal work of Fermi, Pasta and Ulam (Ford, 1992), cellular automata considered by Wolfram and others (Wolfram, 1986), coupled map lattices suggested and studied by Kaneko and others (Kaneko, 1993). As directly relating to the framework of the present book, one has to outline the work of Bunimovich and Sinai and others (Bunimovich and Sinai, 1988; 1993; Bricmont and Kupiainen, 1997; Järvenpää, 2005) devoted to investigation of lattices composed of elements demonstrating hyperbolic chaos. Particularly, it may be lattices of coupled one-dimensional expanding maps, or lattices composed of systems with uniformly hyperbolic attractors. It was shown that hyperbolic nature of chaos and strong chaotic properties, like existence of the absolutely continuous SRB measure, positive topological and metric entropy, persist for the coupled systems while the coupling strength is not too great. These results become essential now, when we can handle feasible systems with uniformly hyperbolic chaotic attractors. To start, it is natural to turn to a situation of minimal number of coupled subsystems manifesting the hyperbolic chaos (Kuptsov and Kuznetsov, 2006). Here we consider a model composed of two pairs of non-autonomous alternately excited van der Pol oscillators discussed in Chap. 4, the whole system consists of four oscillators, and just fits the common topic of the present chapter.

### *8.3.1 Equations and basic modes of operation*

Let us examine a system of two coupled elements, each of which is a pair of alternately excited van der Pol oscillators; so, the model (4.9) just corresponds to a single block. In the following set of equations

$$\begin{aligned} \ddot{x}_1 - (A\cos(2\pi t/T) - x_1^2)\dot{x}_1 + \omega_0^2 x_1 &= \varepsilon y_1 \cos\omega_0 t + d(\dot{x}_2 - \dot{x}_1), \\ \ddot{y}_1 - (-A\cos(2\pi t/T) - y_1^2)\dot{y}_1 + 4\omega_0^2 y_1 &= \varepsilon x_1^2 + d(\dot{y}_2 - \dot{y}_1), \\ \ddot{x}_2 - (A\cos(2\pi t/T) - x_2^2)\dot{x}_2 + \omega_0^2 x_2 &= \varepsilon y_2 \cos\omega_0 t + d(\dot{x}_1 - \dot{x}_2), \\ \ddot{y}_2 - (-A\cos(2\pi t/T) - y_2^2)\dot{y}_2 + 4\omega_0^2 y_2 &= \varepsilon x_2^2 + d(\dot{y}_2 - \dot{y}_1), \end{aligned} \tag{8.24}$$

the variables relating to two subsystems are indicated with subscripts 1 and 2, respectively, and $d$ is parameter of coupling of the subsystems. We assume, as usual, that the period of parameter modulation $T$ is an integer multiple of the period of the auxiliary signal $2\pi/\omega_0$.

Coupling in Eqs. (8.3) is defined in such a way that the terms responsible for the interaction of the subsystems vanish at the coincidence of their states. The corresponding condition determines an invariant manifold of symmetric motions in the phase space of the joined system. This manifold contains an invariant set, which is identical in structure to the attractor of the partial system (4.9), i.e. it is the suspension of the Smale-Williams solenoid.

The coupling terms in Eqs. (8.3) are proportional to differences of time derivatives (the generalized velocities). Hence, the coupling is *dissipative* in the sense that it provides tendency to convergence and equalization of instantaneous states of the subsystems. As individual subsystems are chaotic, the dynamics is determined by competition of two factors: the divergence of states of the subsystems because of intrinsic sensitivity to initial conditions, and the tendency to convergence of the states due to the coupling. At zero, as well as at small values of the coupling parameter $d$, the first factor dominates; chaotic motions in the subsystems are independent or weakly correlated. At large values of the coupling parameter, the second factor prevails, and the complete chaotic synchronization occurs: both subsystems evolve chaotically in time, but in perfect synchrony where the instant states at any time are identical. It is called the complete chaos synchronization (Pikovsky et al., 2002).

Figure 8.15 illustrates dynamics of the model (8.24) at $\omega_0 = 2\pi, T = 10, \varepsilon = 0.5, A = 3$ for two values of the coupling parameter. The smaller value corresponds to chaotic, roughly independent, motions in both subsystems (panel (a)), and the larger one to emergency of chaos synchronization in the course of the time evolution (panel (b)). The relevant features of the processes reveal themselves in large time scales; so, we present fragments of the waveforms separated by relatively long time intervals (marked by three dots). Observe that in the panel (a) the phase differences between the simultaneously active partner oscillators of two subsystems fluctuate from one to other fragment of the waveform. In the second case, the phase difference vanishes in the course of time evolution, and the motions of the subsystems become synchronous.

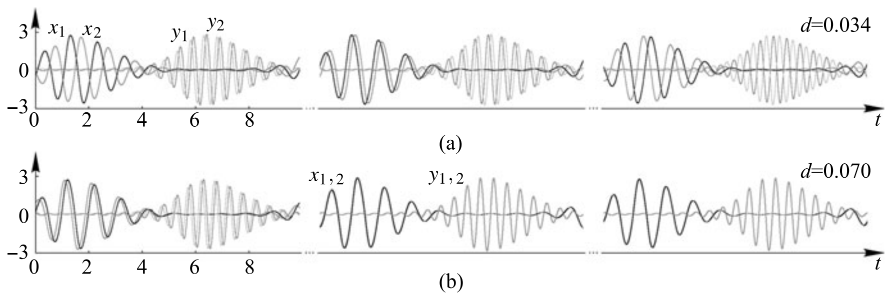


**Fig. 8.15** Fragments of typical time dependence for the dynamical variables of the model (8.24) illustrating nature of behavior in asynchronous **(a)** and synchronous **(b)** chaotic regimes at $\omega_0 = 2\pi, T = 10, A = 3, \varepsilon = 0.5$.

Figure 8.16 shows Lyapunov exponents evaluated for the stroboscopic eight-dimensional Poincaré map of the system and plotted against the coupling parameter at $\omega_0 = 2\pi, T = 10, \varepsilon = 0.5, A = 3$. The data were obtained in computations based on the Benettin algorithm from numerical solution of Eqs. (8.24) supplemented with eight sets of linearized equations for perturbation vectors, which are subjected orthogonalization and normalization at each period of the parameter modulation (Appendix A). Observe that the largest Lyapunov exponent in the whole parameter range remains almost constant close to the value $\ln 2 = 0.693\cdots$. The second Lyapunov exponent is of the same value at zero coupling, but gradually decreases as $d$ grows. Its passage through zero is associated with transition from asynchronous to synchronous behavior approximately at $d_c$=0.069. Other Lyapunov exponents are negative everywhere.

Chaotic attractors in the composite system (8.24) surely relate to the uniformly hyperbolic class in two limit cases.

Certainly, it is so at zero coupling. Here the system decomposes to two independent subsystems, each possessing the hyperbolic attractors of Smale-Williams type

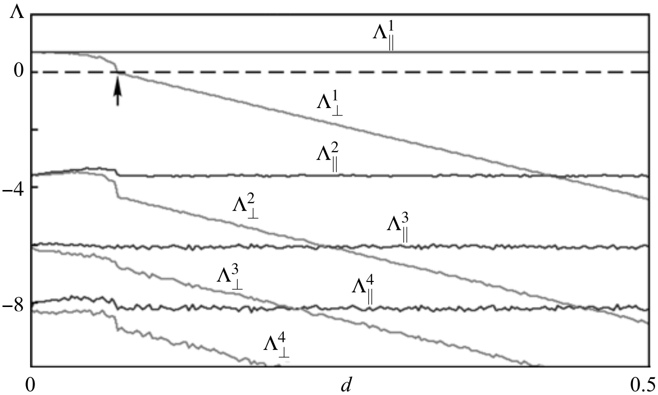


**Fig. 8.16** Lyapunov exponents for the system (8.24) versus parameter of strength of dissipative coupling $\omega_0 = 2\pi, T = 10, \varepsilon = 0.5, A = 3$. The subscripts $(\|, \perp)$ designate the exponents relating, respectively, to symmetric and anti-symmetric (transversal) parts of the Lyapunov spectrum. The synchronization-desynchronization transition is indicated with an arrow.

in stroboscopic map, and the attractor of the whole system is also uniformly hyperbolic. Because of its structural stability, such nature of the attractor persists for close situations of non-zero coupling while it is small enough. The same conclusion follows from the studies (Bunimovich and Sinai, 1988; 1993).

At large couplings, in the situation of synchronous chaotic motion, attractor of the composite system is of the same structure as that of a single block, which is uniformly hyperbolic. The only difference is presence of additional directions associated with strong compression in the phase space of doubled dimension.

On the road from the first to the second situations, under gradual increase of the coupling parameter, the hyperbolicity is violated somewhere because the transition from the first to the second types of dynamics implies change of dimensions of the stable and unstable manifolds; this transition is a separate subject for the analysis.

According to Chap. 4, an illuminating approach to understanding dynamics of a single subsystem is monitoring transformations of phase shifts on successive stages of activity of the oscillators. The same hint is appropriate for the coupled systems.

The top row of Fig. 8.17 shows portraits for attractors of the model (8.24) in the stroboscopic cross-section in projection onto the plane of the phase variables $(\varphi_1, \varphi_2)$ evaluated for oscillators of frequency $\omega_1$ relating to the first and the second subsystems. The diagrams correspond to four values of coupling parameter $d$ indicated on the plots; the remaining parameters are $\omega_0 = 2\pi, T = 20, A = 2, \varepsilon = 0.5$. Panels (a-c) relate to asynchronous dynamics, and panel (d) relates to synchronous regime.

Accounting symmetry of the model in respect to exchange of indices 1 and 2, it is appropriate to introduce the symmetric and anti-symmetric variables defined modulo $2\pi$ instead of two phases $\varphi_1$ and $\varphi_2$ relating to simultaneously active oscillators of both subsystems, namely,

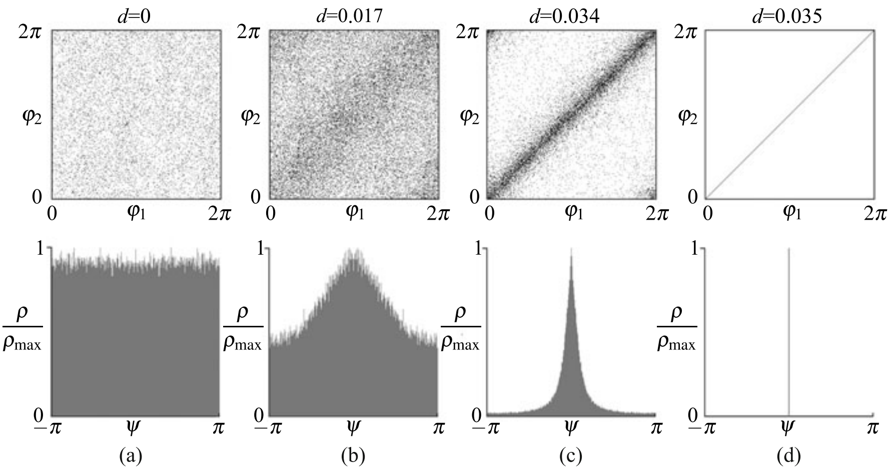


**Fig. 8.17** Portraits of a trajectory on the attractors and histograms for distribution of the phase shifts between the subsystems obtained in computations with model (8.24) in chaotic asynchronous (**a**-**c**) and synchronous (**d**) regimes at $\omega_0 = 2\pi, T = 20, A = 2, \varepsilon = 0.5$.

$$\phi = \varphi_1 + \varphi_2 \quad \text{and} \quad \psi = \varphi_1 - \varphi_2. \tag{8.25}$$

The bottom row of Fig. 8.17 shows histograms for distribution of the phase shifts $\psi$ between the subsystems obtained in computations for model (8.24) at the same parameters. Observe gradual formation of a distribution with pronounced maximum at zero under graduate increase of coupling in non-synchronous regimes, and appearance of Dirac delta function distribution after the synchronization transition.

Figure 8.18 shows iteration diagrams for the phase variables $\phi$ and $\psi$. In diagrams in the top row the symmetric and anti-symmetric phases are plotted at subcritical coupling. In this hyperchaotic regime both variables evolve according to Bernoulli-like maps; two Lyapunov exponents are positive here. The second row shows diagrams for anti-symmetric variables in the nearly critical situation (left) and in the case of coupling strength greater than the critical one. In the last case special procedure was used to obtain the plot from processing the transients; attractor of the synchronous chaotic regime corresponds in these coordinates to a point in the origin as indicated by arrow.

Slightly below the synchronization threshold, a dynamical behavior occurs called the *on-off intermittency* (Platt et al., 1993; Hilborn, 2000; Mosekilde et al., 2002; Schuster and Just, 2005). The system spends most time getting very close to the synchronous state, but from time to time appears to be far from that state; these periods occupy the smaller proportion of time at which we are closer to the point of the transition. Figure 8.19 illustrates this phenomenon for the model (8.24) with the plot of the phase difference between the subsystems depending on time.

Besides the on-off intermittency, transition from non-synchronous to synchronous chaos is accompanied by occurrence of some specific phenomena, like riddling

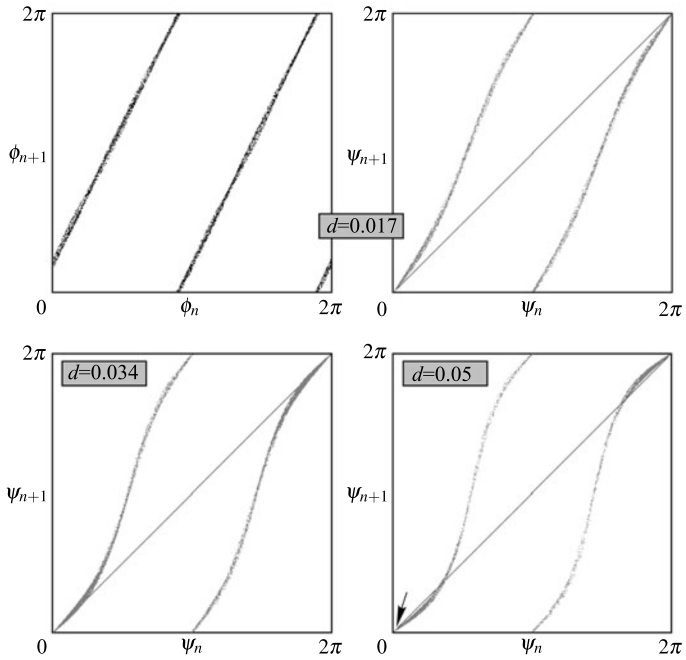


**Fig. 8.18** Iteration diagrams for the model (8.24) at $t_n = nT$ for three values of coupling parameter $d$ and $\omega_0 = 2\pi, T = 20, A = 2, \varepsilon = 0.5$. The top row shows diagrams for symmetric and anti-symmetric phase variables determined according to (8.25) for the case of subcritical coupling. The second row shows diagrams for anti-symmetric variables in nearly critical situation (left) and in the case of coupling larger than the critical value (right). In the last diagram attractor of the synchronous chaotic regime is a point in the origin indicated by the arrow.

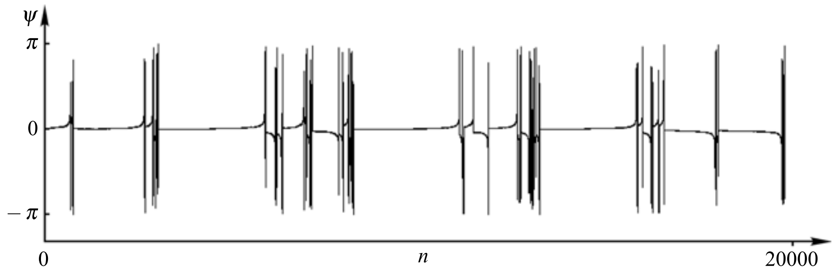


**Fig. 8.19** On-off intermittency in the model (8.24) at $\omega_0 = 2\pi, T = 20, A = 2, \varepsilon = 0.5$ and $d = 0.0347$. The phase differences between two subsystems are plotted evaluated at time instants $nT$.

basins and bubbling attractor, examined in the literature in the context of the chaos synchronization with examples of coupled systems manifesting non-hyperbolic attractors (Anishchenko, 2002; Mosekilde et al., 2002; Ott, 2002; Ashwin, 2005).

Now, they have to be reconsidered to reveal features that may be intrinsic to the case of uniformly hyperbolic chaos in the subsystems.

### 8.3.2 Equations for slow complex amplitudes

More convenient model for detailed studies may be obtained with reformulation of the problem in terms of equations for slow complex amplitudes. Applying this approach to Eqs. (8.24), like described in Sect. 4.1 and 4.3, one can derive the following set of shortened equations

$$\begin{aligned}
\dot{a}_1 &= \frac{1}{2}(A\cos(2\pi t/T) - |a_1|^2)a_1 - \frac{1}{4}i\varepsilon\omega_0^{-1}b_1 + \frac{1}{2}d(a_2 - a_1),\\
\dot{b}_1 &= \frac{1}{2}(-A\cos(2\pi t/T) - |b_1|^2)b_1 - \frac{1}{4}i\varepsilon\omega_0^{-1}a_1^2 + \frac{1}{2}d(b_2 - b_1),\\
\dot{a}_2 &= \frac{1}{2}(A\cos(2\pi t/T) - |a_2|^2)a_2 - \frac{1}{4}i\varepsilon\omega_0^{-1}b_2 + \frac{1}{2}d(a_1 - a_2),\\
\dot{b}_2 &= \frac{1}{2}(-A\cos(2\pi t/T) - |b_2|^2)b_2 - \frac{1}{4}i\varepsilon\omega_0^{-1}a_2^2 + \frac{1}{2}d(b_1 - b_2).
\end{aligned} \tag{8.26}$$

Computations confirm that dynamics governed by these equations agrees well with that for the original model (at least at the parameter values assigned in the previous subsection). So we can use this version of the model to explain essential features of the observed behavior.

First, let us discuss Lyapunov exponents of the symmetric invariant set S defined by the relations $a_1 \equiv a_2, b_1 \equiv b_2$, which represents attractor of the composite system associated with chaos synchronization at large couplings. In the subcritical range of the coupling parameter this set is not attractive. This set is the Smale-Williams solenoid in the stroboscopic Poincaré section.

Setting $a_{1,2}(t) = a(t) + \tilde{a}_{1,2}(t), b_{1,2}(t) = b(t) + \tilde{b}_{1,2}(t)$ we obtain in linear approximation for perturbations of the reference trajectory the following equations:

$$\begin{aligned}
\dot{\tilde{a}}_1 &= \frac{1}{2}(A\cos(2\pi t/T) - 3|a|^2)\tilde{a}_1 - a^2\tilde{a}_1^* - \frac{1}{4}i\varepsilon\omega_0^{-1}\tilde{b}_1 + \frac{1}{2}d(\tilde{a}_2 - \tilde{a}_1),\\
\dot{\tilde{b}}_1 &= \frac{1}{2}(-A\cos(2\pi t/T) - 3|b|^2)\tilde{b}_1 - b^2\tilde{b}_1^* - \frac{1}{2}i\varepsilon\omega_0^{-1}a\tilde{a}_1 + \frac{1}{2}d(\tilde{b}_2 - \tilde{b}_1),\\
\dot{\tilde{a}}_2 &= \frac{1}{2}(A\cos(2\pi t/T) - 3|a|^2)\tilde{a}_2 - a^2\tilde{a}_2^* - \frac{1}{4}i\varepsilon\omega_0^{-1}\tilde{b}_2 + \frac{1}{2}d(\tilde{a}_1 - \tilde{a}_2),\\
\dot{\tilde{b}}_2 &= \frac{1}{2}(-A\cos(2\pi t/T) - 3|b|^2)\tilde{b}_2 - b^2\tilde{b}_2^* - \frac{1}{2}i\varepsilon\omega_0^{-1}a\tilde{a}_2 + \frac{1}{2}d(\tilde{b}_1 - \tilde{b}_2).
\end{aligned} \tag{8.27}$$

It may be rewritten for symmetric variables $\tilde{a}_{||} = \tilde{a}_1 + \tilde{a}_2, \tilde{b}_{||} = \tilde{b}_1 + \tilde{b}_2$ as

$$\begin{aligned}
\dot{\tilde{a}}_{||} &= \frac{1}{2}(A\cos(2\pi t/T) - 3|a|^2)\tilde{a}_{||} - a^2\tilde{a}_{||}^* - \frac{1}{4}i\varepsilon\omega_0^{-1}\tilde{b}_{||}, \\
\dot{\tilde{b}}_{||} &= \frac{1}{2}(-A\cos(2\pi t/T) - 3|b|^2)\tilde{b}_{||} - b^2\tilde{b}_{||}^* - \frac{1}{2}i\varepsilon\omega_0^{-1}a\tilde{a}_{||},
\end{aligned} \tag{8.28}$$

and for anti-symmetric ones $\tilde{a}_\perp = \tilde{a}_1 - \tilde{a}_2, \tilde{b}_\perp = \tilde{b}_1 - \tilde{b}_2$ as

$$\begin{aligned}
\dot{\tilde{a}}_\perp &= \frac{1}{2}(A\cos(2\pi t/T) - 3|a|^2)\tilde{a}_\perp - a^2\tilde{a}_\perp^* - \frac{1}{4}i\varepsilon\omega_0^{-1}\tilde{b}_\perp - d\tilde{a}_\perp, \\
\dot{\tilde{b}}_\perp &= \frac{1}{2}(-A\cos(2\pi t/T) - 3|b|^2)\tilde{b}_\perp - b^2\tilde{b}_\perp^* - \frac{1}{2}i\varepsilon\omega_0^{-1}a\tilde{a}_\perp - d\tilde{b}_\perp.
\end{aligned} \tag{8.29}$$

From these equations it is obvious that spectrum of Lyapunov exponents decomposes onto two parts, the symmetric one obtained from Eqs. (8.28) and anti-symmetric or transversal exponents from (8.29).

The equations for symmetric perturbations (8.28) coincide exactly with respective equations for a single subsystem (4.19). Thus, the Lyapunov exponents are simply equal to those obtained for the single system.

As to the second part of the spectrum, one can notice that substitution $\tilde{a}_\perp = \tilde{a}e^{-dt}, \tilde{b}_\perp = \tilde{b}e^{-dt}$ transforms (8.29) exactly to (8.28). It means that the transversal Lyapunov exponents are connected with those relating to symmetric perturbations by relations $\lambda_\perp^i = \lambda_{||}^i - d$, or, for the Poincaré map, $\Lambda_\perp^i = \Lambda_{||}^i - dT$ where $T$ is the period of modulation, and $i$ is index numbering the Lyapunov exponents from 1 to 4. The dependence of $\Lambda_\perp^i$ on coupling parameter is linear (this is clearly visible in Fig. 8.16).

Transition from synchronous to non-synchronous chaos observed with decrease of the coupling parameter $d$ occurs at zero value of the largest transversal exponent, so, the critical coupling is $d_c = \Lambda_{||}^1/T$. Accounting that $\Lambda_{||}^1 \approx \ln 2$, we obtain an approximate estimate for the critical coupling parameter $d_c \approx 0.693/T$. It agrees well with the computations.

Let us derive an approximate map describing dynamics in terms of the phases. To do this, we note that the effect of coupling appears on time scale of order $T$ while the phase doubling in individual subsystems is characterized by essentially less time scale. So, the phase doubling may be accounted neglecting the coupling and regarded as happening independently in both subsystems.

Due to the coupling, a relatively slow process of evolution of the phase difference between the subsystems takes place for each pair of simultaneously active oscillators, which can be described as follows. Accounting identical time dependence of the bifurcation parameter modulation in coupled pairs of oscillators $a_1$ and $a_2$, it is reasonable to assume that their amplitudes are approximately equal to each other in the whole period of activity: $a_1 \approx A(t)e^{i\varphi}, a_2 \approx A(t)e^{i\theta}$. Substituting these expressions into respective equations (8.26), multiplying them by the exponentials $e^{-i\varphi}, e^{-i\theta}$, and subtracting the equations, we take the imaginary part and obtain the equation for the evolution of the anti-symmetric phase variable $\psi = \varphi - \theta$ of the form

$$\dot{\psi} = -d\sin\psi. \tag{8.30}$$

It may be solved analytically; the convenient representation of the solution is $\psi = \psi_0 + \arctan \dfrac{(1-e^{-dt})\tan\psi_0}{1+e^{-dt}\tan^2\psi_0}$, where $\psi_0$ designates the initial value of $\psi$. The same is true in the second half of the modulation period in respect to the complex amplitudes $b_1$ and $b_2$. Summarizing, the transformation of the phase in one modulation period consists of the slow evolution of the anti-symmetric variable in accordance with Eq. (4.19) of full duration $T$, and of a fast event of doubling of both phases $\varphi$ and $\theta$. So, we have to write

$$\begin{aligned} \varphi_{n+1} &= 2\left(\varphi_n + \frac{1}{2}\arctan\frac{(1-e^{-dT})\tan(\theta_n-\varphi_n)}{1+e^{-dT}\tan^2(\theta_n-\varphi_n)}\right) + c(\bmod 2\pi), \\ \theta_{n+1} &= 2\left(\theta_n + \frac{1}{2}\arctan\frac{(1-e^{-dT})\tan(\varphi_n-\theta_n)}{1+e^{-dT}\tan^2(\theta_n-\varphi_n)}\right) + c(\bmod 2\pi), \end{aligned} \tag{8.31}$$

where $c$ is some constant.[3]

Figure 8.20 shows the plots for the anti-symmetric variable $\psi_n = \varphi_n - \theta_n$ according to the relations (8.31). They have to be compared with empirical plots in Fig. 8.18. Observe that the forms of the curve evolve with growth of the coupling parameter in agreement with qualitative explanations and numerical results. At small coupling, the map for the anti-symmetric phase looks equivalent to Bernoulli map; here the slope of the curve in the origin is greater than 1. At the critical situation $d = d_c$ the curve touches the angle bisector line, and for $d > d_c$ one observes intersections of the curve with that line; in the origin it corresponds to stable fixed point associated with the regime of complete phase synchronization. Figure 8.21 shows a plot illustrating the on-off intermittency close to the critical value of the coupling parameter in the simplified model (8.31). Observe good qualitative correspondence with Fig. 8.19.

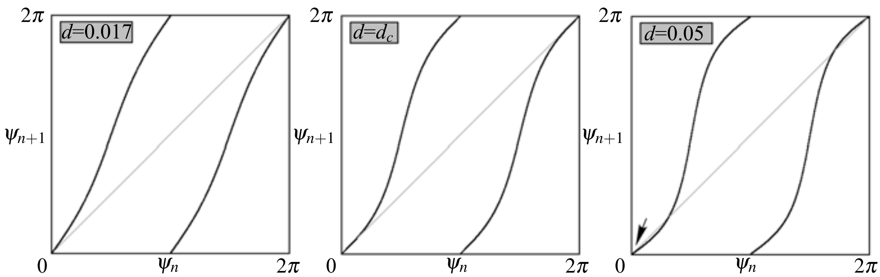


**Fig. 8.20** Plots of the analytic approximation for the map for the anti-symmetric phase according to Eqs. (8.31) for three values of coupling parameter $d$ at $T = 20$. The left diagram corresponds to subcritical situation (no synchronization), the right one to supercritical coupling (synchronization takes place associated with the fixed point on the plot indicated with arrow), and the central diagram relates to the intermediate critical situation.

[3] From this presentation one can easily see how to compose coupled map lattices associated with systems constituted by large number of the elementary blocks, like those studied in (Bunimovich and Sinai, 1988; 1993).

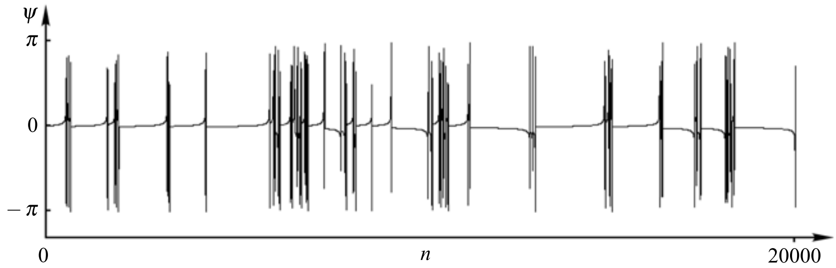


**Fig. 8.21** On-off intermittency in the map (8.31) at $T = 20$ and $d = 0.03462$. The anti-symmetric phase variable is plotted versus the discrete time $n$.

One has to recognize that the model (8.31) is not perfect because it does not embrace some subtle details of the synchronization transition, like riddling basins. In the case of coupled elements with hyperbolic attractor this phenomenon is not so pronounced, but it can be revealed in a narrow parameter range near the transition. To illustrate this, we turn to computations based on Eqs. (8.26).

To proceed we note that the symmetric invariant set S of the system, which is the Smale-Williams solenoid in the stroboscopic Poincaré section, contains invariant subsets, including, particularly, the unstable periodic orbits of different periods (cycles), and the degrees of instability of these subsets in respect to the transversal perturbations differ, generally speaking, from that averaged over the whole set S.[4] Close to the synchronization threshold this circumstance determines effects of riddling basins as well as appearance of the so-called bubbling attractor.

To be concrete, several periodic orbits were determined in computations for the model (8.26) at $T = 4, \varepsilon = 0.2\pi, A = 8$. The relatively small modulation period $T$ is selected here to make the examined effects more pronounced. For these orbits Floquet multipliers $\mu$ were evaluated, and the Lyapunov exponents $\lambda$ are expressed as $\lambda = P^{-1} \ln \mu$, where $P = pT$ is the period of the orbit.

Figure 8.22 plots the largest transversal Lyapunov exponents for the periodic orbits with numbers $p$ ranging from 1 to 7. Observe that with decrease of the coupling parameter, the periodic orbits become transversely unstable at different parameter values in some range around the critical point where it happens for the symmetric invariant set in the sense of a typical trajectory belonging to it. In the region slightly above the synchronization threshold, due to existence of transversally unstable invariant subsets, the basin of attraction for the symmetric attractor is riddled (Mosekilde et al., 2002; Ashwin, 2005). To visualize this basin we consider a two-dimensional section in the phase space, on which dots will be marked belonging and not belonging to the basin in white and black, respectively. For this, we scan a square domain on the plane of variables Re $a_1$ and Re $a_2$, assigning other variables some values associated with an arbitrarily chosen point on the symmetric invariant set. In the plot, the diagonal Re $a_1$= Re $a_2$ represents the symmetric attractor. Then, the computations are performed at each pixel for sufficiently large number

[4] In the approximate model (8.38) this difference is neglected.

of steps of iteration of the stroboscopic Poincaré map, and presence or absence of synchronization is diagnosed by monitoring the norm of the state difference for the subsystem, starting from certain step.[5]

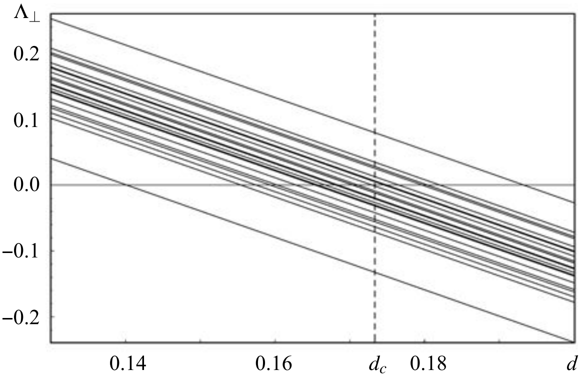


**Fig. 8.22** The largest transversal Lyapunov exponents for cycles with periods ranging from 1 to 7 versus the coupling parameter at $A = 8$, $T = 2$, $\varepsilon = 0.05$. The dotted line marks the synchronization threshold for the symmetric attractor.

It was found possible to detect confidently the effect of the basin riddling for symmetric attractor of the system (8.26) only in very small neighborhood of the synchronization transition. Figure 8.23 shows the results of the procedure of visual-

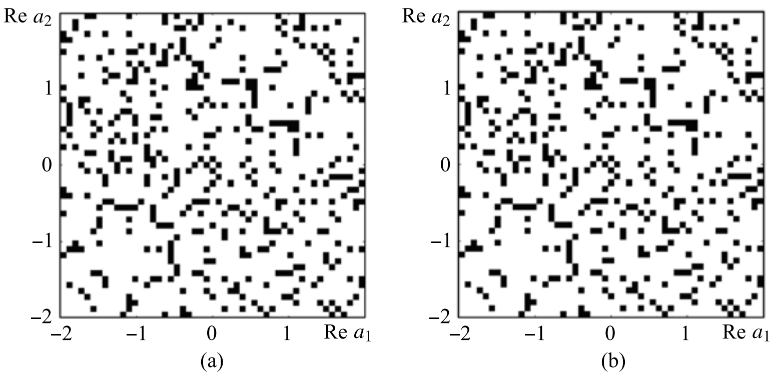


**Fig. 8.23** Riddling of the basin of symmetric attractor of the system (8.26) depicted with low **(a)** and high **(b)** resolution of the recognition procedure. Black color marks the points, from which the system is detected not to arrive at the symmetric attractor. Parameters assigned are $A = 8, T = 2, \varepsilon = 0.05, d = 0.173$. Im $a_1(0) =$ Im $a_2(0) = 0.37, b_1(0) = b_2(0) = -0.05 + 0.07i$.

[5] Rigorously speaking, this procedure guarantees the recognition of convergence or divergence from the symmetric attractor with some probability; it is not absolutely reliable. However, for qualitative illustrations we need here, it is sufficient.

ization of the riddling at $d = 0.173$. One can see that intrinsic feature of the basin is absence of any areas of notable size which would not contain points from the basin. With increase of resolution of the recognition procedure each structural element of the picture breaks down onto smaller disconnected elements, and so on. Such structure may be explained by a rather low density of the invariant subsets in the symmetric attractor responsible for origin of the riddling. In turn, this is connected with hyperbolic nature of the attractor of a single subsystem.

We now consider the effect of "bubbling" of the attractor, which is also associated with the presence of transverse instability of the invariant subsets of the set S (Anishchenko, 2002; Mosekilde et al., 2002; Ott, 2002). Suppose the system is in the supercritical region near the threshold of synchronization. Choose initial conditions so that the system goes into a symmetric attractor, i.e. the distance between the subsystems $\sqrt{|a_1 - a_2|^2 + |b_1 - b_2|^2}$ decreases for a sufficiently large observation time. Then, we retain the previous initial conditions and parameters, but in the course of the numerical solution add a little random noise to the variables. Under its influence, the system can fall in a neighborhood of transverse unstable set, and it will lead to a burst of desynchronized oscillations. After some time the system returns to a symmetric attractor and will remain in his neighborhood as long as the other random shift will cause a new burst.

The "bubbling" is illustrated in Fig. 8.24. In panel (b) one can see that the presence of noise of small amplitude (of order 0.001) causes bursts of oscillations whose amplitude exceeds the amplitude of noise by orders of magnitude. However, the system turns out to be quite rare in the vicinity of transversely unstable invariant sets.

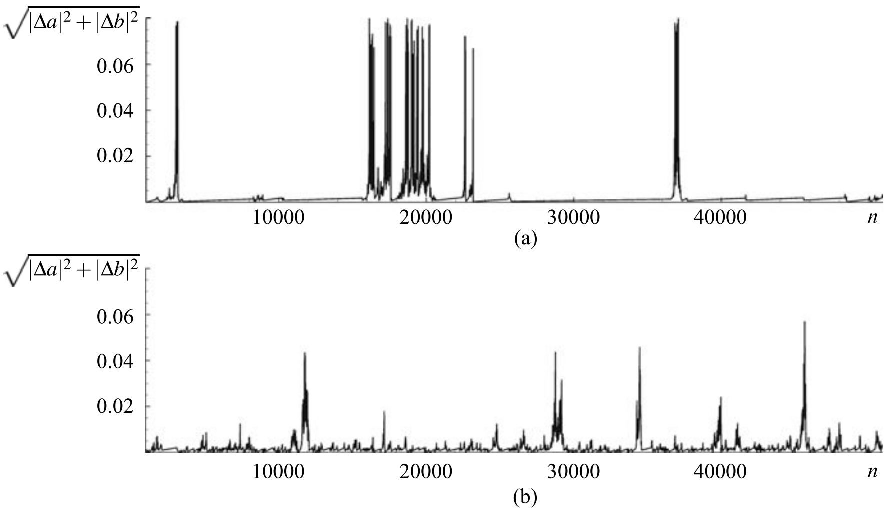


**Fig. 8.24** Illustration of "bubbling attractor": dependence of the distance between instant states of the subsystems in model (8.26) versus number of steps of the stroboscopic Poincaré map at $A = 8, T = 2, \varepsilon = 0.05$. Small noise is added in the course of integration at each step of the finite-difference scheme of order 0.001. The coupling parameter is $d = 0.173$ **(a)** and $d = 0.174$ **(b)**.

As seen from panel (b), a little increase of the coupling parameter leads to essential decrease in probability of appearance of bursts, and the peaks in this figure are lower than those in the previous plot. In other words, in the case of riddling, the effect of bubbling attractor also disappears rapidly with increasing $d$.

## References


Anishchenko, V.S.: Nonlinear Dynamics of Chaotic and Stochastic Systems: Tutorial and Modern Developments. Springer, Heidelberg (2002).

Anishchenko, V.S., Kopeikin, A.S., Kurths, J., Vadivasova, T.E., Strelkova G.I.: Studying hyperbolicity in chaotic systems. Physics Letters A **270**, 301–307 (2000).

Anosov, D.V., Gould, G.G., Aranson, S.K., Grines, V.Z., Plykin, R.V., Safonov, A.V., Sataev, E.A., Shlyachkov, S.V., Solodov, V.V., Starkov, A.N., Stepin, A.M.: Dynamical Systems IX: Dynamical Systems with Hyperbolic Behaviour (Encyclopaedia of Mathematical Sciences) (v. 9). Springer-Verlag, New York (1995).

Arnold, V.I.: Ordinary Differential Equations. The MIT Press, Somerville, MA (1978).

Arnold, V. I., Avez, A.: Ergodic Problems in Classical Mechanics. Benjamin, New York (1968).

Ashwin, P.: Riddled basins and coupled dynamical systems. In: Chazottes, J.-R. and Fernandez, B.(eds.): Dynamics of Coupled Map Lattices and of Related Spatially Extended Systems, pp. 181–208. Springer, Berlin (2005).

Bricmont, J., Kupiainen, A.: Infinite-dimensional SRB measures. Physica D **103**, 18–33 (1997).

Bunimovich, L.A, Sinai, Ya.G.: Spacetime chaos in coupled map lattices. Nonlinearity **1**, 491–516 (1988).

Bunimovich, L.A., Sinai, Ya.G.: Statistical mechanics of coupled map lattices. In: Kaneko, K. (ed.) Theory and Application of Coupled Map Lattices, pp. 169–189. John Wiley & Sons Ltd., New York (1993).

Devaney, R.L.: An Introduction to Chaotic Dynamical Systems. Westview Press, New York (2003).

Farmer, J., Ott, E., Yorke, J.: The dimension of chaotic attractors. Physica D **7**, 153–180 (1983).

Ford, J.: The Fermi-Pasta-Ulam problem: Paradox turns discovery. Physics Reports **213**, 271–310 (1992).

Grassberger, P., Procaccia, I.: Measuring the strangeness of strange attractors. Physica D **9,** 189–208 (1983).

Hilborn, R.C.: Chaos and Nonlinear Dynamics. Oxford University Press, Cambridge (2000).

Isaeva, O.B., Jalnine, A.Yu., Kuznetsov, S.P.: Arnold's cat map dynamics in a system of coupled nonautonomous van der Pol oscillators. Phys. Rev. E **74**, 046207 (2006).

Järvenpää, E.: SRB-measures for coupled map lattices. In: Chazottes, J.-R. and Fernandez, B.(eds.): Dynamics of Coupled Map Lattices and of Related Spatially Extended Systems, pp. 95–114. Springer (2005).

Kaneko, K. (ed.): Theory and Application of Coupled Map Lattices. John Wiley & Sons Ltd., Chichester (1993).

Kuptsov, P.V., Kuznetsov, S.P.: Transition to a synchronous chaos regime in a system of coupled non-autonomous oscillators presented in terms of amplitude equations. Nonlinear Dynamics (Izhevsk) **2**(3), 307–331 (2006) (In Russian).

Kuznetsov, S.P., Sokha, Y.I.: Hyperchaos in model nonautonomous system with a cascade excitation transmission through the spectrum. Izvestija VUZov – Applied Nonlinear Dynamics (Saratov) **18**, 24–32 (2010).

Landau, L.D., Lifshitz, E.M.: Fluid Mechanics (Course of Theoretical Physics, vol.6). Pergamon Press, London (1959).

Letellier C., Rössler, O.E.: Hyperchaos. Scholarpedia, **2**, 1936 (2007).

Matsumoto, T., Chua, L.O., Kobayashi, K.: Hyperchaos laboratory experiment and numerical confirmation. IEEE Trans, Circuits & Syst. **33**, 1143–1147 (1986).
Monin, A.S., Yaglom, A.M.: Statistical Fluid Mechanics, Volume II: Mechanics of Turbulence. Dover Publication, New York (2007).
Mosekilde, E., Maistrenko, Yu., Postnov, D.: Chaotic Synchronization: Applications To Living Systems. World Scientific Publication, Singapore (2002).
Ott, E.: Chaos in dynamical systems. Cambridge University Press, Cambridge (2002).
Pikovsky, A., Rosenblum, M., Kurtz, J.: Synchronization: A Universal Concept in Nonlinear Sciences. Cambridge University Press, Cambridge (2002).
Platt, N., Spiegel, E.A., Tresser C.: On-off intermittency: A mechanism for bursting. Phys. Rev. Lett. **70**, 279–282 (1993).
Reiterer, P., Lainscsek, C., Schürrer, F., Letellier C., Maquet, J.: A nine-dimensional Lorenz system to study high-dimensional chaos. Journal of Physics A **31**, 7121–7139 (1998).
Rössler, O.E.: An equation for hyperchaos. Physics Letters A **71**, 155–157 (1979).
Schuster, H.G., Just, W. Deterministic Chaos: An Introduction. Wiley-VCH Verlag GmbH & Co. KGaA, Weinheim, FRG (2005) .
Stoop, R., Peinke, J., Parisi, J., Röhricht B., Hübener, R. P.: A p-Ge semiconductor experiment showing chaos and hyperchaos. Physica D **35**, 425–435 (1989).
Wolfram, S.: Theory and applications of cellular automata. World Scientific Publication, Singapore (1986).

# Chapter 9
# Autonomous Systems Based on Dynamics Close to Heteroclinic Cycle

**Abstract** This chapter is devoted to autonomous models generating successive trains of oscillations with chaotic phase, which are designed on a base of systems with heteroclinic cycles in the phase space as suggested in our joint work (Kuznetsov and Pikovsky, 2007). The heteroclinic cycle, or the heteroclinic loop consists of several saddle fixed points and of trajectories joining them. The paradigm example for a heteroclinic cycle (Guckenheimer and Holmes, 1988) is discussed in Sect. 9.1. In a frame of the present research, it is interpreted as a set of equations for real amplitudes of interacting oscillators. The equations are supplemented with appropriate additional coupling terms in such a way that the alternating cyclic excitation of the oscillators occurs accompanied by transformation of the phases in accordance with some chaotic map. The number of oscillators may be three or more; so, in the models constructed in this way, the minimal phase space dimension is six. In Sect. 9.2—9.4 we discuss three models, one with attractor of Smale-Williams type, one possessing attractor with dynamics governed approximately by the Arnold cat map, and an example of hyperchaos that corresponds to attractor with two positive Lyapunov exponents. All these examples are designed on a base of equations written for complex amplitudes, and they implement non-resonance mechanism of the excitation transfer between the alternately exciting oscillators. In Sect. 9.5 we advance a model composed of a large number of van der Pol oscillators. Because of slow variation of the natural frequencies of the oscillators around the ring structure of the device, it appears possible to use resonance mechanism for the excitation transfer; so, the system may have prospects for implementing high-frequency chaos generators.

## 9.1 Heteroclinic connection: an example of Guckenheimer and Holmes

Normalized equation for complex amplitude of a single van der Pol oscillator above the threshold of the Andronov-Hopf bifurcation is $\dot{a} = (1 - |a|^2)a$, and respective

S. P. Kuznetsov, *Hyperbolic Chaos*

equation for the squared real amplitude is $\dot{r} = 2(1-r)r$, where $r = |a|^2$. Consider a symmetric system of some number of elements of such kind, which are arranged in a ring and mutually affect each other via nonlinear multiplying factor, and each amplitude variable suppresses those for the previous and the next elements in the ring in different degrees. A simple example composed of three elements is a set of equations

$$\begin{aligned}
\dot{r}_1 &= 2\left(1 - r_1 - \frac{1}{2}r_3 - 2r_2\right) r_1, \\
\dot{r}_2 &= 2\left(1 - r_2 - \frac{1}{2}r_1 - 2r_3\right) r_2, \\
\dot{r}_3 &= 2\left(1 - r_3 - \frac{1}{2}r_2 - 2r_1\right) r_3.
\end{aligned} \tag{9.1}$$

This just corresponds to the paradigm model of Guckenheimer and Holmes (Guckenheimer and Holmes, 1988) rewritten in terms of squared variables with concretized values of the coefficients.

Qualitatively, the behavior of the system may be explained as follows. Let us suppose that initially all three variables are relatively small, but, say, $r_1$ is the largest. Then, it grows in accordance with the first equation, reaches a level of order 1 and nearly saturates. Now, it suppresses strongly the variable $r_3$, because $r_1$ enters the third equation with factor 2, but it does not restrain the growth of the variable $r_2$, as $r_1$ is present in the second equation with factor $\frac{1}{2}$. At the next stage, the variable $r_2$ grows, saturates, and suppresses the variable $r_1$, but allows growth of $r_3$, and so on. So, the elements become active by turns in cyclic order $r_1 \to r_2 \to r_3 \to r_1 \to \cdots$. Each next repetition of the process is longer in time because the successive suppressions of the excitations become deeper.

In the phase space of the system (9.1) there exist three saddle fixed points $(r_1, r_2, r_3) = (1,0,0), (0,1,0)$, and $(0,0,1)$. They are connected by a contour consisting of three smooth curved segments, each representing simultaneously the outgoing separatrix of one saddle and the ingoing separatrix of another (Fig. 9.1(a)). Motion close to the contour corresponds to bypasses around all three segments in the phase space visiting narrower neighborhoods of the saddles; there the motions are very slow, so, the successive time intervals of the bypasses grow gradually and tend to infinity (Fig. 9.1(b)).

Of course, concrete coefficients in (9.1) may be of other values. Moreover, analogous dynamics may be arranged as well with larger number of the elements and, respectively, of the involved saddles.

Currently, there exists quite extensive literature devoted to dynamical phenomena associated with the heteroclinic cycles and to its applications, e.g. in the context of fluid convection, biological populations, neuroscience, etc. (Mercader et al., 2002; Huisman and Weissing, 2001; Rabinovich et al., 2006).

Now we proceed with interpretation of $r_1, r_2, r_3$ as squared amplitudes of three oscillators, $r_k = |a_k|^2, k = 1,2,3$. The equations for the complex amplitudes are

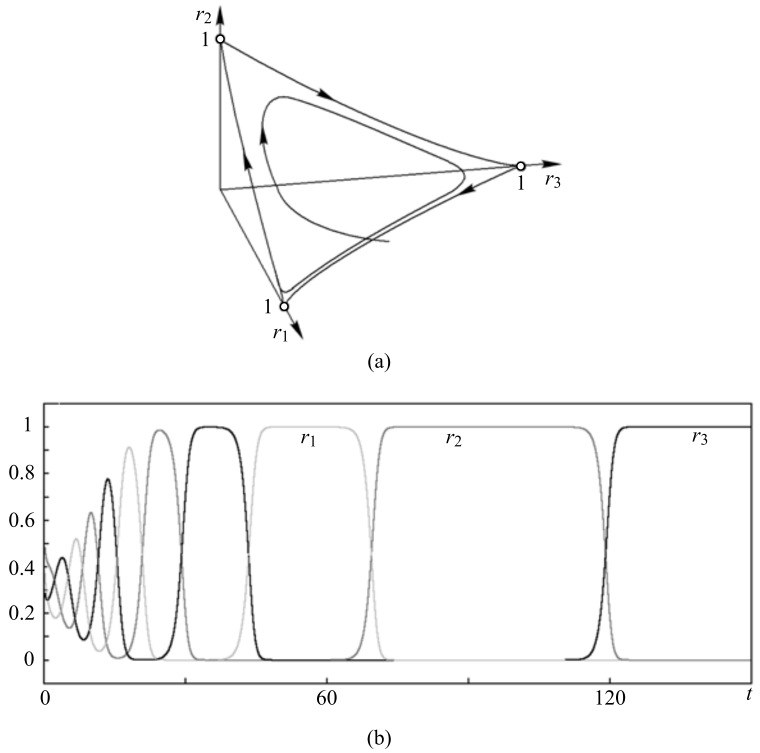


**Fig. 9.1** A heteroclinic cycle in the phase space of the system (9.1) **(a)**, and state variables $r_{1,2,3}$ versus time; observe oscillations with a growing period **(b)**.

$$
\begin{aligned}
\dot{a}_1 + i\omega_1 a_1 &= \left(1 - |a_1|^2 - \frac{1}{2}|a_3|^2 - 2|a_2|^2\right) a_1, \\
\dot{a}_2 + i\omega_2 a_2 &= \left(1 - |a_2|^2 - \frac{1}{2}|a_1|^2 - 2|a_3|^2\right) a_2, \\
\dot{a}_3 + i\omega_3 a_3 &= \left(1 - |a_3|^2 - \frac{1}{2}|a_2|^2 - 2|a_1|^2\right) a_3,
\end{aligned}
\tag{9.2}
$$

where $\omega_{1,2,3}$ designate the frequency parameters. Obviously, the dynamics for the squared amplitudes $r_k = |a_k|^2$ will be precisely the same as that governed by Eqs. (9.1).

## 9.2 Attractor of Smale-Williams type in a system of three coupled self-oscillators

Let us modify Eqs. (9.2) to obtain an autonomous system with attractor of Smale-Williams type in the Poincaré map (Kuznetsov and Pikovsky, 2007). We turn to a symmetric case and set $\omega_{1,2,3} = \omega_0$. Next, we introduce some additional coupling terms in the equations expressed via quadratic nonlinear terms to ensure transfer of the excitation to each next oscillator after its suppression stage from the previously active partner. Setting $a_k = x_k + iy_k$, in terms of the real and imaginary parts, we write down

$$\begin{aligned}
\dot{x}_1 &= \omega_0 y_1 + \left(1 - (x_1^2 + y_1^2) - \frac{1}{2}(x_3^2 + y_3^2) - 2(x_2^2 + y_2^2)\right) x_1 + \varepsilon x_3 y_3, \\
\dot{y}_1 &= -\omega_0 x_1 + \left(1 - (x_1^2 + y_1^2) - \frac{1}{2}(x_3^2 + y_3^2) - 2(x_2^2 + y_2^2)\right) y_1, \\
\dot{x}_2 &= \omega_0 y_2 + \left(1 - (x_2^2 + y_2^2) - \frac{1}{2}(x_1^2 + y_1^2) - 2(x_3^2 + y_3^2)\right) x_2 + \varepsilon x_1 y_1, \\
\dot{y}_2 &= -\omega_0 x_2 + \left(1 - (x_2^2 + y_2^2) - \frac{1}{2}(x_1^2 + y_1^2) - 2(x_3^2 + y_3^2)\right) y_2, \\
\dot{x}_3 &= \omega_0 y_3 + \left(1 - (x_3^2 + y_3^2) - \frac{1}{2}(x_2^2 + y_2^2) - 2(x_1^2 + y_1^2)\right) x_3 + \varepsilon x_2 y_2, \\
\dot{y}_3 &= -\omega_0 x_3 + \left(1 - (x_3^2 + y_3^2) - \frac{1}{2}(x_2^2 + y_2^2) - 2(x_1^2 + y_1^2)\right) y_3.
\end{aligned} \tag{9.3}$$

Here $\varepsilon$ is the coefficient of the additional coupling. In the process of the dynamics, the added terms serve as germs for excitation of each next oscillator at the beginning of the epochs of its activity. It occurs just at passages of the orbit near the saddle fixed points on the underlying heteroclinic cycle. The oscillators become active following the order $1 \to 2 \to 3 \to 1 \to \cdots$. Each new transfer of the excitation is accompanied by the phase doubling. Indeed, let $x_k \sim \sin(\omega_0 t + \varphi), y_k \sim \cos(\omega_0 t + \varphi)$; then the coupling term in the equation for the next oscillator contains the doubled phase: $x_k y_k \sim \sin(\omega_0 t + \varphi)\cos(\omega_0 t + \varphi) = \frac{1}{2}\sin(2\omega_0 t + 2\varphi)$. That oscillator undergoes excitation in the presence of this stimulating oscillating force; so it will inherit this doubled phase at the stage of activity, and so on. The mechanism of transfer of the excitation is non-resonance: indeed, the frequency of the stimulating force is twice as large as the natural frequency of the oscillator. Everything works, however, if one sets the frequency parameters relatively small.

To illustrate functioning of the model in computations, we fix $\omega_0$=1 and $\varepsilon$=0.03. At these parameter values, testing different initial conditions, only one attractor could be observed.

Figure 9.2 shows typical time dependence for the variables $x_1$,$x_2$, and $x_3$ as obtained from the computer solution of Eqs. (9.3). Observe that in the course of time evolution, three oscillators become excited one after another in accordance with the above qualitative description. The process is not periodic, although there is a rather well-defined mean period of the amplitude dynamics (in contrast to the model without the added coupling terms, cf. Fig. 9.1).

To give evidence for the phase doubling, which is crucial for occurrence of the attractor of Smale-Williams type, let us construct the Poincaré map. Here it will be done with some trick taking into account the symmetry of the system. Namely, in the

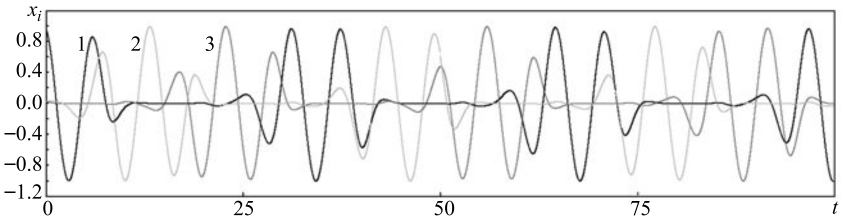


**Fig. 9.2** Time dependence for $x_1$ (black curve), $x_2$ (light gray curve), and $x_3$ (dark gray curve), obtained from the numerical computer solution of Eqs. (9.3) $\omega_0 = 1$ and $\varepsilon = 0.03$.

six-dimensional phase space $\{x_1, y_1, x_2, y_2, x_3, y_3\}$ let us define three hyper-surfaces by the equations

$$\begin{aligned} S_1 &= x_1^2 + y_1^2 - x_3^2 + y_3^2 = 0, \\ S_2 &= x_2^2 + y_2^2 - x_1^2 + y_1^2 = 0, \\ S_3 &= x_3^2 + y_3^2 - x_2^2 + y_2^2 = 0, \end{aligned} \tag{9.4}$$

and examine successive intersections of them in the direction of growth of the values of the quantities $S_j$. The intersection of a surface $S_j = 0$ by a trajectory corresponds to the condition that amplitude of the rising oscillator $(x_j, y_j)$ just overtakes that of the previously excited partner. The intersections follow in the order $S_1 \to S_2 \to S_3 \to \cdots$. A given point on a surface $S_j = 0, j = 1,2,3$ corresponds to a five-dimensional vector $\mathbf{v}_n$. On the next intersection of a surface of the family (9.4) by the trajectory started at $\mathbf{v}_n$ we obtain a new vector; this determines the map $\mathbf{v}_{n+1} = \mathrm{T}(\mathbf{v}_n)$. The spaces of images and pre-images may be identified because of the cyclic symmetry of the system. The usual Poincaré map will correspond to a threefold iteration of the map $\mathbf{T}$.

At each intersection of a surface $S_j = 0$ at time instant $t_n$ we define a phase for the $j$-th oscillator as $\varphi_n = \arg(x_j(t_n) + i y_j(t_n))$. The diagram for $\varphi_{n+1}$ versus $\varphi_n$ is shown in Fig. 9.3. The presence of the phase doubling mechanism is evident from

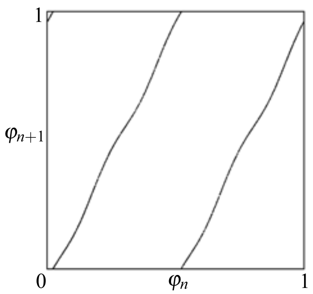


**Fig. 9.3** Iteration diagram for phases obtained in computations for the model (9.3) at $\omega_0 = 1$ and $\varepsilon = 0.03$; the phases are determined at each successive intersection of the family of surfaces $S_j$.

the picture: the diagram looks topologically similar to the expanding circle map $\varphi_{n+1} = 2\varphi_n + \text{const}\ (\bmod 2\pi)$.

Figure 9.4 shows projections of the attractor in the Poincaré map onto three planes of the variables $(x_j, y_j)$ corresponding to three partial oscillators. Because of strong transversal compression in the phase space, the fractal structure of the attractor is not distinguishable on diagrams (a) and (c) for the oscillators, whose amplitudes are equal in the condition of the Poincaré section, but it can be seen on the portrait for the rest oscillator (b) possessing the smallest amplitude at this moment in time.

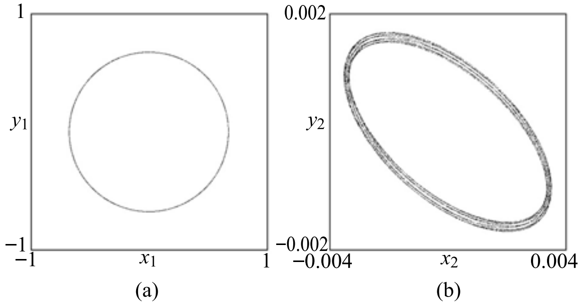


**Fig. 9.4** Portraits of attractor for the model (9.3) in the cross-section of the phase space by the surface $S_1 = 0$ (see (9.4)) depicted in projection onto planes of the variables $(x_1, y_1)$ **(a)**, $(x_2, y_2)$ **(b)**, and $(x_3, y_3)$ **(c)** at $\omega_0 = 1$ and $\varepsilon = 0.03$.

Computation of the spectrum of Lyapunov exponents for the attractor in accordance with the Benettin algorithm requires simultaneous numerical solution of Eqs. (9.3) together with collection of six replicas of the linearized variation equations for perturbation vectors accompanied by Gram-Schmidt orthogonalization and normalization at successive steps of the algorithm with estimate of rates of variation of respective accumulating sums for logarithms of the norm ratios (Appendix A). In the dynamical regime under consideration it yields

$$\begin{aligned} &\lambda_1 = 0.06305, \quad &&\lambda_2 = 0.00000, \quad &&\lambda_3 = -0.2101, \\ &\lambda_4 = -0.2259, \quad &&\lambda_5 = -0.3395, \quad &&\lambda_6 = -1.99993. \end{aligned} \tag{9.5}$$

One Lyapunov exponent is positive, the next one is close to zero (it corresponds, clearly, to the perturbation directed along the orbit), and the remaining four exponents are negative.

For the map **T**, the Lyapunov exponents may be expressed via the non-zero exponents of the flow system by means of the relation $\Lambda_m = T_{av}\lambda_m$, where $T_{av}$ is the average time interval between successive intersections of the surfaces (9.4). Following from the numerical simulations, in the dynamical regime we consider, $T_{\text{av}} \approx 10.96$. Hence, $\Lambda_1 \approx 0.691$ that agrees well with the value $\ln 2 \approx 0.693$ expected from the approximation based on the expanding circle map.

Calculation of the attractor dimension from the Kaplan-Yorke formula (Appendix D) yields for the flow system $D_{KY} = 2 + \lambda_1/|\lambda_3| \approx 2.30$.

## 9.3 Attractor with dynamics governed by the Arnold cat map

Let us start again with the system (9.2) at $\omega_{1,2,3} = \omega_0$, but introduce the additional coupling terms in other way, namely, each partial oscillator is excited by a product of variables relating to two other oscillators. Then, we arrive at the equations

$$\begin{aligned}
\dot{x}_1 &= \omega_0 y_1 + \left(1 - (x_1^2 + y_1^2) - \frac{1}{2}(x_3^2 + y_3^2) - 2(x_2^2 + y_2^2)\right) x_1 + \varepsilon(x_2 y_3 + x_3 y_2),\\
\dot{y}_1 &= -\omega_0 x_1 + \left(1 - (x_1^2 + y_1^2) - \frac{1}{2}(x_3^2 + y_3^2) - 2(x_2^2 + y_2^2)\right) y_1,\\
\dot{x}_2 &= \omega_0 y_2 + \left(1 - (x_2^2 + y_2^2) - \frac{1}{2}(x_1^2 + y_1^2) - 2(x_3^2 + y_3^2)\right) x_2 + \varepsilon(x_1 y_3 + x_3 y_1),\\
\dot{y}_2 &= -\omega_0 x_2 + \left(1 - (x_2^2 + y_2^2) - \frac{1}{2}(x_1^2 + y_1^2) - 2(x_3^2 + y_3^2)\right) y_2,\\
\dot{x}_3 &= \omega_0 y_3 + \left(1 - (x_3^2 + y_3^2) - \frac{1}{2}(x_2^2 + y_2^2) - 2(x_1^2 + y_1^2)\right) x_3 + \varepsilon(x_2 y_1 + x_1 y_2),\\
\dot{y}_3 &= -\omega_0 x_3 + \left(1 - (x_3^2 + y_3^2) - \frac{1}{2}(x_2^2 + y_2^2) - 2(x_1^2 + y_1^2)\right) y_3.
\end{aligned} \tag{9.6}$$

The added coupling terms are selected in symmetric form to exclude the presence of the non-oscillating components, which could disturb the required phase transfer. To illustrate the dynamics we fix $\omega_0$=1 and $\varepsilon = 0.03$. The computations indicate that a unique attractor is observed regardless of initial conditions.

The oscillators become excited following the order $1 \to 2 \to 3 \to 1$. Each new transfer of the excitation is accompanied by assigning new phase with a sum of two previous phases. Indeed, let us suppose that two partner elements transferring the excitation to the given one oscillate as $x_j \sim \sin(\omega_0 t + \varphi), y_j \sim \cos(\omega_0 t + \varphi)$ and $x_k \sim \sin(\omega_0 t + \phi), y_k \sim \cos(\omega_0 t + \phi)$. Then the respective coupling term contains a sum of the phases

$$\begin{aligned}
& x_j y_k + x_k y_j \sim \sin(\omega_0 t + \varphi)\cos(\omega_0 t + \phi) + \sin(\omega_0 t + \phi)\cos(\omega_0 t + \varphi)\\
&= \sin(2\omega_0 t + \varphi + \phi).
\end{aligned}$$

As the excitation takes place in the presence of this stimulating oscillating force, the oscillator will inherit the sum of previous phases; so, the successive transformations will follow the relation $\varphi_{n+1} = \varphi_n + \varphi_{n-1} \pmod{2\pi}$ called the Fibonacci map. It is connected with the Arnold cat map. Indeed, setting $q_n = 2\pi\varphi_n, p_n = 2\pi\varphi_{n-1}$, we have $p_{n+1} = q_n, q_{n+1} = p_n + q_n \pmod 1$, and the two-fold iteration just corresponds to the map

$$p_{n+2} = p_n + q_n, \quad q_{n+2} = p_n + 2q_n \pmod 1. \tag{9.7}$$

Figure 9.5 illustrates evolution of the variables $x_1$,$x_2$, and $x_3$, as functions of time obtained from the computer solution of Eqs. (9.6) after the decay of transients. Observe that the whole process is chaotic and manifests successive excitation of the partial oscillators in proper order with some characteristic average time period.

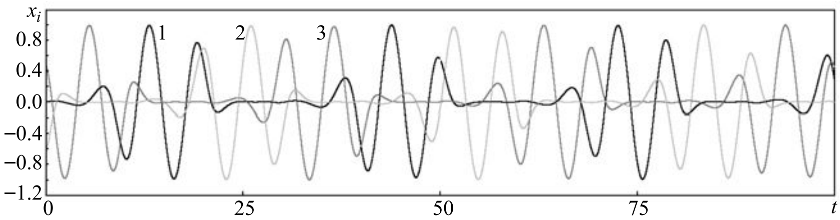


**Fig. 9.5** Time dependence for $x_1$ (black curve), $x_2$ (light gray curve), and $x_3$ (dark gray curve), obtained from the numerical computer solution of Eqs. (9.6) at $\omega_0 = 1$ and $\varepsilon = 0.03$.

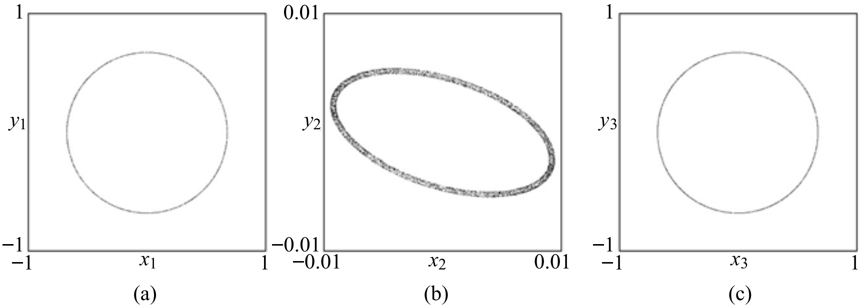


**Fig. 9.6** Portraits of the attractors of the model (9.6) in the cross-section of the phase space by the surface $S_j = 0$ (see (9.4)) depicted in projection onto planes of the variables $(x_j, y_j)$ **(a)**, $(x_{j+1}, y_{j+1})$ **(b)**, and $(x_{j+2}, y_{j+2})$ **(c)** at $\omega_0 = 1$ and $\varepsilon = 0.03$.

We can construct the Poincaré map in the same way as described in the previous section, namely, in the six-dimensional phase space $\{x_1, y_1, x_2, y_2, x_3, y_3\}$ we define three surfaces determined by Eqs. (9.6) and examine successive intersections of these surfaces by a trajectory. In this way we define a five-dimensional map $\mathbf{v}_{n+1} = \mathbf{T}(\mathbf{v}_n)$: the pre-image is a vector $\mathbf{v}_n$ associated with a point on the surface $S_j$, and the image is a vector $\mathbf{v}_{n+1}$ on the next intersected surface $S_k = 0$, which follows the order $S_1 \to S_2 \to S_3 \to \cdots$. Like in the previous subsection, the spaces of images and pre-images may be identified due to the symmetry of the system. Figure 9.6 shows projections of the attractor in the Poincaré map onto three planes of the variables $(x_j, y_j)$ corresponding to three partial oscillators.

For a sequence of successive intersections of the surfaces $S_j = 0$ we can define phases of the oscillations as $\varphi_n = \arg[x_j(t_n) + iy_j(t_n)]$. Figure 9.7 demonstrates that they indeed obey the Fibonacci map $\varphi_{n+1} = \varphi_n + \varphi_{n-1} + \text{const}$ with a good accuracy. As mentioned above, the second iteration of the Fibonacci map is the Arnold cat map. Figure 9.8 illustrates the action of the map obtained from the numerical solution of Eqs. (9.6) with a traditional picture of the cat face. It may be compared to Fig. 1.6 in Chap. 1.

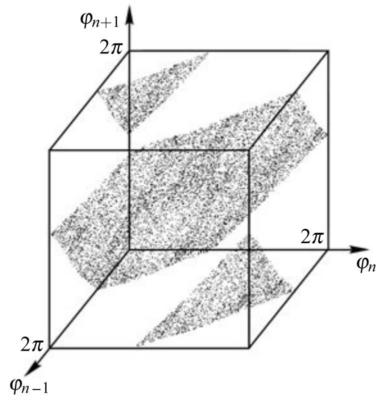


**Fig. 9.7** Three-dimensional representation of the dependence of $\varphi_{n+1}$ on $\varphi_n$ and $\varphi_{n-1}$ in model (9.6) with $\omega_0 = 1$ and $\varepsilon = 0.03$.

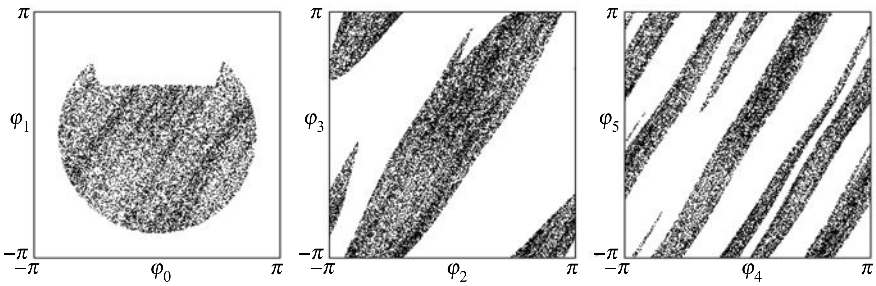


**Fig. 9.8** Diagram for phases of partial oscillators in the model (9.6) with $\omega_0 = 1$ and $\varepsilon = 0.03$ representing successive steps of evolution of the cloud of representative points in a form of the cat face.

Computation of the Lyapunov exponents yields

$$\begin{aligned} &\lambda_1 = 0.04786, \quad \lambda_2 = 0.00000, \quad \lambda_3 = -0.04840, \\ &\lambda_4 = -0.3184, \quad \lambda_5 = -0.3673, \quad \lambda_6 = -2.00002. \end{aligned} \tag{9.8}$$

There is one positive exponent, one zero exponent associated with a shift along the trajectory, and others negative. Taking into account that the average time between the intersections of the surfaces $S_j = 0$ at the given parameters is approximately

$T_{\mathrm{av}} \approx 9.94$, one can evaluate the Lyapunov exponents for the map $\mathbf{v}_{n+1} = \mathbf{T}(\mathbf{v}_n)$: as $\Lambda_m = T_{\mathrm{av}}\lambda_m$, $\Lambda_1 \approx 0.476$, and $\Lambda_3 \approx -0.481$. These numbers should be compared with logarithms of square roots of the eigenvalues for the map (9.7) $\ln \frac{1}{2}(1+\sqrt{5}) \approx 0.481$ and $\ln \frac{1}{2}(\sqrt{5}-1) \approx -0.481$. Note that for the cat map a sum of the Lyapunov exponents vanishes. In the system (9.6) the attractor in the Poincaré map is concentrated close to a two-dimensional torus surface, the dynamics on which are governed approximately by the cat map. This assertion agrees with the fact that the sum of the largest two non-zero Lyapunov exponents is very small: $\lambda_1 + \lambda_3 \approx -0.0005$. In fact, due to numerical statistical errors it is hard to distinguish it from zero. Therefore we conclude that the Lyapunov dimension of the attractor is nearly 3, and the dimension of the attractor in the Poincaré map is close to 2. This explains the visible absence of a fractal structure in Fig. 9.6 (c).

## 9.4 Model with hyperchaos

Hyperchaos is a dynamical regime with two or more positive Lyapunov exponents (Rössler, 1979; Matsumoto et al., 1986; Stoop et al., 1989; Reiterer et al., 1998; Letellier and Rössler, 2007). Let us introduce a system with a hyperchaotic attractor basing on the system of three interacting oscillators evolving close to the heteroclinic cycle. In contrast to two previous models, the present one will be non-symmetric. In Eqs. (9.2) we assign $\omega_1 = 3\omega_0, \omega_{2,3} = \omega_0$, and introduce additional coupling characterized by constants $\varepsilon_{1,2,3}$ as follows:

$$
\begin{aligned}
\dot{x}_1 &= 3\omega_0 y_1 + \left(1 - (x_1^2+y_1^2) - \frac{1}{2}(x_3^2+y_3^2) - 2(x_2^2+y_2^2)\right) x_1 + \varepsilon_1 x_2^2 y_2, \\
\dot{y}_1 &= -3\omega_0 x_1 + \left(1 - (x_1^2+y_1^2) - \frac{1}{2}(x_3^2+y_3^2) - 2(x_2^2+y_2^2)\right) y_1, \\
\dot{x}_2 &= \omega_0 y_2 + \left(1 - (x_2^2+y_2^2) - \frac{1}{2}(x_1^2+y_1^2) - 2(x_3^2+y_3^2)\right) x_2 + \varepsilon_2 x_3, \\
\dot{y}_2 &= -\omega_0 x_2 + \left(1 - (x_2^2+y_2^2) - \frac{1}{2}(x_1^2+y_1^2) - 2(x_3^2+y_3^2)\right) y_2, \\
\dot{x}_3 &= \omega_0 y_3 + \left(1 - (x_3^2+y_3^2) - \frac{1}{2}(x_2^2+y_2^2) - 2(x_1^2+y_1^2)\right) x_3 + \varepsilon_3 (x_1 y_2 + x_2 y_1), \\
\dot{y}_3 &= -\omega_0 x_3 + \left(1 - (x_3^2+y_3^2) - \frac{1}{2}(x_2^2+y_2^2) - 2(x_1^2+y_1^2)\right) y_3.
\end{aligned}
\tag{9.9}
$$

In computations we set $\omega_0 = 1, \varepsilon_1 = \varepsilon_2 = 0.004, \varepsilon_3 = 0.1$. Starting with various initial conditions the system was observed to arrive always to one and the same attractor. Figure 9.9 shows the variables $x_1, x_2$, and $x_3$, as functions of time obtained from the computer solution of Eqs. (9.9) after the decay of transients. Successive excitations of the partial oscillators follow, like in the previous models, the sequence

$$1 \to 2 \to 3 \to 1 \to 2 \to 3 \to \cdots .$$

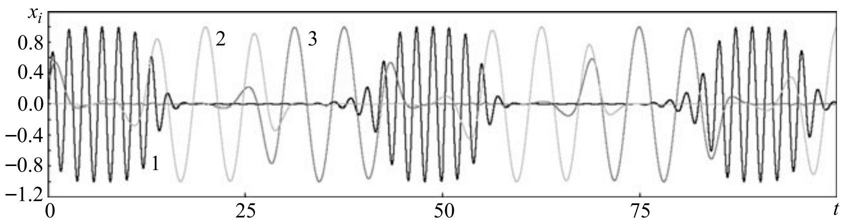


**Fig. 9.9** Time dependence for $x_1$ (black curve), $x_2$ (light gray curve), and $x_3$ (dark gray curve), obtained from the numerical computer solution of Eqs. (9.9) at $\omega_0 = 1, \varepsilon_1 = \varepsilon_3 = 0.004, \varepsilon_2 = 0.1$.

Let us consider the phases the oscillators accept at the cross-sections of the surfaces determined by the conditions (9.4); then we will have a sequence

$$\varphi_1 \to \varphi_2 \to \varphi_3 \to \varphi_1' \to \varphi_2' \to \varphi_3' \to \cdots .$$

Excitation of the oscillator 1 is stimulated by the force proportional to the term $x_2^2 y_2$. The dominant contribution is due to the third harmonic of the basic frequency $\omega_0$ as it is in resonance with the oscillator 1. Hence, at the beginning of the epoch of activity the oscillator 1 adopts the phase

$$\varphi_1' = 3\varphi_2 + \text{const.} \tag{9.10}$$

Oscillator 2 in the course of the excitation is driven in resonance by the force proportional to $x_3$, so it takes up the phase from the oscillator 3:

$$\varphi_2' = \varphi_3 + \text{const.} \tag{9.11}$$

Finally, oscillator 3 is driven by the signal $x_1 y_2 + x_2 y_1$. At the beginning of the active epoch it is excited in a non-resonance manner (this is the reason why we assign a relatively large value for $\varepsilon_3$), and accepts the phase

$$\varphi_3' = \varphi_1 + \varphi_2 + \text{const.} \tag{9.12}$$

Figure 9.10 demonstrates that the phase relations indeed occur in the dynamics governed by Eqs. (9.9) following from computations.

One may remove the constants in (9.9)—(9.11) by appropriate shifts of origins for the variables $\varphi_{1,2,3}$ and write down the relation between the pairs $(\varphi_3, \varphi_2)$ and $(\varphi_3', \varphi_2')$ in the matrix form

$$\begin{pmatrix} \varphi_3' \\ \varphi_2' \end{pmatrix} = \begin{pmatrix} 1 & 3 \\ 1 & 0 \end{pmatrix} \begin{pmatrix} \varphi_3 \\ \varphi_2 \end{pmatrix} . \tag{9.13}$$

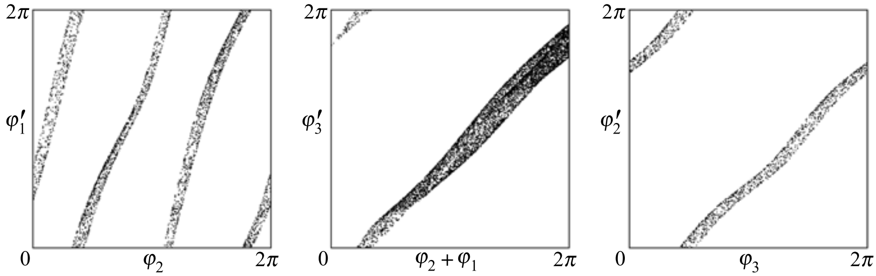


**Fig. 9.10** Phase transformation plots obtained in computations for the model (9.9) at $\omega_0 = 1, \varepsilon_1 = \varepsilon_3 = 0.004, \varepsilon_2 = 0.1$.

The matrix here has two eigenvalues larger than 1, namely,

$$s_1 = (\sqrt{13}+1)/2 = 2.30277\cdots, \quad s_2 = (\sqrt{13}-1)/2 = 1.30277\cdots. \tag{9.14}$$

Hence, the Poincaré map corresponding to a complete bypass around the heteroclinic contour is expected to have two positive Lyapunov exponents associated with the dynamics of the phase variables.

The Lyapunov exponents for the model (9.9) evaluated from the computations are the following:

$$\begin{aligned} \lambda_1 &= 0.01878, & \lambda_2 &= 0.00621, & \lambda_3 &= 0.00000, \\ \lambda_4 &= -0.3680, & \lambda_5 &= -0.4313, & \lambda_6 &= -2.00003. \end{aligned} \tag{9.15}$$

The presence of two positive Lyapunov exponents affirms the hyperchaotic nature of the dynamics. The third exponent is close to zero and has to be interpreted as being linked with infinitesimal shift along the orbit. Other exponents are negative; they correspond to approach of trajectories to the attractor.

In the present case, all consecutive transformations $\varphi_1 \to \varphi_2 \to \varphi_3 \to \varphi_1$ are different; so, one should consider the overall transformation with the return onto a cross-section, say, $S_1 = 0$, as the Poincaré map. As evaluated from the computations, at the assigned parameters the average time between successive returns is $T_{\rm av} \approx 41.475$. The largest Lyapunov exponents for the Poincaré map are evaluated via the exponents of the flow system as $\Lambda_1 = T_{\rm av}\lambda_1 \approx 0.779$ and $\Lambda_2 = T_{\rm av}\lambda_2 \approx 0.258$. They may be compared with the estimates obtained from the qualitative consideration of the dynamics of phases as $\ln s_1 = 0.834$ and $\ln s_2 = 0.265$. Observe quite a good correspondence.

The Lyapunov dimension of the attractor estimated from the Kaplan-Yorke formula is 3.068.

It may be suggested that attractor in the Poincaré map of the considered model is hyperbolic, but verification of this assertion would require reformulation of the algorithm for cone criterion presented in Chap. 7 because the unstable manifold for this attractor is two-dimensional.

## 9.5 An autonomous system with attractor of Smale-Williams type with resonance transfer of excitation in a ring array of van der Pol oscillators

Examples examined in Sect. 9.2—9.4 are designed departing from equations of interacting oscillators written for complex amplitudes. If one intends to organize such dynamics in practice, it would be possible on a base of high-frequency oscillations in situation of applicability of description in terms of slow complex amplitudes. On the other hand, non-resonance mechanism of transfer of excitation between the alternately active oscillators is able to ensure phase doubling or other chaotic transformation for phases only at relatively low natural frequencies. These two conditions contradict each other; so, practical implementation is questionable. One way to overcome this difficulty is to consider a large number of oscillators arranged in such a way that the neighbors transferring each other the excitation possess close natural frequencies, which decrease gradually from the beginning to the end of the chain. The final stage of the excitation transfer at the closure of the chain is of special kind being accompanied by doubling of the respective frequency and the oscillation phase. In the present section this idea is considered in application to the ring model composed of van der Pol oscillators, following (Kruglov and Kuznetsov, 2011).

As mentioned in Chap. 4, a single autonomous van der Pol oscillator is governed by a differential equation

$$\ddot{x} - (A - x^2)\dot{x} + \omega_0^2 x = 0,$$

where $\omega_0$ is the natural frequency. At positive values of the parameter $A$ it demonstrates self-oscillations associated with the attractive limit cycle. Let us consider the following ring model composed of $N+1$ coupled van der Pol oscillators:

$$\begin{aligned}
&\ddot{x}_0 - (A + \frac{3}{2}x_N^2 + x_0^2 - 2S)\dot{x}_0 + \omega_0^2 x_0 = \varepsilon x_N^2,\\
&\ddot{x}_1 - (A + \frac{3}{2}x_0^2 + x_1^2 - 2S)\dot{x}_1 + 2^{-2/N}\omega_0^2 x_1 = \varepsilon x_0,\\
&\ddot{x}_2 - (A + \frac{3}{2}x_1^2 + x_2^2 - 2S)\dot{x}_2 + 2^{-4/N}\omega_0^2 x_2 = \varepsilon x_1,\\
&\cdots\cdots\cdots\cdots\\
&\ddot{x}_N - (A + \frac{3}{2}x_{N-1}^2 + x_N^2 - 2S)\dot{x}_N + 2^{-2}\omega_0^2 x_N = \varepsilon x_{N-1},\\
&S = \sum_{k=0}^{N} x_k^2.
\end{aligned} \tag{9.16}$$

Structure of the factors at the first derivatives ensures a situation that each given oscillator contributes to strong suppression of all other partners, except one numbered with the next index. Hence, the system manifests cyclic propagation of the localized excitation around the ring in direction of increasing indices, in accordance with mechanism explained in Sect. 9.1. Due to presence of the additional coupling characterized by parameter $\varepsilon$ the excitation of each $j$-th oscillator is stimulated by oscillations from $(j-1)$-th partner. As $N$ is large enough, the natural frequencies of the neighbor oscillators are close, and the stimulation is practically resonance. Only at the edge of the chain, the transfer from $N$-th oscillator to zero one is arranged in other way: the first one has the natural frequency twice less that the last one, and the resonance stimulation is produced by the second harmonic component of the coupling term proportional to $x_N^2$ in the first eq. (9.16).

Figure 9.11 shows in panel (a) the time dependence for generalized coordinates of oscillators in the ring structure for $N$=14 obtained from numerical computer solution of Eqs. (9.16) after exclusion of the transients.

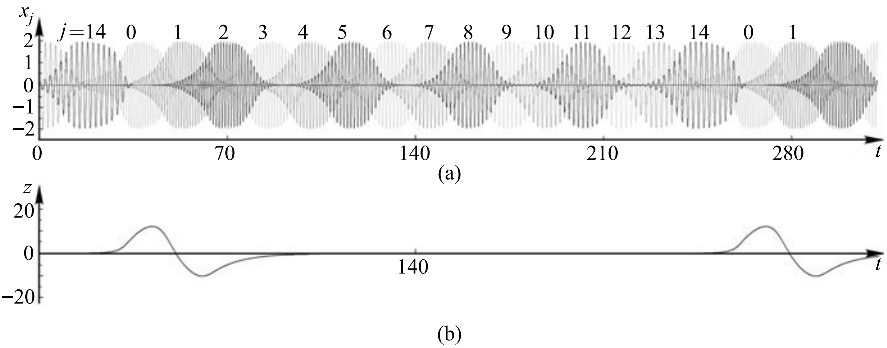


**Fig. 9.11** Time dependence for $x_j, j=0,\ldots,N$ and auxiliary variable $z$ used for construction of the return map obtained from the numerical computer solution of Eqs. (9.16) at $N=14, A=1, \omega_0=2\pi, \varepsilon=0.2$.

In accordance with the idea of the design, the oscillatory excitation has to undergo doubling of phase with each bypass of the ring. This property is crucial for the realization of attractor of Smale-Williams type, and it is highly desirable to illustrate it in the numerical computations.

It is not so trivial to construct appropriate Poincaré map: simple definitions similar to (9.4) appear to be unsuccessful. The single van der Pol system is not so close to perfect symmetry intrinsic to the amplitude equations, and it is problematic to locate the instant of the cross-section relatively to envelope of the oscillations with inaccuracy essentially less than the period associated with the natural frequency to have good definition of the phases.

To settle this problem, let us introduce an auxiliary variable z obeying the differential equation

$$\dot{z}+\gamma z=+x_0^2+\omega_0^{-2}\dot{x}_0^2-x_1^2-2^{2/N}\omega_0^{-2}\dot{x}_1^2. \tag{9.17}$$

Here the right-hand part is the difference of squared amplitudes for the oscillatory elements 0 and 1, and $\gamma$ is positive constant. The behavior of the variable z is illustrated by panel (b) of Fig. 9.11 at particular $\gamma=0.1$. The value z grows during the epoch of activity of the oscillator 0, then decreases below zero during epoch of activity for the oscillator 1, and then decays nearly to zero until the next activation of the oscillator 0 occurs. For the record of the system states and evaluation of the phases $\varphi = \arg(x_0 + i\dot{x}_0/\omega_0)$ we take sequence of the instants of the transitions from positive to negative values of the variable.

Figure 9.12 shows the diagram for $\varphi_{n+1}$ versus $\varphi_n$. Observe that it looks topologically corresponding to the Bernoulli map: one complete revolution for pre image gives rise to two revolutions for image. Accounting strong compression in other directions in the phase space (excluding the cyclic phase variable and the neutral direction along the phase trajectory), it gives a reason for the conjecture that hyperbolic attractor does exist, which corresponds to suspension (special flow) over the Smale-Williams solenoid.

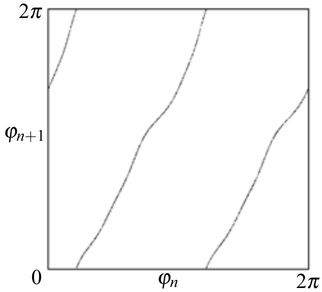


**Fig. 9.12** Iteration diagram for phases obtained in computations for the model (9.16) at $N = 14, A = 1, \omega_0 = 2\pi, \varepsilon = 0.2$. The phases are determined at instants of each successive passage of them by the auxiliary variable z evolving in accordance with Eq. (9.17) from positive to negative values.

Figure 9.13 presents portraits of the attractor in projection onto the phase plane of oscillator $j = 0$. Panel (a) shows the attractor for the flow system in projection from the phase space of dimension $2(N+1)$. In panel (b) attractor in the cross-section defined with the help of the auxiliary variable is plotted. The last one is, in fact, a picture of solenoid; the intrinsic fine transversal Cantor-like structure may be resolved under magnification as shown by the inset.

Figure 9.14 shows portraits of the attractor for the flow system in some other projections, with coordinate axes corresponding to neighboring oscillators in the ring. The first picture on the plane $(x_N, x_0)$ is of specific kind; all the rest ones are qualitatively similar to each other. It is so because just transfer of the excitation from the $N$-th oscillator to zero one is arranged through the quadratic coupling term and the second harmonic; all others are stimulated directly by linear terms in the equations.

By means of the Benettin algorithm (Appendix A) applied to the set of Eqs. (9.16) and respective variation equations, the larger Lyapunov exponents were evaluated:

$$\lambda_1 = 0.003044, \quad \lambda_2 = 0.000002, \quad \lambda_3 = -0.3353, \quad \lambda_4 = -0.6318\cdots. \quad (9.18)$$

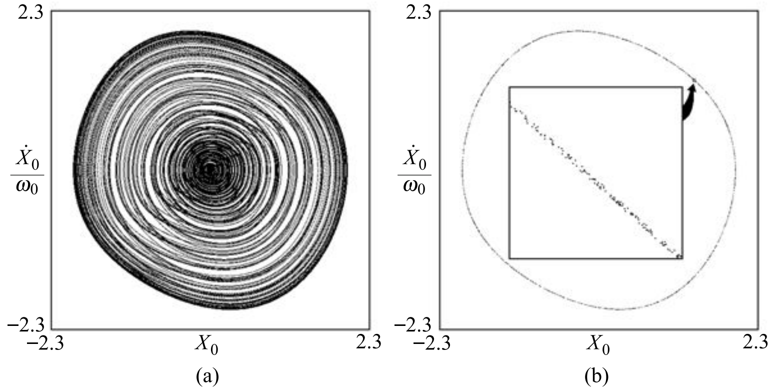


**Fig. 9.13** Attractor of the model (9.16) at $N = 14, A = 1, \omega_0 = 2\pi, \varepsilon = 0.2$ in projection onto the phase plane of the oscillator $j = 0$ from the multidimensional phase space of the flow system **(a)** and in the cross-section constructed using the auxiliary variable z as explained in the text **(b)**.

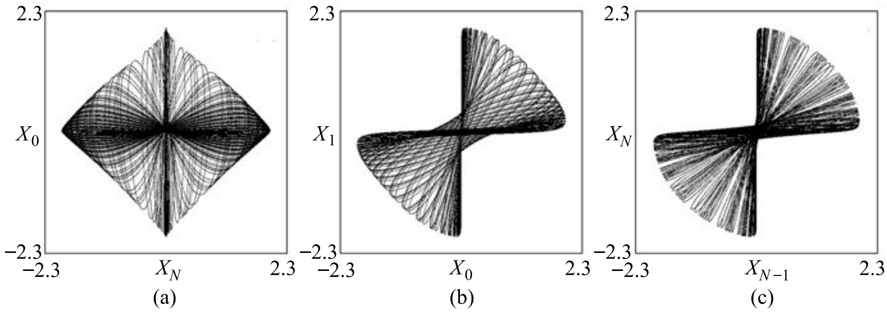


**Fig. 9.14** Portraits of the attractor of the model (9.16) at $N = 14, A = 1, \omega_0 = 2\pi, \varepsilon = 0.2$ in projections from the multidimensional phase space of the flow system onto the planes of generalized coordinates of two neighboring oscillators un the ring structure: $N$ and 0 **(a)**, 0 and 1 **(b)**, $N-1$ and $N$ **(c)**. For other neighboring pairs the diagrams look qualitatively similar to (b) and (c).

The largest Lyapunov exponent is positive that means the dynamics is chaotic. Accounting that intersections of the axis of the auxiliary variable z=0 (see (9.17)) used in the analysis of the phase map occur with average time period $T_{\text{av}} = 227.85$, it is worth considering normalization of the Lyapunov exponent to this time interval that yields $\Lambda_1 = \lambda_1 T_{\text{av}} \approx 0.6934$. Observe a good correspondence with the estimate following from the Bernoulli map for the phases, $\ln 2 \approx 0.6931$. So, we interpret the largest exponent as being associated with the cyclic coordinate in the phase space of dimension $2(N+1)$ along which the expansion takes place. The second exponent is close to zero, up to the numeric error, and should be related to perturbations of a shift along the reference phase trajectory responsible for appearance of a zero term in the spectrum of Lyapunov exponents of the autonomous system. The third exponent is negative, and its absolute value is large enough to ensure overall compression of the phase volume sufficient to evaluate the Kaplan-Yorke dimension of the attractor:

$D_{KY} \approx 2.009$ (in application to the flow system). Although the full spectrum of Lyapunov exponents contains $2(N+1)$ numbers, it seems not necessary to compute all of them because the rest ones correspond to yet stronger compression in the phase space and do not influence the estimate of the dimension.

In conclusion, we can assume that based on similar ring structures, using other methods of introducing of coupling, the dynamics associated with the Arnold cat map and with hyper-chaotic attractors also can be realized in analogy to the previous sections of this chapter.

## References

Guckenheimer, J., Holmes, P.: Structurally stable heteroclinic cycles. Math. Proc. Cambridge Philos. Soc. **103**, 189–192 (1988).

Huisman, J., Weissing, F.J.: Biological conditions for oscillations and chaos generated by multispecies competition. Ecology **82**, 2682–2695 (2001).

Kruglov, V.P., Kuznetsov, S.P.: An autonomous system with attractor of Smale-Williams type with resonance transfer of excitation in a ring array of van der Pol oscillators. CNSNS **16**, 3219–3223 (2011).

Kuznetsov, S.P., Pikovsky, A.: Autonomous coupled oscillators with hyperbolic strange attractors. Physica D **232**, 87–102 (2007).

Letellier C., Rössler, O.E.: Hyperchaos. Scholarpedia **2**, 1936 (2007).

Matsumoto, T., Chua, L.O., Kobayashi, K.: Hyperchaos laboratory experiment and numerical confirmation. IEEE Trans, Circuits & Syst. **33**, 1143–1147 (1986).

Mercader, I., Prat, J., Knobloch, E.: Robust heteroclinic cycles in two-dimensional Rayleigh-Benard convection without Boussinesq symmetry. Int. J. Bifurcation and Chaos **12**, 2501–2522 (2002).

Rabinovich, M.I., Varona, P., Selverston, A.I., Abarbanel, H.D.I.: Dynamical principles in neuroscience. Rev. Mod. Phys. **78**, 1213–1265 (2006).

Reiterer, P., Lainscsek, C., Schürrer, F., Letellier C., Maquet, J.: A nine-dimensional Lorenz system to study high-dimensional chaos. Journal of Physics A **31**, 7121–7139 (1998).

Rössler, O.E.: An equation for hyperchaos. Physics Letters A **71**, 155–157 (1979).

Stoop, R., Peinke, J., Parisi, J., Röhricht B., Hübener, R. P.: A p-Ge semiconductor experiment showing chaos and hyperchaos. Physica D **35**, 425–435 (1989).

# Chapter 10
# Systems with Time-delay Feedback

**Abstract** Besides the alternately excited oscillators, the principle of manipulation by phases in the course of the excitation transfer may be applied to *systems with delayed feedback*. In this case, it is sufficient to have a single self-oscillator manifesting successive stages of activity and suppression, while the excitation transfer accompanied with appropriate phase transformation is carried out through the delayed feedback loop, from one stage of activity to another. In practical implementation, these systems can be even simpler than the alternately excited oscillators. From a mathematical point of view, they are more complex, because presence of the delay implies formally infinite dimension of the state space. Careful mathematical analysis of attractors in such systems, including rigorous foundation of hyperbolicity, is a challenging problem that goes far beyond the scope of this book. In the present chapter, we start with some necessary material concerning the mathematical nature of the differential equations with delay. The next two sections consider models of systems with delay, generating sequences of pulses with the phases of the carrier transformed from pulse to pulse in accordance with expanding circle maps. First, the non-autonomous systems are discussed that operate due to the externally imposed parameter modulation with or without an auxiliary reference signal. Afterwards, we consider an autonomous system with time delay. On the physical level of reasoning it seems confident that chaotic attractors in these systems are of the same nature as those in the above discussed alternately excited oscillatory systems being associated with expanding circle maps for some cyclic variable. Particularly, it is believed that the generated chaos is structurally stable. As one can hypothesize, attractors in these systems as they are treated in a framework of discrete-time description (like the Poincaré maps) belong to the class of solenoids of Smale-Williams embedded in the infinite-dimensional phase space.

S. P. Kuznetsov, *Hyperbolic Chaos*

## 10.1 Some notions concerning differential equations with deviating argument

Time-delay occurs in many systems in nature and technology, particularly, in automatic control theory, electronics, nonlinear optics, physiology, etc. (Kuznetsov, 1982; Vallee et al., 1984; Glass and Mackey, 1988; Hu and Wang, 2002; Chiasson and Loiseaum, 2007). Analysis of the time-delay systems is, therefore, of both theoretical and practical importance. Unlike systems governed by ordinary differential equations, the delay systems are characterized by infinite dimension of their state spaces.

Natural mathematical tool for description of the time-delay systems is the theory of *differential equations with deviating argument* (Bellman and Cooke, 1963; Myskis, 1972; El'sgol'ts and Norkin, 1973; Hu and Wang, 2002). In general, these are equations connecting an unknown vector function and its derivatives taken for different values of the argument. A particular, but sufficiently common form of such equation may be written as

$$\mathbf{x}^{(n)}(t) = \mathbf{f}(t, \mathbf{x}(t), \mathbf{x}^{(1)}(t), \ldots, \mathbf{x}^{(n-1)}(t), \mathbf{x}(t-\tau_0), \mathbf{x}^{(1)}(t-\tau_1), \ldots, \mathbf{x}^{(m)}(t-\tau_m)), \tag{10.1}$$

where $\mathbf{x}$ is a vector of some finite dimension $N$, $\mathbf{f}$ is a vector function, $\mathbf{x}^{(k)}(t)$ is the derivative $d^k\mathbf{x}/dt^k$ evaluated at the instant $t$. The values $\tau_i, i = 0, \ldots, m$ are assumed to be positive constants.

Equation (10.1) is said to be of *retarded type* if the maximal order of derivatives at shifted arguments is less than the order of the derivative in the left-hand part: $0 \leqslant m < n$. If $m = n$ it is called an equation of *neutral type*, and for $m > n$ it is an equation of *leading type*. Well studied is the retarded type; to less extent it may be said about the neutral type. For the leading type development of the consistent theory is difficult and problematic because the initial-value problem appears to be ill-posed. Below, we deal only with equations of retarded type.

To explain the main feature of the delay systems, consider a simple particular case of (10.1), namely, an equation with $N = 1, n = 1, m = 0$:

$$\dot{x} = f(x(t), x(t-\tau)). \tag{10.2}$$

To start integration at a given time $t$ =0 and proceed at $0 < t \leqslant \tau$ we need to evaluate step by step the right-hand part, which depends on the variable $x$ at delayed time instants from the interval $[-\tau, 0]$. Hence, the unknown function $x(t)$ must be specified somehow on this interval $[-\tau, 0]$. *This function must be regarded as a kind of initial condition*. The same reasoning is suitable for any other point in time $t$, after which we wish to continue the solution. In a framework of dynamical system theory, we have to say that *the instant state of the system* (10.2) *at some $t$ is determined by a function defined in a time interval of duration equal to the retarding constant*: $x(t')|_{t' \in [t-\tau, t]} = \xi(t')$. Thus, the phase space for this system is the space of functions of one real argument defined in interval of length $\tau$. This space is infinite-dimensional. Indeed, one can think of these functions as vectors; the components of such vector are values of the function at the set of points of the interval of length $\tau$.

Integration of the equation forward in time is not difficult; in principle it is reduced to step-by-step solution of successive set of ordinary differential equations:

$$\begin{aligned} \dot{x}_1 &= f(x_1, \xi), \quad 0 \leqslant t \leqslant \tau, \\ \dot{x}_2 &= f(x_2, x_1), \quad \tau \leqslant t \leqslant 2\tau, \\ \dot{x}_3 &= f(x_3, x_2), \quad 2\tau \leqslant t \leqslant 3\tau, \end{aligned} \tag{10.3}$$

and so on. In the case of several retarding constants one should use the maximal one to specify a length of the interval determining domain of definition for the initial functions.

Numerical integration of the equations of retarded type by finite-difference method is organized similar to that for ordinary differential equations.

A feature is that we have to deal with *array of values of the unknown function sampled with the integration step and relating to a time interval of required duration*, which represents the initial function. With data from this array, we evaluate the right-hand part of the equation and perform a time step of integration. One can use methods analogous to those of Euler or Runge-Kutta of different orders; if necessary, an interpolation procedure consistent in accuracy with the finite-difference scheme may be applied over the array of the data. As a step has been made, the array is updated, and the procedure goes on.

In contrast to ordinary differential equations, really hard is a question on possibility to trace dynamics *backward* in time. If trying to do so, we have to deal actually with the equation of leading type that is the ill-posed problem, as mentioned above.

Is it possible to generalize the hyperbolic theory and to introduce uniformly hyperbolic attractors in systems governed by the differential equations with deviating argument? It seems that this question was not examined in mathematical literature, but it certainly deserves attention of mathematicians. On the other hand, accounting close relation of the differential-delay equations with ordinary equations via the "step method" (expressed by relations (10.3)) and applicability of approaches developed for design of systems with uniformly hyperbolic attractors to the time-delayed systems (see below), one can expect that the answer will be positive.

To get impression on possible behavior of neighboring orbits in the time-delayed system, let us consider a particular question on stability analysis of a fixed point in the model (10.2). Let the fixed point solution be $x = x_0$, and we consider dynamics close to it setting $x(t) = x_0 + \tilde{x}(t)$. Substitution in (10.2) yields

$$\dot{\tilde{x}} = a\tilde{x}(t) + b\tilde{x}(t-\tau), \tag{10.4}$$

where $a = f_1'(x_0, x_0)$ and $b = f_2'(x_0, x_0)$ are derivatives of the function $f$ in respect to the first and the second arguments evaluated at these arguments equal to $x_0$. The exponential substitution $\tilde{x}(t) \sim e^{\lambda t}$ reduces (10.4) to the transcendent characteristic equation:

$$\lambda = a + be^{-\lambda\tau}. \tag{10.5}$$

Equations of such kind for the case of retarding type problems can have only a restricted number of roots in the right half-plane of complex variable $\lambda$, which are associated with instability. However, there is an infinite set of complex roots in the left half-plane; their real parts asymptotically tend to $-\infty$.[1] It means that a saddle-fixed point in the time-delayed system has a finite-dimensional unstable subspace, and an infinite-dimensional stable subspace. Of analogous type will be structure of other typical saddle orbits in the state space of time-delayed systems.

Methods of computation of Lyapunov exponents for the time-delay systems were discussed, e.g. in (Farmer, 1982; Giacomelli and Politi, 1996; Le Berre et al., 1987; Lepri et al., 1994; Balyakin and Ryskin, 2007; Pazó, D. and López, 2010).

The Lyapunov exponents may be introduced in a similar way as for ordinary differential equations. Say, for a system (10.2) the largest Lyapunov exponent is obtained from simultaneous numerical solution of that equation along the reference trajectory and the variation equation

$$\dot{\tilde{x}} = f_1'(x(t), x(t-\tau))\tilde{x}(t) + f_2'(x(t), x(t-\tau))\tilde{x}(t-\tau). \tag{10.6}$$

The perturbation vector at some instant $t$ in the computations is represented as an array of values $(\tilde{x}_0, \tilde{x}_1, \tilde{x}_2, \ldots, \tilde{x}_M)$, where $\tilde{x}_k = \tilde{x}(t-kh)$, $h$ is a step of the finite-difference scheme, and $M = \tau/h$ is a number of steps in the delay time interval. Using the norm definition $\|\mathbf{x}\| = \sqrt{x_0^2 + x_1^2 + \cdots + x_M^2}$ one renormalizes the perturbation vector to have a fixed norm and continues the procedure accumulating the sums of logarithms of the norm ratios before and after the normalization. The rate of growth of the accumulating sums determines the Lyapunov exponent.

Supplementing the procedure with additional equations for perturbation vectors, and with Gram-Schmidt orthogonalization (using the dot product defined as $\mathbf{x} \cdot \mathbf{y} = \sqrt{x_0 y_0 + x_1 y_1 + \cdots + x_M y_M}$) in straight analogy with the method described in Appendix A, one can evaluate more than one Lyapunov exponents, but not the complete spectrum (as it is infinite in the original equation although restricted in the finite-difference numerical scheme). It is reasonable to agree that the number of terms in the spectrum of Lyapunov exponents really deserving consideration and catching essential features of the dynamics is just the number sufficient to get a correct estimate of the dimension for the attractor from Kaplan-Yorke formula (Appendix D) (Farmer, 1982; Blokhina et al., 2007).

It is appropriate for the time-delayed systems to consider construction analogous to the Poincaré maps in ordinary differential equations (Kuznetsov, 1982; Giacomelli and Politi, 1996).

In this respect, the simplest is the case of non-autonomous systems represented by equation

$$\dot{\mathbf{x}} = \mathbf{f}(t, \mathbf{x}(t), \mathbf{x}(t-\tau)), \tag{10.7}$$

[1] For equations of neutral type the infinite set of roots has asymptotically equal real parts, and may be placed either in right, or in a left half-plane depending on concrete equations and parameters. In leading type case the placement is inversed in comparison with the retarding equation that implies infinite number of unstable roots.

with the right-hand parts periodic in time: $\mathbf{f}(t,\mathbf{x},\mathbf{y}) \equiv \mathbf{f}(t+T,\mathbf{x},\mathbf{y})$, where $T$ is a period. Then, the description may be formulated in terms of functional stroboscopic map

$$\mathbf{X}_{n+1}(t) = \mathbf{F}(\mathbf{X}_n(t)). \tag{10.8}$$

Here the functions $\mathbf{X}_n(t)$ are defined in an interval of length $\tau$ and are related with the original variable $\mathbf{x}(t)$ as $\mathbf{X}_n(t) = \mathbf{x}(t+nT)$. Concrete examples of such systems will be discussed in Sect. 10.2.

In autonomous systems one has to introduce some condition on the function $\mathbf{x}(t)$, which is valid at once in each characteristic period of the dynamics, and introduce a functional map, which generates a sequence of the states at successive instants of validity of this condition. An example will be discussed in Sect. 10.3.

## 10.2 Van der Pol oscillator with delayed feedback, parameter modulation and auxiliary signal

Consider a model system described by the equation of the following form (Kuznetsov and Ponomarenko, 2008):

$$\ddot{x} - (A\cos(2\pi t/T) - x^2)\dot{x} + \omega_0^2 x = \varepsilon x(t-\tau)\dot{x}(t-\tau)\cos\omega_0 t. \tag{10.9}$$

Here, $x$ is a dynamic variable of van der Pol oscillator with the operating frequency $\omega_0$, in which the parameter controlling the bifurcation of limit cycle varies slowly in time with period $T$ and amplitude $A$, so that the oscillator alternately manifests activation and damping. To the right-hand side of the equation a term is added responsible for the delayed feedback. It is a product of the dynamical variable delayed by $\tau$, its derivative, and the auxiliary signal at the frequency $\omega_0$. Parameter $\varepsilon$ determines strength of the delayed feedback. We assume that $N = \omega_0 T/2\pi$ is an integer, so that the external driving is periodic. A block-diagram of the system is shown in Fig. 10.1.

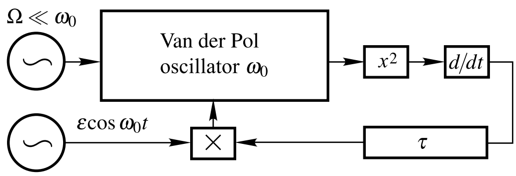


**Fig. 10.1** Block diagram of the system with delay.

### 10.2.1 Attractor of Smale-Williams type in the time-delayed system

Functioning of the system (10.9) as a generator of chaos can be explained as follows. Due to the periodic variation of the parameter responsible for the emergence of the generation, the oscillator alternately manifests stages of activity and damping. Having made proper selection of the retarding time, for example $\tau = \frac{3}{4}T$, one can ensure such a situation that the emergence of self-sustaining oscillations at each next stage of activity is stimulated by a signal emitted at the previous activity epoch. Suppose that it was characterized by some phase $\varphi$, i.e. $x(t) \sim \sin(\omega_0 t + \varphi)$ and $\dot{x}(t) \sim \cos(\omega_0 t + \varphi)$. Then the term in the right-hand part of the equation will contain a component at the fundamental frequency $\omega_0$ with the doubled phase shift constant. Indeed,

$$\begin{aligned} x(t-\tau)\dot{x}(t-\tau)\cos\omega_0 t &\sim \sin 2(\omega_0(t-\tau)+\varphi)\cos\omega_0 t \\ &= \frac{1}{2}\sin(\omega_0 t - 2\omega_0\tau + 2\varphi) + \cdots, \end{aligned} \tag{10.10}$$

where the dots designate a non-resonant term. Therefore, at a new stage of activity the phase of the oscillator will be determined by the phase of the resonant component of the stimulating signal, and at successive stages of activity we obtain the Bernoulli map $\varphi_{n+1} = 2\varphi_n + \mathrm{const}(\mathrm{mod}\ 2\pi)$, in the state space that corresponds to expansion along the angular coordinate $\varphi$. If in other directions compression of the phase volume takes place, such dynamics must correspond to the presence of attractor of Smale-Williams type for the mapping of the phase space in one period of external driving.

For the numerical solution the finite difference method of Runge-Kutta was used, modified with respect to the system with time delay. The retarded values for variable $x$ required to perform steps of the difference scheme are extracted from the stored array of data obtained in the previous steps of the integration. An interpolation scheme was used providing the required order of accuracy. At the beginning of the computations, the array of data is usually filled with random values; then the long enough initial stage of calculations is performed for the system to reach the attractor, and only after that processing procedures including plotting the data are performed.

In Fig. 10.2 panel (a) shows the dynamical variable plotted versus time as obtained from numerical solution of Eqs. (10.9) for oscillations corresponding to the motion on the attractor. Chaos manifests itself in randomness of phases of the oscillations relative to the envelope at successive stages of activity. Panel (b) is a diagram for the phases identified at successive stages of activity; it demonstrates nice agreement with the Bernoulli map, as expected from the qualitative consideration of the operation of the scheme. Panels (b) and (c) show portraits of the attractor. One is projection of the attractor from the extended (including the time axis) phase space of the non-autonomous infinite-dimensional flow system, the other is a portrait of the attractor in the stroboscopic Poincaré section. In the last diagram the transversal

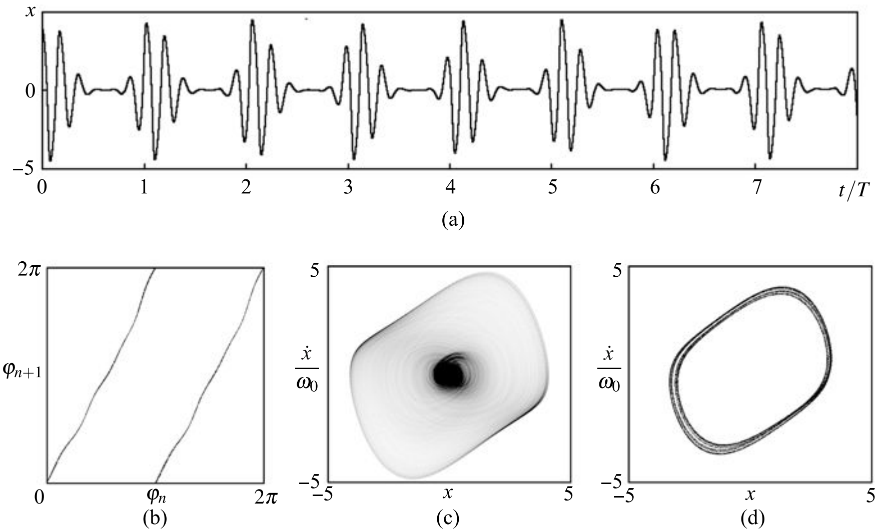


**Fig. 10.2** Waveform of the dynamical variable $x$ according to the results of the numerical solution of Eq. (10.9) at $\omega_0 = 2\pi, T = 6, \tau = \frac{3}{4}T, A = 5.5, \varepsilon = 0.2$ **(a)**. Diagram illustrating the transformation of phases in the successive stages of the activity **(b)**. Attractor of the system in the projection from the infinite dimensional space of states on the phase plane of the oscillator **(c)** and a portrait of the attractor in the Poincaré section **(d)**.

fractal structure is visible, which is a characteristic feature of attractor of Smale-Williams type.

To calculate the Lyapunov exponents the method is used based on the Benettin algorithm with modifications corresponding to the class of delay systems (Farmer, 1982; Giacomelli and Politi, 1996; Le Berre et al., 1987; Lepri et al., 1994; Balyakin and Ryskin, 2007; Pazó, D. and López, 2010). It exploits data of joint numerical integration of Eq. (10.9) and a collection of $m$ variation equations

$$\begin{aligned} &\ddot{\tilde{x}} - (A\cos(2\pi t/T) - x^2)\dot{\tilde{x}} + 2x\dot{x}\tilde{x} + \omega_0^2\tilde{x} \\ &= \varepsilon[\tilde{x}(t-\tau)\dot{x}(t-\tau) + x(t-\tau)\dot{\tilde{x}}(t-\tau)]\cos\omega_0 t \end{aligned} \tag{10.11}$$

to get $m$ larger Lyapunov exponents. In numerical calculations, a perturbation vector is given by the instantaneous values of $\tilde{x}, \dot{\tilde{x}}$ and an array of data corresponding to the values of the variable $\tilde{x}$ in the interval of delay.

Since the system is non-autonomous, it is convenient to organize the computations, considering the stroboscopic dynamics, with time intervals of duration $T$. Upon completion of each stage, the perturbation vectors are orthogonalized by means of the Gram-Schmidt process and normalized to a fixed constant. Lyapunov exponents are obtained from the rate of growth of the cumulative sums of logarithms of the ratios characterizing increase or decrease of the norms of the vectors.

At the chosen parameters the computations yield the following values normalized as for the stroboscopic map (the time scale is the period of modulation $T$):

$$\Lambda_1 = 0.688, \quad \Lambda_2 = -0.837, \quad \Lambda_3 = -4.287\ldots. \tag{10.12}$$

The only positive exponent of the attractor is close to $\ln 2 = 0.693\ldots$, which is consistent with the approximate description of the dynamics in terms of Bernoulli map for the phase variable. Estimate of the dimension with Kaplan-Yorke formula yields for the attractor of the stroboscopic map $D_{KY} = 1 + \Lambda_1/|\Lambda_2| \approx 1.82$. Dimension of the attractor in the extended phase space of the continuous time system is greater by one ($D \approx 2.82$).

It was discovered that in this system hard excitation occurs with hysteresis in a quite wide range of parameters. To study the question, it is convenient to supplement Eq. (10.9) with an additional parameter $h$, which regulates relative duration of excitation and damping stages of the oscillator:

$$\ddot{x} - (h + A\cos(2\pi t/T) - x^2)\dot{x} + \omega_0^2 x = \varepsilon x(t-\tau)\dot{x}(t-\tau)\cos\omega_0 t. \tag{10.13}$$

The above-described mode of operation corresponds to excitation of each new train of oscillations by the stimulating signals transmitted in the delayed feedback loop. Its value is proportional to the squared amplitude of oscillations at the previous stage of activity. If one sets the initial conditions with characteristic amplitude small enough, the excitation does not occur because of negligible level of the squared amplitude, and the oscillations do not develop. Generation regime can be restored by increasing parameter $h$, i.e. by increase of the part of the modulation period, during which the oscillations are linearly unstable. With gradual growth of $h$, at some point one observes an abrupt transition to the large-amplitude chaotic regime. Now, if one starts to decrease $h$, it does not lead immediately to breakdown of the chaotic oscillations since the excitation in the system is transferred from the previous stages of activity to the following ones. Only at large enough negative values of $h$ the oscillations disappear. The hysteresis phenomenon we have described is illustrated in Fig. 10.3. The insets show iteration diagrams for phases associated with certain places on the hysteresis loop. In the course of computation, small random perturbation was added at each step of the numeric integration on a level of order $\Delta x \sim 0.001$ to ensure departure of the system from the trivial stationary state at zero.

The mechanism of functioning of the model and numerical results, confirming its implementation, suggest that the observed low-dimensional chaotic attractor is uniformly hyperbolic, namely, it is a suspension of attractor of Smale-Williams embedded in an infinite state space of the system with delay. Despite hypothetical nature of this conclusion, the considered scheme of the chaotic generator is interesting in itself, because it is prominent for generation of chaotic regimes insensitive to variations of parameters, technical fluctuations and design details, e.g. in the systems of radio-engineering and electronics, nonlinear optics, etc.

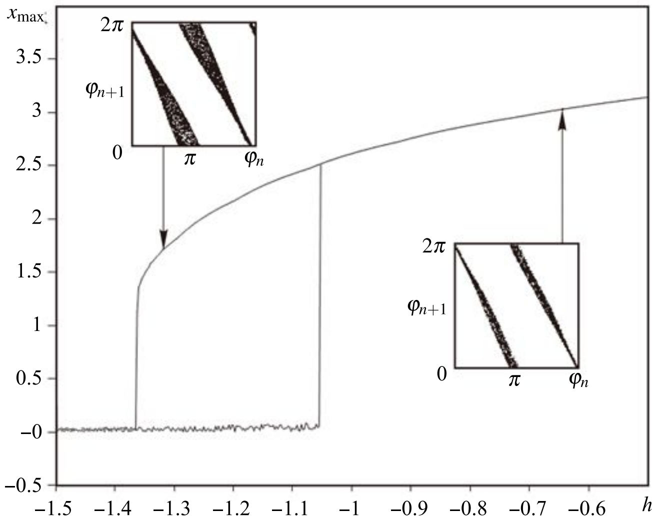


**Fig. 10.3** A diagram illustrating the hard excitation and hysteresis in the system: dependence of the maximum amplitude of the parameter $h$ in (10.13) at $\omega_0 = 2\pi, T = 24, \tau = 12, A = 3, \varepsilon = 0.3$. The parameter $h$ is varied, first, from left to right that corresponds to motion along the lower branch, and then from right to left that corresponds to motion along the upper branch of the hysteresis loop.

## *10.2.2 Hyperchaotic attractors*

An interesting question is the following. Accounting infinite dimensional nature of the dynamics, can we obtain hyperchaos characterized by two or more positive Lyapunov exponents? In the hyperbolic theory it corresponds to attractors with dimension of the unstable manifolds two or more. Remarkably, it may be done in the above model without structural modification, simply by means of appropriate selection of parameters. Namely, one has to increase the ratio of the delay time to the period of parameter modulation in such a way that the signal arriving through the feedback loop would stimulate excitation not at the nearest next stage of activity, but with elapse of one, two, or more activity stages (Fig. 10.4). The mode of operation discussed in the previous section corresponds to delay time marked with the arrow

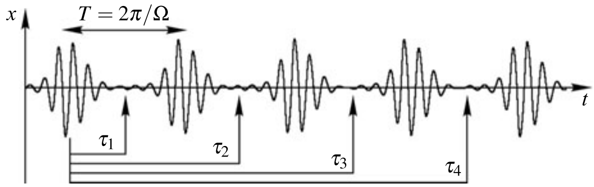


**Fig. 10.4** A diagram illustrating selection of delay time for implementation of regimes with different numbers of positive Lyapunov exponents.

$\tau_1$ while larger delay times, which give rise to hyperchaotic regimes, are indicated with the arrows $\tau_2, \tau_3, \tau_4$.

Let us hereafter concretize the delay times as follows:

$$\tau = \left(k - \frac{1}{2}\right) T, \tag{10.14}$$

where $k$ is a positive integer. Then, with argumentation similar to that in the previous section, we arrive at the mapping for phases of successive trains of oscillations

$$\varphi_n = 2\varphi_{n-k} + \text{const.} \tag{10.15}$$

It reduces to the Bernoulli map in the case $k = 1$. At $k \geqslant 2$ this relation must be interpreted as a map on a $k$-dimensional torus: a vector $\mathbf{v}_{n-1} = (\varphi_{n-1}, \dots, \varphi_{n-k})$ is mapped to vector $\mathbf{v}_n = (\varphi_n, \dots, \varphi_{n-k+1})$. The map possesses a special degeneracy, namely, the complete sequence of phase variables $\varphi_n$ is composed of $k$ independent subsequences in such a way that in the course of the time evolution their terms alternate. For each subsequence, at $k$ steps of discrete time small perturbations undergo doubling, being clear from (10.15). Thus, the map (10.13) has $k$ Lyapunov exponents of equal value $\Lambda_i = k^{-1} \ln 2, i = 1, 2, \dots, k$.

Relating the original system (10.9) the map (10.15) is an approximation. Nevertheless, in application to the regimes of active operation (pulsations), in a wide range of parameters, the conclusion concerning a number of positive Lyapunov exponents must remain valid, although the consecutive terms of the sequence of the phases will no longer be completely independent. It means that the degeneracy is lifted, and the Lyapunov exponents will not be precisely equal. In the infinite-dimensional phase space of the delay system, such dynamics will give rise to a stretch of phase volume along $k$ directions, associated with cyclic coordinates $\varphi_1, \dots, \varphi_k$, and the remaining directions will correspond to compression. It will be hyperchaotic attractor with $k$ positive and others negative Lyapunov exponents.

Figure 10.5 shows waveforms for the oscillating variable versus time plotted in sustained chaotic regimes at different ratios of the delay time and the modulation period selected in accordance with (10.14) for $k = 1, 2, 3, 4$. Thus, panel (a) corresponds to situation of stimulation of excitation by the feedback signal just at the next activity stage, and panels (b)—(d) correspond to stimulation through one, two, and three elapsed intermediate activity stages.

As can be seen, in all cases the process looks like a sequence of oscillating trains following each other with time interval $T$, and the carrier phase evolves from pulse to pulse in a chaotic manner. To demonstrate that chaos indeed appears due to the above-described mechanism of the phase transfer from the previous stages of activity, in Fig. 10.6 the iteration diagrams are shown for the phases. Phases corresponding to each next stage of activity are determined at certain instants fixed with respect to the waveform of slow parameter modulation, according to the formula $\varphi_n = \arg(x - i\omega_0^{-1}\dot{x})$. The same parameter values were assigned as those for computation of the waveforms in Fig. 10.5. The plots are shown in coordinates $(\varphi_n, \varphi_{n-k})$, where $k = 1, 2, 3, 4$ for panels (a), (b), (c) and (d), respectively. Observe that the di-

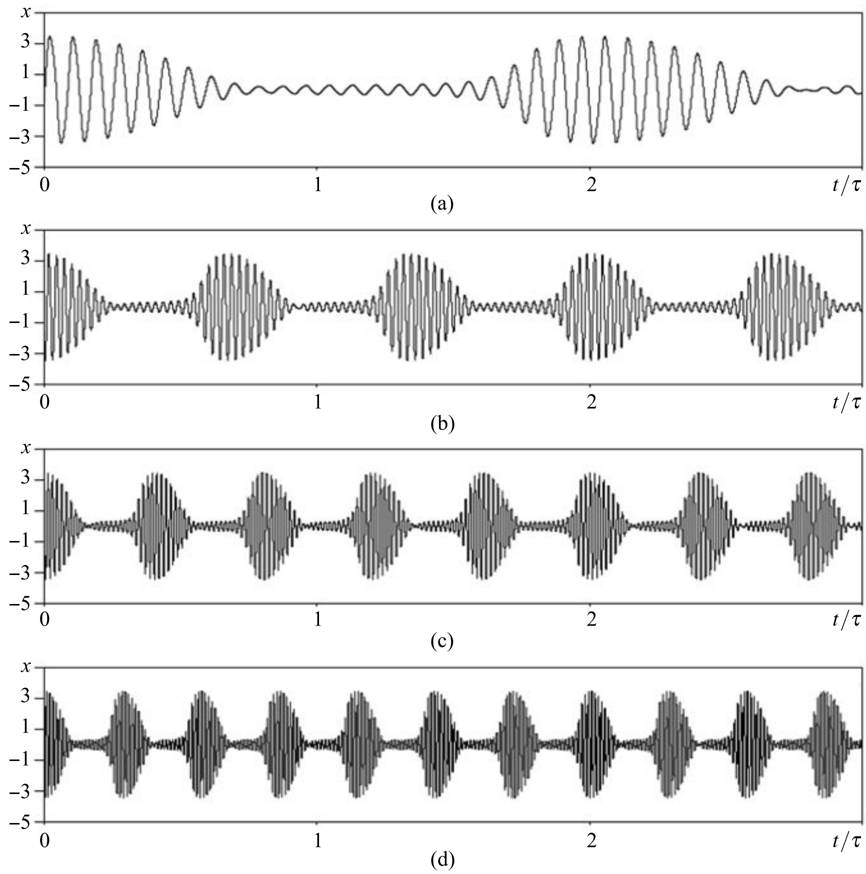


**Fig. 10.5** Waveforms for the oscillating variable versus time obtained from numerical simulation for model (10.9) at $\omega_0 = 2\pi, \varepsilon = 0.3, T = 24, A = 3$, and $k = 1, \tau = 12$ **(a)**; $k = 2, \tau = 36$ **(b)**; $k = 3, \tau = 60$ **(c)**; $k = 4, \tau = 84$ **(d)**.

agrams confirm efficiency of the description in terms of the maps (10.13). Indeed, variation of the phase $\varphi_{n-k}$ implies roughly doubled variation of $\varphi_n$. In Fig. 10.7 we show diagrams for phases in coordinates $(\varphi_n, \varphi_{n-1})$. The fact that the dots nearly uniformly fill a square indicates closeness of the situation to statistical independence of the subsequences. Slightly distinguishable non-uniform structures indicate that a weak statistical dependence is still present, which is not accounted in the simplified description by maps (10.15).

Computations support the conclusions concerning a number of positive Lyapunov exponents in regimes at delay times selected in accordance with (10.15) at different $k$. It is convenient to use Lyapunov exponents normalized to the period $kT : \bar{\Lambda}_i = k\Lambda_i = kT\lambda_i$. In the framework of description by the map (10.15), the first $k$ Lyapunov exponents with this normalization should be equal precisely to $\ln 2 \approx 0.693$.

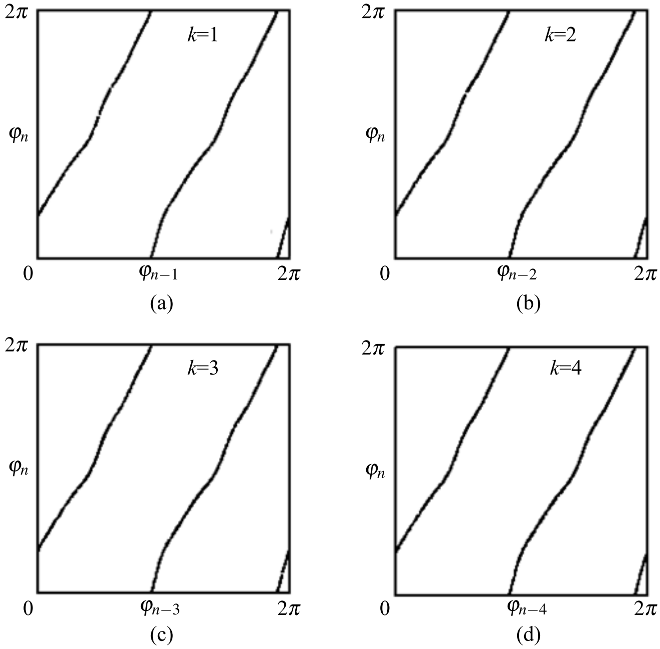


**Fig. 10.6** Iteration diagrams for phases illustrating applicability of the approximated description by the maps (10.15) at different $k$; parameters are the same as in Fig. 10.5.

In computations, in each regime of operation of the system we evaluated a number of Lyapunov exponents for the stroboscopic mapping sufficient for estimate of the attractor dimension from the Kaplan-Yorke formula $D = m + S_m/|\bar{\Lambda}_{m+1}|$, here the integer $m$ is selected in such a way that the sum $S_m = \sum_{i=1}^{m} \bar{\Lambda}_i$ is positive, while $S_{m+1}$ is already negative.

An insightful way of representing the spectrum of Lyapunov exponents, which allows immediate distinguishing the type of hyperchaos regime, is to plot the sums $S_m$ against the number $m$. These graphs are shown in Fig. 10.8. On such a diagram all essential quantifiers of chaos are presented: the value of the plotted function at unit argument is the largest Lyapunov exponent $\bar{\Lambda}_1$; the argument value at the maximum is the number of positive exponents. The maximum of the function corresponds to the Kolmogorov-Sinai entropy according to the Pesin formula $\bar{h} = \sum_{\bar{\Lambda}_k > 0} \bar{\Lambda}_k$. Intersection of the broken line with the abscissa determines the Kaplan-York dimension of the attractor. Observe that in all the cases positive Lyapunov exponents are close to $\ln 2 \approx 0.693$ that agrees with the conclusion based on the approximate maps (10.15).

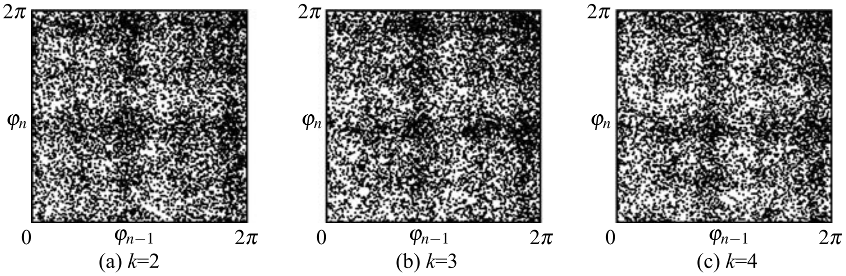


**Fig. 10.7** Diagrams illustrating weak statistical dependence of phases of nearest neighboring activity stages at $k = 2, 3$, and 4; parameters are the same as in Fig. 10.5.

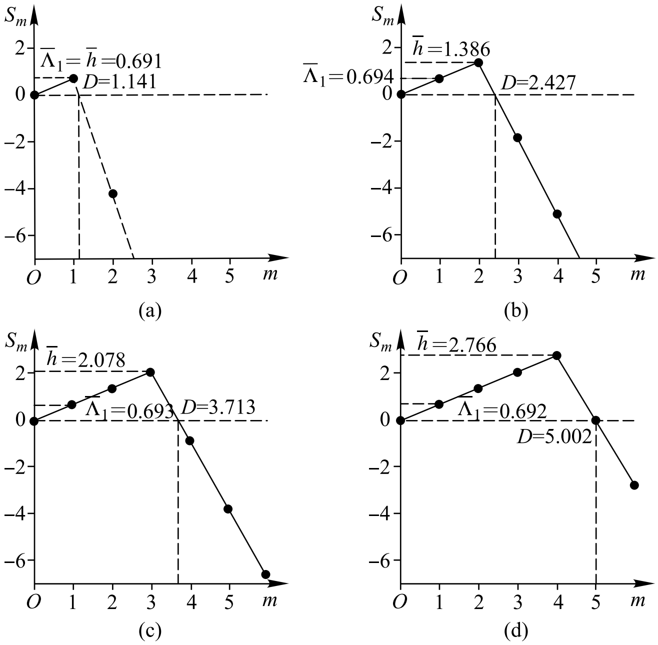


**Fig. 10.8** Plots of sums of Lyapunov exponents on the number of them with indicated values of the largest exponent $\bar{\Lambda}_1$, Kaplan-Yorke dimension $D$, and Kolmogorov-Sinai entropy $\bar{h}$. The data are obtained in computations for the model (10.9) at $\omega_0 = 2\pi, \varepsilon = 0.3, T = 24, A = 3$ for $k = 1, \tau = 12$ **(a)**; $k = 2, \tau = 36$ **(b)**; $k = 3, \tau = 60$ **(c)**; $k = 4, \tau = 84$ **(d)**.

## 10.3 Van der Pol oscillator with two delayed feedback loops and parameter modulation

The system discussed in the previous section is non-autonomous because of two kinds of time dependence of the coefficients. The first is slow variation of a parameter responsible for the birth of self-oscillation in the van der Pol oscillator, and the second is the auxiliary signal of frequency $\omega_0$ equal to the natural frequency of the oscillator. Now, we intend to introduce a model, in which the auxiliary signal is not needed; it makes the scheme simpler in practical implementation (Baranov et al., 2010).

Consider the block diagram in Fig. 10.9. Again, the main element is the van der Pol oscillator, in which the parameter controlling the Andronov-Hopf bifurcation, is slowly modulated in time with period $T$, so that it alternately manifests the excitation and damping. Now, however, the signal from the oscillator passes through *two loops of delayed feedback*, in which the retarding time $\tau_1$ and $\tau_2$ differ by $T$. In one of the feedback circuits the signal undergoes quadratic nonlinear transformation and differentiation, so, the low-frequency component is filtered out (see blocks marked on the diagram, respectively $x^2$ and $d/dt$), and then it is mixed on a quadratic nonlinear element (marked on the diagram as skew cross) with the signal received from the second feedback circuit. The resulting signal contains a component at the difference frequency resonant with the oscillator, and it stimulates the excitation at the beginning of the next stage of activity. The delays are chosen in such a way that to stimulate excitation at the $n+1$-th stage of activity, the signals arrive at the right time from the $(n-1)$-th and $n$-th stages of activity, respectively, through the first and the second feedback loops.

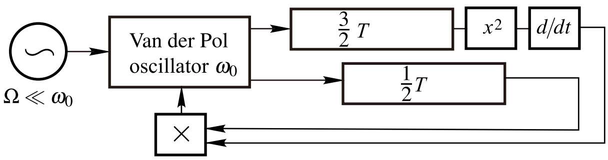


**Fig. 10.9** Block diagram of the system with two delayed feedback loops.

A formal model for the device is a differential equation with two delays

$$\ddot{x} - (A\cos(2\pi t/T) + h - x^2)\dot{x} + \omega_0^2 x = \varepsilon x(t-\tau_1)x(t-\tau_2)\dot{x}(t-\tau_2). \tag{10.16}$$

Here, $x$ is an oscillating variable of the van der Pol oscillator; $\varepsilon$ is a parameter characterizing depth of the delayed feedback, the value of $A$ determines magnitude of the modulation of parameter responsible for the excitation of the oscillator in respect to the average level determined by a value of $h$. To be concrete, we select the delay time constants as $\tau_1 = \dfrac{1}{2}T$ and $\tau_2 = \dfrac{3}{2}T$.

Let us assume for a while that $h=0$. Then, the oscillator will be alternately in active and passive stages of equal duration, respectively, while $A\cos(2\pi t/T) > 0$ or $A\cos(2\pi t/T) < 0$. Suppose the oscillations at the activity stages numbered with $n$ and $n-1$ were $\varphi_n$ and $\varphi_{n-1}$, respectively, i.e. $x \sim \sin(\omega_0 t + \varphi_n)$ and $x \sim \sin(\omega_0 t + \varphi_{n-1})$. Then, substitution in the right-hand part of (10.16) yields

$$
\begin{aligned}
& x(t-\frac{1}{2}T)x(t-\frac{3}{2}T)\dot{x}(t-\frac{3}{2}T) \\
& \sim \sin\left(\omega_0 t - \frac{1}{2}\omega_0 T + \varphi_n\right)\sin\left(\omega_0 t - \frac{3}{2}\omega_0 t + \varphi_{n-1}\right)\cos\left(\omega_0 t - \frac{3}{2}\omega_0 T + \varphi_{n-1}\right) \\
& = \frac{1}{2}\sin\left(\omega_0 t - \frac{1}{2}\omega_0 T + \varphi_n\right)\sin(2\omega_0 t - 3\omega_0 T + 2\varphi_{n-1}) \\
& = -\frac{1}{4}\cos\left(\omega_0 t - \frac{5}{2}\omega_0 T + 2\varphi_{n-1} - \varphi_n\right) + \cdots,
\end{aligned}
$$

where three dots designate a non-resonance term (the third harmonic). Hence, the phase of oscillations at the next activity stage will be expressed as

$$\varphi_{n+1} = -\varphi_n + 2\varphi_{n-1} + \text{const}\ (\bmod 2\pi). \tag{10.17}$$

In the following, for the phase difference $\Delta\varphi_n = \varphi_n - \varphi_{n-1}$ the expanding circle map, or Bernoulli map, holds:

$$\Delta\varphi_{n+1} = -2\Delta\varphi_n\ (\bmod 2\pi). \tag{10.18}$$

The last map is chaotic, with the Lyapunov exponent $\Lambda_1 = \ln 2 \approx 0.693$. The map (10.17) has the same value of the largest Lyapunov exponent, and additionally, the zero value exponent $\Lambda_2 = 0$.

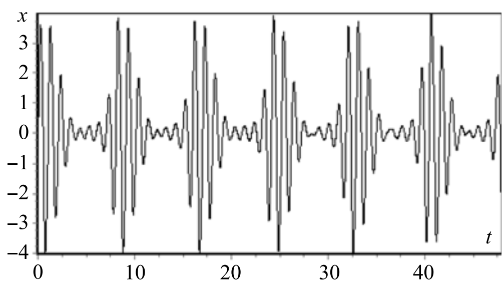


**Fig. 10.10** Waveform for the oscillating variable obtained in computations for the model (10.16) at $\omega_0 = 2\pi, T = 8, A = 4, h = 0, \varepsilon = 0.05, \tau_1 = \frac{1}{2}T$ and $\tau_2 = \frac{3}{2}T$.

Calculations show that the expected type of chaotic dynamics occurs in a quite wide range of parameters. For detailed analysis, the following parameter values are selected: $\omega_0 = 2\pi, T = 8, A = 4, h = 0, \varepsilon = 0.05$. Figure 10.10 shows the generalized coordinate of the oscillator versus time for these parameters. The process is a sequence of trains of oscillations following each other after a time interval $T$. However, the filling phase of the carrier varies from pulse to pulse in a chaotic manner. The presence of chaos is caused by the above-described mechanism of the transfer of phase from the previous stages of the process. Figure 10.11 (a) shows the iteration diagram for phases in the form of three-dimensional graphics, which demonstrates approximate correspondence of the respective function of two variables and expression (10.17). Figure 10.11 (b) shows the iteration diagram for the phase differences between neighboring activity stages, which is observed to be in good agreement with relation (10.18).

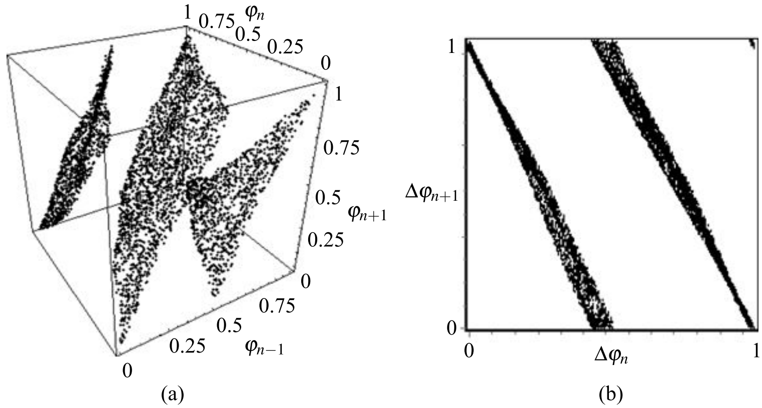


**Fig. 10.11** Diagrams illustrating the transformation of phases in the successive stages of the activity of oscillator **(a)** and for phase differences **(b)** in model (10.16) at $\omega_0 = 2\pi, T = 8, A = 4, h = 0, \varepsilon = 0.05, \tau_1 = \frac{1}{2}T$ and $\tau_2 = \frac{3}{2}T$.

Figure 10.12 shows in panel (a) a portrait of a trajectory on the attractor plotted on the phase plane of the van der Pol oscillator. In fact, the attractor of the system with delay is an object in an infinite-dimensional state space; so the picture should be viewed as a two-dimensional projection of the trajectory. Panel (b) shows a portrait of the attractor in the stroboscopic cross-section.

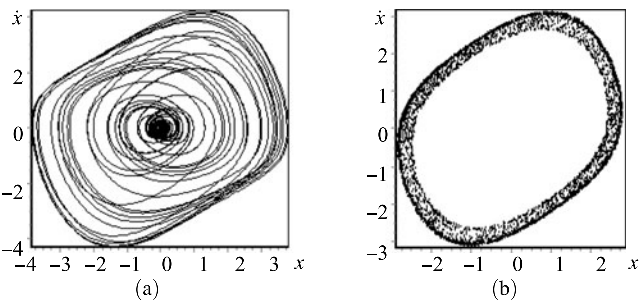


**Fig. 10.12** Two-dimensional projection of a trajectory on the attractor **(a)** and portrait of the attractor in stroboscopic cross-section **(b)** obtained in the numerical solution of Eq. (10.16) at $\omega_0 = 2\pi, T = 8, A = 4, h = 0, \varepsilon = 0.05$.

To calculate the Lyapunov exponents the method was used similar to that discussed in the previous section. It exploits data of joint numerical integration of Eq.

(10.16) and a collection of the variation equations for the perturbation vectors

$$\begin{aligned}
&\ddot{\tilde{x}} + 2x\tilde{x}\dot{x} - (A\cos(2\pi t/T) + h - x^2)\dot{\tilde{x}} + \omega_0^2 x \\
&= \varepsilon\tilde{x}\left(t - \frac{1}{2}T\right) x\left(t - \frac{3}{2}T\right) \dot{x}\left(t - \frac{3}{2}T\right) + \varepsilon x\left(t - \frac{1}{2}T\right) \tilde{x}\left(t - \frac{3}{2}T\right) \dot{x}\left(t - \frac{3}{2}T\right) \\
&\quad + \varepsilon x\left(t - \frac{1}{2}T\right) x\left(t - \frac{3}{2}T\right) \dot{\tilde{x}}\left(t - \frac{3}{2}T\right).
\end{aligned} \tag{10.19}$$

Figure 10.13 shows plots for the largest three Lyapunov exponents versus the parameter of modulation depth $A$ at fixed other parameters. It should be noted that the largest two exponents in a wide range remains almost constant and close to the values ln2 and 0, respectively, in agreement with analyses based on the map (10.17) for transformation of phases. Particularly, at $A = 4$ the first five exponents are found $\Lambda_1 = 0.693, \Lambda_2 = 0.000, \Lambda_3 = -1.140, \Lambda_4 = -1.333, \Lambda_5 = -3.807$. Hence, the Kaplan-Yorke dimension for attractor in stroboscopic cross-section is $D_{KY} = 2 + \Lambda_1/|\Lambda_3| \approx 2.61$, and for attractor embedded in the extended state space is $D \approx 3.61$.

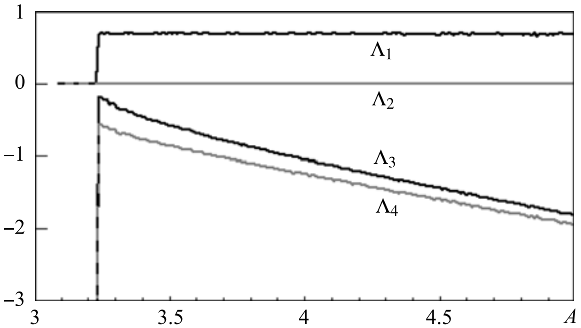


**Fig. 10.13** Dependence of the first four of the Lyapunov exponents on parameter modulation $A$ for stroboscopic map of the model (10.16) at $\omega_0 = 2\pi, T = 8, \varepsilon = 0.05, h = 0$. The computations were performed with gradual decrease of $A$, with the inheritance of the instantaneous states of the system at each step of the parameter variation.

Figure 10.14 shows power spectrum of the oscillator in the present mode of generation of chaos. For its construction a long enough time series was processed sampled from data of numerical simulation of the model (10.16) for motion on the attractor. The spectrum is computed according to the method of statistical evaluation of the spectral power density known in the theory of random processes (Jenkins and Watts, 1968). The procedure is to break the time series into pieces of certain length, performing the Fourier transform for each segment, and then averaging the squares of the amplitudes of spectral components. As can be seen from the figure, the spectrum is concentrated in a certain band near the frequency, $f \approx 1$, i.e. $\omega = 2\pi f \approx \omega_0 = 2\pi$. Note the presence of continuous part of the spectrum that is characteristic for chaotic dynamics. Discrete peaks in the left part of the diagram appear due to the periodic component present in the dynamics of the system because of the slow modulation of the excitation parameter.

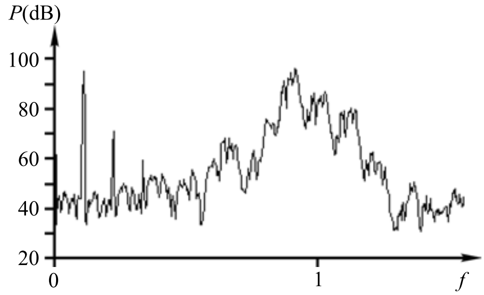


**Fig. 10.14** Power spectrum of the signal generated by the system at $\omega_0 = 2\pi, T = 8, A = 4, \varepsilon = 0.05, h = 0$ obtained by processing the numerical results of the model (10.16).

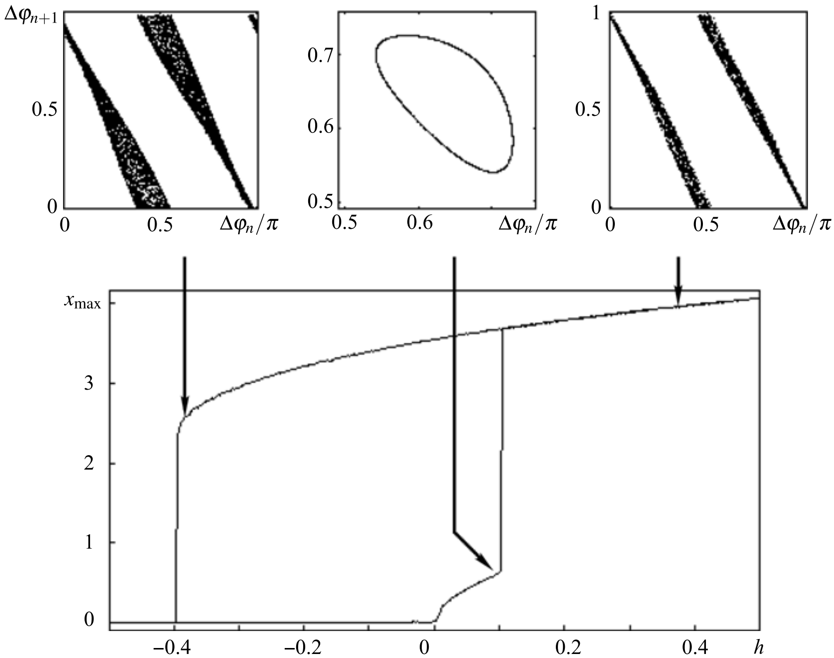


**Fig. 10.15** A diagram illustrating the soft-hard excitation and hysteresis in the system: dependence of the maximum amplitude of the parameter $h$ in (10.16) at $\omega_0 = 2\pi, T = 8, A = 3.9, \varepsilon = 0.05$.

It was observed that the system manifests soft-hard excitation and hysteresis. This phenomenon is illustrated in Fig. 10.15. The amplitude of oscillations is plotted against parameter $h$, which is varied, first, from the left to the right that corresponds to motion along the lower branch, and then from the right to the left that corresponds to motion along the upper branch of the hysteresis loop. Insets in the top part of the picture show the iteration diagrams for phases, corresponding to representative points on the hysteresis loop. When performing calculations in the system a small noise of level 0.001 was added to ensure departure of the system from the trivial zero state. The mechanism for the phenomenon is similar to that discussed in the previous section.

As one can guess, this system should be related to a class of systems with *partially hyperbolic attractors* (Pesin, 2004; Bonatti et al., 2005; Pesin, 2007) due to the presence of a neutral direction at points of the attractor associated with the near-zero Lyapunov exponent. A rigorous justification of this conjecture seems to be rather complex mathematical problem because of infinite-dimensional nature of the system.

It is worth mentioning that another version of a scheme of generator of chaos based on van der Pol oscillator with two delayed feedback loops was advanced and analyzed in (Kuznetsov and Pikovsky, 2008). It differs from (10.16) with the degree of the nonlinear transformations of signals in the feedback circuits; in model (Kuznetsov and Pikovsky, 2008) these transformations are cubic and quadratic, while those in the model (10.16) are linear and quadratic, respectively.

## 10.4 Autonomous time-delay system

To construct an *autonomous* model with the mechanism of generation of chaos similar to that in the previous sections, but without external driving, an appropriate starting point is the *logistic delay equation.* It was offered in due time in the context of population biology (Fowler, 1982) and reads

$$\dot{r} = \mu(1 - r(t-\tau))r(t). \tag{10.20}$$

Here $r$ is positive population variable normalized in such a way that the saturation occurs at $r = 1$; $\mu > 0$ is parameter of the birth rate at small populations; $\tau$ is parameter of the delay time characterizing lag of the effect of saturation. Under condition $\tau < \pi/2\mu$ the system has a stable stationary state $r = 1$. For $\tau > \pi/2\mu$ self-oscillations of the population arise. At large values of delay $\tau$ they have a form of periodic sequence of pulses (Fig. 10.16). The period grows with parameter $\tau$ as $P \cong (1+e^{\mu\tau})/\mu$, and minimal level of the population reached in between the pulses is estimated as $r_{\min} \cong \mu\tau\exp(-e^{\mu\tau} + 2\mu\tau - 1)$, i.e. manifests the double exponentially decrease with increase of $\tau$ (Fowler, 1982).

Now, we regard the positive variable $r$ as squared amplitude of some oscillatory process with frequency $\omega_0$. For this, we set $r = x^2 + y^2$ and require the new variables to satisfy the equations

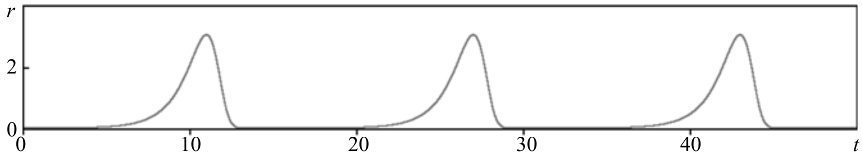


**Fig. 10.16** Self-pulsations in the logistic-delay equation (10.20) at $\mu = 1.6, \tau = 2$; the observed period of pulsations is $T_{\mathrm{av}} \approx 16.0$.

$$\begin{aligned} \dot{x} &= -\omega_0 y + \frac{1}{2}\mu(1 - x^2(t-\tau) - y^2(t-\tau))x, \\ \dot{y} &= \omega_0 x + \frac{1}{2}\mu(1 - x^2(t-\tau) - y^2(t-\tau))y. \end{aligned} \tag{10.21}$$

Next, we add in the first equation an additional term $\varepsilon x(t-\tau)y(t-\tau)$, where $\varepsilon$ is a small parameter, and arrive at the set of equations (Kuznetsov and Pikovsky, 2010)

$$\begin{aligned} \dot{x} &= -\omega_0 y + \frac{1}{2}\mu(1 - x^2(t-\tau) - y^2(t-\tau))x + \varepsilon x(t-\tau)y(t-\tau), \\ \dot{y} &= \omega_0 x + \frac{1}{2}\mu(1 - x^2(t-\tau) - y^2(t-\tau))y. \end{aligned} \tag{10.22}$$

In the case of generation of pulses with extremely low level of minimal amplitude between them, just the additional term will initiate formation of the next pulse of oscillations in the system. Due to this, the period of pulses becomes less than that in system (10.20). If we assume that during a current pulse the variables behave as $x \approx f(t)\cos(\omega_0 t + \varphi), y \approx f(t)\sin(\omega_0 t + \varphi)$, the additional term is expressed as

$$\varepsilon x(t-\tau)y(t-\tau) \approx \frac{1}{2}\varepsilon f^2(t-\tau)\sin(2\omega_0(t-\tau) + 2\varphi). \tag{10.23}$$

It represents a stimulating signal, which initiates oscillations corresponding to the next stage of activity and the phase shift of this signal is transferred to these oscillations. Hence, the phase for the train of oscillations is transformed from the previous train with doubling:

$$\varphi_{n+1} = 2\varphi_n + \text{const.} \tag{10.24}$$

It corresponds to expanding circle map, or the Bernoulli map, which is chaotic and characterizing by the Lyapunov exponent $\Lambda = \ln 2 \approx 0.693$.

As it is common in time-delayed systems, the phase space for the model (10.22) is infinite-dimensional. Indeed, to identify an instant state of the system at some $t = t_0$ and determine uniquely further evolution in time one has to specify functions $x(t)$ and $y(t)$ in time interval $t \in [t_0 - \tau, t_0]$; it corresponds to a point in the phase space. Attractor will be an object embedded in this infinite-dimensional space. One can introduce a mapping of the state space into itself that corresponds to transformation from one oscillation train to the next one. It will be the infinite-dimensional Poincaré map for the system. Dynamics determined by this map is of such nature that on the attractor there is expansion along a direction associated with the phase variable $\varphi$, and compression in other directions. Accounting Bernoulli type of the map for the phase, it must be attractor of Smale-Williams type.

Figure 10.17 shows the time dependence for dynamical variables which illustrate operation of the system (10.22) in accordance with the above qualitative considerations. Indeed, the process looks like a sequence of pulses, trains of oscillations. An average period of their appearance is less than that in model (10.20) and equals $T \cong 11.657$ in the regime under discussion. Portrait of the attractor projected from the infinite-dimensional phase space is presented in Fig. 10.18 in coordinates $(x, y, \rho_\tau)$, where $\rho_\tau = \sqrt{x^2(t-\tau)+y^2(t-\tau)}$. It looks similar to analogous representation of attractor in ordinary differential equations constructed on a base of predator-prey model in Sect. 5.2 (Fig. 5.6(b)).

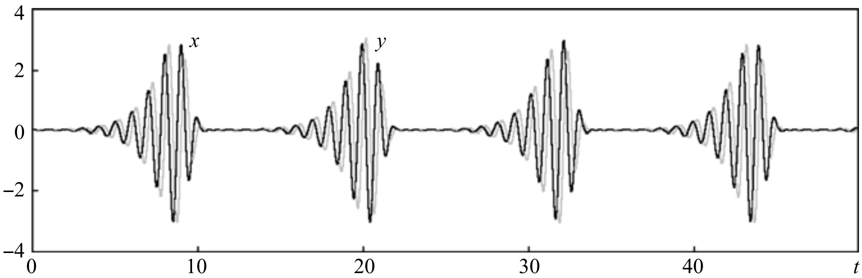


**Fig. 10.17** Waveforms for the dynamical variables $x$ (black) and $y$ (gray) according to the results of the numerical solution of Eq. (10.22) at $\omega_0 = 2\pi, \mu = 1.6, \omega_0 = 2\pi, \tau = 2, \varepsilon = 0.05$; the observed period of pulsations is $T_{\text{av}} \approx 11.657$.

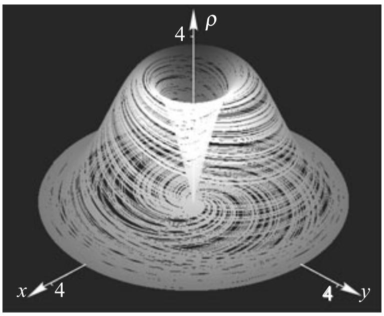


**Fig. 10.18** Portrait of the attractor projected from the infinite-dimensional phase space of the model (10.22) at $\omega_0 = 2\pi, \mu = 1.6, \omega_0 = 2\pi, \tau = 2, \varepsilon = 0.05$.

Three larger Lyapunov exponents evaluated numerically for the system (10.22) are

$$\lambda_1 = 0.0544, \quad \lambda_2 = 0.0005, \quad \lambda_3 = -1.982. \tag{10.25}$$

The largest exponent $\lambda_1$ is positive and corresponds with good accuracy to that obtained from the approximation based on the Bernoulli map. Indeed, accounting that the characteristic period of pulses is about $T \cong 11.657$, for the stroboscopic map the respective exponent is $\Lambda_1 = 0.646$, close to the expected value ln 2. The second exponent is close to zero up to numerical precision; accounting the autonomous nature of the system it is interpreted as being associated with perturbations of infinitesimal shift along the phase trajectory. Other exponents are negative. Estimate of the attractor dimension for the Poincaré map from the Kaplan-Yorke formula yields $D_{KY} \approx 2.027$ for the flow system.

Figure 10.19 demonstrates that transformation of phases of the oscillations from pulse to pulse follows the Bernoulli map. A phase associated with certain pulse is determined at each instant of maximal squared amplitude $x^2 + y^2$ from the relation $\phi = \arg(x - iy)$, and the data are plotted in coordinates $(\phi_n, \phi_{n+1})$.

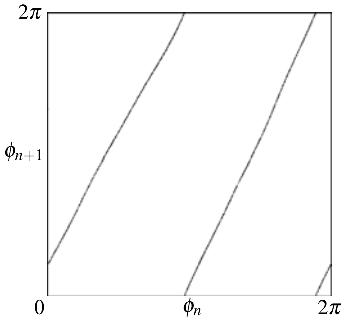


**Fig. 10.19** Diagram illustrating the transformation of phases in the successive stages of the activity plotted according to the results of the numerical solution of Eq. (10.22) at $\omega_0 = 2\pi, \mu = 1.6, \omega_0 = 2\pi, \tau = 2, \varepsilon = 0.05$.

## References


Balyakin, A.A., Ryskin, N.M.: Features of computation of spectrum of Lyapunov exponents in distributed self-oscillatory systems with delayed feedback. Izvestija VUZov-Applied Nonlinear Dynamics (Saratov) **15**, 3–21 (2007).

Baranov, S.V., Kuznetsov, S.P., Ponomarenko, V.I.: Chaos in the phase dynamics of Q-switched van der Pol oscillator with additional delayed-feedback loop. Izvestija VUZov-Applied Nonlinear Dynamics (Saratov) **18** (1), 11–23 (2010) .

Bellman, R., Cooke, C.L.: Differential-difference Equations. Academic Press, New York (1963).

Blokhina, E.V., Kuznetsov, S.P., Rozhnev, A.G.: High-dimensional chaos in a gyrotron. IEEE Transactions on Electron Devices **54**, 188–193 (2007).

Bonatti, C., Diaz, L.J., Viana, M.: Dynamics Beyond Uniform Hyperbolicity. A Global Geometric and Probobalistic Perspective. Encyclopedia of Mathematical Sciences. Vol.102. Springer, Berlin, Heidelberg, New York (2005).

Chiasson, J.N., Loiseaum, J.J. (eds.): Applications of Time Delay Systems (Lecture Notes in Control and Information Sciences, Vol. 352). Springer, Heidelberg (2007).

El'sgol'ts, L.E., Norkin, S.B.: Introduction to the Theory and Application of Differential Equations with Deviating Arguments. Academic Press, New York (1973).

Farmer, J.D.: Chaotic attractors of an infinite-dimensional dynamical system. Physica D **4**, 366–393 (1982).

Fowler, A.C.: An asymptotic analysis of the delayed logistic equation when the delay is large. IMA Journal of Applied Mathematics **28**, 41–49 (1982).

Giacomelli, G., Politi, A.: Relationship between delayed and spatially extended dynamical systems. Phys. Rev. Lett. **76**, 2686–2689 (1996).

Glass, L., Mackey, M.C.: From Clocks to Chaos: The Rhythms of Life. Princeton University Press, Princeton (1988).

Hu, H.Y., Wang, Z.H.: Dynamics of Controlled Mechanical Systems with Delayed Feedback. Springer, Berlin (2002).

Jenkins, G.M., Watts, D.G.: Spectral Analysis and its Application. Holden-Day, Inc., San Francisco (1968).

Kuznetsov, S.P.: Complex dynamics of oscillators with delayed feedback. Radiophysics & Quantum Electronics **25**, 996–1009 (1982).

Kuznetsov, S.P., Pikovsky, A.: Hyperbolic chaos in the phase dynamics of a Q-switched oscillator with delayed nonlinear feedbacks. Europhysics Letters **84**, 10013 (2008).

Kuznetsov, S.P., Pikovsky, A.: Attractor of Smale-Williams type in an autonomous time-delay system. Preprint nlin. arXiv: 1011.5972 (2010).

Kuznetsov, S.P., Ponomarenko, V.I.: Realization of a strange attractor of the Smale–Williams type in a radiotechnical delay-fedback oscillator. Tech. Phys. Lett. **34**, 771–773 (2008).

Le Berre, M., Ressayre, E., Tallet, A., Gibbs, H.M., Kaplan, D.L., Rose M.H.: Conjecture on the dimensions of chaotic attractors of delayed-feedback dynamical systems.Phys. Rev. A **35**, 4020–4022 (1987) .

Lepri, S., Giacomelli, G., Politi, A., Arecchi, F.T.: High-dimensional chaos in delayed dynamical systems. Physica D **70**, 235–249 (1994).

Myskis, A.D.: Linear differential equations with retarded argument, Nauka, Moscow (1972).

Pazó, D., López, J.M.: Characteristic Lyapunov vectors in chaotic time-delayed systems. Phys. Rev. E **82**, 056201 (2010).

Pesin, Ya.B.: Lectures on Partial Hyperbolicity and Stable Ergodicity. Zurich lectures in advanced mathematics. European Mathematical Society (2004).

Pesin, Ya.: Existence and genericity problems for dynamical systems with nonzero Lyapunov exponents. Regular and Chaotic Dynamics **12**, 476–489 (2007).

Vallee R., Delisle, C., Chrostowski J.: Noise versus chavs in acousto-optic bistability. Physical Review A **30**, 336–342 (1984).

# Chapter 11
# Chaos in Co-operative Dynamics of Alternately Synchronized Ensembles of Globally Coupled Self-oscillators

**Abstract** In many cases dynamics of spatially extended systems can be thought of as cooperative action of a large number of relatively simple elements, like interacting limit-cycle oscillators, and treated as low-dimensional dynamics in terms of appropriate collective modes (Cross and Hohenberg, 1993). In this context, a paradigm concept is the Kuramoto model of ensemble of globally coupled phase oscillators distributed in some range of the natural frequencies, and the synchronization-desynchronization transition in such ensemble (Kuramoto, 1984; Strogatz, 2000; Pikovsky et al., 2002; Acebrón, 2005). Now, an interesting question arises about a possibility of occurrence of *hyperbolic attractors* on the level of the collective modes. This problem may be of interest in various fields, e.g. in hydrodynamics, in laser physics and nonlinear optics, electronics, neurodynamics. In this chapter we start from a short introduction to dynamics of a globally coupled ensemble of limit-cycle oscillators and discuss different levels of reduction, including slow complex amplitude equations and phase equations; the last represents exactly the Kuramoto model. Then, we turn to some artificial, but feasible and analytically convenient model of two alternately synchronized and desynchronized interacting ensembles of globally coupled oscillators, which demonstrate transformation of the phase of collective excitation in the course of dynamic evolution in accordance with the expanding circle map at successive stages of synchronization of the subsystems. The consideration is based on a joint work with Pikovsky and Rosenblum (Kuznetsov et al., 2010).

## 11.1 Kuramoto transition in ensemble of globally coupled oscillators

Consider an ensemble of van der Pol oscillators characterized by some distribution over their natural frequencies and interacting through a common field arising due to the global dissipative coupling of all the oscillators. A set of governing equations for the model reads:

S. P. Kuznetsov, *Hyperbolic Chaos*

$$\ddot{x}_\omega - (A - x_\omega^2)\dot{x}_\omega + \omega^2 x_\omega = \kappa < \dot{x}_\omega >, \tag{11.1}$$

where $\kappa$ is the coupling parameter, $A$ is the parameter responsible for the birth of the limit cycle in a single oscillator, and the notion $< \dot{x}_\omega >= \int \dot{x}_\omega f(\omega) d\omega$ means averaging of the variable $\dot{x}_\omega$ over the ensemble. The distribution of natural frequencies of the members of the ensemble over some frequency range is characterized by a function $f(\omega)$, normalized in such a way that $\int f(\omega) d\omega = 1$. The distribution is unimodal; it means that the function has a unique maximum and decays monotonically on both sides of this point with deflection of the frequency.

Supposing that parameters $A$ and $\kappa$ are relatively small, the central frequency $\omega_0$ is large enough, and the range of natural frequencies is relatively narrow, one can reformulate the problem using the method of *slow amplitudes*. To do so, introduce the complex amplitude $a_\omega$ for each oscillator in such a way that the coordinate and velocity variables are expressed as

$$x_\omega = a_\omega e^{i\omega_0 t} + a_\omega^* e^{-i\omega_0 t} \quad \text{and} \quad \dot{x}_\omega = i\omega_0 a_\omega e^{i\omega_0 t} - i\omega_0 a_\omega^* e^{-i\omega_0 t}. \tag{11.2}$$

It implies that the additional condition $\dot{a}_\omega e^{i\omega_0 t} + \dot{a}_\omega^* e^{-i\omega_0 t} = 0$ is assumed. Then, substitution in Eq. (11.1) yields

$$\begin{aligned} &2i\omega_0 \dot{a}_\omega e^{i\omega_0 t} + (\omega^2 - \omega_0^2)(a_\omega e^{i\omega_0 t} + a_\omega^* e^{-i\omega_0 t}) \\ &= (A - a_\omega^2 e^{2i\omega_0 t} - 2|a_\omega|^2 - a_\omega^{*2} e^{-2i\omega_0 t})(i\omega_0 a_\omega e^{i\omega_0 t} - i\omega_0 a_\omega^* e^{-i\omega_0 t}) + \kappa < \dot{x}_\omega > . \end{aligned} \tag{11.3}$$

Now, we multiply the relation by $e^{-i\omega_0 t}$ and carry out the averaging over a period of fast oscillations. It is easily to find out that $\overline{< \dot{x}_\omega > e^{-i\omega_0 t}} = i\omega_0 < a >$, where the overline designates the time averaging. Instead of the frequency of the oscillators it is convenient hereafter to introduce and use the quantity characterizing the detuning $\Omega = (\omega^2 - \omega_0^2)/2\omega_0 \approx \omega - \omega_0$. Then, we get

$$\dot{a}_\Omega = i\Omega a_\Omega + \frac{1}{2}(A - |a_\Omega|^2) a_\Omega + \frac{1}{2}\kappa < a >, \tag{11.4}$$

where $< a >= \int a_\Omega \tilde{f}(\Omega) d\Omega$. The distribution function for the detuning values is expressed in obvious way as $\tilde{f}(\Omega) \approx f(\omega_0 + \Omega)$, and satisfies the normalization condition $\int f(\Omega) d\Omega = 1$.

One more step in simplifying the model is reduction to consideration of ensemble of *phase oscillators*. The individual oscillators are assumed to have constant amplitude corresponding to their limit cycles throughout the process, while the dynamics manifests itself only in evolution of their phases. In the classical theory of synchronization, this corresponds to description in terms of the so-called Adler equation (Pikovsky et al., 2002; Osipov et al., 2007). It is justified if the limit cycle is well pronounced at the selected value of the parameter $A$, distant from the threshold of birth of the limit cycle although it is not too large: the self-oscillations are quasi-harmonic. To reduce the description to the phase equations, we substitute in (11.4)

$$a_\Omega \approx R e^{i\Phi_\Omega}, \tag{11.5}$$

where $R \approx \sqrt{A}$ being constant for all oscillators. After multiplying the equation by $e^{-i\Phi_\Omega}$ and separating the imaginary part, we finally obtain

$$\dot{\Phi}_\Omega = \Omega + \frac{1}{2}\kappa \mathrm{Im}(< e^{i\Phi} > e^{-i\Phi_\Omega}). \tag{11.6}$$

Here $< e^{i\Phi} >= \int e^{i\Phi_\Omega} \tilde{f}(\Omega) d\Omega$, where $\tilde{f}(\Omega)$ is the same distribution function of detuning, which had appeared in the model (11.4). Equation (11.6) corresponds to the *Kuramoto model*, which is extensively examined in (Kuramoto, 1984; Strogatz, 2000; Pikovsky et al., 2002; Acebrón, 2005).

The most interesting feature of the Kuramoto model is the synchronization-desynchronization transition, which occurs at some critical value of parameter $\kappa_c$ as a collective effect in the ensemble of globally coupled oscillators. The coupling may be regarded as a mean field affecting all oscillators. If the coupling constant is above some threshold, this mean field synchronizes some macroscopically significant part of the ensemble, which generates this mean field in self-consistent manner. If the coupling is below the threshold, the ensemble desynchronizes due to the intrinsic frequency difference of the oscillators constituting the ensemble, and the mean field vanishes. As found analytically by Kuramoto, the transition occurs at $\kappa_c = 4/\pi \tilde{f}(0)$.

As the model (11.6) is obtained as approximation for the systems (11.1) and (11.4), one can conclude that the same kind of transition occurs in those models too, although the exact position of the threshold on the parameter axis may be slightly distinct from that evaluated for the Kuramoto model (11.6).

To be concrete, hereafter we assume that the natural frequencies of the oscillators are spread in a finite range $(\omega_{\min}, \omega_{\max})$ in accordance with the distribution function

$$f(\omega) = \begin{cases} \dfrac{\pi}{2}\cos\dfrac{\pi(\omega - \omega_{\min})}{\omega_{\max} - \omega_{\min}}, & \omega \in [\omega_{\min}, \omega_{\max}], \\ 0, & \text{otherwise}. \end{cases} \tag{11.7}$$

The plot of this function is shown in Fig. 11.1. This distribution can be obtained with a help of an auxiliary variable $\xi$ spreading on the unit interval uniformly; one has to set simply $\omega = \omega_{\min} + (\omega_{\max} - \omega_{\min}) \arccos \xi$. For the versions of the model based on slow-amplitude and phase approximations, we set, respectively, $\tilde{f}(\Omega) = f(\omega_0 + \Omega)$.

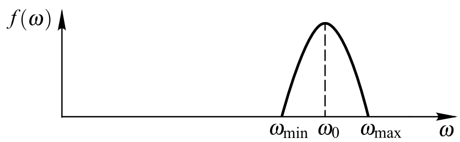


**Fig. 11.1** A plot of the distribution function for the oscillator frequencies in the ensemble.

Equations (11.1), (11.4), or (11.6) correspond to asymptotic of infinitely large number of members of the ensemble called *the thermodynamic limit*. To organize numerical simulations, we assume a finite (though large enough) number of ensemble members $K \gg 1$. Their natural frequencies $\omega_k$ are selected to correspond to the prescribed distribution function $f(\omega)$ in accordance with the relation

$$\omega_k = \omega_{\min} + \frac{(\omega_{\max} - \omega_{\min})}{\pi} \arccos((2k-1)/K - 1), \quad k = 1, 2, \ldots, K. \tag{11.8}$$

The averaging operation over the ensemble for any function $g(x, \dot{x})$ is performed now in accordance with the relation

$$< g(x, \dot{x}) >= \frac{1}{K} \sum_{k=1}^{K} g(x_k, \dot{x}_k). \tag{11.9}$$

In computations the central frequency is specified as $\omega_0 = 2\pi$, so, the unit time corresponds to period of the fast oscillations. Interval of the frequency distribution is of width $\Delta\omega = \omega_{\max} - \omega_{\min} = \dfrac{1}{4}\pi$.

Figure 11.2 illustrates the synchronization-desynchronization transition. Time dependence is plotted for the variables characterizing the mean field versus time for three versions of the model for ensembles of $K = 1000$ units.

Panel (a) relates to the original ensemble of van der Pol oscillators with global dissipative coupling (11.1) at $A = 3$ with frequencies distributed in the range $(2\pi - \pi/8, 2\pi + \pi/8)$ in accordance with the function (11.7) obtained from the formula (11.8). Initial conditions are assigned with randomized phases of all oscillators, while their amplitudes correspond to the limit cycle of a single oscillator. The coupling parameter initially equals a constant $\kappa = 1$, which is above the critical value. Thus, one can observe development of the collective synchronization accompanied by arising oscillations of the mean field $< \dot{x} >$ of significant magnitude. At the middle of the time interval shown on the diagram, the coupling constant is switched to a sub-critical value $\kappa = 0.5$; this event starts the process of gradual destruction of the synchronized state due to the frequency detuning intrinsic to the members of the ensemble.

Panels (b) and (c) correspond, respectively, to description of the phenomenon in terms of slow complex amplitudes with Eqs. (11.4) at $A$=3, and in terms of the ensemble of phase oscillators (11.6). The frequency detuning parameters for the oscillators are obtained from the formula

$$\Omega_k = -(\pi/8) + (1/4) \arccos((2k-1)/K - 1), \quad k = 1, 2, \ldots, K. \tag{11.10}$$

It corresponds to the distribution of frequencies in accordance to (11.7) with $\Delta\omega = \pi/4$. The initial conditions correspond to randomized phases of oscillators, and the coupling parameter is switched from the supercritical to the subcritical values just in the same way as in the panel (a). Again one can observe development of collective synchronization accompanied by arising significant amplitude of the mean field

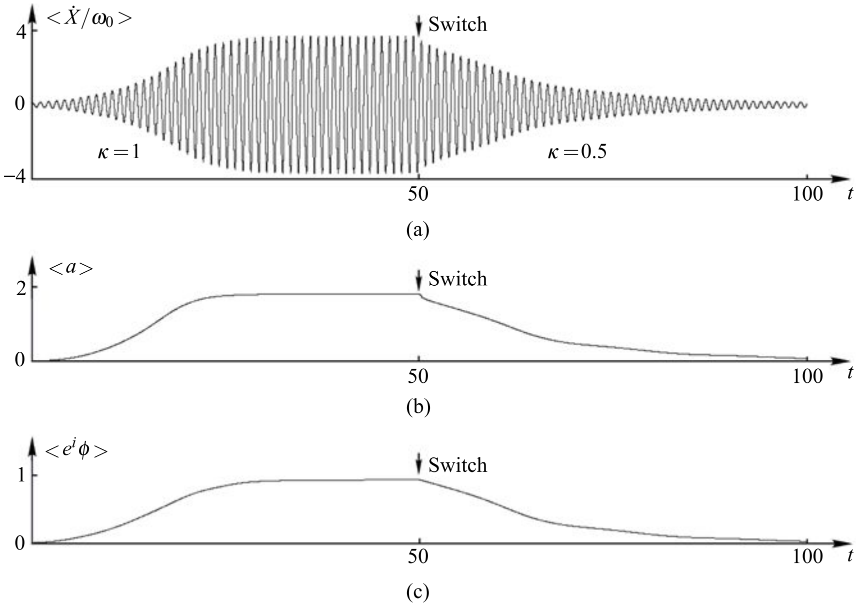


**Fig. 11.2** Time dependence for the variables characterizing the mean field versus time for three versions of the model of $K = 1000$ globally coupled oscillators with frequencies distributed in the range $(2\pi - \pi/8, 2\pi + \pi/8)$. Panel **(a)** corresponds to the original system (11.1), **(b)** to the slow-amplitude version (11.4), and **(c)** to the system of phase oscillators (11.6). Initial conditions relate to states of randomized phases of all oscillators and their amplitudes corresponding to the limit cycle of a single oscillator. The coupling parameter on the first half of the time interval is supercritical, $\kappa = 1$, and in the middle it is switched to a subcritical value $\kappa = 0.5$. Parameter value used in the computations for panels (a) and (b): $A = 3$.

represented by the averages $| < a > |$ and $| < e^{i\Phi} > |$, respectively, and desynchronization after the switch. Geometrically, the scales for the mean-field variables on all three panels are selected to make them visually comparable; so, one can judge about degree of correspondence between the three levels of the description.

## 11.2 Model of two alternately synchronized ensembles of oscillators

Let us turn to the main part of the present chapter aiming to give evidence of possibility of dynamics associated with hyperbolic attractor of Smale-Williams in cooperative behavior of ensemble of oscillators (Kuznetsov et al., 2010).

### *11.2.1 Collective chaos in ensemble of van der Pol oscillators*

In Chap. 4 it was shown how to implement the dynamics described by the Bernoulli map in low-dimensional system of alternately excited self-oscillators. Chaotic nature of the dynamics reveals itself in chaotic evolution of the phases of oscillations generated at successive stages of excitation of the oscillators.

Now, consider a system composed of two ensembles of self-oscillators, similar to each other with natural frequencies distributed in some range, like assumed in the previous section. Oscillator coordinate variables for members of one and the second sub-ensemble will be denoted $x$ and $y$, respectively. To get immediately the model appropriate for numerical simulation, we formulate equations for subsystems composed of a finite (although large) number of oscillators $K$:

$$\begin{aligned}\frac{d^2x_k}{dt^2}-(A-x_k^2)\frac{dx_k}{dt}+\omega_k^2x_\omega &= \kappa f_1(t)\frac{d<x>}{dt}+\varepsilon\frac{d<y^2>}{dt}\sin\omega_0t,\\ \frac{d^2y_k}{dt^2}-(A-y_k^2)\frac{dy_k}{dt}+\omega_k^2y_k &= \kappa f_2(t)\frac{d<y>}{dt}+\varepsilon\frac{d<x^2>}{dt}\sin\omega_0t,\\ k &= 1,2,\dots,K.\end{aligned} \tag{11.11}$$

The averaged quantities in the right-hand parts of the equations are defined as

$$<x>=\frac{1}{K}\sum_{k=1}^{K}x_k,\quad <x^2>=\frac{1}{K}\sum_{k=1}^{K}x_k^2,\quad <y>=\frac{1}{K}\sum_{k=1}^{K}y_k,\quad <y^2>=\frac{1}{K}\sum_{k=1}^{K}y_k^2. \tag{11.12}$$

Parameter $A$ responsible for the birth of the limit cycle is of one and the same value for all members of both sub-ensembles. Parameter $\kappa$ is the coupling constant associated with global dissipative coupling within each sub-ensemble. The strength of this coupling is modulated in time with period $T \gg 2\pi/\omega_0$ in counter-phase in two sub-ensembles; this process is accounted in the equations by the functions $f_1(t)=\sin^2(\pi t/T-\pi/4)$ and $f_2(t)=\sin^2(\pi t/T+\pi/4)$. Interaction between the sub-ensembles is introduced by means of a field, obtained by averaged quadratic terms. The field responsible for the interaction oscillates on a doubled mean frequency, but, due to multiplication of the respective terms by the auxiliary signal of frequency $\omega_0$, it provides resonance effect onto each sub-ensemble from the partner. The ratio $N=\omega_0T/2\pi$ is assumed to be an integer. The distributions of the oscillators in both ensembles over frequencies are identical, characterized by the function (11.7); it is so if the frequencies $\omega_k$ are assigned in accordance with relations (11.8).

Due to presence of the global coupling, each sub-ensemble can undergo the Kuramoto transition: as oscillators synchronize, the collective field emerges with notable amplitude and definite phase of oscillations. As the coupling is turned off, the oscillators desynchronize because of the frequency detuning of individual elements, and the collective field disappears. The operation of the whole system consists of alternating activities of two ensembles with the corresponding alternating growth and decay of their collective mean fields.

Usually, as a single ensemble of oscillators passes through the Kuramoto transition from a non-synchronous state to a synchronous one while the global coupling increases, the phase of the arising collective mode, potentially, of arbitrary value, is determined by fluctuations. In our setup, however, the excitation of collective field in one sub-ensemble is stimulated by a small driving force (proportional to $\varepsilon$) because of action of the partner sub-ensemble; the last is synchronous at that moment and generates notable mean field. This stimulation determines the phase on the appearing collective mode, which accepts this externally designated phase. This is the mechanism of the phase transfer. Because the mutual couplings in our model are proportional to the *second-order* mean fields of doubled characteristic frequency, the phase transfer is accompanied with doubling of the phase. To explain this, let us assume that at the transfer of excitation from the first to the second sub-ensembles we have $d < x > /dt \sim \cos(\omega_0 t + \Phi)$ and $d < x^2 > /dt \sim \cos(2(\omega_0 t + \Phi) + \mathrm{const})$. Then, the driving force affecting the second sub-ensemble contains the resonance component of $(d < x^2 > /dt)\sin\omega_0 t \sim \cos(\omega_0 t + 2\Phi + \mathrm{const})$. Respectively, the arising means field will be of the form $< y > \sim \cos(\omega_0 t + 2\Phi + \mathrm{const})$. As doubling of the phase occurs at each transfer from one subsystem to another and back through the full cycle, we expect that the phase is multiplied by the factor of 4 (up to an additive constant).

In computations the central frequency is $\omega_0 = 2\pi$, so, the unit time corresponds to the period of the fast oscillations. The range of frequency distribution is of width $\Delta\omega = \omega_{\max} - \omega_{\min} = \dfrac{1}{4}\pi$. Number of elements in each of two ensembles is $K = 1000$. Other parameters are $T = 100, \kappa = 1, A = 3, \varepsilon = 0.025$. Initial distribution of phases of the oscillators is uniform in the interval $[0, 2\pi)$ obtained with a standard procedure of pseudo-random numbers generation. Initially, sufficiently long-time interval of transient behavior is excluded from consideration to ensure that we deal with sustained process of the collective dynamics of the two interacting ensembles.

Figure 11.3 shows the graphs of the averaged generalized velocity over each of the ensembles versus time. The presence of intense oscillations of this variable indicates synchronization of the ensemble of oscillators. As seen from the figure, the epochs of intense oscillations for one and the other subsystem alternate with

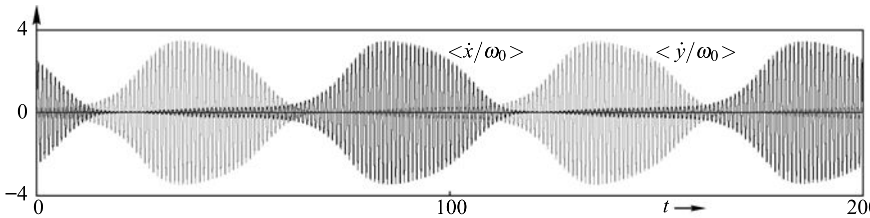


**Fig. 11.3** Graphs for the generalized velocities of the oscillators averaged over the first and the second interacting ensembles, obtained from numerical solution of Eqs. (11.11). The number of oscillators in each ensemble $K = 1000$, the distribution function of frequencies corresponds to the formula (11.7), at $\omega_0 = 2\pi, \omega_{\min}/\omega_0 = 15/16, \omega_{\max}/\omega_0 = 17/16$, the values of other parameters $T = 100, \kappa = 1, A = 3, \varepsilon = 0.025$.

the period $T$. Nevertheless, the dynamics in time is chaotic since the carrier phase relating to the envelope varies from one epoch of the ensemble synchronization to the other being governed by a chaotic map.

According to the approximate qualitative analysis, the phase should be transformed from one epoch to the next synchronization in accordance with the four-fold expanding circle map. Figure 11.4 shows the phase diagram obtained in computations for the collective excitation of one of the ensembles relating to successive epochs of synchronization. The phases are determined by a formula $\Phi = \arg(< x > -i\omega_0^{-1} < \dot{x} >)$ at the time instants $t_n = nT$, and $\Phi_{n+1}$ versus $\Phi_n$ are plotted. As seen, the diagram clearly indicates that the transformation is indeed close to the Bernoulli-type map. The observed scatter of points decreases with increasing number of oscillators $K$, as confirmed in computations.

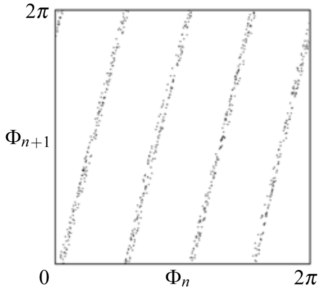


**Fig. 11.4** Diagram for the phases of the collective excitation of one of the ensembles relating to the moments of time $t_n = nT$. The parameters are the same as in Fig. 11.3.

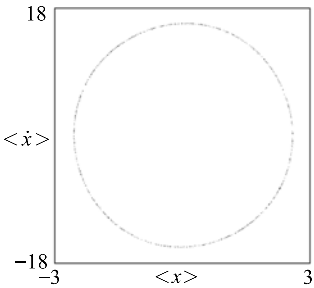


**Fig. 11.5** Portrait of attractor in the stroboscopic section, corresponding to the instants $t_n = nT$, in projection on the plane of averaged generalized coordinates and velocities. The parameters are the same as in Fig. 11.3.

Figure 11.5 shows a portrait of the attractor of the system in the stroboscopic section, in projection on the plane of averaged generalized coordinates and velocities of the oscillators. Transversal Cantor structure, which was expected to be observable on this portrait, is masked by the spread of points, which, apparently, is mainly due to the finite size of the ensemble.

The question about features of Lyapunov spectra of systems of globally coupled oscillators is too multifaceted to discuss here (Nakagawa and Kuramoto, 1995; Strogatz, 2000; Maistrenko et al., 2005); so, we consider only the largest Lyapunov exponent. Its quantitative estimate via the Benettin algorithm at the parameters specified above yields $\lambda = 0.01069 \pm 0.00002$. For the stroboscopic map, accounting that the period of parameter modulation is $T = 100$, we get $\Lambda = 1.069$. It is notably less than the value $\ln 4 = 1.386\cdots$ expected from qualitative analysis of the phase dynamics according to the Bernoulli type map. Nevertheless, it does not contradict the hypothesis of occurrence of suspension of attractor of Smale-Williams type in the phase space of the system responsible for the collective behavior of the oscillatory ensembles.

### *11.2.2 Slow-amplitude approach*

Under some additional assumptions (relatively small $A, \kappa$, and $\varepsilon$; large enough average frequency $\omega_0$; relatively narrow frequency range $\Delta\omega$) the dynamics of two alternately synchronized ensembles may be treated in terms of slow complex amplitudes, like that for a single ensemble in Sect. 11.1. To do so, introduce the complex amplitudes $a_k$ and $b_k$ to oscillators relating to two sub-ensembles in such a way that the coordinate and velocity variables are expressed as

$$\begin{aligned} x_k = a_k e^{i\omega_0 t} + a_k^* e^{-i\omega_0 t}, \quad y_k = b_k e^{i\omega_0 t} + b_k^* e^{-i\omega_0 t}, \\ \dot{x}_k = i\omega_0 a_k e^{i\omega_0 t} - i\omega_0 a_k^* e^{-i\omega_0 t}, \quad y_k = i\omega_0 b_k e^{i\omega_0 t} - i\omega_0 b_k^* e^{-i\omega_0 t}. \end{aligned} \tag{11.13}$$

It implies that the complex amplitudes satisfy the additional conditions

$$\dot{a}_k e^{i\omega_0 t} + \dot{a}_k^* e^{-i\omega_0 t} = 0, \quad b_k e^{i\omega_0 t} + b_k^* e^{-i\omega_0 t} = 0. \tag{11.14}$$

Substitution of relations (11.13) in Eqs. (11.11) with taking into account (11.14) yields

$$\begin{aligned} &2i\omega_0 \dot{a}_k e^{i\omega_0 t} + (\omega^2 - \omega_0^2)(a_k e^{i\omega_0 t} + a_k^* e^{-i\omega_0 t}) \\ &= (A - a_k^2 e^{2i\omega_0 t} - 2|a_k|^2 - a_k^{*2} e^{-2i\omega_0 t})(i\omega_0 a_k e^{i\omega_0 t} - i\omega_0 a_k^* e^{-i\omega_0 t}) \\ &\quad + \kappa f_1(t) < \dot{x}_k > - i\varepsilon < y_k \dot{y}_k > (e^{i\omega_0 t} - e^{-i\omega_0 t}), \\ &2i\omega_0 \dot{b}_k e^{i\omega_0 t} + (\omega_k^2 - \omega_0^2)(b_k e^{i\omega_0 t} + b_k^* e^{-i\omega_0 t}) \\ &= (A - b_k^2 e^{2i\omega_0 t} - 2|b_k|^2 - b_k^{*2} e^{-2i\omega_0 t})(i\omega_0 b_\omega e^{i\omega_0 t} - i\omega_0 b_\omega^* e^{-i\omega_0 t}) \\ &\quad + \kappa f_2(t) < \dot{y}_k > - i\varepsilon < x_k \dot{x}_k > (e^{i\omega_0 t} - e^{-i\omega_0 t}). \end{aligned} \tag{11.15}$$

Now, multiply these expressions by $e^{-i\omega_0 t}$ and carry out the averaging operation over a period of fast oscillations, which is indicated with the overline. It is easily to see that

$$\begin{aligned}
&\overline{< \dot{x}_\omega > e^{-i\omega_0 t}} = i\omega_0 < a >, \quad \overline{< \dot{y}_\omega > e^{-i\omega_0 t}} = i\omega_0 < b >, \\
&\overline{< x_\omega \dot{x}_\omega > (e^{i\omega_0 t} - e^{-i\omega_0 t}) e^{-i\omega_0 t}} \\
&= \overline{< i\omega_0 (a_\omega^2 e^{2i\omega_0 t} - a_\omega^{*2} e^{-2i\omega_0 t}) > (1 - e^{-2i\omega_0 t})} = -i\omega_0 < a^2 >, \\
&\overline{< y_\omega \dot{y}_\omega > (e^{i\omega_0 t} - e^{-i\omega_0 t}) e^{-i\omega_0 t}} = -i\omega_0 < b^2 > .
\end{aligned} \tag{11.16}$$

Instead of the frequencies of the oscillators $\omega_k$ it is convenient now to use the detuning $\Omega_k = (\omega_k^2 - \omega_0^2)/2\omega_0 \approx \omega_k - \omega_0$. Finally, we get

$$\begin{aligned}
\dot{a}_k &= i\Omega_k a_k + \frac{1}{2}(A - |a_k|^2) a_k + \frac{1}{2}\kappa f_1(t) < a > - \frac{1}{2} i\varepsilon < b^2 >, \\
\dot{b}_k &= i\Omega_k b_k + \frac{1}{2}(A - |b_k|^2) b_k + \frac{1}{2}\kappa f_2(t) < b > - \frac{1}{2} i\varepsilon < a^2 >,
\end{aligned} \tag{11.17}$$

where

$$< a > = \frac{1}{K}\sum_{k=1}^{K} a_k, \quad < a^2 > = \frac{1}{K}\sum_{k=1}^{K} a_k^2, \quad < b > = \frac{1}{K}\sum_{k=1}^{K} b_k, \quad < b^2 > = \frac{1}{K}\sum_{k=1}^{K} b_k^2. \tag{11.18}$$

The detuning values $\Omega_k$ are determined in accordance with (11.10).

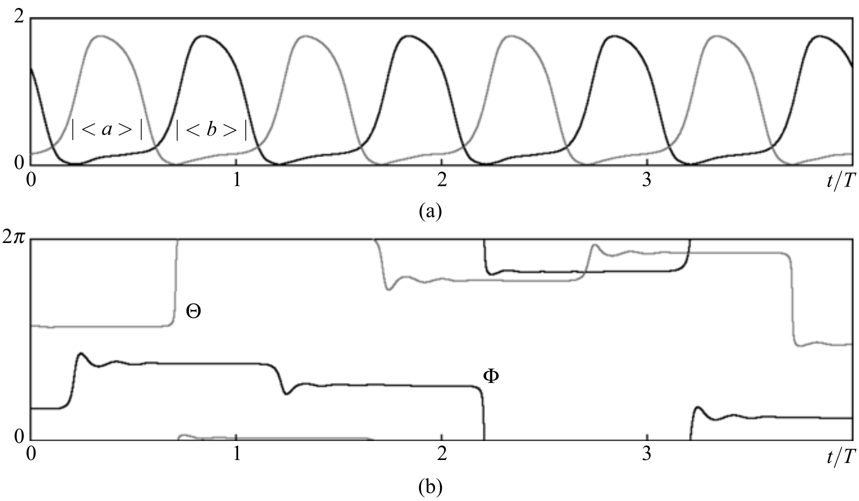


**Fig. 11.6** Graphs of time dependence of modulus **(a)** and phase **(b)** of the complex amplitude averaged over the ensemble for two subsystems, obtained from numerical solution of Eqs. (11.17). The number of oscillators in each ensemble is $K = 1000$, the distribution function of frequencies corresponds to the formula (11.7), the values of other parameters $T = 100, \kappa = 1, A = 3, \varepsilon = 0.025$.

Figure 11.6 shows the graphs for the modulus and phase averaged over the ensemble of the complex amplitude versus time for two subsystems: $< a(t) > =$

$| < a(t) > |e^{i\Phi(t)}, < b(t) >= | < b(t) > |e^{i\Theta(t)}$, see, respectively, diagrams (a) and (b). A number of oscillators in each of two ensembles is $K = 1000$. Other parameters are $T = 100$, $\kappa = 1, A = 3, \varepsilon = 0.1$. Epochs of synchronization correspond to high absolute values of the respective amplitude. As seen, the phase remains roughly constant over time during those epochs. Although the time dependence of the amplitude appears closely periodic in time, in fact, the dynamics is chaotic. Indeed, the phases change from one epoch of synchronization of the ensemble to another, in accordance with the chaotic map. In Fig. 11.7 empirical diagram is shown obtained in the computations phase for the phase $\Phi_n = \arg(< a >)$ of the collective excitation of one of the ensembles at the times $t_n = nT$ relating to the epochs of synchronization of the ensemble.

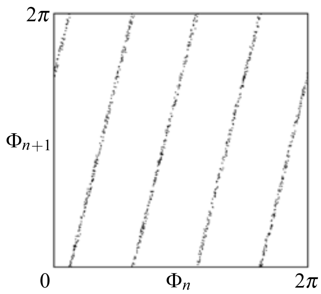


**Fig. 11.7** Diagram for the phases of the collective excitation for one of the ensembles relating to the moments of time $t_n = nT$. The parameters are the same as in Fig. 11.6.

Figure 11.8 shows a portrait of the attractor in the stroboscopic section in a projection on the plane averaged over the ensemble values of generalized coordinates and velocities of the oscillators. By zoom of the image noticeable transverse Cantor structure of the attractor becomes visible (see box in the center of the diagram). It may be conjectured that it is attractor of Smale-Williams type in the reduced low-dimensional phase space of collective variables of the system.

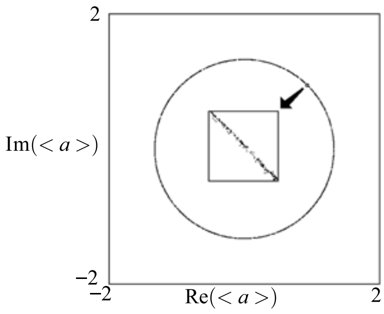


**Fig. 11.8** Portrait of attractor in the stroboscopic section at $t_n = nT$ in projection on the plane of the complex amplitude averaged over the ensemble. The parameters are the same as in Fig. 11.6.

### 11.2.3 Description of the dynamics in terms of ensembles of phase oscillators

Let us undertake a final step in simplifying the model and consider the alternately synchronized ensembles of *phase oscillators*. Now, the individual oscillators will be characterized by one and the same constant amplitude $R$, and the dynamics manifests itself only in evolution of their phases. To reduce the description to the phase equations, we substitute in (11.17)

$$a_k \approx Re^{i\Phi_k}, \quad b_k \approx Re^{i\Theta_k}. \tag{11.19}$$

In selection of $R$ there is certain arbitrariness; a sufficiently good approximation at moderate values of parameter $A$ and relatively small $\kappa$ is $R = \sqrt{A}$.

Substituting (11.19) into Eqs. (11.17), after multiplying the first and the second equations, respectively, by $e^{-i\Phi_k}, e^{-i\Theta_k}$, and taking the imaginary part responsible for the dynamics of phase, we obtain

$$\begin{aligned} \dot{\Phi}_k &= \Omega_k + \frac{1}{2}\mathrm{Im}((\kappa < e^{i\Phi} > -i\varepsilon R < e^{2i\Theta} >)e^{-i\Phi_k}), \\ \dot{\Theta}_k &= \Omega_k + \frac{1}{2}\mathrm{Im}((\kappa < e^{i\Theta} > -i\varepsilon R < e^{2i\Phi} >)e^{-i\Theta_k}), \end{aligned} \tag{11.20}$$

where

$$< e^{im\Phi} >= K^{-1}\sum_{k=1}^{K} e^{im\Phi_k}, \quad < e^{im\Theta} >= K^{-1}\sum_{k=1}^{K} e^{im\Theta_k}, \quad m = 1,2. \tag{11.21}$$

Again, to be concrete, the quantities $\Omega_k$ are supposed to be determined from (11.10).

Figure 11.9 shows graphs for two subsystems for time dependence of the modulus and phase of the complex order parameter. The number of oscillators in each ensemble $K = 1000$, and other parameters are the same as in the previous subsection, $T = 100, \kappa = 1, A = 3, \varepsilon = 0.025$. Fig. 11.10 is a diagram for the phases of the collective excitation $\Theta_n = \arg(< b >)$ at $t_n = nT$. In Fig. 11.11, a portrait of the attractor of the system is shown in the stroboscopic section, in projection on the complex plane of the variable $< b(t) >$.

To conclude, we have proposed and studied a model system, which realizes chaotic dynamics of the phases described by expanding circle map transformation in the course of the transfer of collective excitation alternately between two synchronizing and desynchronizing groups of oscillators. As hoped, it may stimulate search for and discovery of other examples of this kind, perhaps closer to problems of special disciplines such as fluid dynamics, and neurodynamics. It is interesting to note in this context again that the concept of turbulence presented by Ruelle and Takens, the radical for its time, postulated the emergence of *structurally stable hyperbolic strange attractors* (Ruelle and Takens, 1971), not chaotic attractors in broader sense, as this term is commonly used now.

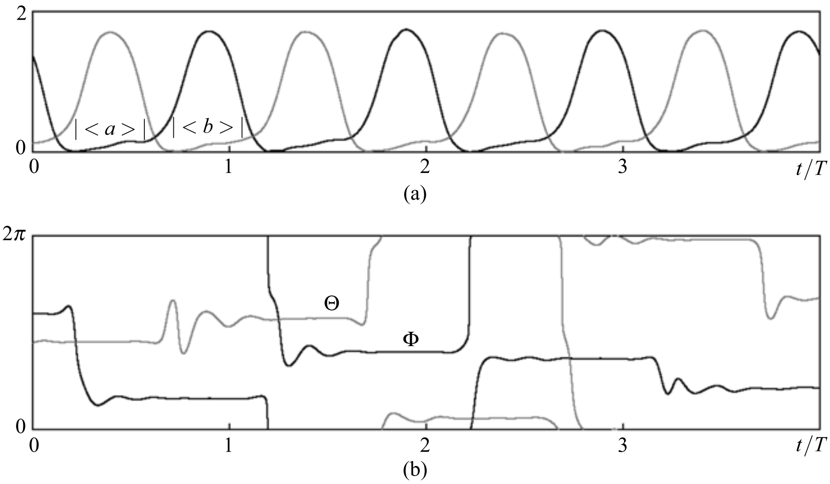


**Fig. 11.9** Graphs of dependence for modulus **(a)** and phase **(b)** of complex order parameters for the two subsystems, obtained by numerical solution of Eqs. (11.20). The number of oscillators in each ensemble is $K = 1000$, the distribution function of frequencies corresponds to the formula (4), the values of other parameters $T = 100, \kappa = 1, A = 3, \varepsilon = 0.025$.

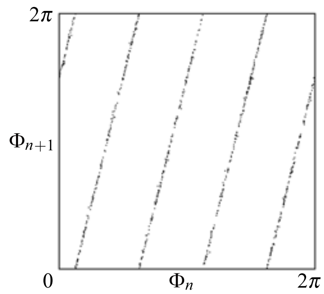


**Fig. 11.10** Diagram for the phases of collective excitation of an ensemble of (11.20) relating to the moments of time $t_n = nT$. The parameters are the same as in Fig. 11.9.

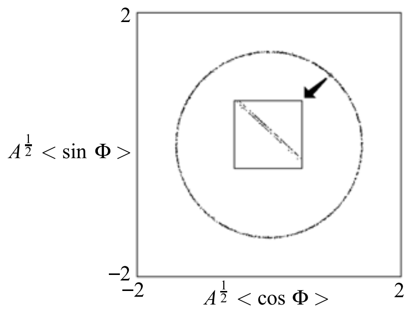


**Fig. 11.11** Portrait of attractor in the stroboscopic section, corresponding to the moment of time $t_n = nT$, projected on the plane of the complex order parameter of one of the ensembles of the phase oscillators (11.20). The parameters are the same as in Fig. 11.9.

Furthermore, it seems realistic to construct artificial systems with collective chaotic phase dynamics based on ensembles of individual elements that can show only regular dynamics. This can be done, say, on the basis of electronic devices, such as arrays of Josephson contacts (Wiesenfeld and Swift, 1995), or with nonlinear optical systems, like arrays of semiconductor lasers (Glova, 2003). Such systems will represent generators of strong chaos providing the power level much higher than that characteristic to the individual elements. Systems of this kind may be of interest for applications requiring the generation of chaotic signals, such as communication schemes (Dmitriev and Panas, 2002; Koronovskii et al., 2009), and noise radar (Lukin, 2001).

## References

Acebrón, J.A., Bonilla, L.L., Pérez Vicente, C.J., Ritort, F.: The Kuramoto model: A simple paradigm for synchronization phenomena. Rev. Mod. Phys. **77**, 137–185 (2005).

Cross, M.C., Hohenberg, P.C.: Pattern formation outside of equilibrium. Rev. Mod. Phys. **65**, 851–1112 (1993).

Dmitriev, A.S., Panas, A.I. Dynamical Chaos: New Information Carriers for Communication Systems. Fizmatlit, Moscow (2002).

Glova, A.F.: Phase locking of optically coupled lasers. Quantum Electronics **33**, 283–306 (2003).

Koronovskii, A.A., Moskalenko, O.I., Hramov, A.E.: On the use of chaotic synchronization for secure communication. Physics-Uspekhi **52**, 1213–1238 (2009).

Kuramoto, Y.: Chemical Oscillations, Waves, and Turbulence, Springer, Berlin (1984).

Kuznetsov, S.P., Pikovsky, A., Rosenblum, M.: Collective phase chaos in the dynamics of interacting oscillator ensembles. Chaos **20**, 043134 (2010).

Lukin, K.A.: Noise radar technology. Telecommunications and Radio-Engineering **16**, 8–16 (2001).

Maistrenko, Y.L., Popovych, O.V., Tass, P.A.: Desynchronization and chaos in the Kuramoto model. In: Chazottes, J.-R and Fernandez, B. (eds.): Dynamics of Coupled Map Lattices and of Related Spatially Extended Systems, pp.285–306. Springer (2005).

Nakagawa, N. and Kuramoto, Y.: Anomalous lyapunov spectrum in globally coupled oscillators. Physica D **80**, 307–316 (1995).

Osipov, G.V., Kurths, J., Zhou, C.: Synchronization in Oscillatory Networks. Springer, Berlin (2007).

Pikovsky, A., Rosenblum, M., Kurtz, J.: Synchronization: A Universal Concept in Nonlinear Sciences. Cambridge University Press, Cambridge (2002).

Ruelle, D., Takens, F.: On the nature of turbulence. Commun. Math. Phys. **20**, 167–192 (1971).

Strogatz, S.H.: From Kuramoto to Crawford: exploring the onset of synchronization in populations of coupled oscillators. Physica D **143**, 1–20 (2000).

Wiesenfeld, K., Swift, J.W.: Averaged equations for Josephson junction series arrays. Phys. Rev. E **51**, 1020–1025 (1995).

# Chapter 12
# Electronic Device with Attractor of Smale-Williams Type

**Abstract** A very interesting question concerns implementation of models discussed in previous chapters (as well as other systems with hyperbolic attractors) as real devices, e.g. in electronics, laser physics, mechanics, etc. In the present chapter an electronic device is considered inspired by the model examined in Sect. 4.2. An advantage of such chaos generator is robustness of the dynamics because of structural stability of the hyperbolic attractor, which may be important for many applications.

## 12.1 Scheme of the device and the principle of operation

Consider an electronic device schematized by the circuit diagram in Fig. 12.1 (Kuznetsov and Seleznev, 2006). It is a non-autonomous system combining two van der Pol oscillators of natural frequencies $\omega_0$ and $2\omega_0$ subjected to appropriate periodic external driving. Each oscillator contains a coil of inductance $L_{1,2}$ and a capacitor of capacitance $C_{1,2}$ selected in such a way that

$$\omega_0 = 1/\sqrt{L_1 C_1}, \quad 2\omega_0 = 1/\sqrt{L_2 C_2}.$$

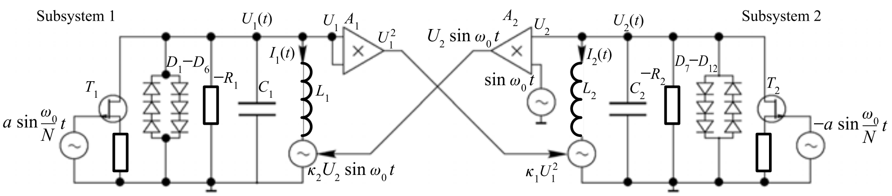


**Fig. 12.1** Circuit diagram of a device composed of two coupled van der Pol oscillators with periodically varying parameters: a physical system having a Smale-Williams type strange attractor.

S. P. Kuznetsov, *Hyperbolic Chaos*

Negative-resistance components based on operational amplifiers are introduced whose respective resistances $(-R_{1,2})$ can be treated as constant parameters in the entire ranges of operating voltage of the corresponding oscillating circuits. A nonlinear conductance that ensures increase in energy loss with oscillation amplitude is implemented by circuit components consisting of two oppositely poled parallel arrays of series-connected semiconductor diodes. A field-effect transistor is used as an almost linearly conducting component, with drain current controlled by the gate voltage slowly varying as a periodic function of time with period $T = 2\pi N/\omega_0$, where $N$ is an integer. During successive half-periods of its variation, one oscillator is active while the other is suppressed and vice versa. Quadratic nonlinear element $A_1$ transforms the signal of the first oscillator into the second harmonic signal, which stimulates activation of the second oscillator in a frequency range around $2\omega_0$. Backward coupling is arranged via the nonlinear element $A_2$ mixing signal from the second oscillator of frequency about $2\omega_0$ with an auxiliary external signal of frequency $\omega_0$ to produce a difference-frequency signal resonant with the first oscillator. It stimulates excitation of the first oscillator as it enters its activity stage. Thus, the excitation is alternately transferred between the oscillators.

The circuit operates as a chaos generator as follows. Suppose that the signal produced by the active first oscillator currently has a phase characterized by the shift constant $\varphi : U_1 \sim \cos(\omega_0 t + \varphi)$. Then, the output of the quadratic nonlinear transformer $A_1$ contains the second harmonic $\cos(2\omega_0 t + 2\varphi)$ with phase $2\varphi$. When the second oscillator becomes active, the generated signal $U_2$ has the phase $2\varphi$. After this signal is heterodyned with the auxiliary signal by means of the element $A_2$, the resulting signal component of frequency $\omega_0$ has the same phase $2\varphi$. Thus, the signal generated by the first oscillator during the next half-period of modulation has the phase $2\varphi$. It is obvious that the phases of the oscillation trains generated during subsequent half-periods can be represented, at least, approximately, by the Bernoulli map

$$\varphi_{n+1} = 2\varphi_n + \text{const} \pmod{2\pi}. \tag{12.1}$$

## 12.2 Experimental observation of the Smale-Williams attractor

The circuit was implemented as a laboratory device (Kuznetsov and Seleznev, 2006). The capacities used were $C_1 = 20$ nF, $C_2 = 5$ nF. Ferrite-core coils had equal inductances $L_1$ and $L_2$ of approximately 1 H. The natural frequencies of the oscillators were, respectively, $f_1 = \omega_0/2\pi = 1090$Hz and $f_2 = 2f_1 = 2180$ Hz. The negative-resistance amplifier and nonlinear conductance were implemented by using a 140UD26 operational amplifier and KD102 diodes, respectively. A time-varying conductance was introduced by using KP303G field-effect transistors. The nonlinear components responsible for the coupling between the subsystems were based on 525PS2 analog frequency multipliers. The output voltages $U_1$ and $U_2$ were fed into a measuring device (oscilloscope or spectrum analyzer), or into a computer via an ADM12-3 analog-to-digital (ADC) converter with 12-bit resolution and a maximum sampling frequency of 3 MHz. The functions $\dot{U}_1$ and $\dot{U}_2$ were obtained by using a standard analog differential amplifier consisting of a 500 pF capacitor and a 62 kΩ resistor combined with a 140UD26 operational amplifier.

In a wide parameter range the experimental system exhibited chaotic oscillations as excitation was alternately transferred between the oscillators by the mechanism discussed above. The operation of the system is illustrated in Fig. 12.2. Panels (a) and (c) show typical waveforms recorded for $N = 8$ and $N = 4$. The time series were obtained with the ADC converter operating at a sampling rate of 200 kHz (approximately 200 data points per period corresponding to the main natural frequency $\omega_0$). Panels (b) and (d) show iteration diagrams obtained from processing the recorded data sampled with time interval equal to a period of the parameter modulation $T = 2\pi N/\omega_0$. The phases were calculated from the formula $\varphi = \arg(U_1 - i\omega_0^{-1}\dot{U}_1)$ by substituting the values of the voltage $U_1$ and the derivative $\dot{U}_1$ at the same instants produced by the analog differentiator. The topological equivalence of the maps to the Bernoulli map (12.1) is obvious; it is essential to infer the hyperbolicity of the attractor from experimental data.

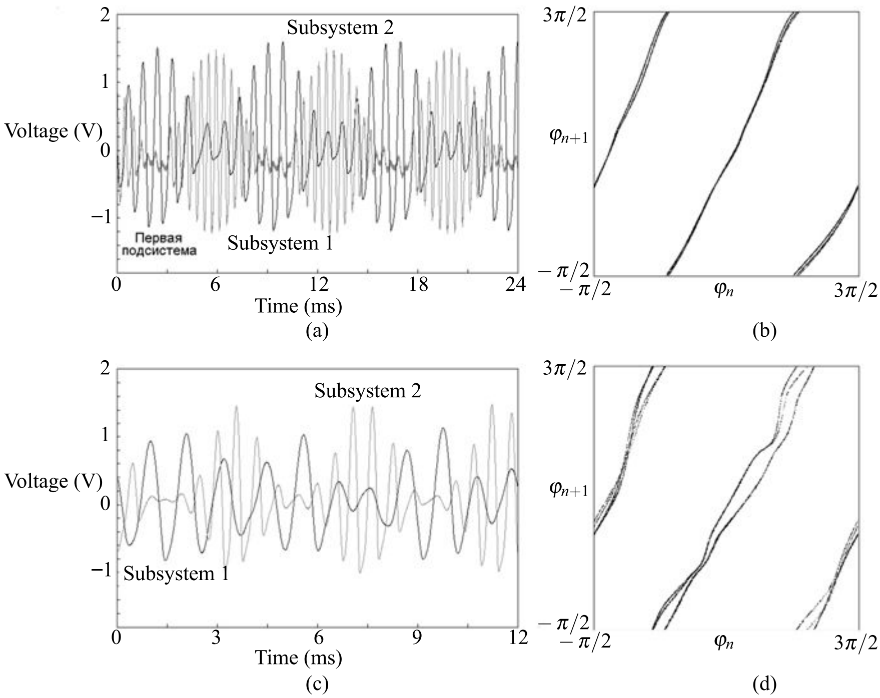


**Fig. 12.2** Samples of waveforms for signals generated by the first (solid curves) and the second (dotted curves) oscillators operating in the chaotic regime, and the empirical iteration diagrams for stroboscopic records of phases of the first oscillator at $N = 8$ (**(a)**,**(b)**) and 4 (**(c)**,**(d)**).

Figure 12.3(a) shows an oscilloscopic image of the chaotic attractor corresponding to $N = 4$ (with horizontal and vertical deflections proportional to $U_1$ and $\dot{U}_1$, respectively) photographed with an exposure time of a few seconds to capture a sufficiently large number of the recurrent loops of a trajectory on the attractor. The image obviously resembles that shown in Fig. 4.6(a). Figure 12.3(b) shows the stroboscopic section of the attractor projected onto the plane $(U_1, \dot{U}_1)$ obtained by processing the bivariate time series used to calculate the diagrams for phases in Fig. 12.2(d). It is obviously similar to the analogous portrait of the Smale-Williams solenoid (Fig. 4.6(b)). An enlarged fragment is shown in inset demonstrating the fine Cantor-like structure of the attractor. The largest Lyapunov exponent of the stroboscopic map evaluated by the method of (Wolf et al., 1985) and by processing a time series sampled with the period $T = 2\pi N/\omega_0$ is $\Lambda \approx 0.73$, in fair agreement with the estimated value $\ln 2 \approx 0.693$. The Grassberger-Procaccia correlation dimension calculated by processing a time series generated at a sampling rate of 200 kHz is $d \approx 2.3$.

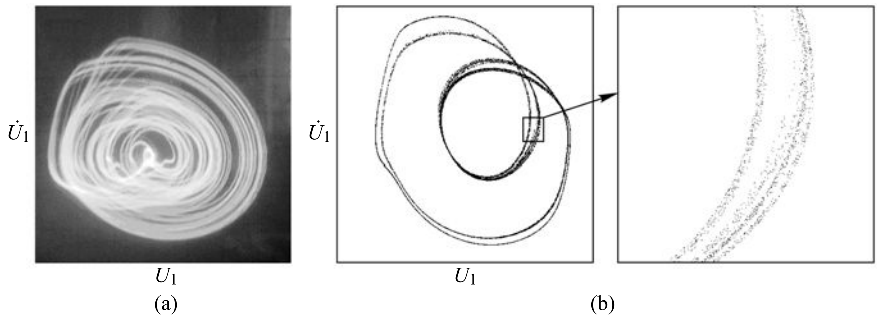


**Fig. 12.3** Portraits of the attractor projected onto the plane of variables $U_1$ and $\dot{U}_1$ for $N = 4$: **(a)** photograph of an oscilloscopic trace image; **(b)** stroboscopic section with period $T = 2\pi N/\omega_0$ at instants corresponding to near-maximum values of $U_1$ with enlarged fragment demonstrating the fine fractal structure of the attractor.

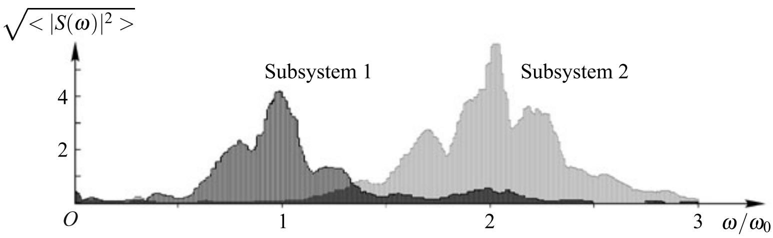


**Fig. 12.4** Spectra of signals produced by the two oscillators operating in the chaotic regime corresponding to $N = 4$ redrawn from photographs of the spectrum-analyzer display.

Figure 12.4 shows power spectra of signals generated by both oscillators operating in the chaotic regime at $N = 4$. Note that the spectra are continuous and are localized around the natural frequencies $\omega_0$ and $2\omega_0$, respectively. They are obviously similar to those obtained for the model discussed in Chap. 4. Unfortunately, some numerical results relating to that model cannot be verified by the experiment. For example, it is hard to determine the complete Lyapunov spectrum or to verify the hyperbolicity criterion. Nevertheless, all in all, the results obtained strongly support the assertion that the dynamics of the experimental device correspond to those of the Smale-Williams type attractor in the non-autonomous system similar to that analyzed in the theoretical study and in numerical simulations.

Additionally, it is worth noting that a device implementing similar operation mechanism was suggested on a base of microwave klystron generator (Emel'yanov et al., 2009; 2010). For that device at the moment, only numerical simulation results are available.

## References

Emel'yanov, V.V., Kuznetsov, S.P., Ryskin, N.M.: Hyperbolic chaos generator based on coupled drift klystrons. Technical Physics Letters **35**, 773–776 (2009).

Emel'yanov, V.V., Kuznetsov, S.P., Ryskin, N.M.: Hyperbolic chaos in the klystron-type microwave vacuum tube oscillator. Chaos **20**, 043104 (2010).

Kuznetsov, S.P., Seleznev, E.P.: A strange attractor of the Smale-Williams type in the chaotic dynamics of a physical system. JETP **102**, 355–364 (2006).

Wolf, A., Swift, J.B., Swinney, H.L., Vastano, J.A.: Determining Lyapunov exponents from a time series. Physica D **16**, 285–317 (1985).

# Chapter 13
# Delay-time Electronic Devices Generating Trains of Oscillations with Phases Governed by Chaotic Maps

**Abstract** Here we turn to consideration of systems with time delayed feedback corresponding to models of Cha. 10, which have been implemented as electronic laboratory devices and studied in experiments described in (Kuznetsov and Ponomarenko, 2008; Baranov et al., 2010). In a frame of the hyperbolic theory the status of dynamics observed in these systems is not so well defined because the classic formulation of the theory relates to finite-dimensional systems, while for the time-delay systems the state space is formally infinite-dimensional. Nevertheless, physically operation principle and observed dynamical phenomena look very similar to those in systems of alternately excited oscillators, for which the hyperbolic nature of the chaotic attractor is well established (see Chaps. 4, 7 and 12). On one hand, it implies a challenging problem for mathematicians to give rigorous definitions and foundation for existence of uniformly hyperbolic chaotic attractors embedded in the infinite dimensional state space of the time-delay systems. On the other hand, accounting transparent principle of operation and evident analogy with the alternately excited oscillators, on physical level of reasoning one can confidently suggest that the chaotic dynamics in time-delay systems of the considered class will have the same features relevant to technical applications like structural stability (robustness).

## 13.1 Van der Pol oscillator with delayed feedback, parameter modulation and auxiliary signal

A time-delay system inspired by the model considered in Subsection 10.2.1 was implemented as a laboratory electronic experimental device and studied in (Kuznetsov and Ponomarenko, 2008). It is based on a single van der Pol oscillator with periodically modulated control parameter to arrange alternating stages of activity and damping, and contains delayed feedback loop with quadratic nonlinear transformation of the signal and mixing with auxiliary external reference signal. At each next stage of activity excitation of the van der Pol oscillator is stimulated by signal from

S. P. Kuznetsov, *Hyperbolic Chaos*

the delay feedback emitted at a previous stage of activity and transfers the doubled phase of the oscillations.

The electronic circuit is schematically depicted in Fig. 13.1. The active element is a single self-oscillator of van der Pol type implemented as an *LC* circuit. A negative-resistance element is arranged on the operational amplifier DA1, and a nonlinear dissipative element is composed of semiconductor diodes D1–D6. The natural frequency of this oscillator was $f_0 = \omega_0/2\pi = 3$ kHz. The modulation of a parameter responsible for the excitation of self-oscillations was organized by introducing additional dissipation via the field-effect transistor VT1, whose resistance slowly varies with time due to the action of the external periodic signal as $\Delta R \sim A\cos\Omega t = A\cos(2\pi t/T)$. During successive periods of the parameter modulation, the oscillator alternately manifests active oscillatory stages and stages of damping as it is below the generation threshold. The generation at each new activity stage is stimulated by a signal arriving via the delay feedback line from the output of the multiplier DA3. In the feedback line, the signal undergoes quadratic nonlinear transformation (by a multiplier implemented on the amplifier DA2) and differentiation (by a standard scheme of differentiator implemented on resistor R2, capacitor C2, and operational amplifier DA4). Then, the signal is passed via a delay line comprising an analog-to-digital converter (ADC), a computer, and a digital-to-analog converter (DAC), where the delay is realized by a computer program algorithm. The delayed signal is multiplied by an auxiliary signal of frequency $f_0$ supplied from an external generator. Owing to the selection of the delay time $\tau = 3T/4$, the signal emitted at the moment of maximum excitation arrives at the oscillator through the delay line approximately at the beginning of the next stage of activity, thus providing stimulation for the onset of generation. Owing to the presence of the quadratic transformation, the system produces phase doubling on each passage from one to another train of oscillations. The ratio of frequencies of the driving signals in the discussed experiments was $N = \omega_0/\Omega = f_0T = 6$.

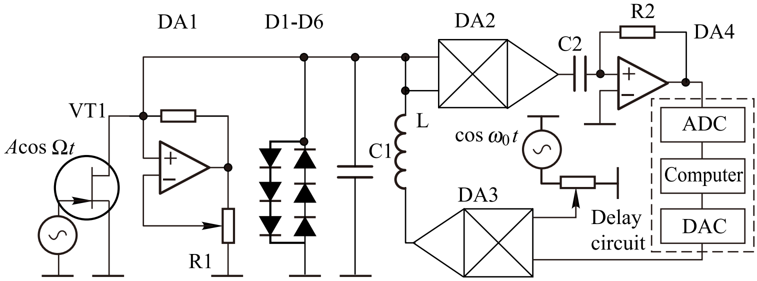


**Fig. 13.1** Circuit diagram of a chaos generator based on a single van der Pol oscillator with periodically modulated parameter and additional time-delayed feedback loop, in which the signal undergoes quadratic nonlinear transformation and mixing with auxiliary signal.

Figures 13.2—13.4 present some experimental data.

Figure 13.2 shows the waveform of the dynamic variable representing sequential trains of oscillations. The chaos is manifested in irregular variations of the position of the carrier oscillations within the envelope in different trains. Figure 13.3 shows a diagram for the phases of oscillations for sequential trains. To depict the diagram, the signal generated by the device was recorded as time series in computer via the ADC for the voltage $U_n$ and the derivative $\dot{U}_n$ obtained from output of the differentiator. The sampling was performed with discrete time step equal to the period of slow parameter modulation at time instants corresponding to the middle of the active stages of the oscillator. The phases were calculated as $\varphi_n = \arg(U_n + i\omega_0^{-1}\dot{U}_n)$. As seen, the phase transformation over one period $T$ corresponds topologically to the expanding circle map, or the Bernoulli map: one bypass for pre-image implies two-fold bypass of the full circle.

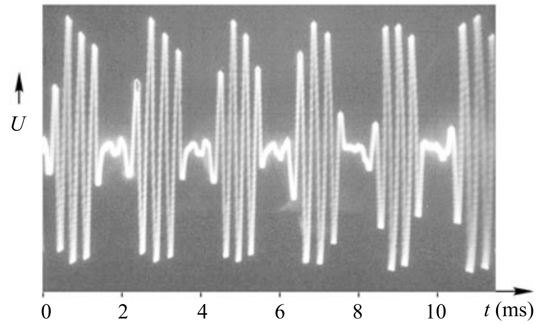


**Fig. 13.2** Waveform of signal generated by the laboratory device as photographed from the oscilloscope screen.

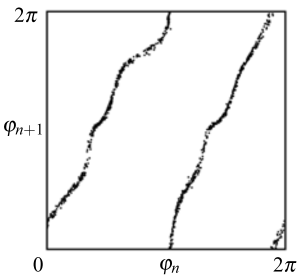


**Fig. 13.3** Diagram for the phases of oscillations for sequential trains obtained by processing the time series of generated signal from the experimental device.

Figure 13.4 shows portraits of the attractor photographed from the oscilloscope screen (a,b). Panel (a) corresponds to projection of the attractor from the multidimensional phase space of the time-delay system onto plane of two variables $(U, \dot{U})$.

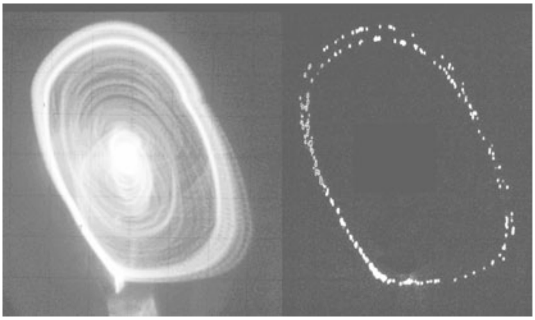

**Fig. 13.4** Portrait of attractor photographed from the oscilloscope screen that corresponds to projection onto plane of two variables $(U,\dot{U})$ from the multidimensional phase space of the time-delay system; stroboscopic portrait of the same attractor.

Panel (b) is stroboscopic cross-section of this attractor; the sampling is performed with time interval equal to period of slow parameter modulation. The stroboscopic image resembles the Smale-Williams solenoid with a noticeable transverse fractal structure characteristic of the attractors of this type.

Figure 13.5 shows the spectral power density obtained by processing the time series of the generated signal recorded in the computer. The spectrum is surely continuous and has a full width at half maximum of about 20% at an average frequency of 3 kHz. Discrete peaks observed in the left-hand part of the plot originate due to presence of periodic component due to the external parameter modulation.

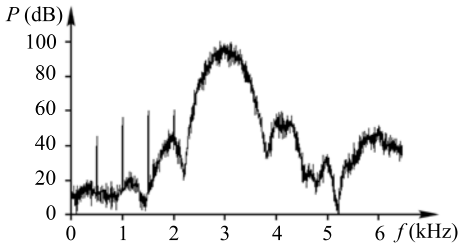


**Fig. 13.5** Plot of spectral power density in the chaotic regime of operation obtained by processing the recorded time series from the experimental device.

As believed, this experiment demonstrates chaotic dynamics associated with attractor of Smale-Williams type embedded in the multidimensional phase space of the time-delay system. Rigorous foundation of this hypothesis, as mentioned, is a challenging problem.

## 13.2 Van der Pol oscillator with two delayed feedback loops and parameter modulation

Now we turn to a version of the time-delay system discussed in Subsection 10.2.2. It is based on a single van der Pol oscillator with two delayed feedback loops, one with linear transmission characteristic, and the other with quadratic nonlinearity producing the second harmonic; both transmitted signals are mixed to produce the difference-frequency signal stimulating excitation at the next stage of activity of the van der Pol oscillator. The arrangement of the device ensures doubling of phase differences of two neighboring oscillation trains in the course of the process.

Figure 13.6 shows the circuit diagram for the system (Baranov et al., 2010). The basic element is the self-oscillator designed using the LC-circuit ($L = 10$ mH, $C_1 = 5$ uF) and the operational amplifier DA1, which introduces a negative resistance. Nonlinearity is provided by two parallel counter-directed chains of semiconductor diodes. The natural frequency of oscillations in the concrete experimental setup was about 700 Hz. Parameter responsible for excitation of the self-oscillator was modulated by an external signal with a frequency of 71 Hz supplied to the gate of the field-effect transistor VT1. The signal from the oscillator was squared with an analog multiplier circuit DA2 and differentiated at the operational amplifier DA4. The signals from the output circuit of differentiation and from the oscillator itself served as two inputs of an analog-digital converter (ADC) and a computer implementing two-channel delay line (delay time was 21 ms and 7 ms, respectively, which is approximately 3/2 and 1/2 of a period of parameter modulation). The output signals transformed back to analog form in the two-channel digital-analog converter (DAC) are input to the analog multiplier whose output is connected to the coil circuit inductance of the self-oscillator. This device corresponds qualitatively to Eq. (10.15). For analysis of the phase relations, the signal from the self-oscillator (the voltage on the capacitor C1) was recorded in a computer together with the second component (derivative of the voltage) obtained by analog differentiator by means of an additional (not shown in the diagram) analog-digital converter.

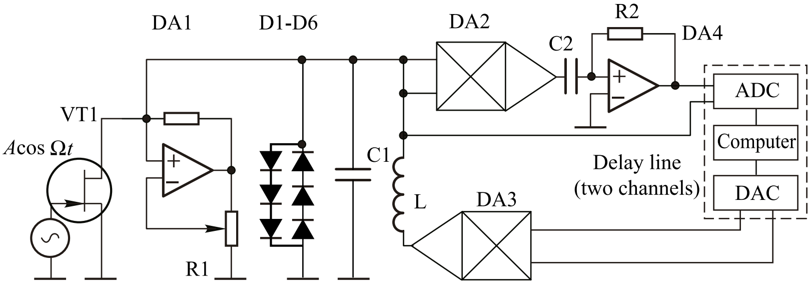


**Fig. 13.6** Schematic diagram of the experimental device.

Figure 13.7 shows a waveform of chaotic signal obtained in the experiment, and the power spectrum of the oscillations in the regime of chaos generation. They are in good qualitative agreement, respectively, with Fig. 10.10 and Fig. 10.14. In Fig. 13.8 iteration diagrams for phases are shown obtained by processing the experimental data recorded from ADC in computer as bivariate time series for the voltage on the capacitor C1 and its time derivative. Panel (a) is three-dimensional plot for phases of three successive oscillation trains, which is in qualitative agreement with relation (10.17). The phases are evaluated at time instants corresponding to the middles of the active stages of the oscillator $\varphi_n = \arg(U_n + i\omega_0^{-1}\dot{U}_n)$. Panel (b) shows a diagram for phase differences $\Delta\varphi_n = \varphi_n - \varphi_{n-1}$ and corresponds well to the relation (10.18).

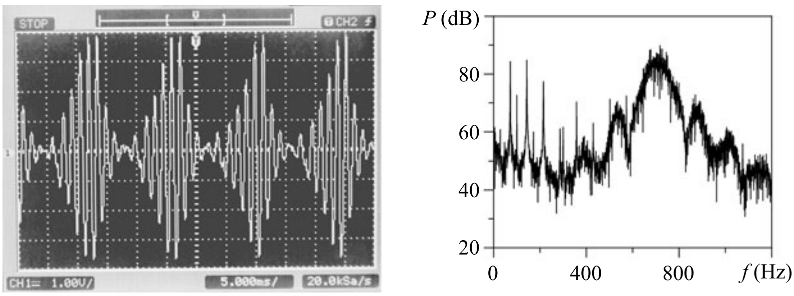


(a) (b)

**Fig. 13.7** Waveform of chaotic signal generated by the experimental device photographed from the oscilloscope screen **(a)** and power spectrum of the signal in this regime **(b)**.

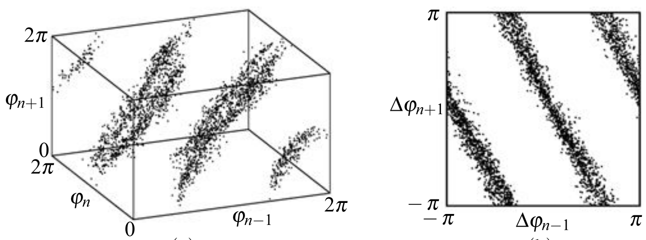


(a) (b)

**Fig. 13.8** Iteration diagrams for phases as three-dimensional plot obtained by processing of recorded experimental data **(a)** and the diagram for phase differences **(b)**.

Figure 13.9 shows portraits of the attractor obtained in the experiment. Panel (a) is photography from the oscilloscope screen; the horizontal and vertical coordinates correspond to voltage on the capacitor C1 and to its time derivative, respectively. Recall that the attractor of the system with delay is an object in an infinite dimensional state space, so the image has to be regarded as a two-dimensional projection of the object. Panel (b) provides a picture of the attractor in the stroboscopic section. This

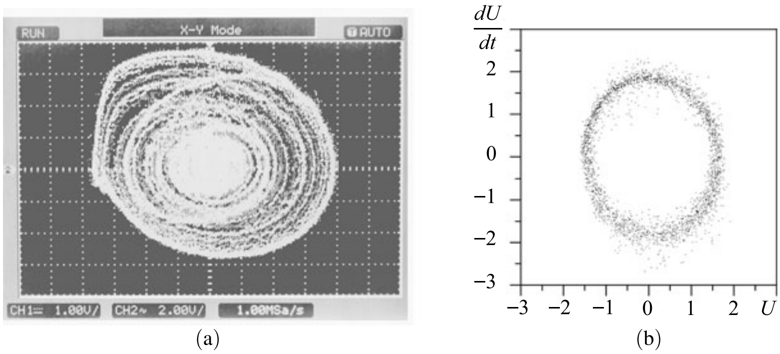


**Fig. 13.9** Portrait of the attractor in the projection onto the phase plane of the oscillator, photographed from the oscilloscope screen **(a)**, and a portrait of the attractor in the stroboscopic section, built by processing the experimental data **(b)**.

attractor embedded in the multidimensional state space of the time-delay system apparently relates to the class of partially hyperbolic attractors, like that discussed in Sect. 10.3.

The experiment confirmed occurrence of the effect of hard excitation. When adjusting the negative resistance introduced into the oscillator circuit due to the presence of operational amplifier, it was possible to observe hysteresis, as illustrated in Fig. 13.10. With gradual motion in the course of parameter variation from the left to the right along the lower branch of the plot, there are no intense oscillations in the system. They arise via abrupt transition at certain threshold, but they persist in the course of parameter variation in reverse direction in a relatively wide range that corresponds to motion from the right to the left along the top branch of the hysteresis loop on the plot.

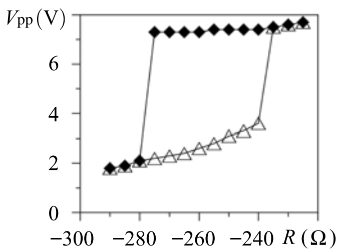


**Fig. 13.10** Diagram illustrating hysteresis accompanying excitation of oscillations in the experimental device. The voltage $V_{pp}$ ("peak-to-peak") is plotted for the signal generated by the system versus the negative resistance introduced into the oscillator circuit due to the presence of an operational amplifier.

## References

Baranov, S.V., Kuznetsov, S.P., Ponomarenko, V.I.: Chaos in the phase dynamics of Q-switched van der Pol oscillator with additional delayed-feedback loop. Izvestija VUZov-Applied Nonlinear Dynamics (Saratov) **18** (1), 11–23 (2010) .

Kuznetsov, S.P., Ponomarenko, V.I.: Realization of a strange attractor of the Smale-Williams type in a radiotechnical delay-fedback oscillator. Tech. Phys. Lett. **34**, 771–773 (2008).

# Chapter 14
# Conclusion

The material presented in this book shows significant progress in the main directions of the research program outlined in the Preface. We can say now that we have a collection of realistic concrete examples of physically realizable systems with chaotic dynamics, to which the principles of the hyperbolic theory are applicable ("systems with axiom A").

Several approaches to constructing systems with uniformly hyperbolic chaotic attractors are developed. Among them are: exploiting models driven by short periodic pulses; organizing dynamics in successive stages, each governed by special form of differential equations; composing systems of oscillators excited alternately and transferring the excitation of each other with transformations of phases described by maps with chaotic dynamics. As well, the delayed feedback systems may be designed to implement the last principle. Also we have shown how one can apply the parametric excitation principle to generation of the hyperbolic chaos.

We have presented and examined a number of concrete systems in which the presence of uniformly hyperbolic chaotic attractors is confirmed at the level of computer validation of cone criterion or is assumed on the basis of qualitative arguments and data of computations. Many examples belong to a class of non-autonomous systems with periodic variation in time of coefficients in the governing equations, but there are also examples of autonomous systems with attractors of Smale-Williams type in the Poincaré map. Due to the intrinsic structural stability, these models can be transformed to a certain extent, without violating the hyperbolic nature of the dynamics, and this is a way to get many other new systems with uniformly hyperbolic chaos. Based on some of the proposed schemes, electronic devices were implemented, in which the dynamics on a hyperbolic attractor has been demonstrated in experiments.

At the moment, the examples of dynamics on the uniformly hyperbolic chaotic attractors we have discussed relate to purposefully designed devices, not to systems of natural origin (where they occur, as thought, extremely rare). However, a border here is conditional, of course. You may recall that the van der Pol oscillator commonly recognized now as a universal model in the theory of oscillations originally came into use in the application to an electronic device, the vacuum-tube generator.

S. P. Kuznetsov, *Hyperbolic Chaos*

It is hoped that models with hyperbolic attractors also may be useful for description of some systems of natural origin, for example, in neurodynamics. Above we mentioned the work, which discussed a possibility of occurrence of an attractor of Plykin type in the neuron model of Hindmarsh-Rose (Belykh et al., 2005). Also in the context of neurodynamics systems with blue sky catastrophes were considered (Shilnikov and Cymbalyuk, 2005; Shilnikov and Kolomiets, 2008); in extended models with the phase space dimension four and more situations may arise, corresponding to the presence of attractors of Smale-Williams type.

A possibility of physical realization of hyperbolic chaos opens up prospects for applications for the well-developed mathematical theory and provides a basis for comparative studies of hyperbolic and non-hyperbolic chaos, including those in computations and in experiments. Also, it becomes interesting and informative to re-examine a field of research, consisting of the construction of complex systems on the basis of the elements with hyperbolic chaos, like chains, lattices, and networks (Bunimovich and Sinai, 1988; 1993; Bricmont and Kupiainen, 1997; Järvenpää, 2005; Kuptsov and Kuznetsov, 2009). One might think that models, specifically designed in order to realize the hyperbolic chaos, will be useful for understanding some fundamental issues still challenging researchers, for example, the problem of turbulence.

An interesting question is about the diagnostic of hyperbolic chaos in physical experiment. Although in this respect the mathematical techniques, such as the cone criterion, seem to be unsuitable, the problem does not look hopeless. At least in the case of the Smale-Williams attractor a productive and convincing approach to recognize the respective type of dynamics is plotting diagrams for the cyclic phase variables demonstrating agreement with expanding mapping of the circle or Anosov torus maps. This may be applied in both computer calculations, and processing of experimental data.

Speaking about possible technical applications of systems with hyperbolic attractors, special attention should be paid to their most important property of structural stability, or roughness.

Recently, a problem of generation of the so-called robust chaos is widely discussed (Banerjee et al., 1998; Elhadj and Sprott, 2008; Drutarovský and Galajda P., 2007; Deshpande et al., 2010). This refers to chaotic dynamics of such kind, when parameter variation is not accompanied with “windows” of regularity (periodicity), and the dependence of the largest Lyapunov exponent in a wide range is a smooth function. It is emphasized that such chaos is desirable in applications, including in the communication systems, the random number generators, encryption schemes. To implement such signals, it was suggested to use components having the characteristics as functions with break points. In practice, the ideal breaks are unfeasible, and it is problematic to eliminate completely the windows of regularity in this way. At the same time, in systems with uniformly hyperbolic attractors the needed properties of chaos appear as a natural attribute because of inherent structural stability.

During the last 20 years the active researches are directed on elaboration of applications of chaotic signals for communication and information systems (Yang, 2001, 2004; Dmitriev and Panas, 2002; Argyris et al., 2006; Koronovskii et al., 2009).

While the arguments in favor of this development look convincing (great information capacity of signals; possibility of controlling the dynamics by small external perturbations; a variety of methods to enclose information in a signal; rich possibilities for encryption of information), it should be noted that the expected potential benefits are far not achieved yet. A possible reason is that with the signals generated by non-hyperbolic attractors, we can not stand on a strong theoretical foundation. On the other hand, for hyperbolic attractors a complete mathematical description of chaos does exist; for example, one can mention a possibility of exhaustive enumeration of orbits belonging to the attractor using finite Markov partitions and respective symbolic dynamics. Therefore, it is likely that involvement of the hyperbolic chaos may realize the expected advantages of the information and communication systems based on chaotic signals.

Of special interest for communication systems may be the principle of manipulation of the phases (Kuznetsov, 2005; Kuznetsov and Seleznev, 2006; Isaeva et al., 2006; Kuznetsov and Pikovsky, 2007; Kuznetsov and Ponomarenko, 2008; Kuznetsov and Pikovsky, 2008; Kuznetsov, 2011). Chaos manifests itself in this case as irregular variation of phase of carrier in a generated sequence of oscillation trains. So, on this basis it is possible to implement systems in which the signal transmission in communication channel will be much less sensitive to noises, losses and distortions than in schemes proposed so far (Yang, 2001, 2004; Dmitriev and Panas, 2002; Argyris et al., 2006; Koronovskii et al., 2009). In this connection it is appropriate to recall the advantages of frequency or phase modulations over amplitude modulation in the traditional communication technologies.

## References


Argyris, A., Syvridis, D., Larger, L. et al.: Chaos-based communications at high bit rates using. commercial fibre-optic links. Nature **438**, 343–346 (2006).

Banerjee, S., Yorke, J.A., Grebogi, C.: Robust chaos. Phys. Rev. Lett. **80**, 3049–3052 (1998).

Belykh, V., Belykh, I., Mosekilde, E.: The hyperbolic Plykin attractor can exist in neuron models. Int. J. of Bifurcation and Chaos **15**, 3567–3578 (2005).

Bricmont, J., Kupiainen, A.: Infinite-dimensional SRB measures. Physica D **103**, 18–33 (1997).

Bunimovich, L.A, Sinai, Ya.G.: Spacetime chaos in coupled map lattices. Nonlinearity **1**, 491–516 (1988).

Bunimovich, L.A., Sinai, Ya.G.: Statistical mechanics of coupled map lattices. In: Kaneko, K. (ed.) Theory and application of coupled map lattices, pp. 169–189. John Wiley & Sons Ltd., New York (1993).

Deshpande, A., Chen, Q., Wang,Y., Lai, Y.-C., Do Y.: Effect of smoothing on robust chaos. Phys. Rev. E **82**, 026209 (2010).

Dmitriev, A.S., Panas, A.I. Dynamical Chaos: New Information Carriers for Communication Systems. Fizmatlit, Moscow (2002).

Drutarovský, M., Galajda, P.: A Robust Chaos-Based True Random Number Generator Embedded in Reconfigurable Switched-Capacitor Hardware. Radioengineering **16** , 120–127 (2007).

Elhadj, Z., Sprott, J.C.: On the robustness of chaos in dynamical systems: Theories and applications. Front. Phys. China **3**, 195–204 (2008).

Isaeva, O.B., Jalnine, A.Yu., Kuznetsov, S.P.: Arnold's cat map dynamics in a system of coupled nonautonomous van der Pol oscillators. Phys. Rev. E **74**, 046207 (2006).

Järvenpää, E.: SRB-measures for coupled map lattices. In: Chazottes, J.-R. and Fernandez, B.(eds.): Dynamics of Coupled Map Lattices and of Related Spatially Extended Systems, pp.95–114. Springer, (2005).

Koronovskii, A.A., Moskalenko, O.I., Hramov, A.E.: On the use of chaotic synchronization for secure communication. Physics-Uspekhi **52**, 1213–1238 (2009).

Kuptsov, P.V., Kuznetsov, S.P.: Violation of hyperbolicity in a diffusive medium with local hyperbolic attractor. Phys. Rev. E **80**, 016205 (2009).

Kuznetsov, S.P.: Example of a physical system with a hyperbolic attractor of the Smale-Williams type. Phys. Rev. Lett. **95**, 144101 (2005).

Kuznetsov, S.P.: On Feasibility of a Parametric Generator of Hyperbolic Chaos. JETP **106**, 380–387 (2008)

Kuznetsov, S.P.: Dynamical chaos and uniformly hyperbolic attractors: from mathematics to physics. Physics-Uspekhi **54** (2), 119 (2011).

Kuznetsov, S.P., Pikovsky, A.: Autonomous coupled oscillators with hyperbolic strange attractors. Physica D **232**, 87–102 (2007).

Kuznetsov, S.P., Pikovsky, A.: Hyperbolic chaos in the phase dynamics of a Q-switched oscillator with delayed nonlinear feedbacks. Europhysics Letters **84**, 10013 (2008).

Kuznetsov, S.P., Ponomarenko, V.I.: Realization of a strange attractor of the Smale–Williams type in a radiotechnical delay-fedback oscillator. Tech. Phys. Lett. **34**, 771–773 (2008).

Kuznetsov, S.P., Seleznev, E.P.: A strange attractor of the Smale–Williams type in the chaotic dynamics of a physical system. JETP **102**, 355–364 (2006).

Shilnikov, A., Cymbalyuk, G.: Transition between Tonic Spiking and Bursting in a Neuron Model via the Blue-Sky Catastrophe. Phys. Rev. Lett. **94**, 048101 (2005).

Shilnikov, A., Kolomiets, M.: Methods of the qualitative theory for the Hindmarsh-Rose model: a case study. Int. J. of Bifurcation and Chaos **18**, 2141–2168 (2008).

Yang, T.: Chaotic Communication Systems. Nova Biomedical (2001).

Yang, T.: A survey of chaotic secure communication systems. International Journal of Computational Cognition **2**, 81–130 (2004).

# Appendix A
# Computation of Lyapunov Exponents: The Benettin Algorithm

A convenient and widely used algorithm for evaluation of Lyapunov exponents (Benettin et al., 1980) is shortly explained here. To be concrete, we discuss a continuous-time autonomous system governed by equation

$$d\mathbf{x}/dt = \mathbf{F}(\mathbf{x}). \tag{A.1}$$

Generalizations to the non-autonomous case and to diffeomorphisms are simple and straightforward.

First, we undertake the numerical solution of Eq. (A.1) up to arrival of the orbit at the attractor.

Then, to compute the largest Lyapunov exponent we proceed with simultaneous integration of Eq. (A.1) together with the variation equation

$$\frac{d\tilde{\mathbf{x}}}{dt} = \mathbf{A}\left(\mathbf{x}(t)\right)\tilde{\mathbf{x}}. \tag{A.2}$$

Here $\mathbf{A}(\mathbf{x}(t))$ is a matrix derivative composed of the partial derivatives of components of the vector function $\mathbf{F}(\mathbf{x})$ over the components of the vector $\mathbf{x}$. We perform integration on some appropriately chosen time interval $T$ starting at $t = t_0$ from $\mathbf{x}(t_0)$ and with some vector $\tilde{\mathbf{x}}(t_0)$ of certain norm $\|\tilde{\mathbf{x}}(t_0)\| = \sqrt{\sum_{i=1}^{N} \tilde{x}_i^2(t_0)}$. As $\tilde{\mathbf{x}}$ obeys the linear equation, this norm can be chosen arbitrarily, say, $\|\tilde{\mathbf{x}}(t_0)\| = 1$. At $t_1 = t_0 + T$ we redefine the perturbation to have the norm equal to the initial value but keeping direction of the vector unchanged, namely, $\tilde{\mathbf{x}}^0(t_1) = \tilde{\mathbf{x}}(t_1)/\|\tilde{\mathbf{x}}(t_1)\|$ (Fig. A.1). Now, continue the procedure with numerical solution from the initial point $\mathbf{x}(t_1)$ with the perturbation $\tilde{\mathbf{x}}^0(t_1)$. Next, obtain the state $\mathbf{x}(t_2)$ at $t_2 = t_0 + 2T$ and perturbation $\tilde{\mathbf{x}}(2T)$, and redefine the perturbation as $\tilde{\mathbf{x}}^0(t_2) = \tilde{\mathbf{x}}(t_2)/\|\tilde{\mathbf{x}}(t_2)\|$, and so on. For $M$ steps of the algorithm the total factor determining the change of the perturbation norm will be $P = \prod_{k=1}^{M} \|\tilde{\mathbf{x}}_k(t_0 + kT)\|$. Obviously, evolution of the magnitude of the perturbation is determined by the largest Lyapunov exponent, so, it is estimated as

$$\lambda_1 \cong \frac{1}{MT} \ln P = \frac{1}{MT} \sum_{k=1}^{M} \ln \|\tilde{\mathbf{x}}_k(t_0 + kT)\|, \tag{A.3}$$

where $M$ is supposed to be large enough. This successive renormalization of the perturbation vectors is essential feature of the computational algorithm.

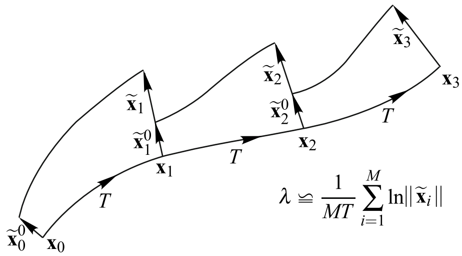


**Fig. A.1** An illustration for Benettin's algorithm of evaluation of the largest Lyapunov exponent (see text).

To compute more than one Lyapunov exponent we monitor a collection of the respective number of perturbation vectors evolving in time along the reference phase trajectory and at each step of the algorithm redefine the perturbation vectors applying the Gram-Schmidt orthogonalization process.

It works as follows. Suppose, at some step of algorithm the perturbation vectors evolve from $\mathbf{x}_1^0(t_{k-1}), \mathbf{x}_2^0(t_{k-1}), \mathbf{x}_3^0(t_{k-1}), \ldots$ at $t_{k-1} = t_0 + (k-1)T$ to $\mathbf{x}_1(t_k), \mathbf{x}_2(t_k)$, $\mathbf{x}_3(t_k), \ldots$ at $t_k = t_0 + kT$. Then, we set

$$\begin{aligned}
&\tilde{\mathbf{x}}_1^0(t_k) = \tilde{\mathbf{x}}_1(t_k)/\|\tilde{\mathbf{x}}_1(t_k)\|, \\
&\tilde{\mathbf{x}}_2^0(t_k) = \mathbf{a}_2/\|\mathbf{a}_2\|, \quad \mathbf{a}_2 = \tilde{\mathbf{x}}_2(t_k) - \langle \tilde{\mathbf{x}}_2(t_k), \tilde{\mathbf{x}}_1(t_k)\rangle\, \tilde{\mathbf{x}}_1^0(t_k), \\
&\tilde{\mathbf{x}}_3^0(t_k) = \mathbf{a}_3/\|\mathbf{a}_3\|, \quad \mathbf{a}_3 = \tilde{\mathbf{x}}_3(t_k) - \langle \tilde{\mathbf{x}}_3(t_k), \tilde{\mathbf{x}}_1(t_k)\rangle\, \tilde{\mathbf{x}}_1^0(t_k) - \langle \tilde{\mathbf{x}}_3(t_k), \tilde{\mathbf{x}}_2(t_k)\rangle\, \tilde{\mathbf{x}}_2^0(t_k), \\
&\ldots\ldots\ldots\ldots
\end{aligned} \tag{A.4}$$

Here the brackets designate the dot product: $\langle \mathbf{u}, \mathbf{v}\rangle = \mathbf{u} \cdot \mathbf{v} = \sum_{i=1}^{N} u_i v_i$. The obtained vectors $\mathbf{x}_1^0, \mathbf{x}_2^0, \ldots$ are used to start a next step of the algorithm at $t_k = kT$. In the course of the computations, the accumulated sums $S_m(M) = \sum_{i=1}^{M} \ln \|\tilde{\mathbf{x}}_m(kT)\|$ are calculated, and the Lyapunov exponents are evaluated from the relations

$$\lambda_m \approx S_m(M)/MT. \tag{A.5}$$

## References

Benettin, G., Galgani, L., Giorgilli, A., Strelcyn, J.-M.: Lyapunov characteristic exponents for smooth dynamical systems and for Hamiltonian systems: A method for computing all of them. Meccanica **15**, 9–30 (1980).

# Appendix B
# Hénon and Ikeda Maps

In some physical systems description by iterated maps appears in a very natural way. Say, considering a particle moving under action of periodic pulses (kicks), one can express the coordinate and velocity just before the next kick via the state before the previous kick and consider dynamics in discrete time with this mapping. Particularly, well-known maps of Hénon (Hénon, 1976) and Ikeda (Ikeda et al., 1980) may be obtained in appropriate setup; it reveals physical significance of these models.

Accounting framework of the current book, it is worth stressing that chaotic attractors in the Hénon and Ikeda maps do not relate to the class of uniformly hyperbolic ones. Transformation of the phase space volumes in the course of dynamical evolution is similar to that mentioned in Chap. 1 in the context of Fig. 1.4 accompanied by formation of local singularities of the density of the "phase fluid". It is associated with an inevitable presence of tangencies between stable and unstable manifolds of orbits on the attractors as illustrated in Chap. 7.

Consider the following simple physical system (Fig. B.1). Let a particle of mass $m$ be able to move along the $x$ axis with friction force proportional to the velocity, $f = -kv$. Suppose further that pulsed kicks effect the particle with period $T$ of intensity depending on the instantaneous position of the particle, i.e. the momentum transferred is expressed by some function $P(x)$.

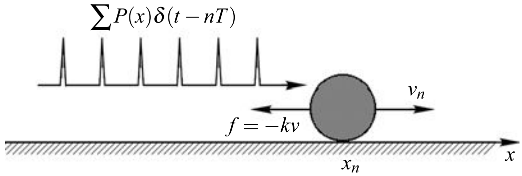


**Fig. B.1** Mechanical system whose dynamics are described by the Hénon map.

Assume that just before the $n$-th kick the particle coordinate is $x_n$, and the velocity is $v_n$. Immediately after the kick the velocity is $v_n + P(x_n)/m$ and then it decreases exponentially according to the expression $v(t) = (v_n + P(x_n)/m)e^{-kt/m}$. At the instant before the next kick we get

$$\begin{aligned} v_{n+1} &= (v_n + P(x_n)/m)\, e^{-kT/m}, \\ x_{n+1} &= x_n + \int_0^T v(t)dt = x_n + (mv_n + P(x_n)) \left(1 - e^{-kt/m}\right) k^{-1}. \end{aligned} \tag{B.1}$$

In terms of variable $y = x - mk^{-1}(e^{kT/m} - 1)v$ introduced instead of $v$, Equations (B.1) may be rewritten as

$$x_{n+1} = f(x_n) + by_n, \quad y_{n+1} = x_n, \tag{B.2}$$

where

$$b = -e^{-kT/m} \text{ and } f(x) = x(1-b) + P(x)(1+b)k^{-1}. \tag{B.3}$$

Now, let us concretize the spatial distribution of the force field in such a way that $f(x) = 1 - ax^2$. Then, (B.2) reads

$$x_{n+1} = 1 - ax_n^2 + by_n, \quad y_{n+1} = x_n. \tag{B.4}$$

In 1976 Hénon introduced this map from purely abstract motivation to get a simple model with chaotic attractor. Now, it is evident that this map may serve for description of simple physical systems, one of which just has been considered. Other examples are dissipative oscillator and rotator under pulsed periodic driving (Heagy, 1992). In physical setup *negative values are natural for the parameter b*, although in the original work of Hénon occasionally the sign of that parameter was set opposite.

Observe that the map is invertible: one can easily express $x_n$ and $y_n$ via $x_{n+1}$ and $y_{n+1}$ uniquely.

Evaluation of the Jacobi determinant for the Hénon map yields

$$J = \begin{vmatrix} \partial x_{n+1}/\partial x_n & \partial x_{n+1}/\partial x_n \\ \partial x_{n+1}/\partial x_n & \partial x_{n+1}\partial x_n \end{vmatrix} = \begin{vmatrix} -2a & b \\ 1 & 0 \end{vmatrix} = -b. \tag{B.5}$$

If we consider a cloud of representative points occupying an area $S$ on the phase plane $(x,y)$, then, at each successive step of iterations the area will be multiplied by factor $|b|$ so, at $|b| < 1$ the system is dissipative.

Figure B.2 shows attractor of the map at parameters $a = 1.4$, $b = 0.3$ corresponding to the original work of Hénon.

Figure B.3 shows a chart of dynamical regimes on the parameter plane $(a,b)$. Distinct gray scales correspond to observed periodic dynamics of different periods. One special gray tone is used for the chaos. The bottom part of the diagram corresponds to presence of attractive stable fixed point. As the parameter $a$ grows, attractors corresponding to periodic oscillations arise out of period 2, then periods 4, 8, etc.; there is a sequence of period doubling bifurcations. The bifurcation lines in the parameter plane represent borders of respective areas of these periodic regimes. They accumulate according to the Feigenbaum law to the limit critical line, which represents the border of chaos (Feigenbaum, 1979; Vul et al., 1984; Schuster and

Just, 2005). Observe small areas of periodic motions scattered over the region occupied by chaos; because of their characteristic shape, they are called the "shrimps" (Gallas, 1993, 1994). Presence of these formations is a visually illustrative feature of non-hyperbolic nature of chaos.

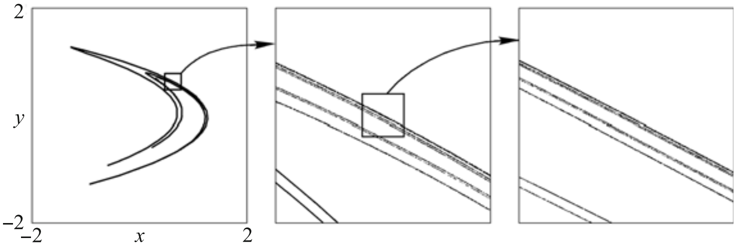


**Fig. B.2** Strange attractor of the Hénon map (B.4) at $a = 1.4, b = 0.3$.

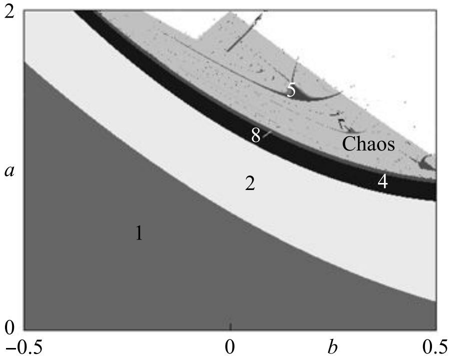


**Fig. B.3** Chart of dynamical regimes on the parameter plane of the Hénon map (B.4). White area in the top left part of the diagram corresponds to divergence of iteration of the map. The numbers 1, 2, 4,... indicate the periods of motion associated with the respective areas.

Figure B.4 shows the larger one of two Lyapunov exponents of the Hénon map (B.4) obtained numerically and plotted versus parameter $a$ at constant $b = 0.3$. Observe a characteristic feature of the dependence intrinsic to the non-hyperbolic chaos. On a background of a set of positive Lyapunov exponent indicating chaos there occur densely deep narrow drops to negative values of the Lyapunov exponent in the *windows of periodicity* (or, *windows of regularity*). In the chart of dynamical regimes of Fig. B.3 the diagram B.4 corresponds to a path on the parameter plane along a vertical line $b = -0.3$; there occur the drops to negative Lyapunov exponent values as the path crosses the "shrimps".

Now, let us turn to another system, an oscillator with cubic nonlinearity driven by periodic short pulses. The model equation is

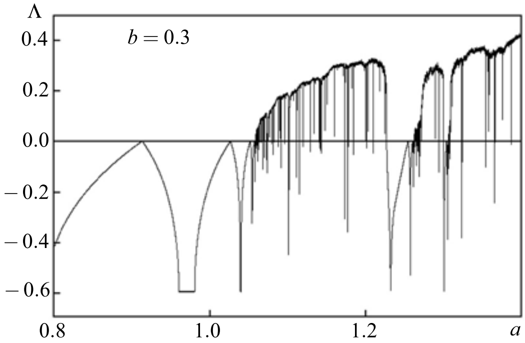


**Fig. B.4** The largest Lyapunov exponent of the Hénon map (B.4) versus parameter a at constant $b = 0.3$.

$$\ddot{x} + \gamma\dot{x} + \omega_0^2 x + \beta x^3 = \Sigma C\delta(t - nT), \tag{B.6}$$

where $x$ is the dynamical variable, $\omega_0$ is natural frequency, $\gamma$ is a coefficient of dissipation, and $\beta$ is parameter of nonlinearity. External driving is represented by a sequence of pulses accounted by Dirac delta function, which follow with period $T$ and have magnitude characterized by constant $C$. We suppose for simplicity that the period of pulses contains an integer number of periods of natural frequency, $\omega_0 T/2\pi = N$.

In assumption that $\omega_0$ and $T$ are relatively large, while $\gamma$, $\beta$, and $C$ are relatively small, one can use the slow amplitude method in intervals between the kicks. For this, we introduce the complex amplitude $a(t)$ and set

$$x = ae^{i\omega_0 t} + a^* e^{-i\omega_0 t}, \quad \dot{x} = i\omega_0(ae^{i\omega_0 t} - a^* e^{-i\omega_0 t}). \tag{B.7}$$

These relations suggest that the complex amplitude satisfies a condition

$$\dot{a}e^{i\omega_0 t} + \dot{a}^* e^{-i\omega_0 t} = 0. \tag{B.8}$$

Substituting the relations (B.7) into (B.6) with zero right-hand part, and accounting (B.8), after averaging over a period of fast oscillations we obtain

$$\dot{a} = -\frac{\gamma}{2}a + \frac{3}{2}\frac{i\beta}{\omega_0}|a|^2 a. \tag{B.9}$$

Now, suppose that just after the $n$-th kick at $t$=$nT$ the complex amplitude is $a_n = \frac{1}{2}(x_n - i\omega_0^{-1}\dot{x}_n)$. To obtain the amplitude just before the next pulse, we integrate Eq. (B.9) in period $T$ with the initial condition $a(nT + 0) = a_n$. It can be done analytically. Indeed, substitution $a = re^{i\varphi}$ yields $\dot{r} + ir\dot{\varphi} = -\frac{1}{2}\gamma r + \frac{3}{2}i\beta\omega_0^{-1}r^3$, and after separation of the real and imaginary parts,

$$\dot{r} = -\frac{1}{2}\gamma r, \quad \dot{\varphi} = \frac{3}{2}\beta\omega_0^{-1}r^2. \tag{B.10}$$

The following hold

$$\begin{aligned} r(\Delta t) &= r_n e^{-\frac{1}{2}\gamma\Delta t}, \\ \varphi(\Delta t) &= \varphi_n + \frac{3}{2}\beta\omega_0^{-1}r_n^2\int_0^{\Delta t} e^{-\frac{1}{2}\gamma\tau}d\tau = \varphi_n + 3\beta\omega_0^{-1}\gamma^{-1}(1-e^{-\frac{1}{2}\gamma\Delta t})r_n^2. \end{aligned} \tag{B.11}$$

Substituting $\Delta t = T$, we obtain

$$\begin{aligned} a((n+1)T-0) &= r_n e^{-\frac{1}{2}\gamma T} e^{i\varphi_n + 3i\beta\omega_0^{-1}\gamma^{-1}(1-e^{-\frac{1}{2}\gamma\Delta t})r_n^2} \\ &= a_n e^{-\frac{1}{2}\gamma T} e^{3i\beta\omega_0^{-1}\gamma^{-1}(1-e^{-\frac{1}{2}\gamma\Delta t})|a_n|^2}. \end{aligned} \tag{B.12}$$

The delta-function kick is accompanied by instant transfer of the momentum; as seen from (B.6) the velocity $\dot{x}$ is changed by the value $C$, while the coordinate $x$ just after the kick retains its value. Thus, we have to set

$$a_{n+1} = \frac{1}{2}(x(nT-0) - i\omega_0^{-1}(\dot{x}(nT-0)+C)) = a(nT-0) - \frac{1}{2}i\omega_0^{-1}C. \tag{B.13}$$

Combining with (B.12) implies that

$$a_{n+1} = -\frac{1}{2}i\omega_0^{-1}C + a_n e^{-\frac{1}{2}\gamma T} e^{3i\beta\omega_0^{-1}\gamma^{-1}(1-e^{-\frac{1}{2}\gamma T})|a_n|^2}. \tag{B.14}$$

Finally, by the change of variable and parameters

$$Z = ia\left(\frac{3\beta(1-e^{-\gamma T/2})}{\omega_0\gamma}\right)^{1/2}, \quad A = \frac{C}{2\omega_0}\left(\frac{3\beta(1-e^{-\gamma T/2})}{\omega_0\gamma}\right)^{1/2}, \quad B = e^{-\gamma T/2}. \tag{B.15}$$

we arrive at the convenient form of the map

$$Z_{n+1} = A + BZ_n e^{i|Z_n|^2}. \tag{B.16}$$

This map was introduced firstly for rather different physical setup, namely, for optical circular resonator filled by medium with the refractive index varying proportional to squared amplitude of electric field of the propagating electromagnetic wave (Ikeda et al., 1980). After that, this map called the Ikeda map became a popular model; it was studied extensively and used often in literature for illustrations of phenomena of chaotic dynamics.

It is worth noticing that applicability of the map (B.16) to quantitative description of the nonlinear optical system is doubtful. Correctly, that system is described by the time-delayed equations written out and examined by the same authors (Ikeda et al., 1980). As to the map (B.16), it was introduced heuristically, and never was derived for the nonlinear optical system on a firm theoretical basis. By contrast, for the nonlinear oscillator this map really delivers a reasonable description valid in appropriate asymptotic (Kuznetsov et al., 2008).

The map (B.16) is represented as a single relation for the complex variable $Z$, but in terms of real variables it is in fact two-dimensional. Evaluation of Jacobi matrix for this map yields $J = B^2$; so, at $B < 1$ the map is dissipative (area compressing). Figure B.5 shows portraits of attractors for the Ikeda map at different values of parameter $A$ at $B$=0.2.

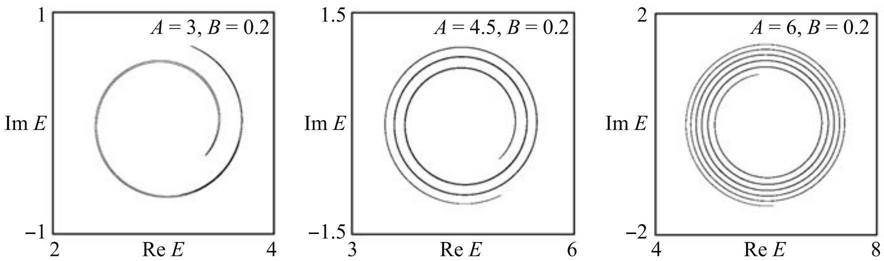


**Fig. B.5** Strange chaotic attractor of the Ikeda map (B.16) at $B = 0.2$ for three different values of the intensity of external driving.

In Fig. B.6 a chart of dynamical regimes on the parameter plane ($A$, $B$) is presented. If one increases the parameter of intensity of driving $A$ at fixed dissipation $B$, the transition to chaos occurs, as a rule, through the period-doubling bifurca-

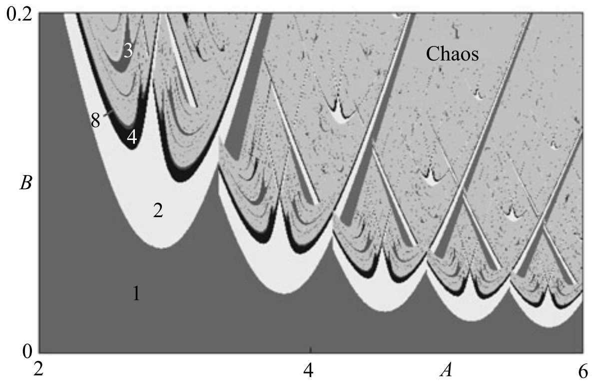


**Fig. B.6** Chart of dynamic regimes on the parameter plane for the Ikeda map (B.16).

tion cascade. However, globally the border of chaos is arranged in complex manner. Particularly, there are narrow strips of periodic dynamics entering deeply inside area occupied by chaos and containing scattered small domains of periodicity, the "shrimps".

Figure B.7 shows the larger one of two Lyapunov exponents of the Ikeda map (B.4) obtained numerically and plotted versus parameter $A$ at constant $B = 0.2$. Again, one can see, in a wide range mostly occupied by chaos, a set of deep narrow drops to negative values of the Lyapunov exponent associated with windows of periodicity. In the chart of dynamical regimes it corresponds to a path on the parameter plane along a horizontal line with the drops to negative Lyapunov exponent values as the pass crosses the "strips" and the "shrimps".

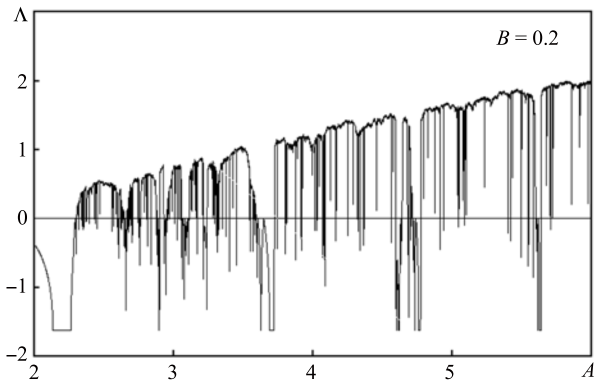


**Fig. B.7** The largest Lyapunov exponent of the Ikeda map (B.16) versus parameter $A$ at constant value of $B = 0.2$.

In Hénon map and Ikeda map under appropriate selection of parameters the configuration of mapping corresponding to the Smale horseshoe (Appendix C) can be verified. It proves complex and chaotic nature of trajectories in the phase space, but chaotic attractors, if occur, do not relate to the uniformly hyperbolic class. A visible indicator of non-hyperbolicity is presence of tiny domains of periodicity surrounded by chaos on the charts of dynamical regimes of Figs. B.3 and B.5. It indicates the absence of the structural stability. In Chap. 7 the Hénon map and Ikeda map are used as examples of non-hyperbolic behavior to oppose them against the systems with uniformly hyperbolic attractors.

## References

Gallas, J.A.C.: Structure of the parameter space of the Hénon map. Phys.Rev.Lett.**70**, 2714 (1993).

Gallas, J.A.C.: Dissecting shrimps: results for some one-dimensional physical systems. Physica A **202**, 196 (1994).

Feigenbaum, M.J.: The universal metric properties of nonlinear transformations. J. Stat. Phys. **21**, 669–706 (1979).

Heagy J.F.: A physical interpretation of the Hénon map. Physica D **57**, 436–446 (1992).

Hénon, M.: A two-dimensional mapping with a strange attractor. Commun. Math. Phys. **50**, 69–77 (1976).

Ikeda, K., Daido, H., Akimoto, O.: Optical turbulence: chaotic behavior of transmitted light from a ring cavity. Phys. Rev. Lett. **45**, 709–712 (1980).

Kuznetsov, A.P., Savin, A.V., Savin, D.V.:On some properties of nearly conservative dynamics of Ikeda map and its relation with the conservative case. Physica A **387**, 1464–1474 (2008).

Schuster, H.G., Just, W. Deterministic Chaos: An Introduction. Wiley-VCH Verlag GmbH & Co. KGaA, Weinheim, FRG (2005) .

Vul, E.B., Sinai, Y.G., Khanin, K.M.: Feigenbaum universality and the thermodynamic formalism. Russ. Math. Surv. **39**, 1–40 (1984).

# Appendix C
# Smale's Horseshoe and Homoclinic Tangle

In Cha. 1 we mentioned complex dynamics associated with stretching, folding, and compression of phase space volume in two-dimensional setting (Fig. 1.4). Formalization of that construction is the so-called *Smale horseshoe* (Smale, 1967; Guckenheimer and Holmes, 1983; Anosov et al., 1995; Devaney, 2003; Schuster and Just, 2005). It is a simple model map invented by Smale as a counterexample to assumption that in high dimensions structurally stable systems are typical. There is no uniformly hyperbolic attractor in this map. Instead, there is a non-trivial chaotic invariant set of saddle type. Presence of the horseshoe is an indicator of complexity of dynamics and chaos on some set of orbits, although physically it may be unobservable as the invariant set is not attractive.

Consider a region in the form of a stadium, which consists of three parts, the square $S$, and half-disks, $D_0$ and $D_1$ docked on two sides. Let the action of the map correspond to stretching this area horizontally, compression in the vertical direction, so it becomes long and narrow strip. Next, we deform it so that it takes a form of a horseshoe, and impose it into the original area, as shown in Fig. C.1. This is Smale's horseshoe map.

All the points belonging to the domains $D_0$ and $D_1$, are mapped inside $D_0$ and eventually attracted to a stable fixed point located in this area. Non-trivial dynamics corresponds to a set of orbits starting from domain $S$. It is clear that after the first iteration of the map some of them leave the domain of S and fall into the $D_0$ or $D_1$; they are not our interest.

Where are the starting points placed, which remain inside the domain S after the first iteration? Obviously, they occupy two narrow vertical bands $V_0$ and $V_1$, which, when stretched horizontally, just become equal in width to the area $S$. And how do placed images of points belong to $S$ at the previous time step? They occupy two narrow horizontal bands $H_0$ and $H_1$, which correspond to the two halves of the horseshoe. At the intersection of these bands the points live that remain in $S$ for iterating twice.

Now consider the horseshoe map in two steps of the iterations (see bottom picture in Fig. C.2). Now, there are four vertical stripes, two of which are located in a strip $V_0$ (denote them by $V_{00}$ and $V_{01}$) and two are situated in the band $V_1$ (denote them by

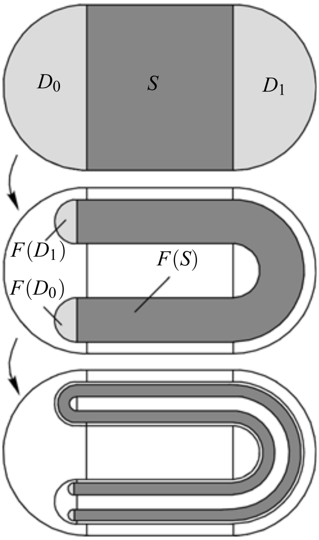


**Fig. C.1** Smale's horseshoe map: transformation of the initial stadium domain with iterating once and twice.

$V_{10}$ and $V_{11}$). Points belonging to these strips survive in the region $S$ with twice iterating. Next, there are four horizontal stripes, two of which are located in the strip $H_0$ (they are $H_{00}$ and $H_{10}$) and two in the strip $H_1$ (they are $H_{01}$ and $H_{11}$). They represent a set where the orbits arrive started in $S$ after twice iterating. The union of overlaps of these strips determines a set of starting points of orbits, which do not leave the region $S$ with four times iterating. With increase of number of considered iterations, each time within each vertical and horizontal strip two more narrow sub-strips are selected and left for following steps of the construction. In the limit of infinite number of iterating, the set of vertical strips and of the horizontal ones form a Cantor set. The intersection of these two sets is a "Cantor grid", which is an invariant set $\Omega$, whose elements survive in the area of $S$ forever, for an arbitrarily large number of iterating of the horseshoe map. Complete description of the invariant set $\Omega$ in terms of symbolic dynamics is achieved by introducing appropriate binary numbering of horizontal and vertical lines, like that introduced in Fig. C.2 for the first two steps of the construction.

Elements of the set $\Omega$ are encoded by two-side infinite binary sequences, and dynamics in this representation is determined as a shift by one step at each once iterating (Bernoulli shift). It implies the presence of chaos. Indeed, given an element of this set by a random, say, with a coin toss, we can obtain two sequences of random digits and use them as head and tail of the two-side binary sequence determining position of some point belonging to the set $\Omega$ in the domain $S$. Starting at that point, and considering dynamics in forward and in inverse time we observe visiting the horizontal and vertical bands of Fig. C.2(a) in accordance with prescribed random sequences. Periodic symbolic sequences correspond to periodic orbits of

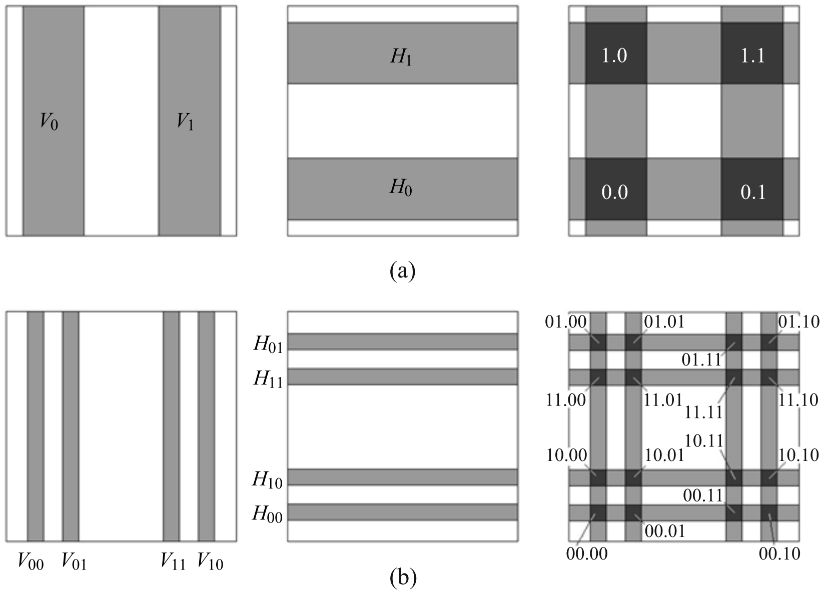


**Fig. C.2** Initial two steps of constructing invariant set Ω of points surviving in the region S. The right-hand pictures on panels **(a)** and **(b)** show in dark gray the sets of survivors with twice and four times iterating, respectively.

the horseshoe map; they form an infinite countable set. The set of all nonperiodic sequences is of cardinality of continuum.

It should be noted that all conclusions about the complex dynamics of the horseshoe map are based essentially only on topological arguments. Configuration of regions may look not exactly like that in Fig. C.1; only topological consistency is needed. Deduction for complex dynamics associated with existence of chaotic orbits and of an infinite number of periodic orbits is in any case a significant result, although, in the case of chaos established by the horseshoe map argumentation chaotic motion as sustained physically relevant regime may not occur because of non-attractive nature of the invariant set Ω.

Existence of the invariant set Ω is closely linked with the remarkable object called the *homoclinic tangle* (Guckenheimer and Holmes, 1983; Neimark and Landa, 1992; Anosov et al., 1995; Hilborn, 2000; Ott, 2002). Figure C.3 shows disposition of stable and unstable manifolds for a saddle-fixed point existing in the domain $S$ for the horseshoe map. Existence of intersection of these manifolds at the homoclinic point $\Gamma$ implies existence of an infinite collection of other homoclinic points! Indeed, the point $\Gamma$ is mapped to some other point, which must lay at intersection of the stable and unstable manifolds; that point, in turn, is mapped to a point of the same nature and so on. These multiple intersections are seen in panel (b), where prolonged segments of the manifolds are shown.

Occurrence of the homoclinic tangle is an equivalent indicator of complex dynamics in a sense of presence of non-attractive chaotic invariant set in the phase space of the system. Simple examples of physically relevant models, in which these phenomena take place, are the Hénon map and Ikeda map discussed in Appendix B.

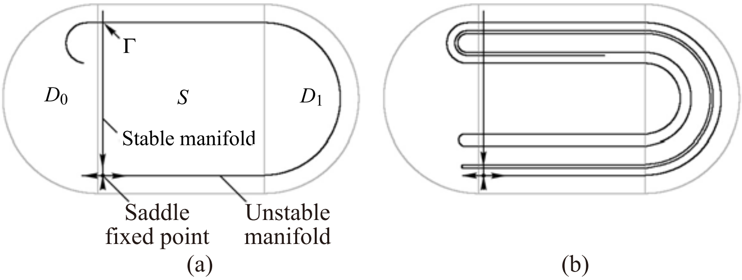


**Fig. C.3** Disposition of stable and unstable manifolds for a saddle-fixed point of the horseshoe map intersecting at the homoclinic point $\Gamma$ **(a)** and illustration of formation of the homoclinic tangle **(b)**.

## References

Anosov, D.V., Gould, G.G., Aranson, S.K., Grines, V.Z., Plykin, R.V., Safonov, A.V., Sataev, E.A., Shlyachkov, S.V., Solodov, V.V., Starkov, A.N., Stepin, A.M.: Dynamical Systems IX: Dynamical Systems with Hyperbolic Behaviour (Encyclopaedia of Mathematical Sciences) (v. 9). Springer-Verlag, New York (1995).

Devaney, R.L.: An Introduction to Chaotic Dynamical Systems. Westview Press, New York (2003).

Guckenheimer, J., Holmes, P.: Nonlinear Oscillations, Dynamical Systems, and Bifurcations of Vector Fields. Springer-Verlag (1990).

Hilborn, R.C.: Chaos and Nonlinear Dynamics. Oxford University Press, Cambridge (2000).

Neimark, Yu.I., Landa, P.S.: Stochastic and Chaotic Oscillations. Springer-Verlag, Berlin (1992).

Ott, E.: Chaos in dynamical systems. Cambridge University Press, Cambridge (2002).

Schuster, H.G., Just, W. Deterministic Chaos: An Introduction. Wiley-VCH Verlag GmbH & Co. KGaA, Weinheim, FRG (2005) .

Smale, S.: Differentiable dynamical systems. Bull. Amer. Math. Soc. (NS) **73**, 747–817 (1967).

# Appendix D
# Fractal Dimensions and Kaplan-Yorke Formula

Essential attribute of chaotic attractors is intrinsic Cantor-like transversal structure provided by the repetitive transformations of stretching, folding, and transversal compression for the phase space volume (see Chap. 1). A tool for quantitatively characterizing this structure is delivered by the fractal geometry (Mandelbrot, 1982; Beck and Schlogl, 1993; Ott, 2002; Schuster and Just, 2005). Fractal dimension generalizes the familiar notion of dimension (1 for curves, 2 for surfaces, 3 for volumes), but for non-trivial sets, like strange attractors, it may be non-integer containing a fractional part.

The simplest definition relates the so-called *box-counting dimension*, or *capacity*. It is based on covering the set by boxes of equal size $\varepsilon$ without overlap (Fig. D.1), and considering dependence on the needed number of the elements of this size. The dimension is defined then as

$$D_0 = -\lim_{\varepsilon \to 0} \frac{\log N(\varepsilon)}{\log \varepsilon}. \tag{D.1}$$

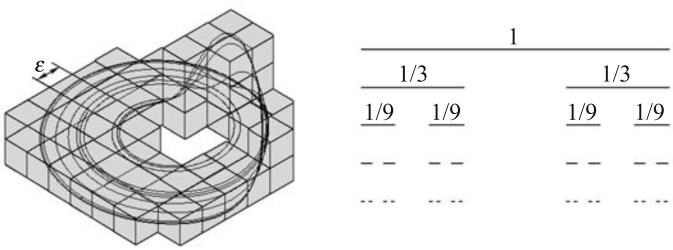


(a) (b)

**Fig. D.1** Covering of an attractor by boxes of fixed size $\varepsilon$ **(a)** and constructing classic Cantor set by successive steps of removing the middle thirds of segments obtained in the previous steps **(b)**.

For example, a classic Cantor set (which appears just in the above dissipative baker map in cross-section of the picture in Fig. 1.3 by a vertical line) obviously can be covered by $N = 2^n$ intervals of length $\varepsilon = 3^{-n}$ (it just corresponds to the $n$-th step of its construction). Taking the limit $n \to \infty$, which corresponds to $\varepsilon \to 0$, we obtain from (1.13) $D = \log 2/\log 3 = 0.6309\ldots$ Dimension of the attractor of the baker map may be easily found to be larger by one, namely, $D_b = 1.6309\ldots$.

As it is, to characterize strange attractors with sufficient completeness, it is necessary to introduce not one but a set of dimensions. Why is it so that a single dimension $D_0$ is not enough?

Imagine that the attractor is essentially not uniform: some of elements of covering are visited more frequently than others. This is in no way reflected in the definition of $D_0$, although, evidently, it should be significant for such a quantitative characterization of the attractor, which pretends to be a dimension.

To account the different probabilities of visiting the cells one needs to account the invariant measure. As noted in Chap. 1, the natural invariant measure of any region of phase space $S$ may be defined as the probability of residence in the area for a typical orbit: $p(S) = \lim\limits_{T\to\infty} (\tau(S,T)/T)$, where $\tau(S,T)$ is the residence time in $S$ at observation interval $T$. Assuming that the invariant measure is defined for the attractor, we attribute certain measure $p_i$ to each $i$-th cell, which is probability of residence there of a typical orbit. Now, consider a sum $I(\varepsilon) = -\sum\limits_{i=1}^{N(\varepsilon)} p_i \log p_i$. It may be interpreted as amount of information needed to specify a cell of residence at given instant. It is clear that the sum will increase with decreasing size of the cells. We can assume that this growth should obey a power law, $I(\varepsilon) \cong \varepsilon^{-D_1}$, or, equivalently that one can define a limit

$$D_1 = -\lim_{\varepsilon\to 0}(I(\varepsilon)/\log\varepsilon) = \lim_{\varepsilon\to 0}\left(\sum_{i=1}^{N(\varepsilon)} p_i \log_\varepsilon p_i\right). \tag{D.2}$$

It is called *the information dimension*.

Moreover, in 1983 an infinite family of generalized dimensions was introduced in use in the nonlinear dynamics called *the Rényi dimensions* on behalf of the Hungarian mathematician who proposed them earlier in another context (Grassberger, 1983; Hentschel and Procaccia, 1983).

Assume that the size of boxes covering the attractor is $\varepsilon$, and the probability of residence in the $i$-th cell is $p_i$. Then for any real number $q$, the dimension $D_q$ is defined as the limit

$$D_q = \frac{1}{q-1}\lim_{\varepsilon\to 0}\left(\log_\varepsilon \sum_{i=1}^{N(\varepsilon)} p_i^q\right). \tag{D.3}$$

Note that at $q = 0$ it turns to the capacity dimension, and at $q = 1$ it is the information dimension. The last follows from evaluating the limit $q \to 1$ by means of the l'Hôpital's rule.

One more special case is the so-called *correlation dimension* $D_2$, which is distinguished because of existence of relatively simple procedure of estimate in computations suggested by (Grassberger and Procaccia, 1983).

In more accurate mathematical analysis, improved definitions were developed accounting possibility of covering sets with elements of different forms and sizes (Hausdorff dimension) (Guckenheimer and Holmes, 1983; Beck and Schlogl, 1993; Ott, 2002).

Remind now that formation of fractal Cantor-like structure in strange attractors occurs due to stretching and compressions of phase volume, which are associated with presence of positive and negative Lyapunov exponents, respectively. Hence, one can ask about a relation between the dimensions and the Lyapunov spectrum. An answer for this question is somewhat given by the *Kaplan-Yorke formula* (Kaplan and Yorke, 1979).

Let the dimension of the phase space of a dissipative system be $N$, then we have $N$ Lyapunov exponents, which are assumed to be numbered in descending order: $\lambda_1, \lambda_2, \ldots, \lambda_N$. If the attractor is chaotic, the largest exponent is positive. On the other hand, the sum of all Lyapunov exponents is negative. Therefore, calculating the sums $S_m = \sum_{k=1}^{m} \lambda_k$ for $m = 1, 2, \ldots$ we will get a result at first positive and then negative values (Fig. D.2). We select such $m$ for which $S_m > 0$, but $S_{m+1} < 0$. Consider the subspace spanning over the perturbation vectors associated with the first $m$ exponents. In this space, the phase volume will increase in the course of the dynamics. On the other hand, in the subspace spanning over $m+1$ vectors the phase volume will be compressed. Along other dimensions the compression is even stronger, so, we will ignore those dimensions.

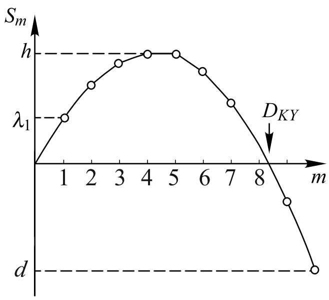


**Fig. D.2** Illustration of dependence of a sum of Lyapunov exponents on the number of terms accounted. Particularly, $S_1$ is the largest Lyapunov exponent $\lambda_1$, the maximum value of $S_m$ is the Kolmogorov-Sinai entropy $h$, $S_N$ is negative constant $d$, characterizing the contraction rate for approach to the attractor. A point of intersection of the graph with the horizontal axis yields the Kaplan-Yorke dimension according to formula (D.7).

In the subspace of dimension $m+1$ consider covering of the attractor by boxes of size $\varepsilon$ assuming the orientations of the edges correspond to the directions associated with the Lyapunov exponents $\lambda_1, \lambda_2, \ldots, \lambda_{m+1}$. Let the number of cells needed be $N(\varepsilon)$. Due to dynamics of representative points along respective orbits, the domain covered by the boxes after some time $T$ transforms to another domain, strongly elongated in the direction corresponding to the largest exponent $\lambda_1$ and flattened in the direction associated with the last one taken into consideration, $\lambda_{m+1}$ (Fig. D.3). Each box transforms to a parallelepiped of size $\varepsilon_1 \times \varepsilon_2 \times \varepsilon_3 \times \cdots \times \varepsilon_{m+1}$, where $\varepsilon_i = \varepsilon e^{\lambda_i T}$. Covering of one parallelepiped by boxes of size $\varepsilon_{m+1}$ requires $n = \prod_{i=1}^{m} (\varepsilon_i/\varepsilon_{m+1}) = \prod_{i=1}^{m} \left( \varepsilon e^{\lambda_i T} / \varepsilon e^{-|\lambda_{m+1}|T} \right)$ cells. Doing so with all $N(\varepsilon)$ parallelepipeds we obtain a new covering of the attractor with the number of cells

$$
\begin{aligned}
N(\varepsilon_{m+1}) = nN(\varepsilon) &= N(\varepsilon) \prod_{i=1}^{m} \left( \varepsilon e^{\lambda_i T} / \varepsilon e^{-|\lambda_{m+1}|T} \right) \\
&= N(\varepsilon) \prod_{i=1}^{m} \left( e^{\lambda_i T} / e^{-|\lambda_{m+1}|T} \right).
\end{aligned} \tag{D.4}
$$

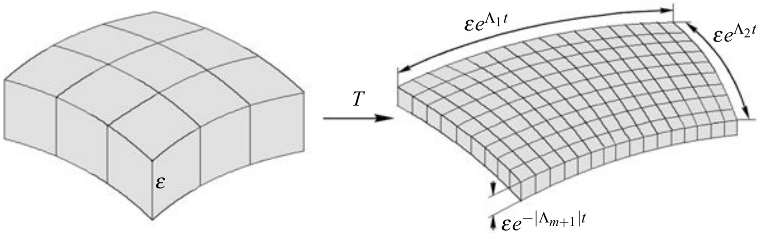


**Fig. D.3** To the derivation of the Kaplan-Yorke formula.

Estimate of the dimension according to (D.1) yields

$$
D \cong -\frac{\log N(\varepsilon_{m+1})}{\log \varepsilon_{m+1}} = \frac{\log N(\varepsilon) + \log \prod_{i=1}^{m} e^{\lambda_i T} - m \log e^{-|\lambda_{m+1}|T}}{-\log \varepsilon + |\lambda_{m+1}|T}. \tag{D.5}
$$

Multiplying the left-and the right-hand parts by $-\log \varepsilon + |\lambda_{m+1}|T$ we obtain

$$
-D \log \varepsilon + D|\lambda_{m+1}|T = \log N(\varepsilon) + \sum_{i=1}^{m} \lambda_i T + m|\lambda_{m+1}|T. \tag{D.6}
$$

Accounting that $D \cong -\log N(\varepsilon)/\log \varepsilon$, we cancel terms in both parts of the relation and finally obtain the *Kaplan-Yorke formula*

$$
D = m + \frac{\sum_{i=1}^{m} \lambda_i}{|\lambda_{m+1}|}. \tag{D.7}
$$

Here, remind that the number $m$ is determined in such a way that $S_m = \sum_{i=1}^{m} \lambda_i > 0$, but already $S_{m+1} = \sum_{i=1}^{m+1} \lambda_i < 0$.

The initial conjecture was that this formula evaluates the information dimension of strange attractors. Indeed, it was proven for attractors of two-dimensional maps. But in general case the conjecture was not confirmed and, generally speaking, it is not valid. Nevertheless, empirically, this formula provides usually sufficiently good results, remarkably close to correct dimensions of attractors in many cases.

It the framework of the present book, one should specially outline that the above derivation exploits essentially assumption of uniform expansion and contraction of the phase volume elements in the course of the dynamical evolution. Hence, we expect that among various chaotic attractors, this formula is especially appropriate just for the uniformly hyperbolic attractors.

To conclude, observe how meaningful the diagram of Fig. D.2 is, which depicts the sums $S_m$ versus the number of accounted Lyapunov exponents $m$. From this plot one can see immediately a set of relevant quantifiers for chaotic attractors: $S_1$ equals the positive Lyapunov exponent responsible for chaos, $S_{\max}$ is the Kolmogorov-Sinai entropy (in accordance with the Pesin formula), the intersection of the plot with the abscissa axis determines the Kaplan-Yorke dimension, and the value $S_N$ determines the rate of compression of the phase volume in the course of approach to the attractor.

## References

Beck, C., Schlogl, F.: Thermodynamics of Chaotic Systems: An Introduction. Cambridge University Press, Cambridge (1993).

Grassberger, P., Procaccia, I.: Measuring the strangeness of strange attractors. Physica D **9,** 189–208 (1983).

Grassberger, P.: Generalized dimensions of strange attractors. Phys. Lett. A **97**, 227–230 (1983).

Guckenheimer, J., Holmes, P.: Nonlinear Oscillations, Dynamical Systems, and Bifurcations of Vector Fields. Springer-Verlag, New York (1983).

Hentschel, H.G.E., Procaccia, I.: The infinite number of generalized dimensions of fractals and strange attractors. Physica D **8**, 435–444 (1983).

Kaplan, J.L., Yorke, J.A.: A chaotic behavior of multi-dimensional differential equations. In: Peitgen, H.-O. and Walther, H.-O. (eds.) Functional Differential Equations and Approximations of Fixed Points. Lecture Notes in Mathematics, **730**, pp. 204–227. Springer-Verlag, Berlin, N.Y. (1979).

Mandelbrot, B.B.: The Fractal Geometry of Nature. W.H. Freeman and Company, New York (1982).

Ott, E.: Chaos in dynamical systems. Cambridge University Press, Cambridge (2002).

Schuster, H.G., Just, W. Deterministic Chaos: An Introduction. Wiley-VCH Verlag GmbH & Co. KGaA, Weinheim, FRG (2005).

# Appendix E
# Hunt's Model: Formal Definition

Hunt's model is an artificially constructed example of a flow non-autonomous system with attractor of Plykin type in stroboscopic Poincaré section developed by T. Hunt in his PhD thesis under supervision of Prof. Robert MacKay (Hunt, 2000). The set of differential equations is formulated for two variables $x$ and $y$, with the right-hand parts depending on $x$, $y$, and the time variable $t$:

$$dx/dt = f_*(x,y,t), \quad dy/dt = g_*(x,y,t). \tag{E.1}$$

Here the functions $f_*$ and $g_*$ are continuously differentiable, and have period $2\pi$ in respect to the argument $t$.

Dynamics of variables $x$, $y$ in the time interval $\Delta t = 2\pi$ is represented in three successive stages, the duration of each is $2\pi/3$. In formulation of the relations, fictitious time $s$ is used, which varies in each stage from 0 to 1. To ensure smoothness of the flow, relationship between $s$ and $t$ is chosen in such a way that the motion of the representative points on the plane of $x$ and $y$ is of zero velocity at the edges of the stages.

In description of the flow, three special curvilinear coordinate systems $(r,\theta)^i$, $i = 1,2,3$ are used in domains $\mathrm{D}_{1,2,3}$ (Fig. 2.6), being linked with the Cartesian coordinates $x$, $y$ by relations

$$\begin{aligned} &x = X + S_i(\pi/2 - |\theta|), \quad y = Y + r\,\mathrm{sgn}\theta, \quad |\theta| \geqslant \pi/2, \\ &x = X + S_i r\cos f_r(\theta), \quad y = Y + r\sin f_r(\theta), \quad |\theta| < \pi/2, \end{aligned} \tag{E.2}$$

where $f_r(\theta) = 2\pi^2 r\theta/(\pi^2(r+1) + 4(r-1)\theta^2)$, $S_1 = -1$ and $S_{2,3} = 1$. Variables $X$ and $Y$ determine location of the origin for the $i$-th coordinate system in the Cartesian coordinates. For brevity, we designate the transformations to new coordinates and back, respectively, as $(r,\theta)^i = (R(x,y,X,Y,S_i), \Theta(x,y,X,Y,S_i))$ and $(x,y) = (F^i(r,\theta,X,Y,S_i), G^i(r,\theta,X,Y,S_i))$. The explicit expressions are derived easily from (E.2).

Let us set $\lambda = (3+\sqrt{5})/2$, $\mu = (3-\sqrt{5})/2$, and introduce some other constants determining geometrical disposition of the construction on the plane $(x,y)$ :

$$X_1 = \frac{1}{4}\left(6\sqrt{5}-6-(3-\sqrt{5})\pi\right), \quad X_2 = 3, \quad X_3 = \frac{1}{4}\left(18-6\sqrt{5}-(\sqrt{5}-1)\pi\right),$$
$$Y_1 = \frac{1}{2}(1+\sqrt{5}), \quad Y_2 = 1, \quad Y_3 = \frac{1}{2}(3+\sqrt{5}), \tag{E.3}$$
$$R_1 = \frac{1}{2}(1+\sqrt{5}), \quad R_2 = 1, \quad R_3 = \frac{1}{2}(\sqrt{5}-1).$$

**1. At the first stage** $t \in [0, 2\pi/3]$ we set $s = \sin^2\left(\frac{3}{4}t\right)$. The origins for the special coordinates move in dependence on $s$ in accordance with

$$X_{i1}(s) = \lambda^s(X_i + \pi/2) - \pi/2, \quad Y_{i1} = \mu^s Y_i, \quad i = 1,2,3. \tag{E.4}$$

Besides, we set $R_{i1}(s) = \mu^s R_i$. Given certain $s$, $x$, $y$, we determine the vector $\mathbf{f}(x,y,s) = (f(x,y,s), g(x,y,s))$ via the following procedure.

**(a)** If $x \leqslant 0$, perform transformation to the coordinate system number 1:

$$(r,\theta)^1 = (R(x,y,-X_{11}(s),Y_{11}(s),-1), \Theta(x,y,-X_{11}(s),Y_{11}(s),-1)), \tag{E.5}$$

and, designating by dot the derivative in respect to $s$, set

$$\dot\theta = (\ln\lambda)\theta, \quad \dot r = (\gamma(\theta,X_{11}(s))h_{12}(r,R_{11}(s)) + (1-\gamma(\theta,X_{11}(s))))(\ln\mu)r. \tag{E.6}$$

Here the functions are introduced:

$$\gamma(\theta,X) = \begin{cases} 1, & |\theta| \leqslant \frac{\pi}{2}, \\ \cos^2\frac{1}{4}\pi(2|\theta|-\pi)X^{-1}, & \frac{\pi}{2} \leqslant \theta \leqslant \frac{\pi}{2}+X, \\ 0, & |\theta| \geqslant \frac{\pi}{2}+X, \end{cases}$$
$$h_{12}(r,R) = \begin{cases} \cos\pi(1-r/\varepsilon), & r < \varepsilon, \\ 1, & \varepsilon \leqslant r \leqslant R-\varepsilon, \\ \frac{5}{4}+\frac{1}{4}\cos\frac{1}{2\varepsilon}\pi(r-R), & |r-R| < \varepsilon, \\ \frac{3}{2}, & r \geqslant R+\varepsilon. \end{cases} \tag{E.7}$$

Then, compute components of the vector field in Cartesian coordinates $(f_1, g_1)$ as

$$f_i = \begin{cases} \dot X - S\,\mathrm{sgn}(\theta)\dot\theta, & |\theta| \geqslant \pi/2, \\ \dot X + S\dot r\cos f_r(\theta) - Sr\sin f_r(\theta)(\dot r\partial f_r(\theta)/\partial r + \dot\theta\partial f_r(\theta)/\partial\theta), & |\theta| \leqslant \pi/2, \end{cases}$$
$$g_i = \begin{cases} \dot Y + \mathrm{sgn}(\theta)\dot r, & |\theta| \geqslant \pi/2, \\ \dot Y + \dot r\sin f_r(\theta) + r\cos f_r(\theta)\left(\dot r\partial f_r(\theta)/\partial r + \dot\theta\partial f_r(\theta)/\partial\theta\right), & |\theta| \leqslant \pi/2, \end{cases} \tag{E.8}$$

where $i = 1$, $S = S_1 = -1$, $\dot X = -(\ln\lambda)(X_{11}+\pi/2)$, $\dot Y = (\ln\mu)Y_{11}$.

**(b)** If $x > 0$, perform analogous computations in the coordinate systems 2 and 3. First, find out

$$(r,\theta)^2 = (R(x,y,X_{21}(s),Y_{21}(s),1),\Theta(x,y,X_{21}(s),Y_{21}(s),1))\,. \tag{E.9}$$

Then, set

$$\begin{aligned}\dot{\theta} &= (\ln\lambda)\theta,\\ \dot{r} &= (\gamma(\theta,X_{21}(s)-X_{31}(s))h_{12}(r,R_{21}(s))\\ &\quad +(1-\gamma(\theta,X_{21}(s)-X_{31}(s))))\,(\ln\mu)r,\end{aligned} \tag{E.10}$$

and with the formula (E.8), where $i = 2$, $S = S_2 = 1$, $\dot{X} = (\ln\lambda)(X_{21} + \pi/2)$, $\dot{Y} = (\ln\mu)Y_{21}$ compute the components of the vector field $(f_2, g_2)$.

Next, find out

$$(r,\theta)^3 = (R(x,y,X_{31}(s),Y_{31}(s),1),\Theta(x,y,X_{31}(s),Y_{31}(s),1)) \tag{E.11}$$

and set

$$\dot{\theta} = (\ln\lambda)\theta, \quad \dot{r} = (\gamma(\theta,X_{31}(s))h_3(r,R_{31}(s)) + (1-\gamma(\theta,X_{31}(s))))\,(\ln\mu)r, \tag{E.12}$$

where

$$h_3(r) = \begin{cases} \cos\pi(1-r/\varepsilon), & r < \varepsilon,\\ 1, & r \geqslant \varepsilon. \end{cases} \tag{E.13}$$

With the formula (E.8), where $i = 3$, $S = S_3 = 1$, $\dot{X} = (\ln\lambda)(X_{31} + \pi/2)$, $\dot{Y} = (\ln\mu)Y_{31}$, obtain components of the vector field $(f_3, g_3)$.

**(c)** Now, determine the vector field

$$\tilde{\mathbf{f}}(x,y,s) = \begin{cases} (f_1,g_1), & x \leqslant 0,\\ w(d_3,d_2)\cdot(f_2,g_2) + w(d_2,d_3)\cdot(f_3,g_3), & x > 0, \end{cases} \tag{E.14}$$

where the function is introduced

$$w = w(u,v) = \sin^2\left(\frac{1}{2}\pi u(u+v)^{-1}\right), \tag{E.15}$$

with arguments expressed as $d_\alpha = \max\{R^\alpha(x,y,X_{\alpha 1}(s),Y_{\alpha 1}(s)) - \mu^s R_\alpha, 0\}$, $\alpha = 2,3$.

**(d)** As a final step of computations at the stage 1 set

$$\mathbf{f}(x,y,s) = \tilde{\mathbf{f}}(x,y,s) + \sum_{i=1}^{3}\beta(\|\mathbf{x}-\mathbf{X}_{i1}\|)\cdot\left(\dot{\mathbf{X}}_{i1}(s) - \tilde{\mathbf{f}}(x,y,s) + (\ln\lambda)(\mathbf{x}-\mathbf{X}_{i1})\right). \tag{E.16}$$

Here $\mathbf{x} = (x,y), \mathbf{X}_{i1}(s) = (S_i X_{i1}, Y_{i1}), \dot{\mathbf{X}}_{i1}(s) = (S_i\dot{X}_{i1}, \dot{Y}_{i1})$, and the function is introduced

$$\beta(\rho) = \begin{cases} 1, & \rho \leqslant \varepsilon/4, \\ \cos^2 \pi(2\rho/\varepsilon - 1/2), & \varepsilon/4 < \rho < \varepsilon/2, \\ 0, & \rho \geqslant \varepsilon/2. \end{cases} \tag{E.17}$$

Here an inaccuracy occurs in the Hunt's work (Aidarova and Kuznetsov, 2009). While the definitions in his text correspond to (E.16) and (E.17), in the code of the program in Mathematical the argument of the function $\beta$ has been incorrectly written as squared norm $\|\mathbf{x} - \mathbf{X}_{i1}\|^2$. Computations indicate its significance: with substitution of the squared norm the hyperbolicity disappears! On the other hand, with the definitions (E.16) and (E.17), the attractor really is detected as a hyperbolic one. However, at $\varepsilon = 0.05$ selected by Hunt, it appears difficult to observe the fractal transversal structure of the attractor in illustrations. Thus, in computations discussed in Chap. 2, an increased parameter value $\varepsilon = 0.17$ was taken, although within the allowable range specified in the work of Hunt.

**2. At the second stage** $t \in [2\pi/3, 4\pi/3]$ set $s = \sin^2\left(\frac{3}{4}t - \frac{1}{2}\pi\right)$. Taking as the origin the point

$$\begin{aligned} X_{22}(s) &= X_2 + (1-s)D, \\ Y_{22}(s) &= Y_2 + (1-s)D, \\ D &= (\lambda - 1)(X_2 + \pi/2) + \mu R_2, \end{aligned} \tag{E.18}$$

we represent an instantaneous state $(x, y)$ in new coordinates as

$$(r, \theta) = (R(x, y, X_{22}(s), Y_{22}(s), 1), \Theta(x, y, X_{22}(s), Y_{22}(s), 1)) \tag{E.19}$$

and set

$$\dot{r} = -D, \quad \dot{\theta} = D. \tag{E.20}$$

Backward transformation to Cartesian coordinates is performed with formula (E.8), where $S = 1, \dot{X} = -D, \dot{Y} = -D$, and components of the vector field $(f_0, g_0)$ are obtained. Finally, set

$$\mathbf{f}(x, y, s) = w(a_2, b_2) \cdot (f_0, g_0), \tag{E.21}$$

where the function $w$ is given by (E.14), and its arguments are expressed as

$$\begin{aligned} a_2 &= \max\left\{R(x, y, X_{22}(s), \frac{1}{2}(Y_2 + Y_{22}(s)), 1) - \frac{1}{2}(-Y_2 + Y_{22}(s)) - \mu R_3, 0\right\}, \\ b_2 &= \max\left\{Y_{22}(s) - 2R_2\mu - R(x, y, X_{22}(s), Y_{22}(s), 1), 0\right\}. \end{aligned} \tag{E.22}$$

**3. At the third stage** $t \in [4\pi/3, 2\pi]$ set $s = \sin^2\left(\frac{3}{4}t - \pi\right)$. Take the point

$$X_{13}(s) = X_1 + (1-s)D, \quad Y_{13}(s) = Y_1 + (1-s)D, \quad D = (\lambda - 1)(X_1 + \pi/2) + \mu R_1 \tag{E.23}$$

as the origin. Transform initial values $(x,y)$ to coordinates $(r,\theta)$:

$$(r,\theta) = (R(x,y,-X_{13}(s),Y_{13}(s),-1), \Theta(x,y,-X_{13}(s),Y_{13}(s),-1)). \tag{E.24}$$

Next, define the flow by formula (E.20) and pass to the Cartesian coordinates by means of (E.8), setting $S=-1$, $\dot{X}=-D$, $\dot{Y}=-D$. Now,

$$\mathbf{f}(x,y,s) = w(a_3,b_3)\cdot(f_0,g_0), \tag{E.25}$$

where the function $w$ is defined by (E.15), and

$$a_3 = \max\left\{R(x,y,-X_{13}(s),\frac{1}{2}(Y_1+Y_{13}(s)),-1) - \frac{1}{2}(-Y_1+Y_{13}(s)) - \mu R_2, 0\right\},$$

$$b_3 = \max\left\{Y_{13}(s) - 2R_1\mu - R(x,y,-X_{13}(s),Y_{13}(s),-1), 0\right\}.$$

**4. Finally**, setting $\mathbf{f}(x,y,s) = (f(x,y,s), g(x,y,s))$, we obtain the equations for the continuous-time model valid at all three stages as follows:

$$dx/dt = \frac{3}{4}|\sin\frac{3}{2}t| f(x,y,s(t)), \quad dy/dt = \frac{3}{4}|\sin\frac{3}{2}t| g(x,y,s(t)). \tag{E.26}$$

In the right-hand parts a factor $s'(t) = \frac{3}{4}|\sin\frac{3}{2}t|$ is taken into account, arising because of the passage from fictitious time $s$ to natural time $t$.

## References

Aidarova, Yu. S., Kuznetsov, S.P.: Chaotic dynamics of the Hunt model, an artificially constructed flow system with a hyperbolic attractor. Preprint. arXiv: 0901.2727 (2009).

Hunt, T.J.: Low Dimensional Dynamics: Bifurcations of Cantori and Realisations of Uniform Hyperbolicity. PhD Thesis. Univercity of Cambridge (2000).

# Appendix F
# Geodesics on a Compact Surface of Negative Curvature

Free mechanical motion of a particle in curved space takes place along the *geodesic lines* of metric identified by a positive-definite quadratic form with smooth coordinate-dependent coefficients. In two dimensions, the square of the infinitesimal displacement is expressed by the relation

$$ds^2 = E(x,y)dx^2 + F(x,y)dxdy + G(x,y)dy^2. \tag{F.1}$$

Through the coefficients of the quadratic form we can obtain the *Gaussian curvature* using the *Brioschi formula* (Struik, 1988)

$$K = \frac{1}{(EG-F^2)^2} \cdot \left( \begin{vmatrix} -\frac{1}{2}E_{yy} + F_{xy} - \frac{1}{2}G_{xx} & \frac{1}{2}E_x & F_x - \frac{1}{2}E_y \\ F_y - \frac{1}{2}G_x & E & F \\ \frac{1}{2}G_y & F & G \end{vmatrix} - \begin{vmatrix} 0 & \frac{1}{2}E_y & \frac{1}{2}G_x \\ \frac{1}{2}E_y & E & F \\ \frac{1}{2}G_x & F & G \end{vmatrix} \right). \tag{F.2}$$

If the curvature is negative, the geodesics are characterized by instability with respect to transversal perturbations; then, if the motion takes place in bounded domain, it is chaotic. Analysis of the dynamics in this situation goes back to Hadamard and others (Anosov, 1967). This problem was one of the main sources of inspiration for the creation of the hyperbolic theory. The purpose of this Appendix is to illustrate the main features of the motion on a compact manifold of negative curvature for a specific example, which follows (Balazs and Voros, 1986).

Surface of constant negative curvature (the Lobachevsky plane or pseudosphere) can be represented by a model of Poincaré, in which points of the surface are mapped as points of the unit disk, and straight lines (i.e. geodesics) are represented by circular arcs orthogonal to the edge of the disc (Fig. F.1(a)). Metric given by the Poincaré model

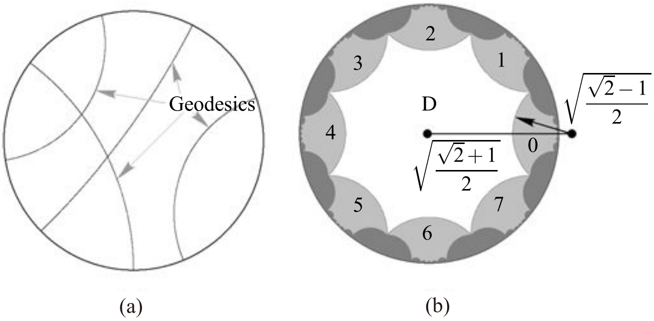


**Fig. F.1** Unit disc representing the Lobachevsky plane in the model of Poincaré with shown representatives of the geodesics. Domain D for consideration of motion of a particle and a set of equivalent domains obtained from D via the variable change (F.7) with $m = 0, 1, \ldots, 7$.

$$ds^2 = \frac{4(dx^2 + dy^2)}{1 - x^2 - y^2} \tag{F.3}$$

corresponds to a constant negative curvature $K = -1$ that may be verified by formula (F.2).

The Lagrange function for the free particle motion contains only the term of the kinetic energy; accounting (F.3) it is expressed as

$$L = W = \frac{2\mu(\dot{x}^2 + \dot{y}^2)}{(1 - x^2 - y^2)^2}, \tag{F.4}$$

where $\mu$ is the mass of the particle. The Euler-Lagrange equations governing the motion of the particle then are obtained in the form

$$\ddot{x} = 2\frac{x\dot{y}^2 - x\dot{x}^2 - 2y\dot{x}\dot{y}}{(1 - x^2 - y^2)^2}, \quad \ddot{y} = 2\frac{y\dot{x}^2 - y\dot{y}^2 - 2x\dot{x}\dot{y}}{(1 - x^2 - y^2)^2}. \tag{F.5}$$

Motion according these equations conserves the kinetic energy $W = 4\mu(\dot{x}^2 + \dot{y}^2)(1 - x^2 - y^2)^{-2}$ and, consequently, occurs along the geodesics of the metric determined by relation (F.3). The velocity, as the rate of increase of distance traveling along the geodesic line, is expressed as

$$\dot{s}^2 = \frac{4(\dot{x}^2 + \dot{y}^2)}{(1 - x^2 - y^2)^2} = 2W\mu^{-1}. \tag{F.6}$$

Consider motion of the particle in a domain of an octagon D bounded by circular arcs (Fig. F.1(b)). Because of symmetry inherent to the pseudosphere, the octagon can be considered equivalent to each of the eight regions attached to the sides, which in the Poincaré model look like distorted octagons of smaller size. The variable changes corresponding to the transformation of each of these regions in the original octagon are given by the relations

$$x' + iy' = \frac{\sqrt{1+\sqrt{2}}(x+iy) + e^{i\pi m/4}\sqrt{2+2\sqrt{2}}}{\sqrt{1+\sqrt{2}} - \sqrt{2+\sqrt{2}}e^{-i\pi m/4}(x+iy)}, \tag{F.7}$$

where $m$ is an index of the respective domain. In the course of the motion, each time when the particle crosses a border of the octagon D, one can think of it as appearing on the opposite side with coordinates reassigned according to (F.7) and velocity components obtained as a derivative of this relation:

$$x' + iy' = \frac{(3+3\sqrt{2})(\dot{x}+i\dot{y})}{\left(\sqrt{1+\sqrt{2}} - \sqrt{2+\sqrt{2}}e^{-i\pi m/4}(x+iy)\right)^2}. \tag{F.8}$$

Points of every two opposite segments of the border of the domain D may be identified; one can think of them as being glued to each other. Topologically, the resulting object may be thought of as a doughnut with two holes, or a sphere with two attached handles. According to the classification adopted in the topology, this is a manifold of genus 2.

Figure F.2 shows a trajectory of free motion of a particle in the domain D obtained from numerical solution of the differential equations (F.5) supplemented with the rules of the border cross-sections (F.7) and (F.8). For longer integration time the orbit is observed to cover the domain densely.

To be sure in its chaotic nature it is worth examining the Lyapunov exponents. Numerically, they may be computed with standard Benettin method solving the equations of motion (F.5) together with a collection of four sets of linearized equations

$$\begin{aligned}
\ddot{\tilde{x}} &= 2\frac{\tilde{x}\dot{y}^2 + 2xy\dot{y}\dot{\tilde{y}} - \tilde{x}\dot{x}^2 - 2x\dot{x}\dot{\tilde{x}} - 2\tilde{y}\dot{x}\dot{y} - 2y\dot{\tilde{x}}\dot{y} - 2y\dot{x}\dot{\tilde{y}}}{(1-x^2-y^2)^2} \\
&\quad +4\frac{(x\dot{y}^2 - x\dot{x}^2 - 2y\dot{x}\dot{y})(x\tilde{x}+y\tilde{y})}{(1-x^2-y^2)^3}, \\
\ddot{\tilde{y}} &= 2\frac{\tilde{y}\dot{x}^2 + 2y\dot{x}\dot{\tilde{x}} - \tilde{y}\dot{y}^2 - 2y\dot{y}\dot{\tilde{y}} - 2\tilde{x}\dot{x}\dot{y} - 2x\dot{\tilde{x}}\dot{y} - 2x\dot{x}\dot{\tilde{y}}}{(1-x^2-y^2)^2} \\
&\quad +4\frac{(y\dot{x}^2 - y\dot{y}^2 - 2x\dot{x}\dot{y})(x\tilde{x}+y\tilde{y})}{(1-x^2-y^2)^3}.
\end{aligned} \tag{F.9}$$

Fortunately, due to special nature of the problem under consideration, there is an alternative approach. One can represent the vector $\tilde{\mathbf{x}} = (\tilde{x}, \tilde{y})$ in locally determined special basis, $(\mathbf{e}_{\|}, \mathbf{e}_{\perp})$, where $\mathbf{e}_{\|}$ is a unit vector directed along the geodesic line, and $\mathbf{e}_{\perp}$ is a unit vector orthogonal to the previous one. Setting $\tilde{\mathbf{x}} = J_{\|}\mathbf{e}_{\|} + J_{\perp}\mathbf{e}_{\perp}$ one can derive the following equations for the coefficients:

$$\ddot{J}_{\|} = 0, \quad \ddot{J}_{\perp} = -K\dot{s}^2 J_{\perp}, \tag{F.10}$$

where $K$ is the Gaussian curvature. These equations hold even for a general case of free motion of a particle in metrics (F.1), with arbitrary dependence of the coefficients on coordinates; then $K$ should be understood as the local curvature depending on the instant coordinates $x$, $y$ in accordance with the formula (F.2).

**Fig. F.2** A representative trajectory of free motion of a particle in compact domain on a surface of constant curvature in accordance with Eqs. (F.5) supplemented with the rules of border cross-sections (F.7) and (F.8).

General solution of the first equation (F.10) is a linear combination of functions 1 and $t$. Hence, it contributes to the spectrum of Lyapunov exponents with two zero values. As to the second equation, for the system under consideration the value $\dot{s}^2$ is equal to the doubled ratio of a constant kinetic energy of the particle to its mass, $2W\mu^{-1}$ (see (F.3)). With the constant negative curvature $K$, the fundamental solutions are $e^{\sqrt{KW\mu^{-1}}t}$ and $e^{-\sqrt{KW\mu^{-1}}t}$. So, the Lyapunov spectrum contains one positive exponent, two zero ones, and one negative one, namely,

$$\lambda_1 = \sqrt{2KW\mu^{-1}}, \quad \lambda_2 = 0, \quad \lambda_3 = 0, \quad \lambda_4 = -\sqrt{2KW\mu^{-1}}. \tag{F.11}$$

Presence of a positive exponent indicates chaotic nature of the dynamics. Observe that the sum of all the exponents is zero that reflects the conservative nature of the system we consider here.

Results of direct numerical calculation of the Lyapunov exponents by the Benettin method are in good agreement with the theoretical result (F.11). For example, for a trajectory with initial conditions $x = 0, y = 0, \dot{x} = 0.6, \dot{y} = 0.8$ we have $W = 2\mu$, and accounting $K = -1$, obtain $\sqrt{2KW\mu^{-1}} = 2$. The result of computation of the Lyapunov exponents in time interval $\Delta t = 1000$ is

$$\lambda_1 = 2.0004, \quad \lambda_2 = 0.0038, \quad \lambda_3 = -0.0038, \quad \lambda_4 = -2.0004. \tag{F.12}$$

Obviously, deflections from (F.11) should be interpreted as inaccuracy of the numerical computations.

## References

Anosov, D.V.: Geodesic flows on closed Riemannian manifolds of negative curvature. Trudy Mat. Inst. Steklov **90**, 3–210 (1967).

Balazs, N.L., Voros, A.: Chaos on the pseudosphere. Physics Reports **143**, 109–240 (1986).

Struik, D.J.: Lectures on classical differential geometry. Dover Publications, NewYork (1988).

# Appendix G
# Effect of Noise in a System with a Hyperbolic Attractor

In this appendix some results are presented concerning effect of noise in a physically realizable flow system with a hyperbolic chaotic attractor of the Smale-Williams type (Jalnine and Kuznetsov, 2008).

Let us examine a system considered in Sect. 4.2 and add random external driving to get a set of stochastic equations

$$\begin{aligned} &\ddot{x} - (A\cos(2\pi t/T) - x^2)\dot{x} + \omega_0^2 x = \varepsilon y \cos\omega_0 t + D\xi(t), \\ &\ddot{y} - (-A\cos(2\pi t/T) - y^2)\dot{y} + 4\omega_0^2 y = \varepsilon x^2 + D\xi(t). \end{aligned} \tag{G.1}$$

Here $\xi(t)$ represents the Gaussian noise; it is assumed that $<\xi(t)>=0$ and $<\xi(t)\xi(t-\tau)>=\delta(\tau)$. Parameter $D$ characterizes the noise intensity and can be varied in a wide range.

For numerical solution of the stochastic equations (G.1) we exploited a second-order method described in (Mannella and Palleschi, 1989). A plot in Fig. G.1(a) shows the results of computation for the noisy system at the parameters $A=3, \varepsilon=0.5, \omega_0=2\pi, T=10$ and at the noise intensity $D=0.01$. In gray color we show 100 superimposed samples of the process under effect of noise starting from identical initial conditions. Due to the noise, in the final part of the interval of observation the states appear to be essentially different because of instability intrinsic to the orbits on the chaotic attractor. As a result, the picture becomes fuzzy. For comparison, the curve shown in black color is related to the system without noise, starting from the same initial conditions.

It is easy to demonstrate qualitatively that a very similar picture is observed in the noiseless system if one considers an ensemble of samples with a slight deviation of the initial conditions. In Fig. G.1(b) we show a set of 100 samples for the system without noise launched from initial conditions with a small random variation near the same initial state as in the previous diagram. The range of the random variations is specially selected to obtain close degree of mutual divergence of the orbits in the considered time interval in comparison with that produced by the effect of noise.

As shown, for the noiseless system the phases determined at successive stages of activity for one of the subsystems obey approximately the Bernoulli map. It is

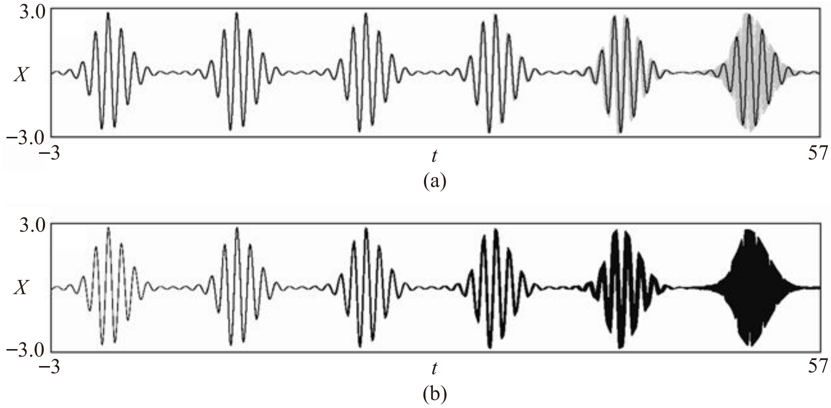


**Fig. G.1** Time dependence for the variable $x$ of the model (G.1): **(a)** superimposed 100 samples obtained at the noise level $D = 0.02$ (gray) and the trajectory without noise (black), all with the same initial conditions; **(b)** superimposed 100 samples for the system without noise $(D = 0)$ for the ensemble of slightly different initial conditions. Here and hereafter the parameters are chosen to be $A = 3.0$, $\varepsilon = 0.5$, $\omega_0 = 2\pi$, and $T = 10$.

interesting to investigate the influence of noise on the iteration diagrams for phases. Taking into account that during the active stage the oscillations of $x(t)$ are close to sinusoidal ones with modulated amplitude and floating phase, we determine the phases at the time moments $t_n = t_0 + nT$ as $\varphi_n = \arg(\dot{x}(t_n) + i\omega_0 x(t_n))$. Figure G.2 shows the iteration diagrams for the phases in the presence of noise (gray) and without noise (black). Note that the presence of noise of sufficiently low intensity does not change the topological nature of the phase map, which remains in the same class as the Bernoulli map $\varphi_{n+1} = 2\varphi_n + \text{const}$.

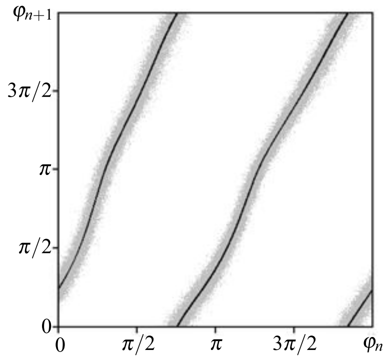


**Fig. G.2** Iteration diagrams for the phase of the first subsystem of the model (G.1) with noise $D = 0.1$.

Another approach that allows us to compare the noisy and the noiseless dynamics is based on the analysis of the Lyapunov exponents. For the model with noise they can be computed using the same linearized variation equations as in Chap. 4, but integrated along the reference trajectory in the noisy system (G.1).

In Fig. G.3 the Lyapunov exponents are plotted versus the noise intensity parameter $D$. At low intensity of noise, the largest Lyapunov exponent is close to $T^{-1}\ln 2$, which corresponds to the approximate description of the dynamics by the Bernoulli map. A notable deflection appears only at a sufficiently high level of noise, namely, at $D \geqslant 0.2$. At $D \sim 0.5$ the effect of noise is already very relevant, the largest Lyapunov exponent crosses zero and becomes negative indicating suppression of the intrinsic dynamical chaos by the external noise. Dependence of other Lyapunov exponents on the noise intensity is not noticeable at all.

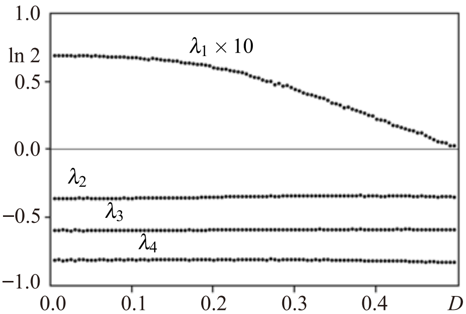


**Fig. G.3** Lyapunov exponents versus intensity of noise for the model (G.1).

For a system with hyperbolic chaotic attractor, presence of noise of low intensity is in some sense inessential: under the slightly varying initial conditions, we can ensure that the phase trajectory of the system without noise remains close to the trajectory of the system with noise over arbitrarily large time interval. This assertion, based on the so-called *shadowing lemma* (Guckenheimer and Holmes, 1983), is justified in the context of the mathematical analysis of noise in (Kiefer, 1974). We have demonstrated this property in computations for the system (G.1).

Suppose two trajectories are launched from identical initial conditions, one in the “pure” system without noise and the other in the system with noise. Obviously, the “noisy” orbit will diverge from the “pure” one. Now, let us try to vary the initial conditions for the pure trajectory to get an approximation for the noisy orbit in the best way at a long time interval. The whole construction is performed for a definite sample of the noisy orbit obtained with the same sample of noise. To explain the method of selection of the initial conditions, it is appropriate to consider the Poincaré map produced by a period-T stroboscopic section of the flow system (G.1) without noise $\mathbf{x}_{n+1} = \mathbf{T}(\mathbf{x}_n)$. In Fig. G.4(a) one can see a portrait of the attractor of the map projected onto the plane $(x, \dot{x}/\omega_0)$. This is solenoid manifesting filaments of an infinite number of wraps possessing the Cantor-like structure in the cross-section. Solid black dots in the picture denote four successive points of the stroboscopic section for one specially chosen trajectory on the attractor. The black lines passing through these dots designate the respective unstable direction $\mathbf{D}^u$, which are tangent to the unstable manifolds $W^u$ at the given points. These directions can be approximated numerically from long-time evolution of an arbitrarily chosen unit perturbation vector $\mathbf{V}_n = (\tilde{x}, \dot{\tilde{x}}/\omega_0, \tilde{y}, \dot{\tilde{y}}/2\omega_0)$ at $t_n = t_0 + nT$, since such a vector governed by the linearized variation equations tends to the unstable direction associated with a single positive Lyapunov exponent.

Now one should take a note of how a cloud of representative points evolves from the same initial conditions in the presence of noise. An illustration is shown in Fig. G.4(b). The dots pictured in gray are obtained in the Poincaré cross-section, i.e., stroboscopically at each next period $T$ from 104 sample orbits of the noisy system at $D = 0.02$. The black dots correspond to the trajectory of the system without noise $(D = 0)$ launched from the same initial conditions. Note that the cloud stretches along the unstable direction tangent to the filaments forming the attractor, but it does not grow in the radial direction.

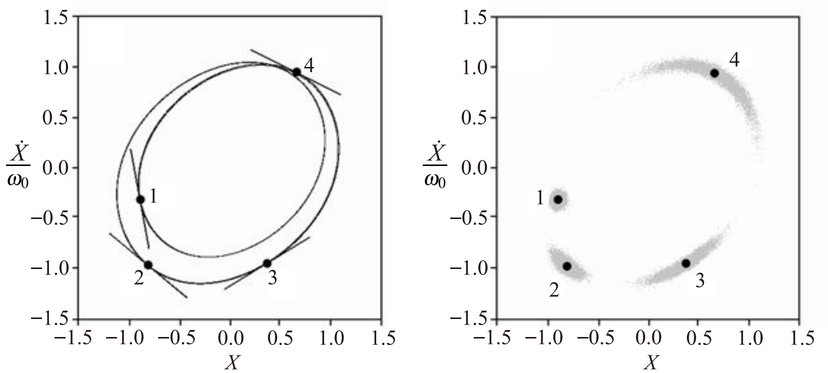


(a) (b)

**Fig. G.4** The stroboscopic cross-section of the attractor of the system (G.1) at $t_0 = 0$ **(a)**. The attractor is projected on the phase plane of the first subsystem. Evolution of the cloud of representative points launched from identical initial conditions in the presence of noise $(D = 0.02)$ **(b)**. The labels 1,2,3,4 indicate the number of steps of the Poincaré map. An ensemble of 104 orbits is shown. Black dots correspond to the system without noise starting from the same initial conditions.

The algorithm for localization of the "pure" trajectory, which approximates a noisy orbit, consists in the following. Let us denote the original noisy orbit as $\mathbf{V}_{\text{noisy}}(t)$, while the pure trajectory in zero approximation is denoted as $\mathbf{V}^{(0)}(t)$. We start first from the initial conditions at $t = t_0$ identical to the noisy and the pure orbit: $\mathbf{V}_{\text{noisy}}(t_0) = \mathbf{V}^{(0)}(t_0)$. The starting point is supposed to belong to the attractor of the system without noise. Then, computing the two trajectories $\mathbf{V}_{\text{noisy}}(t)$ and $\mathbf{V}(0)(t)$, we consider the norm of the difference vector $\|\Delta\mathbf{V}^{(0)}(t_1)\| = \|\mathbf{V}_{\text{noisy}}(t_1) - \mathbf{V}^{(0)}(t_1)\|$ at $t_1 = t_0 + T$. Next, we slightly modify the initial condition for the pure orbit from $\mathbf{V}^{(0)}(t_0)$ to $\mathbf{V}^{(G.1)}(t_0)$ with the purpose to minimize the norm of the difference $\|\mathbf{V}_{\text{noisy}}(t_1) - \mathbf{V}^{(1)}(t_1)\|$. It is provided by variation of the phase of the partial oscillator active at $t = t_0$. For our system it corresponds to variation of the initial state along the unstable direction associated with the point on the attractor, or, that is the same, along a filament of the attractor containing the initial point. The procedure of the search for new initial conditions is explained in detail in (Jalnine and Kuznetsov, 2008).

Suppose we take a new initial condition for the pure orbit $\mathbf{V}^{(1)}(t_0)$. Now with the same sample of the noise we again trace two trajectories, the noisy one starting from $\mathbf{V}_{\text{noisy}}(t_0)$ and the pure one starting from $\mathbf{V}^{(1)}(t_0)$ for a longer time interval up to $t_2 = t_0 + 2T$, and obtain the norm of the difference vector $\|\Delta\mathbf{V}^{(1)}(t_2)\| = \|\mathbf{V}_{\text{noisy}}(t_2) - \mathbf{V}^{(1)}(t_2)\|$ Then, modifying again the initial condition for the pure orbit by variation of the initial phase of the active oscillator, at this time in closer neighborhood of $\mathbf{V}^{(1)}(t_0)$, we try to minimize $\|\mathbf{V}_{\text{noisy}}(t_2) - \mathbf{V}^{(2)}(t_2)\|$ and obtain the new initial condition $\mathbf{V}^{(2)}(t_0)$. The procedure of variation of the initial conditions is the same as the above-described, with only difference being that the maximum variation $\Delta\mathbf{V}^{(2)}$ is chosen from the relation of $\Delta\mathbf{V}^{(2)} = \|\Delta\mathbf{V}^{(1)}(t_2)\|\exp(-2\lambda_1 T)$. Step by step we successively increase the time interval $nT$ and select the initial conditions for the pure orbit $\mathbf{V}^{(n)}(t_0)$, which deliver minimal values for the norms of the differences $\|\mathbf{V}_{\text{noisy}}(t_n) - \mathbf{V}^{(n)}(t_n)\|$. Note that the maximum variation of the initial condition at the $n$-th step of the algorithm decays as $\|\Delta\mathbf{V}^{(n)}\| \sim \exp(-n\lambda_1 T)$. Due to the recurrent nature of the algorithm, it appears that the approximation of the noisy orbit by the pure one holds uniformly during the whole time interval $[t_0, t_0 + nT]$.

Figure G.5 illustrates results of application of several steps of the above algorithm. Parameters of the system are taken the same as those in the previous examples of computations, and the noise intensity is $D = 0.1$.

The first plot in Fig. G.5 corresponds to the initial step of the algorithm: the noisy (gray) and pure (black) trajectories start from identical initial conditions. One can see their sufficiently fast divergence: the phase synchronism disappears already after one period of the parameter modulation $T$. After the first modification of the initial conditions for the pure orbit the divergence is delayed and the phase synchronism persists over $1-2$ periods of $T$, but then the orbits diverge. At the next steps of the algorithm the time intervals of existence of the phase synchronism become longer and longer and occupy finally the whole range in the diagram. Figure G.6 shows in gray color 20 dots of the projection of the noisy 5 orbit at $D = 0.04$ on the plane $(x, \dot{x}/\omega_0)$. In black color 20 dots are shown in the same stroboscopic cross-section of the approximating pure trajectory recovered by the above method.

To characterize the degree of closeness of a noisy orbit to a shadowing pure orbit, we use the following value

$$\rho_k = \frac{1}{kT}\int_{t_0}^{t_0+kT} \left\| V_{\text{noisy}}(t) - V^{(k)}(t) \right\| dt, \tag{G.2}$$

where $k$ designates the duration of the considered time interval in units of the modulation period $T$. Averaging this quantity over the ensemble of initial conditions and

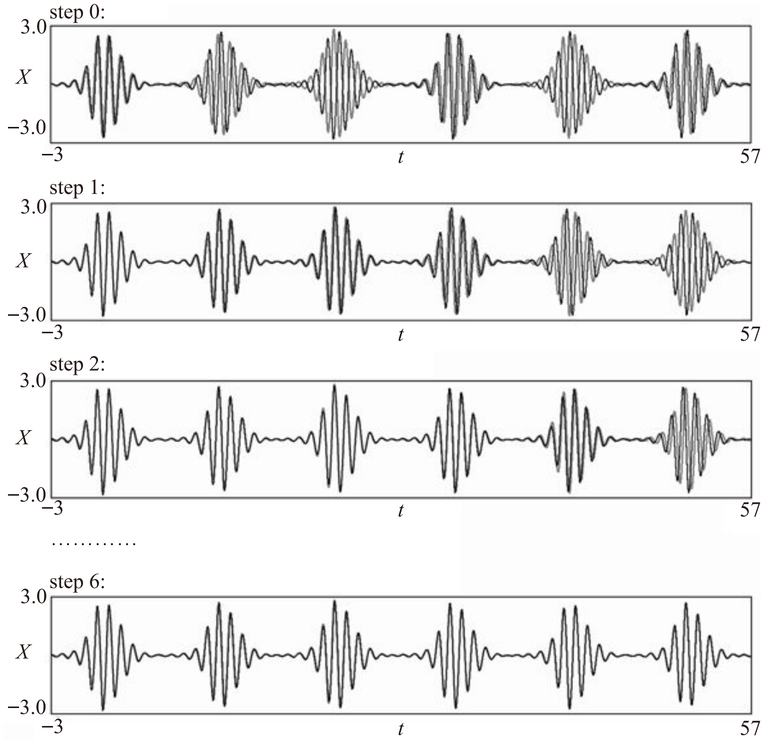


**Fig. G.5** Successive steps of constructing the shadowing trajectory (black) to the given noisy orbits (gray). At the initial step both orbits start from the identical initial conditions. At the last presented diagram the shadowing takes place over the time range of six modulation periods.

the noise samples we obtain a mean deviation $<\rho_k>$, characterizing the degree of closeness of the noisy and shadowing trajectories on the attractor. In Fig. G.7(a) we present plots of the mean deviation $<\rho_k>$ versus $k$ for different noise levels. It can be seen in the figure that the mean deviation depends on $k$ very weakly in the range $k = 8,\ldots,50$. At $k \sim 50 \div 60$ the errors become noticeable due to the finite-digital arithmetic and for the considered level of accuracy further observation of the shadowing becomes impossible.

Figure G.7(b) shows a plot of the mean deviation $<\rho_k>$ computed for $k = 9$ in dependence on the parameter of the noise intensity $D$. For each $D$ we consider a set of 100 orbits launched from different initial conditions and calculated for different noise samples. Each noisy orbit was approximated by the shadowing trajectory with the method described above, and the mean value $<\rho_9>$ was evaluated by averaging over the set of orbits. As seen from the figure, the dependence $<\rho_9>$ versus $D$ is nearly linear in the range from zero to 0.1.

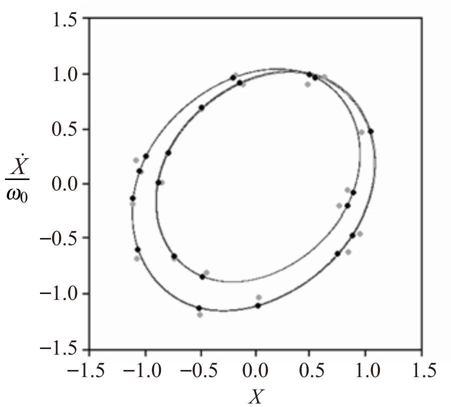


**Fig. G.6** Stroboscopic cross-section of the noisy (light gray) and the shadowing noiseless (black) trajectories on a background of the attractor (dark gray) in projection onto the phase plane of the first subsystem; the noise intensity $D = 0.04$.

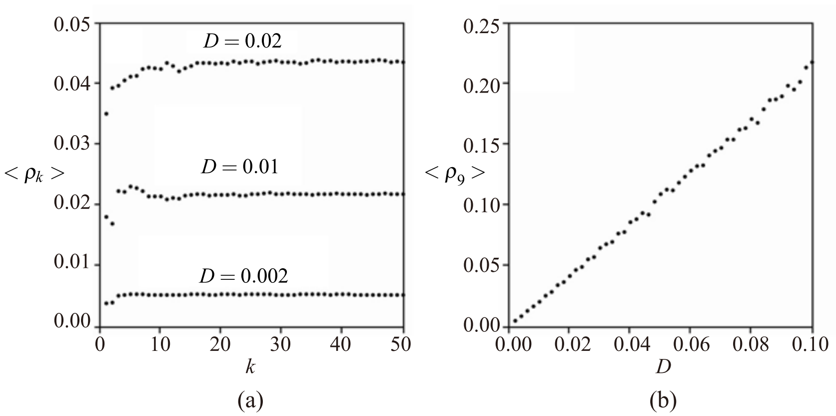


**Fig. G.7** Mean average mutual deviation of noise and shadowing trajectories versus the number of modulation periods taken for the computations at the three noise levels $D = 0.002$, 0.01 and 0.02 **(a)**. The dependence of $< \rho_k >$ on the noise intensity $D$ for $k = 9$ **(b)**.

## References

Guckenheimer, J., Holmes, P.: Nonlinear Oscillations, Dynamical Systems, and Bifurcations of Vector Fields. Springer-Verlag, New York (1983).

Jalnine, A.Yu., Kuznetsov, S.P.: Effect of noise in a nonautonomous system of alternately excited oscillators with a hyperbolic strange attractor. Phys. Rev. E **77**, 036220 (2008).

Kifer, Yu.I.: On small random perturbations of some smooth dynamical systems. Math. USSR Ivestija **8**, 1083–1107 (1974).

Mannella, R. and Palleschi, V.: Fast and precise algorithm for computer simulation of stochastic differential equations. Phys. Rev. A **40**, 3381–3386 (1989).

# Index